Schlumberger

Log Interpretation Principles/Applications

1989

Schlumberger

Log Interpretation Principles/Applications

Seventh printing. March 1998

Schlumberger Wireline & Testing
225 Schlumberger Drive
Sugar Land, Texas 77478

SMP-7017

An asterisk (*) is used throughout this document to denote a mark of Schlumberger.

Schlumberger

Log Interpretation Principles/Applications

Contents

Contents

Contents

Contents

Contents

Contents

Contents

Contents

Contents

Contents

Note: A companion book "Cased Hole Log Interpretation Principles/Applications-1989," provides similar information for cased hole services. Throughout this document references are made to charts, nomograms, and tables necessary for quantitative interpretation of data from our various logging tools. Refer to the *Schlumberger Log Interpretation Charts—1989* book for the most up-to-date version of these charts.

1 Introduction

Electrical well logging was introduced to the oil industry over half a century ago. Since that time, many additional and improved logging devices have been developed and put into general use.

As the science of well logging advanced, the art of interpreting the data also advanced. Today, the detailed analysis of a carefully chosen suite of wireline services provides a method of deriving or inferring accurate values for the hydrocarbon and water saturations, the porosity, the permeability index, and the lithology of the reservoir rock.

Hundreds of technical papers have been written describing the various logging methods, their application, and their interpretation. This abundance of literature is overwhelming in content and frequently unavailable to the average well log user.

This document therefore presents a review of these well logging methods and interpretation techniques. The various openhole services offered by Schlumberger are discussed in some detail, together with essential methods of interpretation and basic applications. The discussion is kept as brief and clear as possible, with a minimum of derivational mathematics.

It is hoped that the document will serve as a useful handbook for anyone interested in well logging. For those who may be interested in more detailed material, the references at the end of each chapter and the other well logging literature can be consulted.

HISTORY

The first electrical log was recorded in 1927 in a well in the small oil field of Pechelbronn, in Alsace, a province of northeastern France. This log, a single graph of the electrical resistivity of the rock formations cut by the borehole, was recorded by the "station" method. The downhole measurement instrument (called sonde) was stopped at periodic intervals in the borehole, measurements were made, and the calculated resistivity was hand-plotted on a graph. This procedure was carried on from station to station until the entire log was recorded. A portion of this first log is shown in Fig. 1-1.

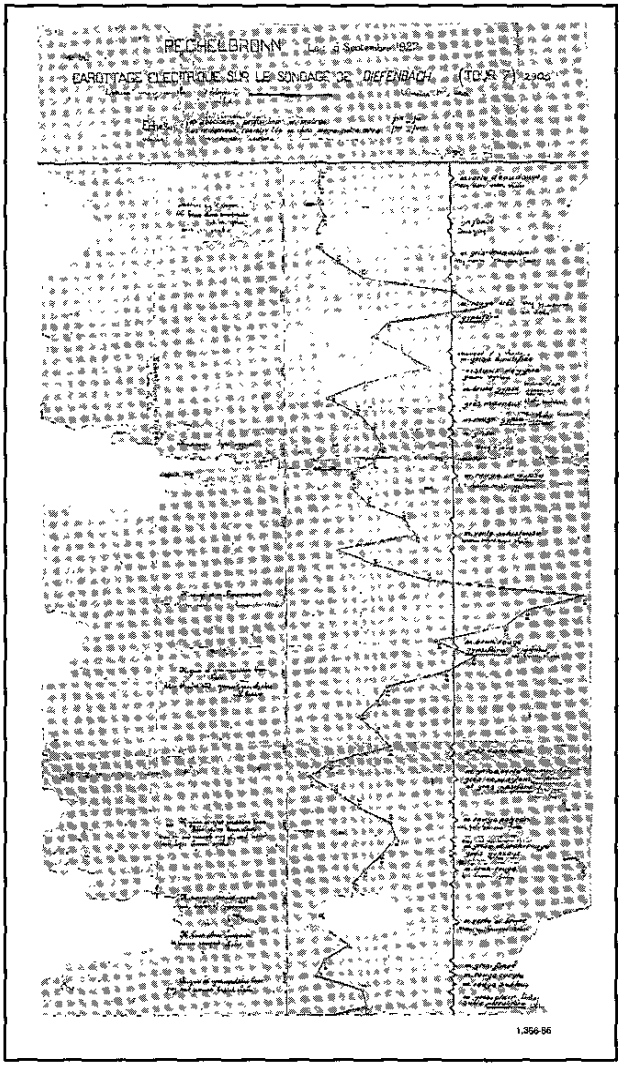

Fig. 1-1—The first log: points plotted on graph paper by Henri Doll.

In 1929, electrical resistivity logging was introduced on a commercial basis in Venezuela, the United States, and Russia, and soon afterwards in the Dutch East Indies. The usefulness of the resistivity measurement for correlation purposes and for identification of potential hydrocarbon-bearing strata was quickly recognized by the oil industry.

In 1931 the spontaneous potential (SP) measurement was included with the resistivity curve on the electrical log. In the same year, the Schlumberger brothers, Marcel and Conrad, perfected a method of continuous recording and the first pen recorder was developed.

The photographic-film recorder was introduced in 1936. By then, the electrical log consisted of the SP curve and short normal, long normal, and long lateral resistivity curves. This combination was predominant in logging activity from 1936 to the late 1950's. After about 1946, these curves were recorded simultaneously.

The development of a dipmeter log began in the early 1930's with the anisotropy dipmeter tool. The three-arm dipmeter device, with an associated photoclinometer, was introduced in 1943; it permitted both the direction and angle of the formation dip to be determined. Each arm contained an SP sensor. In 1946, the SP sensors were replaced by short resistivity devices; this made dip measurements possible in wells where the SP had little correlatable detail.

The first continuously recording electrical dipmeter sonde, which used three microresistivity arrays and contained a fluxgate compass, followed in the mid-1950's. Since then, numerous developments have further refined the measurement of formation dip. Today, a four-arm dipmeter tool records 10 microresistivity curves simultaneously, and a triaxial accelerometer and magnetometers provide highly accurate information on tool deviation and azimuth. The processing of these data into formation dip information is now done exclusively with electronic computers.

The gamma ray (GR) and neutron tools represented the first use of radioactive properties in well logging and the first use of downhole electronics. Unlike SP and resistivity tools, they are able to log formations through steel casing, as well as in air- or gas-filled holes or in oil-based muds. The neutron log was described by Pontecorvo in 1941.

In combination with the GR log, a neutron log enhances lithological interpretations and well-to-well stratigraphic correlations. After about 1949, attention was given to the neutron log as a porosity indicator. However, the early neutron logs were greatly influenced by the borehole environment. It was not until the introduction of the SNP sidewall neutron porosity tool in 1962 and the CNL* compensated neutron tool in 1970 that the neutron gained acceptance as a porosity measurement. The Dual Porosity neutron tool combines those two neutron measurements into a single tool.

Early attempts at porosity determination employed microresistivity measurements. The Microlog tool, introduced in the early 1950's, uses a miniature linear array of three electrodes imbedded in the face of an insulating pad, which is applied to the borehole wall. A borehole caliper is provided by the arm carrying the electrode pad and an opposite backup arm.

The Microlog recording is also useful to delineate permeable beds, and other microresistivity devices help establish the resistivity profile from the invaded zone near the borehole to the noninvaded virgin formation. The Microlaterolog tool was developed for salt muds in 1953. The MicroProximity log and MicroSFL* log have followed.

In 1951, the laterolog tool, the first focused deep-investigating resistivity device, was introduced. It uses a focusing system to constrain the surveying current (emitted from a central electrode) to substantially a horizontal disc for some distance from the sonde. Focused resistivity logs are well adapted for investigation of thin beds drilled with low-resistivity muds. The laterolog device quickly supplanted conventional resistivity logs in salt muds and highly resistive formations.

Over the years, several laterolog tools were developed and used commercially. Today, the DLL* dual laterolog tool, which consists of deep laterolog and shallow laterolog measurements, is the standard. It is usually run with a MicroSFL device as well.

In freshwater muds, the original electrical log has been replaced by the induction log. The induction log was developed in 1949, as an outgrowth of wartime work with mine detectors, for use in oil-base mud. However, its superiority over the electrical log in freshwater muds was soon recognized.

By 1956, a five-coil induction device was combined with the SP curve and a 16-in. normal to make the induction-electrical tool. In 1959, the five-coil device was replaced by one with a six-coil array with deeper investigation.

The DIL* dual induction log, introduced in 1963, is now the standard. It consists of deep induction, medium induction, and shallow resistivity measurements. The shallow resistivity-measuring device is now a focused resistivity device — a Laterolog 8 on the 1963 tool and an SFL device on current tools. A new dual induction log, the Phasor* induction, provides improved thin-bed response, deeper depth of investigation, and greater dynamic resistivity range.

Since the 1930's, logging cables have been used to lower geophones into wells to measure long-interval acoustic travel times from sound sources at the surface.

*Mark of Schlumberger

In the late 1950's, the sonic log gained acceptance as a reliable porosity log; its measurement responds primarily to porosity and is essentially independent of saturation.

The sonic log, coupled with the focused resistivity logs — laterolog and induction — made possible modern formation evaluation from well logs. The sonic log provided a measurement of porosity; the focused resistivity logs, a measurement of true resistivity of the noninvaded virgin formation.

Subsequent improvements in sonic logging included the BHC borehole compensated sonic, the LSS* long-spaced sonic, and the Array-Sonic* tools. The latter tools permit the recording of the entire sonic wavetrain. From an analysis of the wavetrain, the shear and Stoneley transit times can be extracted as well as the compressional transit time.

The logging of formation bulk density, another measurement primarily dependent on formation porosity, was commercially introduced in the early 1960's. An FDC* compensated formation density log, which compensated for the mudcake, quickly followed in 1964. In 1981, the Litho-Density* log provided an improved bulk density measurement and a lithology-sensitive photoelectric absorption cross section measurement.

The recovery of physical rock samples and formation fluid samples with wireline tools also has a rich history. Sidewall coring, using a hollow, cylindrical "bullet" shot into the formation and retrieved by pulling it out, has existed since 1937. Obviously, this technique has undergone continuous improvement over the one-half century since its introduction. For very hard rocks, downhole mechanical coring tools exist that actually drill out the rock samples.

In 1957, a formation tester was introduced. It recovered a sample of the formation fluids and the pore pressure was measured during the sampling process. The FIT formation interval tester and the RFT* repeat formation tester have followed. The older tools could make only one pressure measurement and recover only one fluid sample per trip into the well; the RFT tool can make an unlimited number of pressure measurements and recover two fluid samples per trip.

To handle those formations in which the formation water is fresh, or varies in salinity, or in which the salinity is unknown, dielectric measurements have been developed. The EPT* electromagnetic propagation log was introduced in 1978; the DPT* deep propagation log, in 1985.

The preceding historical sketch has not, by any means, covered all the measurements now made with wireline well logging devices. Other logging measurements include nuclear magnetic resonance, nuclear spectrometry (both natural and induced), and numerous cased hole parameters.

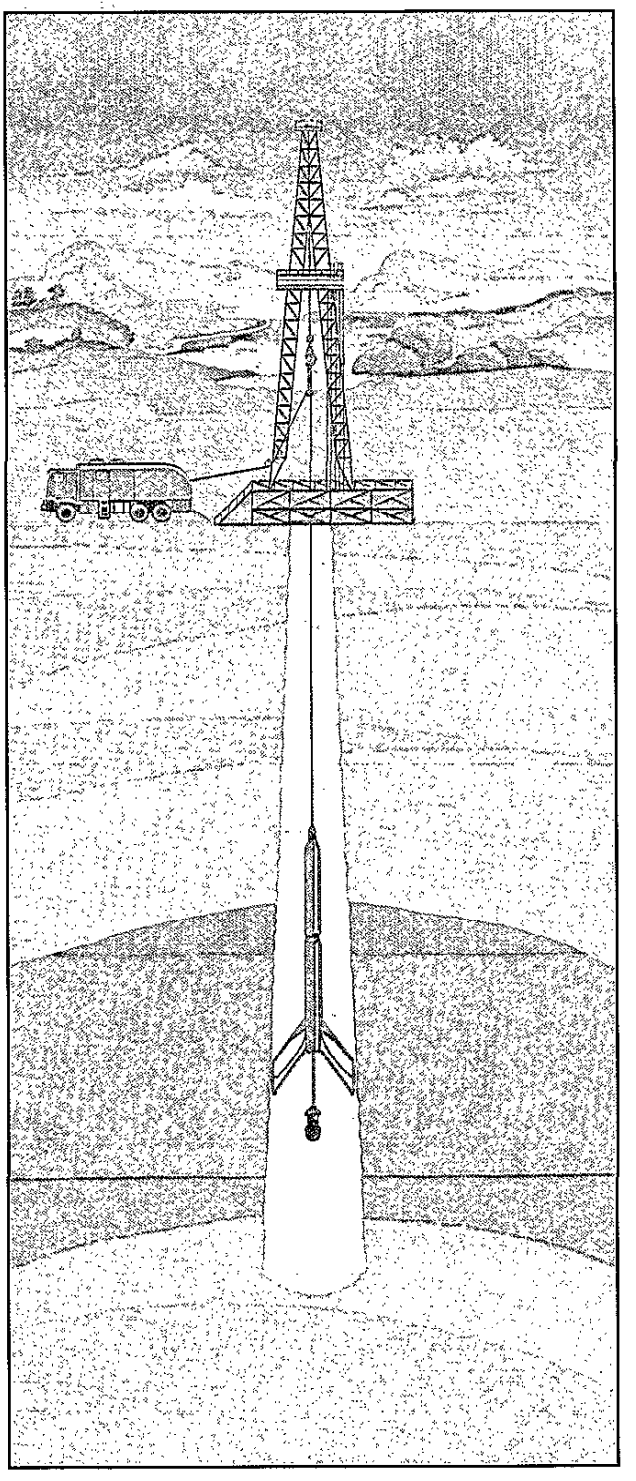

Fig. 1-2—Wireline logging operation.

THE FIELD OPERATION

Wireline electrical logging is done from a logging truck, sometimes referred to as a "mobile laboratory" (Fig. 1-3). The truck carries the downhole measurement in-

struments, the electrical cable and winch needed to lower the instruments into the borehole, the surface instrumentation needed to power the downhole instruments and to receive and process their signals, and the equipment needed to make a permanent recording of the "log."

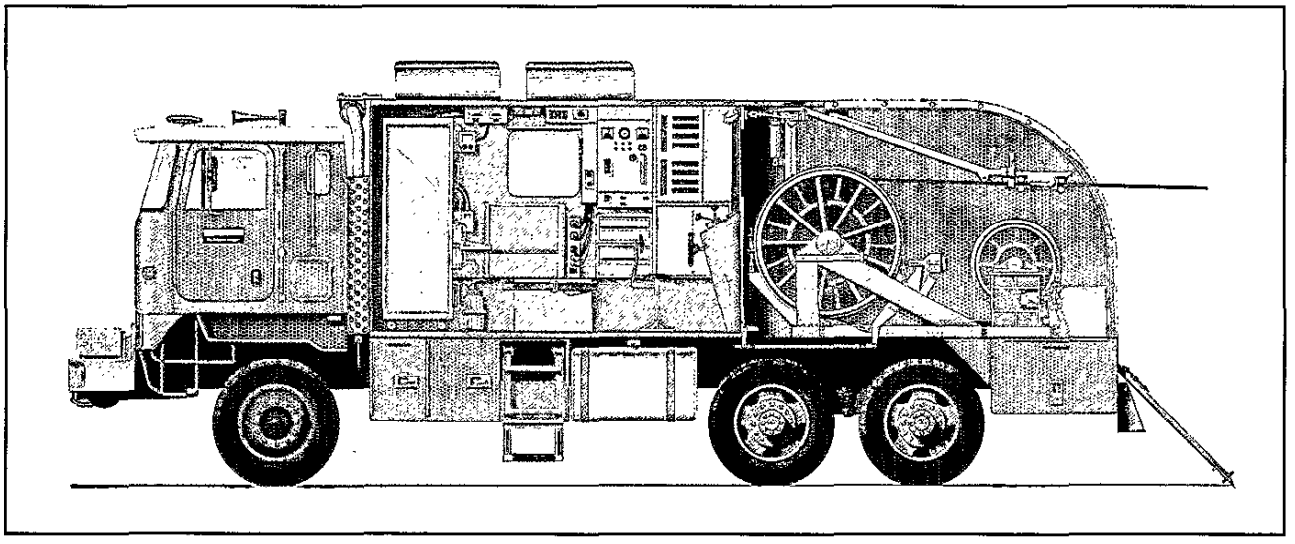

Fig. 1-3—A typical CSU wellsite mobile laboratory. The main winch contains up to 30,000 ft of seven-conductor logging cable; the optional small winch at the rear contains 24,000 ft of slim monoconductor cable for servicing producing wells under pressure. Data acquisition and computer equipment are inside the logging cab. For offshore-remote locations, the cab and winch assemblies are mounted on a skid.

The downhole measurement instruments are usually composed of two components. One component contains the sensors used in making the measurement, called the sonde. The type of sensor depends, of course, upon the nature of the measurement. Resistivity sensors use electrodes or coils; acoustic sensors use transducers; radioactivity sensors use detectors sensitive to radioactivity; etc. The sonde housing may be constructed of steel and/or fiberglass.

The other component of the downhole tool is the cartridge. The cartridge contains the electronics that power the sensors, process the resulting measurement signals, and transmit the signals up the cable to the truck. The cartridge may be a separate component screwed to the sonde to form the total tool, or it may be combined with the sensors into a single tool. That depends, of course, upon how much space the sensors and electronics require and the sensor requirements. The cartridge housing is usually made of steel.

Today, most logging tools are readily combinable. In other words, the sondes and cartridges of several tools can be connected to form one tool and thereby make many measurements and logs on a single descent into and ascent from the borehole.

The downhole tool (or tools) is attached to an electrical cable that is used to lower the tool into and remove from the well. Most cable used in openhole logging today contains seven insulated copper conductors. New cable developments include a fiber optics conductor in the center of six copper conductors. The cable is wrapped with a steel armor to give it the strength to support the tool weight and provide some strength to pull on the tool in case it becomes stuck in the borehole. The cable and tools are run in and out of the borehole by means of a unit-mounted winch.

Well depths are measured with a calibrated measuring wheel system. Logs are normally recorded during the ascent from the well to assure a taunt cable and better depth control.

Signal transmission over the cable may be in analog or digital form; modern trends favor digital. The cable is also used, of course, to transmit the electrical power from the surface to the downhole tools.

The surface instrumentation (Fig. 1-4) provides the electrical power to the downhole tools. More importantly, the surface instrumentation receives the signals from the downhole tools, processes and/or analyzes those signals, and responds accordingly. The desired signals are output to magnetic tape in digital form and to a cathode-ray tube and photographic film in analytical form.

The photographic film is processed on the unit, and paper prints are made from the film. This continuous recording of the downhole measurement signals is referred to as the log.

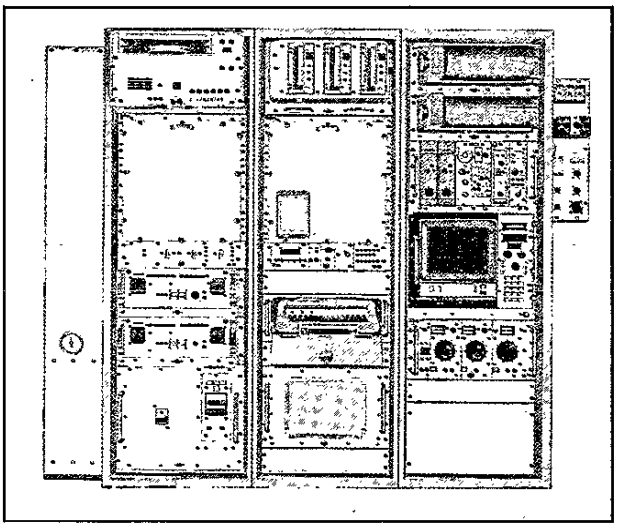

Fig. 1-4—The CSU is a computer-based integrated data acquisition and processing system. The main elements are—Right: a video data display and optical film units to record data. Center: the keyboard/printer unit below three cartridge tape drives. Left: twin DEC 1134 computers each having 256K memory; at the top, a dual hard-disk drive with 42-megabyte capacity and a backup 48-megabyte cartridge tape unit.

LOG DATA ACQUISITION

Wireline-logging technology is being changed by the rapid advancements in digital electronics and data-handling methods. These new concepts have changed our thinking about existing logging techniques and remolded our ideas about the direction of future developments.

Affected are the sensors, the downhole electronics, the cable, the cable telemetry, and the signal processing at the surface.

Basic logging measurements may contain large amounts of information. In the past, some of this data was not recorded because of the lack of high data-rate sensors and electronics downhole, the inability to transmit the data up the cable, and inability to record it in the logging unit. Similarly, those limitations have prevented or delayed the introduction of some new logging measurements and tools. With digital telemetry, there has been a tremendous increase in the data rate that can be handled by the logging cable. Digital recording techniques within the logging unit provide a substantial increase in recording capability. The use of digitized signals also facilitates the transmission of log signals by radio, satellite, or telephone line to computing centers or base offices.

In Table 1-1 the data rate for one of the older tool systems, the induction-sonic combination, is contrasted with the data-rate transmission requirements for some of the newer tools. It illustrates the tremendous increase in the data rate that can now be handled by the newer downhole sensors, by the logging cable, and by the surface instrumentation as a result of digital techniques.

Table 1
Data rate transmission requirements of some well logging tools.

ISF Induction-Sonic	200 Bits/Borehole Ft
High-Resolution Dipmeter	
10 Dip Channels	25,000 Bits/Borehole Ft
Array Sonic	
Full Waveform	60,000 Bits/Borehole Ft
Inelastic Spectroscopy	
Energy Spectrum	20,000 Bits/Second
Well Seismic Tool	
5-Second Wavetrain	80,000 Bits/Second

1,351-86

DATA PROCESSING

Signal processing can be performed at at least three levels: downhole in the tool, uphole in the truck, and at a central computing center. Where the processing is done depends on where the desired results can most efficiently be produced, where the extracted information is first needed, where the background expertise exists, or where technological considerations dictate.

Where it seems desirable, the logging tool is designed so that the data are processed downhole and the processed signal is transmitted to the surface. This is the case when little future use is envisioned for the raw data or when the amount of raw data precludes its transmission. In most cases, however, it is desirable to bring measured raw data to the surface for recording and processing. The original data are thus available for any further processing or display purposes and are permanently preserved for future use.

A wellsite digital computer system, called the CSU* unit, is now standard on all Schlumberger units throughout the world (Fig. 1-4). The system provides the capability to handle large amounts of data. It overcomes many of the past limitations of combination logging systems (the stacking or combination of many measurement sensors into a single logging tool string). It also ex-

pedites field operations. Tool calibration is performed much more quickly and accurately, and tool operation is more efficiently and effectively controlled.

The CSU system provides the obvious potential for wellsite processing of data. Processing of sonic waveforms for compressional and shear velocities is already being done, as is the processing of nuclear energy spectra for elemental composition and, then, chemical composition. More sophisticated deconvolution and signal filtering schemes are practical with the CSU system.

Nearly all the common log interpretation models and equations are executable on the CSU unit. Although not quite as sophisticated as the log interpretation programs available in computing centers, the wellsite interpretation programs significantly exceed what can be done manually. Wellsite programs exist to determine porosity and saturations in simple and complex lithology, to identify lithology, to calculate formation dip, to calculate permeablity, and to determine many more petrophysical parameters. In addition, data (whether recorded, processed, or computed) can be reformatted in the form most appropriate for the user.

The demand for wellsite formation evaluation processing will undoubtedly increase and programs will become more sophisticated.

The computing center offers a more powerful computer, expert log analysts, more time, and the integration of more data. Schlumberger computing centers are located in major oil centers throughout the world. They provide more sophisticated signal processing and formation analysis than the wellsite CSU system. Evaluation programs range in scope from single-well evaluation programs to a series of special application products to reservoir description services that evaluate entire fields. Statistical techniques can be employed more extensively, both in the selection of parameters and in the actual computations.

Log processing seems to be moving more and more toward integrated treatment of all log measurements simultaneously. Programs are being designed to recognize that the log parameters of a given volume of rock are interrelated in predictable ways, and these relationships are given attention during processing. New programs can now use data from more sources, such as cores, pressure and production testing, and reservoir modeling.

DATA TRANSMISSION

The CSU system is able to transmit logs with a suitable communication link. The receiving station can be another CSU system, a transmission terminal, or a central computing center. Data can be edited or reformatted before transmission to reduce the transmission time or to tailor the data to the recipient. Built-in checks on the transmission quality ensure the reliability of the transmitted information.

With the LOGNET* communications network, graphic data or log tapes can be transmitted via satellite from the wellsite to multiple locations (Fig. 1-5). This service is available in the continental U.S. and Canada, onshore and offshore. Virtually any telephone is a possible receiving station.

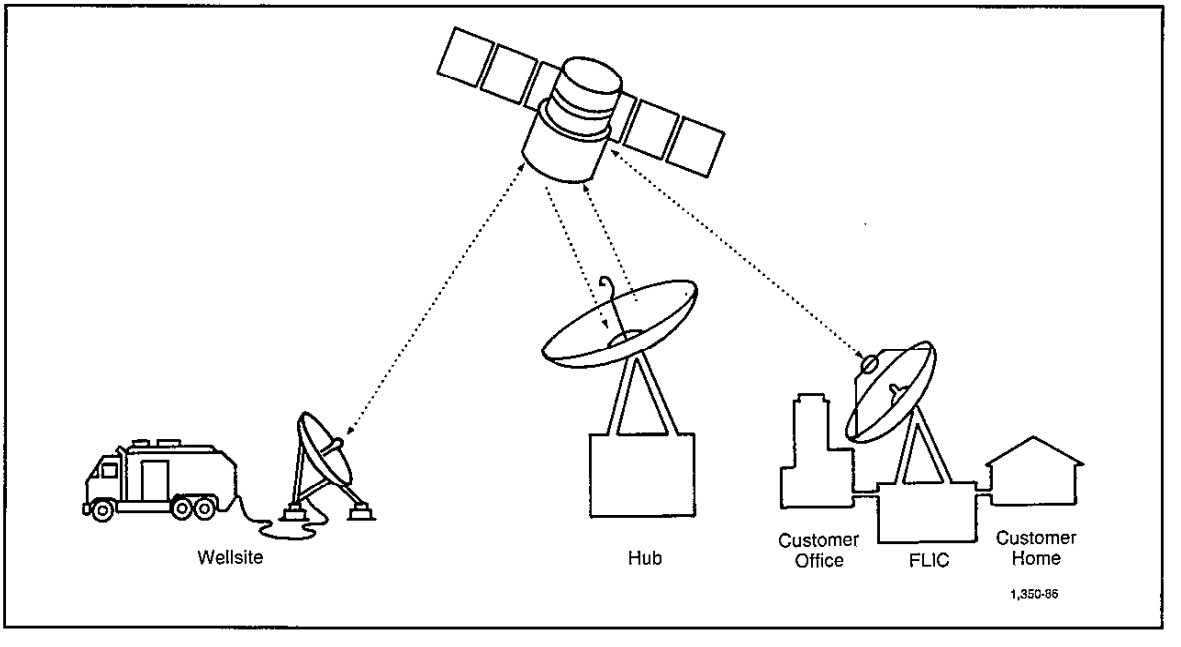

Fig. 1-5—Schematic of LOGNET communications system.

A small transportable communications antenna at the wellsite permits transmission of the well log data via satellite to a Schlumberger computing center and then by telephone to the client's office or home. Since the system is two way, offset logs or computed logs can be transmitted back to the wellsite. The system also provides normal two-way voice communication. There are several receiving station options:

- A standard digital FAX machine will receive log graphic data directly at the office.
- A Pilot 50* portable telecopier plugged into a standard telephone outlet at the office or at home allows clients to take advantage of the 24-hour service.
- A Pilot 100* log station can be installed in the client's office to receive tape and log graphics and to make multiple copies of the log graphics. Since this station is automatic, it can receive data unattended.
- An ELITE 1000* workstation can be installed in the client's office to receive data from the LOGNET communications network. A complete library of environmental corrections as well as the entire range of Schlumberger advanced answer products are available with this new workstation.

All data are encrypted to provide security while transmitting over the airways.

Other local transmission systems exist elsewhere in the world using telephone, radio, and/or satellite communications. In some instances, transmission from the wellsite is possible. In others, transmission must originate from a more permanent communication station. With some preplanning, it is possible to transmit log data from nearly any point in the world to another.

REFERENCES

1. Schlumberger, C., Schlumberger, M., and Leonardon, E.G.: "Electrical Coring; A Method of Determining Bottom-Hole Data by Electrical Measurements," AIME T. P. 462; *Geophys. Prosp. Trans.*, AIME (1932) 110.
2. Schlumberger, C., Schlumberger, M., and Doll, H.G.: "The Electromagnetic Teleclinometer and Dipmeter," *Proc.*, First World Petroleum Congress, London (July 1933).
3. Doll, H.G.: "The SP Dipmeter," *Pet. Tech.* (Jan. 1943) **6**.
4. Stratton, E.F. and Hamilton, R.G.: "Application of Dipmeter Surveys," paper presented at 1947 AIME Annual Meeting, Tulsa, Oct. 8-10.
5. DeChambrier, P.: "The Microlog Continuous Dipmeter," *Geophys.* (April 1953) **18**, No. 4.
6. Allaud, L.A. and Ringot, J.: "The High-Resolution Dipmeter Tool," *The Log Analyst* (May-June 1969) **10**, No. 3.
7. Pontecorvo, B.: "Neutron Well Logging — A New Geological Method Based on Nuclear Physics," *Oil and Gas J.* (Sept. 1941) **40**, No. 18.
8. Tittle, C.W., Faul, H., and Goodman, C.: "Neutron Logging of Drill Holes: The Neutron-Neutron Method," *Geophys.* (April 1951) **16**, No. 4.
9. Russell, J.H. and Bishop, B.O.: "Quantitative Evaluation of Rock Porosity by Neutron-Neutron Method," *Pet. Eng. J.* (April 1954).
10. Bush, R.E. and Mardock, E.S.: "The Quantitative Interpretation of Radioactivity Logs," *J. Pet. Tech.* (1951) **3**, No. 7; *Pet. Trans.*, AIME, **192.**
11. Russell, W.L.: "Interpretation of Neutron Well Logs," *Bull.*, AAPG (1952) **36**, No. 2.
12. Wyllie, M.R.J.: "Procedures for the Direct Employment of Neutron Log Data in Electric-Log Interpretation," *Geophys.* (April 1952) **17**, No. 4.
13. Allen, L.S., Tittle, C.W., Mills, W.R., and Caldwell, R.L.: "Dual-Spaced Neutron Logging for Porosity," *Geophys.* (Jan. 1967) **32**, No. 1.
14. Alger, R.P., Locke, S., Nagel, W.A., and Sherman, H.: "The Dual-Spacing Neutron Log — CNL," *J. Pet. Tech.* (Sept. 1972) **24**, No. 9.
15. Doll, H.G.: "Introduction to Induction Logging and Application to Logging of Wells Drilled With Oil-Base Muds," *J. Pet. Tech.* (June 1949); *Pet. Trans.*, AIME, **186.**
16. Dumanoir, J.L., Tixier, M.P., and Martin, M.: "Interpretation of the Induction-Electrical Log in Fresh Mud," *J. Pet. Tech.* (July 1957) **9**, No. 7; *Trans.*, AIME, **210.**
17. Tixier, M.P., Alger, R.P., Biggs, W.P., and Carpenter, B.N.: "Dual Induction-Laterolog: A New Tool for Resistivity Analysis," paper SPE 713 presented at the 1963 SPE Annual Meeting, New Orleans, Oct. 1963.
18. Doll, H.G.: "The Microlog — A New Electrical Logging Method for Detailed Determination of Permeable Beds," *J. Pet. Tech.* (June 1950) **2**, No. 6; *Pet. Trans.*, AIME, **189.**
19. Doll. H.G.: "The Laterolog: A New Resistivity Logging Method with Electrodes Using an Automatic Focusing System," *J. Pet. Tech.* (Nov. 1951) **3**, No. 11; *Pet. Trans.*, AIME, **192.**
20. Schuster, N.A., Badon, J.D., and Robbins, E.R.: "Application of the ISF/Sonic Combination Tool to Gulf Coast Formations," *Trans.*, Gulf Coast Assoc. Geol. Soc. (Oct. 1971).
21. Doll, H.G.: "The Microlaterolog," *J. Pet. Tech.* (Jan. 1953) **5**, No. 1; *Pet. Trans.*, AIME, **198.**
22. Doll, H.G., Dumanoir, J.L., and Martin, M.: "Suggestions for Better Electric Log Combinations and Improved Interpretations," *Geophys.* (April 1960) **25**, No. 4.
23. Stripling, A.A.: "Velocity Log Characteristics," *J. Pet. Tech.* (Sept. 1958) **10**, No. 9; *Pet. Trans.*, AIME, **213.**
24. Aron, J., Murray, J., and Seeman, B.: "Formation Compressional and Shear Interval-Transit-Time Logging by Means of Long Spacings and Digital Techniques," paper SPE 7446 presented at the 1978 SPE Annual Meeting.
25. Faul, H. and Tittle, C.W.: "Logging of Drill Holes by the Neutron-Gamma Method, and Gamma Ray Scattering," *Geophys.* (1951) **16.**
26. Wahl, J.S., Tittman, J., Johnstone, C.W., and Alger, R.P.: "The Dual Spacing Formation Density Log," *J. Pet. Tech.* (Dec. 1964) **16**, No. 12.
27. Gardner, J.S. and Dumanoir, J.L.: "Litho-Density Log Interpretation," *Trans.*, 1980 SPWLA Annual Logging Symposium.
28. Lock, G.A. and Hoyer, W.A.: "Natural Gamma Ray Spectral Logging," *The Log Analyst* (Sept.-Oct. 1971) **12**, No. 5.
29. Serra, O., Baldwin, J., and Quirein, J.: "Theory, Interpretation, and Practical Applications of Natural Gamma Ray Spectroscopy," *Trans.*, 1980 SPWLA Annual Logging Symposium.

2 Fundamentals of Quantitative Log Interpretation

Almost all oil and gas produced today comes from accumulations in the pore spaces of reservoir rocks — usually sandstones, limestones, or dolomites. The amount of oil or gas contained in a unit volume of the reservoir is the product of its porosity by the hydrocarbon saturation.

In addition to the porosity and the hydrocarbon saturation, the volume of the formation containing hydrocarbons is needed in order to estimate total reserves and to determine if the accumulation is commercial. Knowledge of the thickness and the area of the reservoir is needed for computation of its volume.

To evaluate the producibility of a reservoir, it is necessary to know how easily fluid can flow through the pore system. This property of the formation rock, which depends on the manner in which the pores are interconnected, is its permeability.

The main petrophysical parameters needed to evaluate a reservoir, then, are its porosity, hydrocarbon saturation, thickness, area, and permeability. In addition, the reservoir geometry, formation temperature and pressure, and lithology can play important roles in the evaluation, completion, and production of a reservoir.

POROSITY

Porosity is the pore volume per unit volume of formation; it is the fraction of the total volume of a sample that is occupied by pores or voids. The symbol for porosity is ϕ. A dense, uniform substance, such as a piece of glass, has zero porosity; a sponge, on the other hand, has a very high porosity.

Porosities of subsurface formations can vary widely. Dense carbonates (limestones and dolomites) and evaporites (salt, anhydrite, gypsum, sylvite, etc.) may show practically zero porosity; well-consolidated sandstones may have 10 to 15% porosity; unconsolidated sands may have 30%, or more, porosity. Shales or clays may contain over 40% water-filled porosity, but the individual pores are usually so small the rock is impervious to the flow of fluids.

Porosities are classified according to the physical arrangement of the material that surrounds the pores and to the distribution and shape of the pores. In a clean sand, the rock matrix is made up of individual sand grains, more or less spherical in shape, packed together in some manner where the pores exist between the grains. Such porosity is called intergranular, sucrosic, or matrix porosity. Generally, it has existed in the formations since the time they were deposited. For this reason, it is also referred to as primary porosity.

Depending on how they were actually deposited, limestones and dolomite may also exhibit intergranular porosity. They may also have secondary porosity in the form of vugs or small caves. Secondary porosity is caused by the action of the formation waters or tectonic forces on the rock matrix after deposition. For instance, slightly acidic percolating waters may create and enlarge the pore spaces while moving through the interconnecting channels in limestone formations, and shells of small crustaceans trapped therein may be dissolved and form vugs. Conversely, percolating waters rich in minerals may form deposits that partially seal off some of the pores or channels in a formation, thereby reducing its porosity and/or altering the pore geometry. Waters rich in magnesium salts can seep through calcite with a gradual replacement of the calcium by magnesium. Since the replacement is atom for atom, mole for mole, and the volume of one mole of dolomite is 12% less than that of calcite, the result is a reduced matrix volume and corresponding increase in pore volume.

Stresses in the formation may also occur and cause networks of cracks, fissures, or fractures, which add to the pore volume. In general, however, the actual volume of the fractures is usually relatively small. They do not normally increase the porosity of the rock significantly, although they may significantly increase its permeability.

SATURATION

The saturation of a formation is the fraction of its pore volume occupied by the fluid considered. Water satura-

tion, then, is the fraction (or percentage) of the pore volume that contains formation water. If nothing but water exists in the pores, a formation has a water saturation of 100%. The symbol for saturation is S; various subscripts are used to denote saturation of a particular fluid (S_w for water saturation, S_o for oil saturation, S_h for hydrocarbon saturation, etc.).

Oil, or gas, saturation is the fraction of the pore volume that contains oil, or gas. The pores must be saturated with some fluid. Thus, the summation of all saturations in a given formation rock must total to 100%. Although there are some rare instances of saturating fluids other than water, oil, and gas (such as carbon dioxide or simply air), the existence of a water saturation less than 100% generally implies a hydrocarbon saturation equal to 100% less the water saturation (or $1 - S_w$).

The water saturation of a formation can vary from 100% to a quite small value, but it is seldom, if ever, zero. No matter how "rich" the oil or gas reservoir rock may be, there is always a small amount of capillary water that cannot be displaced by the oil; this saturation is generally referred to as irreducible or connate water saturation.

Similarly, for an oil- or gas-bearing reservoir rock, it is impossible to remove all the hydrocarbons by ordinary fluid drives or recovery techniques. Some hydrocarbons remain trapped in parts of the pore volume; this hydrocarbon saturation is called the residual oil saturation.

In a reservoir that contains water in the bottom and oil in the top the demarcation between the two is not always sharp; there is a more or less gradual transition from 100% water to mostly oil. If the oil-bearing interval is thick enough, water saturation at the top approaches a minimum value, the irreducible water saturation, S_{wi}. Because of capillary forces, some water clings to the grains of the rock and cannot be displaced. A formation at irreducible water saturation will produce water-free hydrocarbons. Within the transition interval some water will be produced with the oil, the amount increasing as S_w increases. Below the transition interval, water saturation is 100%. In general, the lower the permeability of the reservoir rock the longer the transition interval. Conversely, if the transition interval is short, permeability will be high.

PERMEABILITY

Permeability is a measure of the ease with which fluids can flow through a formation. For a given sample of rock and for any homogeneous fluid, the permeability will be a constant provided the fluid does not interact with the rock itself.

The unit of permeability is the darcy, which is very large; so the thousandth part is generally used: the millidarcy (md). The symbol for permeability is k.

In order to be permeable, a rock must have some interconnected pores, capillaries, or fractures. Hence, there exists some rough relationship between porosity and permeability. Greater permeability, in general, corresponds to greater porosity, but this is far from being an absolute rule.

Shales and some sands have high porosities, but the grains are so small that the paths available for the movement of fluid are quite restricted and tortuous; thus, their permeabilities may be very low.

Other formations, such as limestone, may be composed of a dense rock broken by a few small fissures or fractures of great extent. The porosity of such a formation can be low, but the permeability of a fracture can be enormous. Therefore, fractured limestones may have low porosities but extremely high permeabilities.

RESERVOIR GEOMETRY

Producing formations (reservoirs) occur in an almost limitless variety of shapes, sizes, and orientations. Fig. 2-1 shows some of the major reservoir types; almost any combination of these is also possible.

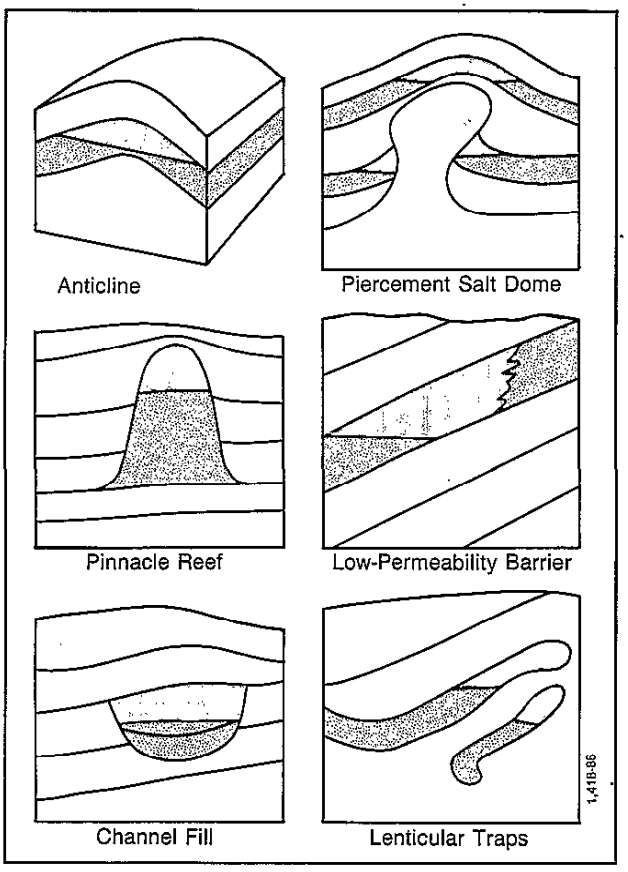

Fig. 2-1—Some typical reservoir shapes and orientations.

The physical shape and orientation of a reservoir can bear heavily on its producibility. Reservoirs can be wide or narrow, thick or thin, large or small. Giant reservoirs, such as some in the Middle East, can cover hundreds of square miles and be thousands of feet thick. Others are tiny, far too small to complete a well in. Configurations vary from simple lens shape to the tortuously complex.

Most reservoir-forming rocks were supposedly laid down in layers like blankets or pancakes. Their physical characteristics thus tend to be quite different in different directions, a condition called anisotropy. This nonuniformity is a very important consideration in reservoir engineering and completion design.

Normally, the permeability of such formations is much higher parallel to than perpendicular to the layering, and the permeabilities of the various layers can also vary widely.

Reservoirs that did not originate as deposited layers of grains do not conform to this laminar model of anisotropy. Carbonate rocks that originated as reefs, rocks subjected to extensive fracturing, or rocks with vuggy porosity are examples.

TEMPERATURE AND PRESSURE

Temperature and pressure also affect hydrocarbon production in several ways. In the reservoir rock, temperature and pressure control the viscosities and mutual solubilities of the three fluids — oil, gas, and water. As a result, the phase relationship of the oil/gas solution may be subject to highly significant variations in response to temperature and pressure changes. For example, as pressure drops gas tends to come out of solution. If this happens in the reservoir rock, the gas bubbles can cause a very substantial decrease in the effective permeability to oil.

The relationships between pressure, temperature, and the phase of hydrocarbon mixtures are extremely variable, depending on the specific types and proportions of the hydrocarbons present. Fig. 2-2 is a simple two-component phase diagram.

Ordinarily, the temperature of a producing reservoir does not vary much, although certain enhanced-recovery techniques (such as steam flood or fire flood) create conspicuous exceptions to this rule. However, some pressure drop between the undisturbed reservoir and the wellbore is inevitable. This pressure drop is called the pressure drawdown; it can vary from a force of a few pounds per square inch (psi) up to full reservoir pressure.

LOG INTERPRETATION

Unfortunately, few of these petrophysical parameters can be measured directly. Instead, they must be derived or inferred from the measurement of other physical parameters of the formations. A large number of parameters can now be measured. They include, among others, the resistivity, the bulk density, the interval transit time, the spontaneous potential, the natural radioactivity, and the hydrogen content of the rock.

Log interpretation is the process by which these measurable parameters are translated into the desired petrophysical parameters of porosity, hydrocarbon saturation, permeability, producibility, lithology, etc.

This translation is further complicated by the drilling process itself. In drilling through a formation, the fluids in the pores of the rock surrounding the borehole may be displaced or contaminated by the invasion of the drilling fluid. Occasionally, the rock matrix may even be altered.

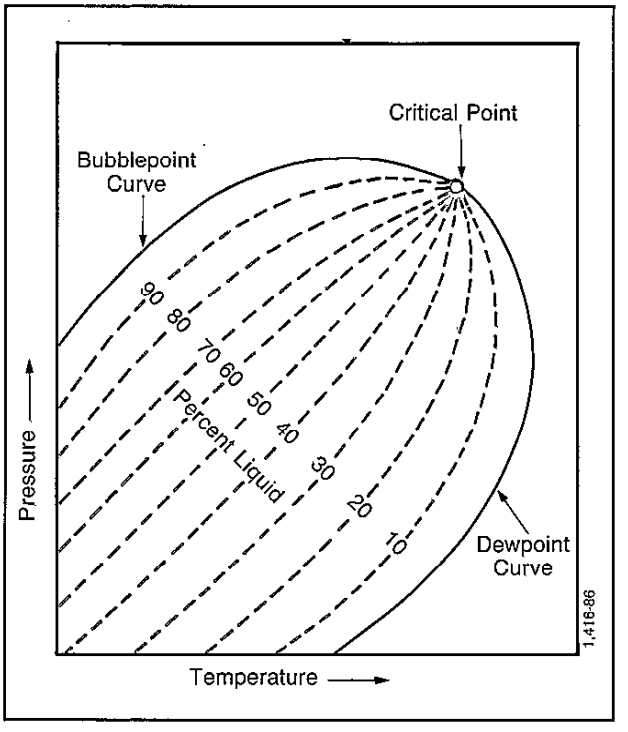

Fig. 2-2—Two-component phase diagram.

Since the petrophysical parameters of the virgin, uncontaminated formation are usually needed, the well logging tool must be able to "see" beyond the contaminated zone into the virgin formation; alternately, the interpretation techniques must be able to compensate for the contamination. In well logging, both approaches are used. Where the physics of the measurement permit, the tool has been designed to have a very significant depth of investigation. When the physics of measurement precludes deep investigation, the interpretation techniques must consider the mud filtrate invasion issues.

It is the purpose of the various well logging tools to provide measurements from which the petrophysical characteristics of the reservoir rocks can be derived or inferred. It is the purpose of quantitative log interpretation to provide the equations and techniques with which these translations can be accomplished. Actually, the basic fundamental premises of log interpretation are few in number and simple in concept.

THE INVASION PROCESS

During the drilling of the well the hydrostatic pressure of the mud column is usually greater than the pore pressure of the formations. This prevents the well from "blowing out." The resultant pressure differential between the mud column and formation forces mud filtrate into the permeable formation, and the solid particles of the mud are deposited on the borehole wall where they form a mudcake. Mudcake usually has a very low permeability (of the order of 10^{-2}-10^{-4} md) and, once developed, considerably reduces the rate of further mud filtrate invasion (Fig. 2-3).

Very close to the borehole most of the original formation water and some of the hydrocarbons may be flushed away by the filtrate. This zone is referred to as the flushed zone. It contains, if the flushing is complete, only mud filtrate; if the formation was originally hydrocarbon bearing, only residual hydrocarbons.

Further out from the borehole, the displacement of the formation fluids by the mud filtrate is less and less complete, resulting in a transition from mud filtrate saturation to original formation water saturation. This zone is referred to as the transition or invaded zone. The extent or depth of the flushed and transition zones depends on many parameters. Among these are the type and characteristics of the drilling mud, the formation porosity, the formation permeability, the pressure differential, and the time since the formation was first drilled. Generally, the lower the formation porosity, the deeper the invasion.The undisturbed formation beyond the transition zone is referred to as the noninvaded, virgin, or uncontaminated zone.

Sometimes in oil- and gas-bearing formations, where the mobility of the hydrocarbons is greater than that of the water because of relative permeability differences, the oil or gas moves away faster than the interstitial water. In this case, there may be formed between the flushed zone and the uninvaded zone an annular zone with a high formation water saturation (Fig. 2-3). Annuli probably occur, to some degree, in most hydrocarbon-bearing formations. Their influence on log measurements depends on the radial location of the annulus and its severity (i.e., magnitude of formation water saturation in the annuli

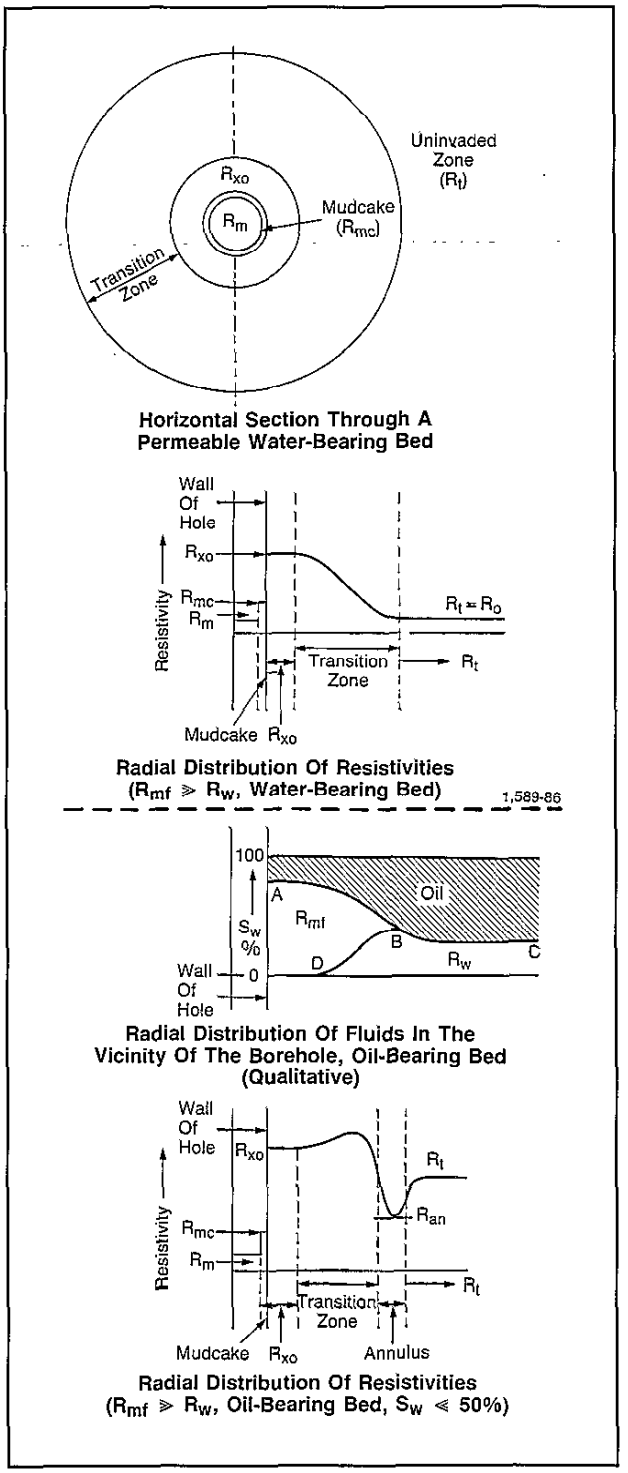

Fig. 2-3—(Upper)—Schematic representation of invasion and resistivity profile in a water-bearing zone.

(Lower)—Invasion and resistivity profile in an oil-bearing zone showing resistivity annulus.

relative to the formation water saturation in the noninvaded zone). Annuli do disappear in time through dispersion.

In fractured formations the mud filtrate invades easily into the fractures, but it may penetrate very little into the unfractured blocks of low-permeability matrix. Therefore, only a small portion of the total original formation fluids (formation water and, if present, hydrocarbons) is displaced by the filtrate — even very close to the borehole. In this case, no true flushed zone exists.

RESISTIVITY

The electrical resistivity of a substance is its ability to impede the flow of electrical current through the substance. The unit used in logging is ohm-meter^2/meter, usually written as ohm-m. Electrical conductivity is the reciprocal of resistivity and is expressed in millimhos per meter (mmho/m).

Most formations logged for potential oil and gas saturation are made up of rocks which, when dry, will not conduct an electrical current; i.e., the rock matrix has zero conductivity or infinitely high resistivity. An electrical current will flow only through the interstitial water saturating the pore structure of the formation, and then only if the interstitial water contains dissolved salts. These salts dissociate into positively charged cations (Na^+, Ca^{++}, ...) and negatively charged anions (Cl^-, SO_4^{--}, ...). Under the influence of an electrical field these ions move, carrying an electrical current through the solution. Other things being equal, the greater the salt concentration, the lower the resistivity of the formation water and, therefore, of the formation. The greater the porosity of the formation and, hence, the greater the amount of formation water, the lower the resistivity.

Of all the rock parameters measured by today's logging tools, resistivity is of particular importance. It is the one measurement for which tools having a deep depth of investigation (up to several feet beyond the borehole) exist. Resistivity measurements are essential for saturation determinations — particularly saturation determinations in the virgin, noninvaded portion of the reservoir. Resistivity measurements are employed, singly and in combination, to determine formation resistivity in the noninvaded formation (called true resistivity, R_t). Resistivity measurements are also used to determine the resistivity close to the borehole (called flushed-zone resistivity, R_{xo}), where mud filtrate has largely replaced the original pore fluids. Resistivity measurements, along with porosity and water resistivity, are used to obtain values of water saturation. Saturation values from both shallow and deep resistivity measurements can be compared to evaluate the producibility of the formation.

FORMATION FACTOR AND POROSITY

It has been established experimentally that the resistivity of a clean, water-bearing formation (i.e., one containing no appreciable amount of clay and no hydrocarbons) is proportional to the resistivity of the brine with which it is fully saturated. The constant of proportionality is called the formation resistivity factor, F. Thus, if R_0 is the resistivity of a nonshaly formation rock 100% saturated with brine of resistivity R_w, then

$$F = R_0/R_w \,. \qquad \text{(Eq. 2-1)}$$

For a given porosity, the ratio R_0/R_w remains nearly constant for all values of R_w below about 1 ohm-m. For fresher, more resistive waters, the value of F may decrease as R_w increases. This phenomenon is attributed to a greater proportionate influence of surface conductance of the rock matrix.

For a given saturating brine water, the greater the porosity of a formation, the lower the resistivity R_0 of the formation, and the lower the formation factor F (from Eq. 2-1). Therefore, the formation factor is inversely related to porosity. It is also a function of pore structure and pore-size distribution.

Archie proposed, based on observations, a formula relating porosity, ϕ, and formation factor, F; the relationship is

$$F = \frac{a}{\phi^m}, \qquad \text{(Eq. 2-2)}$$

where m is the cementation factor or exponent. The cementation exponent and the constant a are determined empirically.

Over the years, experience has generated general acceptance of the following formation factor-porosity relationships (dependent on lithology or pore structure):

$$F = \frac{0.62}{\phi^{2.15}} \text{ for sands, and} \qquad \text{(Eq. 2-3a)}$$

$$F = \frac{1}{\phi^2} \qquad \text{(Eq. 2-3b)}$$

for compacted formations.

The first relationship is popularly referred to as the Humble formula; the second, as the Archie formation factor relationship.

To eliminate the fractional cementation exponent, the Humble formula is sometimes simplified to

$$F = \frac{0.81}{\phi^2}. \qquad \text{(Eq. 2-3c)}$$

Within their normal range of application, these two ways of expressing the Humble formula yield quite similar results.

While the Humble formula is satisfactory for sucrosic rocks, better results are obtained using $F = 1/\phi^2$ in chalky rocks and $F = 1/\phi^{2.2}$ to $1/\phi^{2.5}$ in compact or oolicastic rocks. In some severely oolicastic rocks, m may even be as high as 3.

The Humble and Archie formulas for several values of m are presented graphically on Chart Por-1.

WATER SATURATION

Neither oil nor gas conducts electrical current; both are excellent insulators. Indeed, oil is widely used as an insulator in some electrical equipment. Thus, in a formation containing oil or gas, the resistivity is a function not only of F and R_w but also of S_w. S_w is the fraction of the pore volume occupied by formation water and $(1-S_w)$ is the fraction of the pore volume occupied by hydrocarbons.

Archie determined experimentally that the water saturation of a clean formation can be expressed in terms of its true resistivity as

$$S_w^n = \frac{FR_w}{R_t}, \qquad \text{(Eq. 2-4a)}$$

where n is the saturation exponent.

Although laboratory measurements do show some variation in the value of n, most formation samples yield a saturation exponent of about 2. Therefore, in log interpretation practice, n is taken equal to 2 unless it is known to be otherwise.

Accepting $n = 2$, Eq. 2-4a may be written as

$$S_w = \sqrt{\frac{FR_w}{R_t}}. \qquad \text{(Eq. 2-4b)}$$

This equation is often popularly referred to as the Archie water saturation equation. It is the foundation stone of most electrical log interpretation techniques.

In Eq. 2-3, FR_w is equal to R_0, the resistivity of the formation when 100% saturated with water of resistivity R_w. The water saturation equation, Eq. 2-4b, may then be written:

$$S_w = \sqrt{\frac{R_0}{R_t}}. \qquad \text{(Eq. 2-5)}$$

Early quantitative electric log interpretation used this formula. It simply involved the comparison of R_t, recorded in a potential hydrocarbon-bearing reservoir rock, to R_0, recorded in a known 100% water-bearing reservoir rock. Its use assumes that the two beds have similar porosities and formation factors and contain formation waters of similar salinity. The most appropriate application of Eq. 2-5 is therefore a thick reservoir rock of constant porosity, which has a water column at its base and an oil column at its top.

The ratio R_t/R_0 is called the resistivity index. A resistivity index of unity implies 100% water saturation; a resistivity index of 4 corresponds to 50% water saturation; an index of 10, to 31.6% water saturation; an index of 100, to 10% water saturation; etc. Chart Sw-1 graphically solves the Archie water saturation equation.

The water (mud filtrate) saturation, S_{xo}, of the flushed zone can also be expressed by the Archie formula (Eq. 2-4a) as

$$S_{xo} = \sqrt{\frac{FR_{mf}}{R_{xo}}}, \qquad \text{(Eq. 2-6)}$$

where R_{mf} is the resistivity of the mud filtrate and R_{xo} is the resistivity of the flushed zone. S_{xo} is equal to $(1-S_{hr})$, S_{hr} being the residual hydrocarbon saturation in the flushed zone. S_{hr} depends to some extent on the hydrocarbon viscosity; it generally increases as the viscosity increases.

The comparison of the water saturations obtained in the flushed zone (Eq. 2-6) and in the noninvaded zone (Eq. 2-4b) determines the bulk-volume fraction of oil displaced by the invasion process. Since $S_h = (1-S_w)$ and $S_{hr} = (1-S_{xo})$, the bulk volume of moved oil is $\phi(S_{xo} - S_w)$. The ability of the mud filtrate to displace or move oil in the invasion process implies that the formation exhibits relative permeability to oil; conversely, oil production can be expected when the reservoir is put on production.

Eqs. 2-4b and 2-6 can also be combined to yield the ratio of the saturation in the virgin, uncontaminated zone to the saturation in the flushed zone. Dividing the first equation by the second gives

$$\frac{S_w}{S_{xo}} = \left(\frac{R_{xo}/R_t}{R_{mf}/R_w}\right)^{1/2}. \qquad \text{(Eq. 2-7)}$$

Empirical observations suggest that $S_{xo} \approx S_w^{1/5}$. Substituting this relationship into Eq. 2-7 gives

$$S_w = \left(\frac{R_{xo}/R_t}{R_{mf}/R_w}\right)^{5/8}. \qquad \text{(Eq. 2-8)}$$

Chart Sw-2 is a graphical solution of this equation. The chart also provides for S_w solutions when the residual oil saturation is other than average.

This method for determining water saturation is sometimes referred to as the ratio method. It does not require knowledge of porosity or formation factor. It does, however, imply finite values for these parameters. The implied values can be obtained by working back through Eq. 2-4b (or Eq. 2-6) solving for F, and then solving for ϕ, once S_w (or S_{xo}) has been determined from Eq. 2-8 (and Eq. 2-7).

These equations are good approximations in clean formations with fairly regular distribution of porosity (intergranular or intercrystalline porosity). In formations

with fractures or vugs, the equations are still used, but the accuracy may not be as good. (See Chapter 8.)

Resistivity Logging

Evaluating a reservoir for its water and hydrocarbon saturation involves the saturating formation water resistivity, R_w; the formation factor, F, or porosity, ϕ; and the true formation resistivity, R_t. Flushed zone resistivity, R_{xo}, is also of interest because it can be used to obtain S_w when porosity is unknown, to indicate hydrocarbon movability, and where invasion is deep to obtain a better value of R_t.

The resistivity parameter of greatest interest is R_t, because of its relationship to hydrocarbon saturation in the noninvaded, virgin formation. Determination of R_t is, therefore, of paramount importance. In determining R_t and R_{xo} from resistivity logs, several perturbing factors affecting the log readings must be taken into account. These are

- the borehole, filled with fluid,
- the adjacent formations, and
- the influence of R_{xo} (invasion) on the R_t measurement and vice versa.

The effects of the first two factors can be minimized by using logging tools designed to minimize borehole effect and to provide good vertical definition. The third is resolved by using several resistivity devices having different depths of investigation (see Chapter 7).

When $R_{xo} > R_t$ and formation resistivities are low to moderate, the DIL* dual induction log is recommended for R_t determination. This survey, consisting of a deep induction log, a medium induction log, and a shallow investigating resistivity log, will furnish good values of R_t for beds thicker than 4 or 5 ft if invasion is not too deep. Adding a microresistivity log to the suite will permit a better evaluation of R_{xo}, and thus R_t, in more deeply invaded formations. Interpretation charts are available to correct the various induction logs for borehole, adjacent formation, and invasion effects.

When $R_{xo} < R_t$ and formation resistivities are high, the DLL* dual laterolog is recommended for R_t determination (see Fig. 2-4). This log provides a deep laterolog and a shallow laterolog. Adding a microresistivity log to the suite will permit a better evaluation of R_{xo} and R_t. Charts are also available to correct for borehole, adjacent bed, and invasion effects.

Water Resistivities

In addition to formation factor or porosity, values of formation water resistivity, R_w, and mud filtrate resistivity, R_{mf}, are needed for the water saturation calculations. Mud resistivity, R_m, mudcake resistivity, R_{mc}, and R_{mf} are generally measured at the time of the survey on a mud sample from the flowline or mud pit. These values are recorded on the log heading. If a measured value of R_{mf} or R_{mc} is not available, Chart Gen-7 provides an estimate. Since the resistivity of a material is a function of temperature, R_m, R_{mf}, and R_{mc} must be corrected to formation temperature (Chart Gen-9). The accuracy of these values can be improved by using the AMS auxiliary measurement sonde; it makes continuous borehole in-situ measurements of R_m and temperature versus depth.

Formation water resistivity, R_w, can be found from the SP curve, water catalogs, produced water sample, or water saturation equation (Eq. 2-4a) in a 100% water-bearing formation. In a clean formation, the SP curve response is

$$SP = -K \log \frac{R_{mf}}{R_w}, \qquad \text{(Eq. 2-9)}$$

where K is a temperature-dependent constant. Charts SP-1 and -2 solve the SP equation (Eq. 2- 9) for R_w.

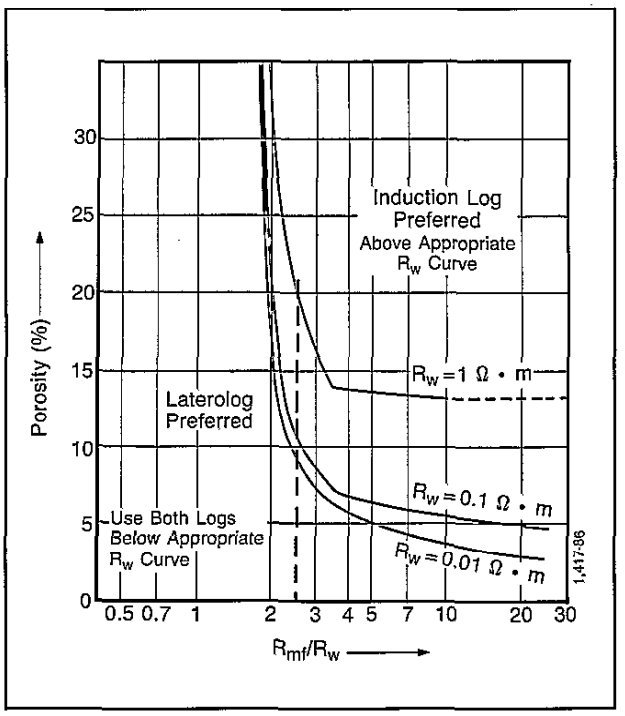

Fig. 2-4—Preferred ranges of application of induction logs and laterologs.

Porosity

Porosity can be obtained from a sonic log, a density log, or a neutron log provided the lithology of the formation is known. If lithology is not known or if mixtures of known minerals exist, a combination of two or more

porosity and lithology-sensitive logs can be used to define the lithology and to provide an accurate value of porosity.

The porosity logs are also somewhat sensitive to the nature of the saturating fluid(s) within the pores investigated by the tool. A combination of two porosity logs can sometimes detect the presence of gas or light oil in the formation.

The sonic tool measures the interval transit time, (t) or the time in microseconds for an acoustic wave to travel through 1 ft (or 1 m) of formation along a path parallel to the borehole.

Porosity can be derived from the interval transit time using an empirical weighted-average or time-average relationship,

$$\phi = \frac{t - t_{ma}}{t_f - t_{ma}}, \qquad \text{(Eq. 2-10)}$$

where t_f and t_{ma} are the transit times in the pore fluid and rock matrix, respectively. This time-average relationship is good for clean, compacted formations of intergranular porosity containing liquids.

Another empirical relationship for porosity from the interval transit time is

$$\phi = c\left(\frac{t - t_{ma}}{t}\right), \qquad \text{(Eq. 2-11)}$$

where $c \approx 0.67$. This empirical relationship is restricted to the same conditions as the time average relationship except that it can be used in noncompacted as well as compacted formations. Chart Por-3 graphically solves these equations.

The density tool responds to the electron density of the material in the formation. For common formation materials, the electron density is proportional to actual density.

Porosity is derived from the bulk density of clean liquid-filled formations when the matrix density, ϱ_{ma}, and the density of the saturating fluids, ϱ_f, are known:

$$\phi = \frac{\varrho_{ma} - \varrho_b}{\varrho_{ma} - \varrho_f}. \qquad \text{(Eq. 2-12)}$$

Chart Por-5 graphically solves this equation.

The presence of shale or gas in the formation complicates the response, but this can be resolved using an appropriate combination of porosity logs (see Chapters 5 and 6).

In addition to a bulk density measurement, the Litho-Density* log also provides a measurement of the photoelectric cross section. This cross section is influenced primarily by the mineralogy of the rock matrix. Used in combination with porosity logs, the composition of complex mineral mixtures can be defined with the photoelectric cross section measurement.

The neutron log responds chiefly to the presence of hydrogen atoms. If the pore space in the formation is liquid filled, the response is basically a measure of porosity. The log is usually scaled in porosity units on the basis of a limestone or sandstone matrix. Corrections must be made if the formation lithology differs from that for which the tool is calibrated. Again, shale and gas affect the porosity readings and must be accounted for (see Chapter 5). Chart Por-13 converts the neutron log reading into porosity.

Shaly Formations

Not all rocks are perfect insulators when dry. Many ores, such as galena and chalcopyrite, have high conductivities and conduct electrical current even when totally dry. Obviously, the resistivity and water saturation equations, which assume that the saturating fluid is the only electrically conductive medium, do not apply when the rock matrix is also conductive. Fortunately, in most oil provinces a significant quantity of conductive mineral in a potential reservoir rock is rare, but when the rock does contain a conductive mineral, the log interpretation must consider that conductivity.

Clays and shales, however, are not rare, and they do contribute to formation conductivity. Shale exhibits conductivity because of the electrolyte that it contains and because of an ion-exchange process whereby ions move under the influence of the impressed electric field between exchange sites on the surface of the clay particles. The effect of the shaliness on shaly sand conductivity is often disproportionately large relative to the quantity of shale. The actual effect depends on the amount, type, and distribution of the shale and on the nature and relative amount of the formation water.

Evaluation of shaly formations, usually shaly sands, is somewhat complex. All logging measurements are influenced by the shale, and corrections for shale content are required.

Through the years, investigators have proposed various interpretation models for shaly sands. In some cases, the model is based upon the shale existing in a particular geometry within the shaly sand; for example, the shale may exist in the form of thin laminae between layers of clean sand, or as grains or nodules in the sand matrix structure, or may be dispersed throughout the pore system of the sand in the form of accumulations adhering to or coating the sand grains. Other shaly sand models are based upon some specific characteristic of the shale, such as its cation exchange capacity or surface area.

Regardless of the basic assumption, most shaly sand interpretation models employ a weighted-average technique to evaluate the relative contributions of the sand and shale phases to the overall shaly sand response. For ex-

*Mark of Schlumberger

ample, in the case of bulk density as measured by a density log, the relationship is

$$\varrho_b = \phi\,(S_{xo}\,\varrho_{mf} + S_{hr}\,\varrho_h) + V_{sh}\,\varrho_{sh} + (1 - \phi - V_{sh})\,\varrho_{ma}, \quad \text{(Eq. 2-13)}$$

where V_{sh} is the bulk-volume fraction of shale, ϱ_{sh} is its density, ϱ_h is the apparent density of the hydrocarbon, and the other terms are as previously defined.

There are many formulas that relate resistivity to water saturation in shaly sands. Most are generally of the form

$$\frac{1}{R_t} = \frac{S_w^2\,(1 - V_x)}{FR_w} + \frac{CV_x}{R_x}, \quad \text{(Eq. 2-14)}$$

where V_x is a term related to the volume, or some specific volumetric characteristic, of the shale or clay; R_x is a term related to the resistivity of the shale or clay; and C, if it occurs in the formula, is a term related to the water saturation, S_w.

It should be noted that when the shale volume is zero (i.e., a clean sand), the equation (Eq. 2-14) reduces to the Archie water saturation equation (Eq. 2-4a). This is true for all shaly sand water saturation interpretation techniques.

REFERENCES

1. Archie, G.E.: "The Electrical Resistivity as an Aid in Determining Some Reservoir Characteristics," *J. Pet. Tech.* (Jan. 1942) 5, No. 1.
2. Archie, G.E.: "Classification of Carbonate Reservoir Rocks and Petrophysical Considerations," *Bull.*, AAPG (Feb. 1952) **36**, No. 2.
3. Winsaver, W.O., Shearin, H.M., Jr., Masson, P.H., and Williams, M.: "Resistivity of Brine-Saturated Sands in Relation to Pore Geometry," *Bull.*, AAPG (Feb. 1952) **36**, No. 2.
4. Poupon, A., Loy, M.E., and Tixier, M.P.: "A Contribution to Electrical Log Interpretation in Shaly Sands," *J. Pet. Tech.* (March 1963).
5. Wyllie, M.R.J., Gregory, A.R., and Gardner, G.H.F.: "An Experimental Investigation of Factors Affecting Elastic Wave Velocities in Porous Media," *Geophys.* (July 1958) **23**, No. 3.
6. Raymer, L.L., Hunt, E.R., and Gardner, J.S.: "An Improved Sonic Transit Time-to-Porosity Transform," *Trans.*, 1980 SPWLA Annual Logging Symposium.
7. Alger, R.P., Raymer. L.L., Hoyle, W.R., and Tixier, P.: "Formation Density Log Applications in Liquid-Filled Holes," *J. Pet. Tech.* (March 1963).
8. Worthington, P.F.: "The Evaluation of Shaly-Sand Concepts in Reservoir Evaluation," *The Log Analyst* (Jan.-Feb. 1985).
9. *Log Interpretation Charts*, Schlumberger Well Services, Houston (1989).

3

Spontaneous Potential and Natural Gamma Ray Logs

The spontaneous potential (SP) curve and the natural gamma ray (GR) log are recordings of naturally occurring physical phenomena in in-situ rocks. The SP curve records the electrical potential (voltage) produced by the interaction of formation connate water, conductive drilling fluid, and certain ion-selective rocks (shale). The GR log indicates the natural radioactivity of the formations. Nearly all rocks exhibit some natural radioactivity and the amount depends on the concentration of potassium, thorium, and uranium. There are two types of GR logs. One, the standard GR log, measures only the total radioactivity. The other, the NGS* natural gamma ray spectrometry log, measures the total radioactivity and the concentrations of potassium, thorium, and uranium producing the radioactivity.

Both the SP curve and GR log are generally recorded in Track 1 (left track) of the log. They are usually recorded in conjunction with some other log — such as the resistivity or porosity log. Indeed, nearly every log now includes a recording of the SP curve and/or GR log.

Although relatively simple in concept, the SP curve and GR logs are quite useful and informative. Among their uses are the following:

- Differentiate potentially porous and permeable reservoir rocks (sandstone, limestone, dolomite) from nonpermeable clays and shales.
- Define bed boundaries and permit correlation of beds.
- Give a qualitative indication of bed shaliness.
- Aid in lithology (mineral) identification.
- In the case of the SP curve, permit the determination of formation water resistivity, R_w.
- In the case of the GR and NGS logs, detect and evaluate deposits of radioactive minerals.
- In the case of the NGS log, define the concentrations of potassium, thorium, and uranium.

*Mark of Schlumberger

THE SP CURVE

The SP curve is a recording versus depth of the difference between the electrical potential of a movable electrode in the borehole and the electrical potential of a fixed surface electrode.

Opposite shales the SP curve usually defines a more-or-less straight line on the log, called the shale baseline. Opposite permeable formations, the curve shows excursions from the shale baseline; in thick beds, these excursions (deflections) tend to reach an essentially constant deflection defining a sand line. The deflection may be either to the left (negative) or to the right (positive), depending primarily on the relative salinities of the formation water and of the mud filtrate. If the formation water salinity is greater than the mud filtrate salinity, the deflection is to the left. For the reversed salinity contrast, the deflection is to the right.

The position of the shale baseline on the log has no useful meaning for interpretation purposes. The SP sensitivity scale is chosen and the shale baseline position is set by the engineer running the log so that the curve deflections remain in the SP track. The SP log is measured in millivolts (mV).

An SP curve cannot be recorded in holes filled with nonconductive muds because such muds do not provide electrical continuity between the SP electrode and the formation. Furthermore, if the resistivities of the mud filtrate and formation water are about equal, the SP deflections will be small and the curve will be rather featureless.

Origin of the SP

The deflections on the SP curve result from electric currents flowing in the mud in the borehole. These SP currents are caused by electromotive forces in the formations, which are of electrochemical and electrokinetic origins.

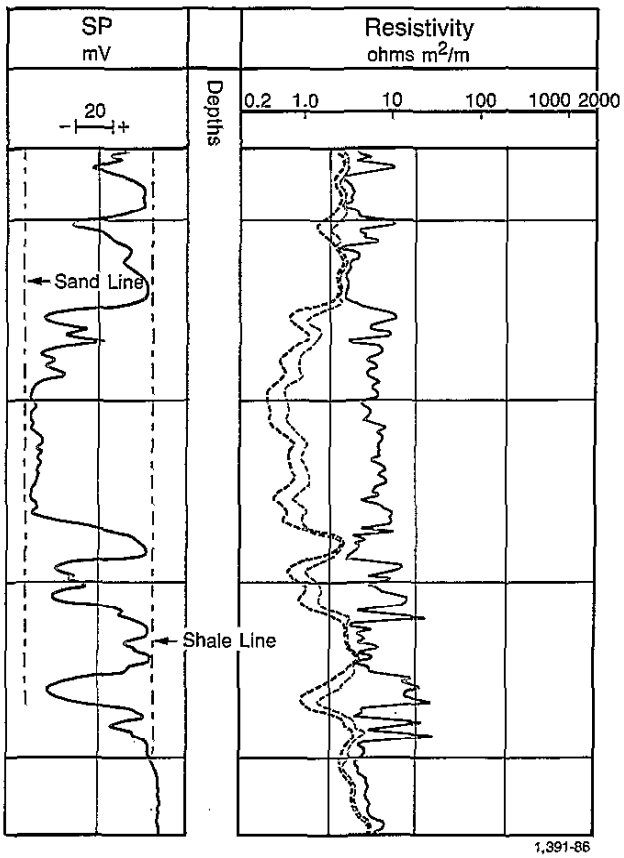

Fig. 3-1—Example of SP log in a sand-shale series.

Electrochemical Component of the SP

Consider a permeable formation with thick shale beds above and below; assume, too, that the two electrolytes present, mud filtrate and interstitial formation water, contain sodium chloride (NaCl) only. Because of the layered clay structure and the charges on the layers, shales are permeable to the Na^+ cations but impervious to the Cl^- anions. Only the Na^+ cations (positive charges) are able to move through the shale from the more concentrated to the less concentrated NaCl solution. This movement of charged ions is an electric current, and the force causing them to move constitutes a potential across the shale.

The curved arrow in the upper half of Fig. 3-2 shows the direction of current flow corresponding to the passage of Na^+ ions through the adjacent shale from the more saline formation water in the bed to the less saline mud.

Since shales pass only the cations, shales resemble ion-selective membranes, and the potential across the shale is therefore called the membrane potential.

Another component of the electrochemical potential is produced at the edge of the invaded zone, where the mud filtrate and formation water are in direct contact. Here Na^+ and Cl^- ions can diffuse (move) from either solution to the other. Since Cl^- ions have a greater mobility than Na^+ ions, the net result of this ion diffusion is a flow of negative charges (Cl^- ions) from the more concentrated to the less concentrated solution. This is equivalent to a conventional current flow in the opposite direction, indicated by the straight Arrow A in the upper half of Fig. 3-2. The current flowing across the junction between solutions of different salinity is produced by an electromagnetic force (emf) called liquid-junction potential. The magnitude of the liquid-junction potential is only about one-fifth the membrane potential.

If the permeable formation is not shaly, the total electrochemical emf, E_c, corresponding to these two phenomena, is equal to

$$E_c = -K \log \frac{a_w}{a_{mf}}, \qquad \text{(Eq. 3-1)}$$

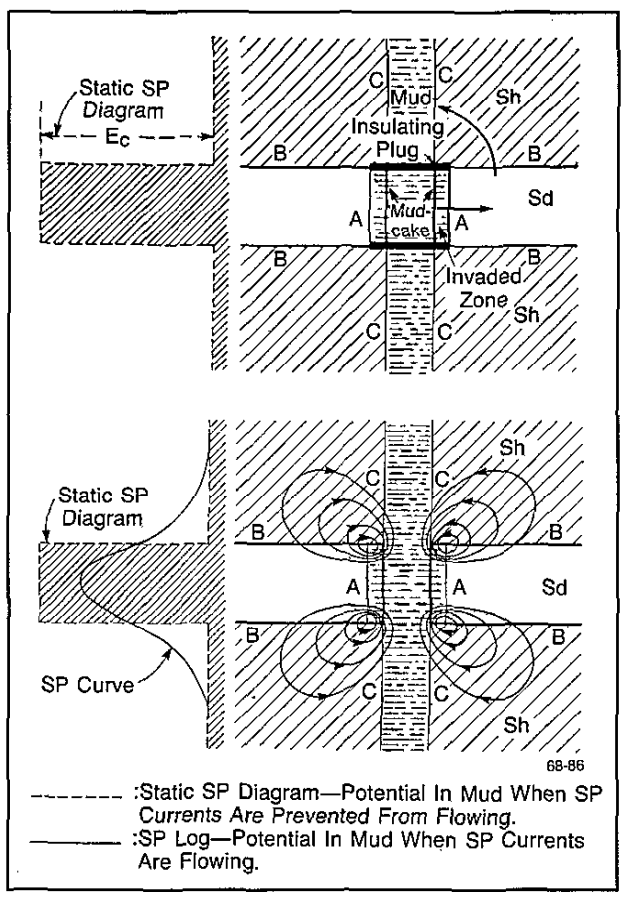

Fig. 3-2—Schematic representation of potential and current distribution in and around a permeable bed.

where a_w and a_{mf} are the chemical activities of the two solutions (formation water and mud filtrate) at formation temperature; K is a coefficient proportional to the absolute temperature, and, for NaCl formation water and mud filtrate, is equal to 71 at 25° C (77° F). The chemical activity of a solution is roughly proportional to its salt content (i.e., to its conductivity). If the solutions contain substantial amounts of salts other than NaCl, the value of K at 77° F may differ from 71.

If the permeable formation contains some shale or dispersed clay, the total electrochemical emf and, hence, the SP deflections will be reduced since the clay in the permeable formation produces an electrochemical membrane of opposite polarity to that of the adjacent shale bed.

Electrokinetic Component of the SP

An electrokinetic potential, E_k (also known as streaming potential or electrofiltration potential), is produced when an electrolyte flows through a permeable, nonmetallic, porous medium. The magnitude of the electrokinetic potential is determined by several factors, among which are the differential pressure producing the flow and the resistivity of the electrolyte.

In the borehole, an electrokinetic emf, E_{kmc}, is produced by the flow of mud filtrate through the mudcake deposited on the borehole wall opposite permeable formations. In practice, little or no electrokinetic emf is actually generated across the permeable formation itself. This is because practically all the differential pressure between the borehole and undisturbed virgin formation is expended across the less permeable mudcake. Any remaining differential pressure across the formation is normally not great enough to produce any appreciable electrokinetic emf.

An electrokinetic emf, E_{ksh}, may, however, be produced across the shale, since it may have sufficient permeability to permit a tiny amount of filtration flow from the mud.

Each of these electrokinetic emf's contributes to a more negative SP reading opposite the permeable bed and opposite the shale, respectively. The net contribution to the SP deflection (measured from the shale line) is, therefore, the difference between the contributions of the mudcake and the shale electrokinetic effects. In practice, these electrokinetic emf's are similar in magnitude, and the net electrokinetic contribution to the SP deflection is therefore usually small, normally regarded as negligible. This is particularly true if the formation water is rather saline (resistivity less than 0.1 ohm-m) and the differential pressure has a normal value of only a few hundred pounds per square inch (psi) or less.

It is, however, possible for electrokinetic effects to become more important in cases of unusually large pressure differentials (e.g., in depleted formations of low pressure or when very heavy drilling muds are used). In these cases, the electrokinetic emf's may be quite significant and the mudcake and shale electrokinetic effects may not cancel each other.

Important electrokinetic effects may also be seen in very low-permeability formations (less than a few millidarcies) in which an appreciable part of the pressure differential is applied across the formation itself. If formation permeability is so low that little or no mudcake is formed, most of the pressure differential between the formation pore pressure and hydrostatic head of the mud column is applied to the formation. If the formation water is brackish, if the mud is resistive, and if the formation is clean and has some porosity, the electrokinetic effect may be quite large, sometimes exceedng -200 mV.

These infrequent effects are difficult to detect, but conditions favoring their existence should alert us to the possibility of a large electrokinetic potential. When a significant electrokinetic potential exists the SP deflection cannot be used to calculate a reliable value of formation water resistivity, R_w.

SP Versus Permeability and Porosity

The movement of ions, which causes the SP phenomenon, is possible only in formations having a certain minimum permeability. (A small fraction of a millidarcy is sufficient.) There is no direct relationship between the value of permeability and the magnitude of the SP deflection, nor does the SP deflection have any direct relation to the porosity.

Static SP

The lower portion of Fig. 3-2 depicts how the SP currents flow in the borehole and formations. The current directions shown correspond to the more usual case where the salinity of the formation water is greater than that of the mud filtrate. Thus, the potential observed opposite the permeable sandstone bed is negative with respect to the potential opposite the shale. This negative variation corresponds to an SP curve deflection toward the left on the SP log (also illustrated on the figure).

If the salinity of the mud filtrate is greater than that of the formation water, the currents flow in the opposite direction. In that case, the SP deflection opposite a permeable bed is positive (to the right). Positive deflections are usually observed in freshwater-bearing formations. If the salinities of the mud filtrate and formation water are similar, there is no SP potential or current flow and, hence, no SP deflection opposite a permeable bed.

As shown on Fig. 3-2, the SP currents flow through four different media: the borehole, the invaded zone, the noninvaded part of the permeable formation, and the surrounding shales. In each medium, the potential along a line of current flow drops in proportion to the resistance encountered; the total potential drop along a line of current flow is equal to the total emf.

The deflections on the SP curve are, however, a measurement of only the potential drop in the borehole resulting from the SP currents. This potential drop represents only a fraction (although usually the major fraction) of the total emf because there are also potential drops in the formation. If the currents could be prevented from flowing by means such as the insulating plugs schematically indicated in the upper part of Fig. 3-2, the potential differences observed in the mud would equal the total emf. The SP curve recorded in such an idealized condition is called the static SP curve. The static SP, or SSP, is the SP deflection opposite a thick, clean formation. The deflection is measured from the shale baseline and its magnitude, from Eq. 3-2, is

$$SSP = -K \log \frac{a_w}{a_{mf}}. \qquad \text{(Eq. 3-2)}$$

Fortunately, because the borehole presents a much smaller cross-sectional area to current flow relative to the formations, most of the SP voltage drop does occur in the borehole provided formation resistivities are low to moderate and beds are moderately thick. Therefore, the recorded SP deflection does approach the static SP value in most thick permeable beds.

Determination of SSP

The value of SSP can be determined directly from the SP curve if, in a given horizon, there are thick, clean, water-bearing beds. A line is drawn through the SP (negative) maxima opposite the thick permeable beds, and another line (shale baseline) is drawn through the SP opposite the intervening shale beds (see Fig. 3-1). The difference, in millivolts, between these lines is the SSP; any SP anomalies should be discounted.

Many times, it is difficult to find thick, clean, permeable invaded beds in the zone under study. When beds are thin but still clean, the SP must be corrected to find a value of SSP. Corrections for the effect of bed thickness and/or invasion are given in Charts SP-3 or SP-4. Additional information on SP bed thickness corrections is provided in Refs. 14 and 15.

Shape of the SP Curve

The slope of the SP curve at any level is proportional to the intensity of the SP currents in the borehole mud at that level. As illustrated on Fig. 3-2, the intensity of the currents in the mud is maximum at the boundaries of the permeable formation, and, accordingly, the slope of the curve is maximum (and there is an inflection point) at these boundaries.

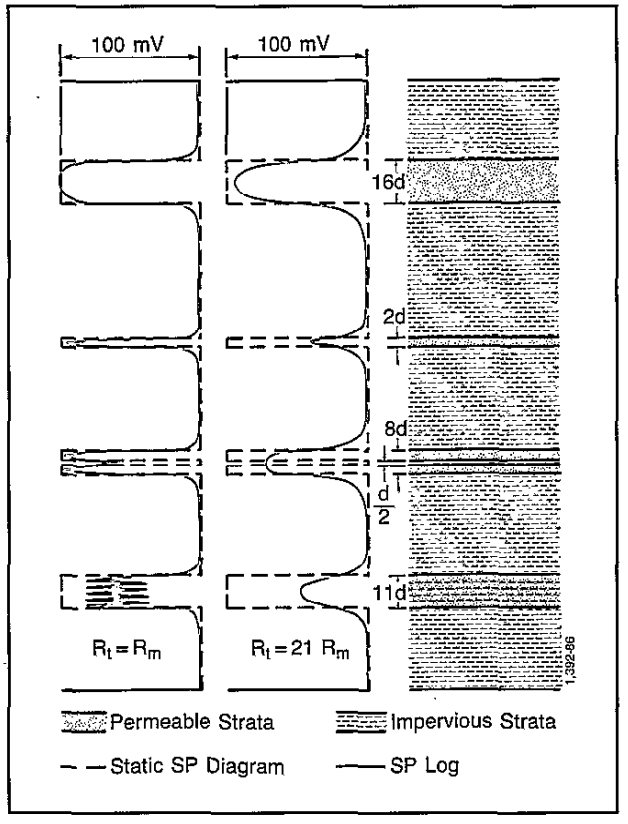

Fig. 3-3—SP curve in beds of different thickness for $R_t = R_m$ (left) and $R_t = 21\ R_m$ (center).

The shape of the SP curve and the amplitude of the deflection opposite a permeable bed depend on several factors. The factors, which affect the distribution of the SP current lines and the potential drops taking place in each of the media through which the SP current flows, are the following:

- Thickness, h, and true resistivity, R_t, of the permeable bed.
- Resistivity, R_{xo}, and diameter, d_i, of the zone contaminated by mud filtrate invasion.
- Resistivity, R_s, of the adjacent shale formation.
- Resistivity, R_m, of the mud and diameter, d_h, of the borehole.

Fig. 3-3 shows a few examples of SP curves computed for $R_t = R_s = R_m$ (left side) and $R_t = R_s = 21\ R_m$ (center); the static SP, SSP, represented by the crosshat-

ched diagrams is assumed to be 100 mV in these examples. In the case of $R_t = R_s = R_m$, the SP curve gives a much sharper definition of the boundaries of the permeable beds, and the SP deflections are greater and more closely approach the SSP value than in the case where the formation-to-mud resistivity ratio is 21.

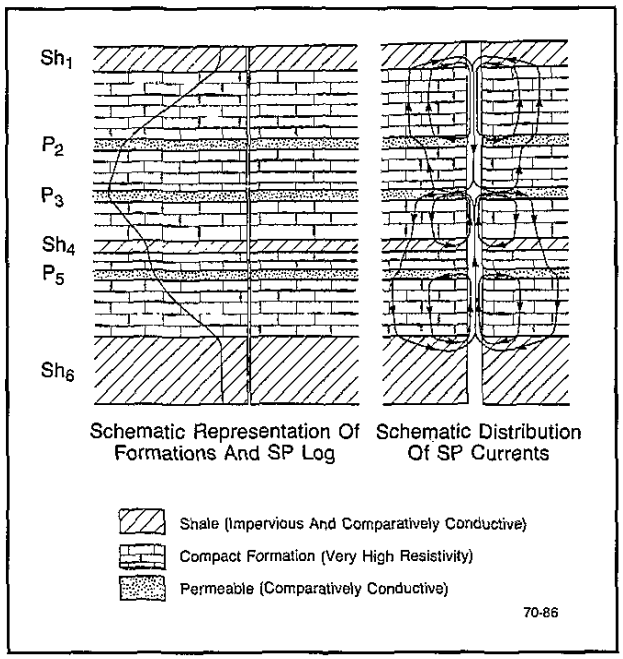

Fig. 3-4—Schematic representation of SP phenomena in highly resistive formations.

Highly Resistive Formations

In some formations, resistivities may be very high except in the permeable zones and in the shales. These high resistivities can significantly alter the distribution of the SP currents and, hence, the shape of the SP curve. As illustrated in Fig. 3-4, the currents flowing from shale bed Sh_1 towards permeable bed P_2 are largely confined to the borehole between Sh_1 and P_2 because of the very high resistivity of the formation in this interval. Accordingly, the intensity of the SP current in the borehole in this interval remains constant. Assuming the hole diameter is constant, the potential drop per foot will be constant, and the SP curve will be a straight sloped line.

In these formations, SP current leaves or enters the borehole only opposite the lower resistivity permeable beds or the shales. Therefore, the SP curve shows a succession of straight portions with a change of slope opposite every permeable interval (with the concave side of the SP curve towards the shale line) and opposite every shale bed (with the convex side of the SP curve towards the shale line). The SP cannot easily be used to define the boundaries of the permeable beds in these situations.

Shale Baseline Shifts

The shale baseline (from which the SP deflections are measured) is usually fairly well defined on the SP log (Fig. 3-1). However, in some wells, baseline shifts are observed. A baseline shift occurs whenever formation waters of different salinities are separated by a shale bed that is not a perfect cationic membrane. Large shifts make definition of the shale baseline and determination of the SSP value quite difficult.

Fig. 3-5 shows a simplification of a field case. The well penetrates a series of sandstones (B, D, F, H) separated by thin shales or shaly sandstones (C, E, G). The SSP of Interval B is indicated by the deflection at the upper boundary to be −42 mV. Shale C is not a perfect cationic membrane and the SP opposite C does not come back to the shale baseline of A. The SP deflection of Interval D, measured from Shale E, indicates that E is a better membrane than C. The shale baseline for Sandstone D is shown by the dashed line farther to the left; the SSP of Interval D is 44 mV or more. Similarly, it can be seen that Shale G is not as good a membrane as E; the SSP of Interval F is negative and equal to at least −23 mV.

When there is no shale bed to separate waters of different salinities in a permeable bed, there is also an SP baseline shift. In such a case, the SP curve shows little

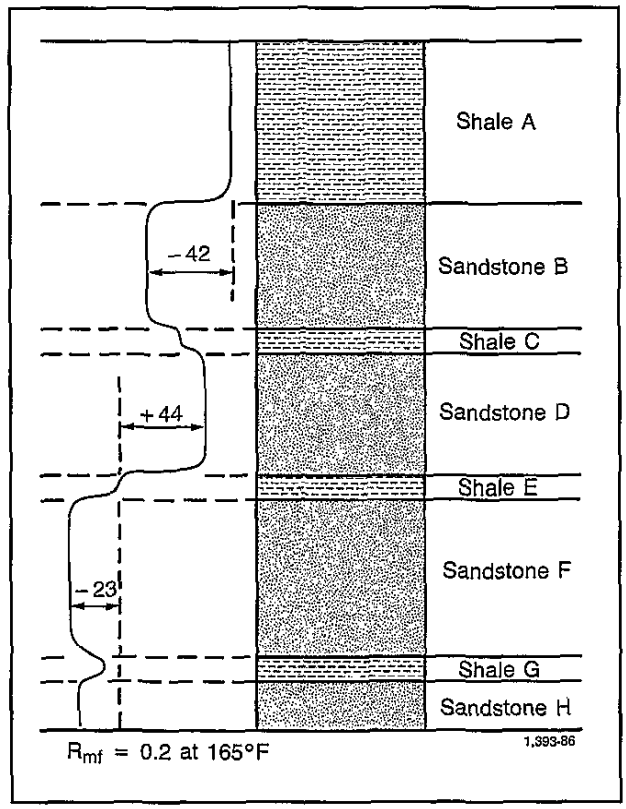

Fig. 3-5—SP baseline shift.

or no variation at the level where the salinity change occurs, but the SP deflections at the upper and lower boundaries of the permeable bed exhibit quite different amplitudes. Indeed, they may exhibit different polarities if the salinity of the mud filtrate is between the salinities of the two different interstitial formation waters. If the permeable bed is not shaly and if the permeable bed and the surrounding shales are sufficiently thick, the SP deflections at the two boundaries are the static SP deflections corresponding to the two different waters.

In all cases, the SP deflection at the shale-permeable bed boundary gives the polarity of the static SP deflection and, generally, a lower limit of its magnitude.

SP Anomalies Related to Invasion Conditions

In very permeable formations, SP anomalies, if not understood or recognized, may cause errors in the evaluation of the SSP.

When a high-porosity saltwater sand with good vertical permeability is invaded by fresh mud filtrate, the lighter filtrate floats up toward the upper boundary of the sand. An invasion profile, such as shown on the right side of Fig. 3-6, develops. Invasion is very shallow near the lower boundary of each permeable interval and deeper near the upper boundary. The SP is affected as follows:

- At the upper boundary the curve is rounded because of the deep invasion.
- At impervious shale streaks the SP may have a sawtoothed profile, as illustrated on the left side of Fig. 3-6; just below the shale streak the SP deflection is less than the SSP, and above the shale streak the SP deflection exceeds the SSP. This anomaly is caused by the accumulation of filtrate below the shale streak. Encircling the hole is a horizontal disk-shaped cell consisting of a shale disk sandwiched between salt water and mud filtrate. The emf of this cell superimposed on the normal SSP produces the anomalous profile.

The invasion may vanish completely in the lower portion of a very permeable bed, producing an invasion profile as shown on Fig. 3-7. Where there is no invasion, a reduced SP deflection is observed; there, the filtrate and the interstitial water are no longer in direct contact. As a result, there is no liquid-junction potential E_j to add to the shale-membrane potential E_{sh}, as is the case where there is invasion. Furthermore, the mudcake now acts as a cationic membrane to produce a mudcake membrane potential E_{mc}, which is of opposite direction to the shale-membrane potential. The efficiency of the mudcake as a membrane is usually much less, however, than that of a good shale so only a reduced SP deflection, as shown on Fig. 3-7, occurs. Since the diameter of invasion in the lower part of a permeable bed may decrease or increase with time, dependent upon mud and hole conditions, this reduced SP phenomenon may also appear and disappear with time. Sometimes the SP is decreased over most of the bed because invasion exists only in a thin plane at the top.

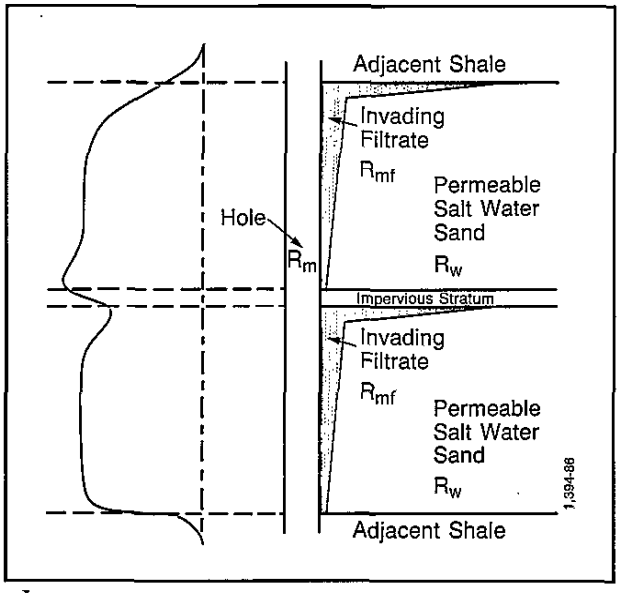

Fig. 3-6—Sawtooth SP.

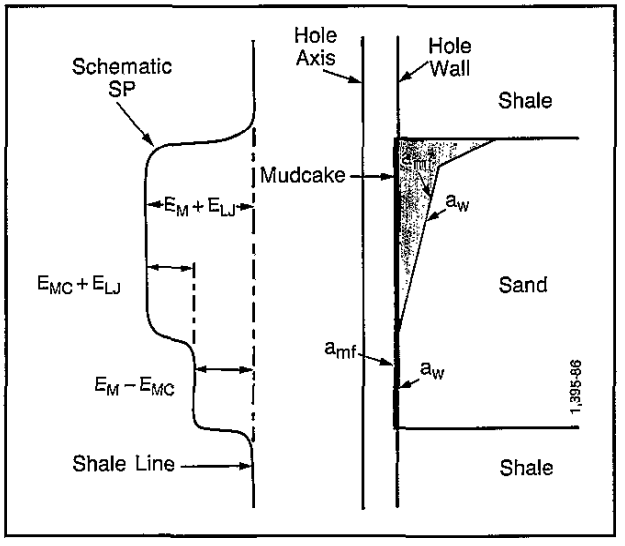

Fig. 3-7—SP reduction by mudcake membrane emf.

Field experience has shown that when there is a significant change in the mud used during drilling, it takes a long time for the recorded SP curve to reflect characteristics of the new mud. Therefore, when the SP curve is needed for R_w determinations, the mud characteristics should be kept fairly constant during drilling. In fact, if the characteristics of the mud must be changed, it is desirable to log the well just prior to the change.

SP Anomalies—Noise

Sometimes a small-amplitude sine-wave signal is superimposed on the SP; this happens when some mobile part of the winch becomes accidentally magnetized. An intermittent contact between casing and cable armor may also cause spurious spikes on the SP curve. In these situations, the SP curve should be read in such a way that the sine-wave amplitude or spike is not added to, or subtracted from, the authentic SP deflection.

Direct currents flowing through the formations near the SP electrode can also result in erroneous SP values, particularly when formation resistivities are high. These currents may be caused by bimetallism, which occurs when two pieces of different metals touch each other and, surrounded with mud, form a weak battery. These currents are small and are not likely to affect the SP except in highly resistive formations. Accordingly, if an SP curve in very resistive formations looks questionable, the SP deflections should preferably be read opposite nonshaly intervals where the resistivities are as low as possible.

It is sometimes difficult to record a good SP on offshore or barge locations; passing ships, cathodic protection devices, and leaky power sources may all contribute to a noisy SP. On land, proximity to power lines and pumping wells may have a similar effect on the SP curve. Many of these disturbances can be minimized by a careful choice of the ground-electrode location.

THE GR LOG

The GR log is a measurement of the natural radioactivity of the formations. In sedimentary formations the log normally reflects the shale content of the formations. This is because the radioactive elements tend to concentrate in clays and shales. Clean formations usually have a very low level of radioactivity, unless radioactive contaminant such as volcanic ash or granite wash is present or the formation waters contain dissolved radioactive salts.

The GR log can be recorded in cased wells, which makes it very useful as a correlation curve in completion and workover operations. It is frequently used to complement the SP log and as a substitute for the SP curve in wells drilled with salt mud, air, or oil-based muds. In each case, it is useful for location of shales and nonshaly beds and, most importantly, for general correlation.

Properties of Gamma Rays

Gamma rays are bursts of high-energy electromagnetic waves that are emitted spontaneously by some radioactive elements. Nearly all the gamma radiation encountered in the earth is emitted by the radioactive potassium isotope of atomic weight 40 (K^{40}) and by the radioactive elements of the uranium and thorium series.

Each of these elements emits gamma rays; the number and energies of which are distinctive of each element. Fig. 3-8 shows the energies of the emitted gamma rays: potassium (K^{40}) emits gamma rays of a single energy at 1.46 MeV, whereas the uranium and thorium series emit gamma rays of various energies.

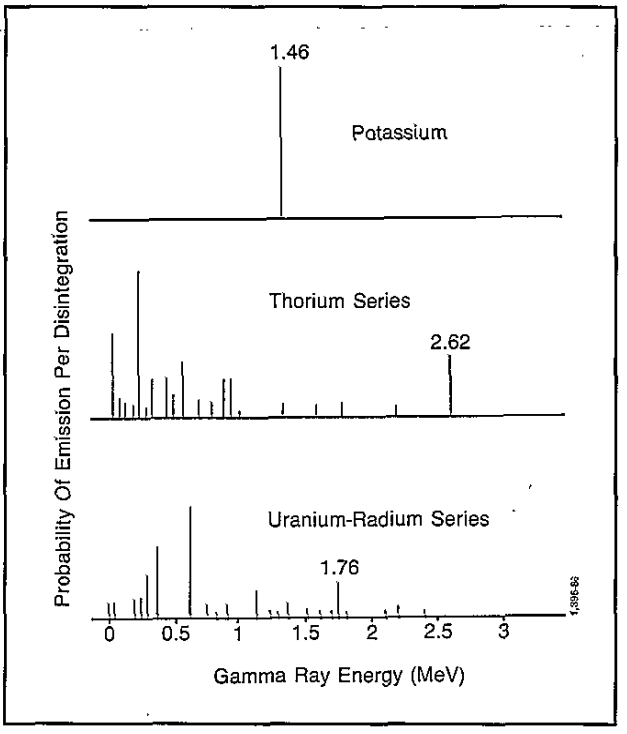

Fig. 3-8—Gamma ray emission spectra of radioactive minerals.

In passing through matter, gamma rays experience successive Compton-scattering collisions with atoms of the formation material, losing energy with each collision. After the gamma ray has lost enough energy, it is absorbed, by means of the photoelectric effect, by an atom of the formation. Thus, natural gamma rays are gradually absorbed and their energies degraded (reduced) as they pass through the formation. The rate of absorption varies with formation density. Two formations having the same amount of radioactive material per unit volume, but having different densities, will show different radioactivity levels; the less dense formations will appear to be slightly more radioactive. The GR log response, after appropriate corrections for borehole, etc., is proportional to the weight concentrations of the radioactive material in the formation:

$$GR = \frac{\Sigma\, \varrho_i\, V_i\, A_i}{\varrho_b}, \qquad \text{(Eq. 3-3)}$$

where

ϱ_i are the densities of the radioactive minerals,

V_i are the bulk volume factors of the minerals,

A_i are proportionality factors corresponding to the radioactivity of the mineral,

and

ϱ_b is the bulk density of the formation.

In sedimentary formations, the depth of investigation of the GR log is about 1 ft.

Equipment

The GR sonde contains a detector to measure the gamma radiation originating in the volume of formation near the sonde. Scintillation counters are now generally used for this measurement. They are much more efficient than the Geiger-Mueller counters used in the past. Because of its higher efficiency, a scintillation counter need only be a few inches in length; therefore, good formation detail is obtained. The GR log may be, and usually is, run in combination with most other logging tools and cased hole production services.

Calibration

The primary calibration standard for GR tools is the API test facility in Houston. A field calibration standard is used to normalize each tool to the API standard and the logs are calibrated in API units. The radioactivities in sedimentary formations generally range from a few API units in anhydrite or salt to 200 or more in shales.

Prior to the API calibration procedure, GR logs were scaled in micrograms of radium-equivalent per ton of formation. Conversions from these units to API units are shown in Table 3-1.

Table 3-1
Conversion from old units to API units for Schlumberger gamma ray logs.

Equipment	Old Unit	API Units Per Old Unit
GNT-F or -G Gamma Ray	1 μgm Ra-eq/ton	16.5
GNT-J, -K Gamma Ray, GLD-K	1 μgm Ra-eq/ton	11.7

1518-86

Borehole Correction Curves

The GR log deflection is a function not only of the radioactivity and density of the formations but also of hole conditions (hole diameter, mud weight, tool size, and tool position) since the material interposed between the counter and the formation absorb gamma rays. Chart Por-7 is used to make these borehole corrections. As might be expected, the corrections are quite significant in large boreholes and in heavy muds.

Many older GR logs were calibrated so that a 3⅝-in. sonde eccentric in a 10-in. uncased borehole filled with 10-lb/gal nonradioactive mud would read directly the true radioactivity of the formations. Chart Por-7, with some minor shifting, is applicable for logs calibrated in this manner.

Applications

The GR log is particularly useful for defining shale beds when the SP is distorted (in very resistive formations), when the SP is featureless (in freshwater-bearing formations or in salty mud; i.e., when $R_{mf} \approx R_w$), or when the SP cannot be recorded (in nonconductive mud, empty or air-drilled holes, cased holes). The bed boundary is picked at a point midway between the maximum and minimum deflection of the anomaly.

The GR log reflects the proportion of shale and, in many regions, can be used quantitatively as a shale indicator. It is also used for the detection and evaluation of radioactive minerals, such as potash or uranium ore. Its response, corrected for borehole effect, is practically proportional to the K_2O content, approximately 15 API units per 1% of K_2O. The GR log can also be used for delineation of nonradioactive minerals.

This traditional correlation log is part of most logging programs in both open and cased hole. Furthermore, because it is readily combinable with most other logging tools, it permits the accurate correlation of logs made on one trip into the borehole with those made on another trip.

THE NGS LOG

Like the GR log, the NGS natural gamma ray spectrometry log measures the natural radioactivity of the formations. Unlike the GR log, which measures only the total radioactivity, this log measures both the number of gamma rays and the energy level of each and permits the determination of the concentrations of radioactive potassium, thorium, and uranium in the formation rocks.

Physical Principle

Most of the gamma ray radiation in the earth originates from the decay of three radioactive isotopes: potassium 40 (K^{40}), with a half-life of 1.3×10^9 years; uranium 238 (U^{238}), with a half-life of 4.4×10^9 years; and thorium 232 (Th^{232}), with a half-life of 1.4×10^{10} years.

Potassium 40 decays directly to stable argon 40 with the emission of a 1.46-MeV gamma ray. However, uranium 238 and thorium 232 decay sequentially through a long sequence of various daughter isotopes before arriving at stable lead isotopes. As a result, gamma rays of many different energies are emitted and fairly complex energy spectra are obtained, as Fig. 3-8 shows. The characteristic peaks in the thorium series at 2.62 MeV and the uranium series at 1.76 MeV are caused by the decay of thallium 208 and bismuth 214, respectively.

It is generally assumed that formations are in secular equilibrium; that is, the daughter isotopes decay at the same rate as they are produced from the parent isotope. This means that the relative proportions of parent and daughter elements in a particular series remain fairly constant; so, by looking at the gamma ray population in a particular part of the spectrum it is possible to infer the population at any other point. In this way, the amount of parent isotope present can be determined.

Once the parent isotope population is known, the amount of nonradioactive isotope can also be found. The ratio of potassium 40 to total potassium is very stable and constant on the earth while, apart from thorium 232, the thorium isotopes are very rare and so can be neglected. The relative proportions of the uranium isotopes depend somewhat on their environment, and there is also a gradual change because of their different half-lives; at present, the ratio of uranium 238 to uranium 235 is about 137.

Measurement Principle

The NGS tool uses a sodium iodide scintillation detector contained in a pressure housing which, during logging, is held against the borehole wall by a bow spring.

Gamma rays emitted by the formation rarely reach the detector directly. Instead, they are scattered and lose energy through three possible interactions with the formation; the photoelectric effect, Compton scattering, and pair production. Because of these interactions and the response of the sodium iodide scintillation detector, the original spectra of Fig. 3-8 are degraded to the rather "smeared" spectra shown in Fig. 3-9.

The high-energy part of the detected spectrum is divided into three energy windows, W1, W2, and W3; each covering a characteristic peak of the three radioactivity series (Fig. 3-9). Knowing the response of the tool and the number of counts in each window, it is possible to determine the amounts of thorium 232, uranium 238, and potassium 40 in the formation. There are relatively few counts in the high-energy range where peak discrimination is best; therefore, measurements are subject to large statistical variations, even at low logging speeds. By including a contribution from the high-count rate, low-energy part of the spectrum (Windows W4 and W5), these high statistical variations in the high-energy windows can be reduced by a factor of 1.5 to 2. The statistics are further reduced by another factor of 1.5 to 2 by using a filtering technique that compares the counts at a particular depth with the previous values in such a way that spurious

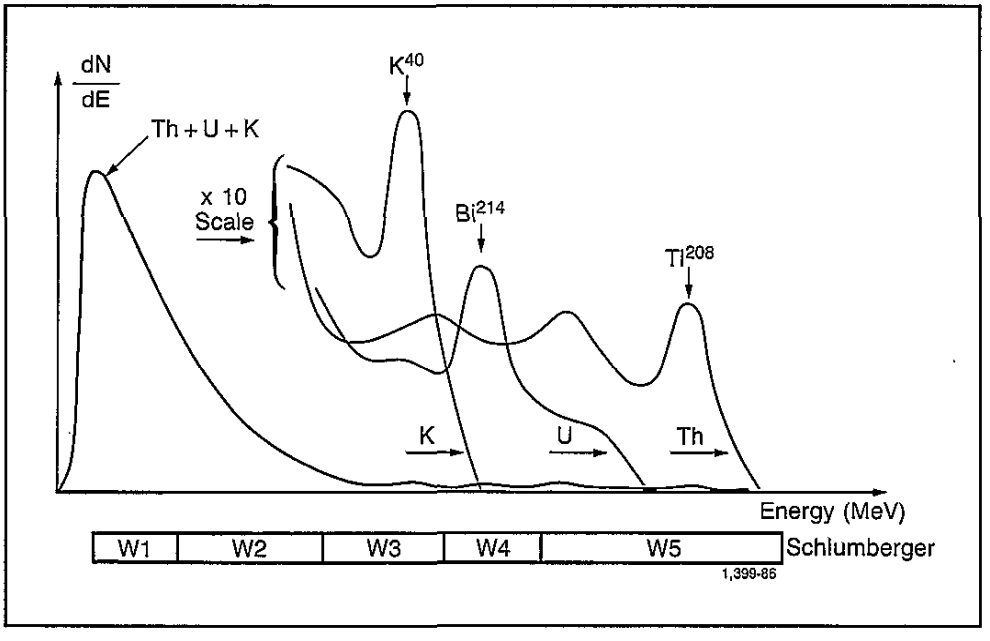

Fig. 3-9—Potassium, thorium, and uranium response curves (NaI crystal detector).

changes are eliminated while the effects of formation changes are retained. Normally, only the final filtered data are presented on film, but the unfiltered raw data are always recorded on tape.

Log Presentation

The NGS log provides a recording of the amounts (concentrations) of potassium, thorium, and uranium in the formation. These are usually presented in Tracks 2 and 3 of the log (Fig. 3-10). The thorium and uranium concentrations are presented in parts per million (ppm) and the potassium concentration in percent (%).

In addition to the concentrations of the three individual radioactive elements, a total (standard) GR curve is recorded and presented in Track 1. The total response is determined by a linear combination of the potassium, thorium, and uranium concentrations. This standard curve is expressed in API units. If desired, a "uranium-free" measurement (CGR) can also be provided. It is simply the summation of gamma rays from thorium and potassium only.

Borehole Correction Curves

The response of the NGS tool is a function not only of the concentration of potassium, thorium, and uranium but also of hole conditions (hole size and mud weight) and of the interactions of the three radioactive elements themselves.

Interpretation

The average concentration of potassium in the earth's crust is about 2.6%. For uranium, it is about 3 ppm; for thorium, it is about 12 ppm. Obviously, individual formations may have significantly greater or lesser amounts and specific minerals usually have characteristic concentrations of thorium, uranium, and potassium. Therefore, the curves of the NGS log can often be used individually or collectively to identify minerals or mineral type. Chart CP-19 shows a chart of potassium content compared with thorium content for several minerals; it can be used for mineral identification by taking values directly from the recorded curves.

Often, the result is ambiguous so other data are needed. In particular, the photoelectric absorption coefficient in combination with the ratios of the radioactive families are helpful: Th/K, U/K, and Th/U. Care needs to be taken when working with these ratios; they are not the ratios of the elements within the formation but rather the ratio of the values recorded on the NGS log, ignoring the units of measurement. Chart CP-18 compares the photoelectric absorption coefficient with the potassium content or the ratio of potassium to thorium for mineral identification.

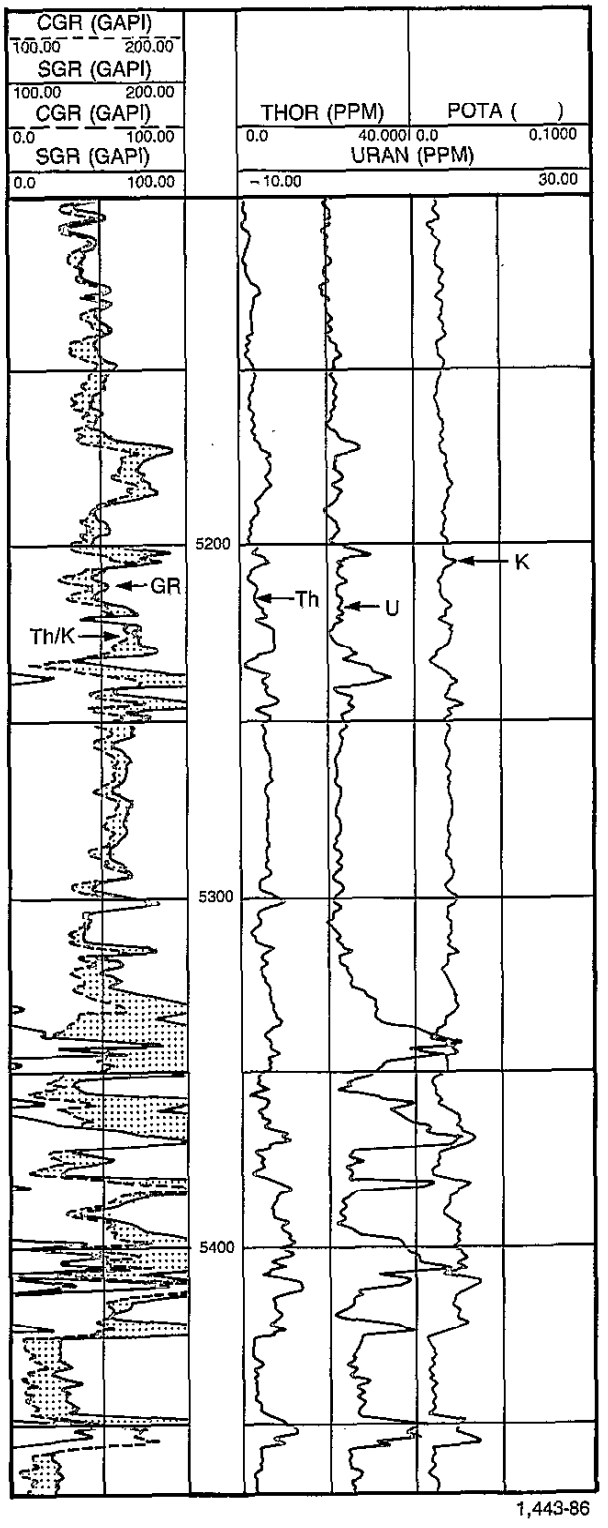

Fig. 3-10—NGS* natural gamma ray spectrometry log.

*Mark of Schlumberger

Applications

The NGS log can be used to detect, identify, and evaluate radioactive minerals. It also can be used to identify clay type and to calculate clay volumes. This, in turn, can provide insight into the source, the depositional environment, the diagenetic history, and the petrophysical characteristics (surface area, pore structure, etc.) of the rock.

The thorium and potassium response or the thorium-only response of the NGS log is often a much better shale indicator than the simple GR log or other shale indicators. Shaly-sand interpretation programs such as GLOBAL* and ELAN* can thereby benefit from its availability. The NGS log can also be used for correlation where beds of thorium and potassium content exist.

The combination of the NGS log with other lithology-sensitive measurements (such as photoelectric absorption, density, neutron, sonic) permits the volumetric mineral analysis of very complex lithological mixtures. In less complex mixtures, it allows the minerals to be identified with greater certainty and volumes to be calculated with greater accuracy.

The uranium response of the NGS log is sometimes useful as a "moved fluid" indicator for in-field wells drilled into previously produced reservoirs. Also, permeable streaks may have higher uranium salt content than less permeable intervals.

REFERENCES

1. Schlumberger, C., Schlumberger, M., and Leonardon, E.G.: "A New Contribution to Subsurface Studies by Means of Electrical Measurements in Drill Holes," *Trans.*, AIME (1934) **110**.
2. Doll, H.G.: "The SP Log: Theoretical Analysis and Principles of Interpretation," *Trans.*, AIME (1948) **179**.
3. Mounce, W.D. and Rust, W.M., Jr.: "Natural Potentials in Well Logging," *Trans.*, AIME (1944) **155**.
4. Wyllie, M.R.J.: "A Quantitative Analysis of the Electro-Chemical Component of the SP Curve," *J. Pet. Tech.* (1949) **1**.
5. Doll, H.G.: "The SP Log in Shaly Sands," *Trans.*, AIME (1950) **189**.
6. Wyllie, M.R.J.: "An Investigation of the Electrokinetic Component of the Self-Potential Curve," *Trans.*, AIME, **192**.
7. Gondouin, M. and Scala, C.: "Streaming Potential and the SP Log," *J. Pet. Tech.* (Aug. 1958).
8. Wyllie, M.R.J., deWitte, A.J., and Warren, J.E.: "On the Streaming Potential Problem," *Trans.*, AIME (1958) **213**.
9. Hill, H.J. and Anderson, A.E.: "Streaming Potential Phenomena in SP Log Interpretation," *Trans.*, AIME (1959) **216**.
10. Gondouin, M., Hill, H.J., and Waxman, M.H.: "A Tri-Chemical Component of the SP Curve," *J. Pet. Tech.* (March 1962).
11. Althaus, V.E.: "Electrokinetic Potentials in South Louisiana Tertiary Sediments," *The Log Analyst* (May-July 1967).
12. Pied, B. and Poupon, A.: "SP Base Line Shifts in Algeria," *Trans.*, 1966 SPWLA Annual Logging Symposium.
13. Segesman, F. and Tixier, M.P.: "Some Effects of Invasion on the SP Curve," *J. Pet. Tech.* (June 1959).
14. Segesman, F.: "New S.P. Correction Charts," *Geophys.* (Dec. 1962) **27**, No.6.
15. Worthington, A.E. and Meldau, E.F.: "Departure Curves for the Self-Potential Log," *J. Pet. Tech.* (Jan. 1958).
16. Poupon, A., Strecker, I., and Gartner, J.: "A Review of Log Interpretation Methods Used in the Niger Delta," *Trans.*, 1967 SPWLA Annual Logging Symposium.
17. Blanchard, A. and Dewan, J.T.: "Calibration of Gamma Ray Logs," *Pet. Eng.* (Aug. 1953).
18. *Recommended Practice for Standard Calibration and Form for Nuclear Logs*, American Petroleum Institute (Sept. 1959) API RP33.
19. Tixier, M.P. and Alger, R.P.: "Log Evaluation of Non-Metallic Mineral Deposits," *Trans.*, 1967 SPWLA Annual Logging Symmposium.
20. Tittman, J.: "Radiation Logging," *Fundamentals of Logging*, Univ. of Kansas (1956).
21. Baldwin, J.L., Quirein, J.A., and Serra, O.: "Theory and Practical Application of Natural Gamma Ray Spectroscopy," *Trans.*, 1980 SPWLA Annual Logging Symposium.
22. Quirein, J.A., Gardner, J.S., and Watson, J.T.: "Combined Natural Gamma Ray Spectral/Litho-Density Measurements Applied to Complex Lithologies," paper SPE 11143 presented at the 1982 SPE Annual Technical Conference and Exhibition.
23. Ellis, D.V.: "Correction of NGT Logs for the Presence of KCl and Barite Muds," *Trans.*, 1982 SPWLA Annual Logging Symposium.
24. *Log Interpretation Charts*, Schlumberger Well Services, Houston (1989).

4 Formation Water Resistivity Determination

Formation water, sometimes called connate water or interstitial water, is the water, uncontaminated by drilling mud, that saturates the porous formation rock. The resistivity of this formation water, R_w, is an important interpretation parameter since it is required for the calculation of saturations (water and/or hydrocarbon) from basic resistivity logs. There are several sources for formation water resistivity information. These include water catalogs, chemical analyses, the spontaneous potential (SP) curve, and various resistivity-porosity computations and crossplots.

R_w FROM WATER CATALOG

In many oil-producing regions, water catalogs have been published that list the resistivity data for many formation waters collected from different fields and different producing horizons of the region. The source of the R_w values may be the measurement of a water sample obtained from production, from a production test, or from a drillstem test. In some cases, the source might be well logs.

These catalogs are compiled and published by local geological or other professional societies, by oil companies or producers, by government entities, and by educational groups. They can verify R_w values obtained from the SP curve or from resistivity-porosity comparisons.

R_w FROM CHEMICAL ANALYSIS

Although direct measurement of formation water resistivity on a produced water sample is always preferred, sometimes only a chemical analysis of the water sample is available, even in catalog listings.

Methods do exist for deriving the electrical resistivity of a solution from its chemical analysis. Chart Gen-8 describes one method. It uses weighting coefficients to convert concentrations of individual ions into equivalent sodium chloride (NaCl) concentrations. The method is based on the work of Dunlap, Desai and Moore, and others.

From the derived equivalent NaCl concentration, R_w at any desired temperature can be obtained from Chart Gen-9.

R_w FROM THE SP

In many cases, a good value of R_w can easily be found from the SP curve recorded in clean (nonshaly) formations. The static SP (SSP) value in a clean formation is related to the chemical activities (a_w and a_{mf}) of the formation water and mud filtrate through the formula:

$$\text{SSP} = -K \log \frac{a_w}{a_{mf}} . \qquad \text{(Eq. 4-1)}$$

For NaCl solutions, $K = 71$ at 77° F (25° C); K varies in direct proportion to temperature:

$$K = 61 + 0.133\ T_{°F} . \qquad \text{(Eq. 4-2)}$$

$$K = 65 + 0.24\ T_{°C} .$$

For pure NaCl solutions that are not too concentrated, resistivities are inversely proportional to activities (Fig. 4-1). However, this inverse proportionality does not hold exactly at high concentrations or for all types of waters. Therefore, equivalent resistivities R_{we} and R_{mfe}, which by definition are inversely proportional to the activities ($R_{weq} = 0.075/a_w$ at 77° F), are used. R_{we} is the equivalent formation water resistivity and R_{mfe} is the equivalent mud filtrate resistivity. Eq. 4-1 can then be written in resistivity terms as:

$$\text{SSP} = -K \log \frac{R_{mfe}}{R_{we}} . \qquad \text{(Eq. 4-3)}$$

Knowing the formation temperature, the static SP value recorded opposite a porous, permeable, nonshaly formation can be transformed into the resistivity ratio R_{mfe}/R_{we}. Chart SP-1 performs this translation graphically.

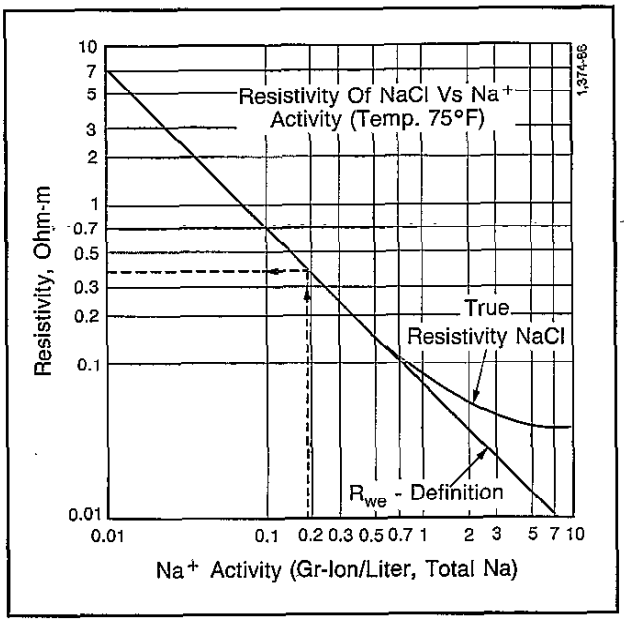

Fig. 4-1—Activity of Na^+ ions vs. NaCl resistivity (Ref. 7).

Determination of R_{mfe}

With the ratio R_{mfe}/R_{we} now determined and the resistivity, R_{mf}, of a sample of mud filtrate measured, the equivalent formation water resistivity, R_{we}, is easily calculated. However, the mud filtrate resistivity reported on the log heading is its actual resistivity, not its equivalent resistivity. To convert the measured mud filtrate resistivity, R_{mf}, into an equivalent mud filtrate resistivity R_{mfe}, the following rules are employed:

1. For predominately NaCl muds
   a. If R_{mf} at 75° F is greater than 0.1 ohm-m, use $R_{mfe} = 0.85\ R_{mf}$ at formation temperature. This relationship is based on measurements made on many typical muds.
   b. If R_{mf} at 75° F is less than 0.1 ohm-m, use the NaCl (solid) curves of Chart SP-2 to derive a value of R_{mfe} from the measured R_{mf} value corrected to formation temperature from Chart Gen-9.
2. For freshwater gypsum muds, the dashed curves of Chart SP-2 are used to convert R_{mf} to R_{mfe}.
3. Lime-based muds, despite their name, usually have a negligible amount of calcium in solution and are treated as regular mud (see Rule 1).

Determination of R_w

Chart SP-2 is also used to convert R_{we} to R_w. The solid curves, for very saline brines, were derived from laboratory data on pure NaCl solutions. These solid curves are used for R_{we} and R_w values less than about 0.1 ohm-m; they assume that in formation waters of this salinity that NaCl is the predominate salt. The dashed curves are derived from a study of a large number of relatively fresh formation waters from oil-producing regions of the western hemisphere. Their departure from the linear relationship of $R_w = R_{we}$ reflects the increasing effect of multivalent cations with the decreasing concentration of these waters. It is assumed that the chloride ion is still the predominant anion in these waters and that the K value associated with NaCl solutions is still reasonably applicable.

ENVIRONMENTAL CORRECTIONS AND PRECAUTIONS

The static SP value can be obtained directly from the SP curve if the bed is clean, thick, porous, permeable, and only moderately invaded; and if the formation water is saline and the drilling mud is not too resistive. These conditions are not always met. When they are not, the recorded SP deflection (in millivolts) must be corrected. Charts SP-3 and SP-4 correct the recorded SP curve to a static SP value for bed thickness, hole size, invasion, and resistivity contrasts.

The use of the SP curve for R_w determination requires a clean, nonshaly bed. Charts SP-3 and SP-4 do not correct for shaliness.

It is assumed that the recorded SP curve seldom contains an electrokinetic potential component. Although this is generally the case, it may not always be so. Very low permeability formations, depleted-pressure formations, or the use of very heavy drilling mud may give rise to a significant electrokinetic potential. In these cases, an R_w value derived from the SP curve will probably be too low. Other sources of R_w data should be explored.

Also, when salts other than NaCl are present in significant quantities, where SP baseline shifts exist, or where R_w is variable, certain precautions are required in calculating R_w from the SP log.

SALTS OTHER THAN NaCl

When the formation water and/or the mud filtrate contain Ca^{++} and Mg^{++} ions in addition to Na^+ ions, the SSP value is given, within a few millivolts, by

$$SSP = -K \log \frac{(a_{Na} + \sqrt{a_{Ca} + a_{Mg}})_w}{(a_{Na} + \sqrt{a_{Ca} + a_{Mg}})_{mf}}, \quad \text{(Eq. 4-4)}$$

where a_{Na}, a_{Ca}, and a_{Mg} are the ionic activities of Na, Ca, and Mg in the formation water and in the mud filtrate. (It is assumed here that the chloride ion is the predominant anion.)

If the concentrations of Na, Ca, and Mg ions are known, the activity of a solution at 75° F (that is, $a_{Na} + \sqrt{a_{Ca} + a_{Mg}}$) can be determined from Fig. 4-2.

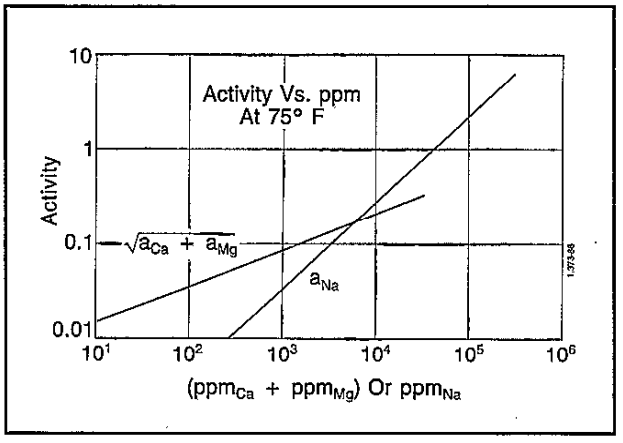

Fig. 4-2—Activity vs. concentration, Na^+ and Ca^+ plus Mg^+.

In fresh formation waters, salts other than NaCl may become more important. In these cases, the R_w-R_{we} relationship may be quite different from that for NaCl. Fig. 4-3 shows R_w-R_{we} curves at 25° C (77° F) for solutions of several different salts. With one exception, these curves are laboratory-derived for pure solutions. The exception is an R_w-R_{we} curve empirically determined for average fresh waters. This curve corresponds to the dashed curves in Chart SP-2.

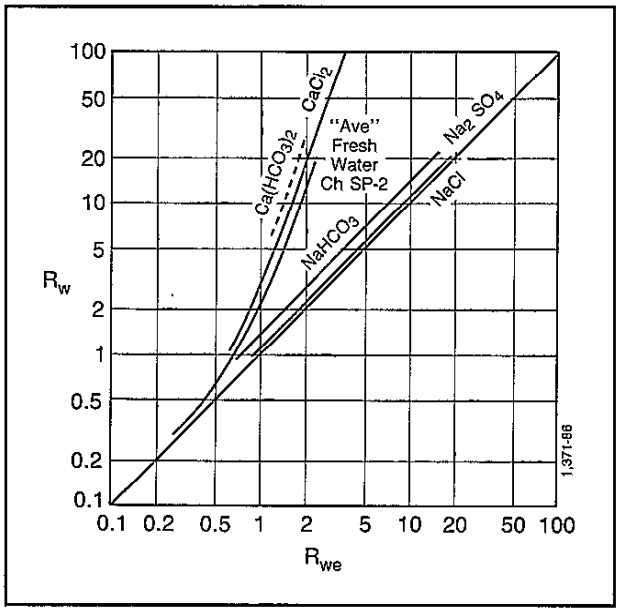

Fig. 4-3—R_w vs. R_{we} for solutions of several salts.

In most formation waters, there is enough NaCl that the K value for NaCl (71 at 77° F) can be used. However, when certain salts are predominant in very fresh waters, the K value may be affected. For example, if both filtrate and formation water were pure sodium bicarbonate solutions ($NaHC0_3$), K would be 56 (instead of the NaCl value of 71) at 77° F. For potassium chloride (KCl) solutions the K would be about 60 at 77° F. Potassium bicarbonate ($KHC0_3$) solutions have a K of about 45 at 77° F.

If extensive logging work is to be done in an area where unusual salts predominate in the formation water, empirical K values (for the type mud used) and empirical R_w-R_{we} charts can be developed for that area.

SP ANOMALIES

Determination of R_w is complicated by imperfect cationic membranes, R_w changes occurring below the oil-water contact, and long vertical transitions from fresh to salt water. For example, in some special areas, notably in Algeria and Nigeria and in mountainous areas, large variations in R_w from one bed to another, or even across oil-water contacts, result in SP anomalies and baseline shifts that make interpretation difficult. Fortunately, it is often possible to recognize and account for this unusual SP behavior and to derive useful R_w values. To do so, the SP curve must be carefully analyzed.

Two general types of SP anomalies are found, depending on how the waters of different resistivities are separated:

- When a good cationic membrane, such as a thin shale streak, separates the two formation waters, there should be no baseline shift and the SP deflections reflect the R_w changes between the two intervals of differing waters.
- If no membrane separates the two waters, such as oil and salt water overlying fresh water in the same permeable zone, there is no change in SP deflection over the zone; there is a large baseline shift from the top to the base of the zone.

An independent means of identifying shale (GR or porosity log crossplot) may be necessary to aid SP interpretation in these cases.

R_w FROM RESISTIVITY-POROSITY LOGS

R_{wa} Log

The R_{wa} log is computed as

$$R_{wa} = \frac{R_t}{F}, \qquad \text{(Eq. 4-5)}$$

where R_t is from a deep-investigation resistivity log, and F is computed from a porosity log reading.

For clean, water-bearing zones, $R_t = R_0 = FR_w$ and the R_{wa} value derived from Eq. 4-5 is equal to R_w. A continuous plot of R_{wa} values over many potential reservoir formations should reveal a rather consistent lower limit to this computed R_{wa} value. If it does, that R_{wa} value is probably the formation water resistivity R_w.

This technique works best over intervals in which the formation water resistivity remains constant or changes only gradually. Fortunately, in most oil-producing provinces this is usually the case, particularly at deeper depths.

R_{wa}-SP Plots

At shallow depths, R_w can change rapidly and makes determination of R_w from the SP curve difficult and uncertain. In such a case, a plot of R_{wa} on a logarithmic scale versus SP deflection on a linear scale is valuable for estimating R_w; it may also point out hydrocarbon-bearing zones.

Fig. 4-4 is a plot of R_{wa} versus SP values from an interval where the salinity changes rapidly. Most points fall in a trend parallel to and just above the R_w line (R_w as computed from the SP curve using Charts SP-1 and SP-2), which indicates slightly greater than average amounts of salts other than NaCl. Points 5 and 11 lie well above the main trend and probably represent hydrocarbon-bearing formations.

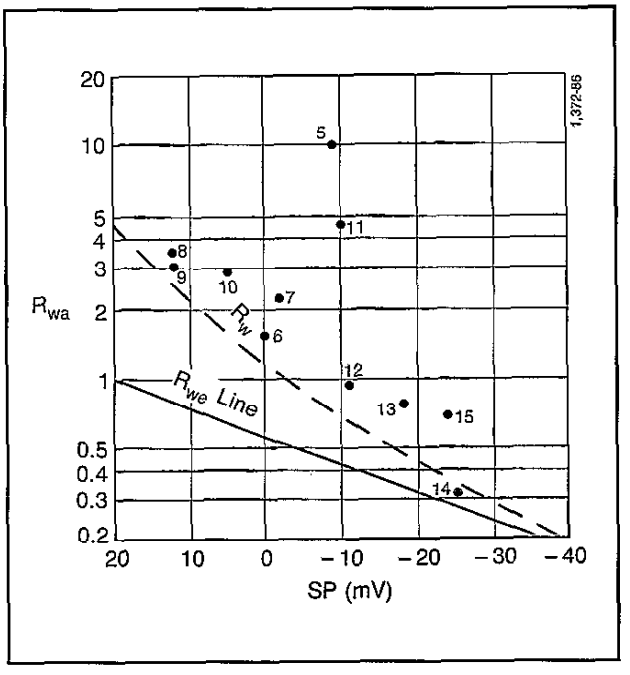

Fig. 4-4—R_{wa} vs. SP for determining R_w and distinguishing hydrocarbon-bearing zones in intervals of changing R_w.

RESISTIVITY-POROSITY PLOTS

Various resistivity-porosity plots, such as resistivity-sonic, resistivity-density, or resistivity-neutron, are described in Chapter 8. R_w can be derived from the slope of the 100% water-saturation line as determined on any one of these plots. As normally plotted, the 100% water-saturation line is the focus of the points falling to "northwest" of the resistivity-porosity plot. With porosity (and formation factor) and true resistivity known, R_w can be calculated ($R_w = R_0/F$).

R_w from R_{xo} and R_t

Equations for S_w and S_{xo} for clean formations given in Chapter 2 can be combined to give

$$\frac{R_{xo}}{R_t} = \left(\frac{S_w}{S_{xo}}\right)^2 \frac{R_{mf}}{R_w}. \quad \text{(Eq. 4-6)}$$

The value of R_{xo}/R_t is equal to R_{mf}/R_w in water zones where S_w and S_{xo} are 1 (i.e., 100%). Thus, by computing R_{xo}/R_t over an interval containing clean, invaded water sands, the value of R_{mf}/R_w can be found. Then, knowing R_{mf} (as reported on the log heading), R_w can be determined.

An equivalent quicklook solution can be obtained by an overlay technique using logarithmically scaled R_t and R_{xo} logs. If one log is placed over the other and shifted so that the two curves coincide in clean water-bearing zones, the 1-ohm-m line on the R_{xo} log grid will lie on the R_t grid at a value equal to R_w/R_{mf}. Knowing R_{mf}, R_w can then be easily calculated.

A similar result can be obtained by simply crossplotting values from an R_{xo} log (such as MicroSFL* or Proximity log) versus corresponding values from a deep resistivity log (such as deep induction log) over an interval containing some water sands. A line through the points corresponding to the highest values of R_{xo}/R_t provides an estimate of R_{mf}/R_w.

REFERENCES

1. Dunlap, H.F. and Hawthorne, R.R.: "The Calculation of Water Resistivities From Chemical Analysis," *Trans.*, AIME (1951) **192.**
2. Moore, E.J., Szasz, S.E., and Whitney, B.F.: "Determining Formation Water Resistivity From Chemical Analysis," *J. Pet. Tech.* (March 1966).
3. Moore, E.J.: "A Graphical Description of New Methods for Determining Equivalent NaCl Concentration From Chemical Analysis," *Trans.*, 1966 SPWLA Annual Logging Symposium.
4. Desai, K.P. and Moore, E.J.: "Equivalent NaCl Solutions From Ionic Concentrations," *The Log Analyst* (May-June 1969) **10**, No. 3.
5. Segesman, F.: "New S. P. Correction Charts," *Geophys.* (Dec. 1962) **27**, No. 6.
6. Worthington, A.E. and Meldau, E.F.: "Departure Curves for the Self-Potential Log," *J. Pet. Tech.* (Jan. 1958).
7. Gondouin, M., Tixier, M.P., and Simard, G.L.: "An Experimental Study of the Influence of the Chemical Composition of Electrolytes on the S. P. Curve," *J. Pet. Tech.* (Feb. 1957).
8. Poupon, A., Strecker, I., and Gartner, J.: "A Review of Log Interpretation Methods Used in the Niger Delta," *Trans.*, 1967 SPWLA Annual Logging Symposium.
9. Cox, J.W. and Raymer, L.L.: "The Effect of Potassium-Salt Muds on Gamma Ray and Spontaneous Potential Measurements," *Trans.*, 1976 SPWLA Annual Logging Symposium.
10. *Log Interpretation Charts*, Schlumberger Well Services, Houston (1989).

5 Porosity Logs

Rock porosity can be obtained from the sonic log, the density log, or the neutron log. For all these devices, the tool response is affected by the formation porosity, fluid, and matrix. If the fluid and matrix effects are known or can be determined, the tool response can be related to porosity. Therefore, these devices are often referred to as porosity logs.

All three logging techniques respond to the characteristics of the rock immediately adjacent to the borehole. Their depth of investigation is very shallow — only a few inches or less — and therefore generally within the flushed zone.

Other petrophysical measurements, such as microresistivity or nuclear magnetism or electromagnetic propagation, are sometimes used to determine porosity. However, these devices are also greatly influenced by the fluid saturating the rock pores. For that reason, they are discussed elsewhere.

SONIC LOGS

In its simplest form, a sonic tool consists of a transmitter that emits a sound pulse and a receiver that picks up and records the pulse as it passes the receiver. The sonic log is simply a recording versus depth of the time, t, required for a sound wave to traverse 1 ft of formation. Known as the interval transit time, transit time, Δt or slowness, t is the reciprocal of the velocity of the sound wave. The interval transit time for a given formation depends upon its lithology and porosity. This dependence upon porosity, when the lithology is known, makes the sonic log very useful as a porosity log. Integrated sonic transit times are also helpful in interpreting seismic records. The sonic log can be run simultaneously with many other services.

Principle

The propagation of sound in a borehole is a complex phenomenon. It is governed by the mechanical properties of several separate acoustical domains. These include the formation, the borehole fluid column, and the logging tool itself.

The sound emanated from the transmitter impinges on the borehole wall. This establishes compressional and shear waves within the formation, surface waves along the borehole wall, and guided waves within the fluid column.

In the case of well logging, the borehole wall, formation bedding, borehole rugosity, and fractures can all represent significant acoustic discontinuities. Therefore, the phenomena of wave refraction, reflection, and conversion lead to the presence of many acoustic waves in the borehole when a sonic log is being run. It is not surprising, in view of these considerations, that many acoustic energy arrivals are seen by the receivers of a sonic logging tool. The more usual energy arrivals are shown in the acoustic waveform displays of Fig. 5-1. These waveforms were recorded with an array of eight receivers located 8 to 11½ ft from the transmitter. The various wave packets have been labeled. Although the wave packets are not totally separated in time at this spacing, the distinct changes corresponding to the onset of the formation compressional and shear arrivals and the Stoneley arrival can be observed.

The first arrival or compressional wave is one that has traveled from the transmitter to the formation as a fluid pressure wave, has been refracted at the borehole wall, has traveled within the formation at the compressional wave velocity of the formation, and has traveled back to the receiver as a fluid pressure wave.

The shear wave is one that has traveled from the transmitter to the formation as a fluid pressure wave, has traveled within the formation at the shear wave velocity of the formation, and has traveled back to the receiver as a fluid pressure wave.

The mud wave (not strongly evident in these wavetrains) is one that has traveled directly from transmitter to receiver in the mud column at the compressional wave velocity of the borehole fluid.

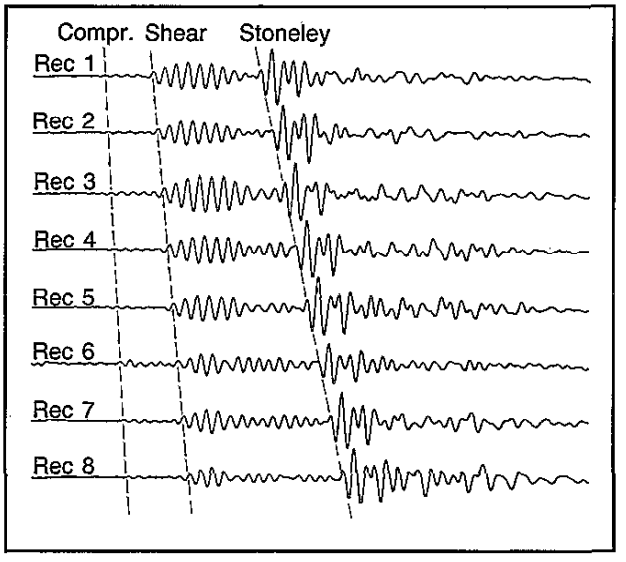

Fig. 5-1—Example waveforms from the eight-receiver Array-Sonic tool.

The Stoneley wave is one of large amplitude that has traveled from transmitter to receiver with a velocity less than that of the compressional waves in the borehole fluid. The velocity of the Stoneley wave is dependent upon the frequency of the sound pulse, hole diameter, formation shear velocity, densities of the formation and fluid, and fluid compressional wave velocity.

Equipment

There are currently three sonic tools in use: the BHC* borehole compensated sonic tool, the LSS* long-spaced sonic tool, and the Array-Sonic* tool. Although the entire sonic waveform can now be recorded with any of these tools, only the Array-Sonic tool has been designed to provide full-waveform recording as a standard feature.

Nearly all BHC logs recorded in the past provide only a measurement of formation compressional interval transit time, t, accomplished through first motion detection at the receiver. In other words, the receiver triggers on the first arrival of compressional energy.

As shown in Fig. 5-2, the BHC system uses one transmitter above and one transmitter below two pairs of sonic receivers. This sonde substantially reduces the spurious effects of hole-size changes and errors from sonde tilt. When one of the transmitters is pulsed the time elapsed between detection of the first arrival at the two corresponding receivers is measured.

The speed of sound in the sonic sonde and in the drilling mud is less than that in the formations. Accordingly, the first arrivals of sound energy at the receivers correspond to sound-travel paths in the formation near the borehole wall.

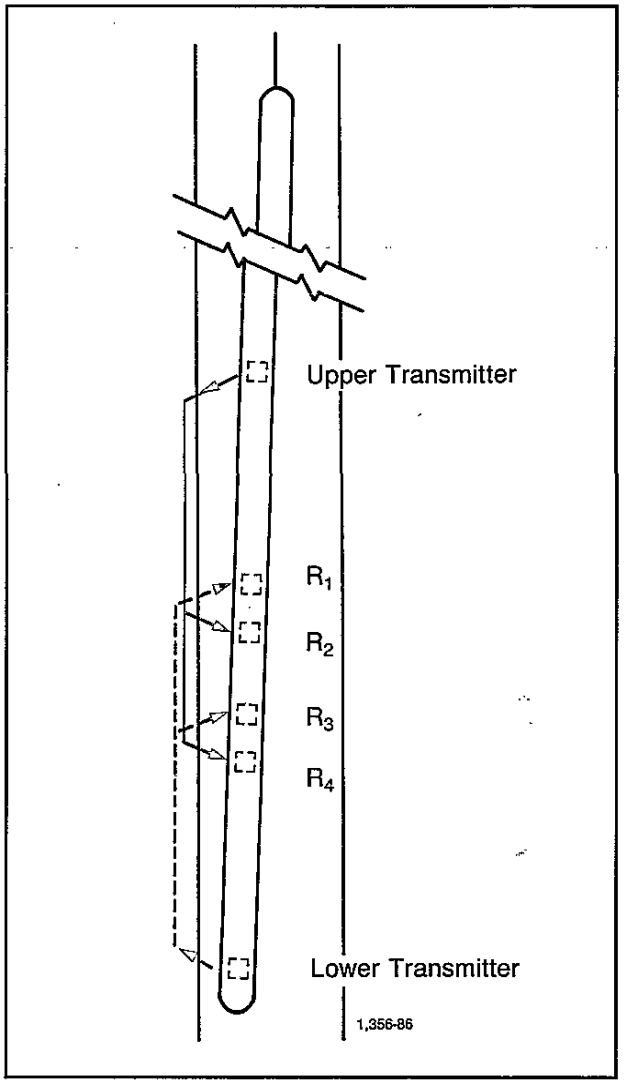

Fig. 5-2—Schematic of BHC sonde, showing ray paths for the two transmitter-receiver sets. Averaging the two Δt measurements cancels errors from sonde tilt and hole-size changes. (Ref. 2)

The BHC tool transmitters are pulsed alternately, and t values are read on alternate pairs of receivers. The t values from the two sets of receivers are averaged automatically by a computer at the surface for borehole compensation. The computer also integrates the transit-time readings to obtain total travel times (see Fig. 5-3).

Sometimes the first arrival, although strong enough to trigger the receiver nearer the transmitter, may be too weak by the time it reaches the far receiver to trigger it. Instead, the far receiver may be triggered by a different, later arrival in the sonic wave train, and the travel time measured on this pulse cycle will then be too large. When this occurs, the sonic curve shows a very abrupt and large

*Mark of Schlumberger

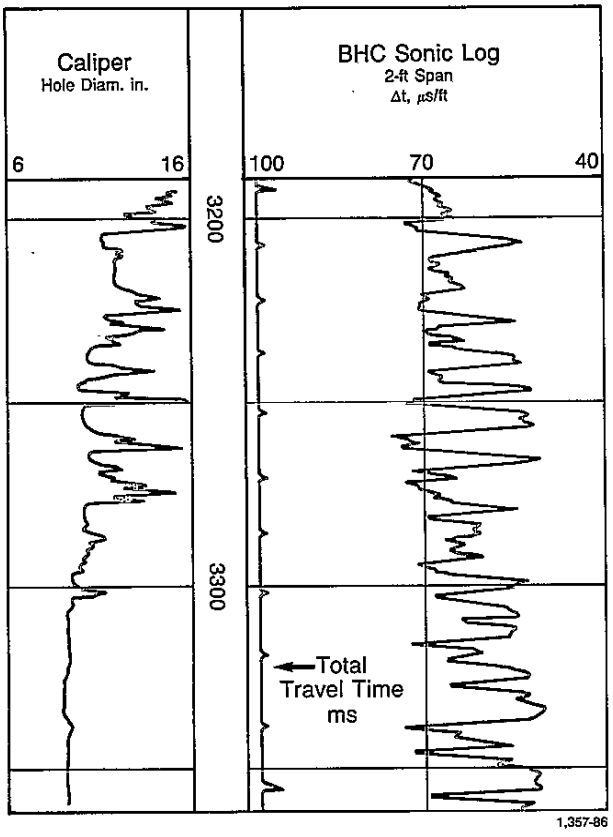

Fig. 5-3—Presentation of sonic log. (Ref. 3)

excursion towards a higher t value; this is known as cycle skipping. Such skipping is more likely to occur when the signal is strongly attenuated by unconsolidated formations, formation fractures, gas saturation, aerated muds, or rugose or enlarged borehole sections.

In early studies of velocity logging, the rock surrounding the wellbore was regarded as an infinite homogeneous medium for the propagation of sound waves. It is now apparent that in some shales a lateral velocity gradient exists. Sound waves travel at lower speeds near the borehole; at some greater distance from the borehole, they propagate at the true speed of sound in the shale. Similar variations may exist in the radial velocity profile in some unconsolidated rocks and in permafrost.

In large-diameter boreholes, it is possible to have a mud wave arrival at the near receiver before the formation signal. This problem is particularly prevalent at shallower depths where sonic logs are often run for seismic purposes.

In all these cases, a sonic tool with long spacing is required to provide a correct measurement of the velocity in the nonaltered zone. When the receivers are far enough from the transmitter, the first arrival is not the refracted ray traveling just inside the borehole wall but a wave penetrating beyond the borehole into the faster nonaltered zone.

LSS sonic tools, with transmitter-receiver spacings of 8 ft and 10 ft or 10 ft and 12 ft, are available. They measure the interval transit time of the formation at a much greater depth into the formation than the usual BHC sonic tool. This tool is more likely to yield a measurement free from the effects of formation alteration, relaxation damage (from drilling process), and enlarged borehole. These more accurate measurements are always desirable when the sonic data are to be used for seismic purposes. Fig. 5-4 compares the transit time recorded with an LSS tool to that from a standard-spacing tool in a formation with alteration.

Using the standard BHC system for borehole compensation with an LSS sonde would make the tool excessively long. An alternate solution called "depth-derived" borehole compensation is used.

The LSS sonde has two transmitters and two receivers arranged as shown in Fig. 5-5. Readings are taken at two different depth positions of the sonde: once when the two receivers straddle the measure point depth and once when the two transmitters straddle the measure point depth.

$$\text{First } t \text{ reading} = T_1 \rightarrow R_1 - T_1 \rightarrow R_2$$

$$\text{Second } t \text{ reading} = T_1 \rightarrow R_2 - T_2 \rightarrow R_2$$

The first t reading is memorized until the sonde has reached the position to make the second t reading, then both are averaged to obtain the borehole compensated measurement.

$$t = \frac{\text{memorized first } t \text{ reading} + \text{second } t \text{ reading}}{2 \times \text{span}}$$

where span is the distance (2 ft) between a pair of receivers.

Assuming the two sonde position depths are accurately known and the sonde tilting is similar for the two positions, the depth-derived borehole compensated system is equivalent to the standard BHC system. Use of the upper transmitter and receiver yields an 8-ft—10-ft sonic t measurement, and use of the lower transmitter and receiver yields a 10-ft—12-ft sonic t measurement.

The Array-Sonic service provides all measurements of the BHC and LSS logs and, in addition, provides several other features. The tool contains two broadband (5 to 18 kHz) piezoelectric transmitters spaced 2 ft apart. Two piezoelectric receivers are located 3 ft and 5 ft from the upper transmitter. These receivers have a dual role. In open hole, they are used in conjunction with the two transmitters to make standard short-spaced 3-ft—5-ft and 5-ft—7-ft depth-derived, borehole-compensated t logs. In cased wells, they are used to make standard 3-ft ce-

ment bond logs (CBL) and 5-ft Variable Density* logs (VDL).

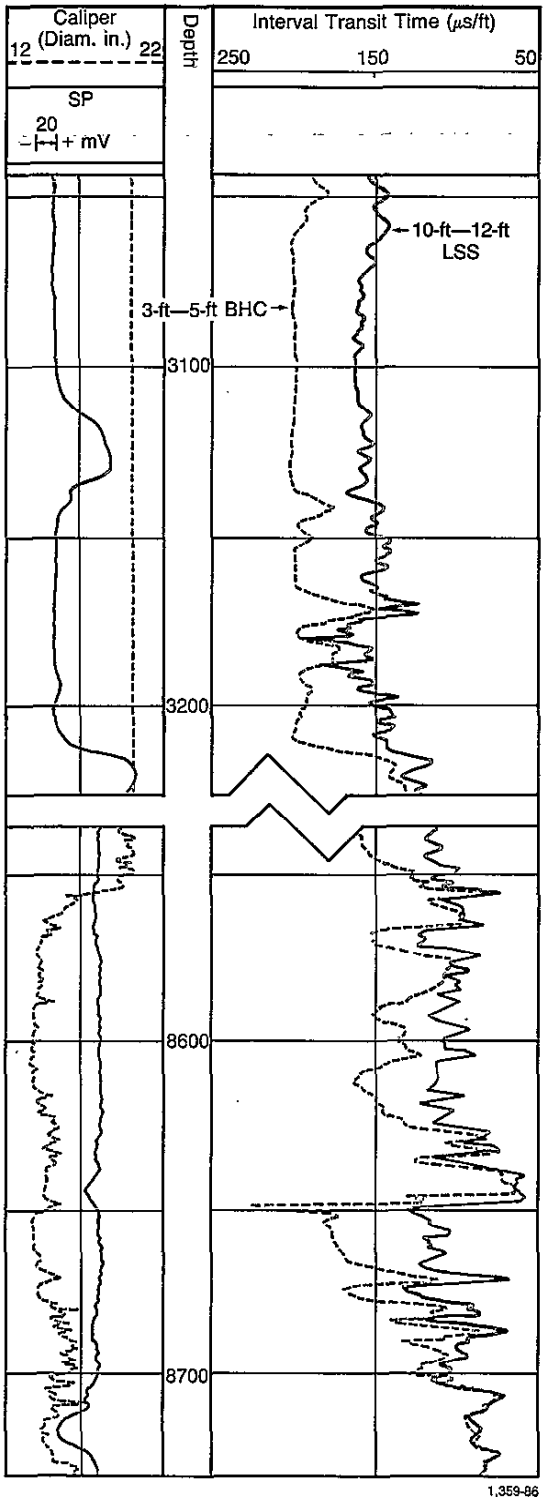

Fig. 5-4—Comparison of LSS and BHC sonic logs in enlarged holes.

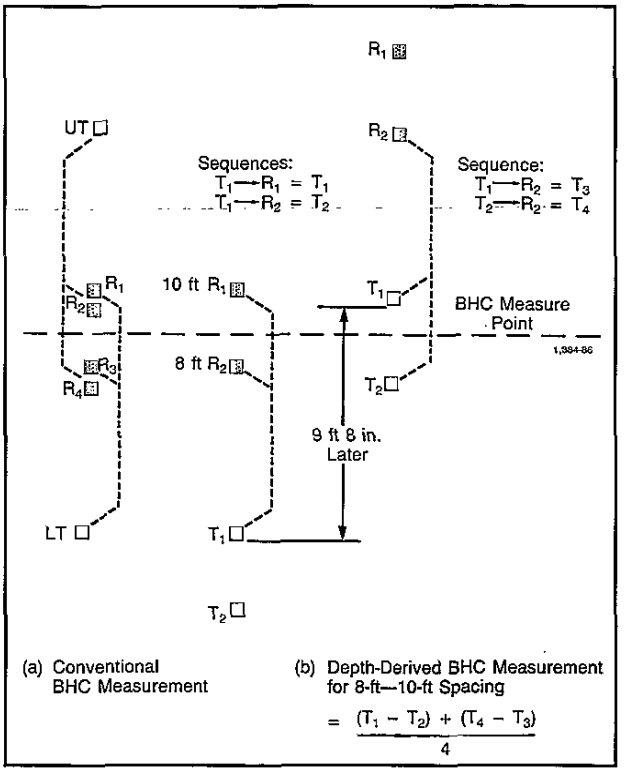

Fig. 5-5—Depth-derived compensation for long-spaced sonic tool.

The Array-Sonic tool (Fig. 5-6) also contains an array of eight wideband piezoelectric receivers. The receivers are spaced 6 in. apart with the closest receiver 8 ft from the upper transmitter. Two of these receivers, Receivers 1 and 5, spaced 2 ft apart, can be used for making standard long-spaced 8-ft—10-ft and 10-ft—12-ft depth-derived borehole-compensated t logs. Measurement hardware also exists, consisting of a closely spaced transmitter-receiver pair, to make a continuous mud t log. Borehole fluid is drawn through this measurement section as the tool is moved during logging.

The eight-array receiver outputs and the two from the sonic sonde are multiplexed with the mud t receiver output and transmitted to the surface in either analog or digital form. An example of a set of waveforms digitized from the eight-receiver array is shown in Fig. 5-1.

The array waveforms are processed at the wellsite with the CSU* surface instrumentation and array processor or at the computing center using a true full-waveform technique.

Rather than recording just the compressional wave component, a waveform-processing technique is used to find and analyze all propagating waves in the composite waveform. This slowness-time coherence technique (STC)

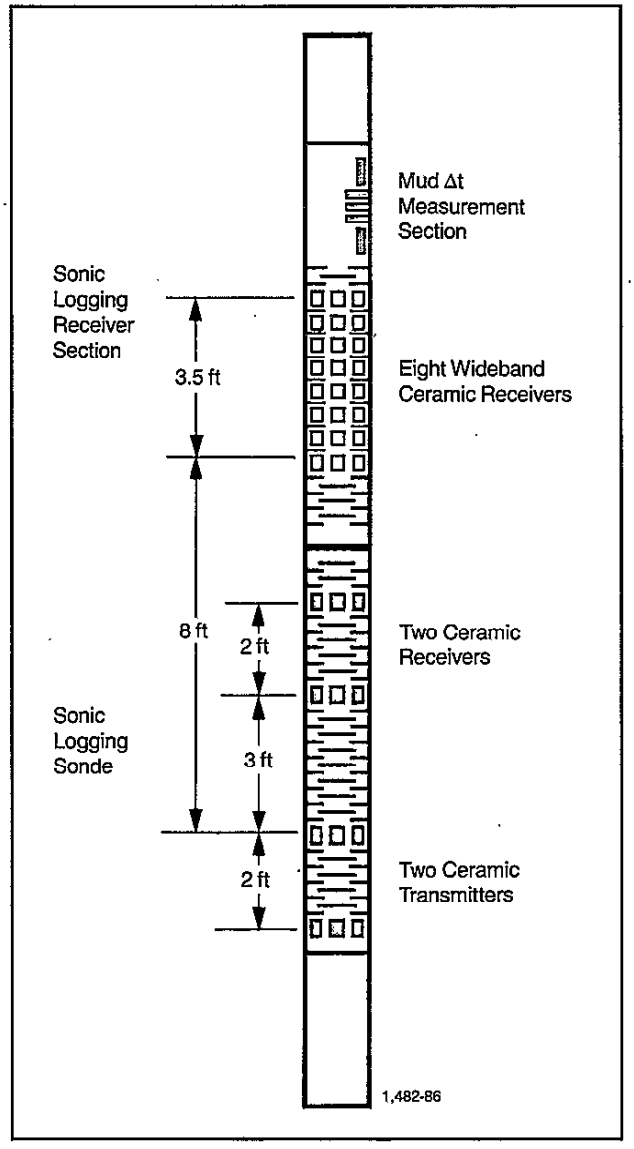

Fig. 5-6—Multipurpose sonic sonde configuration.

uses a semblance algorithm, similar to that employed in seismic processing, to detect arrivals that are coherent across the array of receiver waveforms and to estimate their interval transit time.

Applying this semblance algorithm to the waveforms of Fig. 5-1 produces the coherence map shown in Fig. 5-7. Regions of large coherence correspond to the compressional, shear, and Stoneley arrivals. The apex of each region defines the slowness of that wave. This process is repeated for each set of array waveforms acquired by the tool while moving up the hole and is used to produce a log. A typical log determined in this fashion is shown in Fig. 5-8. Compressional transit time, t_c; shear transit time, t_s; and Stoneley transit time, t_{St}, are presented. In a slow formation, the tool obtains real-time measurements of compressional, Stoneley, and mud wave velocities. Shear wave values are then derived from these velocities.

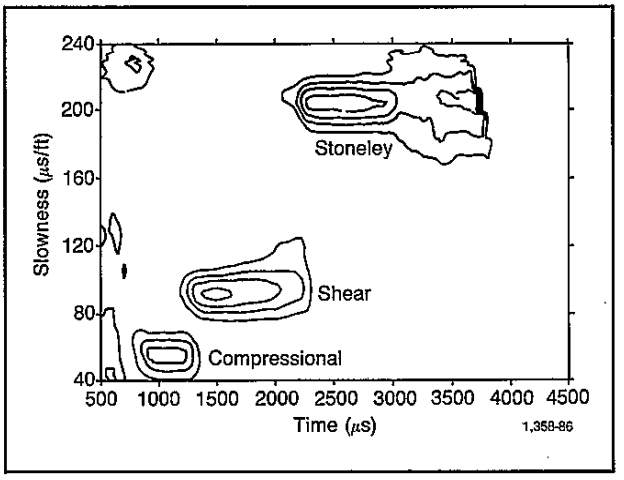

Fig. 5-7—Contour plot of the STC coherence function.

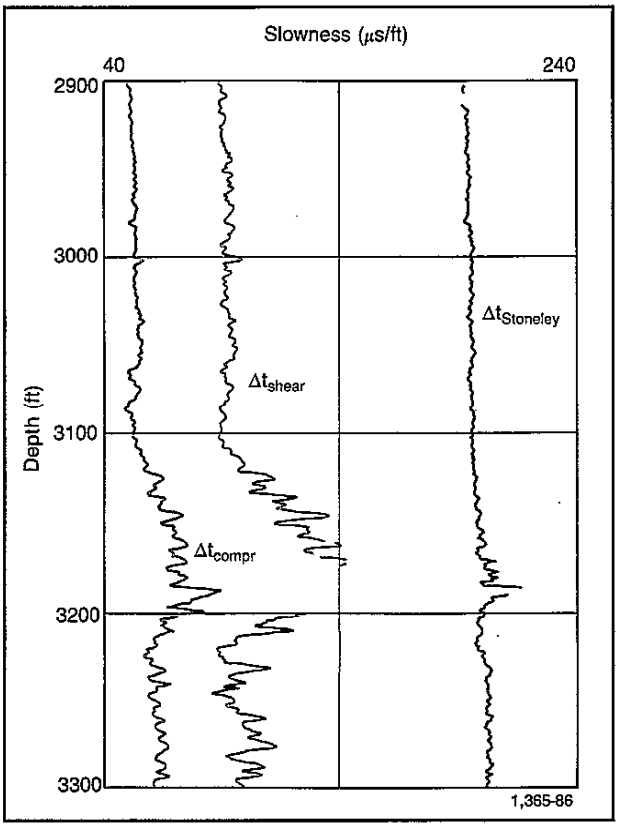

Fig. 5-8—Log of classified component slownesses.

Because of the number of receivers, the full-wavetrain recording, and the digital transmission, the Array-Sonic tool can provide a large amount of acoustic information. Among these data are:

- 3-ft—5-ft t_c (first-motion compressional transit time)
- 5-ft—7-ft t_c
- 8-ft—10-ft t_c
- 10-ft—12-ft t_c
- t_c (wavetrain-derived compressional transit time)
- t_s (wavetrain-derived shear transit time)
- t_{St} (wavetrain-derived Stoneley transit time)
- 6-in. t_c (first-motion compressional transit time)
- Mud transit time
- Amplitude logging
- Energy analysis
- Frequency analysis
- t_c, t_s, and t_{St} through casing
- CBL/VDL data through casing

Log Presentation

Sonic velocities in common formation lithologies range from about 6,000 to 23,000 ft/sec. To avoid small decimal fractions the reciprocal of velocity, t, is recorded (English scale) in microseconds per foot (μs/ft) over a range from about 44 μs/ft for zero-porosity dense dolomite to about 190 μs/ft for water.

The interval transit time is usually recorded on a linear scale in Tracks 2 and 3 of the log (Fig. 5-3). The integrated travel time is given by a series of pips, usually recorded at the left edge of Track 2. Each small pip indicates an increase of 1 ms of the total travel time; a large pip is recorded every 10 ms. The travel time between two depths is obtained by simply counting the pips. The integrated travel time is useful for seismic purposes.

Sonic Velocities In Formations

In sedimentary formations the speed of sound depends on many parameters; principally, it depends on the rock matrix material (sandstone, limestone, dolomite ...) and on the distributed porosity. Ranges of values of sonic velocity and transit time for common rock matrix materials and casing are listed in Table 5-1.

The values listed are for nonporous substances. Porosity decreases the velocity of sound through the rock material and, correspondingly, increases the interval transit time.

Table 1

	v_{ma}(ft/sec)	Δt_{ma}(μs/ft)	Δt_{ma}(μs/ft) (commonly used)
Sandstones	18,000-19,500	55.5-51.0	55.5 or 51.0
Limestones	21,000-23,000	47.6-43.5	47.5
Dolomites	23,000	43.5	43.5
Anhydrite	20,000	50.0	50.0
Salt	15,000	66.7	67.0
Casing (iron)	17,500	57.0	57.0

1,367-86

Porosity Determination (Wyllie Time-Average Equation)

Consolidated and Compacted Sandstones

After numerous laboratory determinations, M.R.J. Wyllie proposed, for clean and consolidated formations with uniformly distributed small pores, a linear time-average or weighted-average relationship between porosity and transit time:

$$t_{LOG} = \phi\, t_f + (1 - \phi)\, t_{ma} \quad \text{(Eq. 5-1a)}$$

or

$$\phi = \frac{t_{LOG} - t_{ma}}{t_f - t_{ma}}, \quad \text{(Eq. 5-1b)}$$

where

t_{LOG} is the reading on the sonic log in μs/ft,

t_{ma} is the transit time of the matrix material,

and

t_f is the transit time of the saturating fluid (about 189 μs/ft for freshwater mud systems).

Generally, consolidated and compacted sandstones have porosities from 15 to 25%. In such formations, the response of the sonic log seems to be relatively independent of the exact contents of the pores: water, oil, gas, or even disseminated shale. However, in some higher porosity sandstones (30% or greater) that have very low water saturation (high hydrocarbon saturation) and very shallow invasion, the t values may be somewhat greater than those in the same formations when water saturated.

If any shale laminae exist within the sandstone, the apparent sonic porosity values are usually increased by an amount proportional to the bulk volume fraction of laminae. The t readings are increased because t_{sh} is generally greater than t_{ma} of the sandstone matrix.

Carbonates

In carbonates having intergranular porosity the time-average formula still applies, but, sometimes, pore structure and pore size distribution are quite different from that of sandstones. There is often some secondary porosity consisting of vugs and/or fractures with much larger dimensions than the pores of the primary porosity.

In vuggy formations, the velocity of sound seems to depend mostly on the primary intergranular porosity, and the porosity derived from the sonic reading through the time-average formula (ϕ_{SV}) will tend to be too low by an amount approaching the secondary porosity. Thus, if the total porosity (ϕ_t) of a formation exhibiting primary and secondary porosity (ϕ_2) is available (from a neutron and/or density log, for example), the amount of secondary porosity can be estimated:

$$\phi_2 = \phi_t - \phi_{SV}. \qquad \text{(Eq. 5-2)}$$

Uncompacted Sands

Direct application of the time-average equation gives values of porosity that are too high in unconsolidated and insufficiently compacted sands. Uncompacted sands are most prevalent in the geologically younger formations, particularly at shallow depths. However, even at deeper depths these younger sands are often uncompacted when the overburden-to-formation fluid pressure differentials are less than about 4000 to 5000 psi. Such lack of compaction may be indicated when adjacent shales exhibit t values greater than 100 μs/ft.

When the formations are not sufficiently compacted, the observed t values are greater than those that correspond to the porosity according to the time-average formula, but the ϕ versus t relationship is still approximately linear. In these cases, an empirical correction factor, C_p, is applied to Eq. 5-1 to give a corrected porosity, ϕ_{SVcor}:

$$\phi_{SVcor} = \frac{t - t_{ma}}{t_f - t_{ma}} \cdot \frac{1}{C_p}. \qquad \text{(Eq. 5-3)}$$

The value of C_p is given approximately by dividing the sonic velocity in nearby shale beds by 100. However, the compaction correction factor is best determined by comparing ϕ_{SV}, as obtained from Eq. 5-1, with the true porosity obtained from another source. Several approaches are possible.

The R_0 method: Compare the sonic and induction or laterolog values in a clean water sand. The value of R_0 found from the resistivity is divided by R_w to obtain F. Then ϕ is found from F (Chart Por-2) and compared with ϕ_{SV} from Eq. 5-1 (sonic porosity without compaction correction). The value of C_p is equal to ϕ_{SV}/ϕ. This value of C_p can then be used to analyze nearby potential hydrocarbon-bearing sands.

Density-sonic crossplot method: When sonic and density logs are available, ϱ_b (in ordinate) and t (in abscissae) values are crossplotted over several sands in the interval of interest. If the sands contain no gas and some of them are clean, a line drawn from the matrix point through the points lying toward the upper left will be the clean sand line (Fig. 5-9). For any given porosity value on this clean sand line, there will be a value of t. Enter this t in Chart Por-3 and go vertically to the ϕ value. The intersection will give the value for C_p. If a sand is known to be clean and liquid filled, then $C_p = \phi_{SV}/\phi_D$.

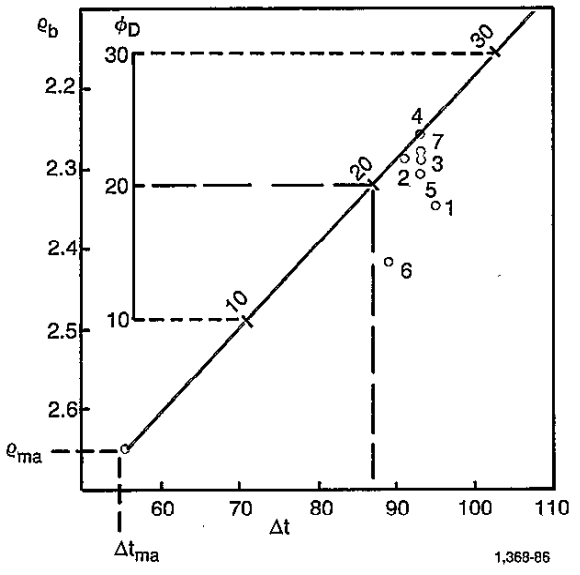

Fig. 5-9—Density-sonic crossplot as used for compaction-factor determination.

Neutron method: The previous two methods require a clean sand. If the sands are shaly, neither method can be safely used. If an SNP or CNL* neutron log is available, ϕ_N may be compared with ϕ_{SV} (or t) using Chart Por-3. Differences between ϕ_N and ϕ_{SV} in water-filled sands are due to lack of compaction. For such sands, $C_p = \phi_{SV}/\phi_N$.

In some shallowly invaded high-porosity rocks with high hydrocarbon saturation, sonic-derived porosity may be too high because of fluid effect. Both oil and gas transmit sound at lower velocities (higher transit times) than does water. Therefore, the transit time-to-porosity transform, which assumes water as the saturating pore fluid, sometimes overstates rock porosity. In these cases, the time average-derived porosity is multiplied by 0.9 in oil-bearing formations and by 0.7 in gas-bearing forma-

tions. These fluid corrections are applied only when the time average-derived porosity is obviously too high.

Empirical Equation Based on Field Observations

The long-standing problems with using the time-average equation, coupled with numerous comparisons of sonic transit time versus porosity, led to the proposal of an empirical transit time-to-porosity transform. The transform is also shown in Chart Por-3. The transform is empirical, being based entirely on comparisons of sonic transit time versus an independent porosity measurement.

The empirical transform exhibits several salient features. First, it appears that all pure quartz sandstones may be characterized by a unique matrix velocity, slightly less than 18,000 ft/sec. A value of 17,850 ft/sec (or t_{ma} = 56 μs/ft) is suggested. Limestone and dolomite also seem to exhibit unique matrix velocities: 20,500 ft/sec (or t_{ma} = 49 μs/ft) for limestone, and 22,750 ft/sec (or t_{ma} = 44 μs/ft) for dolomite.

In sandstone, the transform yields slightly greater porosity values over the low- to medium-porosity range (i.e., the 5 to 25% range) than does the time-average equation using an 18,000 ft/sec matrix velocity. In fact, at 15% porosity the transform indicates a porosity similar to that given by the time-average equation using a matrix velocity of 19,500 ft/sec. Thus, it appears the higher matrix velocities used in sonic interpretation in the past have been selected to force the time-average equation to yield a truer porosity over the low to medium range; this is true for both carbonates and sandstones.

For moderately high porosity sands (30%), the proposed empirical transform generally corresponds to the time-average equation using v_{ma} = 18,000 ft/sec. Above 35% porosity, however, sonic transit time increases much more rapidly than porosity, and its response quickly departs from that predicted by the time-average equation. This is the region in which the time-average equation would require a "lack of compaction" correction. The new transform eliminates the need for the correction factor and yields porosity directly.

This empirical transform can be approximated over the range of normally encountered porosities by the following equation:

$$\phi_{SV} = C \frac{(t_{LOG} - t_{ma})}{t_{LOG}}. \quad \text{(Eq. 5-4)}$$

The value of the constant C has a range of 0.625 to 0.7 depending upon the investigator. Chart Por-3 uses 0.7 for C: this was the value originally proposed. However, more recent transit time-to-porosity comparisons indicate 0.67 is more appropriate.

For the case of a gas-saturated reservoir rock, C becomes 0.6. It should be used when the rock investigated by the sonic tool contains an appreciable amount of hydrocarbon in the gassy (vapor) phase. Because of the very shallow depth of investigation, this condition normally exists only in higher porosity sandstones (greater than 30%).

Correlations with t Curve

Variations of velocity in different types of rock produce a sonic surve with a correlatable character. In addition, the very good vertical definition of the sonic log and the reduced hole effect because of borehole compensation make this log excellent for correlation. It is very helpful in some cases where other logs give poor results (thick shale sections and evaporites). Moreover, some types of formations, evaporites in particular, can be easily identified from their t values.

Abnormal Formation Pressures

Formations having abnormally high fluid pressures are often overlain by overpressured shales, which have an excess of pore water. Sonic transit time is greater in these shales than in normally compacted shales. Thus, a sonic log may be used to predict the possibility of overpressure.

The sonic travel time in shales normally decreases with increasing burial depth. A plot of this trend, t_{sh} versus depth, defines the normal compaction. Departures from this trend toward higher values suggest an abnormal, overpressured section (Fig. 5-10). With experience in the area, the magnitude of the overpressure can often be related to the difference between the actual shale transit time and that expected from the normal compaction trend line.

Shear-Wave Interpretation

All the preceding discussion has concerned compressional transit time interpretation. With the Array-Sonic tool and full-waveform recording, it is now possible to obtain shear-wave transit time measurements on a more routine basis. Application of the shear wave in formation evaluation is only now beginning to be explored. It is obvious that shear-wave velocity data will be useful in calculating rock elastic or inelastic properties and as an adjunct to shear seismic data.

Shear-wave transit time data are also useful in identifying matrix minerals and pore fluids (Fig. 5-11). For example, a crossplot of compressional transit time, t_c, and shear transit time, t_s, can be used to identify the mineral content of the various rocks traversed by the wellbore. The technique is similar to other porosity log crossplotting techniques (e.g., density-neutron, sonic-density, sonci-neutron).

There is evidence that the shear-wave transit time may be useful for fluid identification. Laboratory observations

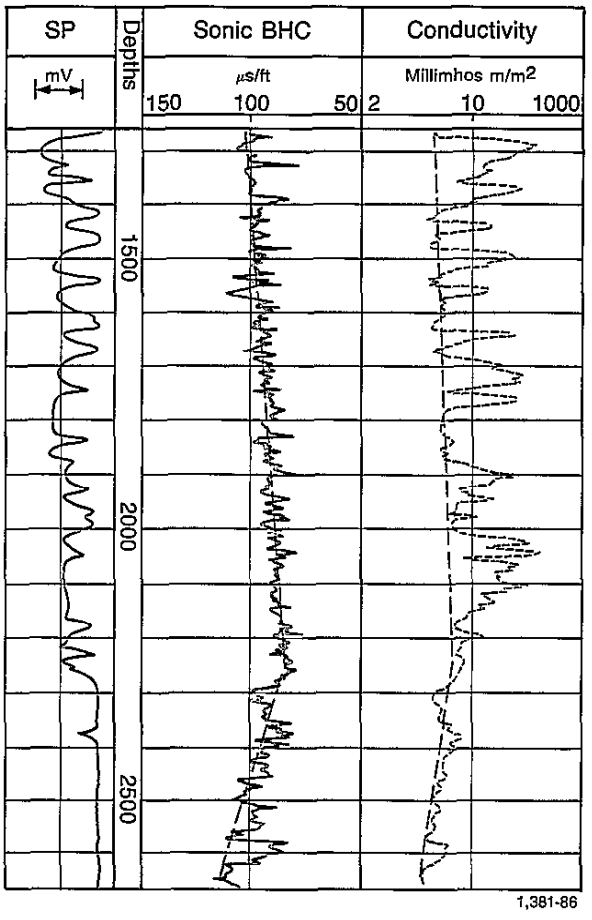

Fig. 5-10—Detecting overpressured zone with the sonic log.

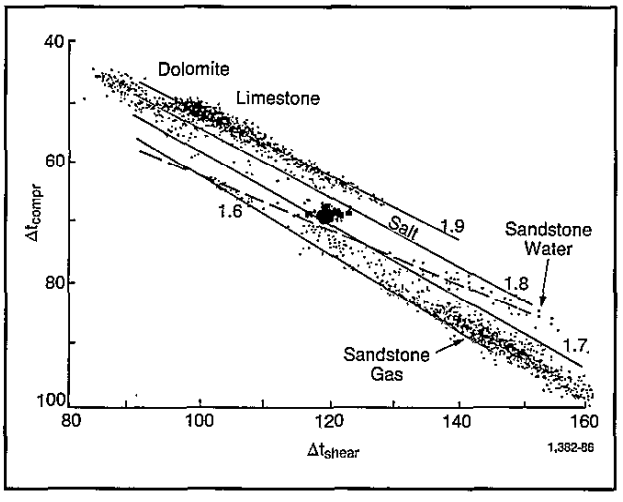

Fig. 5-11—Δt_{compr}—Δt_{shear} crossplots.

suggest that light hydrocarbon saturation decreases the velocity of the compressional wave (relative to brine saturation) through the porous rock and increases the velocity of the shear wave.

A relationship between porosity and shear velocity (or interval transit time) has also been noted. Indeed, the time-average relationship (Eq. 5-1) and the empirical relationship (Eq. 5-4) that relate compressional transit time to porosity appear to apply to shear transit time as well. Of course, appropriate matrix and fluid parameters must be used. For shear-wave propagation, the parameters are approximately:

Sandstone,	t_{ma}	≈	86 μs/ft
Limestone,	t_{ma}	≈	90 μs/ft
Dolomite,	t_{ma}	≈	76 μs/ft
Anhydrite,	t_{ma}	≈	100 μs/ft
Water,	t_{ma}	≈	350 μ/ft

These values are tentative. Further experience with the shear transit time may lead to some refinement. Also, the listing of a shear transit time value for water is somewhat imaginary since water does not support shear-wave propagation. However, the use of the listed value for water in the time-average equation does seem to yield acceptable porosity values.

DENSITY LOGS

Density logs are primarily used as porosity logs. Other uses include identification of minerals in evaporite deposits, detection of gas, determination of hydrocarbon density, evaluation of shaly sands and complex lithologies, determinations of oil-shale yield, calculation of overburden pressure and rock mechanical properties.

Principle

A radioactive source, applied to the borehole wall in a shielded sidewall skid, emits medium-energy gamma rays into the formations. These gamma rays may be thought of as high-velocity particles that collide with the electrons in the formation. At each collision a gamma ray loses some, but not all, of its energy to the electron, and then continues with diminished energy. This type of interaction is known as Compton scattering. The scattered gamma rays reaching the detector, at a fixed distance from the source, are counted as an indication of formation density.

The number of Compton-scattering collisions is related directly to the number of electrons in the formation. Consequently, the response of the density tool is determined essentially by the electron density (number of electrons per cubic centimeter) of the formation. Electron density is related to the true bulk density, ϱ_b, which, in turn,

depends on the density of the rock matrix material, the formation porosity, and the density of the fluids filling the pores.

Equipment

To minimize the influence of the mud column, the skid-mounted source and detector are shielded. The openings of the shields are applied against the wall of the borehole by an eccentering arm. The force exerted by the arm, and the plow-shaped design of the skid, allow it to cut through soft mudcakes. Any mudcake or mud remaining between the tool and the formation is "seen" as part of the formation and must be accounted for.

A correction is needed when the contact between the skid and the formations is not perfect (mudcake or irregularities in the borehole wall). In unfavorable cases this correction can be fairly large. If only one detector is used, the correction is not easy to determine because it depends on the thickness, the weight, and even the composition of the mudcake or mud interposed between the skid and the formations.

In the FDC* compensated formation density tool, two detectors of differing spacing and depth of investigation are used, as shown on Fig. 5-12. The chart of Fig. 5-13 is a plot of long-spacing versus short-spacing count rates. Points for a given value of ϱ_b and various mudcake conditions fall on or very close to an average curve. Using these average curves it is possible to enter the chart with the two count rates and determine the corrected ϱ_b from the plot without any explicit measurement of mudcake density or thickness. This measurement technique is referred to as "spine and ribs."

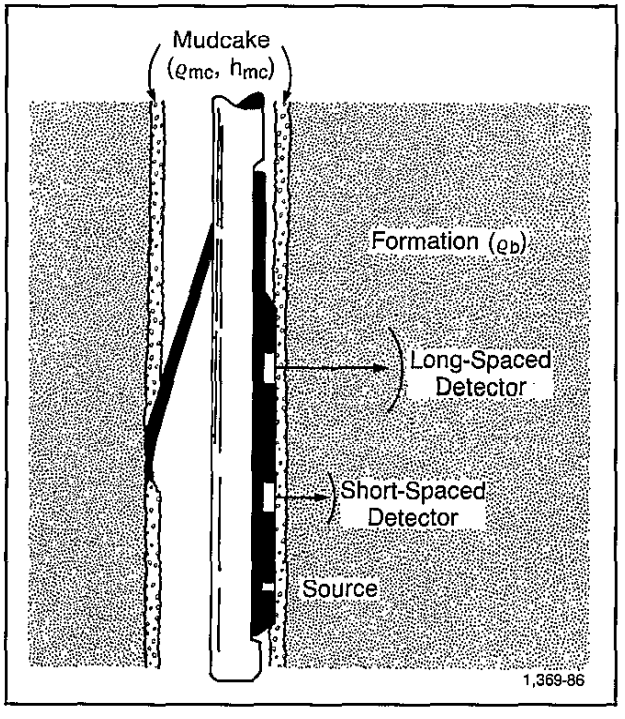

Fig. 5-12—Schematic drawing of the dual spacing Formation Density Logging Device (FDC). (Ref. 16)

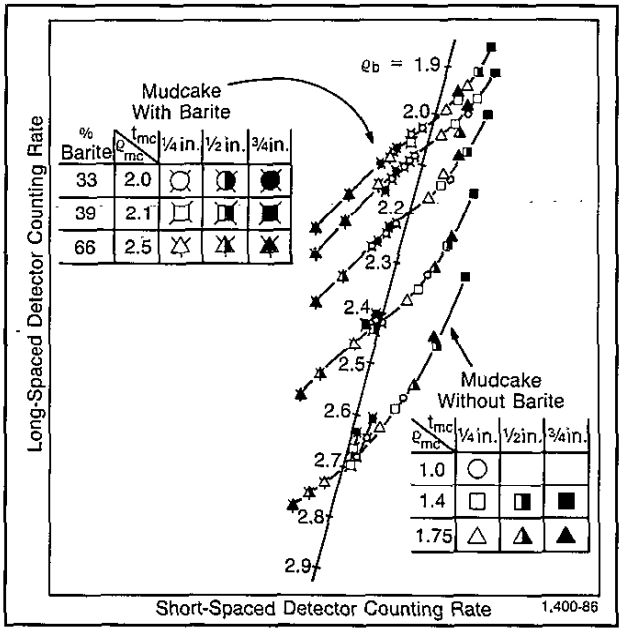

Fig. 5-13—"Spine-and-ribs" plot, showing response of FDC counting rates to mudcake. (Ref. 16)

The correction is made automatically and the corrected ϱ_b curve and $\Delta\varrho$ (the correction made) are recorded directly on the log (Fig. 5-14).

The distance between the face of the skid and the extremity of the eccentering arm is recorded as a caliper log, which helps to assess the quality of contact between the skid and the formation.

Logging Empty Holes

The spine-and-ribs plot for empty holes is not the same as that shown in Fig. 5-13. When the density tool is used in empty hole, the bulk density is automatically computed according to the empty-hole tool response.

Log Presentation

Log information is presented as shown in Fig. 5-14. The bulk density curve, ϱ_b, is recorded in Tracks 2 and 3 with a linear density scale in grams per cubic centimeter. An optional porosity curve may also be recorded in Tracks 2 and 3. This is a continuous solution of Eq. 5-7, using preset values of ϱ_{ma} and ϱ_f selected according to conditions. The $\Delta\varrho$ (which shows how much density compensation has been applied to correct for mudcake and hole rugosity) is usually recorded in Track 3. The caliper is

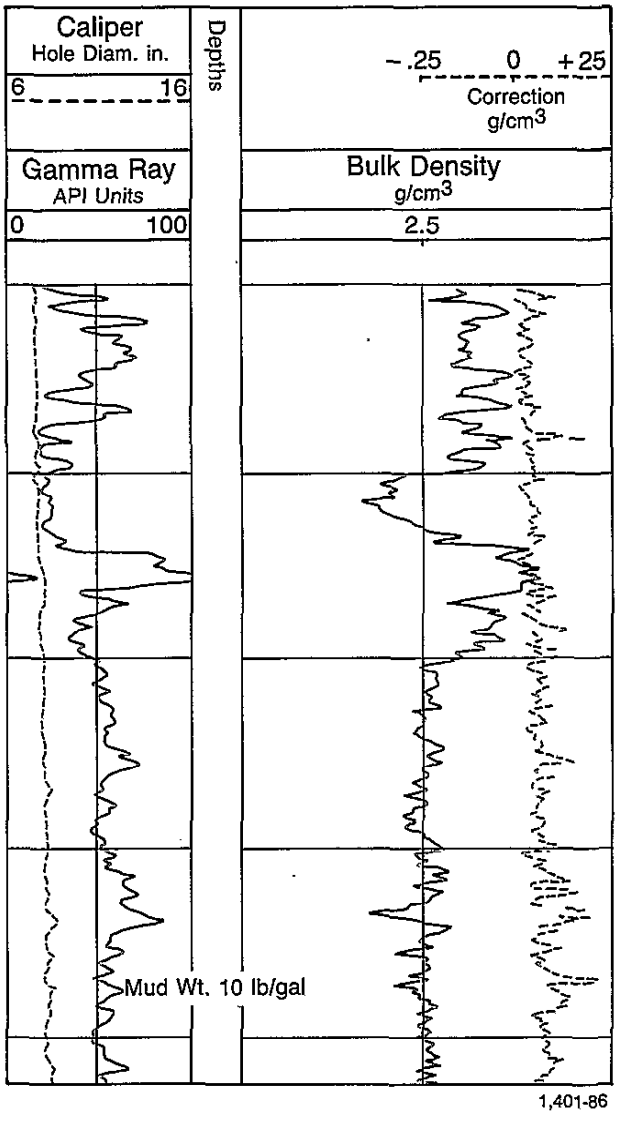

Fig. 5-14—FDC log presentation. (Ref. 16)

recorded in Track 1. A gamma ray (GR) curve may also be simultaneously recorded in Track 1. If a CNL* compensated neutron log is run in combination with the FDC log, it is also recorded in Tracks 2 and 3.

Calibration

The primary calibration standards for the FDC tool are laboratory freshwater-filled limestone formations of high purity and known densities. The secondary (shop calibration) standards are large aluminum and sulfur blocks into which the sonde is inserted. These blocks are of carefully designed geometry and composition, and their characteristics have been related to the limestone formations. With the blocks, two different thicknesses of artificial mudcakes are used to check the automatic mudcake correction. Finally, at the wellsite, a radioactive test jig is used to produce a signal of known intensity to verify the detection system.

Borehole Effect

Chart Por-15 shows the corrections needed for borehole sizes up to 15 in. in mud- and gas-filled boreholes. The corrections are negligible for holes smaller than 10 in. in diameter.

The FDC tool may not always follow the same track up the side of the hole on subsequent — overlap and/or repeat — runs. If the formations are quite heterogeneous—having, for instance, more vugs and/or fissures on one side of the hole wall than on the other—the two runs may disagree slightly. Disagreement is infrequently encountered, however, because the heavy skid tends to ride the downhill side of the hole, which seldom is absolutely vertical.

Electron Density and Bulk Density

The density log responds to the electron density of the formations. For a substance consisting of a single element, the electron density index, ϱ_e, is related to the bulk density, ϱ_b :

$$\varrho_e = \varrho_b \left(\frac{2Z}{A}\right), \qquad \text{(Eq. 5-5a)}$$

where

ϱ_b is the actual bulk density,

Z is the atomic number (number of electrons per atom),

and

A is the atomic weight (ϱ_b/A is proportional to the number of atoms per cubic centimeter of the substance).

For a molecular substance, the electron density index is related to the bulk density:

$$\varrho_e = \varrho_b \quad 2 \left(\frac{\Sigma Z\text{'s}}{\text{Mol. Wt.}}\right), \qquad \text{(Eq. 5-5b)}$$

where

ΣZ's is the sum of the atomic numbers of atoms making up the molecule (equal to the number of electrons per molecule) and Mol. Wt. is the molecular weight.

For most formation substances, the bracketed quantities in Eqs. 5-5a and 5-5b are very close to unity (Column 4 of Tables 5-2 and 5-3). When the density tool is calibrated in freshwater-filled limestone formations, the apparent bulk density, ϱ_a, as read by the tool is related to the electron density index, ϱ_e, by:

$$\varrho_a = 1.0704\ \varrho_e - 0.1883. \qquad \text{(Eq. 5-6)}$$

Table 5-2

Element	A	Z	$2\frac{Z}{A}$
H	1.008	1	1.9841
C	12.011	6	0.9991
O	16.000	8	1.0000
Na	22.990	11	0.9569
Mg	24.320	12	0.9868
Al	26.980	13	0.9637
Si	28.090	14	0.9968
S	32.070	16	0.9978
Cl	35.460	17	0.9588
K	39.100	19	0.9719
Ca	40.080	20	0.9980

1,386-86

For liquid-filled sandstones, limestones, and dolomites the tool reading, ϱ_a, is practically identical to actual bulk density, ϱ_b. For a few substances, such as sylvite, rock salt, gypsum, anhydrite, coal, and gas-bearing formations, the corrections shown in Fig. 5-15 are needed to obtain bulk density values from the density log readings.

Porosity From Density Log

For a clean formation of known matrix density, ϱ_{ma}, having a porosity, ϕ, that contains a fluid of average density, ϱ_f, the formation bulk density, ϱ_b, will be:

$$\varrho_b = \phi\, \varrho_f + (1 - \phi)\, \varrho_{ma}\,. \qquad \text{(Eq. 5-7a)}$$

For usual pore fluids (excepting gas and light hydrocarbons) and for common reservoir matrix minerals, the difference between the apparent density ϱ_a, read by the density log, and the bulk density, ϱ_b, is so trivial that it is disregarded. Solving for ϕ,

$$\phi = \frac{\varrho_{ma} - \varrho_b}{\varrho_{ma} - \varrho_f}, \qquad \text{(Eq. 5-7b)}$$

where $\varrho_b = \varrho_a$ (with exceptions noted).

Common values of ϱ_{ma} are given in Table 5-3.

The fluid in the pores of the permeable formations, within the relatively shallow zone investigated by the tool (about 6 in.), is usually mostly mud filtrate. This mud filtrate may have a density ranging from slightly less than 1 to more than 1.1 depending upon its salinity, temperature, and pressure. Fig. 5-16 shows the densities

Table 5-3

Compound	Formula	Actual Density ϱ_b	$\frac{2\Sigma Z's}{\text{Mol. Wt.}}$	ϱ_e	ϱ_a (as seen by tool)
Quartz	SiO_2	2.654	0.9985	2.650	2.648
Calcite	$CaCO_3$	2.710	0.9991	2.708	2.710
Dolomite	$CaCO_3MgCO_3$	2.850	0.9977	2.863	2.850
Anhydrite	$CaSO_4$	2.960	0.9990	2.957	2.977
Sylvite	KCl	1.984	0.9657	1.916	1.863
Halite	NaCl	2.165	0.9581	2.074	2.032
Gypsum	$CaSO_4 2H_2O$	2.320	1.0222	2.372	2.351
Anthracite Coal		{1.400 / 1.800}	1.0300	{1.442 / 1.852}	{1.355 / 1.796}
Bituminous Coal		{1.200 / 1.500}	1.0600	{1.272 / 1.590}	{1.173 / 1.514}
Fresh Water	H_2O	1.000	1.1101	1.110	1.000
Salt Water	200,000 ppm	1.146	1.0797	1.237	1.135
Oil	$n(CH_2)$	0.850	1.1407	0.970	0.850
Methane	CH_4	ϱ_{meth}	1.2470	1.247 ϱ_{meth}	1.335 ϱ_{meth}—0.188
Gas	$C_{1.1}H_{4.2}$	ϱ_g	1.238	1.238 ϱ_g	1.325 ϱ_g—0.188

1,387-86

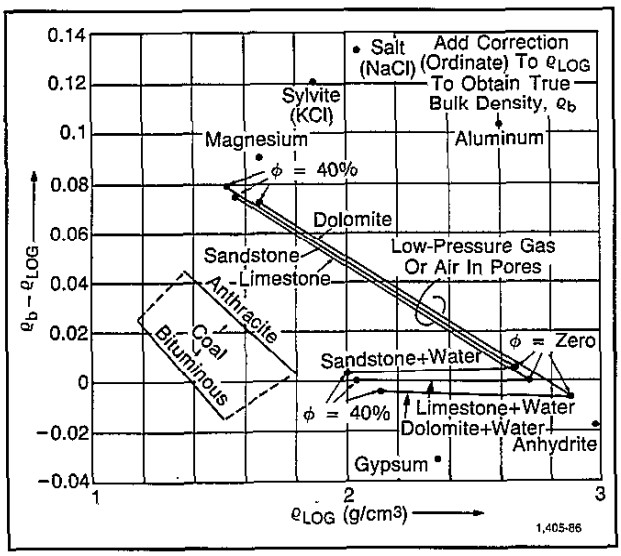

Fig. 5-15—Correction needed to get true bulk density from log density. (Ref. 2)

of water and NaCl solutions at various temperatures, pressures, and salinities. At 75° F and atmospheric pressure, the relation between NaCl water salinity and density may be approximated by

$$\varrho_w = 1 + 0.73\ P, \qquad \text{(Eq. 5-8)}$$

where P is the NaCl concentration in ppm $\times\ 10^{-6}$.

Chart Por-5 shows FDC porosities versus ϱ_b readings for various matrices and ϱ_f values of 1 through 1.2.

Effect of Hydrocarbons

If residual hydrocarbons exist in the region investigated by the FDC tool, their presence may affect the log readings. The effect of oil may not be noticeable because the average fluid density, ϱ_f, (from ϱ_o and ϱ_{mf}) will probably still be close to unity. If there is appreciable residual gas saturation, its effect will be to lower the ϱ_a.

Fig. 5-15 shows the corrections that must be added to the recorded ϱ_a values to obtain true ϱ_b values when low-pressure gas or air ($\varrho_g \approx 0$) occupies the pores.

The apparent density of gas, as seen by the density log, can be computed if the composition and density of the gas are known. Fig. 5-17 is a chart showing, for a gas of specified composition, the values of ϱ_g (actual density) and ϱ_{ga}, the apparent gas density seen by the density tool (based on electron density) as a function of pressure and temperature. In formations saturated with gas in the vicinity of the borehole, use ϱ_{ga} instead of ϱ_f in Eq. 3-7.

Effect of Shale

Interpretation can be affected by shale or clay in the formations. Although the properties of shales vary with the

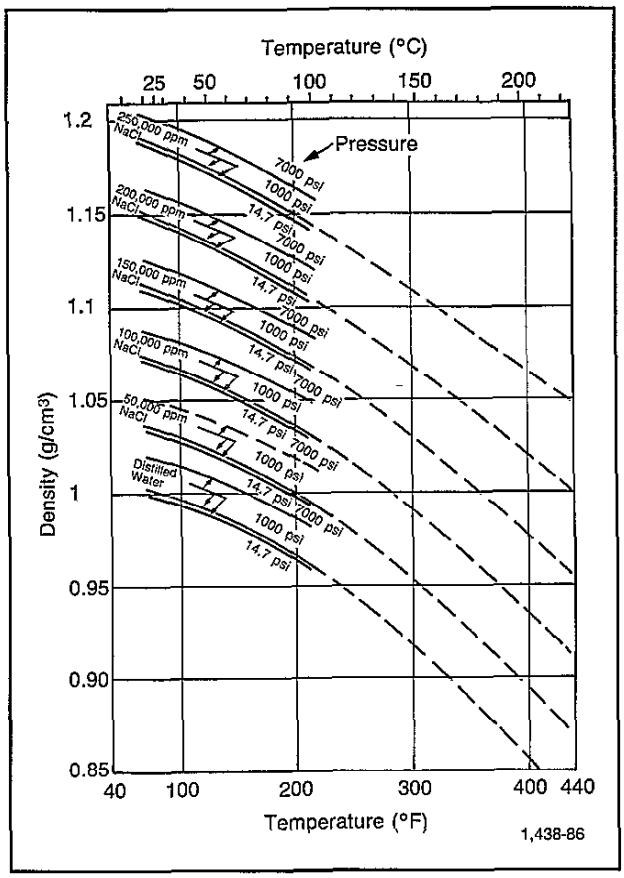

Fig. 5-16—Densities of water and NaCl solutions at varying temperatures and pressures.

formation and locality, typical densities for shale beds and laminar shale streaks are of the order of 2.2 to 2.65 g/cm^3. Shale densities tend to be lower at shallow depths where compacting forces are not as great. Dispersed clay or shale disseminated in the pore spaces may have a somewhat lower density than the interbedded shales.

Effect of Pressure

The bulk density of shale increases with compaction, and in areas where the sediments are relatively young the increase of shale density with depth is apparent on the logs. However, departure from this trend is observed in overpressured zones; shale density decreases with increasing depth (Fig. 5-18). This decrease often appears in shales as much as several hundred feet above high-pressure permeable sands. A high-density zone (the sealing barrier) usually lies at the top of this interval of decreased density. Density logs run at intervals during the drilling of a well can be used to predict abnormally pressured zones so that precautions can be taken to eliminate possible hazards.

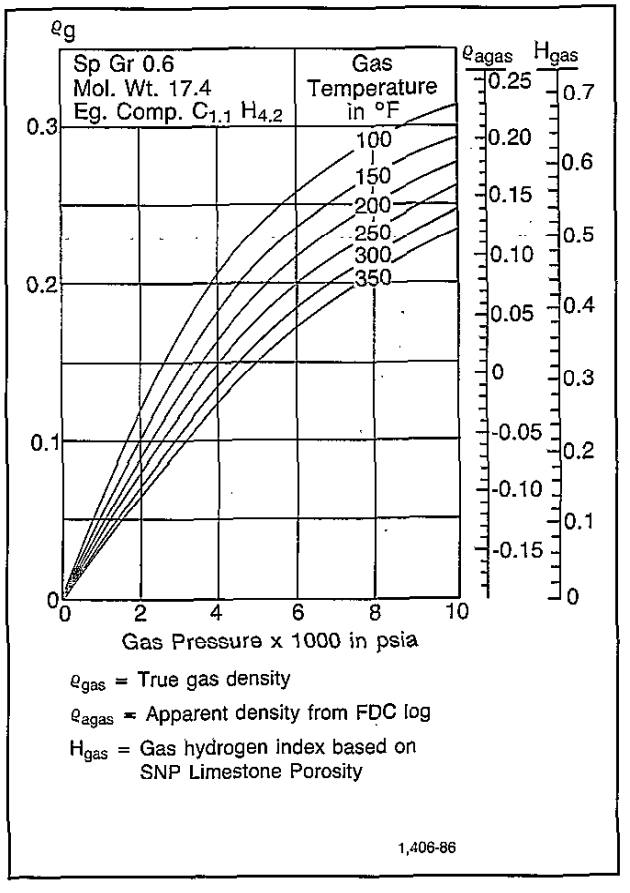

Fig. 5-17—Gas density and hydrogen index as functions of pressure and temperature for a gas mixture slightly heavier than methane ($C_{1.1}$ $H_{4.2}$).

Litho-Density* Log

The Litho-Density log is an improved and expanded version of the FDC log. In addition to the bulk density measurement, the tool also measures the photoelectric absorption index of the formation, P_e. Photoelectric absorption can be related to lithology; whereas the ϱ_b measurement responds primarily to porosity and secondarily to rock matrix and pore fluid, the P_e measurement responds primarily to rock matrix (lithology) and secondarily to porosity and pore fluid.

Equipment

In appearance and operation, the Litho-Density tool is similar to the FDC tool. The tool has a pad, or skid, in which the gamma ray source and two detectors are located. This skid is held against the borehole wall by a spring-activated backup arm. Gamma rays, emitted by the source at an energy of 662 keV, are scattered by the formation and lose energy until absorbed through photoelectric effect.

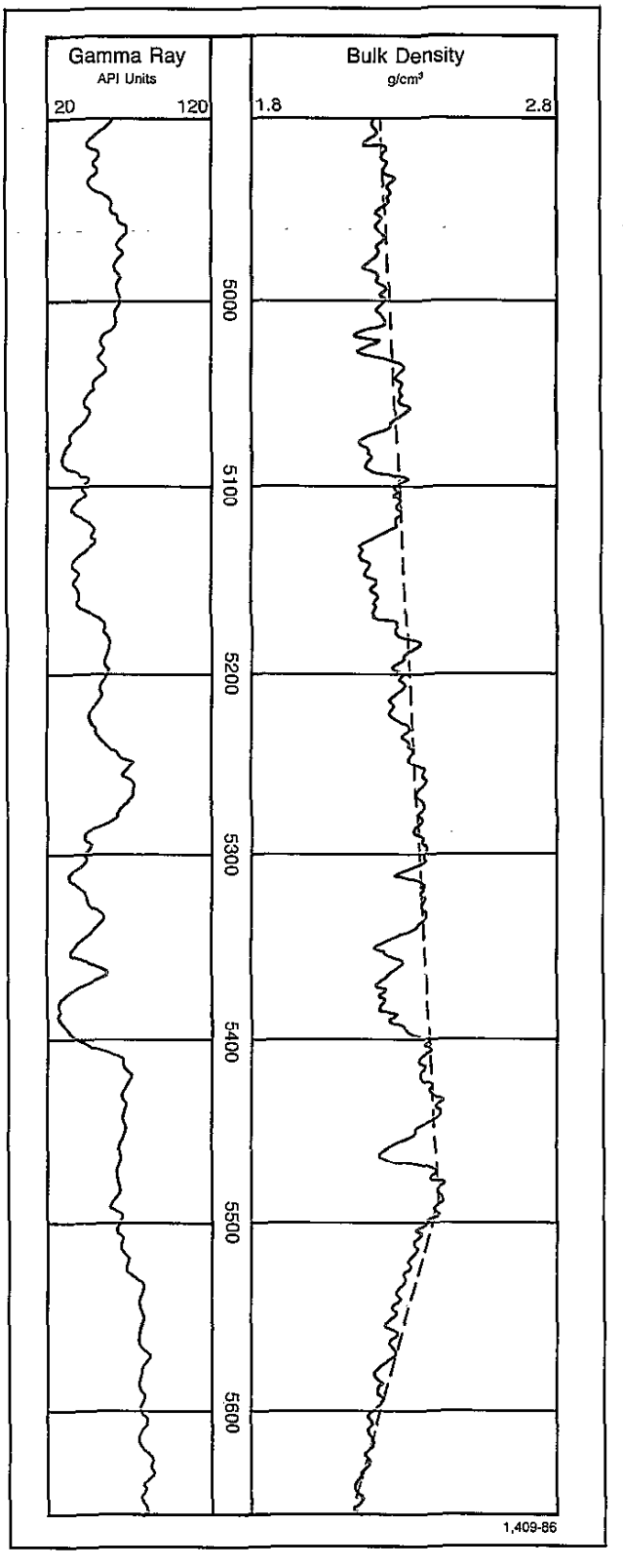

Fig. 5-18—Density log in overpressured shales.

At a finite distance from the source, such as the far detector, the energy spectrum might look as illustrated in Fig. 5-19. The number of gamma rays in the higher energy region (region of Compton scattering) is inversely related only to the electron density of the formation (i.e., an increase in the formation density decreases the number of gamma rays). The number of gamma rays in the lower energy region (region of photoelectric effect) is inversely related to both the electron density and the photoelectric absorption. By comparing the counts in these two regions, the photoelectric absorption index can be determined.

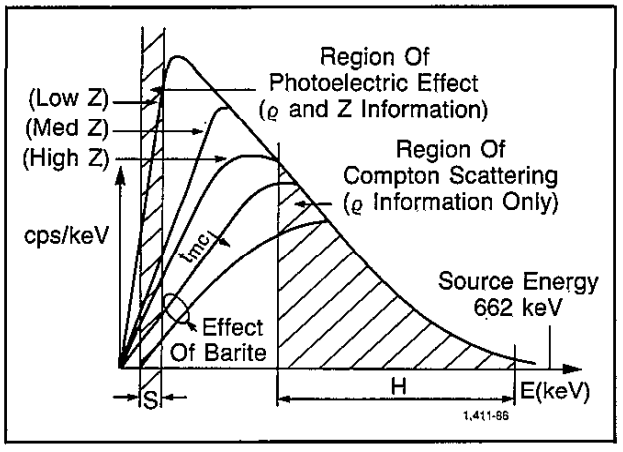

Fig. 5-19—Variations in spectrum for formation with constant density but different Z.

The gamma ray spectrum at the near detector is used only to correct the density measurement from the far detector for the effects of mudcake and borehole rugosity.

Photoelectric Absorption

In nuclear experiments, cross section is defined as a measure of the probability that a nuclear reaction will take place, under specified conditions, between two particles or a particle and another target. It is usually expressed in terms of the effective area a single target presents to the incoming particle. Table 5-4 lists the photoelectric absorption cross section, given in barns per atom, for several elements at the incident gamma ray energy level. The atomic number, Z, for each of these elements is also listed. The photoelectric cross section index, P_e, in barns per electron is related to Z by:

$$P_e = \left(\frac{Z^{3.6}}{10}\right). \qquad \text{(Eq. 5-9)}$$

Table 5-4

Element	Photoelectric Cross Section	Atomic Number Z_e
Hydrogen	0.00025	1
Carbon	0.15898	6
Oxygen	0.44784	8
Sodium	1.4093	11
Magnesium	1.9277	12
Aluminum	2.5715	13
Silicon	3.3579	14
Sulfur	5.4304	16
Chlorine	6.7549	17
Potassium	10.0810	19
Calcium	12.1260	20
Titanium	17.0890	22
Iron	31.1860	26
Copper	46.2000	29
Strontium	122.2400	38
Zirconium	147.0300	40
Barium	493.7200	56

1,388-86

For a molecule made up of several atoms, a photoelectric absorption cross section index, P_e, may be determined based upon atomic fractions. Thus,

$$P_e = \frac{\Sigma\, A_i\, Z_i\, P_i}{\Sigma\, A_i\, Z_i}, \qquad \text{(Eq. 5-10)}$$

where A_i is the number of each atom in the molecule.

Table 5-5 gives the P_e value for several reservoir rocks, minerals, and fluids commonly encountered in the oil field. From this list it is not readily apparent that the cross section is relatively independent of porosity and the saturating fluid. To verify this relative independence, express the photoelectric absorption cross section index in volumetric terms rather than in electron terms.

By definition:

$$U = P_e\, \varrho_e.$$

Since P_e has the units of barns per electron and ϱ_e the units of electrons per cubic centimeter, U has the units of barns per cubic centimeter. This parameter permits the cross sections of the various volumetric components of a formation to be added in a simple weighted average manner. Thus,

$$U = \phi\, U_f + (1 - \phi)\, U_{ma}, \qquad \text{(Eq. 5-11)}$$

where U, U_f, and U_{ma} are the photoelectric absorption cross sections of the mixture, pore fluid, and matrix, respectively; all are expressed in barns per cubic centimeter. Transformation of the mixture response given by Eq. 5-11 back into P_e gives the response shown in Chart CP-16 when P_e is crossplotted against bulk density.

Table 5-5

Name	Formula	Molecular Weight	P_e	ϱ_b	ϱ_a	U
Minerals						
Anhydrite	$CaSO_3$	136.146	5.055	2.960	2.957	14.95
Barite	$BaSO_4$	233.366	266.800	4.500	4.011	1070.00
Calcite	$CaCO_3$	100.090	5.084	2.710	2.708	13.77
Carnallite	$KCl\text{-}MgCl_2\text{-}6H_2O$	277.880	4.089	1.610	1.645	6.73
Celestite	$SrSO_4$	183.696	55.130	3.960	3.708	204.00
Corundum	Al_2O_3	101.900	1.552	3.970	3.894	6.04
Dolomite	$CaCO_3M_gCO_3$	184.420	3.142	2.850	2.864	9.00
Gypsum	$CaSO_4\text{-}2H_2O$	172.180	3.420	2.320	2.372	8.11
Halite	NaCl	58.450	4.650	2.165	2.074	9.65
Hematite	Fe_2O_3	159.700	21.480	5.210	4.987	107.00
Ilmenite	$FeO\text{-}TiO_2$	151.750	16.630	4.700	4.460	74.20
Magnesite	$MgCO_3$	84.330	0.829	3.037	3.025	2.51
Magnetite	Fe_3O_4	231.550	22.080	5.180	4.922	109.00
Marcasite	FeS_2	119.980	16.970	4.870	4.708	79.90
Pyrite	FeS_2	119.980	16.970	5.000	4.834	82.00
Quartz	SiO_2	60.090	1.806	2.654	2.650	4.79
Rutile	TiO_2	79.900	10.080	4.260	4.052	40.80
Sylvite	KCl	74.557	8.510	1.984	1.916	16.30
Zircon	$ZrSiO_4$	183.310	69.100	4.560	4.279	296.00
Liquids						
Water	H_2O	18.016	0.358	1.000	1.110	0.40
Salt Water	(120,000 ppm)		0.807	1.086	1.185	0.96
Oil	$CH_{1.6}$		0.119	0.850	0.948	0.11
	CH_2		0.125	0.850	0.970	0.12
Miscellaneous						
Clean Sandstone			1.745	2.308	2.330	4.07
Dirty Sandstone			2.700	2.394	2.414	6.52
Average Shale			3.420	2.650	2.645	9.05
Anthracite	C:H:O –		0.161	1.700	1.749	0.28
Coal	93:3:4					
Bituminous	C:H:O –		0.180	1.400	1.468	0.26
Coal	82:5:13					

1,390-86

Tool Response

The Litho-Density tool skid and detector system have been designed so that greater counting rates are obtained than with the FDC tool and result in lower statistical variations and better repeatability of the measurements. The geometry of the skid has also been altered so that the density reading has a greater vertical resolution than that of the FDC measurement. The P_e measurement exhibits an even better vertical resolution; this has applications in identifying fractures and laminar formations.

The procedure for mudcake and borehole rugosity compensation with the Litho-Density tool uses "spine and rib" as done with the FDC tool. Because of the fixed radius of curvature of the measuring device surface, borehole size also influences the measurement. The borehole-size correction is shown in Chart Por-5.

NEUTRON LOGS

Neutron logs are used principally for delineation of porous formations and determination of their porosity. They respond primarily to the amount of hydrogen in the formation. Thus, in clean formations whose pores are filled with water or oil, the neutron log reflects the amount of liquid-filled porosity.

Gas zones can often be identified by comparing the neutron log with another porosity log or a core analysis. A combination of the neutron log with one or more other porosity logs yields even more accurate porosity values and lithology identification—even an evaluation of shale content.

Principle

Neutrons are electrically neutral particles, each having a mass almost identical to the mass of a hydrogen atom. High-energy (fast) neutrons are continuously emitted from a radioactive source in the sonde. These neutrons collide with nuclei of the formation materials in what may be thought of as elastic "billiard-ball" collisions. With each collision, the neutron loses some of its energy.

The amount of energy lost per collision depends on the relative mass of the nucleus with which the neutron collides. The greater energy loss occurs when the neutron strikes a nucleus of practically equal mass — i.e., a hydrogen nucleus. Collisions with heavy nuclei do not slow the neutron very much. Thus, the slowing of neutrons depends largely on the amount of hydrogen in the formation.

Within a few microseconds the neutrons have been slowed by successive collisions to thermal velocities, corresponding to energies of around 0.025 eV. They then diffuse randomly, without losing more energy, until they are captured by the nuclei of atoms such as chlorine, hydrogen, or silicon.

The capturing nucleus becomes intensely excited and emits a high-energy gamma ray of capture. Depending on the type of neutron tool, either these capture gamma rays or the neutrons themselves are counted by a detector in the sonde.

When the hydrogen concentration of the material surrounding the neutron source is large, most of the neutrons are slowed and captured within a short distance of the source. On the contrary, if the hydrogen concentration is small, the neutrons travel farther from the source before being captured. Accordingly, the counting rate at the detector increases for decreased hydrogen concentration, and vice versa.

Equipment

Neutron logging tools include the GNT tool series (no longer in use), the SNP sidewall neutron porosity tool (in limited use), and the CNL tool series, which includes the CNL compensated neutron and the Dual-Energy Neutron Log (DNL*). The current tools use americium-beryllium (AmBe) sources to provide neutrons with initial energies of several million electron volts.

The GNT tools were nondirectional devices that employed a single detector sensitive to both high-energy capture gamma rays and thermal neutrons. They could be run in cased or uncased holes. Although the GNT tools responded primarily to porosity, their readings were greatly influenced by fluid salinity, temperature, pressure, borehole size, standoff, mudcake, mud weight, and, in cased holes, by the casing and cement.

In the SNP tool the neutron source and detector are mounted on a skid, which is applied to the borehole wall. The neutron detector is a proportional counter, shielded so that only neutrons having energies above about 0.4 eV (epithermal) are detected.

The SNP tool has several advantages over the GNT tools:

- Because it is a sidewall device, borehole effects are minimized.
- Epithermal neutrons are measured, which minimizes the perturbing effects of strong thermal neutron absorbers (such as chlorine and boron) in the formation waters and matrix.
- Most required corrections are performed automatically in the surface instrumentation.
- It provides a good measurement in empty holes.

The SNP equipment is designed for operation only in open holes, either liquid filled or empty. The minimum hole diameter in which the tool can be used is 5 in. A caliper curve is recorded simultaneously with the SNP neutron data.

The CNL tool is a mandrel-type tool especially designed for combination with any of several other tools to provide a simultaneous neutron log. The CNL tool is a dual-spacing, thermal neutron-detection instrument. The ratio of counting rates from the two detectors is processed by the surface equipment to produce a linearly scaled recording of neutron porosity index. A 16-curie source and longer source-to-detector spacings give the CNL tool a greater radial depth of investigation than that of the SNP tool. The effects of borehole parameters are greatly reduced by taking the ratio of two counting rates similarly affected by these perturbations. The CNL tool can be run in liquid-filled holes, either cased or uncased, but cannot be used in gas-filled holes.

Since thermal neutrons are measured in the CNL tool, the response is affected by elements having a high thermal neutron capture cross section. The tool is sensitive to shale in the formation since shales usually contain small amounts of boron and other rare earth elements having a particularly high thermal neutron capture cross section. If excessive, this effect can mask the tool response to gas in shaly formations.

To improve the response to gas and to enhance interpretation in the presence of thermal neutron absorbers, the DNL tool incorporates two epithermal neutron detectors in addition to the two thermal neutron detectors (Fig. 5-20). Two separate porosity measurements are obtained, one from each pair of detectors. In clean formations the measured porosities generally agree. In shaly formations containing a large number of thermal neutron absorbers, the porosity measured by the epithermal detectors reads lower and agrees more closely with density-derived porosity. A comparison of the two porosity measurements indicates the shale or clay content, or the formation fluid salinity.

At a given source-detector spacing, epithermal neutron count rate is approximately an order of magnitude less than that for thermal neutrons. Therefore, to have reasonable epithermal neutron count rates, the epithermal detectors have been placed nearer to the neutron source than the thermal neutron detectors. The thermal neutron-detector configuration duplicates that of the standard CNL tool.

Since the two pairs of detectors are placed at different spacings and neutrons are detected at different energy levels, the environmental effects can be expected to be significantly different on the two neutron measurements.

If the ratio processing used on the thermal neutron measurement is used for the epithermal measurement, the computed porosity is quite sensitive to borehole effects. As a result of a detailed study of detector response to many environmental variables, an epithermal neutron processing technique has been developed that uses individual detector count rates. The method, which is

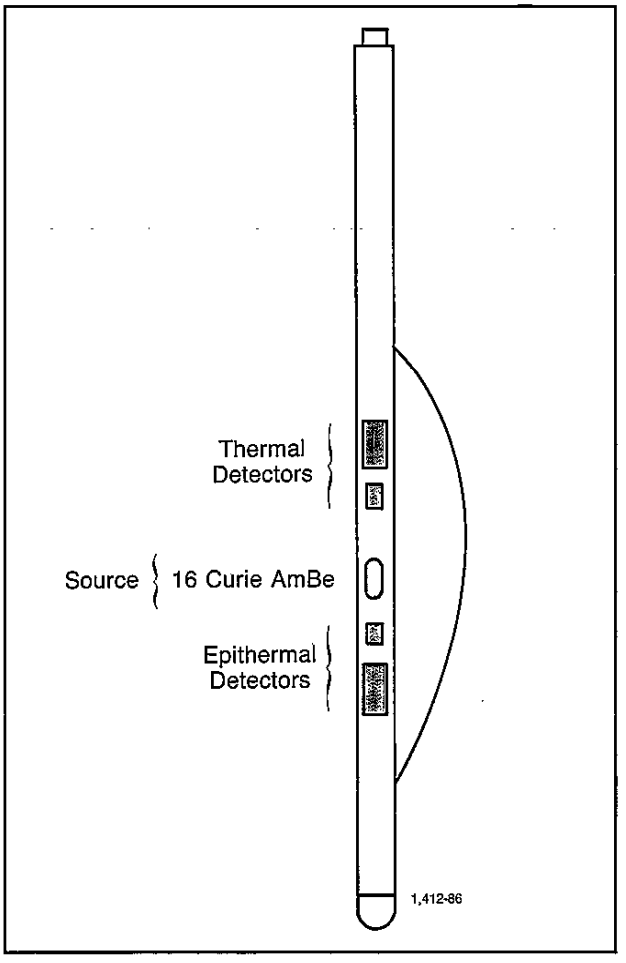

Fig. 5-20—DNL tool configuration, also known as CNT-G.

analogous to the spine-and-ribs analysis developed for the FDC tool, greatly reduces borehole effects on the epithermal neutron porosity measurement. The epithermal count rates can also be used to determine neutron porosity in air-filled boreholes.

The combined epithermal and thermal neutron Dual Porosity measurements provide improved porosity determination. Since the epithermal measurement is relatively free of neutron absorber effects, it yields improved gas detection in shaly reservoirs (Fig. 5-21). A comparison of the two neutron responses also provides information on the presence of materials with significant thermal neutron capture cross sections.

Log Presentation

SNP porosity readings are computed and recorded directly on the log (Fig. 5-22). The CSU* program automatically provides the corrections necessary in liquid-filled holes for mud weight, salinity, temperature, and hole-size variations. Chart Por-15 is used for mudcake correction. In

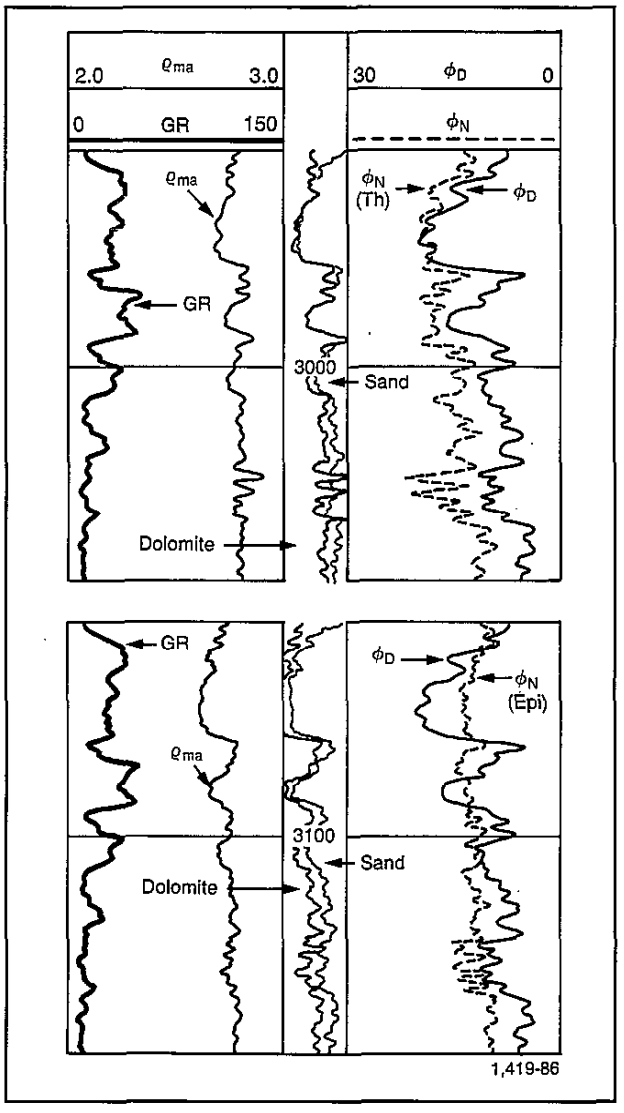

Fig. 5-21—Thermal/epithermal neutron log comparison in a gas zone.

gas-filled holes only the hole-size correction is required; it is done manually using a nomogram. The porosity values are recorded linearly in Tracks 2 and 3.

The CNL log and the DNL log are recorded in linear porosity units for a particular matrix lithology. When a CNL tool is run in combination with another porosity tool, all curves can be recorded on the same porosity scale. This overlay presentation permits visual qualitative interpretation of porosity and lithology or the presence of gas. Fig. 5-23 is an example of a combination CNL-FDC log.

Calibration

The primary calibration standard for GNT neutron logs was the API neutron pit in Houston. The response of the

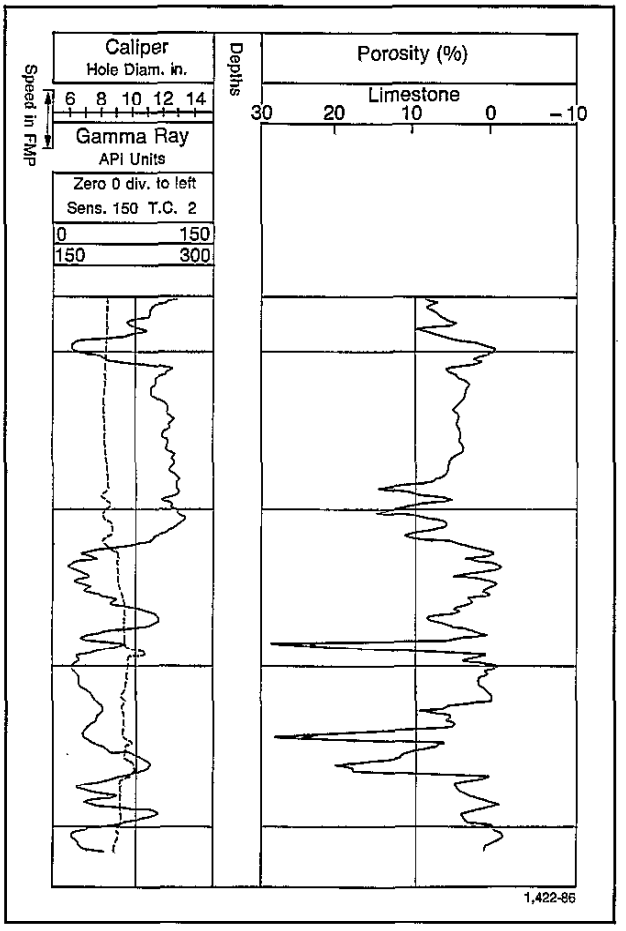

Fig. 5-22—Presentation of SNP log.

logging tool in a 19% porosity water-filled limestone was defined as 1,000 API units. Secondary calibrating devices, accurately related to the API pit, were used for the field calibration.

Prior to the API calibration procedure, neutron logs were scaled in counts per second. Conversion factors are provided in Table 5-6 to rescale them for comparison with neutron logs scaled in API units. Present neutron logs are scaled directly in porosity units.

Table 5-6

Tool Type Source: PuBe or AmBe	Spacing in.	API Units per Std. CPS
GNT-F, G, H	15.5	1.55
GNT-F, H	19.5	5.50
GNT-G	19.5	5.70
GNT-J, K	16	2.70

1,389-86

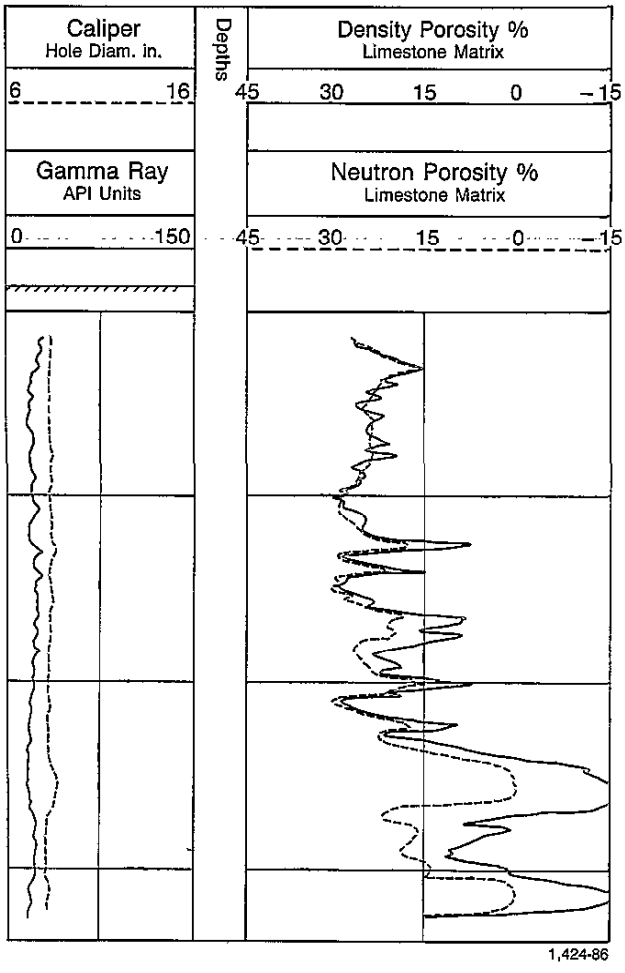

Fig. 5-23—Presentation of CNL-FDC log.

SNP tool calibration is based on numerous readings in formations of high purity and accurately known porosity. An environmental calibrator is used as a secondary standard at the wellsite. This device provides readings corresponding to 11% and 22% porosity in limestone.

The primary calibration standard for CNL tools is a series of water-filled laboratory formations. The porosities of these controlled formations are known within ± 0.5 porosity units. The secondary (shop) standard is a water-filled calibrating tank. A wellsite check is made by using a fixture that reproduces the count rate ratio obtained in the tank.

Investigation Characteristics

The typical vertical resolution of the SNP and CNL tools is 2 ft. However, a new method of processing the count rates of the CNL tool is now available that increases the vertical resolution to 1 ft by exploiting the better vertical resolution of the near detector.

The radial investigation depends on the porosity of the formation. Very roughly, at zero porosity the depth of investigation is about 1 ft. At higher porosity in liquid-filled holes, the depth of investigation is less because neutrons are slowed and captured closer to the borehole. For average conditions, the depth of investigation for the SNP tool is about 8 in. in a high-porosity rock; it is about 10 in. for the CNL tool in similar conditions. Both tools sample a somewhat larger volume of formation than the FDC tools.

Tool Response

As already stated, the responses of the neutron tools primarily reflect the amount of hydrogen in the formation. Since oil and water contain practically the same amount of hydrogen per unit volume, the responses reflect the liquid-filled porosity in clean formations. However, the tools respond to all the hydrogen atoms in the formation, including those chemically combined in formation matrix minerals.

Thus, the neutron reading depends mostly on the hydrogen index of the formation. The hydrogen index is proportional to the quantity of hydrogen per unit volume, with the hydrogen index of fresh water at surface conditions taken as unity.

Hydrogen Index of Salt Water

Dissolved sodium chloride (NaCl) takes up space and thereby reduces the hydrogen density. An approximate formula for the hydrogen index of a saline solution at 75° F is

$$H_w = 1 - 0.4P, \qquad \text{(Eq. 5-12a)}$$

where P is the NaCl concentration in ppm $\times 10^{-6}$. More generally, independent of temperatures,

$$H_w = \varrho_w (1 - P). \qquad \text{(Eq. 5-12b)}$$

In openhole logging, formations are generally invaded and the water in the zone investigated by the neutron logs is considered to have the same salinity as the borehole fluid. The SNP log is automatically corrected for salinity. The salinity correction to the CNL log is provided by Chart Por-14c.

For cased holes, the invaded zone usually disappears with time, and the water salinity is that of the formation water.

Response to Hydrocarbons

Liquid hydrocarbons have hydrogen indexes close to that of water. Gas, however, usually has a considerably lower hydrogen concentration that varies with temperature and pressure. Therefore, when gas is present near enough to the borehole to be within the tool's zone of investigation,

a neutron log reads too low a porosity. This characteristic allows the neutron log to be used with other porosity logs to detect gas zones and identify gas/liquid contacts. A neutron and density log combination provides a more accurate porosity and a value of minimum gas saturation. (Hydrocarbon effect will be discussed further in Chapter 6 in the Crossplotting Section.)

The quantitative response of the neutron tool to gas or light hydrocarbon depends primarily on hydrogen index and another factor—the "excavation effect." The hydrogen index can be estimated from the composition and density of the hydrocarbon. For light hydrocarbons (gases), Fig. 5-15 provides an estimate of its hydrogen index, H_h. The hydrogen index of heavier hydrocarbons (oils) can be approximated by the equation:

$$H_o = 1.28\ \varrho_o. \qquad \text{(Eq. 5-13)}$$

This equation assumes the chemical composition of the oil is n CH_2. H_o is derived from the comparison of the hydrogen density and molecular weight of water to those of oil.

Another set of equations can be used to estimate the hydrogen index of hydrocarbon fluids:

For light hydrocarbons ($\varrho_h < 0.25$),

$$H_h \approx 2.2\ \varrho_h. \qquad \text{(Eq. 5-14a)}$$

For heavy hydrocarbons ($\varrho_h > 0.25$),

$$H_h \approx \varrho_h + 0.3. \qquad \text{(Eq. 5-14b)}$$

Still another proposal suggests the equation

$$H_h = 9 \left(\frac{4 - 2.5\ \varrho_h}{16 - 2.5\ \varrho_h}\right) \varrho_h. \qquad \text{(Eq. 5-15)}$$

Mathematical investigations indicate that the effect of gas in the formation near the borehole is greater than would be expected by taking into account only its smaller hydrogen density. Previous calculations had been made as if the gas-filled portion of the porosity were replaced by rock matrix. The new calculations show that when this additional rock matrix is "excavated" and replaced with gas, the formation has a smaller neutron-slowing characteristic. The calculated difference in the neutron log readings has been termed the excavation effect. If this effect is ignored, too-high values of flushed-zone gas saturation and too-low values of porosity are given.

Fig. 5-24 shows the corrections needed for excavation effect. The values of porosity for sandstone, limestone, and dolomite lithologies are plotted. Intermediate porosity values can be interpolated.

The ordinate scale is used to correct neutron log porosities. An additional ordinate scale is provided for correcting porosities derived from a neutron-density crossplot that does not contain the excavation effect correction. Excavation effect corrections have already been incorporated into Chart CP-5.

The corrections for excavation effect given by Fig. 5-23 can be approximated by the formula

$$\Delta\phi_{Nex} = K\ [2\ \phi^2\ S_{wH} + 0.04\ \phi]\ (1 - S_{wH}), \qquad \text{(Eq. 5-16)}$$

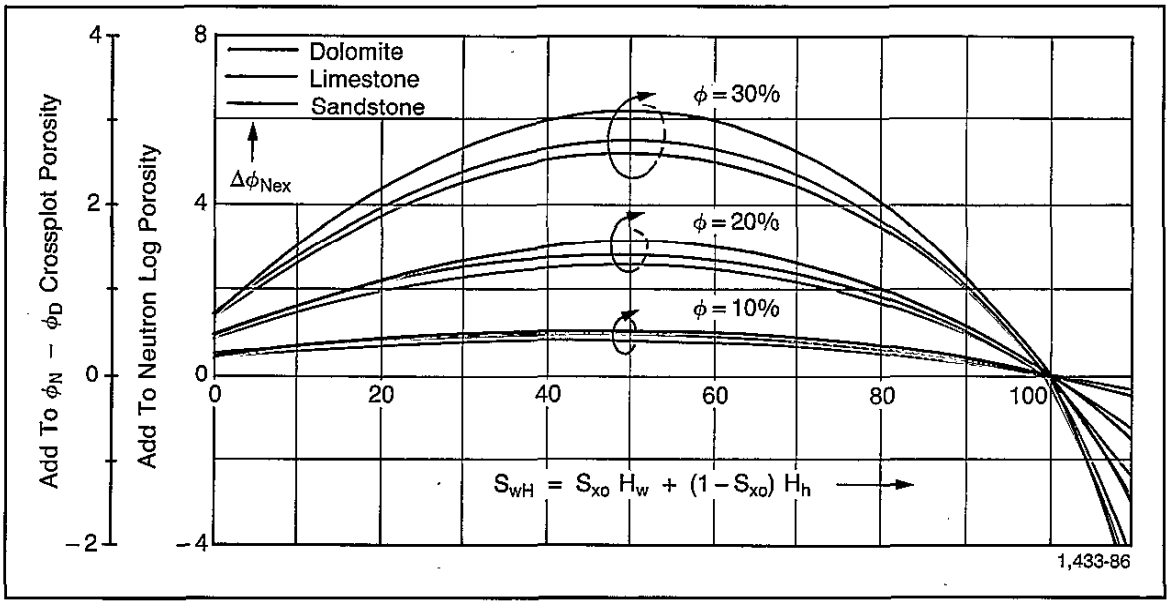

Fig. 5-24—Correction for excavation effect as a function of S_{xo} for three values of porosity and for $H_g = 0$. Effects of limestone, sandstone, and dolomite included within the shaded bands.

where $\Delta\phi_{Nex}$, ϕ, and S_{wH} are in fractional units. For sandstone the coefficient, K, is 1; for limestone it is about 1.046, and for dolomite it is about 1.173. Note that the second term of this equation is rather small and can often be disregarded.

Shales, Bound Water

Neutron tools see all hydrogen in the formation even if some is not associated with the water saturating the formation porosity. For example, it sees bound water associated with the shales. Shales in general have an appreciable hydrogen index; in shaly formations the apparent porosity derived from the neutron response will be greater than the actual effective porosity of the reservoir rock.

Also, the neutron tool measures water of crystallization. For example, nonporous gypsum ($CaSO_4 + 2H_2O$) has a large apparent porosity because of its significant hydrogen content.

Effect of Lithology

The readings of all neutron logs are affected to some extent by the lithology of the matrix rock. SNP and CNL logs are usually scaled for a limestone matrix. Porosities for other lithologies are obtained from Chart Por-13 (Fig. 5-25) or from scales on the log headings. The SNP corrections apply only to logs run in liquid-filled holes. When the hole is gas filled, the lithology effect is reduced to a negligible level, and porosity may be read directly subject to limitations. Lithology corrections to the DNL log are also made using Chart Por-13. The SNP response is used for the epithermal neutron measurement, and the CNL response is used for the thermal neutron measurement.

Determining Porosity From Neutron Logs

Subject to various assumptions and corrections, values of apparent porosity can be derived from any neutron log. However, certain effects, such as lithology, clay content, and amount and type of hydrocarbon, can be recognized and corrected for only if additional porosity information — from sonic and/or density logs — is available. Any interpretation of a neutron log alone should be undertaken with a realization of the uncertainties involved.

SNP Corrections

Most of the SNP corrections (e.g., mud weight, salinity, borehole diameter, temperature) and the porosity computation are automatically performed in the tool instrumentation. However, because the SNP tool is a directional sidewall device, it averages the hydrogen concentration of whatever material lies in front of the pad, including the mudcake.(A chart for mudcake correction is provided on Chart Por-15a.) The pad is pressed against the hole wall with great force so that much of the softer mudcake is scraped away. Moreover, the backup pad is small and tends to cut through the mudcake. To get the mudcake thickness in front of the pad, take the difference between caliper reading and bit size. (Do not divide by two.)

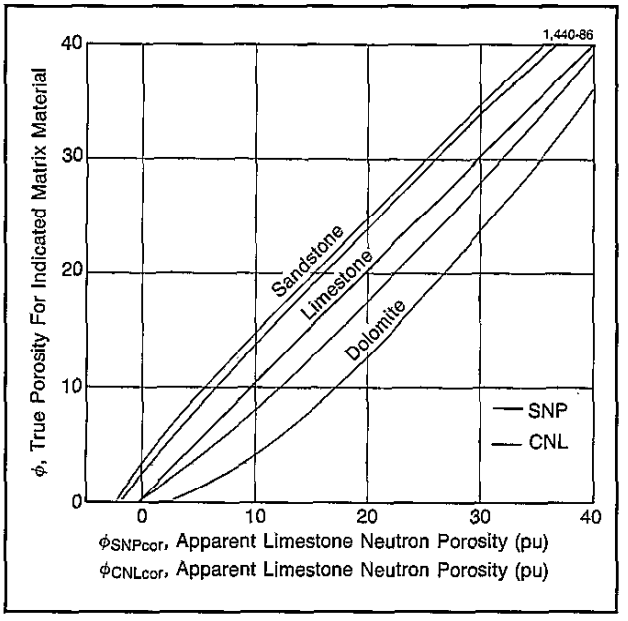

Fig. 5-25—Neutron porosity equivalence curves (Por-13a).

Thermal Neutron Measurement

The CNL and DNL tools are designed to minimize the effects of hole size, mudcake, etc. on the thermal neutron measurement. When either tool is run in combination with the FDC tool, the caliper signal provides an automatic hole size correction. However, for the other perturbing influences, and for hole size when the FDC tool is not run, automatic correction is not possible because the variables are not measured or controlled. Moreover, some of these effects vary with porosity.

The standard conditions for CNL tool and DNL tool calibration are:

- 7⅞-in. borehole diameter
- Fresh water in borehole and formation
- No mudcake or standoff
- 75° F temperature
- Atmospheric pressure
- Tool eccentered in hole.

If there are departures from these conditions, the logs will require corrections. The combined correction for all

factors, usually small, yields a value of corrected neutron porosity index. Chart Por-14c provides the corrections to the CNL and DNL thermal neutron measurements for borehole size, mudcake thickness, borehole and formation-water salinities, mud weight, standoff, pressure, and temperature.

Applications

Determining porosity is one of the most important uses of neutron logs. Corrections for lithology and borehole parameters are necessary for accurate porosity determinations.

The SNP log is specifically designed for open holes and provides porosity readings having minimum borehole effect. It can also be effectively used in gas-filled holes.

The compensation features of the CNL and Dual Porosity tools greatly reduce the effects of borehole parameters, and the tools are designed for combination with other openhole or cased hole tools. In combination with another porosity log (or other porosity data) or when used in a resistivity crossplot, the neutron log is useful to detect gas-bearing zones. For this application, the neutron-density combination is best in clean formations since the responses to gas are in opposite directions. In shaly formations, the neutron-sonic combination is an effective gas detector since shale affects each similarly. For greater accuracy in determining porosity and gas saturation in gas zones, the neutron log should be corrected for excavation effect.

The neutron log is used in combination with other porosity logs for lithology and shaly-sand interpretation. A comparison of the DNL epithermal neutron and thermal neutron measurements can identify shales and clays and other rocks containing neutron absorbers.

Also, count rates from the epithermal detectors of the DNL tool can be used for determining porosity in empty holes.

LOGGING-WHILE-DRILLING FORMATION DENSITY AND POROSITY

A logging-while-drilling tool has been developed to provide density and porosity logs comparable in quality to those obtained with current wireline techniques. This device is called the Compensated Density Neutron (CDN*) since it combines the two most important nuclear measurements in one drill collar.

The density measurement employs two gain-stabilized, photomultiplier/crystal scintillation detectors. Low density "windows" in the drill collar enable spectroscopy methods to be employed. The formation's photoelectric absorption factor (P_e) is also measured and is used for lithology identification.

Use of a 1.5 Ci Cs137 source results in a statistical precision of about 0.01 g/cc for the density measurement at a rate of penetration (ROP) of 50 ft/hr. The measurement is made through "windows" in a full gauge stabilizer that minimizes borehole standoff effects. Residual density errors are accounted for by using the traditional "spine and ribs" compensation technique. An independent measurement of the mud density is made continuously in the downhole tool which provides useful additional information for the correction of borehole standoff effects.

The borehole-compensated thermal neutron measurement provides a high quality porosity log formulated in terms of the traditional near/far ratio-porosity transform. A 7.5 Ci AmBe source provides a statistical precision of about 0.5 pu at 30 pu formation porosity with an 8-in. borehole and an ROP of 50 ft/hr. An extensive set of laboratory measurements and mathematical modeling results have been used to quantify environmental effects on both the density and porosity measurements.

The density and P_e response, and the neutron porosity log are similar to the wireline Litho-Density and CNL logs (Fig. 5-26).

The tool provides for efficient rig floor handling procedures and continues Schlumberger's commitment to nuclear source safety. Both the density and neutron sources are retrievable by conventional wireline fishing techniques, minimizing the possibility of having to abandon the source downhole in the event that the drill pipe becomes stuck (Fig. 5-27).

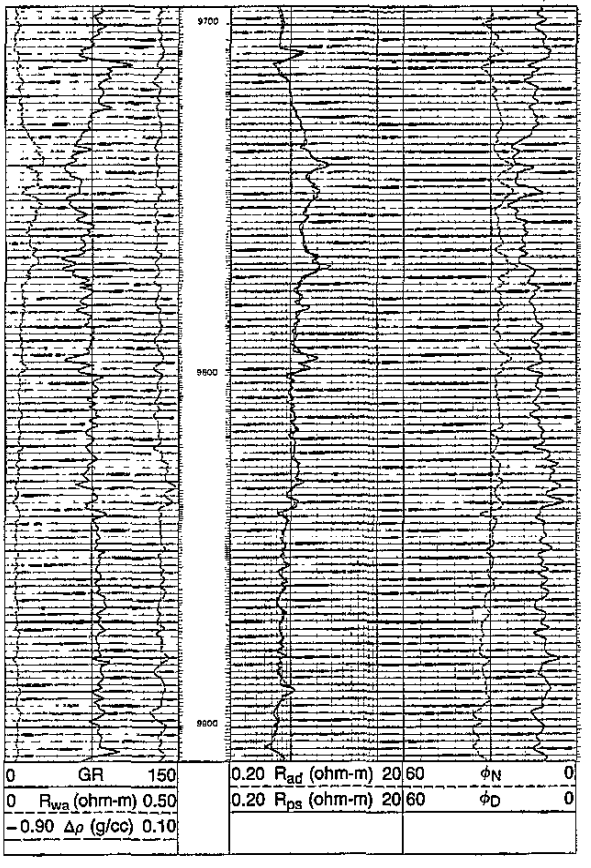

Fig. 5-26—Combined presentation of the CDN tool and the Compensated Dual Resistivity (CDR*) tool. Tick marks indicate the sampling rate of each measurement.

*Mark of Schlumberger

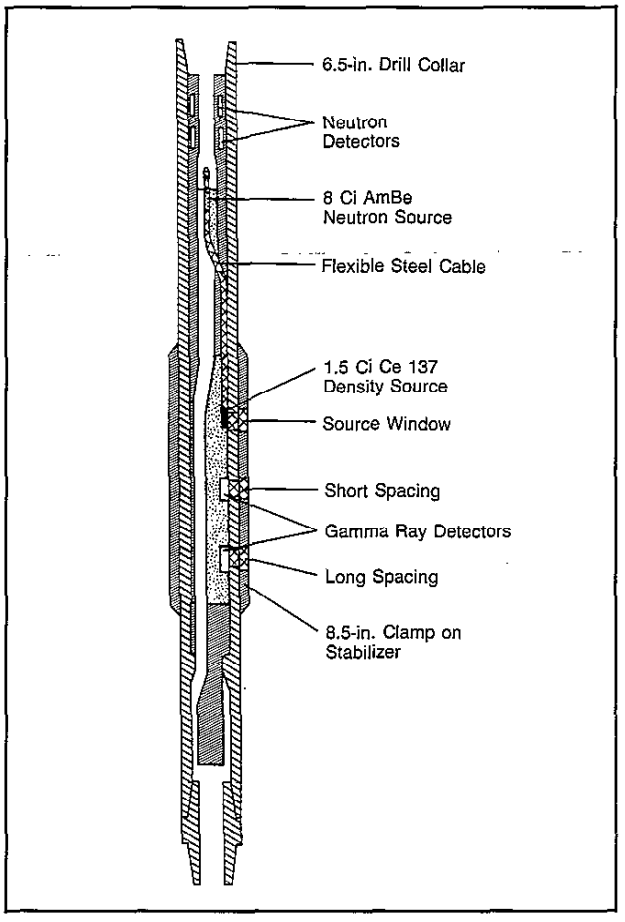

Fig. 5-27—Schematic of the CDN tool.

REFERENCES

1. Kokesh, F.P. and Blizard, R.B.: "Geometric Factors in Sonic Logging," *Geophys.* (Feb. 1959) **24**, No. 1.
2. Kokesh, F.P., Schwartz, R.J., Wall, W.B., and Morris, R.L.: "A New Approach to Sonic Logging and Other Acoustic Measurements," *J. Pet. Tech.* (March 1965) **17**, No. 3.
3. Hicks, W.G.: "Lateral Velocity Variations Near Boreholes," *Geophys.* (July 1959) **XXIV**, No. 3.
4. Hicks, W.G. and Berry, J.E.: "Application of Continuous Velocity Logs to Determination of Fluid Saturation of Reservoir Rocks," *Geophys.* (July 1956) **21**, No. 3.
5. Wyllie, M.R.J., Gregory, A.R., and Gardner, G.H.F.: "Elastic Wave Velocities in Heterogeneous and Porous Media," *Geophys.* (Jan. 1956) **21**, No. 1.
6. Wyllie, M.R.J., Gregory, A.R., and Gardner, G.H.F.: "An Experimental Investigation of Factors Affecting Elastic Wave Velocities in Porous Media," *Geophys.* (July 1958) **23**, No. 3.
7. Tixier, M.P., Alger, R.P., and Doh, C.A.: "Sonic Logging," *J. Pet. Tech.* (May 1959) **11**, No. 5.
8. Pickett, G.R.: "Acoustic Character Logs and Their Applications in Formation Evaluations," *J. Pet. Tech.* (June 1963) **15**, No. 6.
9. Morris, R.L., Grine, D.R., and Arkfeld, T.E.: "Using Compressional and Shear Acoustic Amplitudes for the Location of Fractures," *J. Pet. Tech.* (June 1964) **16**, No. 6.
10. Aron, J., Murray, J., and Seeman, B.: "Formation Compressional and Shear Interval-Transit-Time Logging by Means of Long Spacing and Digital Techniques," paper SPE 7446 presented at the 1978 SPE Annual Technical Conference and Exhibition.
11. Raymer, L.L., Hunt, E.R., and Gardner, J.S.: "An Improved Sonic Transit Time-to-Porosity Transform," *Trans.*, 1980 SPWLA Annual Logging Symposium, paper P.
12. Leslie, H.D. and Mons, F.: "Sonic Waveform Analysis: Applications," *Trans.*, 1982 SPWLA Annual Logging Symposium, paper GG.
13. Morris, C.F., Little, T.M., and Letton, W.: "A New Sonic Array Tool for Full Waveform Logging," paper SPE 13285 presented at the 1984 SPE Annual Technical Conference and Exhibition.
14. Alger, R.P., Raymer, L.L., Hoyle, W.R., and Tixier, M.P.: "Formation Density Log Applications in Liquid-Filled Holes," *J. Pet. Tech.* (March 1963).
15. Tittman, J. and Wahl, J.S.: "The Physical Foundations of Formation Density Logging (Gamma-Gamma)," *Geophys.* (April 1965).
16. Wahl, J.S., Tittman, J., and Johnstone, C.W.: "The Dual Spacing Formation Density Log," *J. Pet. Tech.* (Dec. 1964).
17. Gaymard, R. and Poupon, A.: "Response of Neutron and Formation Density Logs in Hydrocarbon-Bearing Formations," *The Log Analyst* (Sept.-Oct. 1968).
18. Hottman, C.E. and Johnson, R.K.: "Estimation of Formation Pressures from Log-Derived Shale Properties," *J. Pet. Tech.* (June 1965).
19. Fertl, W.H. and Timko, D.J.: "Occurrence and Significance of Abnormal Pressure Formations," *Oil and Gas J.* (Jan. 5, 1970).
20. Fertl, W.H. and Timko, D.J.: "How Abnormal-Pressure-Detection Techniques are Applied," *Oil and Gas J.* (Jan. 12, 1970).
21. Gardner, J.S. and Dumanoir, J.L.: "Litho-Density Log Interpretation," Trans., 1980 SPWLA Annual Logging Symposium, paper N.
22. Ellis, D., Flaum, C., Roulet, C., Marienbach, E. and Seeman, B.: "The Litho-Density Tool Calibration," paper SPE 12084 presented at the 1983 SPE Annual Technical Conference and Exhibition.
23. Tittman, J.: "Radiation Logging," *Fundamentals of Logging*, Univ. of Kansas (1956).
24. Tittman, J., Sherman, H., Nagel, W.A., and Alger, R.P.: "The Sidewall Epithermal Neutron Porosity Log," *J. Pet. Tech.* (Oct. 1966).
25. Alger, R.P., Locke, S., Nagel, W.A., and Sherman, H.: "The Dual Spacing Neutron Log," paper SPE 3565 presented at the 1971 SPE Annual Technical Conference and Exhibition.
26. *Recommended Practice for Standard Calibration and Form for Neutron Logs*, API RP33, American Petroleum Institute (Sept. 1959).
27. Segesman, F. and Liu, O.: "The Excavation Effect," *Trans.*, 1971 SPWLA Annual Logging Symposium.
28. Davis, R.R., Hall, J.E., Flaum, C., and Boutemy, Y.L.: "A Dual Porosity CNL Logging System," paper SPE 10296 presented at the 1981 SPE Annual Technical Conference and Exhibition.
29. Scott, H.D., Flaum, C., and Sherman, H.: "Dual Porosity CNL Count Rate Processing," paper SPE 11146 presented at the 1982 SPE Annual Technical Conference and Exhibition.
30. Sherman, H. and Locke, S.: "Effect of Porosity on Depth of Investigation of Neutron and Density Sondes," paper SPE 5510 presented at the 1975 SPE Annual Technical Conference and Exhibition.
31. Edmundson, H. and Raymer, L.L.: "Radioactive Logging Parameters for Common Minerals," *Trans.*, 1979 SPWLA Annual Logging Symposium, paper O.
32. Flaum, C.: "Dual Detector Neutron Logging in Air-Filled Boreholes," *Trans.*, 1983 SPWLA Annual Logging Symposium, paper BB.
33. Galford, J.E., Flaum, C., Gilchrist, W.A., and Duckett, S.: "Enhanced Resolution Processing of Compensated Neutron Logs," paper SPE 15541 presented at the 1986 SPE Annual Technical Conference and Exhibition.
34. Gilchrist, A., Galford, J., and Soran, P., and Flaum, C.: "Improved Environmental Corrections for Compensated Logs," paper SPE 15540 presented at the 1986 SPE Annual Technical Conference and Exhibition.
35. *Log Interpretation Charts*, Schlumberger Well Services, Houston (1989).

6 Lithology and Porosity Determination

The measurements of the neutron, density, and sonic logs depend not only on porosity (ϕ) but also on the formation lithology, on the fluid in the pores, and, in some instances, on the geometry of the pore structure. When the lithology and, therefore, the matrix parameters (t_{ma}, ϱ_{ma}, ϕ_{ma}) are known, correct porosity values can be derived from these logs, appropriately corrected for environmental effects, in clean water-filled formations. Under these conditions, a single log, either the neutron or the density or, if there is no secondary porosity, the sonic, can be used to determine porosity.

Accurate porosity determination is more difficult when the matrix lithology is unknown or consists of two or more minerals in unknown proportions. Determination is further complicated when the response of the pore fluids in the portion of the formation investigated by the tool differs appreciably from that of water. In particular, light hydrocarbons (gas) can significantly influence the response of all three porosity logs.

Even the nature or type of pore structure affects the tool response. The neutron and density logs respond to total porosity—that is, the sum of the primary (intergranular or intercrystalline) porosity and the secondary (vugs, fissures, fractures) porosity. The sonic logs, however, tend to respond only to evenly distributed primary porosity.

To determine porosity when any of these complicating situations exists requires more data than provided by a single porosity log. Fortunately, neutron, density, and sonic logs respond differently to matrix minerals, to the presence of gas or light oils, and to the geometry of pore structure. Combinations of these logs and the photoelectric cross section index, P_e, measurement from the Litho-Density* log and the thorium, uranium, and potassium measurement from the NGS* natural gamma ray spectrometry log can be used to unravel complex matrix or fluid mixtures and thereby provide a more accurate porosity determination.

The combination of measurements depends upon the situation. For example, if a formation consists of only two known minerals in unknown proportions, the combination of density and neutron logs or the combination of bulk density (ϱ_b) and photoelectric cross section will define the proportions of the two minerals and a better value of porosity. If it is known that the lithology is more complex but consists of only quartz, limestone, dolomite, and anhydrite, then a relatively accurate value of porosity can again be determined from the density-neutron combination; however, the mineral fractions of the matrix cannot be precisely determined.

Crossplots are a convenient way to demonstrate how various combinations of logs respond to lithology and porosity. They also provide visual insight into the type of mixtures that the combination is most useful in unraveling. Charts CP-1 through -21 present many of these combinations.

Fig. 6-1 (Chart CP-1e) is an example in which neutron and density porosities are crossplotted on linear scales. Points corresponding to particular water-saturated pure lithologies define curves (sandstone, limestone, dolomite, etc.) that can be graduated in porosity units, or a single mineral point (e.g., salt point) may be defined. This chart is entered with porosities computed as if the matrix had the same properties as water-saturated limestone; as a result, the limestone line is the straight line of equal density and neutron porosities.

When the matrix lithology is a binary mixture (e.g., sandstone-lime or lime-dolomite or sandstone-dolomite) the point plotted from the log readings will fall between the corresponding lithology lines.

NEUTRON-DENSITY CROSSPLOTS

Charts CP-1a and -1b are for SNP neutron versus density data. These charts were constructed for clean, liquid-saturated formations and boreholes filled with water or water-base mud. The charts should not be used for air-

*Mark of Schlumberger

or gas-filled boreholes; in these, the SNP matrix effect is changed. Charts CP-1e and -1f are similar plots for CNL* neutron versus density data.

The separations between the quartz, limestone, and dolomite lines indicate good resolution for these lithologies. Also, the most common evaporites (rock salt, anhydrite) are easily identified.

In the example shown on Fig. 6-1, $\phi_{Dls} = 15$ and $\phi_{Nls} = 21$. This defines Point P, lying between the limestone and dolomite curves. Assuming a matrix of limestone and dolomite and proportioning the distance between the two curves, the point corresponds to a volumetric proportion of about 30% dolomite and 70% limestone; porosity is 18%.

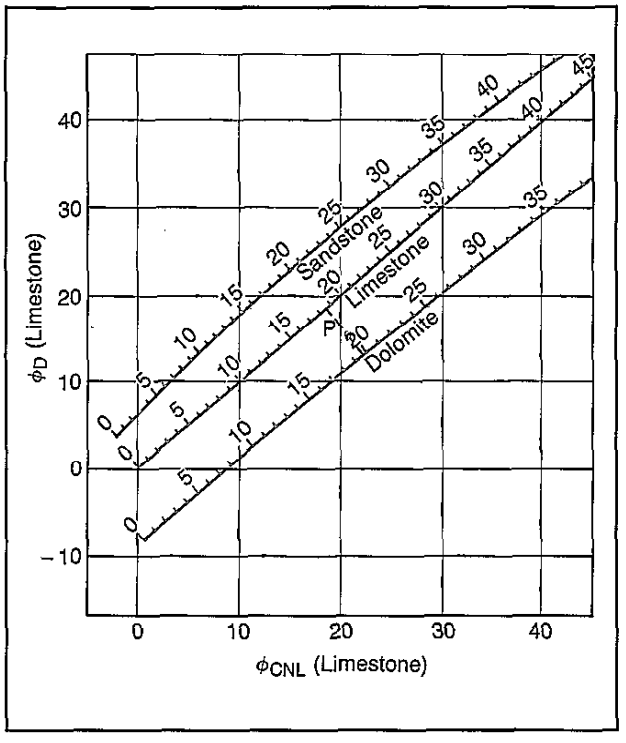

Fig. 6-1—Porosity and lithology determination from Litho-Density and CNL neutron logs in water-filled holes.

An error in choosing the matrix pair does not result in large error in the porosity value found, as long as the choice is restricted to quartz (sandstone or chert), limestone, dolomite, and anhydrite; shaliness and gypsum are excluded. For instance, in the above example, if the lithology were sandstone and dolomite instead of limestone and dolomite, the porosity found would be 18.3%; the mineral proportions would, however, be about 40% sandstone and 60% dolomite.

In fact, the plotted Point P of Fig. 6-1 could correspond to various mixtures of sandstone, limestone, and dolomite. In all cases, the porosity would be in the 18% range. Thus, although the rock volumetric fractions estimated from the neutron-density data could be considerably in error, the porosity value will always be essentially correct if only sandstone, limestone, and/or dolomite are present. This feature of the neutron-density combination, coupled with its use as a gas-finder, has made it a very popular log combination.

SONIC-DENSITY CROSSPLOT

Crossplots of sonic t versus density ϱ_b or ϕ_D have poor porosity and reservoir rock (sandstone, limestone, dolomite) resolution, but they are quite useful for determining some evaporite minerals. As can be seen from Fig. 6-2 (Chart CP-7), an error in the choice of the lithology pair from the sandstone-limestone-dolomite group can result in an appreciable error in porosity. Likewise, a small error in the measurement of either transit time or bulk density can result in an appreciable error in porosity and lithology analysis. The good resolution given by the chart for salt, gypsum, and anhydrite is shown by the wide separation of the corresponding mineral points on the figure. Several log-data points are shown that correspond to various mixtures of anhydrite and salt and, perhaps, dolomite.

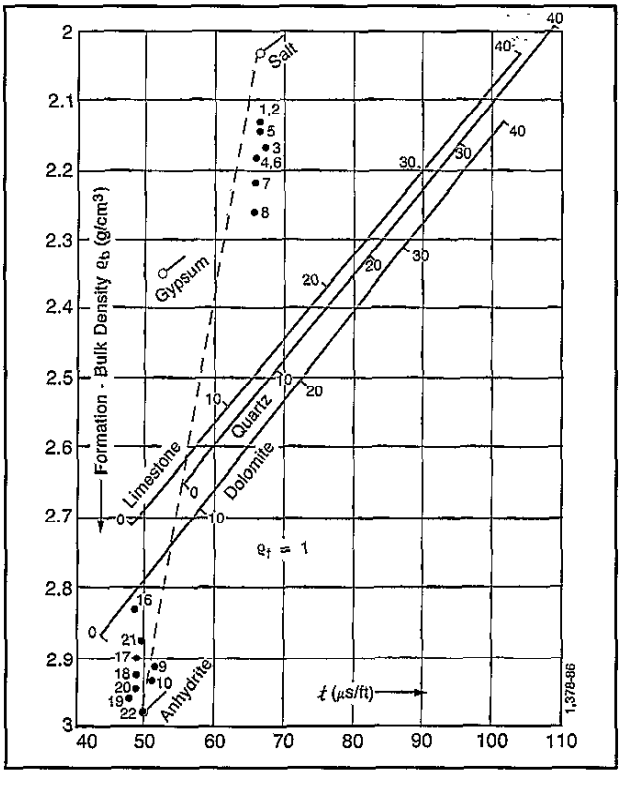

Fig. 6-2—Porosity and lithology determination from FDC density and sonic logs.

SONIC-NEUTRON CROSSPLOTS

Chart CP-2a is a plot of sonic t versus porosity from an SNP log. As with the density-neutron plots, resolution between sandstone, limestone, and dolomite lithologies is good, and errors in choosing the lithology pair will have only a small effect on the porosity value found. However, resolution is lost if evaporites are present. Chart CP-2b is a similar plot of sonic t versus porosity from the CNL log.

The sonic crossplots (Charts CP-2 and -7) are constructed for both the weighted-average (Wyllie) and the observed (Raymer, Hunt, and Gardner) sonic transit time-to-porosity transforms. Chart CP-2c is shown in Fig. 6-3. For mineral identification and porosity determination, use the transform previous experience has shown most appropriate for the area.

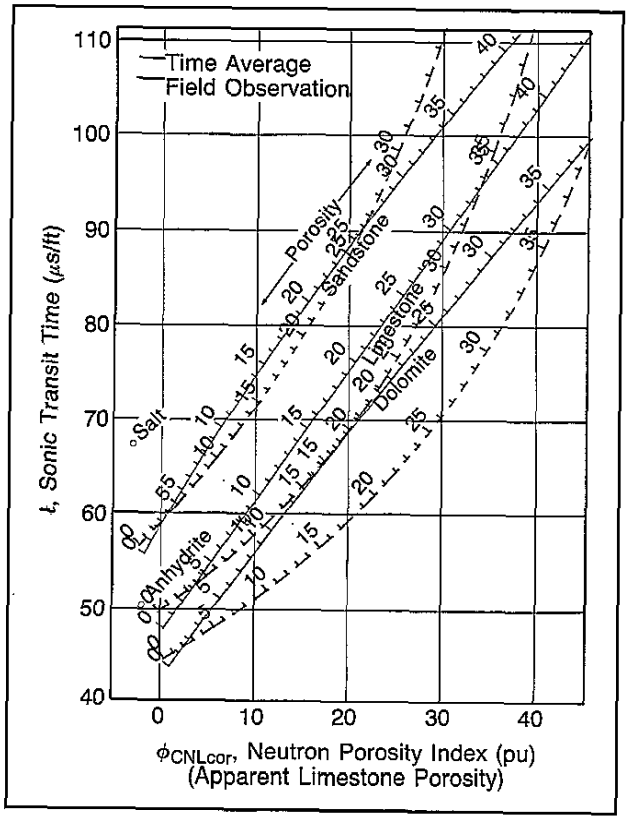

Fig. 6-3—Porosity and lithology determination from sonic log and CNL* compensated neutron log; t_f = 189 μs/ft.

DENSITY-PHOTOELECTRIC CROSS SECTION CROSSPLOTS

The photoelectric cross section index, P_e, curve is, by itself, a good matrix indicator. It is slightly influenced by formation porosity; however, the effect is not enough to hinder a correct matrix identification when dealing with simple lithologies (one-mineral matrix). P_e is little affected by the fluid in the pores.

The bulk density versus photoelectric cross section index crossplot (Charts CP-16 and -17, Fig. 6-4) can be used to determine porosity and to identify the mineral in a single-mineral matrix; the charts can also be used to determine porosity and the mineral fractions in a two-mineral matrix where the minerals are known. To use these charts the two minerals known or assumed to be in the matrix must be selected. A rib is then drawn through the log point to equal porosity points on the spines of the assumed minerals. These spines correspond to pure mineral matrices. The ribs are constant porosity approximates for any matrix mixture of the two minerals assumed. The distances from the log point to the pure mineral spines approximate the relative proportions of the minerals in the matrix.

If the porosity value from Chart CP-16 or -17 is equal to that of Chart CP-1, the choice of minerals is correct and the porosity is liquid filled. If the two values are different, choosing another pair of minerals may reconcile the difference.

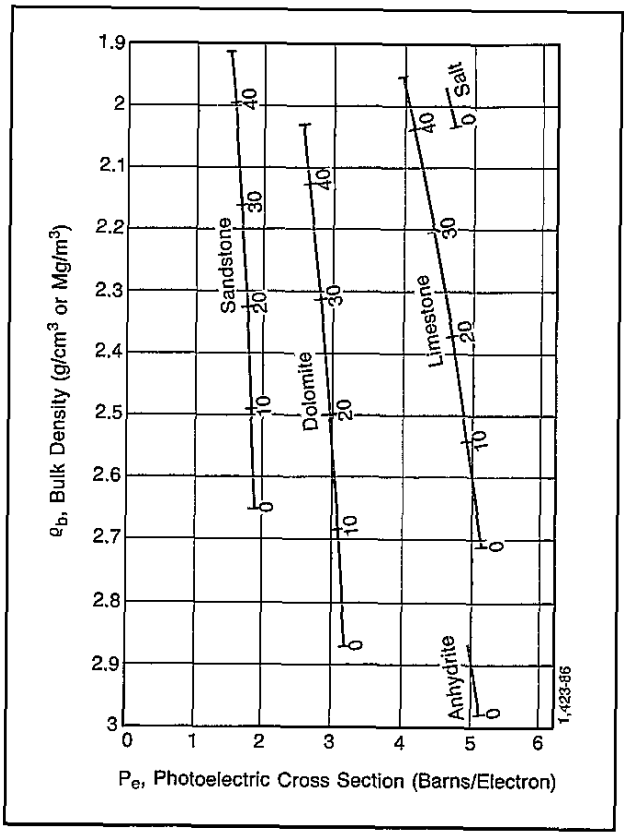

Fig. 6-4—Porosity and lithology determination from Litho-Density* log; fresh water, liquid-filled holes, ϱ_f = 1.0.

If one knows which pair of minerals is present in the matrix and the ϱ_b-ϕ_N porosity is less than the ϱ_b-P_e porosity, the presence of gas may be suspected. The location of the log point on the porosity rib of the ϱ_b-P_e plot permits the computation of the matrix density (mixture of two minerals in known proportions). If ϱ_{maa} (from the ϱ_b-ϕ_N plot) is less than ϱ_{maa} (from the ϱ_b - P_e plot), the presence of gas is confirmed.

NGS CROSSPLOTS

Because some minerals have characteristic concentrations of thorium, uranium, and potassium, the NGS log can be used to identify minerals or mineral type. Chart CP-19 compares potassium content with thorium content for several minerals; it can be used for mineral identification by taking values directly from the recorded NGS curves. Usually, the result is ambiguous and other data are needed. In particular, P_e is used with the ratios of the radioactive families: Th/K, U/K, and Th/U. Use care when working with these ratios because they are not the ratios of the elements within the formation but rather the ratios of the values recorded on the NGS log, ignoring the units of measurement. Charts have been constructed that allow P_e to be compared with either the potassium content, Fig. 6-5 (Chart CP-18 top), or the ratio of potassium to thorium, Fig. 6-6 (Chart CP-18 bottom).

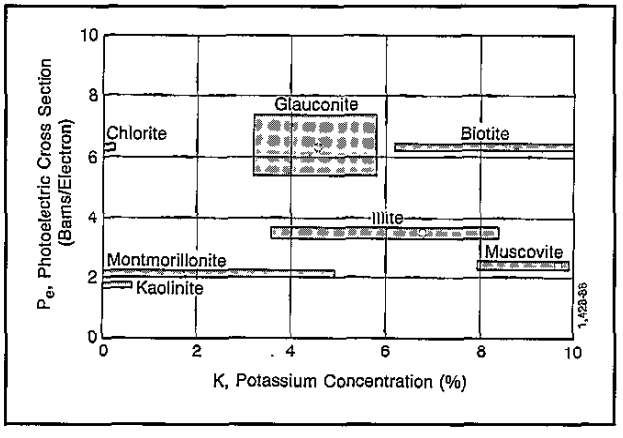

Fig. 6-5—Mineral identification from Litho-Density log and natural gamma ray spectrometry log.

The major occurrences of the three radioactive families are as follows:

- Potassium - micas, feldspars, micaceous clays (illite), radioactive evaporites
- Thorium - shales, heavy minerals
- Uranium - phosphates, organic matter

The significance of the type of radiation depends on the formation in which it is found. In carbonates, uranium

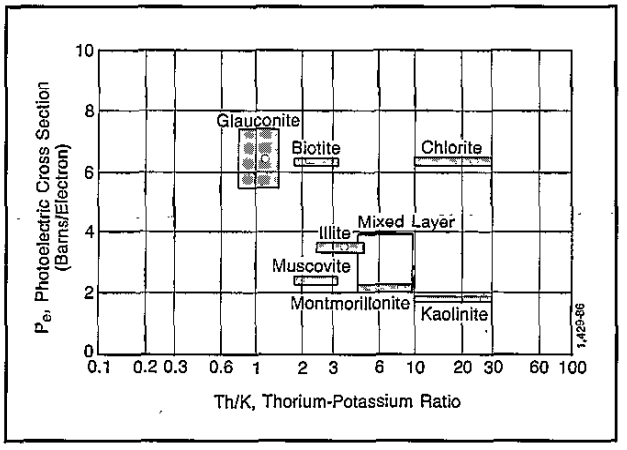

Fig. 6-6—Mineral identification from Litho-Density log and natural gamma ray spectrometry log.

usually indicates organic matter, phosphates, and stylolites. The thorium and potassium levels are representative of clay content. In sandstones, the thorium level is determined by heavy minerals and clay content, and the potassium is usually contained in micas and feldspars. In shales, the potassium content indicates clay type and mica, and the thorium level depends on the amount of detrital material or the degree of shaliness.

High uranium concentrations in a shale suggest that the shale is a source rock. In igneous rocks the relative proportions of the three radioactive families are a guide to the type of rock, and the ratios Th/K and Th/U are particularly significant.

The radioactive minerals found in a formation are, to some extent, dependent on the mode of sedimentation. The mode of transportation and degree of reworking and alteration are also factors. As an example, because thorium has a very low solubility, it has limited mobility and tends to accumulate with the heavy minerals. On the other hand, uranium has a greater solubility and mobility, and so high uranium concentrations are found in fault planes, fractures, and formations where water flow has occurred. Similarly, high concentrations can build up in the permeable beds and on the tubing and casing of producing oil wells. Chemical marine deposits are characterized by their extremely low radioactive content, with none of the three families making any significant contribution. Weathered zones are often indicated by pronounced changes in the thorium and potassium content of the formation but a more or less constant Th/K ratio.

EFFECT OF SHALINESS ON CROSSPLOTS

Shaliness produces a shift of the crossplot point in the direction of a so-called shale point on the chart. The shale point is found by crossplotting the measured values (ϱ_{sh},

ϕ_{Nsh}, t_{sh}) observed in the neighboring shale beds. Generally, the shale point is in the southeast quadrant of neutron-density and sonic-density crossplots, to the northeast on the neutron-sonic crossplot, and in the lower center of the density-photoelectric cross section crossplot. These shale values, however, may only approximate the parameters of the shaly material within the permeable beds.

EFFECT OF SECONDARY POROSITY ON CROSSPLOTS

Sonic logs respond differently to secondary porosity than the neutron and density logs. They largely ignore vuggy porosity and fractures and respond primarily to intergranular porosity; neutron and density tools respond to the total porosity.

Thus, on crossplots involving the sonic log, secondary porosity displaces the points from the correct lithology line and indicates something less than the total porosity; the neutron-density crossplots yield the total porosity.

THE SECONDARY POROSITY INDEX LOG

In clean, liquid-filled carbonate formations with known matrix parameters, a secondary porosity index ($I_{\phi 2}$) can be computed as the difference between total porosity, as determined from neutron and/or density logs, and porosity from the sonic log

$$I_{\phi 2} = \phi - \phi_{SV} \cdot \qquad \text{(Eq. 6-1)}$$

A relative secondary porosity index is sometimes computed as the ratio of the absolute index, defined above, to total porosity.

EFFECT OF HYDROCARBONS ON CROSSPLOTS

Gas or light hydrocarbons cause the apparent porosity from the density log to increase (bulk density to decrease) and porosity from the neutron log to decrease. On a neutron-density crossplot this results in a shift (from the liquid-filled point of the same porosity) upward and to the left, almost parallel to the isoporosity lines. If a gas correction is not made, the porosity read directly from the crossplot chart may be slightly too low. However, the lithology indication from the chart can be quite erroneous.

Arrow B-A on Fig. 6-7 illustrates the correction for this hydrocarbon shift. Log Point B is for a clean limestone containing gas of density 0.1 g/cm^3. Corrected Point A falls near the limestone line, and porosity can be read directly.

The hydrocarbon shift $(\Delta \varrho_b)\,h$ and $(\Delta \phi_N)\,h$ are given by

$$(\Delta \varrho_b)h = - A\phi S_{hr} \qquad \text{(Eq. 6-2)}$$

and

$$(\Delta \phi_N)h = - B\phi S_{hr} - \Delta \phi_{Nex}, \qquad \text{(Eq. 6-3)}$$

where $\Delta \phi_{Nex}$ is excavation effect (discussed in Chapter 5).

For oil-bearing formations

$$A = (1.19 - 0.16\, P_{mf})\, \varrho_{mf} - 1.19\, \varrho_h - 0.032 \qquad \text{(Eq. 6-4)}$$

and

$$B = 1 - \frac{\varrho_h + 0.30}{\varrho_{mf}\,(1 - P_{mf})} \cdot \qquad \text{(Eq. 6-5)}$$

For gas-bearing formations

$$A = (1.19 - 0.16\, P_{mf})\, \varrho_{mf} - 1.33\, \varrho_h \qquad \text{(Eq. 6-6)}$$

and

$$B = 1 - \frac{2.2\, \varrho_h}{\varrho_{mf}\,(1 - P_{mf})}, \qquad \text{(Eq. 6-7)}$$

where

S_{hr} = residual hydrocarbon saturation,

ϱ_h = hydrocarbon density in grams per cubic centimeter,

ϱ_{mf} = mud filtrate density in grams per cubic centimeter,

and

P_{mf} = filtrate salinity in parts per million NaCl.

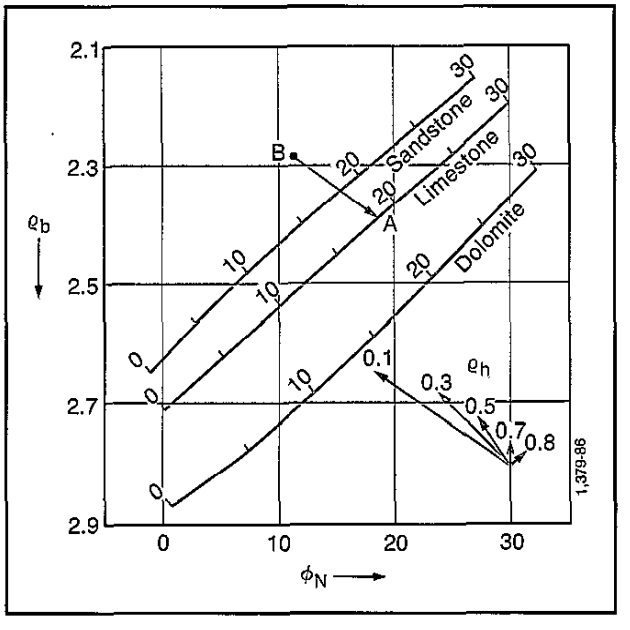

Fig. 6-7—Effect of hydrocarbon. Arrow B-A represents correction of log Point B for hydrocarbon effect for a gas case. The arrows at lower right represent approximate hydrocarbon shifts for various values of ϱ_h for ϕ S_{hr} = 0.15, P_{mf} = 0, and ϱ_{mf} = 1.

The arrows at the lower right of Fig. 6-7 show, for various hydrocarbon densities, the approximate magnitudes and directions of the hydrocarbon shifts as computed from the above relations for $\phi S_{hr} = 15\%$. (Fresh mud filtrate was assumed and excavation effect was neglected.) This value of ϕS_{hr} could occur in a gas sand (e.g., $\phi = 20\%$, $S_{hr} = 75\%$).

Gas will also shift the points on a sonic-neutron plot as a result of the decrease in ϕ_N. Similarly, gas will shift points on a sonic-density plot as a result of the increase in ϕ_D because of the presence of gas. In uncompacted formations, the sonic t reading may also be increased by the effect of the gas.

Hydrocarbon shifts in oil-bearing formations are usually negligible; for clean formations, porosities can be read directly from the porosity graduations on the chart.

M-N PLOT

In more complex mineral mixtures, lithology interpretation is facilitated by use of the M-N plot. These plots combine the data of all three porosity logs to provide the lithology-dependent quantities M and N. M and N are simply the slopes of the individual lithology lines on the sonic-density and density-neutron crossplot charts, respectively. Thus, M and N are essentially independent of porosity, and a crossplot provides lithology identification.

M and N are defined as:

$$M = \frac{t_f - t}{\varrho_b - \varrho_f} \times 0.01 \qquad \text{(Eq. 6-8)}$$

$$N = \frac{\phi_{Nf} - \phi_N}{\varrho_b - \varrho_f}. \qquad \text{(Eq. 6-9)}$$

For fresh muds, $t_f = 189$, $\varrho_f = 1$, and $\phi_{Nf} = 1$. Neutron porosity is in limestone porosity units. The multiplier 0.01 is used to make the M values compatible for easy scaling.

If the matrix parameters (t_{ma}, ϱ_{ma}, ϕ_{Nma}) for a given mineral are used in Eqs. 6-8 and 6-9 in place of the log values, the M and N values for that mineral are defined. For water-bearing formations, these will plot at definitive points on the M-N plot. Based on the matrix and fluid parameters listed in Table 6-1, M and N values are shown in Table 6-2 for several minerals in both fresh mud- and salt mud-filled holes. (N is computed for the CNL log.)

Fig. 6-8 is an M-N plot showing the points for several single-mineral formations. This plot is a simplified version of Chart CP-8.

Points for a mixture of three minerals will plot within the triangle formed by connecting the three respective single-mineral points. For example, suppose a rock mixture exhibits N = 0.59 and M = 0.81; in Fig. 6-8 this point falls within a triangle defined by the limestone-dolomite-quartz points. It would therefore be interpreted in most cases as representing a mixture of limestone, dolomite, and quartz. However, it could also be a limestone-quartz-anhydrite mixture or, less likely, a dolomite-quartz-gypsum mixture, since the point is also contained in those triangles. The combination selected would depend on the geological probability of its occurrence in the formation.

Table 6-1
Matrix and fluid coefficients of several minerals and types of porosity (liquid-filled boreholes).

Mineral	Δt_{ma}	ϱ_{ma}	ϕ_{maSNP}	ϕ_{maCNL}
Sandstone 1 ($V_{ma} = 18{,}000$), $\phi > 10\%$	55.5	2.65	−0.035*	−0.05*
Sandstone 2 ($V_{ma} = 19{,}500$), $\phi > 10\%$	51.2	2.65	−0.035*	−0.05*
Limestone	47.5	2.71	0.00	0.00
Dolomite 1 ($\phi = 5.5\%$ to 30%)	43.5	2.85	0.035*	0.085*
Dolomite 2 ($\phi = 1.5\%$ to 5.5% & > 30%)	43.5	2.85	0.02*	0.065*
Dolomite 3 ($\phi = 0.0\%$ to 1.5%)	43.5	2.85	0.005*	0.04*
Anhydrite	50.0	2.98	−0.005	−0.002
Gypsum	52.0	2.35	0.49**	
Salt	67.0	2.03	0.04	−0.01

Fluids		Δt_f	ϱ_f	ϕ_{fN}
Primary Porosity (Liquid-Filled):	Fresh Mud	189.0	1.00	1
	Salt Mud	185.0	1.10	
Secondary Porosity (In Dolomite):	Fresh Mud	43.5	1.00	1
	Salt Mud		1.10	
(In Limestone):	Fresh Mud	47.5	1.00	1
	Salt Mud		1.10	
(In Sandstone):	Fresh Mud	55.5	1.00	1
	Salt Mud		1.10	

*Average values.
**Based on hydrogen-index computation.

1564-86

Table 6-2
Values of M and N for common minerals.

Mineral	Fresh Mud ($\varrho_f = 1$)		Salt Mud ($\varrho_f = 1.1$)	
	M	N*	M	N*
Sandstone 1 $v_{ma} = 18{,}000$	0.810	0.636	0.835	0.667
Sandstone 2 $v_{ma} = 19{,}500$	0.835	0.636	0.862	0.667
Limestone	0.827	0.585	0.854	0.621
Dolomite 1 $\phi = 5.5$-30%	0.778	0.489	0.800	0.517
Dolomite 2 $\phi = 1.5$-5.5%	0.778	0.500	0.800	0.528
Dolomite 3 $\phi = 0$-1.5%	0.778	0.513	0.800	0.542
Anhydrite $\varrho_{ma} = 2.98$	0.702	0.504	0.718	0.533
Gypsum	1.015	0.296	1.064	0.320
Salt			1.269	1.086

1565-86

*Values of N are computed for CNL neutron log.

Secondary porosity, shaliness, and gas-filled porosity will shift the position of the points with respect to their true lithology, and they can even cause the M-N points to plot outside the triangular area defined by the primary mineral constituents. The arrows on Fig. 6-8 indicate the direction a point is shifted by the presence of each. In the case of shale, the arrow is illustrative only since the position of the shale point will vary with area and formation.

In combination with the crossplots using other pairs of porosity logs and lithology-sensitive measurements, the M-N plot aids in the choice of the probable lithology. This information is needed in the final solution for porosity and lithology fractions.

MID PLOT

Indications of lithology, gas, and secondary porosity can also be obtained using the matrix identification (MID) plot.

To use the MID plot, three data are required. First, apparent total porosity, ϕ_{ta}, must be determined using the appropriate neutron-density and empirical (red curves) neutron-sonic crossplots (Charts CP-1 and -2). For data plotting above the sandstone curve on these charts, the apparent total porosity is defined by a vertical projection to the sandstone curve.

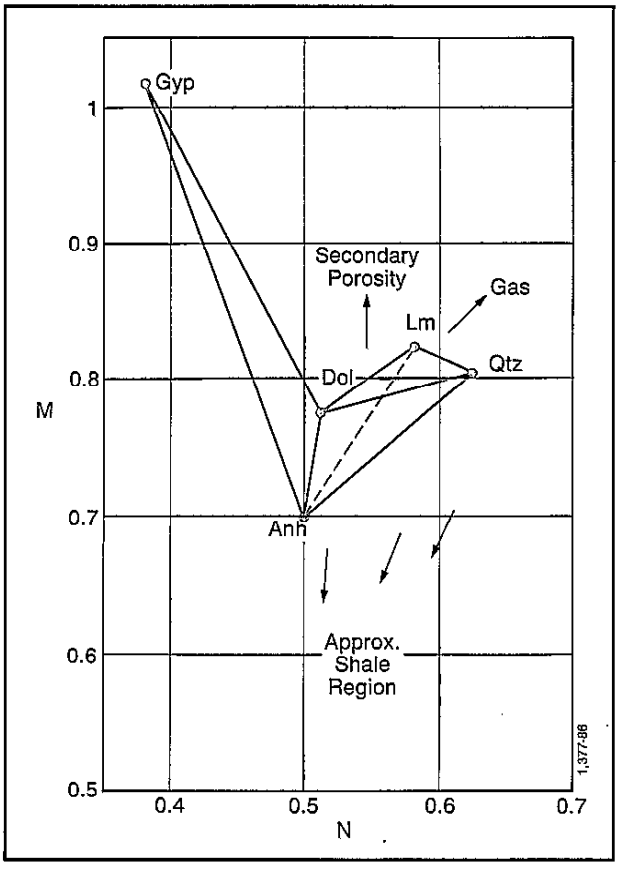

Fig. 6-8—M-N plot showing points for several minerals (N is calculated using SNP neutron log). Arrows show direction of shifts caused by shale, gas, and secondary porosity.

Next, an apparent matrix transit time, t_{maa} and an apparent grain density, ϱ_{maa}, are calculated:

$$\varrho_{maa} = \frac{\varrho_b - \phi_{ta}\,\varrho_f}{1 - \phi_{ta}} \qquad \text{(Eq. 6-10)}$$

$$t_{maa} = \frac{t - \phi_{ta}\,t_f}{1 - \phi_{ta}} \quad \text{time-average relationship} \qquad \text{(Eq. 6-11a)}$$

$$t_{maa} = t - \frac{\phi_{ta}\,t}{c} \quad \text{field-observed relationship} \qquad \text{(Eq. 6-11b)}$$

where

ϱ_b is bulk density from density log,
t is interval transit time from sonic log,
ϱ_f is pore fluid density,
t_f is pore fluid transit time,
ϕ_{ta} is apparent total porosity,

and

c is a constant ($c \approx 0.68$).

The apparent total porosity is not necessarily the same in the equations. For use in the t_{maa} equations (Eq. 6-11), it is the value obtained from the neutron-sonic crossplot (Chart CP-2). For use in the ϱ_{maa} equation (Eq. 6-10), it is the value obtained from the neutron-density crossplot (Chart CP-1).

Chart CP-14 (Fig. 6-9) can be used to solve graphically for ϱ_{maa} (Eq. 6-10) and for t_{maa} using the empirical field-observed transit time-to-porosity relationship (Eq. 6-11b). The northeast half (upper right) of the chart solves for the apparent matrix interval transit time, t_{maa}. The southwest half (lower left of the same chart) solves for the apparent matrix grain density, ϱ_{maa}.

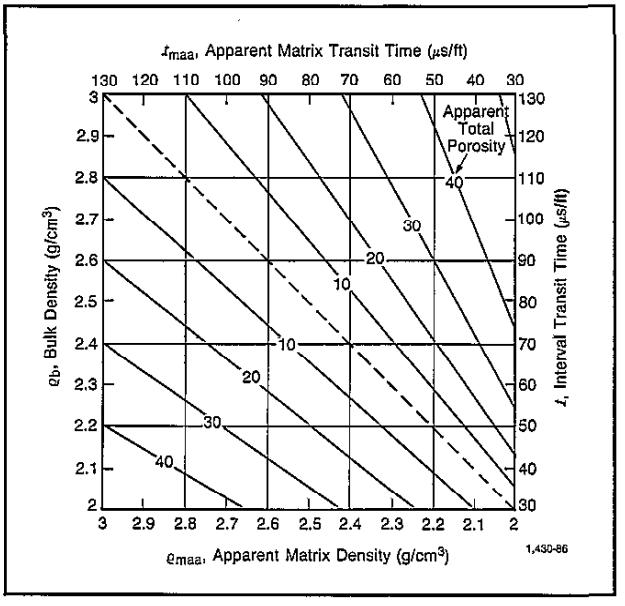

Fig. 6-9—Determination of apparent matrix parameters from bulk density or interval transit time and apparent total porosity; fluid density = 1.

The crossplot of the apparent matrix interval transit time and apparent grain density on the MID plot will identify the rock mineralogy by its proximity to the labeled points on the plot. On Chart CP-15 the most common matrix minerals (quartz, calcite, dolomite, anhydrite) plot at the positions shown (Fig. 6-10). Mineral mixtures would plot at locations between the corresponding pure mineral points. Lithology trends may be seen by plotting many levels over a zone and observing how they are grouped on the chart with respect to the mineral points.

The presence of gas shifts the plotted points to the northeast on the MID plot. Secondary porosity shifts points in the direction of decreased t_{maa}; i.e., to the left. For the SNP log, shales tend to plot in the region to the right of anhydrite on the MID plot. For the CNL log, shales tend to plot in the region above the anhydrite point.

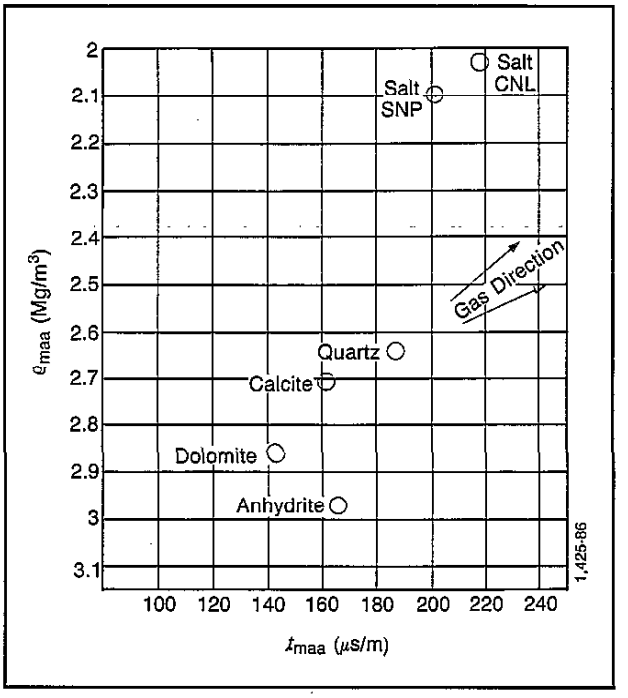

Fig. 6-10—Matrix identification (MID) plot.

Sulfur plots off the chart to the northeast at $t_{maa} \approx 122$ and $\varrho_{maa} \approx 2.02$. Thus, the direction to the sulfur point from the quartz, calcite, dolomite, anhydrite group is approximately the same as the direction of the gas-effect shift. Gypsum plots to the southwest.

The concept of the MID plot is similar to that of the M-N plot. However, instead of having to compute values of M and N, values of ϱ_{maa} and t_{maa} are obtained from charts (Chart CP-14). For most accurate results, log readings should, of course, be depth matched and corrected for hole effect, etc. The need for such corrections can often be seen from the trend of the plotted points on the MID plot (Fig. 6-10).

ϱ_{maa} vs. U_{maa} MID PLOT

Another crossplot technique for identifying lithology uses data from the Litho-Density log. It crossplots the apparent matrix grain density, ϱ_{maa}, and the apparent matrix volumetric cross section, U_{maa} (in barns per cubic centimeter).

The apparent matrix grain density is obtained as previously described in the MID plot discussion. Charts CP-1 and -14 are used for its determination.

The apparent matrix volumetric cross section is computed from the photoelectric cross section index and bulk density measurements

$$U_{maa} = \frac{P_e \varrho_e - \phi_{ta} U_f}{1 - \phi_{ta}}, \qquad \text{(Eq. 6-12)}$$

where

P_e is photoelectric absorption cross section index,

ϱ_e is electron density $\left(\varrho_e = \frac{\varrho_b + 0.1883}{1.0704}\right)$,

and

ϕ_{ta} is apparent total porosity.

The apparent total porosity can be estimated from the density-neutron crossplot if the formation is liquid filled.

Chart CP-20 solves Eq. 6-12 graphically. A simplified version is shown in Fig. 6-11.

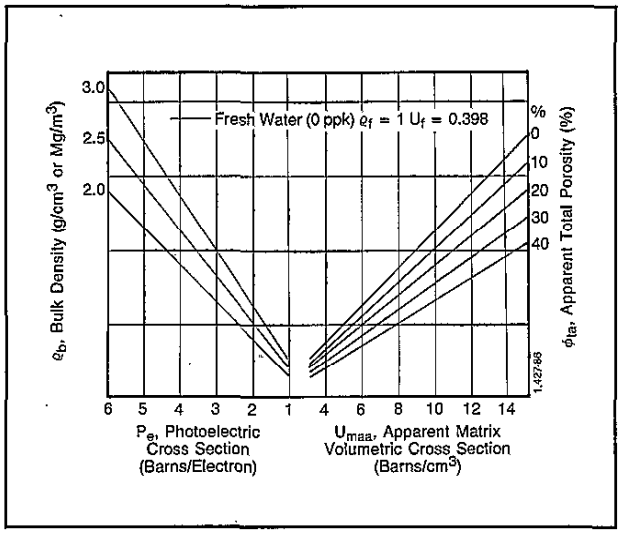

Fig. 6-11—Matrix identification plot; ϱ_{maa} vs. U_{maa}.

Table 6-3 lists the photoelectric absorption cross section index, the bulk density, and the volumetric cross section for common minerals and fluids. For the minerals, the listed value is the matrix value (ϱ_{ma}, U_{ma}); for the fluids, it is the fluid value (ϱ_f, U_f). Chart CP-21 (Fig. 6-12) shows the location of these minerals on a ϱ_{maa} versus U_{maa} crossplot. The triangle encompassing the three common matrix minerals of quartz, calcite, and dolomite has been scaled in the percentages of each mineral. For example, a point exhibiting an apparent matrix grain density of 2.76 g/cm³ and volumetric cross section of 10.2 barns/cm³ would be defined by the crossplot as 40% calcite, 40% dolomite, and 20% quartz provided no other minerals exist and the pores are liquid saturated.

On this crossplot, gas saturation displaces points upwards on the chart and heavy minerals displace points to the right. Clays and shales plot below the dolomite point.

Table 6-3

	P_e	Sp.gr	ϱ_{bLOG}	U
Quartz	1.810	2.65	2.64	4.780
Calcite	5.080	2.71	2.71	13.800
Dolomite	3.140	2.85	2.85	9.000
Anhydrite	5.050	2.96	2.98	14.900
Halite	4.650	2.17	2.04	9.680
Siderite	14.700	3.94	3.89	55.900
Pyrite	17.000	5.00	4.99	82.100
Barite	267.000	4.48	4.09	1065.000
Water (fresh)	0.358	1.00	1.00	0.398
Water (100K ppm NaCl)	0.734	1.06	1.05	0.850
Water (200K ppm NaCl)	1.120	1.12	1.11	1.360
Oil (n(CH_2))	0.119	ϱ_o	1.22 ϱ_o − .118	0.136 ϱ_o
Gas (CH_4)	0.095	ϱ_g	1.33 ϱ_g − .188	0.119 ϱ_g

1566-86

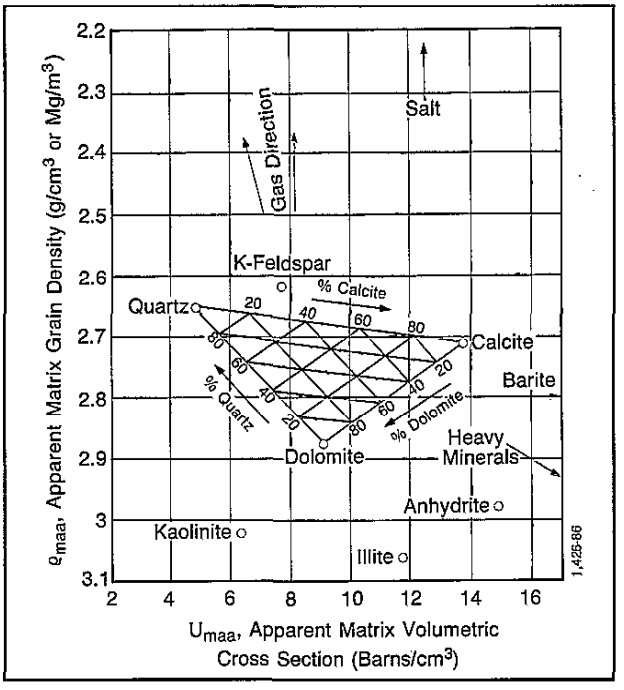

Fig. 6-12—Matrix identification plot.

COMPLEX LITHOLOGY MIXTURES

Mathematically, the transformation of the basic measurement of a porosity or other appropriate log into porosity and/or lithology and/or pore fluid identification is simply the solution of one or more simultaneous equations. When the rock matrix contains only a single known mineral and the saturating fluid is also known, any one of the porosity logs can be used for porosity identification. In other words, a single equation (single log measurement) is sufficient to solve for a single unknown (in this case, the porosity).

If, however, in addition to porosity, the rock matrix is an unknown mixture of two known minerals, then two independent equations (two log measurements) are needed to solve for the two unknowns (in this case, the porosity and the mineral fractions). For example, in a limestone-dolomite mixture, the combination of neutron and density logs could be used. Their responses to porosity and lithology are

$$\varrho_b = \phi\varrho_f + (1 - \phi)\,(L\varrho_{maL} + D\varrho_{maD}) \qquad \text{(Eq. 6-13)}$$

and

$$\phi_N = \phi\,\phi_f + (1 - \phi)\,(L\phi_{maL} + D\phi_{maD})\,, \qquad \text{(Eq. 6-14)}$$

where

ϱ_b and ϕ_N are the measured bulk density and apparent limestone porosity from the density and neutron logs, respectively;

ϱ_f and ϕ_f are the density and hydrogen index of the fluid saturating the pores investigated by the density and neutron logs;

ϕ is the porosity;

ϱ_{maL} and ϱ_{maD} are the grain densities of limestone and dolomite, respectively;

ϕ_{maL} and ϕ_{maD} are the hydrogen indices of limestone and dolomite;

and

L and D are the fractions of limestone and dolomite in the rock matrix mixture.

Three unknowns exist in the above two equations; they are ϕ, L, and D. However, since the mineral fractions of the rock matrix must total unity, the dolomite fraction could be expressed in terms of the limestone fraction as $D = 1 - L$, thereby reducing the number of unknowns in the above equations to two; or a third material balance equation of $L + D = 1$ could be included. In either event, solution for ϕ, L, and D is possible since the number of equations (and independent log measurements) equals the number of unknowns.

The several crossplot charts that plot one log measurement against another are simply approximate graphical solutions of the responses of two log measurements for porosity and lithology determination. Charts CP-1, -2, -7, -16, and -17 are examples. These charts can also be used when the rock matrix is composed of a single, but unknown, mineral. The problem is the same; it is one of two equations and two unknowns. The unknowns, in this situation, are porosity and mineral identification (i.e., its ϱ_{ma} and ϕ_{ma} characteristics). It is presumed that ϱ_{ma} and ϕ_{ma} are known for most minerals expected to be encountered in sedimentary rocks.

When more unknowns exist, such as in a rock matrix made up of three minerals, another independent equation (or log measurement) is required. The sonic log might be added to the neutron-density combination. The equations become for a limestone-dolomite-quartz mixture:

$$\varrho_b = \phi\varrho_f + (1 - \phi)\,(L\varrho_{maL} + D\varrho_{maD} + S\varrho_{maS}) \qquad \text{(Eq. 6-15)}$$

$$\phi_N = \phi\,\phi_f + (1 - \phi)\,(L\phi_{maL} + D\phi_{maD} + S\phi_{maS}) \qquad \text{(Eq. 6-16)}$$

$$t = \phi\,t_f + (1 - \phi)\,(Lt_{maL} + \phi t_{maD} + St_{maS}) \qquad \text{(Eq. 6-17)}$$

$$1 = L + D + S\,. \qquad \text{(Eq. 6-18)}$$

Simultaneous solution of these four equations yields values for the four unknowns (L, D, S, and ϕ). The M-N plot (Chart CP-8), the ϱ_{maa} versus t_{maa} MID plot (Chart CP-15), and the ϱ_{maa} versus U_{maa} Matrix Identification plot (Chart CP-21) are graphical solutions to four unknowns, four equation systems.

Even more complex mixtures can be unraveled by adding more equations (log measurements). Of course, the additional log measurements must respond to the same, but not necessarily all, unknown petrophysical parameters; they should not introduce additional unknowns into the problem.

It is not easy to develop graphical techniques that can solve systems of five, six, and more simultaneous equations for a large number of unknown petrophysical parameters. These problems are best handled by computer programs. One such program is Litho-Analysis*.

LITHO-ANALYSIS PROGRAM

This program uses the uranium, thorium, and potassium concentration measurements from the NGS log; the bulk density and photoelectric cross section index measurements from the Litho-Density log; and the apparent porosity measurement from the CNL log. Lithology mixtures containing quartz (sandstone), calcite (limestone), dolomite, anhydrite, halite (salt), two shales (low- and high-potassium clays), feldspar, and mica can be unraveled into the fractions of each mineral present.

Response equations and parameter selections are obtained from the comparison of thorium and potassium measurements and from the apparent matrix density and apparent volumetric photoelectric cross section index (Chart CP-21). The thorium and potassium response equations are used to estimate the volumes of clays, mica, and feldspar. The apparent

matrix density (ϱ_{maa}) and volumetric cross section (U_{maa}) data can then be corrected for clay, mica, and feldspar. A three-mineral analysis is then done using the corrected ϱ_{maa} and U_{maa} data. A test ensures that the clay correction is within the limits for the assumed lithology model. If it is not within limits, either the estimate of clay volume or the lithology model, or both, are changed.

The general case of two clays and feldspar can be modeled by observing the rather close proximity of the 100% kaolinite, montmorillonite, and chlorite clay points on Chart CP-19. This suggests defining (1) a low-potassium clay point, Cl_1; (2) a high-potassium clay point, Cl_2, which is generally illite; and (3) a low-thorium, high-potassium point; i.e., feldspar, Fel; and (4) a clean matrix point, Mat. This model is depicted by Fig. 6-13. The line connecting the two clay points is called the clay line, and the line from the origin through the feldspar point is called the feldspar line. W_{Cl} is obtained by linear interpolation between the clay and feldspar lines.

The following four-mineral natural gamma ray spectral interpretation model is assumed:

$$W_{Cl} = W_{Cl_1} + W_{Cl_2} \qquad \text{(Eq. 6-19)}$$

$$Th = Th_{Cl_1} W_{Cl_1} + Th_{Cl_2} W_{Cl_2} + Th_{Mat} W_{Mat} + Th_{Fel} W_{Fel} \qquad \text{(Eq. 6-20)}$$

$$K = K_{Cl_1} W_{Cl_1} + K_{Cl_2} W_{Cl_2} + K_{Mat} W_{Mat} + K_{Fel} W_{Fel} \qquad \text{(Eq. 6-21)}$$

$$1 = W_{Cl_1} + W_{Cl_2} + W_{Mat} + W_{Fel}, \qquad \text{(Eq. 6-22)}$$

with W_{Cl} as a known function of Th and K. The model is shown by Fig. 6-14. The resulting mineral weight fractions can readily be converted to volume fractions.

The Litho-Density measurements of bulk density and effective photoelectric cross section are sensitive to the presence of any of the six sedimentary categories: carbonates, evaporites, silicates, clays, micas, feldspar. Chart CP-21 presents a crossplot of U_{maa} versus ϱ_{maa}. The locations of the various mineral points represent theoretical locations based upon the chemical compositions of the various minerals.

The fundamental Litho-Density interpretation problem is the correction of the apparent matrix volumetric cross section and apparent matrix density for the presence of feldspar, mica, or clay. The presence of evaporites must also be considered. Assuming the type of clay is known and assuming, for discussion, that initially no evaporites exist, the Litho-Density variables are corrected for the presence of feldspar and clay. This problem can be expressed mathematically as

$$\varrho_{maa} - P_4\varrho_4 - P_5\varrho_5 = P_1\varrho_1 + P_2\varrho_2 + P_3\varrho_3 \qquad \text{(Eq. 6-23)}$$

$$U_{maa} - P_4U_4 - P_5U_5 = P_1U_1 + P_2U_2 + P_3U_3, \qquad \text{(Eq. 6-24)}$$

$$1 - P_4 - P_5 = P_1 + P_2 + P_3, \qquad \text{(Eq. 6-25)}$$

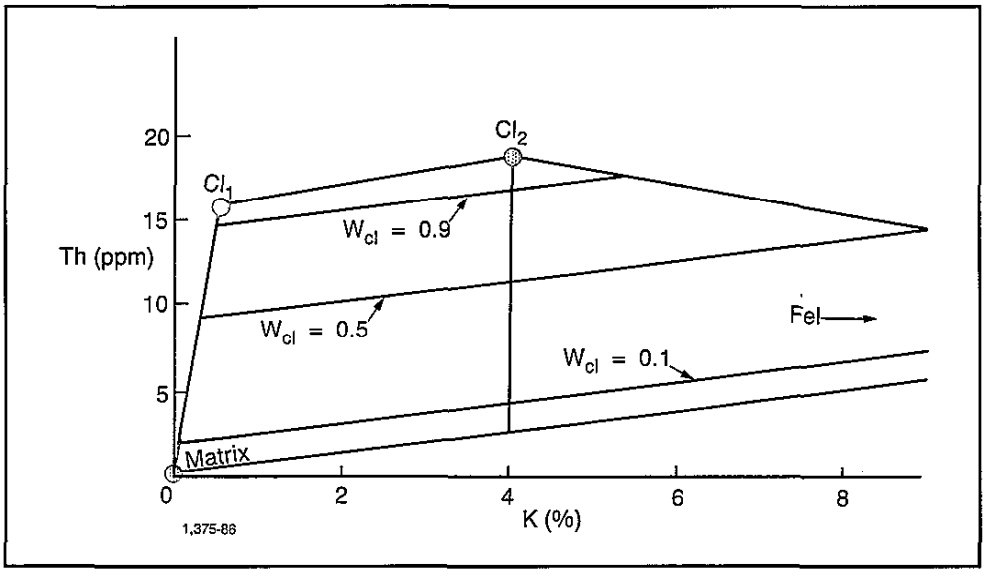

Fig. 6-13—Estimation of total clay percentage.

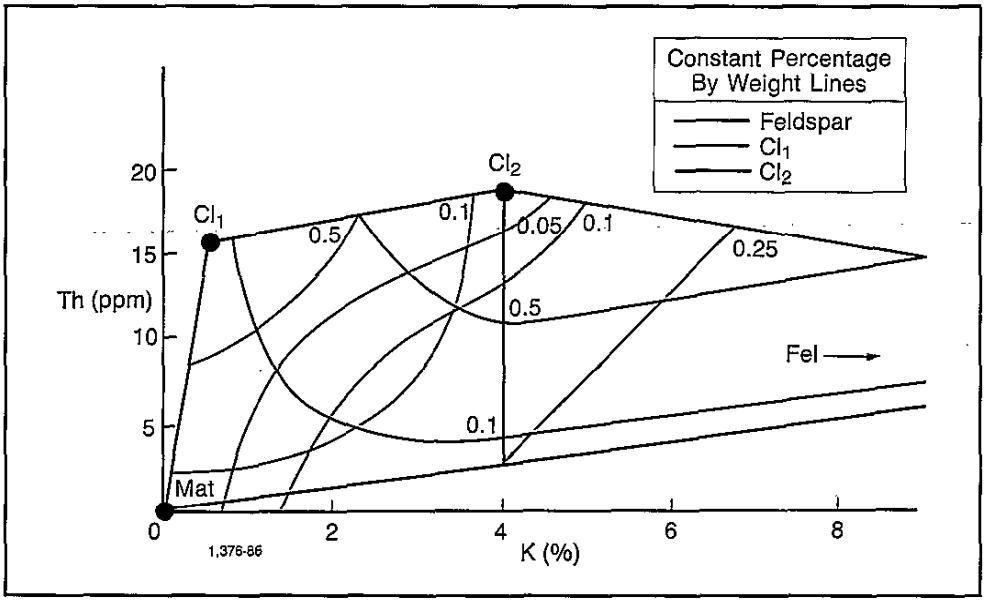

Fig. 6-14—Four-mineral spectral model.

where

ϱ_1 is the density of mineral 1,

P_1 is the proportion of mineral 1 in formation matrix,

and

U_1 is the volumetric cross section of mineral 1.

Indices 1, 2, and 3 correspond to the three selected matrix minerals (say, quartz, calcite, and dolomite) and form the vertices of the chosen triangle of Chart CP-21. Indices 4 and 5 correspond to the feldspar and clay corrections obtained from the spectral measurement of Th and K.

There are now three unknowns (P_1, P_2, and P_3) and three equations. Minimum and maximum amounts of clay can be set by not allowing a negative P_1.

PRESENCE OF EVAPORITES

Eqs. 6-19 through 6-25, with some constraints on the proportion of clay, define the basic Litho-Analysis model. However, a test must be applied to detect evaporites—anhydrite and salt. The Litho-Analysis model accepts the existence of two models: (1) a calcite, quartz, dolomite (plus the allowance of a clay/feldspar correction) model; and (2) an anhydrite, salt, dolomite model. Then, the probability of each model is computed. The final estimates of calcite, quartz, dolomite, anhydrite, and salt are just those obtained from the Litho-Density measurements (with Model 1 corrected for clay, feldspar) for each of the two models. However, they are weighted in accordance with the probability of the respective models.

This probability logic is rather complex. It is sufficient to say, for example, that the probability of anhydrite or salt increases as the ϱ_{maa} versus U_{maa} point moves away from the calcite, quartz, dolomite triangle towards the anhydrite or salt point, and the neutron porosity decreases. However, the probability of anhydrite or salt decreases with increasing clay fraction.

A Litho-Analysis computation is shown in Table 6-4 with corresponding X-ray diffraction data.

Table 6-4
Comparison of Litho-Analysis data with X-ray diffraction on cores.

	Depth (ft) 11,403	11,405	11,415	11,416	Data
Sand	85%	75%	82%	79%	Litho-Analysis
	91	73	86	78	X-ray diffraction
Limestone	0%	19%	12%	8%	Litho-Analysis
	0	19	3	3	X-ray diffraction
Dolomite	0%	0%	0%	0%	Litho-Analysis
	0	0	0	0	X-ray diffraction
Feldspar	0%	0%	0%	0%	Litho-Analysis
	Trace	1	0	Trace	X-ray diffraction
Siderite	—	—	—	—	Litho-Analysis
	Trace	0%	1%	1%	X-ray diffraction
Illite	0%	0%	0%	0%	Litho-Analysis
	2	1	2	4	X-ray diffraction
Clay 2	15%	6%	6%	13%	Litho-Analysis
	7	6	8	14	X-ray diffraction

1567-86

FLUID IDENTIFICATION

Most of the discussion to this point has involved the use of porosity logs in determining porosity when the rock lithology is not known or when the rock matrix consists of two or more known minerals in unknown proportions. These techniques generally require that the fluid saturating the rock pores is known and is a liquid.

Similar combinations of porosity logs can be used to determine porosity when the fluid or fluids saturating the pores are unknown but the rock lithology is known. In this case, the tool response equation for the density log is

$$\varrho_b = \phi\,[S_h\,\varrho_h + (1 - S_h)\,\varrho_w] + (1 - \phi)\,\varrho_{ma}\,, \qquad \text{(Eq. 6-26)}$$

where

S_h is hydrocarbon saturation in the zone investigated by the density log

and

ϱ_h is hydrocarbon density.

Similar tool response equations can be written for the neutron and sonic logs.

To determine porosity from Eq. 6-26, the density, and hence the nature, of the saturating hydrocarbon and/or the fractions of hydrocarbon and water saturation must be known. If only one of these parameters is known, the other can be found by combining the density log with another porosity log—usually the neutron log. Chart CP-5 graphically solves the density log response equation (Eq. 6-26) and a similar neutron log response equation when the nature of the saturating hydrocarbon is known approximately. Porosity and gas saturation or water saturation can be determined.

If the nature of the saturating hydrocarbon is not known but its fraction of saturation is known, the chart (CP-9) "Porosity Estimation in Hydrocarbon-Bearing Formations" permits the estimation of porosity from a comparison of the density and neutron logs. Hydrocarbon saturation can be estimated from a microresistivity or shallow dielectric measurement. The density of the hydrocarbon saturation can be estimated from Chart CP-10.

REFERENCES

1. Raymer, L.L. and Biggs, W.P.: "Matrix Characteristics Defined by Porosity Computations," *Trans.*, 1963 SPWLA Annual Logging Symposium.
2. Poupon, A., Hoyle, W.R., and Schmidt, A.W.: "Log Analysis in Formations with Complex Lithologies," *J. Pet. Tech.* (Aug. 1971).
3. Gardner, J.S. and Dumanoir, J.L.: "Litho-Density Log Interpretation," *Trans.*, 1980 SPWLA Annual Logging Symposium, paper N.
4. Serra, O., Baldwin, J., and Quirein, J.: "Theory, Interpretation, and Practical Applications of Natural Gamma Ray Spectroscopy," *Trans.*, 1980 SPWLA Annual Logging Symposium, paper Q.
5. Gaymard, R. and Poupon, A.: "Response of Neutron and Formation Density Logs in Hydrocarbon-Bearing Formations," *The Log Analyst* (Sept.-Oct. 1968).
6. Burke, J.A., Campbell, R.L., Jr., and Schmidt, A.W.: "The Litho-Porosity Crossplot," *The Log Analyst* (Nov.-Dec. 1969).
7. Hassan, M. and Hossin, A.: *Contribution a L'etude des Comportements du Thorium et du Potassium Dans les Roches Sedimentaries,* C. R. Acad. Sci., Paris (1975).
8. Edmundson, H. and Raymer, L.L.: "Radioactive Logging Parameters for Common Minerals," *The Log Analyst* (Sept.-Oct. 1979).
9. Suau, J. and Spurlin, J.: "Interpretation of Micaceous Sandstones in the North Sea," *Trans.*, 1982 SPWLA Annual Logging Symposium.
10. Quirein, J.A., Gardner, J.S., and Watson, J.T.: "Combined Natural Gamma Ray Spectral/Litho-Density Measurements Applied to Complex Lithologies," paper SPE 11143 presented at the 1982 SPE Annual Technical Conference and Exhibition.
11. Delfiner, P.C, Peyret, O., and Serra, O.: "Automatic Determination of Lithology From Well Logs," paper SPE 13290 presented at the 1984 SPE Annual Technical Conference and Exhibition.
12. *Log Interpretation Charts*, Schlumberger Well Services, Houston (1989).

7 Resistivity Logs

The resistivity of a formation is a key parameter in determining hydrocarbon saturation. Electricity can pass through a formation only because of the conductive water it contains. With a few rare exceptions, such as metallic sulfide and graphite, dry rock is a good electrical insulator. Moreover, perfectly dry rocks are very seldom encountered. Therefore, subsurface formations have finite, measurable resistivities because of the water in their pores or absorbed in their interstitial clay.

The resistivity of a formation depends on:

- Resistivity of the formation water.
- Amount of water present.
- Pore structure geometry.

The resistivity (specific resistance) of a substance is the resistance measured between opposite faces of a unit cube of that substance at a specified temperature. The meter is the unit of length and the ohm is the unit of electrical resistance. In abbreviated form, resistivity is

$$R = r\,A/L\,, \qquad \text{(Eq. 7-1)}$$

where

R is resistivity in ohm-meters,

r is resistance in ohms,

A is area in square meters,

and

L is length in meters.

The units of resistivity are ohm-meters squared per meter, or simply ohm-meters (ohm-m).

Conductivity is the reciprocal of resistivity and is expressed in mhos per meter. To avoid decimal fractions, conductivity is usually expressed in millimhos per meter (mmho/m), where 1000 mmho/m = 1 mho/m:

$$C = \frac{1000}{R}\,. \qquad \text{(Eq. 7-2)}$$

Formation resistivities are usually from 0.2 to 1000 ohm-m. Resistivities higher than 1000 ohm-m are uncommon in permeable formations but are observed in impervious, very low porosity (e.g., evaporites) formations.

Formation resistivities are measured by either sending current into the formation and measuring the ease of the electrical flow through it or by inducing an electric current into the formation and measuring how large it is.

CONVENTIONAL ELECTRICAL LOGS

During the first quarter-century of well logging, the only resistivity logs available were the conventional electrical surveys. Thousands of them were run each year in holes drilled all over the world. Since then, more sophisticated resistivity logging methods have been developed to measure the resistivity of the flushed zone, R_{xo}, and the true resistivity of the uninvaded virgin zone, R_t.

The conventional electrical survey (ES) usually consisted of an SP, 16-in. normal, 64-in. normal, and 18-ft 8-in. lateral devices. Since the ES log is the only log available in many old wells, the measurement principles and responses are covered in this section. For more detailed information on old electric logs, refer to Ref. 22.

Principle

Currents were passed through the formation by means of current electrodes, and voltages were measured between measure electrodes. These measured voltages provided the resistivity determinations for each device.

In a homogeneous, isotropic formation of infinite extent, the equipotential surfaces surrounding a single current-emitting electrode (A) are spheres. The voltage between an electrode (M) situated on one of these spheres and one at infinity is proportional to the resistivity of the homogeneous formation, and the measured voltage can be scaled in resistivity units.

Resistivity Devices

In the normal device (Fig. 7-1), a current of constant intensity is passed between two electrodes, A and B. The resultant potential difference is measured between two other electrodes, M and N. Electrodes A and M are on the sonde. B and N are, theoretically, located an infinite distance away. In practice, B is the cable armor, and N is an electrode on the bridle (the insulation-covered lower end of the cable) far removed from A and M. The distance AM is called the spacing (16-in. spacing for the short normal, 64-in. spacing for the long normal), and the point of inscription for the measurement is at O, midway between A and M.

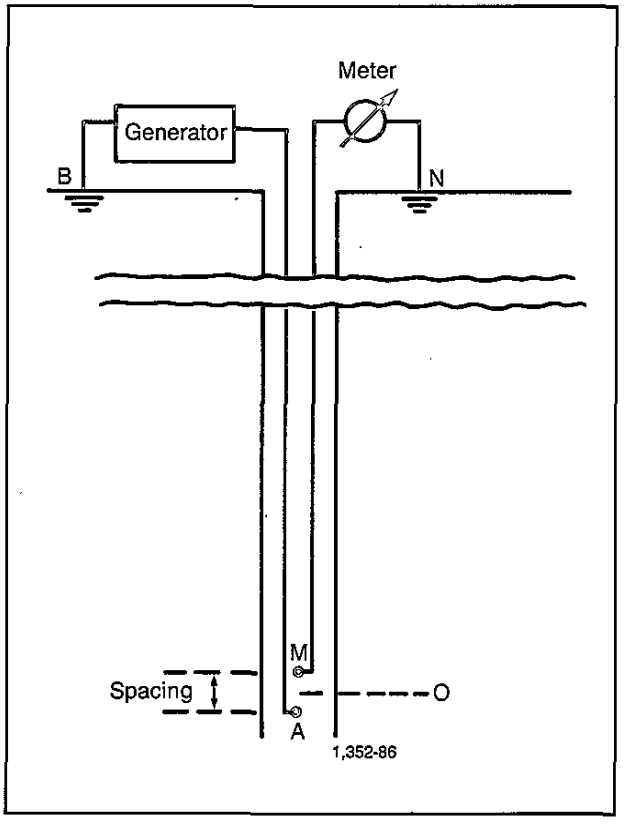

Fig. 7-1—Normal device—basic arrangement.

In the basic lateral device (Fig. 7-2), a constant current is passed between A and B, and the potential difference between M and N, located on two concentric spherical equipotential surfaces centered on A, is measured. Thus, the voltage measured is proportional to the potential gradient between M and N. The point of inscription is at O, midway between M and N. The spacing AO is 18 ft 8 in. The sonde used in practice differs from that shown in Fig. 7-2 in that the positions of the current and measuring electrodes are interchanged; this

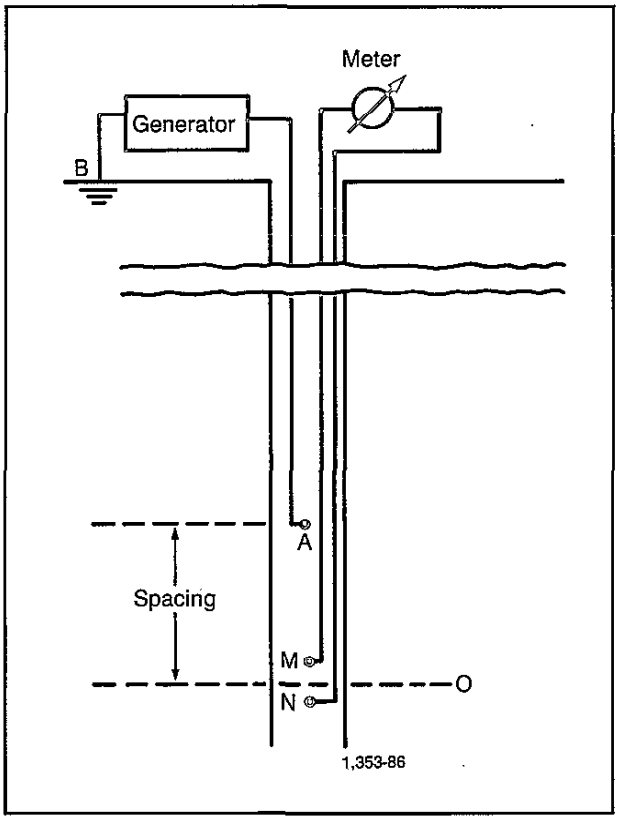

Fig. 7-2—Lateral device—basic arrangement.

reciprocal sonde records the same resistivity values as the basic sonde described above. Also, all electrodes are in the borehole, with N located 50 ft 10 in. above M.

Generally, the longer the spacing, the deeper the device investigates into the formation. Thus, of the ES resistivity logs, the 18-ft 8-in. lateral has the deepest investigation and the 16-in. normal the shallowest. In practice, however, the apparent resistivity, R_a, recorded by each device is affected by the resistivities and geometrical dimensions of all media around the device (borehole, invaded and uncontaminated zones, and adjacent beds).

Normal and Lateral Curves

In the following examples, the shapes of the normal and lateral curves are described for a few typical cases. All cases correspond to noninvaded formations. To read the conventional resistivity logs correctly, a knowledge of these typical curve shapes is required.

Fig. 7-3 illustrates the response of the normal device in beds more resistive than the surrounding formations. (The resistivities of the various media are indicated on the figure.)

The upper part shows the response in a thick bed (h = 10 AM). The curve is symmetrical and a maximum is observed at the center of the bed, where the reading is almost equal to R_t (no invasion). The apparent bed thickness on the normal curve is less than actual bed thickness by an amount equal to the spacing.

The lower part shows the response in a bed with a thickness less than the spacing. The curve is still symmetrical but is reversed. A minimum apparent resistivity, actually less than surrounding formation resistivity, is observed opposite the bed even though bed resistivity is greater than surrounding bed resistivity. Two spurious peaks appear, one above and one below the bed; the distance between the two peaks is equal to bed thickness plus the spacing of the normal.

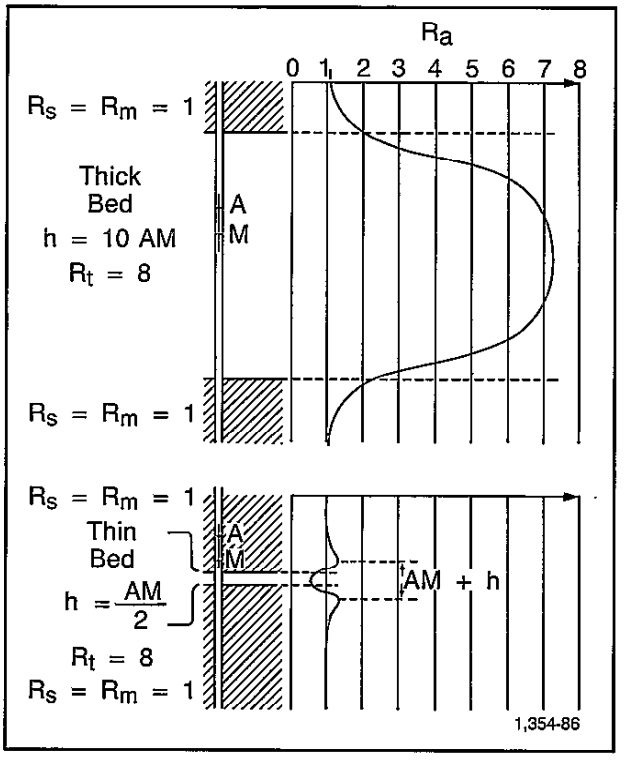

Fig. 7-3—Normal curves—bed more resistive than adjacent formations.

Fig. 7-4 illustrates the response of the normal device in thick and thin beds less resistive than the surrounding formations. The curves are symmetrical and the apparent bed thickness is greater than actual bed thickness by an amount equal to the AM spacing.

Fig. 7-5 illustrates the response of the lateral device in beds more resistive than the surrounding formations. Since the usual lateral spacing is 18 ft 8 in., the cases represented correspond to bed thicknesses of about 190, 28, and 9 ft. All curves are dissymmetrical. In the cases of the 190- and 28-ft beds, note the comparatively low readings in the upper 19 ft of the resistive bed and the high resistivity readings near the lower boundary. For the 190-ft bed, the curve presents a fairly long plateau with readings about equal to R_t; a minimum bed thickness of about 50 ft is needed to obtain these plateau readings uninfluenced by surrounding formations. In the case of the thin bed, there is a fairly sharp resistivity peak opposite the bed, followed by low readings over the "blind zone" below the bed, then a spurious "reflection" peak equal to the AO spacing below the bed. The relationship shown on the figure $(R_{amax}/R_{amin}) \leq (R_t/R_s)$ is of interest, even if accuracy of bed R_t cannot be expected.

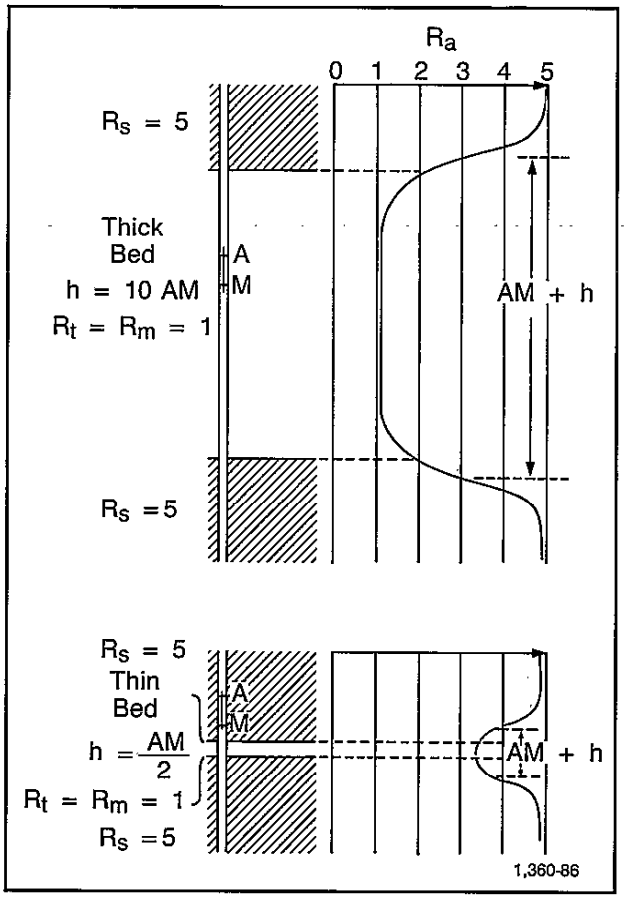

Fig. 7-4—Normal curves—bed less resistive than adjacent formations.

Fig. 7-6 illustrates the response of the lateral device in beds less resistive than the surrounding formations. The curves are again dissymmetrical. In both cases, the anomaly extends below the bed for a distance slightly greater than the AO spacing.

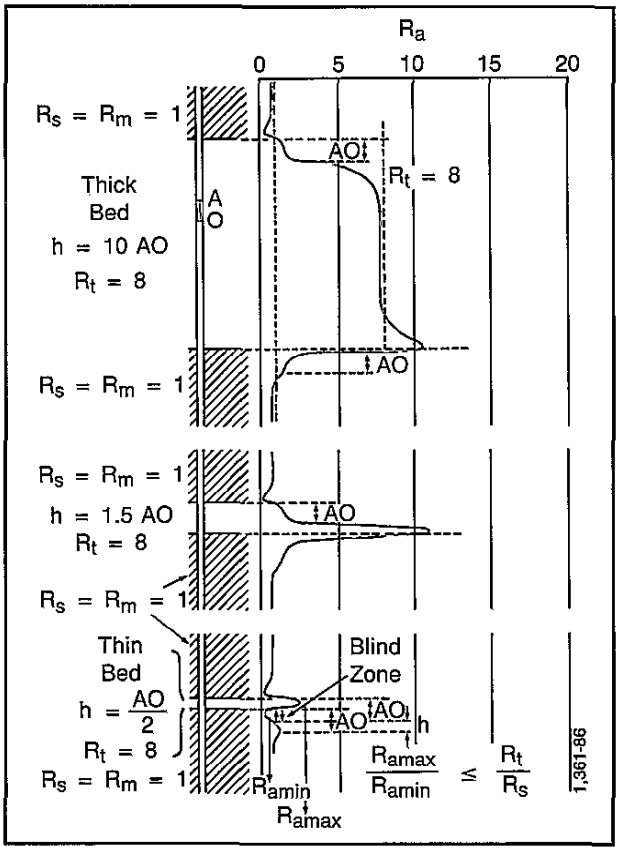

Fig. 7-5—Lateral curves—bed more resistive than adjacent formations.

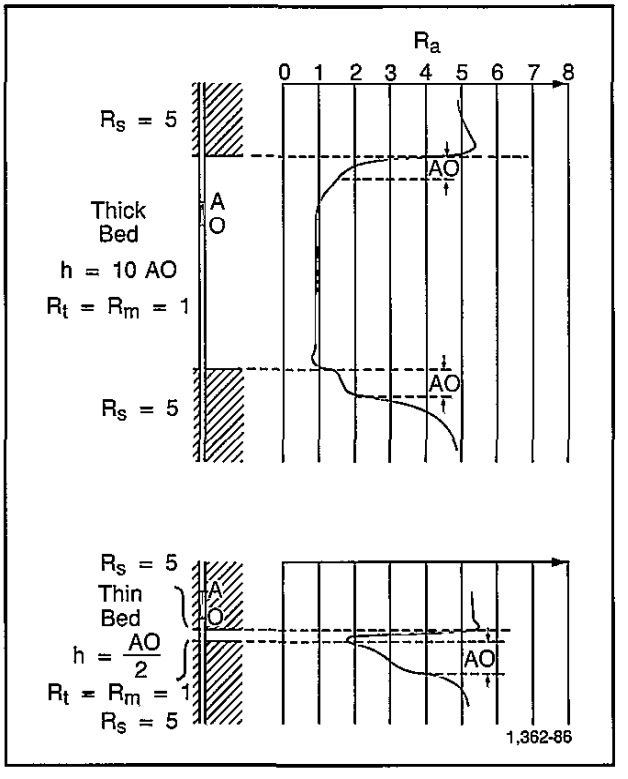

Fig. 7-6—Lateral curves—bed less resistive than adjacent formations.

Figs. 7-3 through 7-6 correspond to formations having moderate resistivities. In highly resistive formations, the normal curves are no longer symmetrical. Fig. 7-7 illustrates a thick bed of infinite resistivity. A two-electrode normal device would still give a symmetrical curve (dash-dot trace), but a three-electrode normal device, as was actually employed, gives a triangular-shaped curve (solid trace) with the peak of the triangle located at a distance AN below the upper boundary. The lateral curve also has a triangular shape, with the peak opposite the lower boundary. Also note that the lateral curve reads very low in the upper 19 ft of the bed.

If the borehole is bottomed in a thick formation of infinite resistivity, the lateral curve reads zero and the normal device gives a constant reading as long as the N electrode remains in the resistive bed (Fig. 7-8). The shapes of the normal and lateral curves become very complicated in highly resistive formations.

R_t From the ES Log

General rules for obtaining R_t from electrical logs are based on the relative resistivity of the bed compared to the resistivities of the mud and surrounding formation. Therefore, formations are subdivided into three classes, depending on the ratio $R_{16''}/R_m$. These simplifying rules are derived from a study of resistivity departure curves.

1. Low Resistivity—when $R_{16''}/R_m < 10$ (invasion up to $2d$)

   The shorter spacings, such as 16- and 64-in. normals, are most useful in finding R_t. Often, $R_m \cong R_s$, in which case the apparent value of the 64-in. normal can be easily corrected to R_t, depending on the ratio $R_{64''}/R_s$ and the bed thickness (see Fig. 7-9).

2. Medium Resistivity—when $10 < R_{16''}/R_m < 50$

   In this case, the 64-in. normal is very useful in the lower portion of the resistivity range; when $R_{16''}/R_m > 20$, the 18-ft 8-in. lateral becomes important, either to find R_t or to confirm the apparent 64-in. normal value. The lateral has an unsymmetrical curve, and R_t must be picked as shown in Fig. 7-9.

3. High Resistivity—when $R_{16''}/R_m > 50$

   The 64-in. normal is greatly affected by invasion so the 18-ft 8-in. lateral is the best choice for estimating R_t.

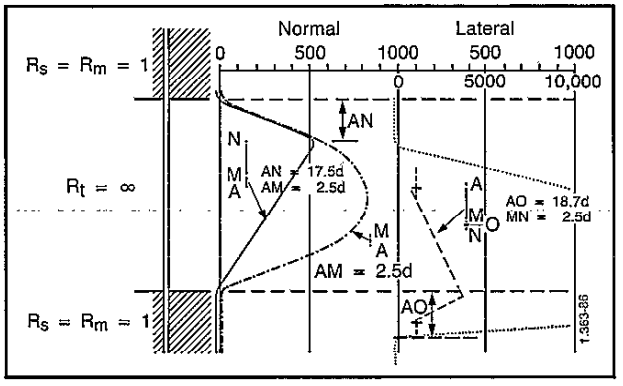

Fig. 7-7—Two-electrode and three-electrode normals and lateral curves in thick bed of infinite resistivity.

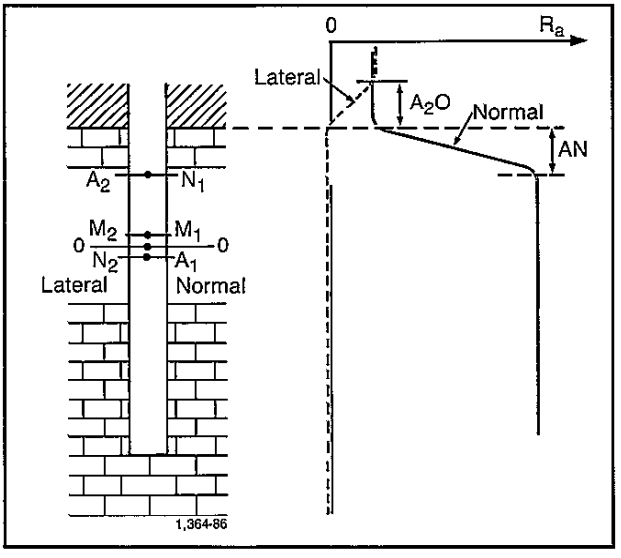

Fig. 7-8—Normal and lateral curves in highly resistive bed incompletely penetrated by borehole.

FOCUSING ELECTRODE LOGS

The responses of conventional electrical logging systems can be greatly affected by the borehole and adjacent formations. These influences are minimized by a family of resistivity tools that uses focusing currents to control the path taken by the measure current. These currents are emitted from special electrodes on the sondes.

The focusing electrode tools include the laterolog and SFL* spherically focused devices. These tools are much superior to the ES devices for large R_t/R_m values (salt muds and/or highly resistive formations) and for large resistivity contrasts with adjacent beds (R_t/R_s or R_s/R_t). They are also better for resolution of thin to moderately thick beds. Focusing electrode systems are available with deep, medium, and shallow depths of investigation.

Devices using this principle have as quantitative applications the determination of R_t and R_{xo}. The deep-reading devices include the Laterolog 7, the Laterolog 3, and the deep laterolog of the DLL* dual laterolog tool. The medium- to shallow-reading devices, all integral with combination tools, are the Laterolog 8 of the DIL* dual induction-laterolog tool, the shallow laterolog of the DLL tool, and the SFL of the ISF and DIL-SFL combinations.

Laterologs 3, 7, and 8 are now obsolete but their design principles will be discussed since many wells have been logged with these devices over the years.

Laterolog 7

The LL7 device comprises a center electrode, A_O, and three pairs of electrodes: M_1 and M_2; M'_1 and M'_2; and A_1 and A_2 (Fig. 7-10). The electrodes of each pair are symmetrically located with respect to A_O and are electrically connected to each other by short-circuiting wire.

A constant current, i_o, is emitted from A_O. Through bucking electrodes, A_1 and A_2, an adjustable current is emitted; the bucking current intensity is adjusted automatically so that the two pairs of monitoring electrodes, M_1 and M_2 and M'_1 and M'_2, are brought to the same potential. The potential drop is measured between one of the monitoring electrodes and an electrode at the surface (i.e., at infinity). With a constant i_o current, this potential varies directly with formation resistivity.

Since the potential difference between the M_1-M_2 pair and the M'_1-M'_2 pair is maintained at zero, no current from A_O is flowing in the hole between M_1 and M'_1 or between M_2 and M'_2. Therefore, the current from A_O must penetrate horizontally into the formations.

Fig. 7-10 shows the distribution of current lines when the sonde is in a homogeneous medium; the "sheet" of i_o current retains a fairly constant thickness up to a distance from the borehole somewhat greater than the total length A_1A_2 of the sonde. Experiments have shown that the sheet of i_o current retains substantially the same shape opposite thin resistive beds.

The thickness of the i_o current sheet is approximately 32 in. (distance O_1O_2 on Fig. 7-10), and the length A_1A_2 of the sonde is 80 in.

Fig. 7-11 compares the curves obtained experimentally opposite a thin resistive bed using the conventional devices (16-in. and 64-in. normals and 18-ft 8-in. lateral) with the corresponding LL7 recording. The conventional devices give poor results; the LL7 curve, in spite of difficult conditions (R_t/R_m is 5000), shows the bed very clearly and reads close to R_t.

Laterolog 3

The LL3 tool also uses currents from bucking electrodes to focus the measuring current into a horizontal sheet

* Mark of Schlumberger

Bed Thickness (e)	Qualifications	Device	Response
A. In low resistivity, when $R_{16''}/R_m < 10$ (invasion up to 2d)			
e > 20 ft (> 4 AM′)		Long Normal	$R_{64''} = R_t$
e ≅ 15 ft (3 AM′)	$R_m \cong R_s$ $R_{64''}/R_s \geq 2.5$	Long Normal	$R_{64''} = \frac{2}{3} R_t$
e ≅ 15 ft (3 AM′)	$R_m \cong R_s$ $R_{64''}/R_s \leq 1.5$	Long Normal	$R_{64''} = R_t$
e ≅ 10 ft (2 AM′)	$R_m \cong R_s$ $R_{64''}/R_s \geq 2.5$	Long Normal	$R_{64''} = \frac{1}{2} R_t$
e ≅ 10 ft (2 AM′)	$R_m \cong R_s$ $R_{64''}/R_s = 1.5$	Long Normal	$R_{64''} = \frac{2}{3} R_t$
5 ft < e < 10 ft	When oil bearing and SP is −50 to −80 mV	Short Normal	$R_{16''} \cong R_t$
5 ft < e < 10 ft	Surrounding beds homogeneous	Lateral in resistive bed	$R_t \geq R_{max} \times R_s/R_{min}$
Thin beds (in general)	Surrounding beds homogeneous	Lateral in conductive bed	$R_{19''} \cong R_t$

B. Rules for using lateral (AO = 18 ft 8 in.)

e > 40 ft (> 2 AO)

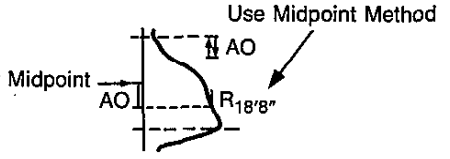

e ≅ 28 ft (= 1.5 AO)

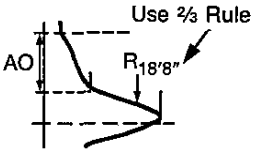

e ≅ 24 ft (= 1.3 AO)

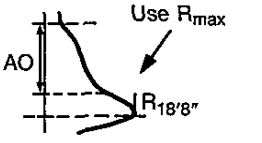

5 ft < e < 10 ft — Resistive bed and surrounding beds homogeneous

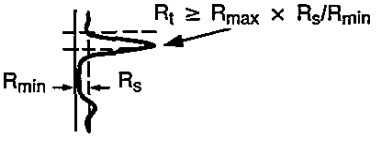

When $R_{16''}/R_m > 50$, these values must be corrected for the borehole: Chart B-2.

C. Response of Laterolog 7

e > 3 ft

For $d_i = 20$ in., $R_{LL} \cong 0.2\ R_{xo} + 0.8\ R_t$

For $d_i = 40$ in., $R_{LL} \cong 0.4\ R_{xo} + 0.6\ R_t$

For $d_i = 80$ in., $R_{LL} \cong 0.6\ R_{xo} + 0.4\ R_t$

Thus, the best results occur when $R_{xo} < R_t$ and $R_{mf}/R_w < 4$.

1,370-86

Fig. 7-9—R_t estimation from electrical logs.

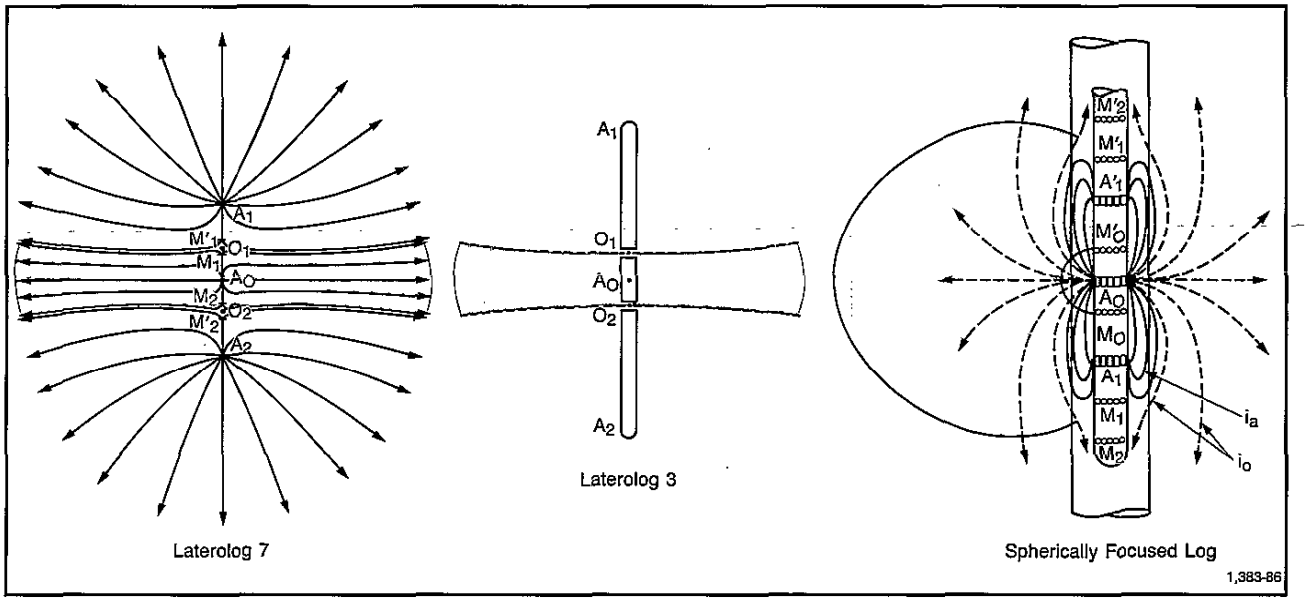

Fig. 7-10—Schematics of focusing electrode devices.

penetrating into the formation (Fig 7-10). Symmetrically placed on either side of the central A_O electrode are two very long (about 5-ft) electrodes, A_1 and A_2, which are shorted to each other. A current, i_o, flows from the A_O electrode, whose potential is fixed. From A_1 and A_2 flows a bucking current, which is automatically adjusted to maintain A_1 and A_2 at the potential of A_O. All electrodes of the sonde are thus held at the same constant potential. The magnitude of the i_o current is then proportional to formation conductivity.

The i_o current sheet is constrained to the disk-shaped area. The thickness, O_1O_2, of the current sheet is usually about 12 in., much thinner than for the LL7 device. As a result, the LL3 tool had a better vertical resolution and shows more detail than did the LL7 tool. Furthermore, the influences of the borehole and of the invaded zone were slightly less.

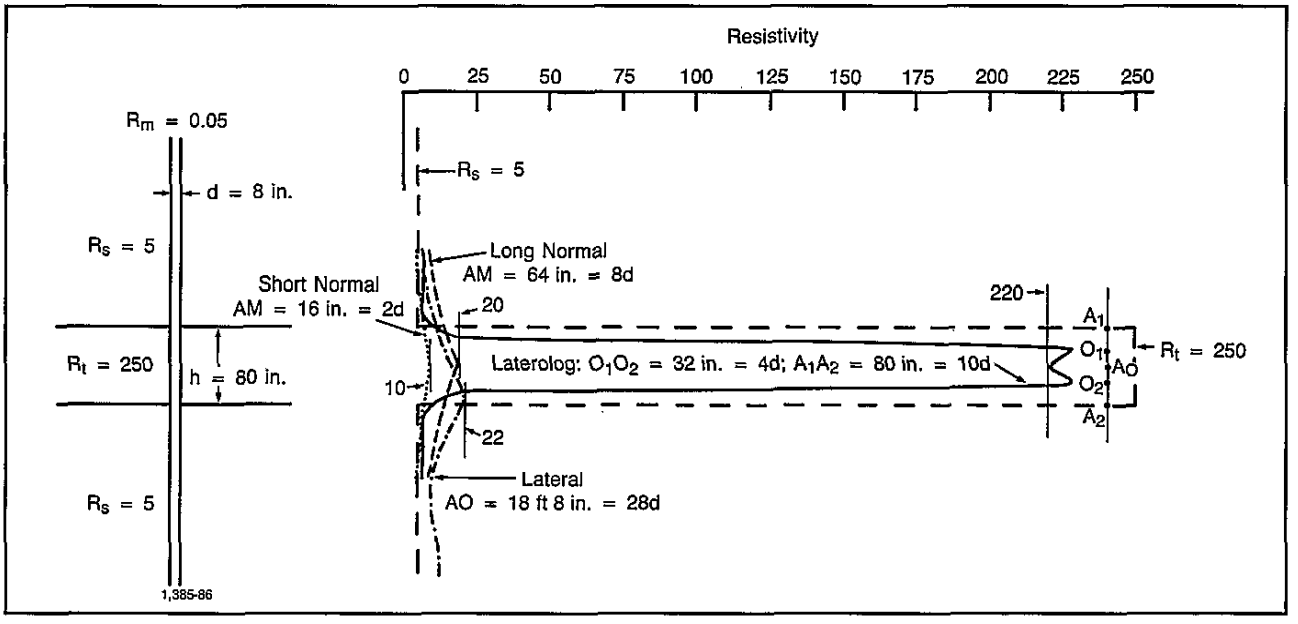

Fig. 7-11—Response of Laterolog 7 and ES opposite a thin, resistive, noninvaded bed with very salty mud (laboratory determinations).

Laterolog 8

The shallow-investigation LL8 measurement is recorded with small electrodes on the dual induction-laterolog sonde. The device is similar in principle to the LL7 tool except for its shorter spacings. The thickness of the i_0 current sheet is 14 in., and the distance between the two bucking electrodes is somewhat less than 40 in. The current-return electrode is located a relatively short distance from A_O. With this configuration, the LL8 device gives sharp vertical detail, and the readings are more influenced by the borehole and the invaded zone than are those of the LL7 and LL3 tools.

Dual Laterolog-R_{xo} System

The objective of any deep-reading resistivity device is to measure the true formation resistivity, R_t. Deep-reading resistivity tools were designed so that, as much as possible, their response is determined by the resistivity of the virgin formation beyond the invaded zone. Unfortunately, no single measurement has yet succeeded in entirely eliminating the effects of the invaded zone.

A solution is to measure the resistivity with several arrays having different depths of investigation. Measurements responding to three appropriately chosen depths of investigation usually approximate the invasion profile well enough to determine R_t.

For best interpretation accuracy such a combination system should have certain desirable features:

- Borehole effects should be small and/or correctable.
- Vertical resolutions of the devices should be similar.
- Radial investigations should be well distributed; i.e., one reading as deep as practical, one reading very shallow, and the third reading in between.

This need resulted in the development of the DLL dual laterolog-MicroSFL tool with simultaneous recordings. Fig. 7-12 is a sketch of the tool showing the electrode array used for the two laterolog devices. Both use the same electrodes and have the same current-beam thickness, but have different focusing to provide their different depth of investigation characteristics. Fig. 7-13 illustrates the focusing used by the deep laterolog device (left) and by the shallow laterolog device (right).

The DLL tool has a response range of 0.2 to 40,000 ohm-m, which is a much wider range than covered by previous laterolog devices.

To achieve accuracy at both high and low resistivities, a "constant-power" measuring system is employed. In this system, both measure current (i_0) and measure voltage (V_0) are varied and measured, but the product of the two (i.e., power), i_0V_0, is held constant.

The deep laterolog measurement (LLD) of the DLL tool has a deeper depth of investigation than previous

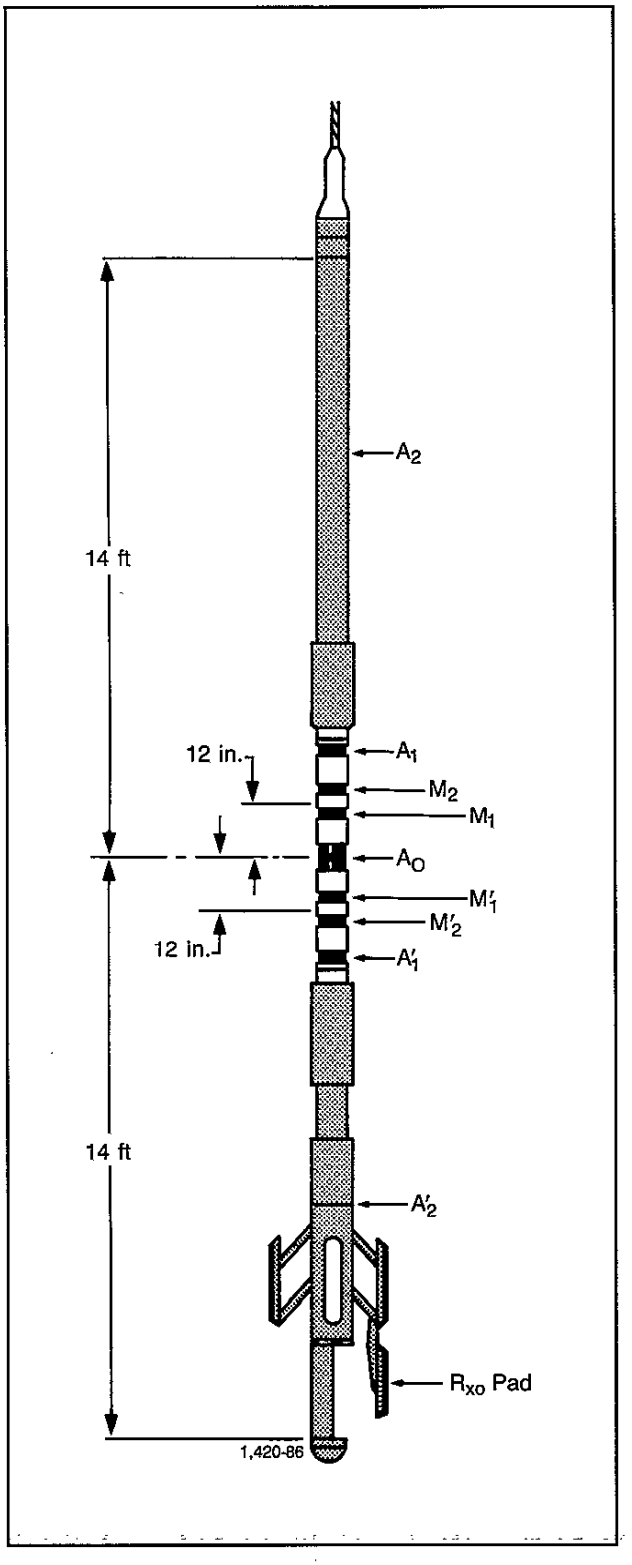

Fig. 7-12—Schematic diagram of the Dual Laterolog-R_{xo} tool.

laterolog tools and extends the range of formation conditions in which reliable determinations of R_t are possible.

To achieve this, very long guard electrodes are needed; the distance between the extreme ends of the guard electrodes of the DLL-R_{xo} tool is approximately 28 ft. The nominal beam thickness of 2 ft, however, insures good vertical resolution.

The shallow laterolog measurement (LLS) has the same vertical resolution as the deep laterolog device (2 ft), but it responds more strongly to that region around the borehole normally affected by invasion. It uses a type of focusing called "pseudolaterolog," wherein the focusing current is returned to nearby electrodes instead of to a remote electrode. This causes the measure current to diverge more quickly once it has entered the formations, thus producing a relatively shallow depth of investigation.

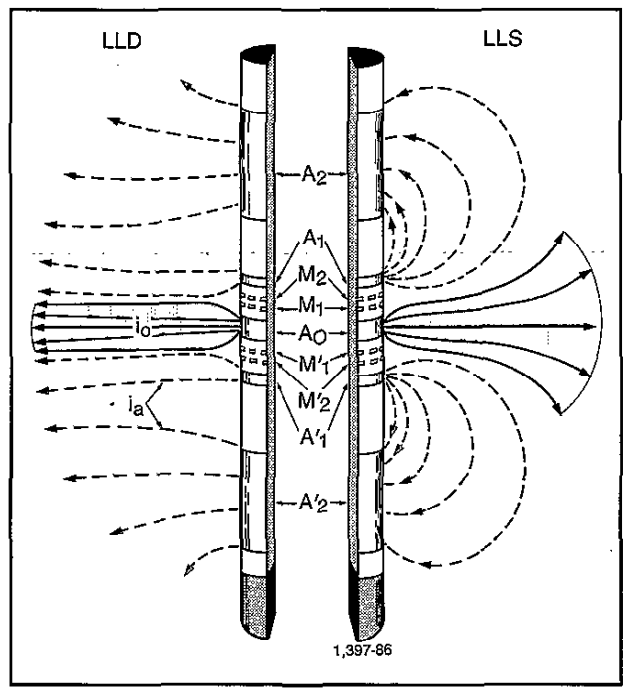

Fig. 7-13—Schematic of the Dual Laterolog.

Delaware Effect

If both B and N electrodes are placed downhole, LLD readings may exhibit a "Delaware effect" (or gradient) in sections located just below thick nonconductive beds such as anhydrite. It appears as abnormally high resistivity for about 80 ft below the resistive bed.

Fig. 7-14 illustrates the effect and its cause. As B electrode enters the thick anhydrite, the current flow is confined to the borehole, and if the bed is thick enough (several hundred feet) practically all the current will flow in that part of the borehole below B. Then when N electrode enters the bed, it can no longer remain at zero potential as intended. It is exposed to an increasing negative potential as it rises farther from the bed boundary. This potential causes a gradual increase (gradient) in the recorded resistivity.

The LLD device uses surface electrodes for current return so it is not subject to Delaware effect. However, a small anti-Delaware effect has been observed that produces resistivities that are slightly low immediately below the resistive bed. This problem was minimized by using cable armor as the reference electrode for the measure potential.

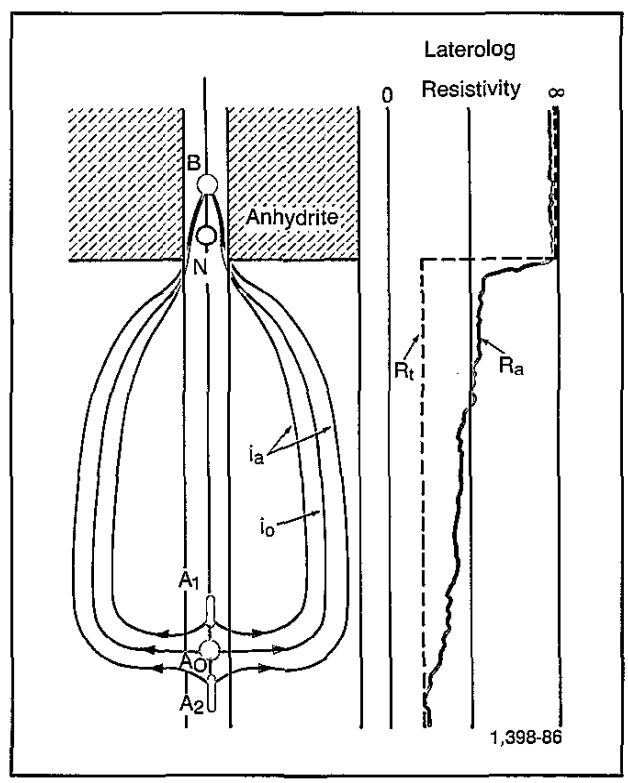

Fig. 7-14—Principle of Delaware effect.

Groningen Effect

An effect similar to the Delaware gradient was later noticed on the LLD curve. It is called the "Groningen" effect, after the large Dutch gas field where the anomaly was first discovered. The Groningen effect occurs for about 100 ft below a thick, highly resistive bed. Since the measure and bucking current cannot flow easily through the highly resistive bed, it returns through the mud column and creates a negative potential on the "zero reference electrode." If casing has been set in the resistive zone, it helps to "short circuit" the current and the Gron-

ingen effect is even more pronounced. An induction log is recommended for serious formation evaluation in these "shielded" conductive beds.

Scales

A problem common to all resistivity and conductivity devices is providing a scale that can be read accurately over the full range of response. Years ago, most laterologs were recorded on linear scales. Because of the very large range of resistivities often encountered, the required scale was relatively insensitive. Very low readings, whether resistivity or conductivity, were virtually unreadable. Backup curves of increased sensitivity were introduced, but they were difficult to read and cluttered the log in formations of high contrast.

For a while, the hybrid scale, first used on the LL3 tool, was employed. It presented linear resistivity over the first half of the grid track (log), and linear conductivity over the last half. Thus, one galvanometer could record all resistivities from zero to infinity. Although somewhat awkward to use because of the odd scale divisions (see Fig. 7-15a), the hybrid scale did provide acceptable sensitivity in both low-resistivity and low-conductivity formations.

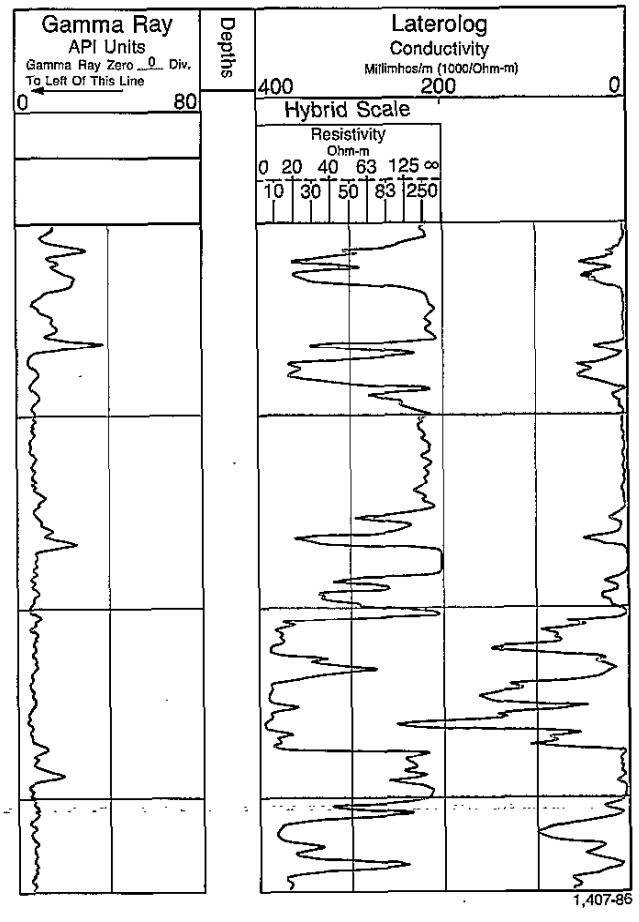

Fig. 7-15a—Laterolog recorded on hybrid scale.

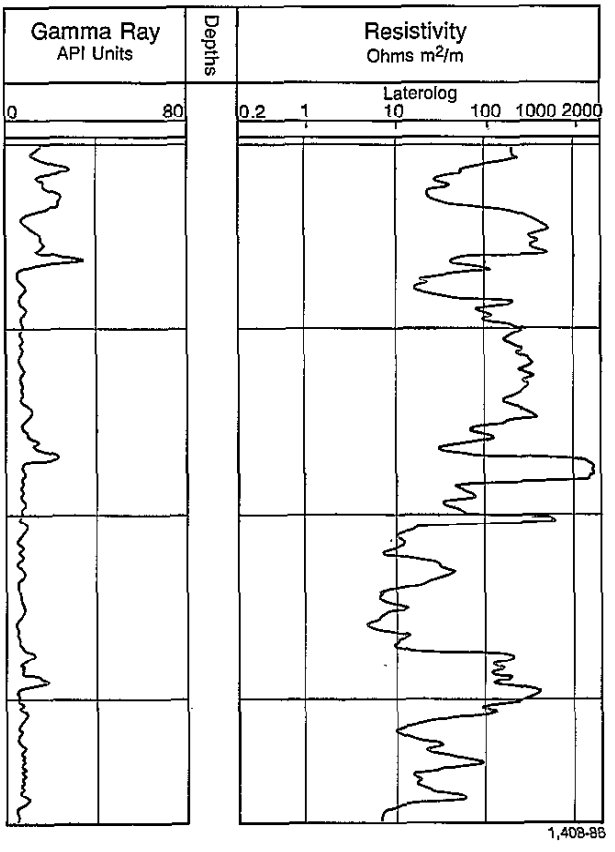

Fig. 7-15b—Laterolog over same interval as in Fig. 7-15a recorded on logarithmic scale.

Today, the logarithmic scale is the most acceptable scale for recording resistivity curves. Its standard form is a split four-cycle grid covering the range from 0.2 to 2000 ohm-m (see Fig. 7-15b). Even this range is sometimes not sufficient for the DLL-R_{xo} measurements; when needed, a backup trace is used to cover the range from 2000 to 40,000 ohm-m.

Spherically Focused Log

The SFL device measures the conductivity of the formation near the borehole and provides the relatively shallow investigation required to evaluate the effects of invasion on deeper resistivity measurements. It is the short-spacing device now used on the DIL-SFL tool—developed to replace the 16-in. normal and LL8 devices.

The SFL system differs from previous focused electrode devices. Whereas the LL7 and LL8 systems attempt to focus the current into planar discs, the SFL system establishes essentially constant potential shells around the current electrode. The SFL device is able to preserve the spherical potential distribution in the formation over a wide range of wellbore variables, even when a conduc-

tive borehole is present. To accomplish this, the SFL device is composed of two separate, and more or less independent, current systems. The bucking current system serves to "plug" the borehole and establish the equipotential spheres. The i_0 survey current system causes an independent survey current to flow through the "volume of investigation"; the intensity of this current is proportional to formation conductivity.

The SFL device consists of current-emitting electrodes, current-return electrodes, and measure electrodes. Two equipotential spheres about the tool's current source are established. The first sphere is about 9 in. away from the survey current electrode; the other is about 50 in. away. A constant potential of 2.5 mV is maintained between these two spherical surfaces. Since the volume of formation between these two surfaces is constant (electrode spacing is fixed) and the voltage drop is constant (2.5 mV), the conductivity of this volume of formation can be determined by measuring the current flow.

Influence of Wellbore Variables and Log Corrections

The laterolog and SFL readings, like most resistivity measurements, are influenced by the borehole mud, the adjacent (shoulder) beds, and the invaded zone. Charts have been constructed from a series of mathematical simulations to correct the log readings for these influences. The corrections must always be made in this order—borehole, bed thickness, invasion.

Borehole Effect

Charts Rcor-2a and -2b are borehole-correction charts for deep and shallow laterolog readings for a centered sonde. Eccentering has little effect on the LLD curve, but it can be detrimental to the LLS reading when the ratio R_t/R_m is high. Chart Rcor-2c is for eccentered sondes. Chart Rcor-1 provides borehole corrections for the LL8 and SFL devices employed on the DIL-LL8 and DIL-SFL tools. Chart Rcor-3 corrects the SFL device used on the Phasor induction tool for borehole effects.

Adjacent Bed Effect

Chart Rcor-8 gives the shoulder bed-effect corrections needed for the deep and shallow laterolog readings of the DLL tool in noninvaded beds with infinitely thick shoulder beds of similar resistivity.

Readings must be corrected for borehole effect before the shoulder-bed charts are entered. Fig. 7-16 provides bed-thickness corrections for the LL3 and LL7 measurements.

Pseudogeometrical Factors

Geometrical factor can be defined as that fraction of the total signal that would originate from a volume having a specific geometrical orientation with the sonde in an infinite homogeneous medium. The only logging devices for which this concept is reasonably rigorous are the induction tools. However, for comparative evaluations, it is useful to construct charts based on pseudogeometrical factors for other resistivity devices. Such a chart is shown in Fig. 7-17, where the integrated pseudogeometrical factors of progressively larger cylinders are plotted versus the diameters of the cylinders. The apparent resistivity, R_a, measured in a thick bed is given approximately by

$$R_a = J(d_i)\, R_{xo} + [1 - J(d_i)]\, R_t, \quad \text{(Eq. 7-3)}$$

where $J(d_i)$ is the pseudogeometrical factor. A pseudogeometrical factor relating to an electrode-type resistivity device is applicable in only one set of conditions; therefore, charts of this type are not valid as general-purpose invaded-zone correction charts. The most useful feature of this chart is its graphic comparison of the relative contribution of the invaded zone to the responses of the various tools and, therefore, of the relative depths of investigation of the individual tools.

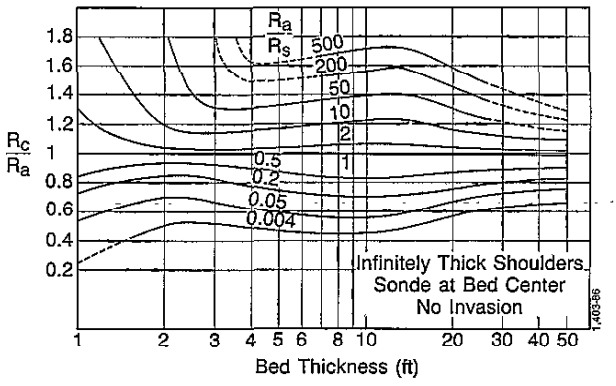

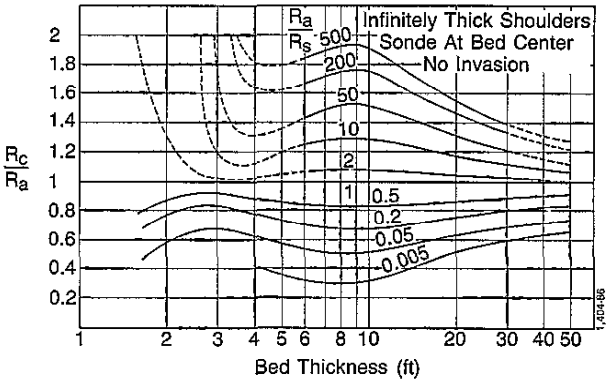

Fig. 7-16b—Shoulder-bed correction, Laterolog 7.

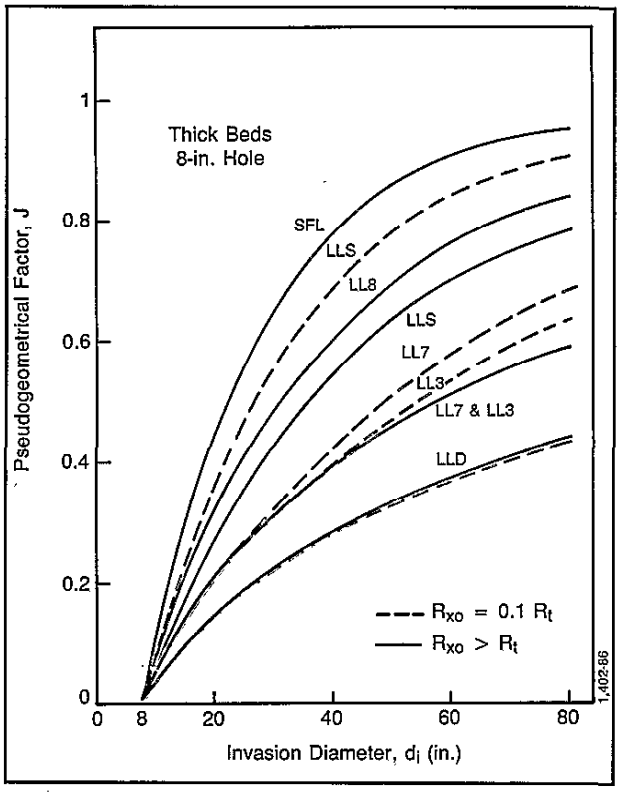

Fig. 7-17—Radial pseudogeometrical factors, fresh muds (solid) and salty muds (dashed).

Note the excellent spread in radial characteristics of the deep and shallow laterolog measurements. This feature permits accurate resistivity analysis over a wide range of invasion conditions.

Invasion Correction

Eq. 7-3 contains three unknowns: the flushed zone resistivity, R_{xo}; the true resistivity of the virgin, uncontaminated zone, R_t; and the diameter of invasion, d_i. If a step profile of invasion is assumed, a combination of deep and shallow laterolog measurements with a very shallow R_{xo} resistivity measurement, such as the MicroSFL or microlaterolog, can be used to solve for the three unknowns.

Chart Rint-9 performs this solution graphically. The true resistivity value obtained can be used in the Archie water saturation equation to determine saturation, or the R_{xo}/R_t resistivity ratio can be used for the same purpose in the ratio water saturation equation.

INDUCTION LOGGING

The induction logging tool was originally developed to measure formation resistivity in boreholes containing oil-base muds and in air-drilled boreholes. Electrode devices did not work in these nonconductive muds, and attempts to use wall-scratcher electrodes were unsatisfactory.

Experience soon demonstrated that the induction log had many advantages over the conventional ES log when used for logging wells drilled with water-base muds. Designed for deep investigation, induction logs can be focused in order to minimize the influences of the borehole, the surrounding formations, and the invaded zone.

Principle

Today's induction tools have many transmitter and receiver coils. However, the principle can be understood by considering a sonde with only one transmitter coil and one receiver coil (Fig. 7-18).

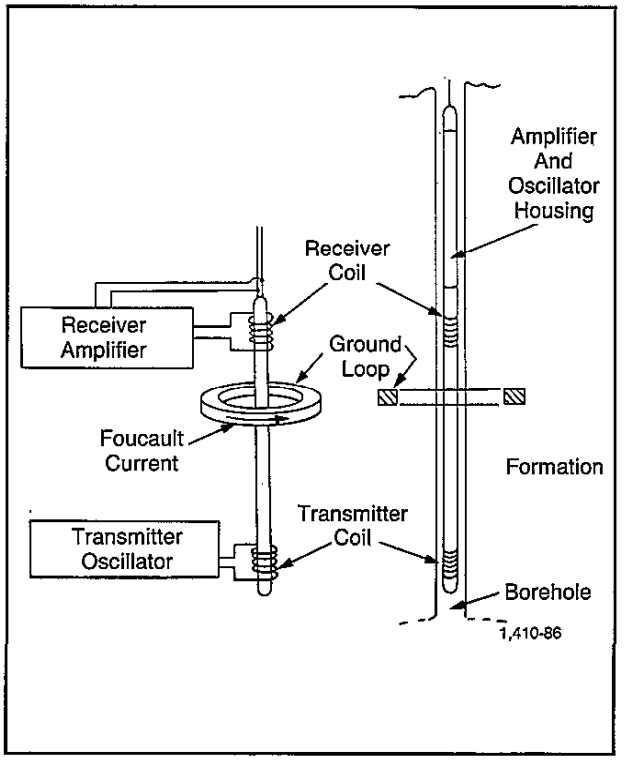

Fig. 7-18—Basic two-coil induction log system.

A high-frequency alternating current of constant intensity is sent through a transmitter coil. The alternating magnetic field created induces currents in the formation surrounding the borehole. These currents flow in circular ground loops coaxial with the transmitter coil and create, in turn, a magnetic field that induces a voltage in the receiver coil.

Because the alternating current in the transmitter coil is of constant frequency and amplitude, the ground loop

currents are directly proportional to the formation conductivity. The voltage induced in the receiver coil is proportional to the ground loop currents and, therefore, to the conductivity of the formation.

There is also a direct coupling between the transmitter and receiver coils. The signal originating from this coupling is eliminated by using "bucking" coils.

The induction tool works best when the borehole fluid is an insulator—even air or gas. The tool also works well when the borehole contains conductive mud unless the mud is too salty, the formations are too resistive, or the borehole diameter is too large.

Geometrical Factor

If the model is simplified (sonde centered and formation homogeneous and isotropic), the tool response can be calculated as the sum of the elementary signals created by all formation loops coaxial with the sonde. This neglects the mutual and self-inductance of the ground loops. Each elementary signal is proportional to the loop conductivity and to a geometrical factor that is a function of the loop position with reference to the transmitter and receiver coils. Therefore,

$$E = K \Sigma g_i C_i, \qquad \text{(Eq. 7-4)}$$

where

E is the induced electromotive force,

K is the sonde constant,

g is the geometrical factor for that particular loop,

C is the conductivity of that loop,

and

$\Sigma g_i = 1$.

The geometrical factor, g_i, corresponding to a medium is defined as the proportion of the total conductivity signal contributed by the given medium. As shown in Chart Gen-3, the formation can be split into cylinders coaxial with the sonde (tool being centralized); they correspond to the mud column, invaded zone, virgin zone, and shoulder beds. The total signal can be expressed by

$$C_I = G_m C_m + G_{xo} C_{xo} + G_t C_t + G_s C_s, \qquad \text{(Eq. 7-5)}$$

where

$$G_m + G_{xo} + G_t + G_s = 1$$

and where G is the geometrical factor for a defined region.

Thus, a volume of space defined only by its geometry relative to the sonde has a fixed and computable geometrical factor (G) (see Fig. 7-19). This permits the construction of mathematically sound correction charts to account for the effects of borehole mud, invaded zone, and adjacent beds on the R_t measurement, providing symmetry of resolution exists.

Because induction tools are designed to evaluate R_t, it is important to minimize terms relative to the mud, the invaded zone, and the shoulder beds. This is done by minimizing the corresponding geometrical factors with a focused signal.

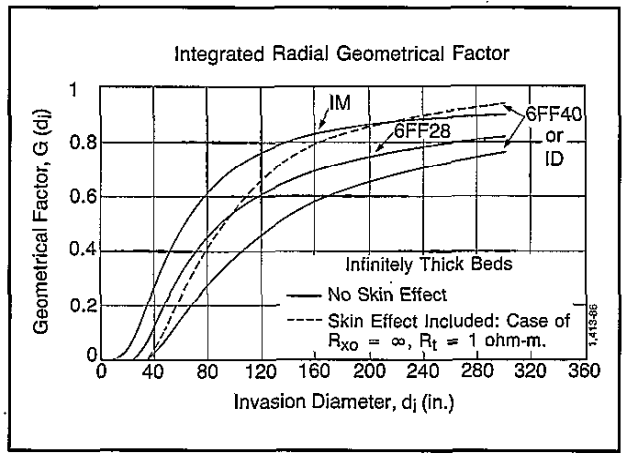

Fig. 7-19—Geometrical factors. Dashed curve includes skin effect, under conditions shown, for the 6FF40 or the deep induction (ID) devices.

Focusing

The simple two-coil system does not represent the tool used today. However, it can be considered the building block from which today's multicoil sonde was built. The response of a multicoil sonde is obtained by breaking it down into all possible two-coil combinations of transmitter-receiver pairs. The response of each coil pair is weighted by the product of the number of turns on the two coils and by the product of their cross-sectional area. The responses of all coil pairs are added, with due regard to the algebraic sign of their contributions and their relative positions.

Multicoil sondes, or focused sondes, offer certain advantages. Vertical resolution is improved by suppressing the response from the shoulder formations, and depth of investigation is improved by suppressing the response from the mud column and the formation close to the hole.

Deconvolution

Deconvolution is the extraction of desirable components of a complex signal by variously weighting the gross measurement at different points relative to the objective zone. Deep induction measurements are made possible,

without sacrificing vertical resolution, by a deconvolution that gives greater proportional weight to the signal measured at the sonde center than to signals measured above and below that point.

In the past, various weighted deconvolutions were used to account for differing values of shoulder-bed resistivity, but this practice has been abandoned in the interest of standardization. Most of today's logs are run with shoulder-bed resistivity settings of 1 ohm-m, and deconvolution is performed by the CSU* surface equipment software. Deconvolution is done before skin-effect boost is applied.

Skin Effect

In very conductive formations the induced secondary currents in the ground loops are large, and their magnetic fields are important. The magnetic fields of these ground loops induce additional emf's (electrical voltages) in other ground loops. These induced emf's are out of phase with those induced by the transmitter coil of the induction tool. This interaction between the ground loops causes a reduction of the conductivity signal recorded on the induction logs, which is called "skin effect." It is a predictable phenomenon. Fig. 7-20 shows the response of the tool compared to the actual formation conductivity of the formation. Skin effect becomes significant when formation conductivity exceeds 1,000 mmho/m.

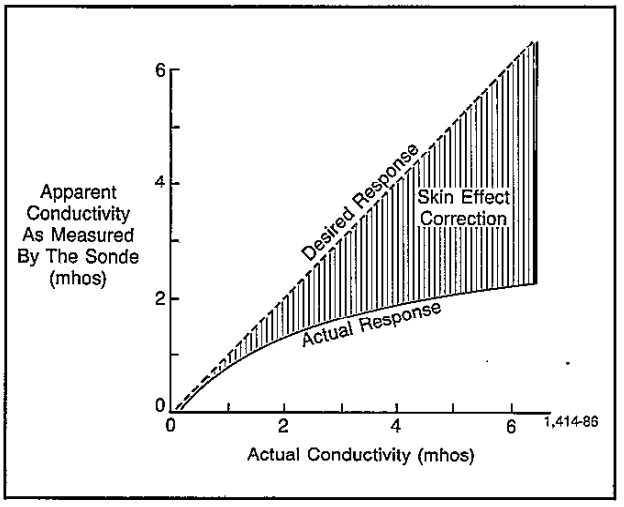

Fig. 7-20—Actual response of an induction log compared to the "desired" response.

Schlumberger induction logs are automatically corrected for skin effect during recording. The correction is based on the magnitude of the uncorrected tool response, treated as if it were from a homogeneous medium. A secondary skin-effect correction may be required when the media surrounding the sonde are not of uniform conductivity. These corrections are usually incorporated in the various interpretation charts that involve induction logs.

Equipment

The induction tool has been the basic resistivity tool used in logging low- to medium-resistivity formations drilled with fresh water, oil, or air for over 25 years. During that period, several types of equipment have been developed and used.

1. The 6FF40 induction-electrical survey (IES) tool included a six-coil focused induction device of 40-in. nominal spacing (hence, the nomenclature, 6FF40), a 16-in. normal, and an SP electrode. The tool was first introduced in the late 1950's and was the standard induction tool throughout the 1960's. It has since been replaced by improved tools.
2. The DIL-LL8 system used a deep-reading induction device (the ID, which was similar to the 6FF40), a medium induction device (the IM), an LL8 device (which replaces the 16-in. normal), and an SP electrode.

   The IM device has a vertical resolution similar to that of the 6FF40 (and ID) but only about half the depth of investigation (see Fig. 7-19). The LL8 was a focused, shallow-investigation device with better thin-bed resolution and less borehole influence than the 16-in. normal. It was also void of some disturbing characteristics of normal devices—such as reversals in thin resistive beds.
3. The induction-SFL (ISF) tool incorporated a deep induction device similar to the 6FF40, the SFL device, and an SP electrode. The tool was combinable with the borehole compensated sonic tool and with a gamma ray (GR) device. The combination offered, in certain geological horizons, the ability to evaluate the hydrocarbon potential of the well in a single logging run. The sonic log provided porosity evaluation and the ISF log provided saturation evaluation.
4. The DIL-SFL tool is similar to the DIL-LL8 tool except that the SFL has replaced the LL8 as the shallow-investigation device. The SFL measurement is less influenced by the borehole than is the LL8 measurement (see Chart Rcor-1).
5. The Phasor* Induction SFL tool has a deep-reading induction device (IDPH), a medium-reading induction device (IMPH), an SFL device, and an SP electrode. The tool employs a digital transmission and processing system and a continuous calibration verification system. It also can be operated at frequencies of 10 and 40 kHz, as well as at 20 kHz (the operating frequency of most previous induction devices).

* Mark of Schlumberger

6. The 6FF28 IES tool (2⅝-in. diameter) is a scaled-down version of the 6FF40 device, having a 28-in. primary coil spacing, and includes a standard 16-in. normal device and an SP electrode. It is used for logging in small holes and for through-drillpipe operations.

Log Presentation and Scales

The SP and/or GR curves are recorded in Track 1 for all tools.

Fig. 7-21 illustrates the original IES presentation. The induction conductivity curve is sometimes recorded over both Tracks 2 and 3. The linear scale is in millimhos per meter (mmho/m), increasing to the left. In Track 2 both the 16-in. normal and the reciprocated induction curves are recorded on the conventional linear resistivity scale.

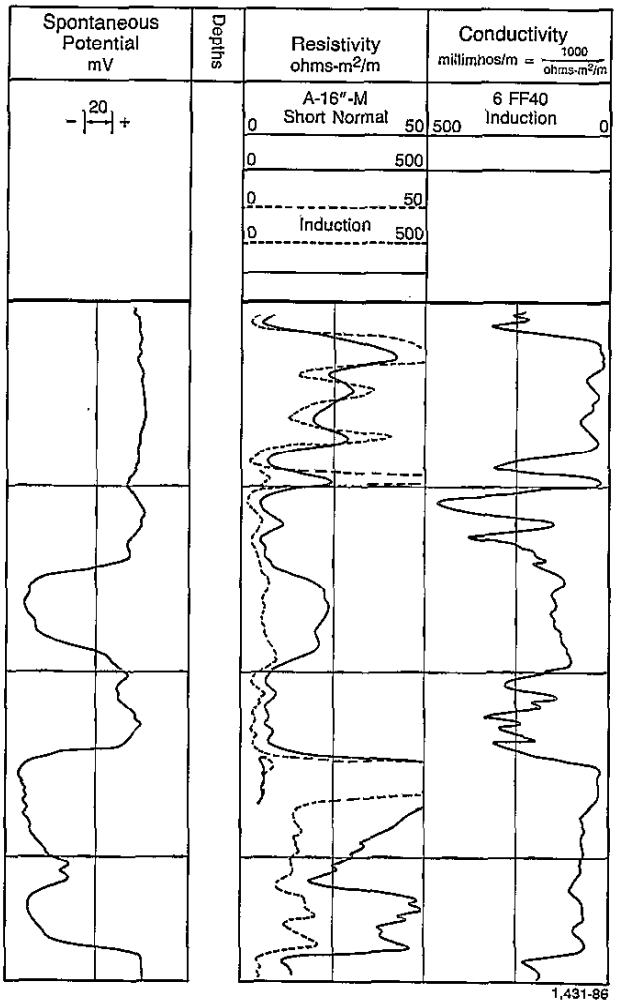

Fig. 7-21—Induction-electrical log presentation.

The DIL-LL8 log introduced the logarithmic grid; the standard presentation is shown in Fig. 7-22. Four decades of resistivity (usually 0.2 ohm-m to 2,000 ohm-m) were recorded over Tracks 2 and 3.

The DIL-SFL log, in combination with the sonic log, required a modification of this grid. Two decades of resistivity on logarithmic grid are presented in Track 2. The sonic transit time is presented in Track 3 on linear grid. The log presentation is shown in Fig. 7-23.

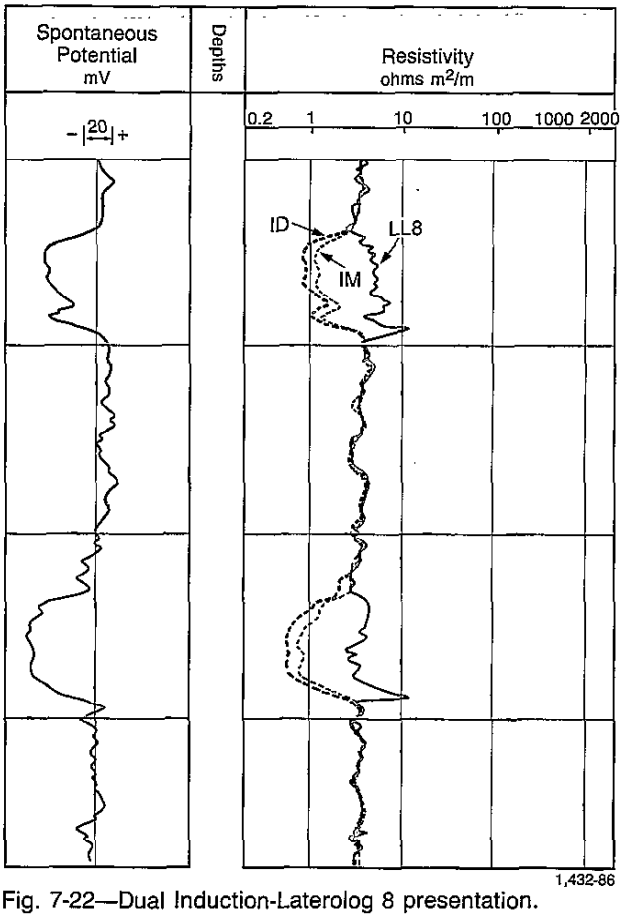

Fig. 7-22—Dual Induction-Laterolog 8 presentation.

Environmental Corrections Prior to Phasor Induction

As is true for all resistivity measurements, induction measurements may be influenced by the borehole, by surrounding beds, and by invasion. The induction log must be corrected for these effects before the measurements can be used. Since the induction logs have been specifically designed to minimize these effects, they are not normally large and can, in many situations, be ignored without major consequence. Nevertheless, it is wise to make these environmental corrections. There are three: a borehole correction, a surrounding bed correction, and an invasion correction. Charts are available to assist in making the corrections, and they must be made in the stated order: borehole, bed thickness, invasion.

Borehole Correction

Conductivity signals from the mud can be evaluated using geometrical factors. Chart Rcor-4 gives corrections for various curves (6FF40, ID, IM, 6FF28, IDPH, IMPH) and for various standoffs.

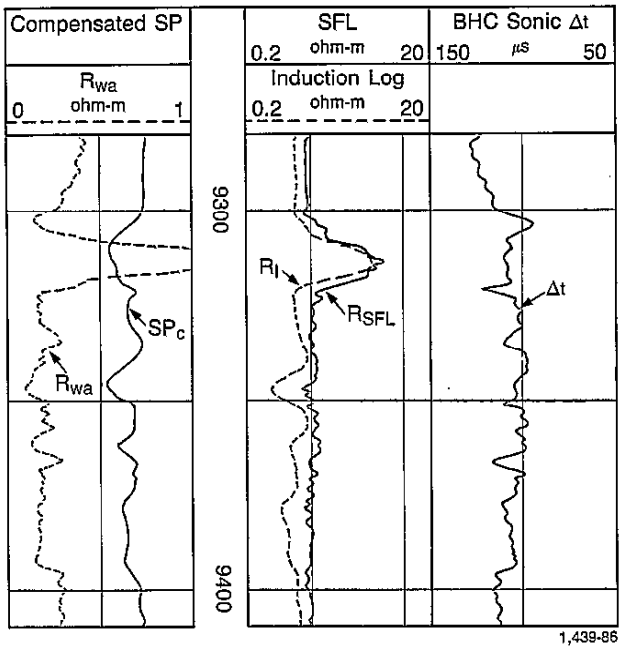

Fig. 7-23—ISF/sonic presentation.

The nominal borehole signal, based on bit size, is sometimes removed from the recorded log; when the hole signal is significant, consult the log heading to ascertain whether this was done. The precaution applies particularly to the medium induction devices because they are strongly influenced by borehole size.

Surrounding Bed Correction

Charts Rcor-5 and -6 provide bed-thickness corrections for the ID and IM, respectively. The need for a correction in thin beds is generally well recognized. Not so well recognized is the need for a correction when bed thickness is in the 10- to 30-ft range and bed resistivity exceeds 5 ohm-m.

The ID correction curves are valid for the 6FF40 measurement; these two induction devices are, for all practical purposes, identical. The ID correction curves are also valid for the 6FF28 provided the bed thickness is adjusted for the shorter coil spacing before entry into the chart.

To correct the ID (and 6FF40 and 6FF28) in thin conductive beds, Chart Rcor-7 is used. Chart Rcor-9 provides bed-thickness corrections for the Phasor induction measurements. The charts reflect the much superior bed-thickness response of the Phasor tool. For beds thicker than 6 ft, little or no surrounding bed correction is required.

Invasion Correction

The invasion correction charts are derived from geometrical factor considerations. If a step profile of invasion is assumed (a step profile is one in which the invading mud filtrate pushes all the connate water before it in a piston-like process), the responses of, say, the DIL-SFL measurements are as follows:

$$C_{ID} = G_m C_m + G_{xo} C_{xo} + G_t C_t, \qquad \text{(Eq. 7-6)}$$

$$C_{IM} = G'_m C_m + G'_{xo} C_{xo} + G'_m C_t, \qquad \text{(Eq. 7-7)}$$

$$R_{SFL} = J_m R_m + J_{xo} R_{xo} + J_t R_t, \qquad \text{(Eq. 7-8)}$$

where m refers to the mud column, xo to the flushed zone, and t to the uncontaminated noninvaded formation; C and R are the conductivities and resistivities, respectively, of these zones; and G, G', and J are the geometrical factors of these zones for the ID, IM, and SFL, respectively; all are a function of the same diameter of invasion, d_i. There are three unknowns in these response equations—R_{xo}, R_t, and d_i. (The diameter of invasion and borehole size automatically define all the geometrical factors.)

Solving the equations from the input of the ID, IM, and SFL measurements will yield d_i, R_{xo}, and R_t. Charts Rint-2, -3, -5, -10, -11, and -12 provide a graphical solution for these terms for combinations of induction measurements and mud conditions (mud type and resistivity contrast).

High-Resistivity Formations

In high-resistivity formations, the conductivity signal measured by the induction tool is very small. After calibration there is still an uncertainty of about ± 2 mmho/m on the standard induction measurements (6FF40, ID, IM, 6FF28). This can represent an error of 20% on the signal from a formation of 100 ohm-m (or 10 mmho/m). This error can be significantly reduced by downhole calibration if a suitable impervious, thick formation of exceedingly high resistivity is present.

The calibration accuracy of the Phasor induction tool is much superior. Its uncertainty is less than ± 0.75 mS/m when operated at 20 kHz and about ± 0.40 mS/m when operated at 40 kHz.

Effect of Dipping Beds

Modern computers have allowed the development of increasingly sophisticated models of resistivity logging tool response to actual logging geometries. A recent study was made to analyze the effect of dipping beds on the induction response.

Fig. 7-24 shows the effect of dip on the ID response for 5- and 10-ft resistive and conductive beds, for 0° to 90° dip angles in 10° increments. The resistivity contrast between the bed and shoulders is 20:1 in all cases. The logs were deconvolved and boosted in the same manner as field logs.

The following conclusions were reached as a result of this study: dip makes beds appear thicker than they are; center-bed R_t readings become averaged with R_t readings become averaged with R_s in a generally predictable but not easily quantified manner; thin beds are more affected than thick beds; and resistive beds are affected more than conductive beds.

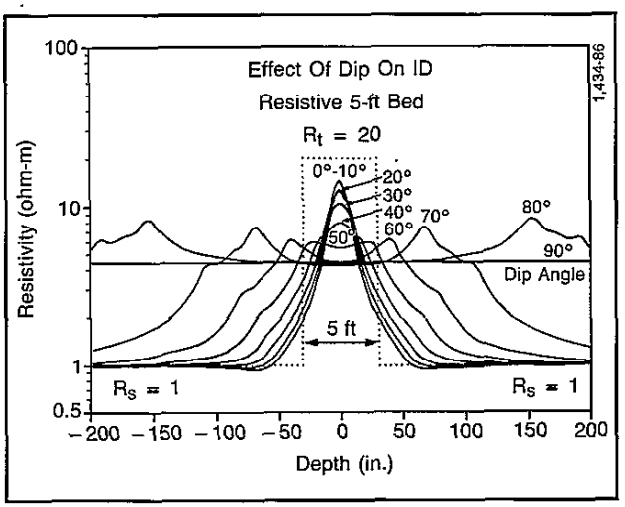

Fig. 7-24a—Effect of dip on ID response in a thin 5-ft resistive bed.

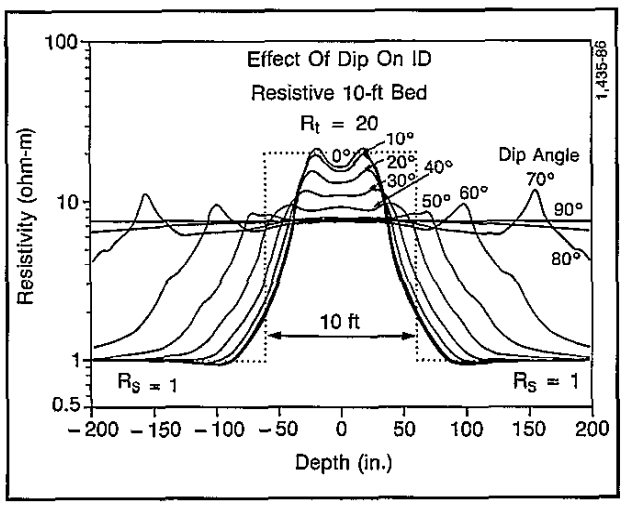

Fig. 7-24b—Effect of dip on ID response in a thick 10-ft resistive bed.

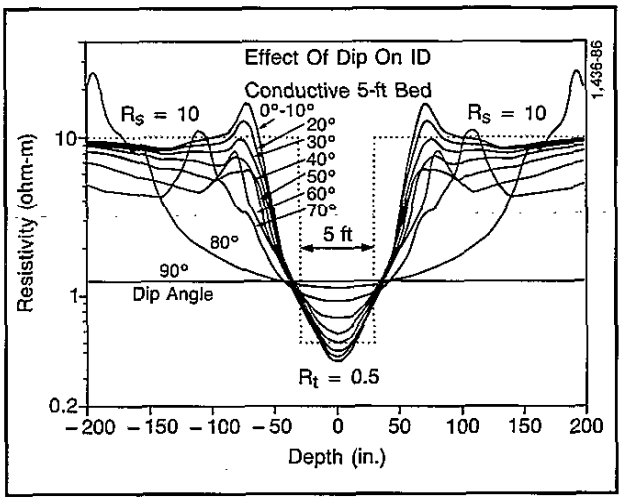

Fig. 7-24c—Effect of dip on ID response in a thin 5-ft conductive bed.

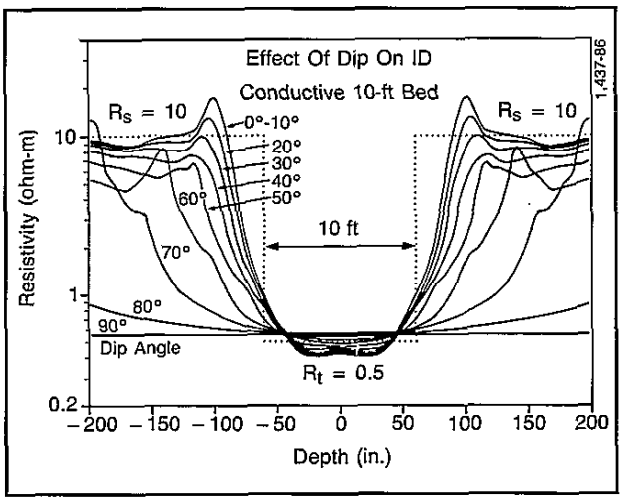

Fig. 7-24d—Effect of dip on ID response in a thick 10-ft conductive bed.

Annulus

In a hydrocarbon-bearing formation of high permeability with very low water saturation, an annulus of high formation water saturation may form between the flushed zone, R_{xo}, and the virgin zone, R_t. If mud filtrate resistivity, R_{mf}, is greater than formation water resistivity, R_w, the annulus may have a resistivity lower than either R_{xo} or R_t; in some cases, its resistivity may be significantly lower. This has the effect of reducing the induction resistivity reading so that an erroneously low value is obtained after applying standard corrections. The effect is most often noted on the IM measurement, but it can influence the ID as well, depending on the exact location of the annulus and its magnitude.

Indeed, there is some evidence that an annulus exists to some degree in most, if not all, hydrocarbon-bearing formations. In most, however, its effect on the induction measurements is negligible. During the drilling of the well, the annulus can wax and wane and move. Thus, in a given formation it may be quite evident on one logging run but essentially absent on another.

Salt Muds

Fig. 7-19 shows that the geometrical factor of all material within a 65-in.-diameter cylinder of the ID array is about 0.2. If R_{xo} is equal to 4 R_t, then C_{xo} equals $C_t/4$, and the induction tool response is

$$\begin{aligned} C_{ID} &= G_{xo}C_{xo} + G_tC_t \\ &= (0.2)\ (C_t/4) + (0.8)\ C_t \\ &= 0.85\ C_t. \end{aligned}$$

In the same conditions, but using salty mud so that R_{xo} equals $R_t/4$, the response is

$$\begin{aligned} C_{ID} &= (0.2)\ 4\ C_t + (0.8)\ C_t \\ &= 1.6\ C_t, \end{aligned}$$

which illustrates the "conductivity-seeking" characteristic of the induction devices and shows why they must be used with discretion in salt-mud environments. As a rule, R_t should be less than about 2.5 R_{xo} and d_i no greater than 100 in. for satisfactory R_t determination from deep induction logs.

However, if formation resistivities are low, invasion is shallow, and the borehole is to gauge and 9 in. or less, the induction tool may perform quite satisfactorily in salt mud.

Phasor Induction SFL Tool

The Phasor Induction SFL tool uses a conventional dual induction-SFL array to record resistivity data at three depths of investigation. In addition to the usual inphase (R-signal) induction measurements, the tool makes a high-quality measurement of the induction quadrature signal (X-signals). These measurements are combined with new advances in signal processing to provide a dual induction SFL log with thin-bed resolution down to 2 ft, and with full correction for such environmental distortions such as shoulder effect and borehole effect.

Since its introduction in the early 1960's, the dual induction tool has evolved into the primary logging service for openhole formation evaluation in fresh and oil-based muds. Previous tools have, however, produced logs with response limitations. These limitations have usually required tedious hand correction. In extreme cases tool response limitations have produced features on logs that were mistaken for geological features. Although the distortions of the formation resistivity caused by resolution effect and shoulder effect are fully predictable from electromagnetic theory, automatic correction algorithms were not successful before now because of the nonlinearity of the R-signal measurement, which was the only measurement made in the older tools.

New developments in electronics technology, recent work on computing the response of the induction tool in realistic formation models, and modern signal processing theory have combined to allow the development of the newer tool which is able to overcome the limitations of previous tools.

Central to this development is a nonlinear deconvolution technique that corrects the induction log in real time for shoulder effect and improves the thin-bed resolution over the full range of formation conductivities. This algorithm, called Phasor Processing, requires the use of the induction quadrature signals, or X-signals, which measure the nonlinearity directly. Phasor Processing corrects for shoulder effect and provides thin-bed resolution down to 2 ft in many cases.

By adding borehole geometry measurements in the same tool string, borehole effect can also be corrected in real time. With these environmental effects removed, a real-time inversion of the data into a three-parameter invasion model can be done at the wellsite.

The Phasor induction design provides several additional advantages over existing tools. These include improvements in the calibration system, sonde error stability, SFL response, and a reduction of signal and cable noise. Each of these improvements contributes toward providing more accurate formation resistivity measurements over a wider range of resistivity and borehole conditions.

Phasor Tool Description and Features

The Phasor Induction SFL tool can be combined with other cable telemetry tools. Measurements returned to the surface include deep (ID) and medium (IM) R-signals, ID and IM X-signals, SFL voltage and current, SFL focus current, spontaneous potential (SP), SP-to-Armor voltage, and array temperature. All measurements except SP are digitized downhole with high-resolution analog-to-digital converters, and all measure channels are recalibrated every 6 in. during logging.

The operating frequency of the induction arrays is selectable at 10 kHz, 20 kHz, or 40 kHz, with a default frequency of 20 kHz. The tool also provides measurements of important analog signals and continuous monitoring of digital signals as an aid to failure detection and analysis. A schematic of the tool is shown in Fig. 7-25. Depths of investigation and vertical resolution of the measurements is listed on the following page:

Median Radial Depths of Investigation		
(above 100 ohm-m homogeneous formation)		ID: 62 in. (158 cm)
		IM: 31 in. (79 cm)
		SFL: 16 in. (41 cm)
(at 0.1 ohm-m homogeneous formation)		ID: 48 in. (122 cm)
		IM: 26 in. (66 cm)
		SFL:16 in. (41 cm)
Vertical Resolution (bed thickness for full R_t determination—no invasion)		IDPH: 8 ft (246 cm)
		IMPH: 6 ft (185 cm)
	*	IDER: 3 ft (92 cm)
		IMER: 3 ft (92 cm)
	†	IDVR: 2 ft (61 cm)
		IMVR: 2 ft (61 cm)
		SFL: 2 ft (61 cm)

*ER-Enhanced Resolution Phasor
†VR-Very Enhanced Resolution Phasor

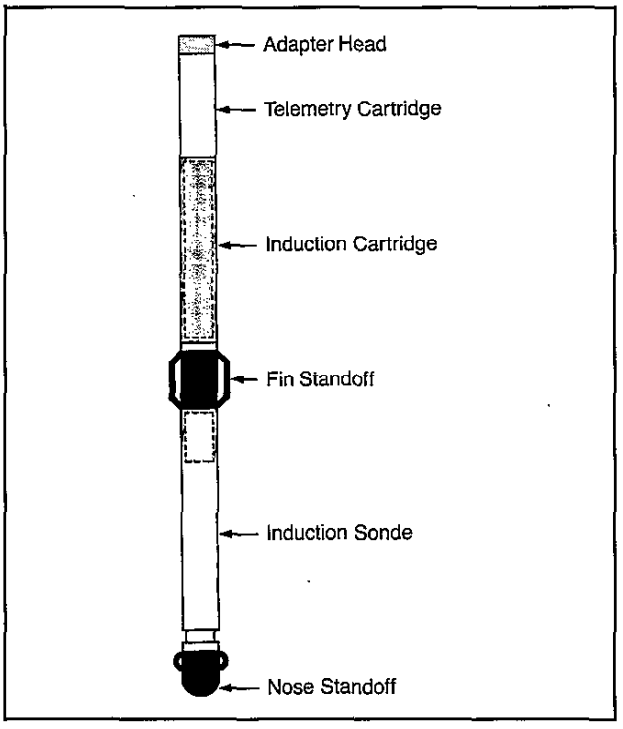

Fig. 7-25—Schematic of the Phasor Induction SFL tool.

Tool design improvements, X-signal measurements, Phasor processing, and borehole corrections provide more accurate resistivity values than other induction tools in all resistivity and bed thickness ranges and borehole conditions. A comparison in the same Texas well between the previous dual induction tool and the Phasor Induction SFL tool with 2-ft vertical resolution (Fig. 7-26) demonstrates the improvement in resolution and accuracy of the Phasor logs.

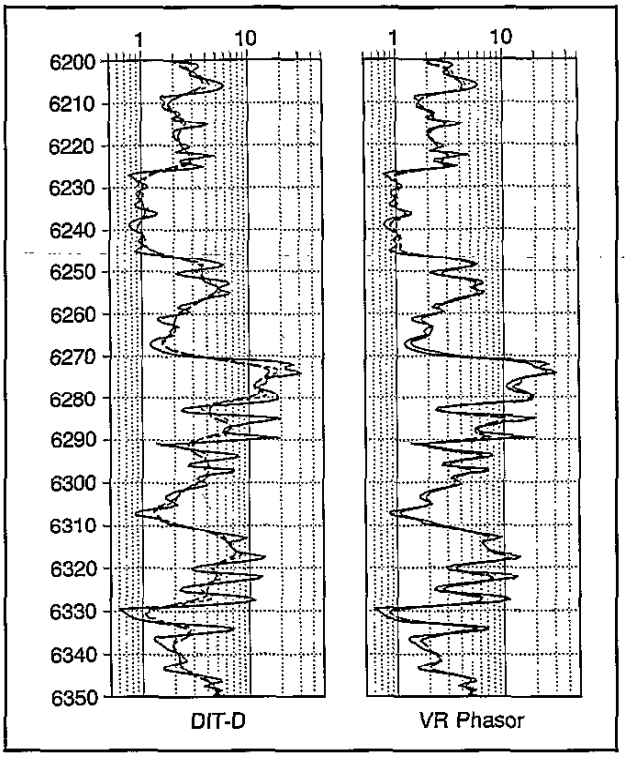

Fig. 7-26—Dual Induction SFL tool recorded in a Texas well versus Phasor Induction SFL tool with 2-ft vertical resolution.

The difference Phasor Processing makes at various resistivity levels is shown in Fig. 7-27a. A set of formation conductivity contrasts produces different response characteristics on the traditional ILD log depending on the average conductivity level. At high resistivity (low conductivity) around 100 ohm-m, the log shows considerable blurring of the thin beds and shoulder effect in the thicker zones. At moderate resistivity, around 10 ohm-m, the log has less shoulder effect. At low resistivity, shoulder effect has disappeared, but the log has developed horns and overshoots. The VR Phasor logs of the same formations (Fig. 7-27b) read correctly regardless of the formation conductivity.

Environmental Corrections

The Phasor Induction tool provides a comprehensive set of automatic corrections for environmental effects. The main ones are:

- Shoulder effect and thin-bed resolution.
- Skin effect.
- Borehole and cave effect.
- Large boreholes.
- Invasion effects.

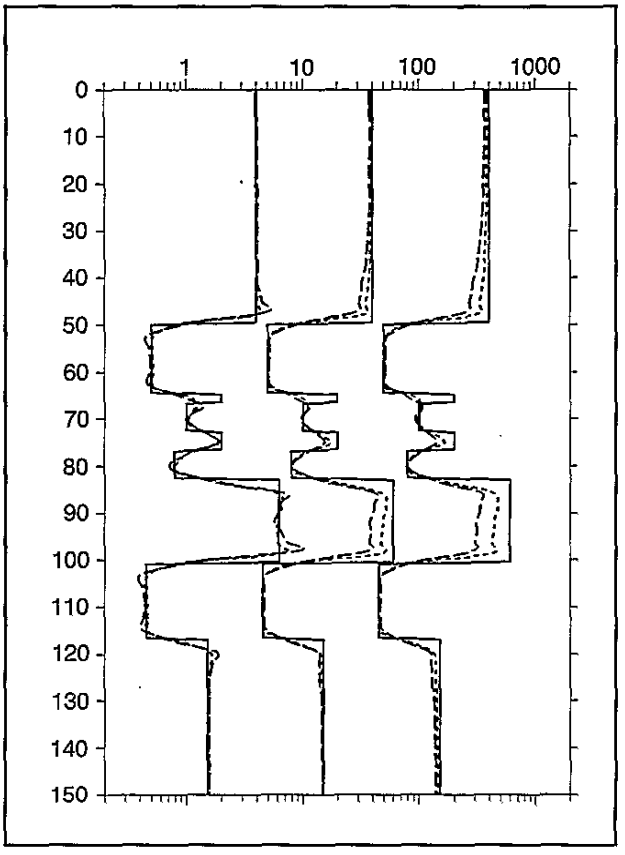

Fig. 7-27a—Varying formation conductivity produces different responses on the traditional ILD measurement.

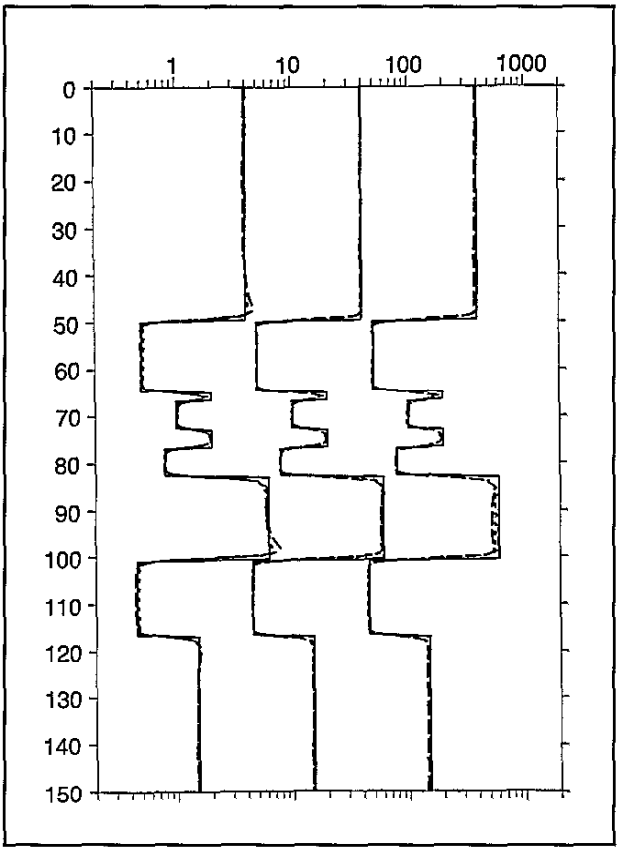

Fig. 7-27b—VR Phasor logs of the same model formations read correctly over the conductivity range.

Shoulder Effect and Vertical Resolution

Shoulder effect is the response of an induction tool to distant conductive beds when in a relatively nonconductive bed thicker than 8 ft. Thin-bed effect appears in beds thinner than the full resolution of ID or IM. The vertical resolution width of the traditional ID is about 8 ft, and IM about 6 ft. The Phasor deconvolution method corrects for shoulder effect and improves thin-bed resolution down to as low as 2 ft.

The ID and IM Phasor logs are available in three vertical resolution "widths": IDPH and IMPH with 8-ft and 6-ft resolution widths to match the resolution of traditional logs, IDER and IMER with 3-ft resolution for improved resolution over a wide range of environmental conditions, and IDVR and IMVR with 2-ft resolution for ultimate resolution over a more limited range of environmental conditions. All Phasor logs are completely corrected for shoulder effect, have vertical response functions that are constant with formation conductivity changes, and have more nearly linear radial responses. Fig. 7-28 shows the improvements of Phasor Processing over traditional processing on the ID measurement for the three resolution widths. These are computed logs in a formation model taken from an Oklahoma well.

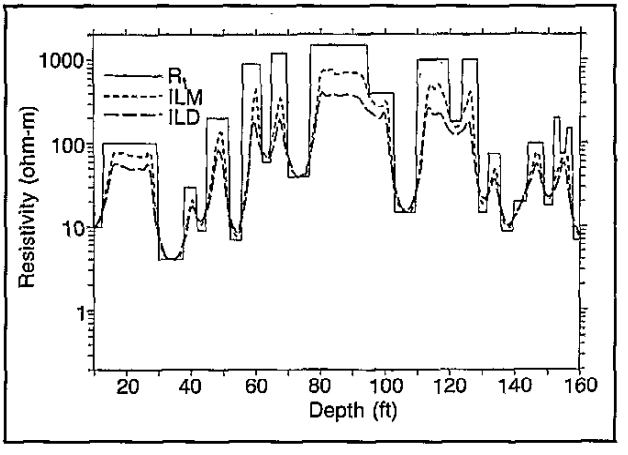

Fig. 7-28a—Traditional dual induction ILD and ILM logs compared to: Phasor IDPH, IMPH.

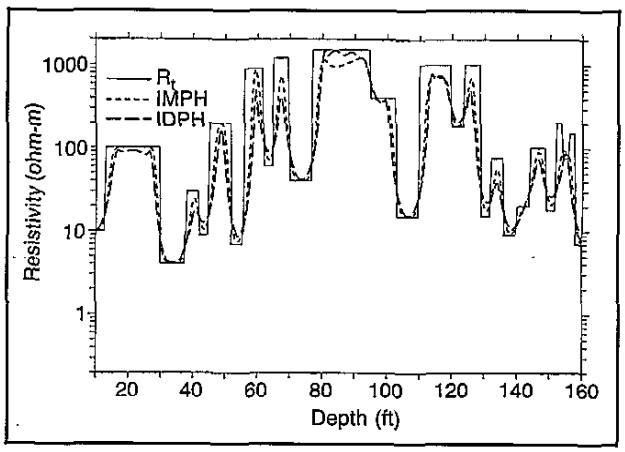

Fig. 7-28b—Traditional dual induction ILD and ILM logs VR Phasor IDER, IMER.

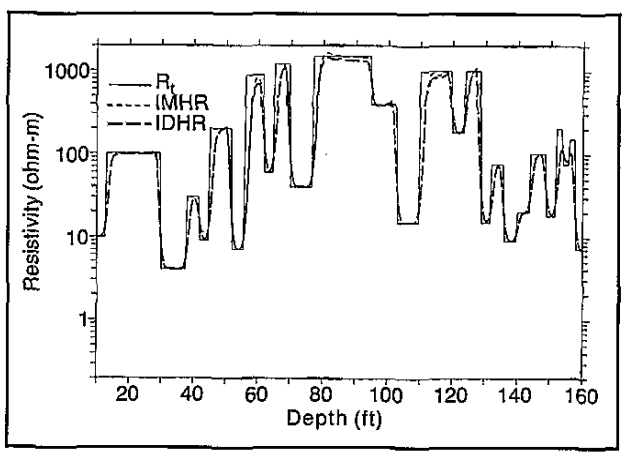

Fig. 7-28c—Traditional dual induction ILD and ILM logs VR Phasor.

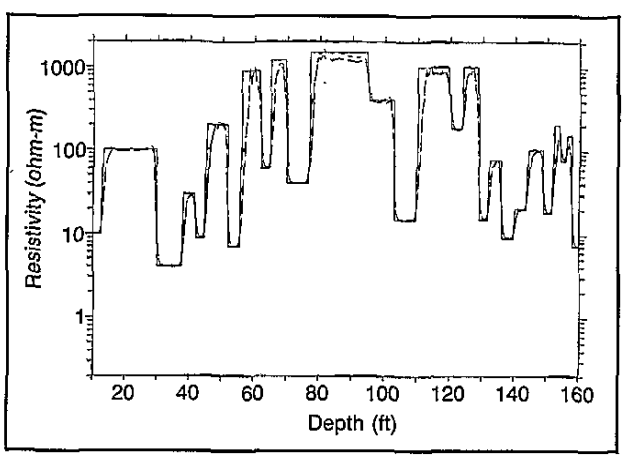

Fig. 7-28d—Traditional dual induction ILD and ILM logs and IDVR, IMVR.

Skin Effect

The problems at low resistivity are more related to skin effect than the problems at high resistivities. The Phasor ID measurement, with skin effect corrected by the X-signal, can read as low as 0.05 ohm-m.

Skin effect is more subtle than the lowest conductivity a tool can read. A log example from a Gulf Coast well is displayed in Fig. 7-29 showing the ID with traditional and VR Phasor Processing. The traditional log shows overshoot at the bed boundaries and incorrect center-bed readings. The VR Phasor log shows that the overshoot problems have been corrected and center-bed improvements made. Note how the IDVR and IMVR curves are parallel.

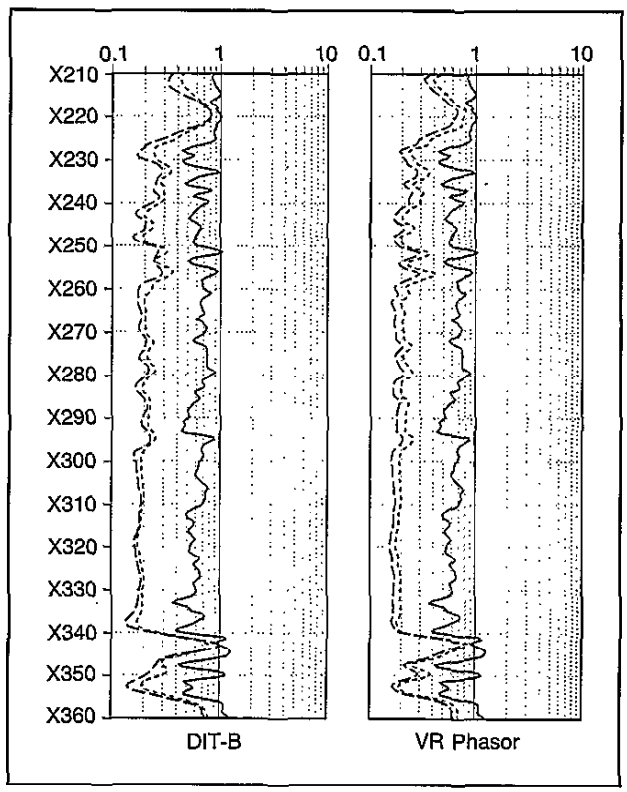

Fig. 7-29—Gulf Coast well with traditional induction ILD, ILM (left), and VR Phasor Processing IDVR, IMVR (right).

Borehole and Cave Effect

Since the induction tool is a "conductivity seeking" device, it can respond strongly to high conductivity in the borehole. Charts for previous tools were based on data determined experimentally and are valid only in smooth holes. Models have been developed that compute the borehole signal with arbitrary formation and borehole conductivities, and in any borehole size and at any standoff. These correction algorithms for the Phasor Induction SFL tool are available for real-time logging. The algorithms use measured information

about the borehole environment, such as hole diameter and borehole conductivity, to determine the correction needed at a given depth.

Large Boreholes

The Phasor Induction SFL tool, in conjunction with specially equipped neutron, density, and sonic devices, can provide excellent logs in large boreholes. The example of Fig. 7-30a shows an overlay of the Phasor ID measurements in a well drilled with a 12.5-in. bit and later reamed with a 23-in. bit. Both logs were automatically corrected for shoulder effect and for borehole and cave effect. Comparisons of the ID curves (Fig. 7-30b) and the invasion-corrected R_t values show that the Phasor Induction SFL tool along with the new modeling techniques allows quality log results in large boreholes. The expense of drilling small holes for logging and then reaming for large casing sizes can now be eliminated.

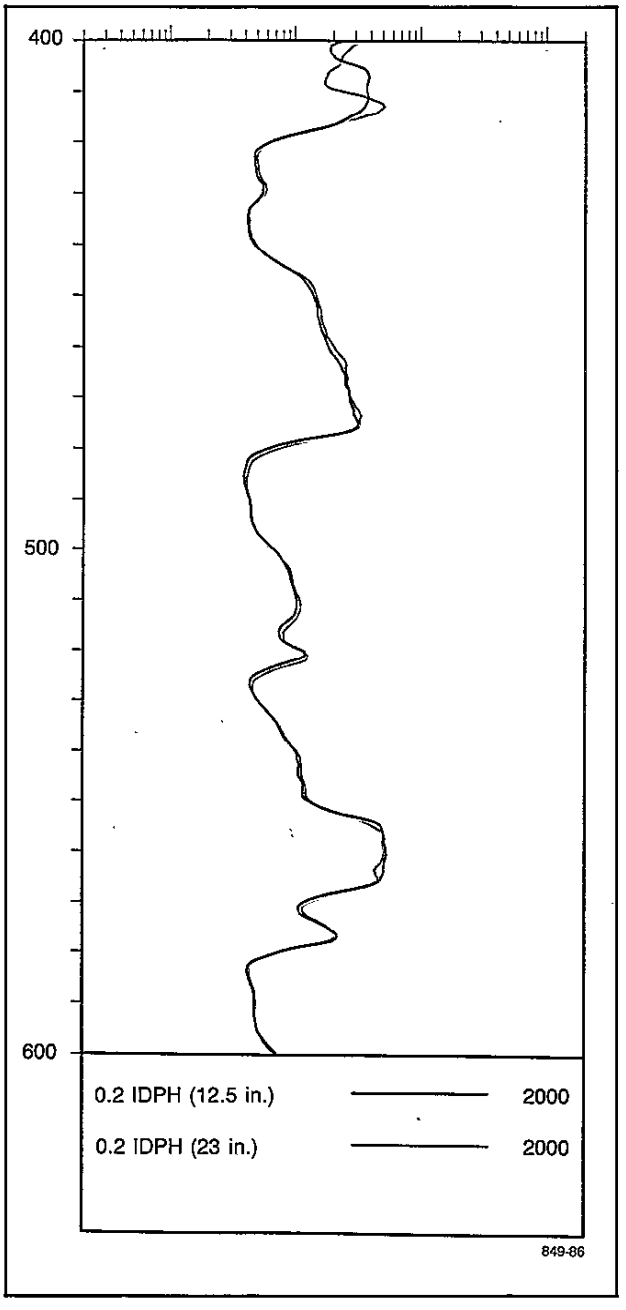

Fig. 7-30a—Phasor IDPH logs in 12.5-in. and 23-in. holes.

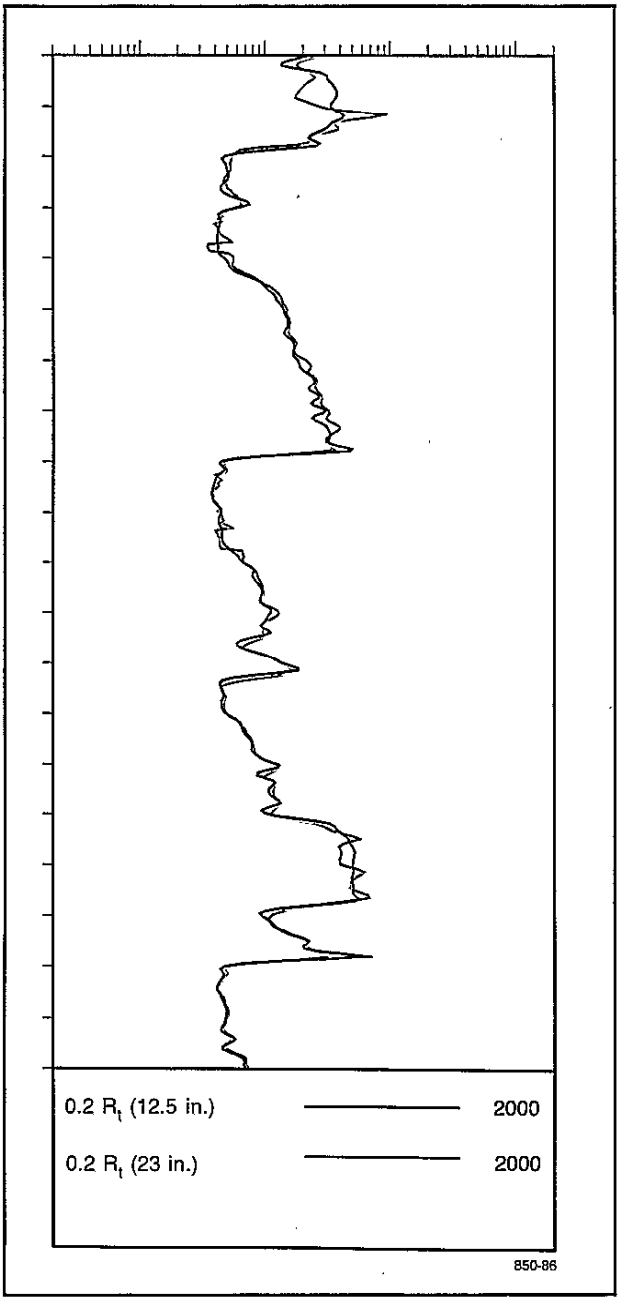

Fig. 7-30b—Invasion-corrected R_t curves.

Invasion Corrections

$R_{xo} > R_t$: the original dual induction tool was developed to determine R_t in the presence of invasion. The three measurements, at three different depths of investigation, are used to solve for parameters of a simple invasion model assuming only a flushed zone and a virgin zone. The solution can be presented in graph form as a "tornado" chart. The Phasor Induction SFL tool has the same task, but, because of the use of the X-signals, the character of the Phasor tornado charts is different. Fig. 7-31 shows the chart for an R_{xo} value of 10 ohm-m. Note that invasion diameters of up to 200 in. can be determined. An algorithm was devised to interpolate between the computed tornado chart data points to produce a log of R_{xo}, R_t, and d_i. Data from cases computed at three R_{xo} values are used in the computation.

$R_{xo} < R_t$: Fig. 7-32 shows a limited set of cases for $R_{xo} < R_t$. Although the recommended tool for these cases has always been the dual laterolog, the figure shows that as long as invasion is moderate, the Phasor induction measurement does a good job. The additional depth of investigation of ID provided by the X-signal aids in separating out these data. The invasion profiling algorithm includes these cases as well as the normal $R_{xo} > R_t$ cases.

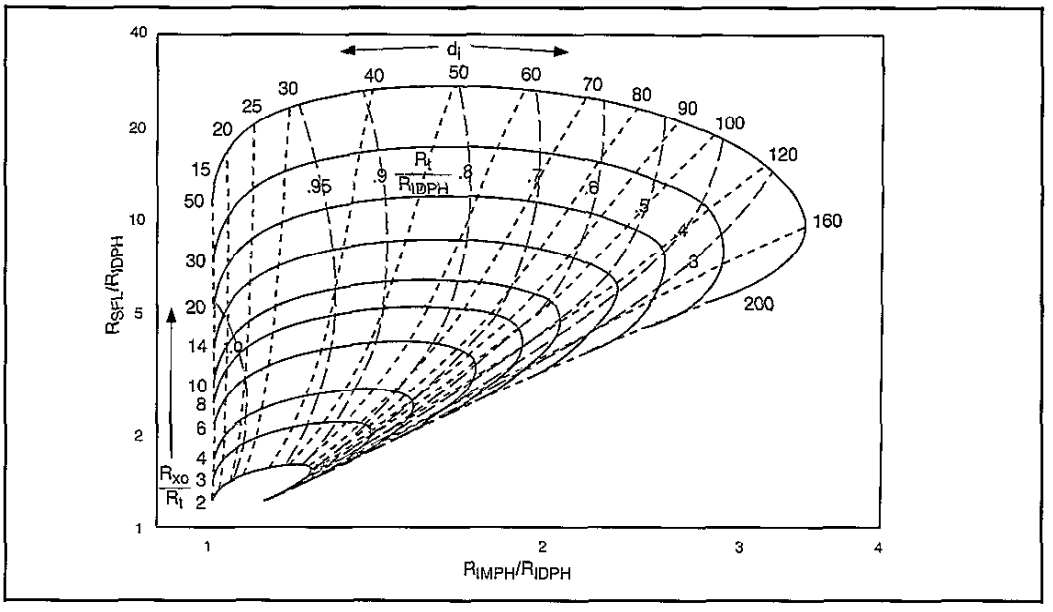

Fig. 7-31—Phasor Induction tornado chart for R_{xo} = 10.

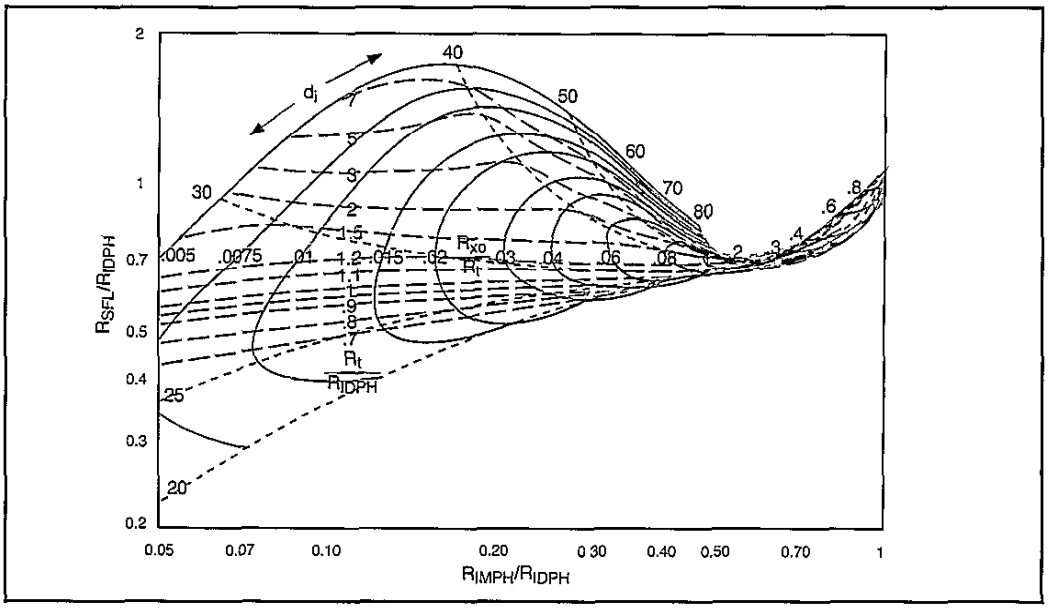

Fig. 7-32—Phasor Induction tornado chart for $R_{xo} < R_t$.

A Phasor log is shown in Fig. 7-33a where the ID measurement in the zone just below 3265 ft reads higher than either the IM or SFL curves. Interpretation through the $R_{xo} < R_t$ chart data produces the R_{xo}, R_t, and d_i log of Fig. 7-33b. A Dual Laterolog-MicroSFL tool was run in this well as the normal resistivity tool for this resistivity regime. The MicroSFL curve, plotted on the invasion-corrected Phasor induction logs, shows the close agreement of the two methods of R_{xo} measurement. For wells where it is expected that some zones will have $R_{xo} < R_t$, the addition of a MicroSFL tool is highly recommended to estimate shallow invasion parameters and to indicate non-step-profile invasion.

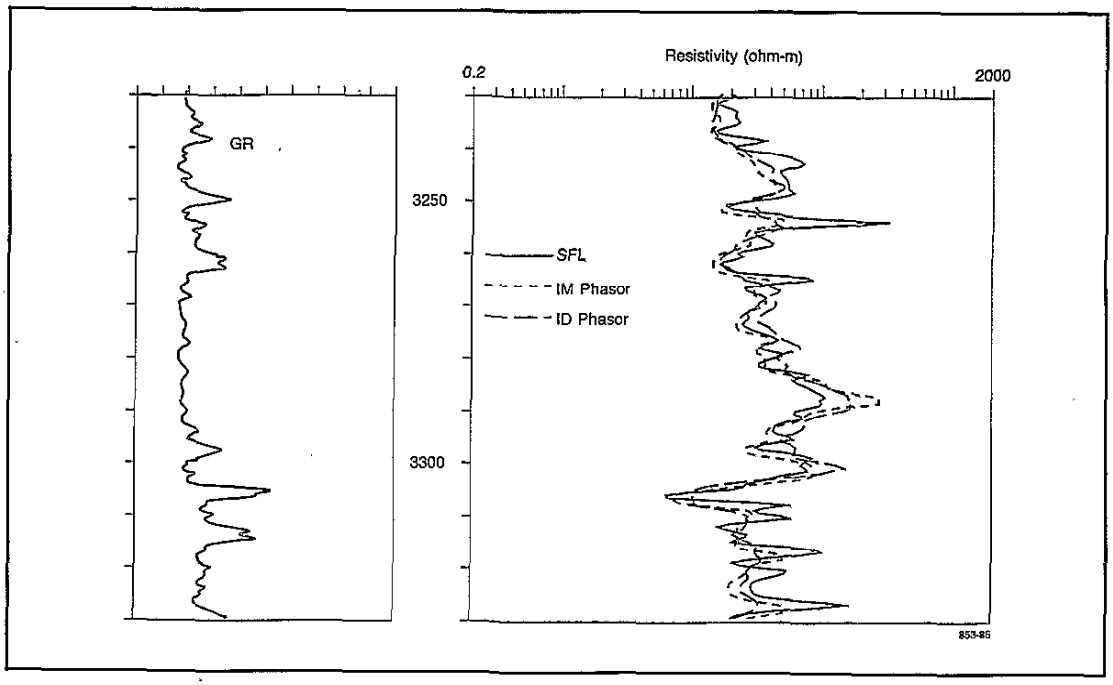

Fig. 7-33a—Phasor log with $R_{xo} < R_t$ zone.

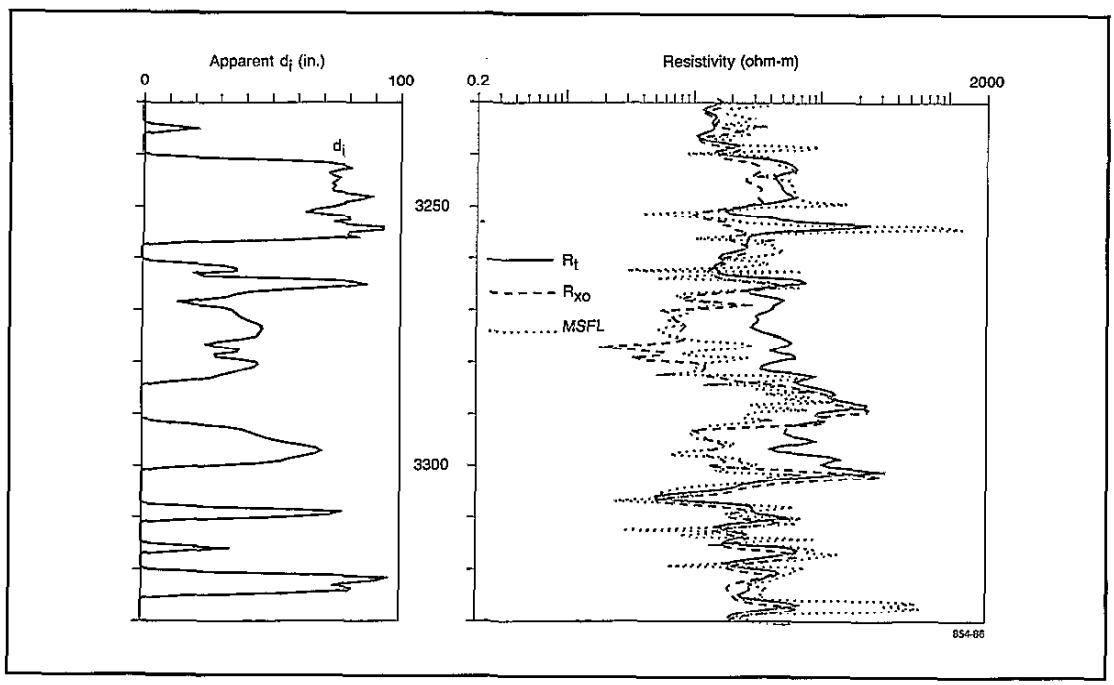

Fig. 7-33b—Phasor invasion interpretation with MicroSFL curve.

Interpretation in the Presence of Transition Zones

Traditional methods of invasion interpretation are based on the assumption of step-profile invasion. The Phasor Induction SFL tool brings new methods of interpretation to more realistic invasion profiles where transition zones can complicate the induction log. Two types of transitions are expected to be common: a "slope" profile with a continuous transition from R_{xo} to R_t over some radial distance, and the annulus profile. Studies[30] have shown that slope profiles produce little error in the estimate of R_t made by tornado chart methods. Annulus profiles can cause significant errors in estimating R_t, but they can be detected by comparison of Phasor logs made at all three operating frequencies, or by the addition of an R_{xo} device such as the MicroSFL tool.[30]

Oil-Based Mud

The Phasor induction service also provides better resistivity values in wells drilled with oil-based mud systems. Establishing an invasion profile requires three measurements with varying depths of investigation. When oil-based mud is used, the SFL device cannot be used for the shallow resistivity measurement, but the Phasor's X-signals provide some additional depth information. Various combinations of the R- and X-signal measurements were tested for invasion interpretation, particularly at shallow invasion diameters. The chart of Fig. 7-34 was the best compromise and is applicable only below 10 ohm-m. Above that resistivity, the X-signals are not sufficiently localized to provide accurate invasion interpretation. Note that the raw, unboosted ID and IM measurements are used as "medium" and "shallow," respectively. The axes are reversed from those of the usual tornado chart.

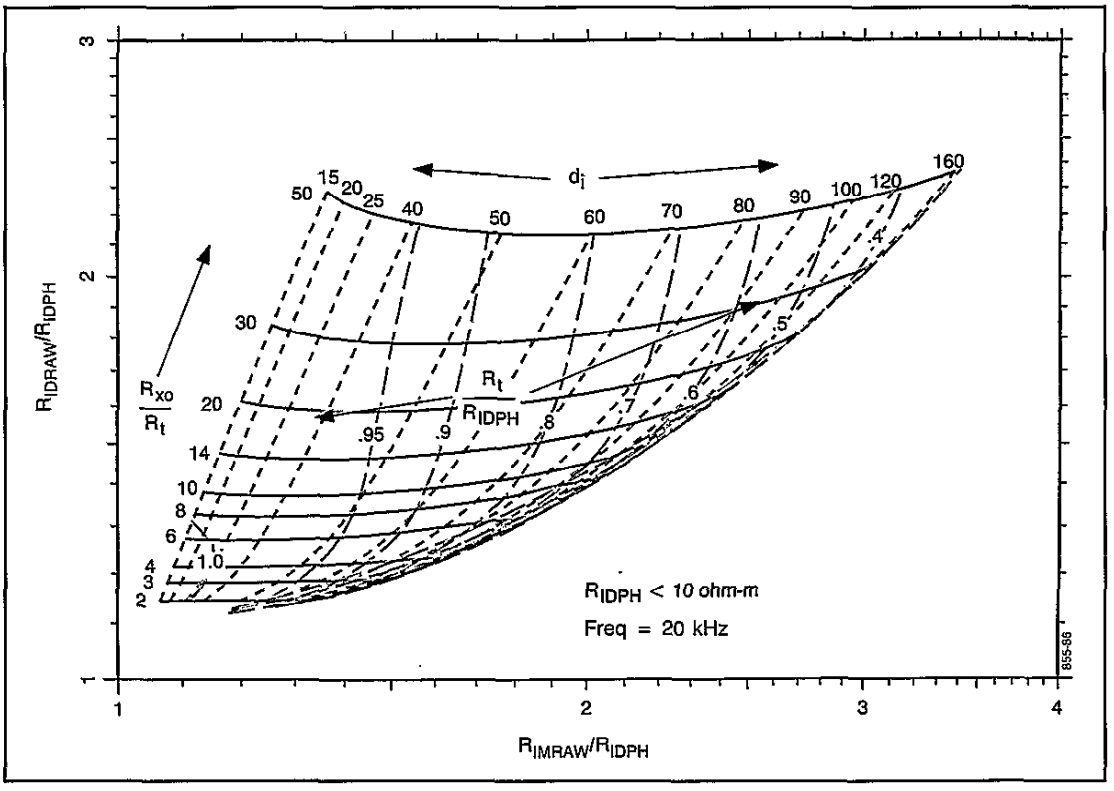

Fig. 7-34—Phasor Induction oil-based mud invasion interpretation, applicable only below 10 ohm-m.

Phasor Case Studies

Case studies illustrate the effectiveness of the Phasor induction measurements and the environmental corrections algorithms.

The first example is from a gas well in Oklahoma, and shows the large errors that can be caused by shoulder effect. The traditional dual induction log is shown in Fig. 7-35a. The zones from 9255 to 9295 ft and 9490 to 9540 ft are low-porosity limestone with gas production from fractures; the log exhibits classic shoulder effect on ID and IM, with both tools seeing the very conductive shoulders. The environmentally corrected Phasor (7-ft) logs are shown in Fig. 7-35b. Borehole effect in these zones is negligible, so all the differences come from the Phasor shoulder-effect correction. The invasion correction is shown in Fig. 7-35c, with R_t, R_{xo}, and an apparent d_i resulting from the tornado chart algorithm.

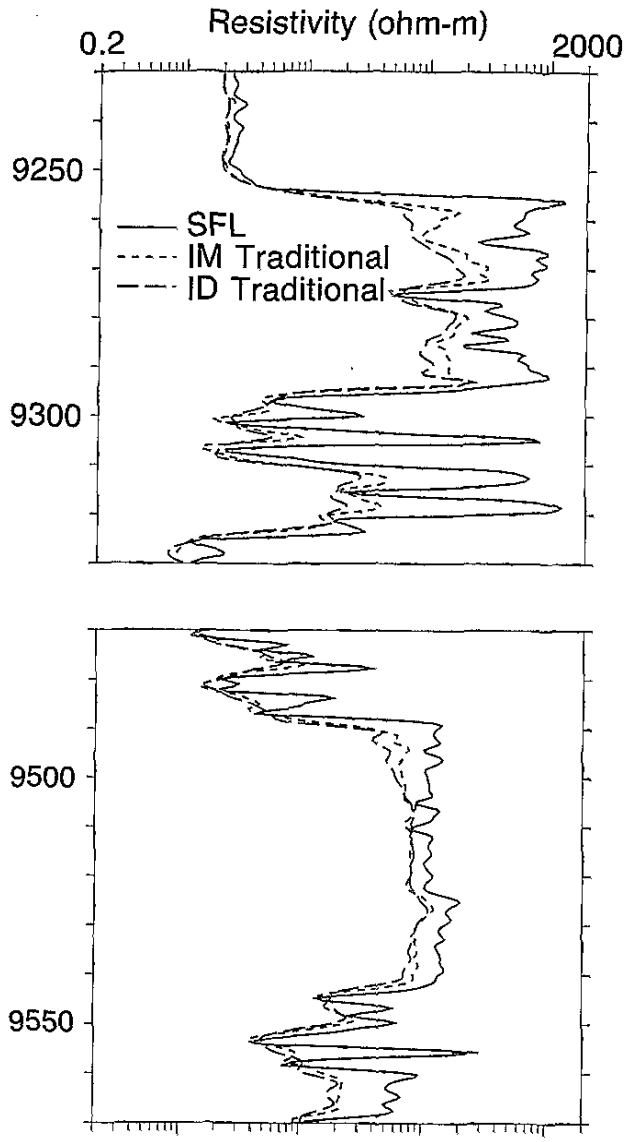

Fig. 35a—Dual Induction SFL log.

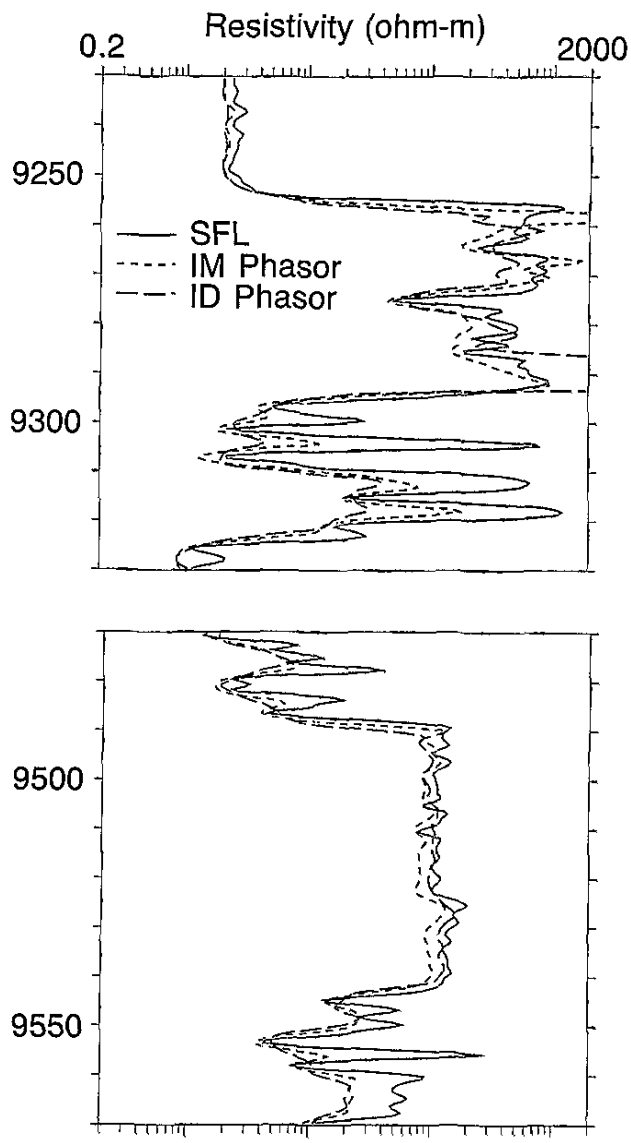

Fig. 35b—Phasor Processed (7-ft) log.

The corrections shown are what one expects from the published thin-bed charts; however, the best test of the corrections is a computed log with a known input formation. Fig. 7-35d shows a computed ID log designed to resemble the zone in the previous example. The solid rectangular curve shows the input formation. The short dashed curve shows the ID as traditionally processed, while the long dashed curve shows the ID Phasor Processed. The Phasor ID curve shows no shoulder effect and agrees with the input formation to better than 0.5 mS/m.

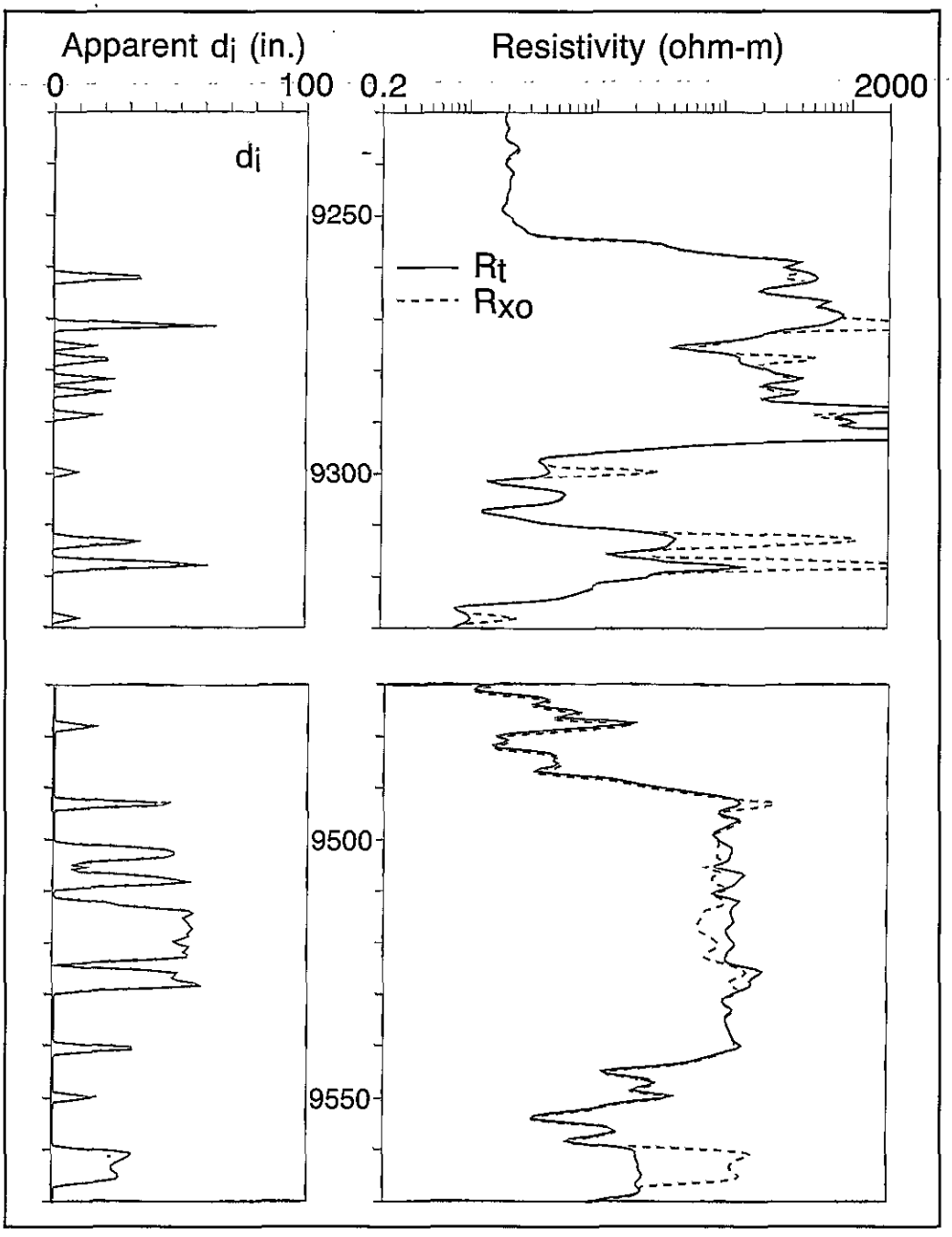

Fig. 7-35c—Phasor invasion interpretation.

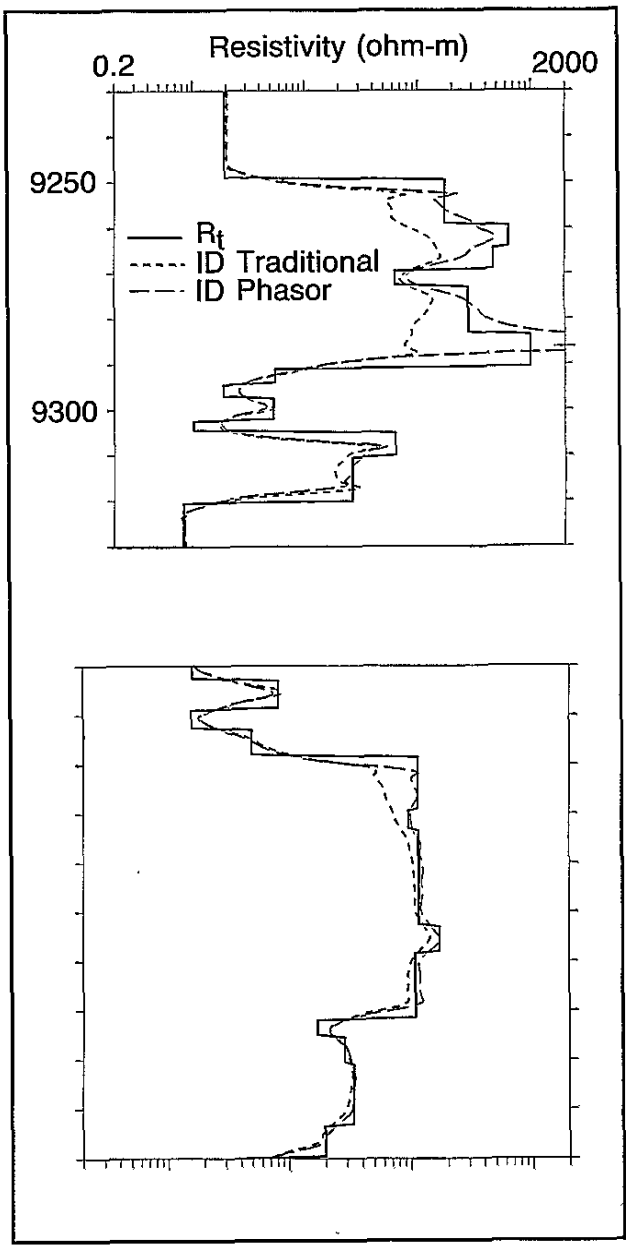

Fig. 7-35d—Computed log showing effect of Phasor Processing.

Another comparison is shown by an Offshore Gulf of Mexico well; Fig. 7-36 shows the traditional dual induction log from this well. Note the zone near 10560 ft with the SFL measurement showing a series of thin beds and the ILD curve anticorrelating with the SFL curve. The VR Phasor (2-ft) log clearly delineates the beds. The invasion interpretation of Fig. 7-36b shows the invaded laminations.

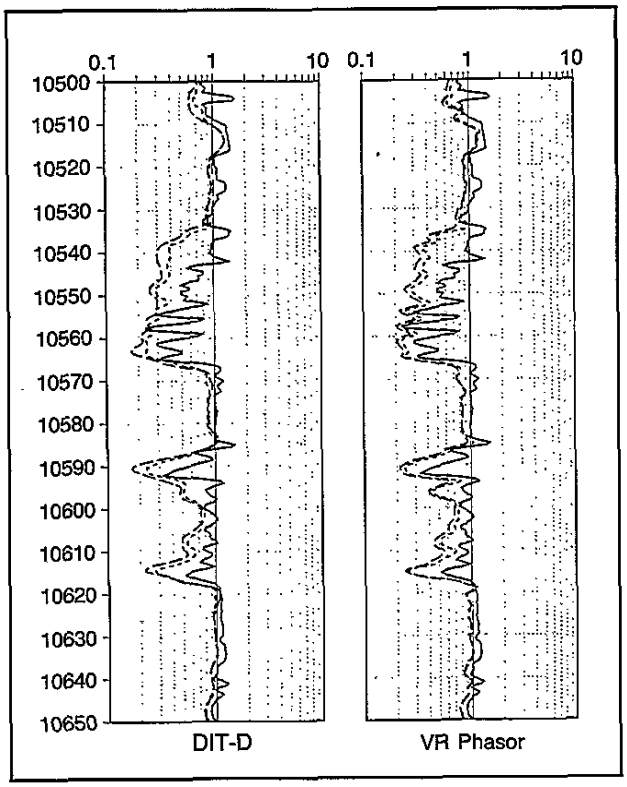

Fig. 7-36a—Offshore Gulf of Mexico well with traditional DIL and VR Phasor (2-ft) log which clearly delineates thin beds.

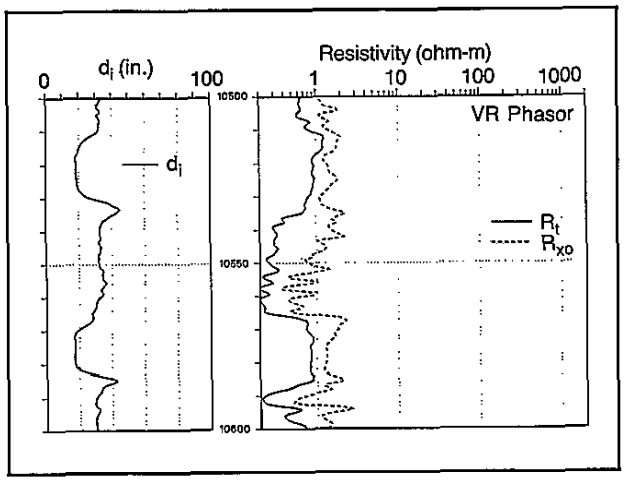

Fig. 7-36b—Phasor invasion interpretation of zone at 10,550 ft.

The third example is from a Canadian well with high resistivities from 125 to 130 m in a dolomitic sandstone which produces water-free gas. Figure 37a shows the traditional logs,

Fig. 37b shows the nuclear logs, and Fig. 37c shows the ER Phasor (3-ft) logs over the interval. ER Phasor logs predict an S_w of 12-14%, a significant reduction from the S_w of about 20% from the traditional logs. The ER Phasor logs also delineate the individual beds within the reservoir.

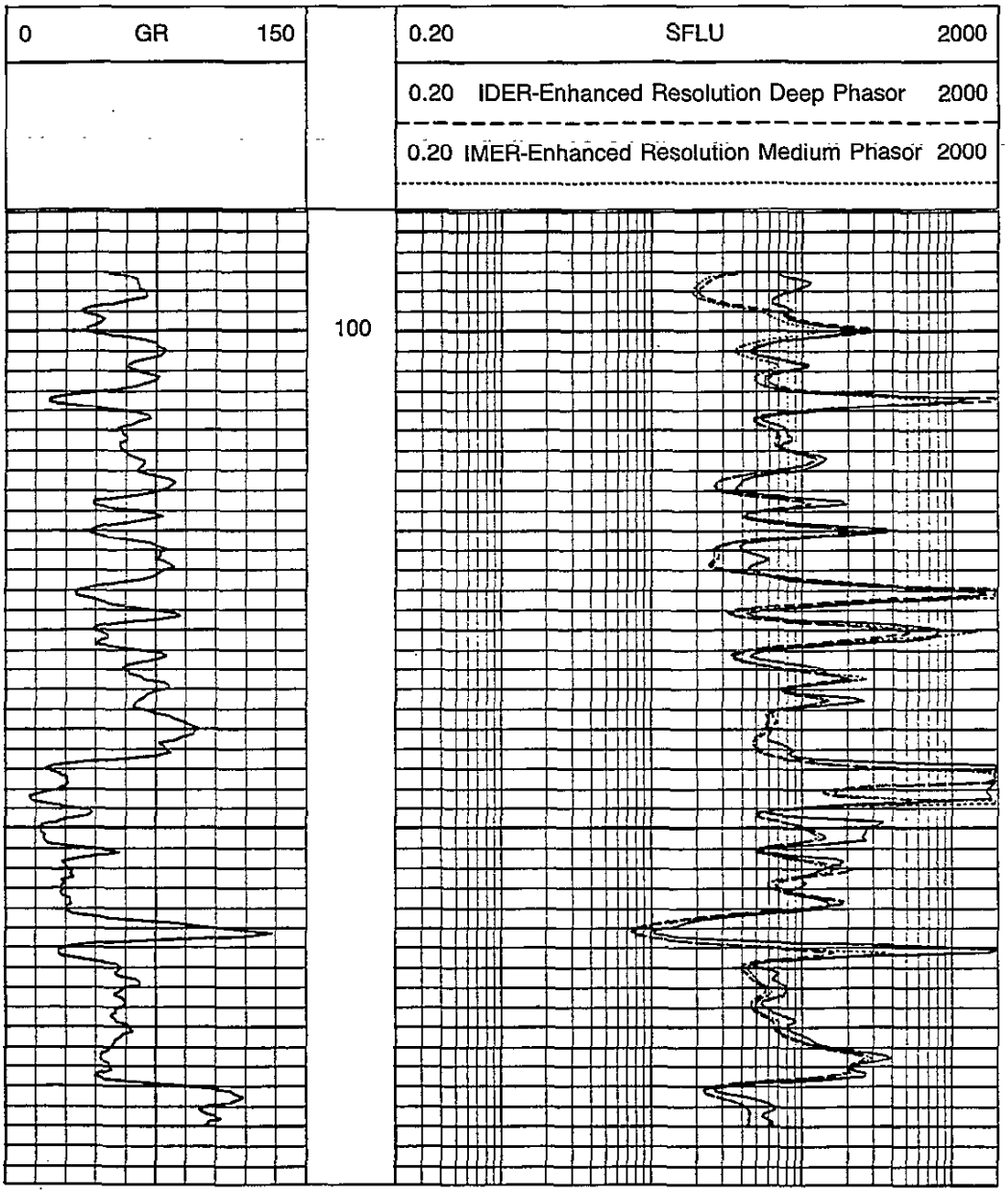

Fig. 7-37a—Canadian well with high resistivities recorded by traditional DIL.

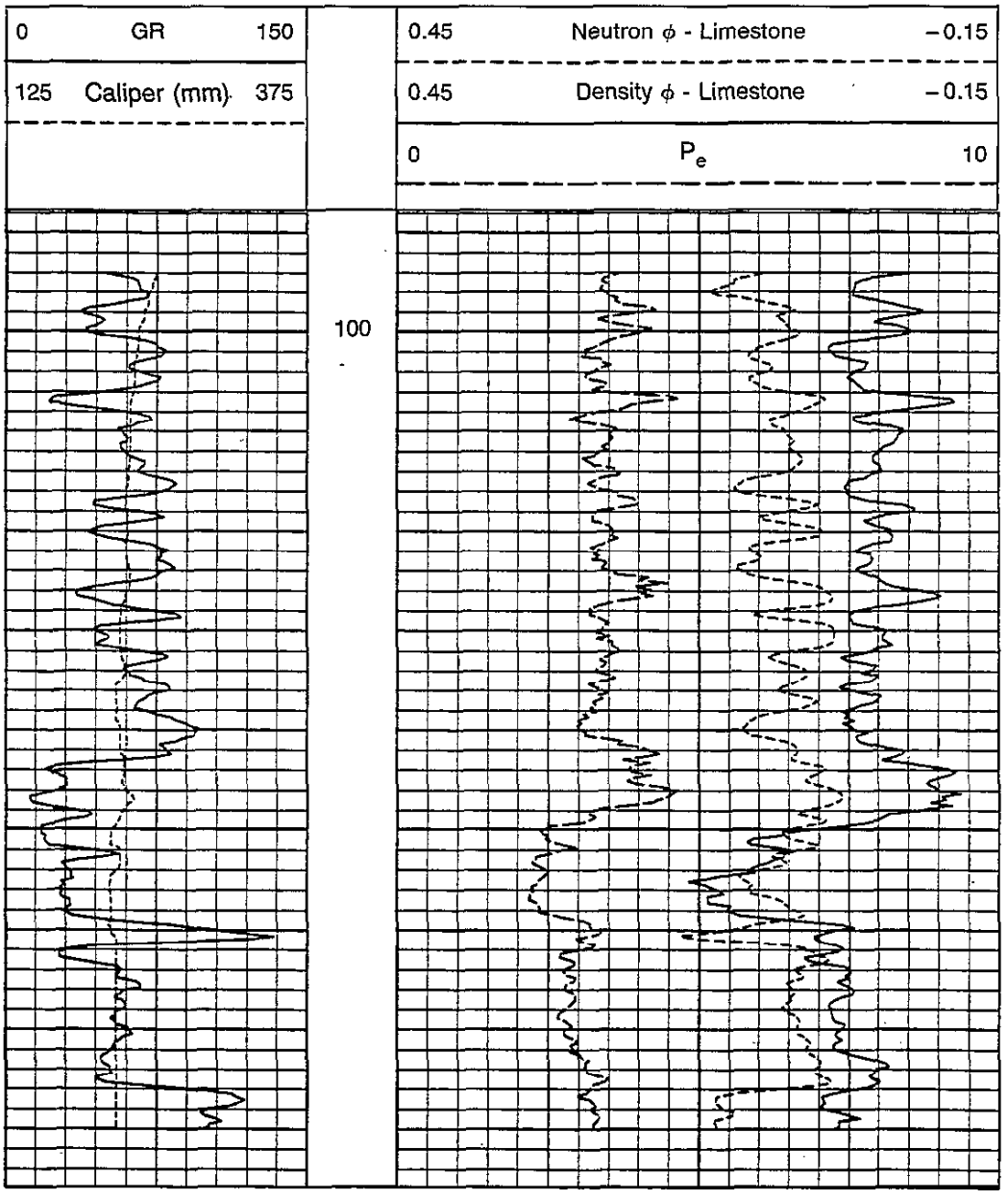

Fig. 7-37b—Nuclear logs reveal dolomitic sandstone which produces water-free gas.

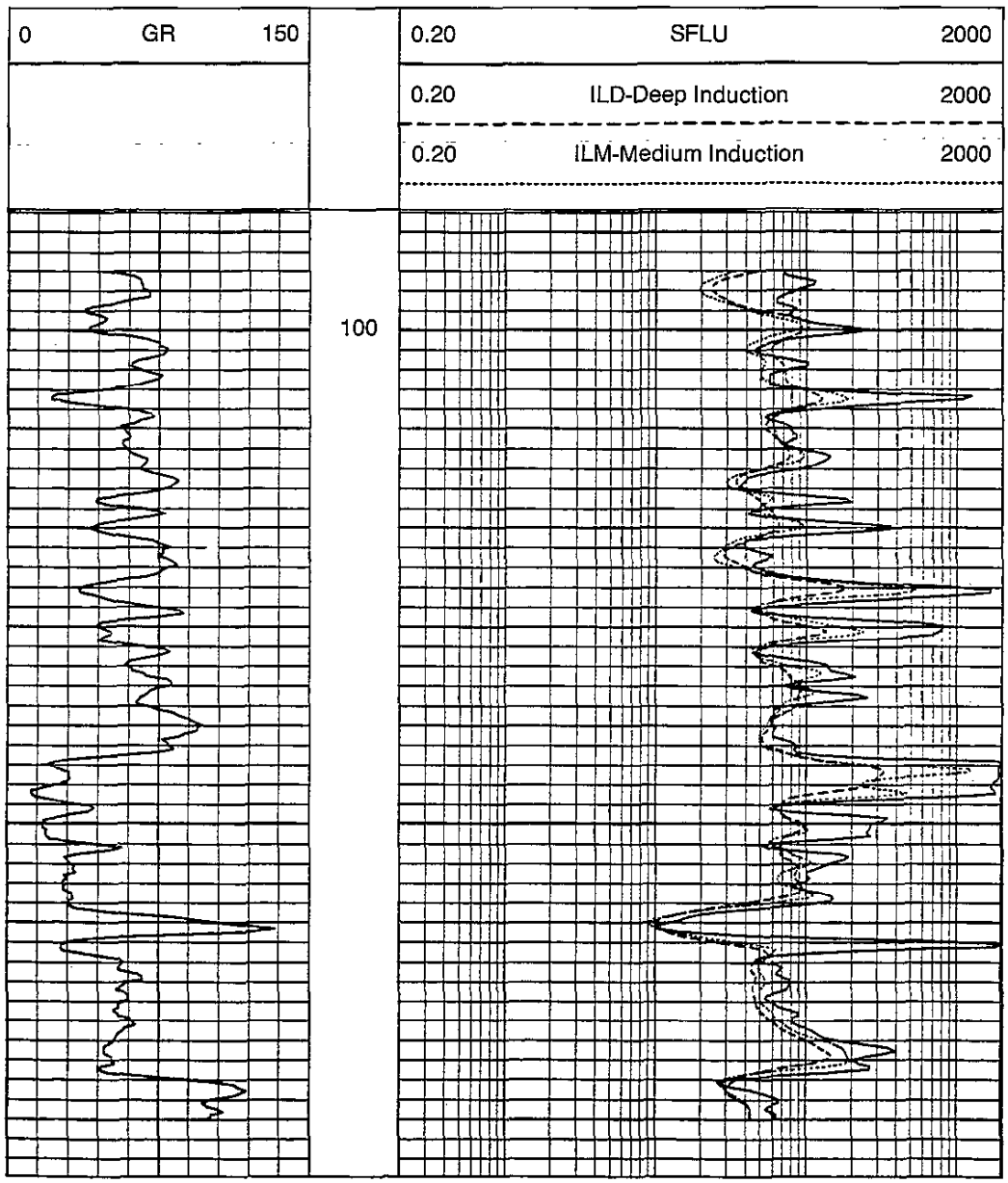

Fig. 7-37c—ER Phasor (3-ft) log with improved resistivity and bed definition.

Induction Versus Laterolog Measurements

Nearly all resistivity measurements are now made with focused devices. These tools are designed to minimize the influence of the borehole fluid and surrounding beds. Two types of tools exist: laterolog and induction tools. They have unique characteristics that favor their use in specific, and often different, situations and applications.

The induction log is generally recommended in holes drilled with only moderately conductive drilling muds, nonconductive muds (e.g., oil-base muds), and in empty or air-drilled holes. The laterolog is generally recommended in holes drilled with very conductive drilling muds (i.e., salt muds).

The induction tool, being a conductivity-sensitive device, is most accurate in low- to medium-resistivity formations. The laterolog tool, being a resistivity device, is most accurate in medium- to high-resistivity formations.

There is an overlap in the areas of applicability. The chart of Fig. 7-38 has been constructed for average cases: d_i from 0 to 80 in. and the possible occurrence of an annulus. This chart is only a guide. For conditions other than those given, the areas of applicability may differ.

As seen from Fig. 7-38, the laterolog measurement is preferred when R_{mf}/R_w falls to the left of the vertical dashed line and to the left of the solid line for the appropriate value of R_w. The induction log is preferred above the appropriate R_w line. To the right of the dashed line and below the appropriate R_w curve, either or both logs may be required for an accurate interpretation.

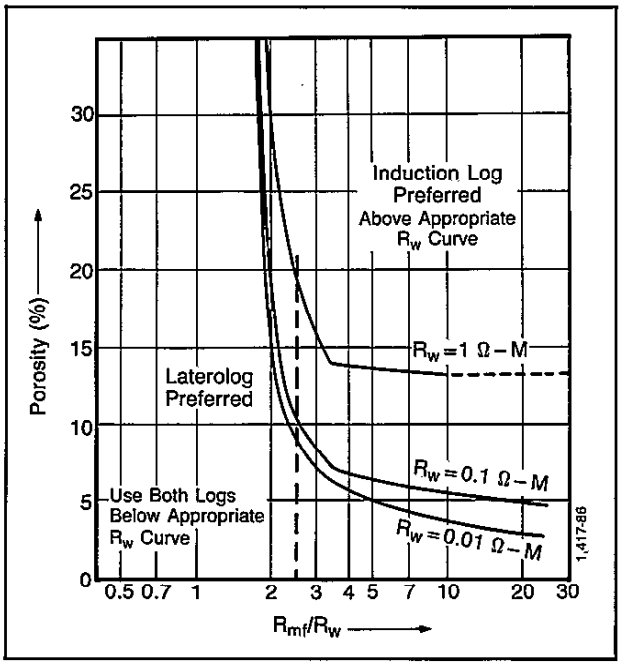

Fig. 7-38—Preferred ranges of application of induction logs and laterologs for usual cases.

The nature of the two tools can be described simply by saying that laterolog devices "see" the more resistive zones; induction tools "see" the more conductive zones. Thus R_{xo} is greater than R_t, the induction tool is preferred for R_t determination, and the laterolog tool is preferred where R_{xo} is less than R_t. Since the induction tool is a conductivity-seeking device it responds strongly to high conductivity in the borehole. Recent modeling efforts have led to codes that compute the borehole signal with arbitrary formation and borehole conductivities, and in any borehole size and at any standoff. A caliper, recorded with the induction tool, is required for the borehole correction.

The results of this method are shown in Fig. 7-39. The well drilled with salty mud was logged with the Phasor induction tool and the DLL tool. The ID log was first corrected for shoulder effect with the Phasor algorithm, then corrected for borehole effect. The resistivity spike at 3057 ft on the uncorrected ID measurement is due to borehole signal; the spikes at 3112 and 3123 are a result of cave effect. The ID log uncorrected is not very useful. After correction, it is much closer to the LLD curve. Although the laterolog tool is preferred in these conditions, the induction log provides acceptable results in this extreme case with Phasor Processing.

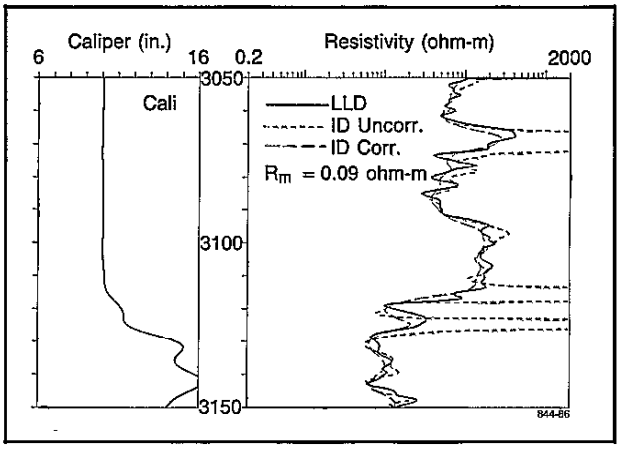

Fig. 7-39—Field log with and without borehole correction.

Induction logs provide acceptable thin-bed resolution, which makes reliable formation evaluation possible in beds down to 3-ft thick (IDER, IMER). The laterolog devices exhibit even better thin-bed resolution. Except for beds with extremely high resistivity, reliable formation evaluation is possible in beds as thin as 3 ft.

Both laterolog and induction measurements are influenced by the borehole and by surrounding beds. Even relatively thick beds may have some effect on their measurements. The measurements of both devices should be corrected for

borehole and surrounding bed effects. Although these corrections are usually small, it is good practice to make them to insure that they are not overlooked in those few cases where they are significant.

To correct either the LLD or the ID measurements for invasion effects, at least three resistivity measurements of differing depths of investigation are required. It is, therefore, strongly recommended that the resistivity log include at least three resistivity measurements. For the laterolog system, this could consist of a DLL-R_{xo} log (LLD, LLS, and MicroSFL measurements). For the induction system, this could consist of the DIL-SFL (ID, IM, and SFL) or, better yet, the Phasor Induction SFL tool (IDPH, IMPH, and SFL).

MICRORESISTIVITY DEVICES

Microresistivity devices are used to measure the resistivity of the flushed zone, R_{xo}, and to delineate permeable beds by detecting the presence of mudcake.

Measurements of R_{xo} are important for several reasons. When invasion is moderate to deep, a knowledge of R_{xo} allows the deep resistivity measurement to be corrected to true formation resistivity. Also, some methods for computing saturation require the R_{xo}/R_t ratio. In clean formations, a value of F can be computed from R_{xo} and R_{mf} if S_{xo} is known or can be estimated.

To measure R_{xo}, the tool must have a very shallow depth of investigation because the flushed zone may extend only a few inches beyond the borehole wall. Since the reading should not be affected by the borehole, a sidewall-pad tool is used. The pad, carrying short-spaced electrode devices, is pressed against the formation and reduces the short-circuiting effect of the mud. Currents from the electrodes on the pad must pass through the mudcake to reach the flushed zone.

Microresistivity readings are affected by mudcake; the effect depends on mudcake resistivity, R_{mc}, and thickness, h_{mc}. Moreover, mudcakes can be anisotropic, with mudcake resistivity parallel to the borehole wall less than that across the mudcake. Mudcake anisotropy increases the mudcake effect on microresistivity readings so that the effective, or electrical, mudcake thickness is greater than that indicated by the caliper.

Older microresistivity equipment included a tool with two pads mounted on opposite sides. One was the microlog pad, and the other was either the microlaterolog or Proximity pad, as required by mud and mudcake conditions. The measurements were recorded simultaneously.

Newer microresistivity equipment includes a microlog tool and a MicroSFL tool. Mounted on the powered caliper device, the microlog can be run simultaneously with any combination of Litho-Density*, CNL*, DIL, NGS, or EPT* logging services.

* *Mark of Schlumberger*

The MicroSFL tool can also be run in combination with other services. It is most commonly combined with the DLL or DIL equipment.

Microresistivity logs are scaled in resistivity units.

- When recorded by itself, the microlog is usually recorded over Tracks 2 and 3 on a linear scale. The microcaliper is shown in Track 1.
- The microlaterolog and Proximity logs are recorded on a four-decade logarithmic scale to the right of the depth track (Fig. 7-40). The caliper is recorded in Track 1. When the microlog is also recorded, it is presented in Track 1 on a linear scale.
- The MicroSFL measurement is also recorded on the logarithmic grid. When run with the DLL or DIL log, it is presented on the same film and on the same resistivity scale.

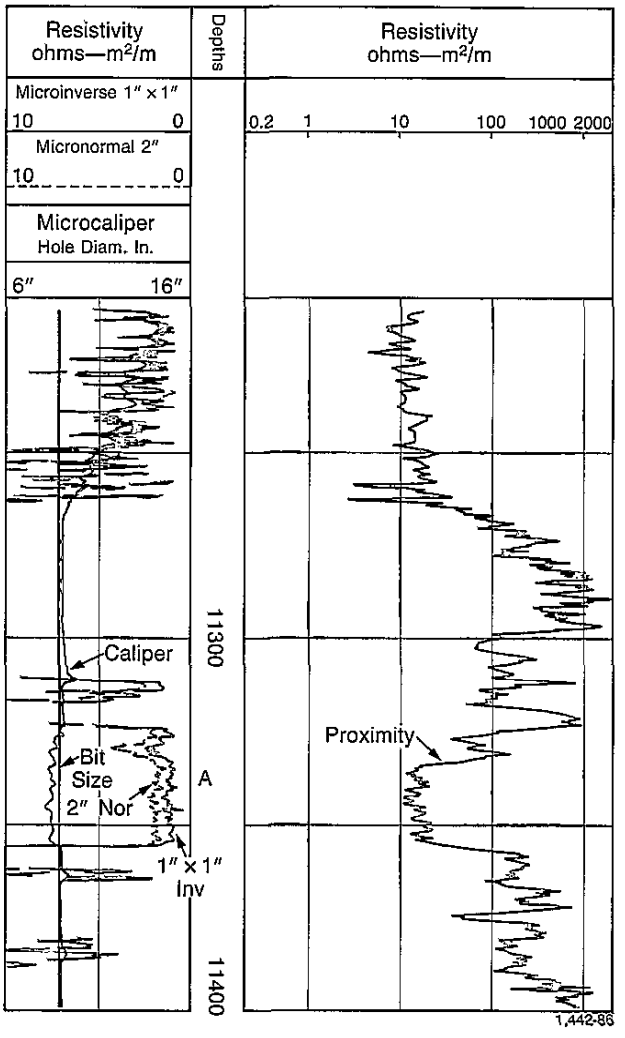

Fig. 7-40—Presentation of Proximity-Microlog.

Microlog

With the microlog tool, two short-spaced devices with different depths of investigation provide resistivity measurements of a very small volume of mudcake and formation immediately adjoining the borehole. Comparison of the two curves readily identifies mudcake, which indicates invaded and, therefore, permeable formations.

Principle

The rubber microlog pad is pressed against the borehole wall by arms and springs. The face of the pad has three small in-line electrodes spaced 1 in. apart. With these electrodes a 1- by 1-in. microinverse ($R_{1"x1"}$) and a 2-in. micronormal ($R_{2"}$) measurement are recorded simultaneously.

As drilling fluid filters into the permeable formations, mud solids accumulate on the hole wall and form a mudcake. Usually, the resistivity of the mudcake is slightly greater than the resistivity of the mud and considerably lower than the resistivity of the invaded zone near the borehole.

The 2-in. micronormal device has a greater depth of investigation than the microinverse. It is, therefore, less influenced by the mudcake and reads a higher resistivity, which produces "positive" curve separation. In the presence of low-resistivity mudcake, both devices measure moderate resistivities, usually ranging from 2 to 10 times R_m.

In impervious formations, the two curves read similarly or exhibit some "negative" separation, and the resistivities are usually much greater than in permeable formations.

Interpretation

Positive separation in a permeable zone is illustrated in Fig. 7-40 at Level A. The caliper shows evidence of mudcake. Although the microlog curves identify permeable formations, quantitative inferences of permeability are not possible.

When no mudcake exists, the microlog readings may yield useful information about borehole condition or lithology, but the log is not quantitatively interpretable.

Under favorable circumstances, R_{xo} values can be derived from the microlog measurements using Chart Rxo-1. R_{mc} values for this purpose can be measured directly or estimated from Chart Gen-7, and h_{mc} is obtained from the caliper curve. Limitations of the method are:

- The ratio R_{xo}/R_{mc} must be less than about 15 (porosity more than 15%).
- h_{mc} must be no greater than 0.5 in.
- Depth of invasion must be over 4 in.; otherwise, the microlog readings are affected by R_t.

Microlaterolog

The microlaterolog tool was designed to determine R_{xo} accurately for higher values of R_{xo}/R_{mc} where the microlog interpretation lacks resolution.

Principle

The microlaterolog pad is shown in Fig. 7-41. A small electrode, A_O, and three concentric circular electrodes are embedded in a rubber pad applied against the hole wall. A constant current, i_o, is emitted through A_O. Through the outer electrode ring, A_1, a varying current is emitted and automatically adjusted so that the potential difference between the two monitoring electrode rings, M_1 and M_2, is maintained essentially equal to zero. The i_o current is forced to flow in a beam into the formation. The resulting current lines are shown on the figure. The i_o current near the pad forms a narrow beam, which opens up rapidly a few inches from the face of the pad. The microlaterolog resistivity reading is influenced mainly by the formation within this narrow beam.

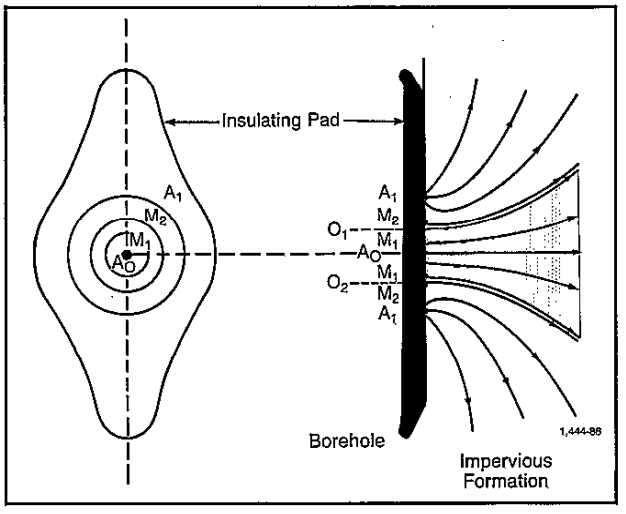

Fig. 7-41—Microlaterolog pad showing electrodes (left) and schematic current lines (right).

Fig. 7-42 compares qualitatively the current-line distributions of the microlaterolog and the microlog devices when the corresponding pad is applied against a permeable formation. The greater the value of R_{xo}/R_{mc}, the greater the tendency for the microlog i_o current to escape through the mudcake to the mud in the borehole. Consequently, for high R_{xo}/R_{mc} values, microlog readings respond very little to variations of R_{xo}. On the contrary, all the microlaterolog i_o current flows into the permeable formation and the microlaterolog reading depends mostly on the value of R_{xo}.

Response

Laboratory tests and computer simulation results have shown that the virgin formation has practically no influence on the microlaterolog readings if the invasion depth is more than 3 or 4 in.

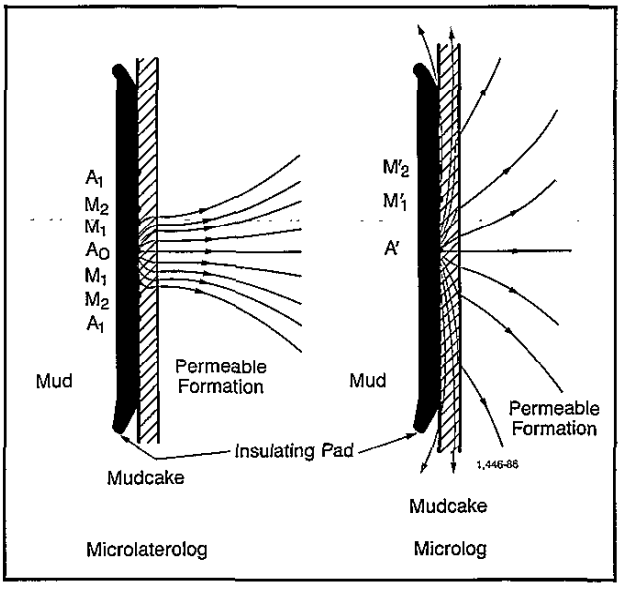

Fig. 7-42—Comparative distribution of current lines of Microlaterolog and Microlog.

The influence of mudcake is negligible for mudcakes less than ⅜ in., but increases rapidly with greater thicknesses. Chart Rxo-2 (top) gives appropriate corrections.

Proximity Log

Principle

The Proximity tool is similar in principle to the microlaterolog device. The electrodes are mounted on a wider pad, which is applied to the wall of the borehole; the system is automatically focused by monitoring electrodes.

Response

Pad and electrode design are such that isotropic mudcakes up to ¾ in. have very little effect on the measurements (see Chart Rxo-2, bottom).

The Proximity tool has a significantly deeper depth of investigation than does the microlog or microlaterolog tools. Thus, if the invasion is very shallow, the Proximity measurement may be influenced by R_t. The resistivity measured can be expressed as:

$$R_P = J_{xo} R_{xo} + (1 - J_{xo}) R_t ,$$

where R_P is resistivity measured by the Proximity log and J_{xo} is the pseudogeometrical factor of the flushed zone. The value of J_{xo}, as a function of invasion diameter, d_i, is given in Fig. 7-43; this chart gives only an approximate value of J_{xo}. J_{xo} depends, to some extent, on the diameter of the borehole and on the ratio R_{xo}/R_t.

If d_i is greater than 40 in., J_{xo} is very close to unity; accordingly, the Proximity log measures R_{xo} directly. If d_i is less than 40 in., R_P is between R_{xo} and R_t, usually much closer to R_{xo} than to R_t. R_P can be fairly close to R_t only if the invasion is nonexistent or extremely shallow; of course, when R_{xo} and R_t are similar, the value of R_P depends very little on d_i.

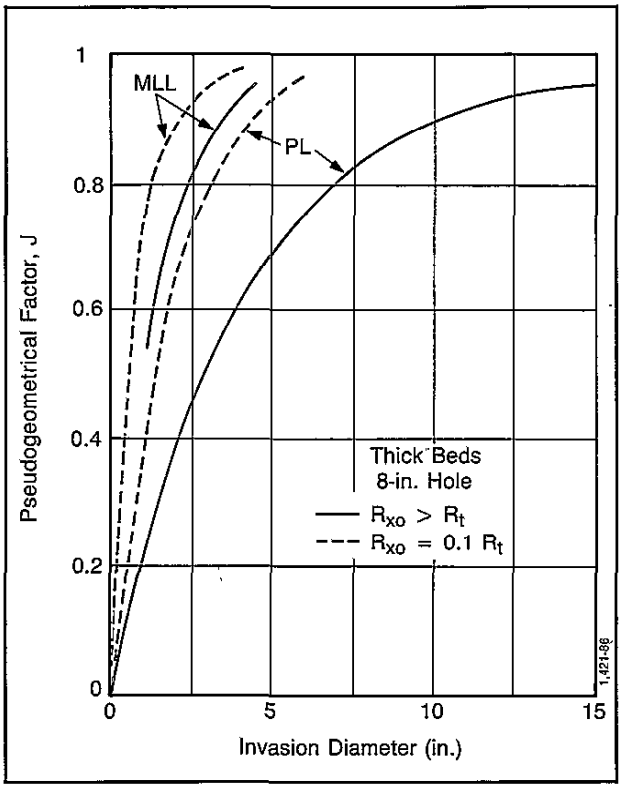

Fig. 7-43—Pseudogeometrical factors, Microlaterolog and Proximity log.

Vertical Resolution

The resolution of the Proximity log is about 6 in. Corrections for the effect of adjacent beds are unnecessary for bed thicknesses greater than 1 ft.

MicroSFL

The MicroSFL is a pad-mounted spherically focused logging device that has replaced the microlaterolog and Proximity tools. It has two distinct advantages over the other R_{xo} devices. The first is its combinability with other logging tools, including the DIL and DLL tools. This eliminates the need for a separate logging run to obtain R_{xo} information.

The second improvement is in the tool's response to shallow R_{xo} zones in the presence of mudcake. The chief limitation of the microlaterolog measurement is its sensitivity

to mudcakes. When mudcake thickness exceeds about ⅜ in., the log readings are severely influenced at high R_{xo}/R_{mc} contrasts. The Proximity log, on the other hand, is relatively insensitive to mudcakes, but it requires an invaded zone with a d_i of about 40 in. in order to provide direct approximations of R_{xo}.

The solution was found in an adaptation of the principle of spherical focusing in a sidewall-pad device. By careful selection of electrode spacings and bucking-current controls, the MicroSFL measurement was designed for minimum mudcake effect without an undue increase in the depth of investigation (see Chart Rxo-3). Fig. 7-44 illustrates, schematically, the electrode arrangement (right) and the current patterns (left) of the MicroSFL tool.

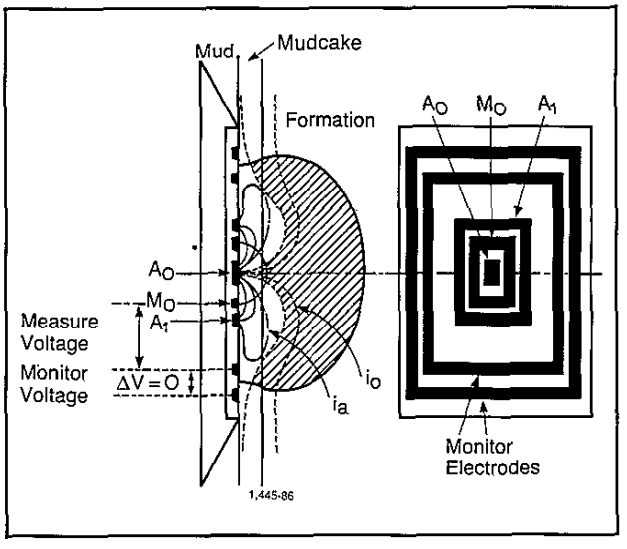

Fig. 7-44—Electrode arrangement of MicroSFL device (right) and current distribution (left).

The surveying current flows outward from a central electrode, A_O. Bucking currents, passing between the electrodes, A_O and A_1, flow in the mudcake and, to some extent, in the formation. The measuring current, i_o, is thereby confined to a path directly into the formation, where it quickly "bells" out and returns to a remote electrode, B. To achieve this, the bucking current is adjusted to make the monitor voltage equal to zero. By forcing the measure current to flow directly into the formation, the effect of mudcake resistivity on tool response is minimized; yet, the tool still has a very shallow depth of investigation.

Synthetic microlog curves can be computed from MicroSFL parameters. Since the measure current sees mostly the flushed zone and the bucking current sees primarily the mudcake, it is possible to mathematically derive micronormal and microinverse curves.

Environmental Corrections

Microresistivity measurements must be corrected for mudcake. Charts Rxo-1, -2, and -3 provide the mudcake correction for the microlog, microlaterolog, Proximity, and MicroSFL values, respectively. The correction is a function of the mudcake thickness and the resistivity contrast between the mudcake and the microresistivity measurement. Mudcake thickness is normally deduced from a comparison of the actual borehole size, as measured with the caliper, to the known bit size.

Resistivity Interpretation

When invasion is very deep an accurate value of R_t is sometimes difficult to measure because the reading of the deep-investigation log is also affected by R_{xo}. This effect is greater for larger values of R_{mf}/R_w because the contrast between R_{xo} and R_t is greater. Conversely, when invasion is very shallow, the measurements of so-called R_{xo} microresistivity logs may be affected by the R_t zone.

It may also become very difficult, or impossible, to make accurate corrections for invasion by filtrates of different characteristics. If a mud change is anticipated, the resistivity logs should be run before the change.

Assuming a sharp transition between the R_{xo} and R_t zone, the interpretation problem involves three unknown parameters: R_{xo}, d_i, and R_t. To solve it three different measurements may be required. These preferably include one whose response is affected mostly by R_t, another affected mostly by R_{xo}, and a third affected mostly by variations in d_i.

Determination of R_{xo}

R_{xo} can be determined from the microlaterolog or MicroSFL logs and can sometimes be derived from the microlog or the Proximity log. These pad devices for R_{xo} determination are sensitive to mudcake effects and borehole rugosity, but are usually insensitive to bed-thickness effects.

In the absence of a microresistivity measurement, a value of R_{xo} may be estimated from the porosity using a formula such as

$$R_{xo} = \frac{0.62\ R_{mf}}{\phi^{2.15}(1 - S_{or})^2}, \qquad \text{(Eq. 7-9)}$$

using ϕ from a porosity log and an estimated value of S_{or} (residual oil saturation). In water-bearing formations, this estimate may be good since S_{or} can be fairly safely assumed to be zero. In hydrocarbon-bearing formations, any uncertainty in S_{or} will, of course, be reflected in the R_{xo} estimation from Eq. 7-9.

Resistivity Invasion Corrections

Three resistivity curves of differing depths of investigation can be used to define R_{xo}, R_t, and d_i. These charts have the

appearance of a tornado and are sometimes referred to as "tornado" charts. There are many of these charts, constructed for various combinations of resistivity devices. Some are entered with R_{xo} plus two deeper resistivity log readings; others are entered with three resistivity log values. All provide the information to correct the deep resistivity reading for the effects of invasion, to define the diameter of the invasion, d_i, and to define the R_{xo}/R_t ratio. Those entered with three resistivity measurements also correct the shallow resistivity reading for any deficiencies in invasion and thereby provide an R_{xo} value.

Unless otherwise stated, all invasion correction charts are for thick beds and 8-in. boreholes; readings should be corrected as necessary for bed thickness and hole size. The charts were constructed assuming a step contact between the R_{xo} and R_t zones (no annulus, no transition zone). In most situations this assumption is adequate. In all charts for the induction log, skin-effect corrections have been incorporated.

Charts Rint-3 and -4 make use of R_{xo}, the deep induction (ID or 6FF40), and the LL8 (Chart Rint-3) or SFL (Chart Rint-5) measurements. If the point lies in the plateau region of the curves, it is apparent that invasion is so shallow that $R_{xo}/R_{ID} \cong R_{xo}/R_t$, and $R_{ID} \cong R_t$. These charts take into account the variation in pseudogeometrical factors with R_{xo}/R_t.

Chart Rint-10 makes use of R_{xo}, the deep induction (ID or 6FF40), and the medium induction measurements for the case of $R_{xo} > R_t$.

Charts Rint-9a and -9b are similar charts for the dual laterolog tools, type DLT-B and types DLT-D/E, respectively. They use R_{xo}, LLD, and LLS measurements. Although the correction is moderate at very shallow invasion, the LLD always requires some invasion correction to obtain R_t.

Charts Rint-2a, -2b, -2c use ID, IM, and LL8 or SFL data. Two charts for each set of measurements exist. One is for use when $R_{xo}/R_m \cong 100$ and another for when $R_{xo}/R_m \cong 20$.

Similar charts exist for the Phasor induction combination of IDPH, IMPH, and SFL (Charts Rint-11a,-11b). These apply to 20-kHz tool operation and include the case of $R_{xo} > R_t$. Similar charts are available for 10- and 40-kHz operation. Notice that the Phasor induction tool provides much better resolution in deeper invasion (invasion greater than 50 in.) than does the dual induction tool.

Many oil-base muds will invade the formations and influence resistivity readings. Chart Rint-12 uses the Phasor induction measurements to define R_t and d_i in low-resistivity rocks drilled with such mud. It uses the deep and medium Phasor induction signals after boosting (IDPH and IMPH) and before boosting (IID and IIM).

Compensated Dual Resistivity

The Compensated Dual Resistivity (CDR*) tool[33] is an electromagnetic propagation tool for logging-while-drilling. The CDR tool provides two resistivity measurements with several novel features. These features have been verified by theoretical modeling, test tank experiments, and log examples.

The CDR tool is a 2-MHz electromagnetic propagation tool built into a drill collar. The drill collar is fully self-contained and has rugged sensors and electronics. The measurement is borehole compensated, which requires two transmitters and two receivers. The two transmitters alternately broadcast electromagnetic waves, and the phase shifts and attenuations are measured between the two receivers and averaged. The phase shift is transformed into a shallow measurement, R_{ps}, and the attenuation is transformed into a deep measurement, R_{ad}.

The CDR tool has several new, important features:

- R_{ad} and R_{ps} provide two depths of investigation and are used to detect invasion while drilling. In a 1-ohm-m formation, the diameters of investigation (50% response) are 30 in. for R_{ps} and 50 in. for Rad.
- R_{ad} and R_{ps} detect beds as thin as 6 in. R_{ad} and R_{ps} cross over precisely at the horizontal bed boundaries. This feature can be used to measure bed thickness.
- R_{ad} and R_{ps} are insensitive to hole size and mud resistivity in smooth boreholes. Borehole corrections are very small even for contrasts of 100:1 between formation and mud resistivities (Charts Rcor-11, 12, and 13).

The features of the CDR tool are best demonstrated by field logs. Fig. 7-45 shows the vertical responses for R_{ad} and R_{ps} for a very thin, resistive bed. This well was drilled with an 8.5-in. bit and oil-based mud. Track 1 shows the CDR tool's gamma ray and an EPT attenuation curve and Track 2 shows the measured CDR tool resistivities. The EPT attenuation and the crossovers of R_{ad} and R_{ps} predict a bed thickness of 2 ft.

There are minimal borehole effects in fresh muds, even in large holes. A good example comes from a well drilled in Texas (Fig. 7-46), where the CDR tool logged the same formations with different size holes. The well was drilled with an 8.5-in. bit, reamed once to 17.5 in., and reamed a second time to 26 in. The CDR tool logged the well at 8.5 in. while drilling, and logged the 17.5-in. and 26-in. holes on wiper trips. A Phasor Induction SFL tool logged the 8.5-in. hole. The wireline SP and CDR tool gamma ray are shown in Track 1 (8.5-in. hole). The Phasor induction resistivities are shown in Track 2 and the CDR tool resistivities are shown in Track 3 for the 8.5-in. hole. The CDR tool resistivities for the 17.5-in. hole and for the 26-in.hole are shown in Tracks 4 and 5.

The CDR tool resistivities and the wireline resistivities are in good agreement. Even in the 26-in. hole, R_{ad} reads

the true resistivity because its diameter of investigation is significantly larger than 26 in. However, R_{ps} is more sensitive to the borehole and the vertical sensitivity is reduced because of the large hole size.

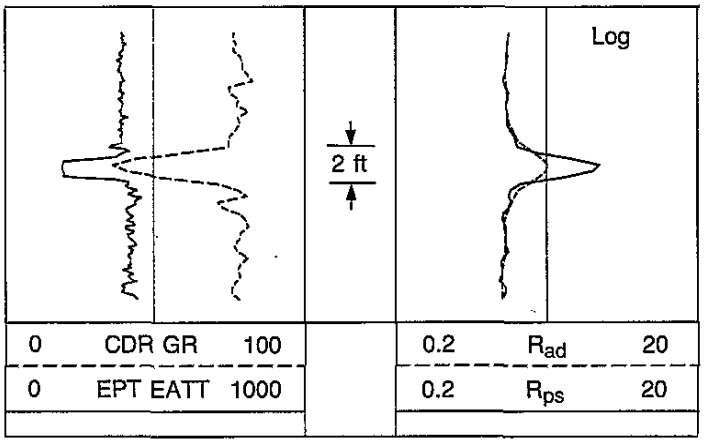

Fig. 7-45—Comparison of CDR tool and the wireline EPT tool response for a thin bed.

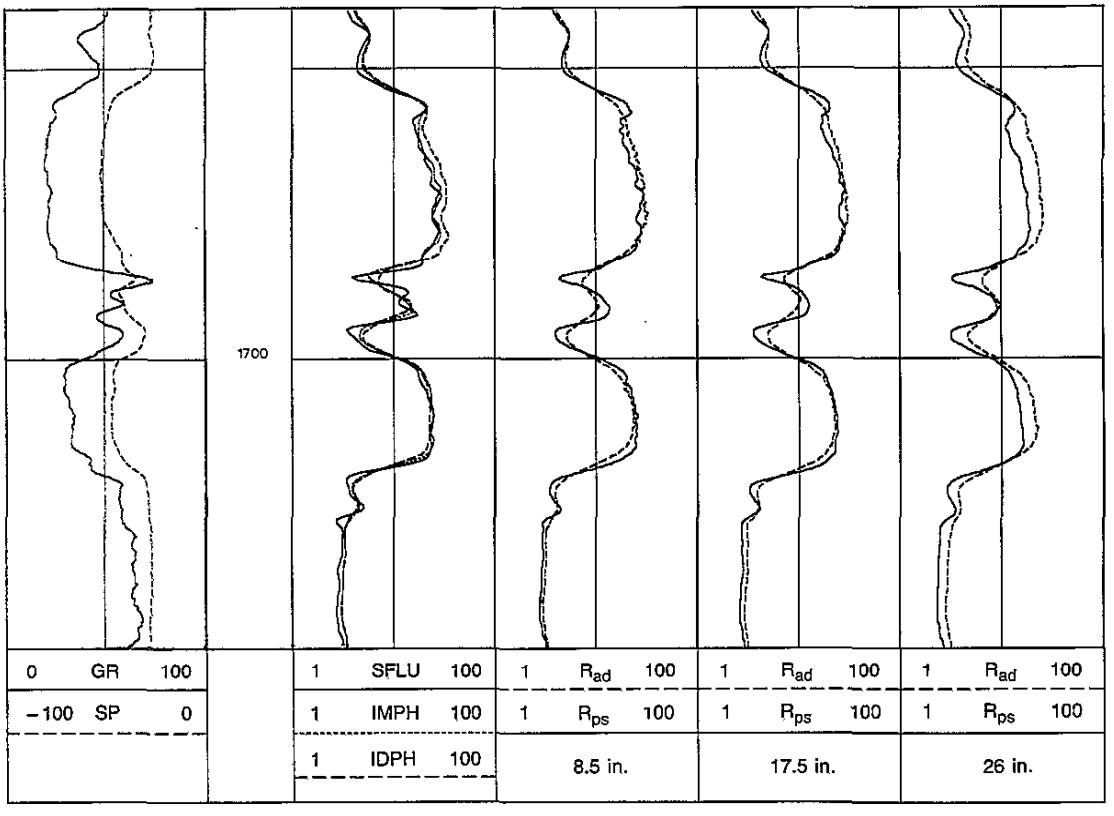

Fig. 7-46—Comparison of CDR tool and Phasor Induction SFL tool of a surface interval showing the effects of borehole size.

Fig. 7-47 shows a case of resistive invasion ($R_{mf} > R_w$) from a well drilled in southern Louisiana. A wireline SP is in Track 1, Phasor Induction tool resistivities are in Track 2, and R_{ad} and R_{ps} are in Track 3. The log shows a series of invaded saltwater sands. Since the mud filtrate is more resistive than the formation water, the IMPH resistivity is higher than the deeper IDPH resistivity. The CDR tool's resistivities reveal a similar profile while drilling. Through most of the upper sand, R_{ps} reads much higher than IDPH, and close to the SFLU. However, the deeper R_{ad} reads close to the IDPH resistivity in these invaded sands. The CDR tool logged these formations 5 to 20 minutes after they were penetrated, while the wireline logs were run about three days later.

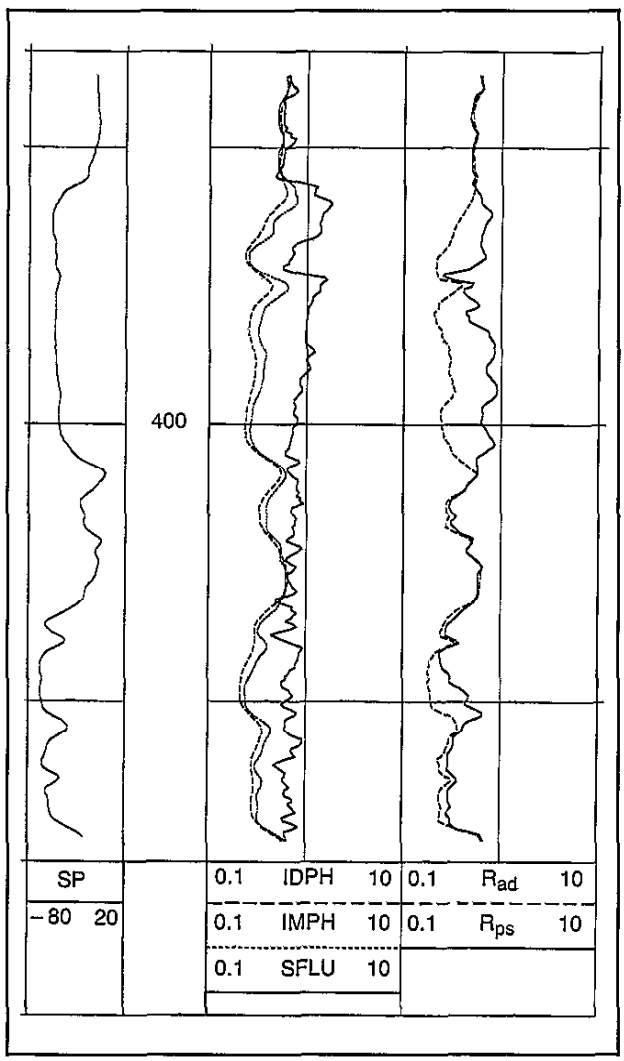

Fig. 7-47—CDR tool and Phasor Induction comparison illustrates invasion.

REFERENCES

1. Schlumberger, C., Schlumberger, M., and Leonardon, E.G.: "Some Observations Concerning Electrical Measurements in Anisotropic Media and Their Interpretation," *Trans.*, AIME (1934) **110**.
2. Schlumberger, C., Schlumberger, M., and Leonardon, E.G.: "Electrical Coring; A Method of Determining Bottom-Hole Data by Electrical Measurements," *Trans.*, AIME (1934) **110**.
3. Schlumberger, C., Schlumberger, M., and Leonardon, E.G.: "A New Contribution to Subsurface Studies by Means of Electrical Measurements in Drill Holes," *Trans.*, AIME (1934) **110**.
4. Lynch, E.J.: *Formation Evaluation*, Harper's Geoscience Series, Harper & Row (1962).
5. Martin, M. and Kunz, K.S.: "Why Those Low Lateral Readings?," *Oil and Gas J.* (Feb. 10, 1958).
6. Doll, H.G.: "The Laterolog," *J. Pet. Tech.* (Nov. 1951).
7. Suau, J., Grimaldi, P., Poupon, A., and Souhaite, P.: "The Dual Laterolog-R_{xo} Tool," paper SPE 4018 presented at the 1972 SPE Annual Meeting.
8. Doll, H.G.: "Introduction to Induction Logging," *J. Pet. Tech.* (June 1949).
9. Dumanoir, J.L., Tixier, M.P., and Martin, M.: "Interpretation of the Induction-Electrical Log in Fresh Mud," *J. Pet. Tech.* (July 1957).
10. Moran, J.H. and Kunz, K.S.: "Basic Theory of Induction Logging," *Geophys.* (Dec. 1962).
11. Tixier, M.P., Alger, R.P., Biggs, W.P., and Carpenter, B.N.: "Combined Logs Pinpoint Reservoir Resistivity," *Pet. Eng.* (Feb.-March 1965).
12. Barber, T.D.: "Introduction of the Digital Dual Induction Tool," paper SPE 12049 presented at the 1983 SPE Annual Technical Conference and Exhibition.
13. Doll, H.G.: "The Microlog," *Trans.*, AIME (1950) **189**.
14. Doll, H.G.: "Filtrate Invasion in Highly Permeable Sands," *Pet. Eng.* (Jan. 1955).
15. Doll, H.G.: "The Microlaterolog," *J. Pet. Tech.* (Jan. 1953).
16. Doll, H.G. and Martin, M.: "Suggestions for Better Electric Log Combinations and Improved Interpretations," *Geophys.* (Aug. 1960).
17. Boyeldieu, C., Coblentz, A., Pelissier-Combescure, J.: "Formation Evaluation in Oil Base Muds," *Trans.*, 1984 SPWLA Annual Logging Symposium.
18. Blakeman, E.R.: "A Method of Analyzing Electrical Logs Recorded on Logarithmic Scale," *J. Pet. Tech.* (Aug. 1952).
19. Barber, T.D.: "Real-Time Environmental Corrections for the DIT-E Digital Dual Induction Tool," *Trans.*, 1985 SPWLA Annual Logging Symposium.
20. Anderson, B.: "The Analysis of Some Unsolved Induction Interpretation Problems Using Computer Modeling," *Trans.*, 1986 SPWLA Annual Logging Symposium.
21. Barber, T.D.: "Invasion Profiling with the Phasor Induction Tool," *Trans.*, 1986 SPWLA Annual Logging Symposium.
22. Frank, Rollyn: *Prospecting With Old E-Logs*, Schlumberger Educational Services, Houston (1986).
23. *Log Interpretation Charts*, Schlumberger Educational Services, Houston (1989).

24. Barber, T. D.: "Phasor Processing of Induction Logs Including Shoulder and Skin Effect Correction," U.S. Patent No. 4,513,376 (1984).
25. Kienitz, C., Flaum, C., Olesen, J-R., and Barber, T.: "Accurate Logging in Large Boreholes," Trans., 1986 SPWLA Annual Logging Symposium.
26. Schaefer, R. T., Barber, T. D., and Dutcher, C. H.: "Phasor Processing of Induction Logs Including Shoulder and Skin Effect Correction," U. S. Patent 4,471,436 (1984).
27. Anderson, B., Safinya, K. A., and Habashy, T.: "Effects of Dipping Beds on the Response of Induction Tools," paper SPE 15488 presented at the 61st Annual SPWLA Technical Conference, October, 1986.
28. Anderson, B., and Barber, T.: "Strange Induction Logs—A Catalog of Environmental Effects," The Log Analyst, XXIX, No. 4, 229-243.
29. Anderson, B., and Barber, T.: "Using Computer Modeling to Provide Missing Information for Interpreting Resistivity Logs," 28th Annual SPWLA Logging Symposium, Texas, June, 1988.
30. Singer, J., and Barber, T.: "The Effect of Transition Zones on the Response of Induction Logs," 28th Annual SPWLA Logging Symposium, June, 1988.
31. Barber, T.: "Induction Log Vertical Resolution Enhancement Physics and Limitations," 28th Annual SPWLA Logging Symposium, June, 1988.
32. *Phasor* Induction Tool*, Schlumberger Educational Services, Houston (1989).
33. Clark, B. *et al.*: "A Dual Depth Resistivity Measurement for FEWD," paper A, 29th Annual SPWLA Logging Symposium, 1988.
34. Anderson, B. and Chew, W.C.: "A New High Speed Technique for Calculating Synthetic Induction and DPT* Logs," paper HH, 25th Annual SPWLA Logging Symposium, 1984.

8 Determination of Saturation

INTRODUCTION

Water saturation is the fraction (or percentage) of the pore volume of the reservoir rock that is filled with water. It is generally assumed, unless otherwise known, that the pore volume not filled with water is filled with hydrocarbons. Determining water and hydrocarbon saturation is one of the basic objectives of well logging.

CLEAN FORMATIONS

All water saturation determinations from resistivity logs in clean (nonshaly) formations with homogeneous intergranular porosity are based on Archie's water saturation equation, or variations thereof. The equation is

$$S_w^n = \frac{F R_w}{R_t} , \qquad \text{(Eq. 8-1)}$$

where

R_w is the formation water resistivity (see Chapter 4),

R_t is the true formation resistivity (see Chapter 7),

and

F is the formation resistivity factor.

F is usually obtained from the measured porosity of the formation through the relationship (Chart Por-1)

$$F = a/\phi^m. \qquad \text{(Eq. 8-2)}$$

For S_{xo}, the water saturation in the flushed zone, a similar expression exists:

$$S_{xo}^n = \frac{F R_{mf}}{R_{xo}} , \qquad \text{(Eq. 8-3)}$$

where

R_{mf} is the mud filtrate resistivity

and

R_{xo} is the flushed zone resistivity.

In these equations, the saturation exponent n is usually taken as 2. Laboratory experiments have shown that this is a good value for average cases. The values of a and m in Eq. 8-2 are subject to more variation: in carbonates, $F = 1/\phi^2$ is usually used; in sands, $F = 0.62/\phi^{2.15}$ (Humble formula), or $F = 0.81/\phi^2$ (a simpler form practically equivalent to the Humble formula). Eq. 8-1 (with $n = 2$) is solved, in nomograph form, in Chart Sw-1.

Chart Sw-1 may also be used to solve Eq. 8-3 for the flushed zone water saturation. To do this, the R_{xo} reading is inserted on the R_t leg of the nomograph and the R_{mf} value is inserted in the R_w leg. Chart Sw-1 is constructed using the Humble porosity-to-formation factor relationship. For any other porosity-to-formation factor relationship the nomograph should be entered with the formation factor.

The accuracy of the Archie equation (Eqs. 8-1 and -3) depends in large measure, of course, on the accuracy of the fundamental input parameters: R_w, F, and R_t. The deep resistivity measurement (induction or laterolog) must be corrected, therefore, for borehole, bed thickness, and invasion. The most appropriate porosity log (sonic, neutron, density, or other) or combination of porosity and lithology measurements must be used to obtain porosity, and the proper porosity-to-formation factor relationship must be used. Finally, the R_w value should be verified in as many ways as possible: calculation from the SP curve, water catalog, calculation from nearby water-bearing formation, and/or water sample measurement.

Resistivity - Vs. - Porosity Crossplots

Combining Eqs. 8-1 and -2, the Archie saturation equation may be written

$$S_w^n = \frac{a R_w}{\phi^m R_t} . \qquad \text{(Eq. 8-4a)}$$

If n and m are equal to 2, and $a = 1$, then

$$\phi\, S_w = \sqrt{R_w/R_t}\,. \qquad \text{(Eq. 8-4b)}$$

Eq. 8-4b shows that for R_w constant, $\phi\, S_w$ is proportional to $1/\sqrt{R_t}$; $\phi\, S_w$ is the quantity of water per unit volume of formation. To emphasize the proportionality between ϕ and $1/\sqrt{R_t}$, Eq. 8-4b may be rewritten:

$$\phi = \frac{\sqrt{R_w}}{S_w}\;\frac{1}{\sqrt{R_t}}\,. \qquad \text{(Eq. 8-4c)}$$

For a 100% water-saturated formation, $S_w = 1$ and $R_t = R_0$. If R_0 for water-saturated formations is plotted on an inverse square-root scale versus ϕ, all points should fall on a straight line given by $\phi = \sqrt{R_w}/\sqrt{R_0}$.

Furthermore, the points corresponding to any other constant value of S_w will also fall on a straight line, since in Eq. 8-4c the coefficient, $\sqrt{R_w/S_w}$, is constant for constant values of R_w and S_w.

Instead of an actual R_t value, it is usually satisfactory to plot the log reading of the deep resistivity device provided the readings are not much influenced by invasion or other environmental factors (e.g., from a deep induction log or deep laterolog).

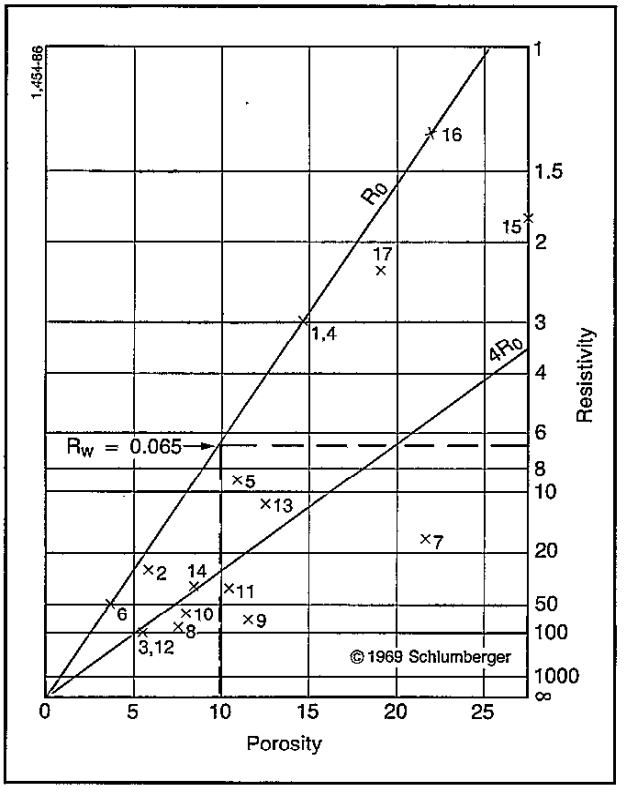

Fig. 8-1—Resistivity-porosity crossplot for determining R_w and S_w.

Fig. 8-1 shows several points plotted over an interval in which formation-water resistivity is constant (as indicated by constant SP deflections opposite the thick, clean permeable beds). Assuming that at least some of the points are from 100% water-bearing formations, the line for $S_w = 1$ is drawn from the pivot point ($\phi = 0$, $R_t = \infty$) through the most northwesterly plotted points. The slope of this line defines the value of R_w. As shown on Fig. 8-1, for $\phi = 10\%$, $R_0 = 6.5$ ohm-m. For this formation, the most appropriate $F-\phi$ relation is $F = 1/\phi^2$. Thus, for $\phi = 10\%$, $F = 100$. Since $R_w = R_0/F$, $R_w = 6.5/100 = 0.065$ ohm-m, as shown.

For other S_w values, R_t and R_0 are related by the equation $R_t = R_0/S_w^2$. For $S_w = 50\%$, $1/S_w^2 = 4$, and $R_t = 4\,R_0$. This relation establishes the line for $S_w = 50\%$.

On Fig. 8-1, for the same porosity as before ($\phi = 10\%$), $R_t = 4$, $R_0 = 4 \times 6.5 = 26$ ohm-m gives a point that defines the line for $S_w = 50\%$. Other S_w lines may be defined in a similar manner.

Charts Sw-15 and -16 provide blank grids for making resistivity-porosity crossplots. Chart Sw-16 is used when $F = 1/\phi^2$ is the more appropriate formation factor-porosity relationship and Chart Sw-15 is used when $F = 0.62/\phi^{2.15}$ is more appropriate.

If the matrix composition remains constant over the formations under investigation, the basic measurement from the sonic, density, or neutron logs can be plotted directly versus R_t with similar results. This is possible because of the linear relationship between porosity and bulk density, sonic transit time or neutron hydrogen index response. An example of a sonic-induction crossplot is shown in Fig. 8-2. The transit time has been plotted against the induction resistivity for several levels. The northwesterly points define the 100% water saturation line. The transit time value at the point where this line intersects the horizontal line of infinite resistivity is the matrix transit time, t_{ma}. In Fig. 8-2, t_{ma} is found to be approximately 47.5 μs/ft (156 μs/m), corresponding to a matrix velocity of 21,000 ft/sec (6,400 m/s).

By knowing t_{ma}, a porosity scale, from Chart Por-3, and a scale of formation factor (e.g., from $F = 1/\phi^2$ using Chart Por-1) can be easily derived. A vertical line drawn through $F = 100$ (or $\phi = 10$) intersects the water line at $R_0 = 5$ ohm-m; accordingly, R_w ($= R_0/F$) is 0.05 ohm-m.

The lines for other S_w values are straight lines, determined as previously described, radiating out from the $R_t = \infty$, $t_{ma} = 47.5$ pivot point.

Density and neutron logs can be crossplotted against resistivity in a manner identical to the sonic logs. For density logs, the intersection of the 100% water line with the infinite resistivity line yields the matrix density value, ϱ_{ma}. For neutron logs, the intersection defines the matrix hydrogen index, or apparent matrix porosity. Knowledge of matrix density or hydrogen index permits the ϱ_b or

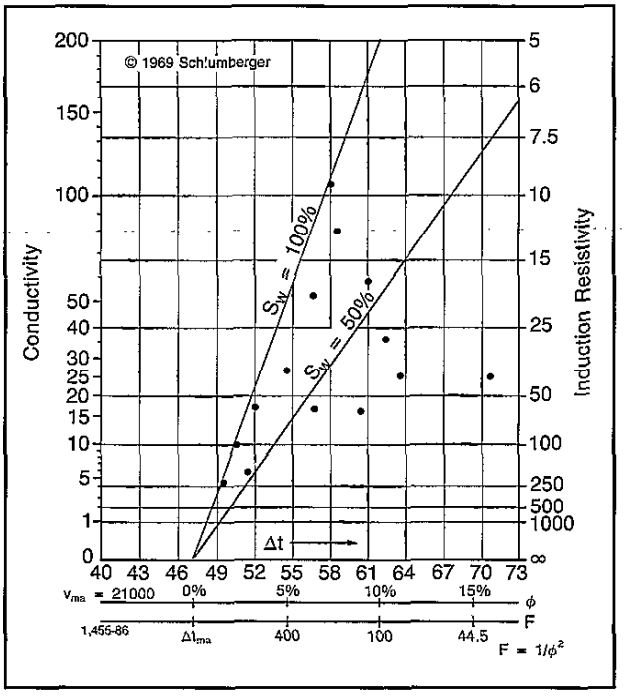

Fig. 8-2—Sonic-induction crossplot.

ϕ_N scale to the rescaled in ϕ and F units. With the F scale defined, R_w can be calculated as for the sonic-resistivity crossplot, and lines of constant water saturation can be constructed in a similar manner.

These resistivity-versus-porosity crossplots require that formation water resistivity be constant over the interval plotted, that lithology be constant, that invasion not be deep, and that the measured porosity log parameter (i.e., t, ϱ_b, ϕ_N) can be linearly related to porosity. This last condition implies that the time average transform for the conversion of t into porosity is appropriate.

The neutron-resistivity crossplot is not as satisfactory in gas-bearing formations as the sonic- or density-resistivity crossplots. The apparent porosity measured by the neutron log in gas zones is often much too low. This results in pessimistic S_w values in gas zones. Indeed, in a gas zone, the neutron-resistivity may indicate a porous gas-bearing zone to be near zero porosity and 100% water bearing. In contrast, the sonic- or density-resistivity tends to be slightly optimistic in gas zones (i.e., porosities may be slightly high and water saturations slightly low).

Microresistivity-Vs.-Porosity Crossplots

A resistivity-porosity plot can also be made using the values from a shallow-investigation resistivity log, such as the microlaterolog or MicroSFL log. If the microresistivity log reads substantially R_{xo}, then a line through points of mud filtrate-saturated formations (S_{xo} = 1) should have a slope related to R_{mf}. R_{mf} is an important parameter, and this check of its value by means of a sonic-microresistivity or density-microresistivity crossplot is often useful.

These plots are also valuable for improved determinations of matrix parameters (either t_{ma} or ϱ_{ma}), particularly in cases where the sonic-resistivity or density-resistivity plot does not give a clear answer because of hydrocarbon saturation. The $F R_{mf}$ line should be easier to determine since S_{xo} is usually fairly high even in hydrocarbon-bearing formations.

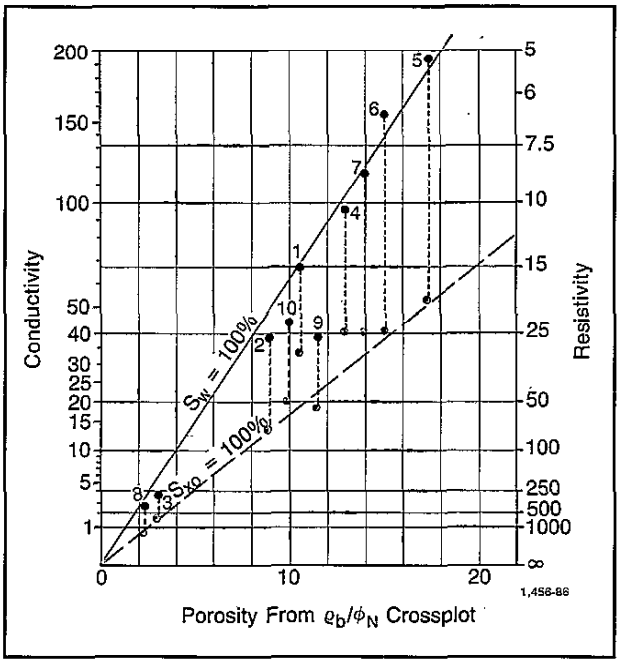

Fig. 8-3—Resistivity-porosity crossplot showing points from deep induction and microlaterolog. S_w = 1 and S_{xo} = 1 lines are shown. (After Baird, 1968)

Fig. 8-3 shows a resistivity-porosity plot in which both the deep induction reading and the microlaterolog at the same levels are plotted in a series of water-bearing formations. The porosity values were derived in this case from a neutron-density crossplot. The plots from the two logs define two trends corresponding respectively to S_w = 1 (using deep induction) and S_{xo} = 1 (using microlaterolog data). The points not in these trends can be divided into two groups.

1. Points whose microlaterolog readings fall on the S_{xo} = 1 line but whose deep induction log readings fall below the S_w = 1 line (Points 2, 9, 10) are probably the result of either deep invasion or adjacent-bed effect in which R_{ID} is greater than R_t.
2. Points whose induction log readings fall on the S_w = 1 line but whose microlaterolog points fall above the S_{xo} = 1 line are possibly due to shallow invasion in

which R_{MLL} is lower than R_{xo}.

Resistivity-porosity plots are thus often more informative if the short-spaced resistivity values are also plotted. Not only does this permit an appreciation of invasion effects but it may also indicate moved oil.

R_{wa} Comparison

If water saturation is assumed to be 100%, the Archie water saturation equation (Eq. 8-1) reduces to

$$R_{wa} = \frac{R_t}{F} \approx \frac{R_{ID}}{F} . \qquad \text{(Eq. 8-5)}$$

The term R_{wa} is used in Eq. 8-5, rather than R_w, to indicate that this is an apparent formation water resistivity. It is only equal to R_w in 100% water-bearing formations. In hydrocarbon-bearing formations, R_{wa} computed from Eq. 8-5 will be greater than R_w. Indeed, by combining Eqs. 8-1 and -5, the relationship between S_w, R_{wa}, and R_w can be shown to be

$$S_w = \sqrt{R_w/R_{wa}} . \qquad \text{(Eq. 8-6)}$$

The R_{wa} technique can, therefore, be useful for identifying potential hydrocarbon-bearing zones and for obtaining R_w values.

In practice, R_{wa} is obtained by simply dividing the deep induction resistivity (or deep laterolog resistivity) by the formation factor obtained from a porosity log or a combination of porosity logs. To be most effective, either a continuous R_{wa} computation is made over a long interval of the borehole or many individual manual computations are made so as to approximate a continuous computation.

For manual computation of R_{wa}, the logs are divided into sections of consistent lithology, shaliness, and R_w. The SP curve is most useful for this, but the GR, resistivity, and other curves should be consulted. The log readings, deep resistivity and porosity (t, ϱ_b, or ϕ_N), are read and tabulated, and the corresponding values of R_{wa} are calculated. Various charts are helpful in these calculations. For example, if porosity is obtained from the FDC* formation density or Litho-Density* log, Chart Por-5 can be used for porosity calculation, Chart Por-1 can be used to convert porosity to formation factor, and Chart Sw-1 (in reverse starting at $S_w = 100\%$) can be used to make the R_{wa} computation.

Since the R_{wa} technique, as normally applied, requires that deep resistivity (R_{deep}) $\cong R_t$, invasion must be shallow enough that the deep resistivity reads essentially the same as the true resistivity. In addition, R_w should be constant or vary in a consistent and recognizable manner over the interpreted intervals, lithology should be essentially constant and known, and permeable zones should be reasonably clean (i.e., shale free). If these conditions are fulfilled, the calculated R_{wa} values will approximate R_w values in clean water-bearing sands. Usually, an R_{wa} value at least three times that of R_w is needed to indicate possible hydrocarbon potential; that corresponds to a water saturation of less than 60%.

A useful feature of the R_{wa} method is that foreknowledge of R_w is not needed; indeed, if some reasonably clean water zones are included in the computations, their R_{wa}'s are R_w.

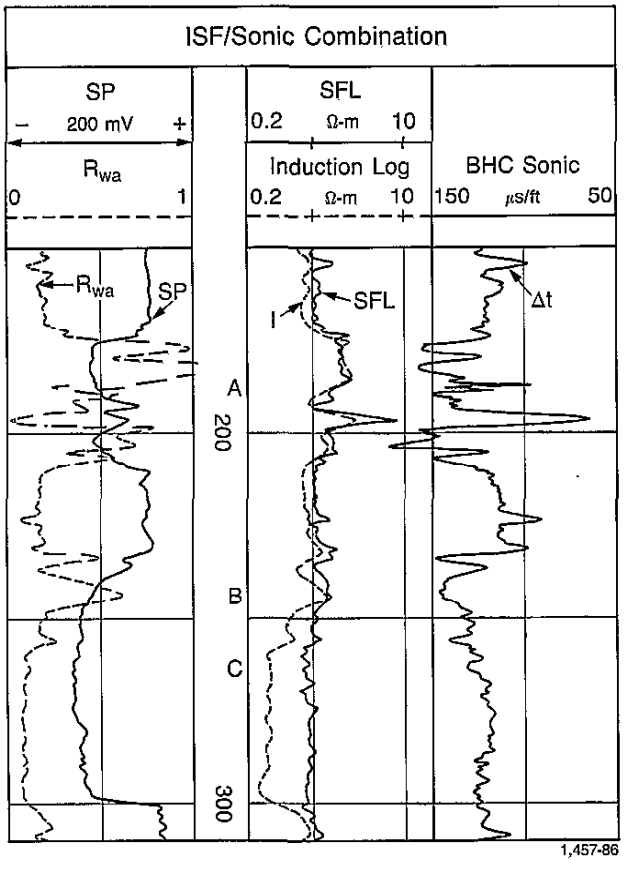

Fig. 8-4—R_{wa} curve recorded on ISF/sonic log.

A continuous log of R_{wa} can be recorded at the wellsite using resistivity and porosity logs. Fig. 8-4 is an example computed from the BHC sonic log and induction-SFL log combination. The R_{wa} computation indicates the lower sand to be predominately water bearing with a good show of hydrocarbons at its top. R_w is indicated to be about 0.08 ohm-m by the consistent R_{wa} computations over Interval C. R_{wa} reaches 0.6 ohm-m at Level B in the top of this zone. That corresponds to a water saturation of 37% ($S_w = \sqrt{R_w/R_{wa}} = \sqrt{0.08/0.6}$). The entire upper sand, Interval A, is indicated as hydrocarbon bearing by the R_{wa} computations, assuming it contains for-

* Mark of Schlumberger

mation water similar to that of the lower zone. Similar SP deflections in the two zones suggest this is the case.

A continuous R_{wa} log provides ready visual identification of water- and hydrocarbon-bearing formations, changes in R_w, in lithology, etc.

LOGARITHMIC OVERLAYS

Logarithmic scaling of resistivity and porosity logs is useful for wellsite interpretations because of the properties of logarithms.

1. The logarithm of the **product** of two numbers is equal to the algebraic sum of the logarithms of the two numbers.
2. The logarithm of the **quotient** of two numbers is equal to the algebraic difference of the logarithms of the two numbers.
3. The logarithm of a number **raised to the power, n,** is equal to the product of n times the logarithm of the number.

On logarithmic scaling, the logarithm of a curve reading is proportional to the distance from the unity index line to the curve. Thus, near the bottom of Fig. 8-5, the length of Line A is proportional to the logarithm of the deep resistivity measurement. Similarly, Line B is proportional to logarithm of F at the same level. The algebraic separation between the two curves, Length A − Length B (= Length C) is proportional to the algorithm of the ratio, R_{deep}/F. Since Length A is less than Length B, the logarithm of the ratio, in this case, is negative. This means the value of the ratio is less than one. Then, measuring the Length C to the left of the index line and reading from the logarithmic scale, the value of the ratio is about 0.4.

For field use it is more convenient to evaluate the quotient (corresponding to the separation, Length C) by using a transparent plastic logarithmic overlay scale applied directly to the separation between the curves.

Log F- Log R_{deep} Overlay

Instead of computing a continuous R_{wa} curve or a series of R_{wa} values, as explained earlier, the formation factor, F, can be recorded directly (or traced) on logarithmic scale on the resistivity log. Then, log F could be compared to log R_{deep}. Writing Eq. 8-5 in terms of logarithms,

$$\log R_{wa} = \log R_{deep} - \log F. \quad \text{(Eq. 8-7)}$$

Thus, log R_{wa}, on a logarithmic scale, is simply the algebraic separation between the two curves, R_{deep} and F.

To read the value of R_{wa}, a transparent overlay scale of Exponent 1 is used. (Exponent 1 means that the logarithmic scale is identical to the one on the field log.) At any given level on the log the unity index line of the overlay is placed on the F curve. Then, R_{wa} is read directly from the position of the R_{deep} curve relative to the scale. As shown in the scales in Fig. 8-5, R_{wa} is about 2.2 ohm-m for the upper level and about 0.027 ohm-m for the lower level.

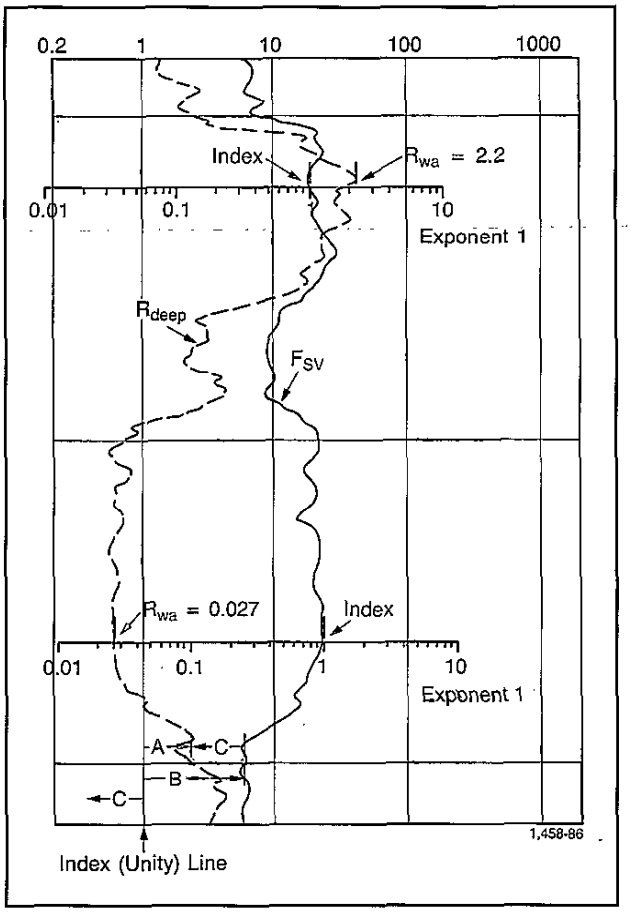

Fig. 8-5—The log R_{deep}-log F overlay.

The value of F could be derived from any porosity log. The sonic log is most popular because it is more compatible with the resistivity log in shaly sands and it readily recognizes gas-bearing zones. The neutron log handles shaly sands also but may overlook gas zones; the density log recognizes gas zones but does not handle shaly sands very well. It is necessary, of course, to record the F log on a logarithmic scaling that matches that of the resistivity log.

R_0 Overlay and F Overlay

It would be just as easy to produce an R_0 curve, for comparison with the R_{deep} curve, by adding the logarithm of R_w to the logarithm of F. This is done by shifting the F curve a distance corresponding to the logarithm of R_w in respect to the resistivity grid. Thus, since $R_0 = FR_w$,

$$\log R_0 = \log F + \log R_w . \quad \text{(Eq. 8-8a)}$$

In case R_w is not known, this could be done by shifting the F curve until it overlays the R_{deep} curve in suspected water-bearing zones.

Apparent water saturation would be determined from the separation between log R_0 and log R_{deep}. Since $S_w^2 = R_0/R_t \approx R_0/R_{deep}$,

$$2 \log S_w \approx \log R_0 - \log R_{deep} . \quad \text{(Eq. 8-8b)}$$

Thus, the separation between the R_0 and R_{deep} curves on a logarithmic scale will be approximately twice the logarithm of S_w. S_w can be obtained by using a logarithmic overlay in which one decade of S_w is equal in length to two decades of R_{deep} or F. The scaling is designated on Fig. 8-6 by the expression "Exponent 0.5."

To use the transparent overlay scale, the unity index line is placed on the R_{deep} curve; S_w is read from the resulting position of the R_0 curve on the scale. At the upper level of Fig. 8-6, S_w is indicated as about 11%.

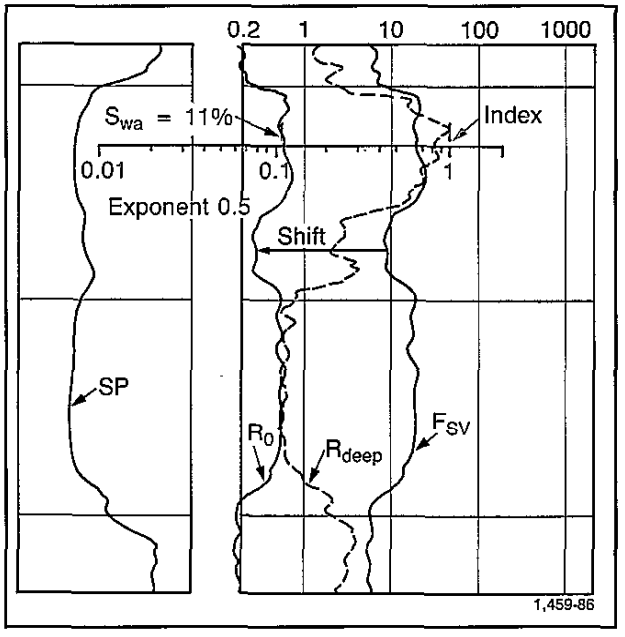

Fig. 8-6—The R_0 overlay.

The F overlay is a variation of the R_0 overlay. S_w is determined by the separation on the logarithmic scale between F_R (as derived from the deep resistivity) and F. F_R is defined as:

$$F_R = \frac{R_{deep}}{R_w} \approx \frac{R_t}{R_w} . \quad \text{(Eq. 8-9a)}$$

The meaning of F_R in terms of S_w is seen by replacing R_t/R_w with F_R in the Archie water saturation equation to give

$$F_R \approx \frac{F}{S_w^2} . \quad \text{(Eq. 8-9b)}$$

In terms of logarithms, Eq. 8-9a becomes

$$\log F_R = \log R_{deep} - \log R_w , \quad \text{(Eq. 8-9c)}$$

and Eq. 8-9b becomes

$$2 \log S_w = \log F - \log F_R . \quad \text{(Eq. 8-9d)}$$

Thus, the log F_R curve is found by shifting the logarithmic R_{deep} curve by a distance equal to log R_w (see Fig. 8-7). If R_w is not known, this shift could also be determined by making the shift such that the F_R and F curves overlay in water-bearing zones.

The S_w scaler used on the transparent overlay to read S_w is the same one used in Fig. 8-6. On Fig. 8-7, S_w at the upper level is again indicated to be about 11%.

In the R_0 overlay technique, the F curve is shifted relative to the R_{deep} curve an amount equal to log R_w. S_w (or more exactly, log S_w) is the resulting separation between the two curves. In the F overlay technique, the R_{deep} curve is shifted relative to the F curve an amount equal to log R_w.

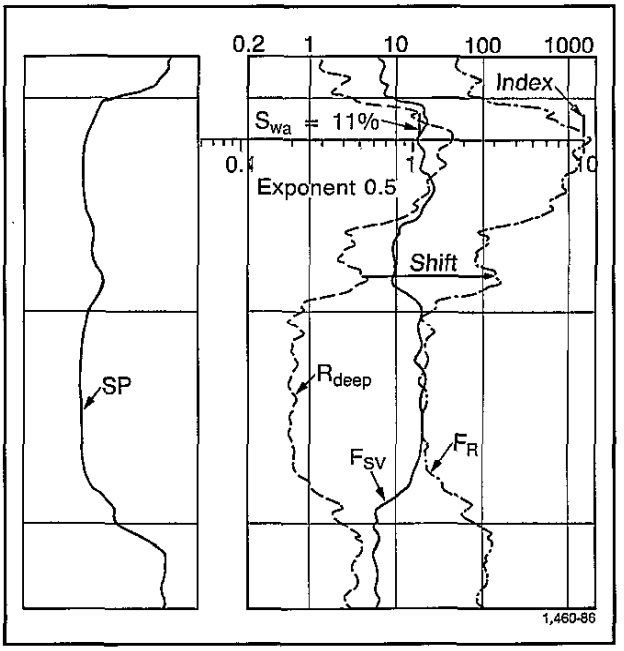

Fig.8-7—The F overlay (log F-log F_R).

RESISTIVITY RATIO METHODS

In resistivity ratio methods, it is assumed that a formation is divided into two distinct regions, a flushed or invaded zone and a noninvaded zone. Both zones have the same F, but each contains water of a distinct resistivity (R_{mf} or R_z in the invaded zone and R_w in the noninvad-

ed zone). The resistivities of the two zones must be measurable or derivable from logs, and methods for determining the resistivity of the water in each zone must be available.

Because of the necessary assumptions, the resistivity ratio methods have limitations, but when no porosity or formation factor data are available, they are sometimes the only choice. The principal limitation arises from the inability of any resistivity device to measure either R_{xo} or R_t totally independent of the other. Simply put, invasion must be deep enough to allow a shallow-investigating resistivity device to measure R_{xo} but not so deep that a deep resistivity device cannot measure R_t.

Another difficulty appears when hydrocarbons are present. In this case, some knowledge or assumption of the value of the flushed or invaded zone saturation is necessary.

Flushed Zone Method

If $n = 2$ is assumed and Eq. 8-1 is divided by Eq. 8-3,

$$\left(\frac{S_w}{S_{xo}}\right)^2 = \frac{R_{xo}/R_t}{R_{mf}/R_w} \cdot \qquad \text{(Eq. 8-10)}$$

This equation gives the ratio of S_w to S_{xo}, and no knowledge of formation factor or porosity is needed. R_{xo} may be found from a MicroSFL log, R_t from an induction or laterolog, and R_{mf}/R_w from measured values or from the SP curve.

The ratio S_w/S_{xo} is valuable in itself as an index of oil movability. If $S_w/S_{xo} = 1$, then no hydrocarbons have been moved by invasion, whether or not the formation contains hydrocarbons. If S_w/S_{xo} is about 0.7 or less, movable hydrocarbons are indicated. The value of S_w/S_{xo}, along with ϕ and S_w, is useful in evaluating reservoirs.

To determine S_w from Eq. 8-10, S_{xo} must be known. For moderate invasion and average residual oil saturation, an empirical relation between S_{xo} and S_w has been found useful: $S_{xo} = S_w^{1/5}$. Inserting this into Eq. 8-10 gives:

$$S_w = \left(\frac{R_{xo}/R_t}{R_{mf}/R_w}\right)^{5/8} \cdot \qquad \text{(Eq. 8-11)}$$

Chart Sw-2 provides a solution of Eq. 8-11 using the values of R_{xo}/R_t and R_{mf}/R_w. Preferably, the chart is entered with R_{mf}/R_w; optionally, the SP can be used. Provision is also made in the upper right portion of the chart for using values of S_{or} (residual oil saturation) other than those given by the fifth-root relation.

The relationship $S_{xo} = S_w^{1/5}$ is strictly empirical and may differ appreciably from the actual case.

Invaded Zone Method

The invaded zone method is useful for water saturation determination when only an ES, IES, or other early resistivity log is available and no porosity log or formation factor data exist. For application of the method, R_i/R_m must be at least 10.

Archie's equation for the invaded zone is

$$S_i^2 = \frac{FR_z}{R_t} \cdot \qquad \text{(Eq. 8-12a)}$$

where R_z is the resistivity of the water in the invaded zone. Because of incomplete flushing, R_z is a mixture of mud filtrate, R_{mf}, and formation water, R_w.

Studies of many logs suggest that S_i and S_w are related by

$$S_i = S_w^{1/2} \cdot \qquad \text{(Eq. 8-12b)}$$

Dividing the noninvaded zone water saturation equation (Eq. 8-1) by Eq. 8-12a and using the relationship presented in Eq. 8-12b yields an expression for S_w:

$$S_w = \frac{R_i/R_t}{R_z/R_w} \cdot \qquad \text{(Eq. 8-13)}$$

To use Eq. 8-13, R_t is taken from a deep resistivity device such as a deep induction or deep laterolog (corrected as necessary for borehole effect and bed thickness). R_i is taken from a shallow resistivity device such as a Laterolog 8, 16-in. normal, or SFL (corrected for borehole effect and bed thickness).

R_z is given by the relationship

$$\frac{1}{R_z} = \frac{z}{R_w} + \frac{1-z}{R_{mf}} \cdot \qquad \text{(Eq. 8-14)}$$

where z is the fraction of the invaded zone pore water, which is formation water, and $1 - z$ is the fraction that is mud filtrate. Experience has indicated that z varies from 0.075 in cases of normal invasion to 0.035 in cases of deep invasion or vuggy formations.

Fig. 8-8 solves Eq. 8-13. It is entered with R_{mf}/R_w on the appropriate z scale and R_i/R_t (oblique lines) to determine S_w. When R_i/R_t is close to unity, some caution is required. The formation may be extremely invaded or there may be little invasion, or it may be dense and impermeable. On the other hand, many good hydrocarbon-bearing reservoirs will have $R_i/R_t \approx 1.0$.

Porosity Balance

To verify that invasion falls within the limits required by the resistivity ratio methods, the porosity balance can be used. It requires an independent value of porosity; this can be obtained from cores, logs, reservoir analysis, etc. This "porosity check" can verify the applicability of the

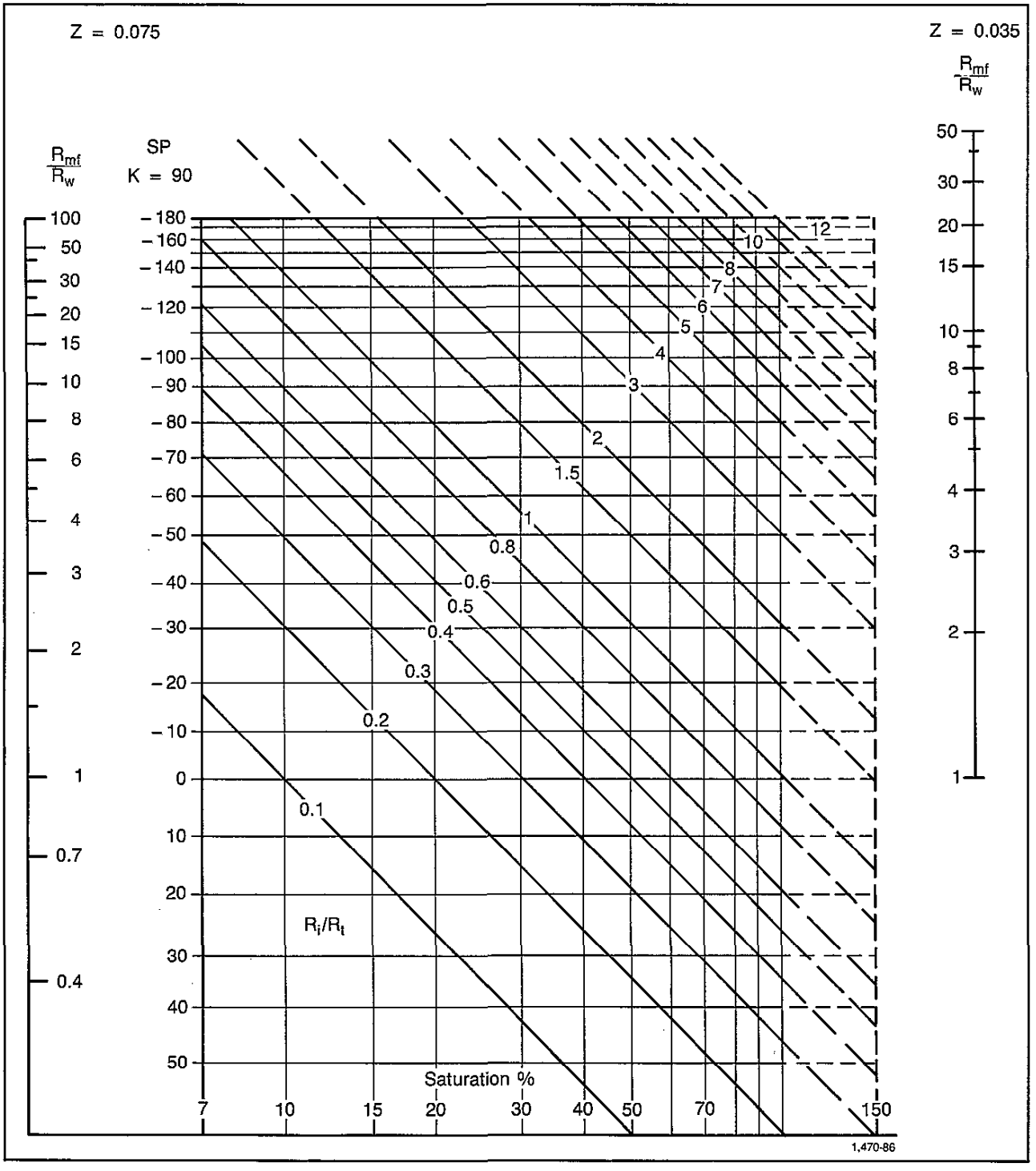

Fig. 8-8—Empirical resistivity-ratio method. (Ref. 4)

ratio method and the validity of the S_w value derived. If the porosity check indicates the ratio method results are in error, the porosity balance will indicate how the error can be corrected.

For comparison with the independent value of porosity, ϕ_t, a porosity value, ϕ_c, is derived from S_{wc}. (S_{wc} is

the value of S_w from the ratio method chart. The subscript t stands for the "true" value and the subscript c for the "calculated" value.) This is done by computing a formation factor, F_c, from the relation

$$F_c = S_{wc}^2 \frac{R_t}{R_w} \qquad \text{(Eq. 8-15)}$$

and then deriving ϕ_c from F_c using the appropriate $F = \phi$ relationship from Chart Por-1. Then:

1. If $\phi_c = \phi_t$, the ratio method solution is correct and $S_{wc} = S_w$.
2. If $\phi_c > \phi_t$, then F_c is too low and S_{wc} is too low. The ratio R_{xo}/R_t or R_i/R_t is too low, probably because invasion is either deeper or shallower than one of the resistivity measurements can handle. The shallow resistivity (R_{xo} or R_i) is too low because of shallow invasion or the deep resistivity (R_t) is too high because of deep invasion.
   a. If $R_{shallow}/R_{deep} < 1.4$ and the induction was used for R_t, use $R_{ID} = R_t$ in Eq. 8-1 to find S_w.
   b. If $R_{shallow}/R_{deep} > 1.4$ and $FR_z > R_{shallow}$, invasion is shallow. Use $R_{deep} = R_t$ in Eq. 8-1 to find S_w.
   c. If $R_{shallow}/R_{deep} > 1.4$ but $FR_z < R_{shallow}$, invasion is deep. Eq. 8-12a is solved for S_w (with $S_w = S_i^2$).
3. If $\phi_c > \phi_t$, then S_{wc} is too high. This occurs when R_{xo}/R_t or R_i/R_t is too high, as might happen in the case of an annulus. Eq. 8-12a is used for S_w determination (with $S_w = S_i^2$).

Other Ratio Charts

Other types of ratio charts allow the direct use of log data (corrected for borehole effect and thickness) in lieu of either or both R_{xo} and R_t. Charts Sw-7a and -7b, which apply to various combinations of shallow resistivity devices (16-in. normal, Laterolog 8, SFL) with the deep induction (ID or 6FF40), are examples.

Reference to the invasion correction charts (Charts Rint-2a, -b, -c) show, to a rough approximation, that R_{xo}/R_t can be related to $R_{shallow}/R_{deep}$ when invasion is within certain limits — neither too deep nor too shallow.

Chart Sw-7a merges the invasion correction chart (Chart Rint-2a) with the flushed-zone saturation chart (Chart Sw-2) or Eq. 8-10. The chart can be entered directly with the ratio of R_{LL8}/R_{ID} and R_{mf}/R_w. Although convenient to use, the water saturation, S_w, obtained is only an approximation. That is because water saturations, although shown as lines on the charts, are actually areas similar to the 100% water saturation area. The actual saturation values shown on the chart apply only when invasion diameter is about 50 in. For deeper or shallower invasion, the water saturation value of a given location on the chart would be slightly higher.

Invasion-Corrected Ratio Methods

The uncertainty in invasion diameter can be eliminated by correcting the log data before using it in a resistivity ratio interpretation method. This requires at least three resistivity measurements of different depths of investigation.

The three resistivity measurements (corrected for borehole effect and bed thickness) are entered in the appropriate invasion correction chart and R_{xo}/R_t obtained. For example, for the DIL-Laterolog 8 data, Chart Rint-2a or -2b would be used (dependent on the R_{xo}/R_m ratio). R_{xo}/R_t is obtained, and ideally R_t, from the R_t/R_{ID} value. R_{xo}/R_t can then be entered into Chart Sw-2 or Eq. 8-10 to determine S_w.

The invasion correction charts generally assume a step profile of invasion. If a transition profile (one in which mud filtrate and formation water are intermixed) or an annulus profile exists, the R_{xo}/R_t and R_t/R_{ID} values given by the charts may be in error. The "porosity balance" may be used to detect and correct the error. An independent source of porosity, such as a porosity log, is required.

Rather than compare porosity computed from the ratio method saturation with true porosity measured by the porosity log, the ratio method water saturation, S_{wR}, (i.e., S_w from Eq. 8-11) is compared to the Archie water saturation, S_{wA}, (i.e, S_w from Eq. 8-1). If S_{wA} and S_{wR} are equal, the assumption of a step-contact invasion profile is verified, and all values found (S_w, R_{xo}/R_t, R_t/R_{ID}, R_t, d_i) are considered good.

If $S_{wA} > S_{wR}$, either invasion is very shallow or a transition type of invasion profile is indicated. In these cases, S_{wA} is considered the better value for S_w. If $S_{wA} < S_{wR}$, an annulus type of invasion profile is indicated. In this case, a more accurate value can be estimated using the relation:

$$S_w = S_{wA} \left(\frac{S_{wA}}{S_{wR}}\right)^{1/4}. \qquad \text{(Eq. 8-16)}$$

Chart Rint-1 helps solve this relationship.

R_{xo}/R_t Overlay

Logarithmic scaling of resistivity logs makes it possible to read saturations by overlaying one resistivity log over another. This is done by applying a resistivity-ratio method directly on the logs and using a simple procedure involving the separation between the curves.

The equation for the water saturation ratio method was given in Eq. 8-11. The simplest case is for $R_{mf} \cong R_w$;

then, Eq. 8-11 reduces to $S_w \cong (R_{xo}/R_t)^{5/8}$. To obtain S_{wa} a transparent overlay is used that corresponds to "Exponent ⅝." This means that the length of a decade on the log scale is ⅝ times as long as a decade on the overlay scale. The unity index line of the overlay scale is placed on the deep resistivity curve, and S_w is read on the overlay scale from the shallow resistivity curve. Fig. 8-9 illustrates the method. S_w is indicated to be 24%.

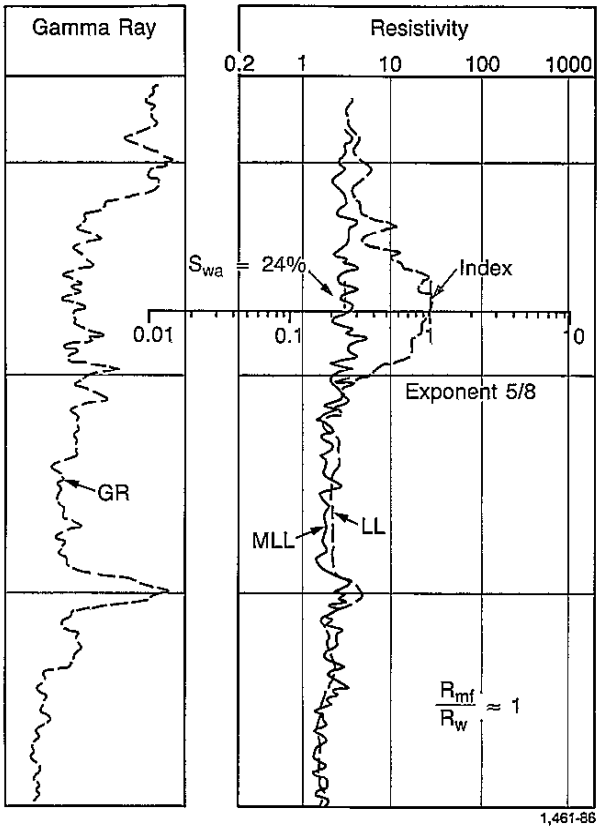

Fig. 8-9—S_{wa} from logarithmic resistivity overlay, case of $R_{mf} \approx R_w$.

When $R_{mf} \neq R_w$ (usually $R_{mf} > R_w$), the procedure for finding S_w involves an additional step. The value of R_{mf}/R_w must be known, or the R_{deep} curve can be shifted to make it coincide with the $R_{shallow}$ curve in known water zones. In the lower zone of Fig. 8-10, expected to be water bearing, this shift is indicated as "a"; it suggests an R_{mf}/R_w value of 3. The entire R_{deep} curve is shifted by this amount to the right (or the $R_{shallow}$ curve could be shifted to the left by the same amount). The unity index line of the Exponent ⅝ overlay scale is placed on the shifted R_{deep} value, and the value of S_w is read from the position of the shallow resistivity curve on the overlay scale. S_w is indicated to be 14%.

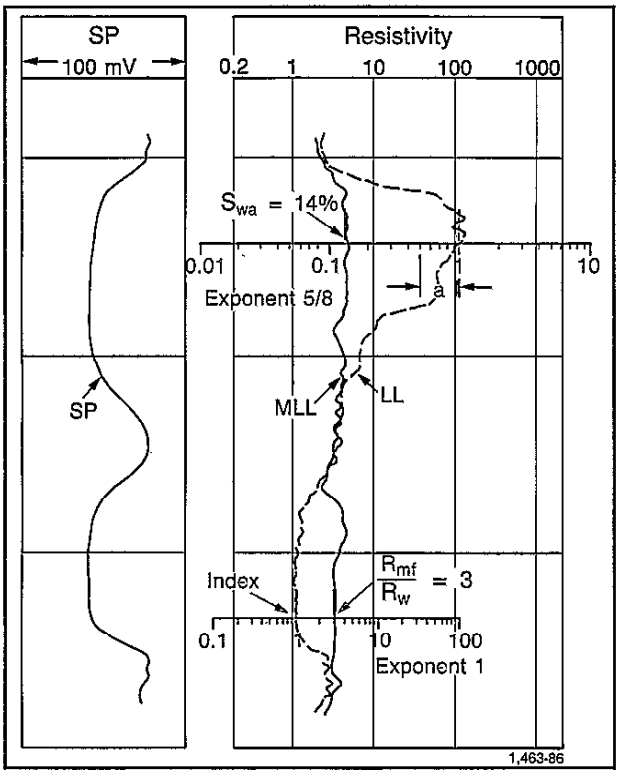

Fig. 8-10—Logarithmic resistivity overlay, case where $R_{mf}/R_w \neq 1$.

R_{xo}/R_t Quicklook

The R_{xo}/R_t quicklook can be used to identify hydrocarbon-bearing formations and to indicate hydrocarbon movability (producibility). When S_w/S_{xo} is 1 in a permeable zone, the zone will produce water or be nonproductive regardless of water saturation. An S_w/S_{xo} significantly less than 1 indicates the zone is permeable and contains some hydrocarbons, and that the hydrocarbons have been flushed (moved) by invasion. Thus, the zone contains producible hydrocarbon.

Eq. 8-10 can be written as

$$\frac{S_w}{S_{xo}} = \left(\frac{R_{xo}/R_t}{(R_{mf}/R_w)_{SP}}\right)^{1/2}, \qquad \text{(Eq. 8-17)}$$

which shows that an indication of S_w/S_{xo} can be obtained by comparing R_{xo}/R_t with R_{mf}/R_w, where the subscript SP emphasizes that R_{mf}/R_w is derivable from the SP. Equivalently, the comparison can be between log R_{xo}/R_t and the SP curve for an indication of log S_w/S_{xo}.

The log R_{xo}/R_t is computed from a comparison of the deep and shallow resistivity measurements or from all three resistivity measurements and is used as an overlay comparison curve with the SP. Separations between the

log R_{xo}/R_t curve, properly scaled to match the SP, and the SP curve provide a quicklook location of producible hydrocarbons.

Originally, log R_{xo}/R_t was computed from R_{LL8}/R_{ID} or R_{SFL}/R_{ID}. Use was made of the observation that over a wide range of invasion diameters (from about 20 to 100 in.) R_{xo}/R_t depends primarily on the value of R_{LLS}/R_{ID} or R_{SFL}/R_{ID} (see Fig. 8-11). The relationship employed for the LL8 device was

$$R_{xo}/R_t = 1.85\,(R_{LL8}/R_{ID}) - 0.85\,. \quad \text{(Eq. 8-18a)}$$

For the SFL device, it was

$$R_{xo}/R_t = 1.45\,(R_{SFL}/R_{ID}) - 0.45\,. \quad \text{(Eq. 8-18b)}$$

Much more sophisticated algorithms are now used to obtain R_{xo}/R_t. All three resistivity measurements of the DIL-SFL tool are employed. As a result, the computed R_{xo}/R_t values more closely duplicate the values given by the invasion correction charts (Chart Rint-11) and by Fig. 8-11 over a greater range of invasion diameters.

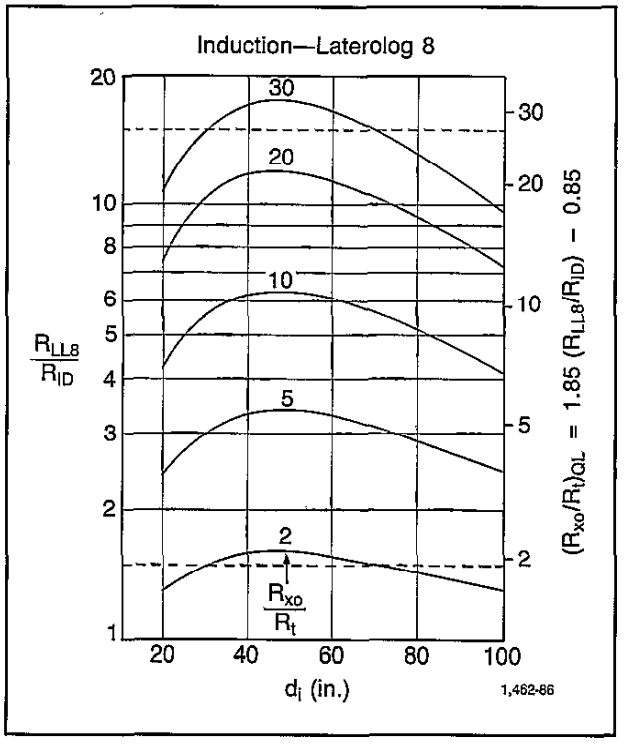

Fig. 8-11—Plot illustrating strong interdependence of R_{LL8}/R_{ID} and R_{xo}/R_t in the range of d_i values from 20 to 100 in. (Ref. 5)

To interpret the R_{xo}/R_t quicklook curve, the impermeable zones must be eliminated by reference to the SP, GR, or microlog curves or by resistivity ratios. Then, if the SP and R_{xo}/R_t (actually $-K$ log R_{xo}/R_t) curves coincide in a permeable zone, the zone will most probably produce water. If, however, the R_{xo}/R_t curve reads appreciably lower (i.e., to the right) than the SP, the zone should produce hydrocarbons. An R_{xo}/R_t value less than the SP amplitude indicates movable hydrocarbons are present.

The R_{xo}/R_t quicklook technique is applicable to fresh mud conditions ($R_{xo} > R_t$) in formations where invasion falls within the limits demanded by the R_{xo}/R_t computation. For the simpler computation technique using Eq. 8-18, that is about 30 to 70 in.; for the more sophisticated techniques, that is between 20 and 120 in. Even in the more restrictive case, however, any errors are optimistic. In other words, water zones may appear to be hydrocarbon productive. This constitutes a safeguard against overlooking pay zones, and is considered a desirable feature in any quicklook approach.

The R_{xo}/R_t technique efficiently handles variations in formation water resistivity, R_w, and in shaliness. Any change in R_w is reflected similarly into both the computed R_{xo}/R_t and the SP amplitude. Thus, comparing the two curves still permits formation fluid identification. Shaliness also affects the two curves in a similar manner. All other things remaining constant, shaliness reduces the R_{xo}/R_t value and the SP amplitude. Finally, the R_{xo}/R_t quicklook technique does not require porosity data nor use of any F - ϕ relationships.

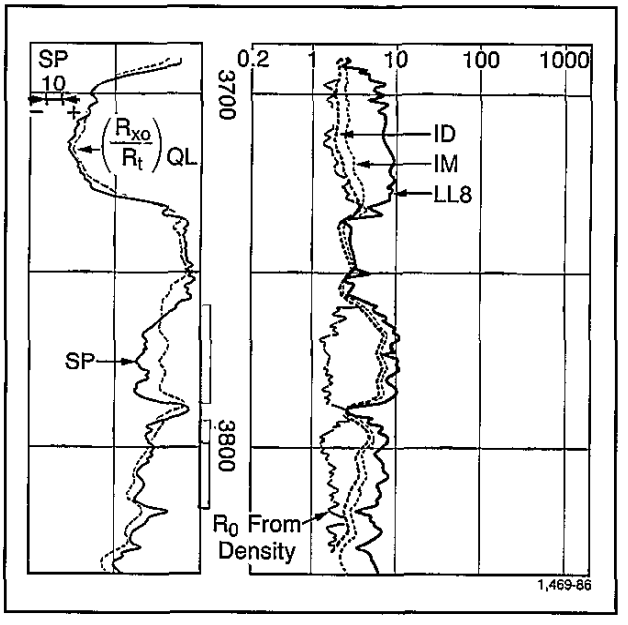

Fig. 8-12—Example of $(R_{xo}/R_t)_{QL}$ curve used for comparison with SP to identify zones with movable hydrocarbons.

Fig. 8-12 is an example of a shaly gas sand at 3760 through 3788 ft and several water-productive sands with

varying amounts of shaliness. The productive gas sand is identified by the separation between the R_{xo}/R_t and SP curves. Water-productive zones are shown by lack of separation. In shaly water zones the variation in the SP curve is essentially the same as the variation in the R_{xo}/R_t ratio — a result of the same shale; so, the comparison is not significantly disturbed by shaliness. Neither is it disturbed by variations in R_w.

Estimates of water saturation and saturation ratio in clean formations can be made by comparing the R_{xo}/R_t and SP curves. Eq. 8-17 permits S_w/S_{xo} to be estimated and Eq. 8-11 (assuming $S_{xo} = S_w^{1/5}$) permits S_w to be estimated.

F-MOP MOVABLE OIL PLOT

The *F*-MOP plot uses two resistivity curves and a porosity curve recorded on logarithmic scale to show hydrocarbon saturation and movability. The recorded curves are F_{deep}, F_{xo}, and F (from a porosity log), where

$$F_{deep} = \frac{R_{deep}}{R_w} \approx FS_w^2 , \quad \text{(Eq. 8-19a)}$$

$$F_{xo} = \frac{R_{xo}}{R_{mf}} \approx FS_{xo}^2 , \quad \text{(Eq. 8-19b)}$$

and

$$F = \frac{a}{\phi^m} .$$

On a logarithmic scale, the apparent formation factor curves, F_{deep} and F_{xo}, are located by shifting the corresponding resistivity curve by log R_w or log R_{mf}, whichever is appropriate. The F curve is a log ϕ curve recorded at the proper sensitivity and polarity.

For an estimate of hydrocarbon movability the S_{xo} value is compared with the S_w value. Values of S_w are found, as shown in Fig. 8-13, with a logarithmic overlay of "Exponent 0.5" applied to the separation between the F and F_{deep} curves. Values of S_{xo} are found in the same manner by applying the scale between the F_{xo} and F curves. In each case, the unity index line of the overlay scale is placed on the F_{xo} or F_{deep} curve.

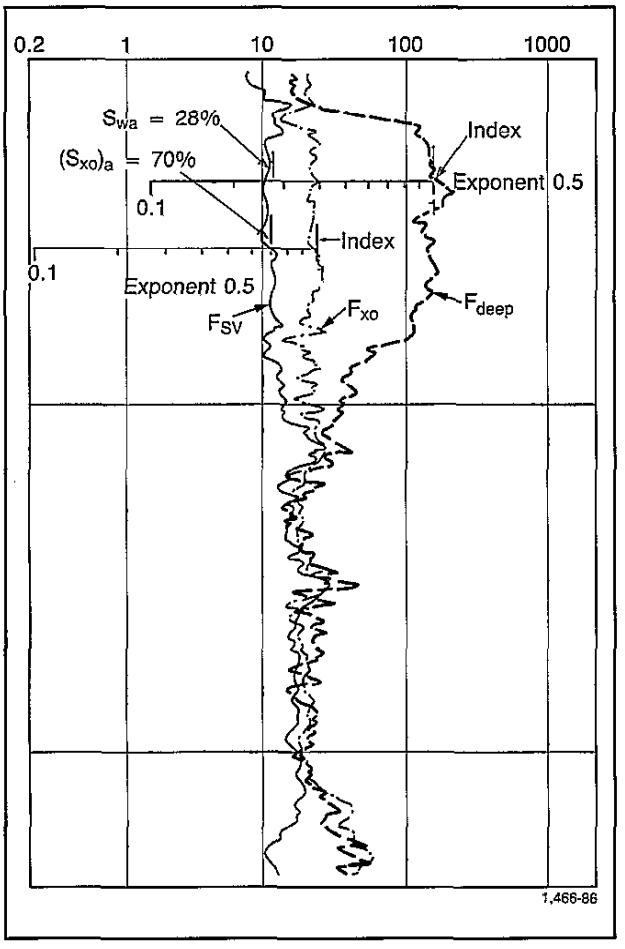

Fig. 8-13—The *F* MOP.

POROSITY AND GAS SATURATION IN EMPTY HOLES

In empty or gas-drilled holes the formations are uninvaded; a combination of density and neutron or deep resistivity logs, or all three, can be used to determine porosity and gas saturation.

Chart Sw-11 presents three methods that use these logs. In this chart the gas density, ϱ_g, and hydrogen index of the gas, H_g, in situ are assumed to be zero.

Density-Neutron Method - The density-neutron method is used where gas saturation is the primary information desired. Porosity can also be obtained. This method should be used when little or no shale is present. Shaliness will result in too high a porosity and too low a gas saturation.

Since $\varrho_g = 0$, the fluid density ϱ_f will be

$$\varrho_f = S_L \varrho_L + S_g \varrho_g = S_L \varrho_L , \quad \text{(Eq. 8-20)}$$

where

S_L is the liquid saturation (water and oil)

and

ϱ_L is the density of the liquid.

The value of ϱ_L is taken as unity, since the densities of formation waters generally exceed 1 and densities of oils are slightly less than 1. The error from these variations is found to be negligible, so

$$\varrho_f \approx S_L . \quad \text{(Eq. 8-21)}$$

Also, taking $H_g = 0$ and $H_L = 1$,

$$\phi_N = \phi S_L H_L + \phi S_g H_g = \phi S_L ,$$

or

$$S_L = 1 - S_g = \phi_N/\phi . \qquad \text{(Eq. 8-22)}$$

Combining Eqs. 8-21 and -22:

$$\varrho_f \simeq \phi_N/\phi . \qquad \text{(Eq. 8-23)}$$

Inserting this into the porosity-density equation (Eq. 5-6) and solving for ϕ gives:

$$\phi = \frac{\varrho_{ma} - \varrho_b + \phi_N}{\varrho_{ma}} . \qquad \text{(Eq. 8-24)}$$

Eq. 8-24 is the basis of the porosity determination, and Eq. 8-22 is used for saturation determinations.

Density-Resistivity Method - This method is also used when gas saturation is of primary interest. The pore liquid must be formation water. Therefore, the method can be used only if no oil is present. From Eq. 8-4b,

$$S_w = (1/\phi)\sqrt{R_w/R_t} . \qquad \text{(Eq. 8-25)}$$

For the case where no oil is present, Eq. 8-21 becomes

$$\varrho_f = S_w = (1/\phi)\sqrt{R_w/R_t} . \qquad \text{(Eq. 8-26)}$$

Inserting this expression for ϱ_f into the density-porosity formula and solving for ϕ,

$$\phi = \frac{\varrho_{ma} - \varrho_b + \sqrt{R_w/R_t}}{\varrho_{ma}} . \qquad \text{(Eq. 8-27)}$$

With ϕ determined from Eq. 8-27, S_w is found from Eq. 8-25.

Density-Neutron-Resistivity Method - This method provides a fractional analysis of all fluid present. Porosity and gas saturation are derived by using Eqs. 8-24 and -22. Porosity and resistivity are then used to compute water saturation. Oil saturation is found as $S_o = 1 - (S_g + S_w)$.

SHALY FORMATIONS

Shales are one of the more important common constituents of rocks in log analysis. Aside from their effects on porosity and permeability, this importance stems from their electrical properties, which have a great influence on the determination of fluid saturations.

Shales are loose, plastic, fine-grained mixtures of clay-sized particles or colloidal particles and often contain a high proportion of clay minerals. Most clay minerals are structured in sheets of alumina-octahedron and silica-tetrahedron lattices. There is usually an excess of negative electrical charges within the clay sheets. The substitution of Al^{+++} by ions of lower valence is the most common cause of this excess; the structure of the crystal remains the same. This local electrical imbalance must be compensated to maintain the electrical neutrality of the clay particle. The compensating agents are positive ions — cations or counterions — which cling to the surface of the clay sheets in a hypothetical dry state. The positive surface charge is usually measured in terms of milli-ions equivalents per 100 grams of dry clay minerals and is called the cation exchange capacity (CEC). When the clay particles are immersed in water, the Coulomb forces holding the positive surface ions are reduced by the dielectric properties of water. The counterions leave the clay surface and move relatively freely in a layer of water close to the surface (the electrical balance must be maintained so that the counterions remain close to the clay water interface) and contribute to the conductivity of the rock.

Since the Archie water saturation equation, which relates rock resistivity to water saturation, assumes that the formation water is the only electrically conductive material in the formation, the presence of another conductive material (i.e., shale) requires either that the Archie equation be modified to accommodate the existence of another conductive material or that a new model be developed to relate rock resistivity to water saturation in shaly formations. The presence of clay also complicates the definition or concept of rock porosity. The layer of closely bound surface water on the clay particle can represent a very significant amount of porosity. However, this porosity is not available as a potential reservoir for hydrocarbons. Thus, a shale or shaly formation may exhibit a high total porosity yet a low effective porosity as a potential hydrocarbon reservoir.

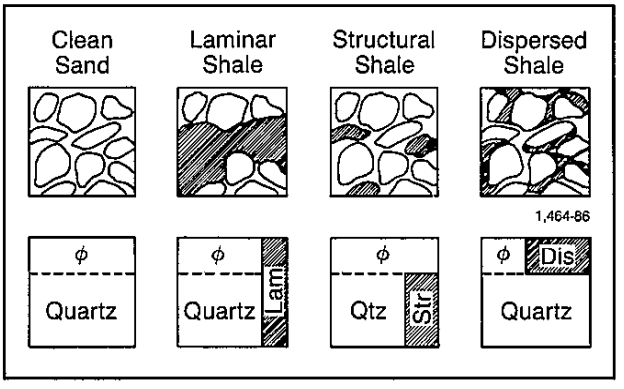

Fig. 8-14—Forms of shale classified by manner of distribution in formation. Pictorial representations above, volumetric representations below.

The way shaliness affects a log reading depends on the amount of shale and its physical properties. It may also depend on the way the shale is distributed in the formation. Shaly material can be distributed in the formation in three ways.

1. Shale can exist in the form of laminae between which are layers of sand. The laminar shale does not affect the porosity or permeability of the sand streaks themselves. However, when the amount of laminar shale is increased and the amount of porous medium is correspondingly decreased, overall average effective porosity is reduced in proportion.
2. Shale can exist as grains or nodules in the formation matrix. This matrix shale is termed structural shale; it is usually considered to have properties similar to those of laminar shale and nearby massive shales.
3. The shaly material can be dispersed throughout the sand, partially filling the intergranular interstices. The dispersed shale may be in accumulations adhering to or coating the sand grains, or it may partially fill the smaller pore channels. Dispersed shale in the pores markedly reduces the permeability of the formation.

All these forms of shale can, of course, occur simultaneously in the same formation.

Over the years, a large number of models relating resistivity and fluid saturations have been proposed. Many have been developed assuming the shale exists in a specific geometric form (i.e., laminar, structural, dispersed) in the shaly sand. All these models are composed of a clean sand term, described by the Archie water saturation equation, plus a shale term. The shale term may be fairly simple or quite complex; the shale term may be relatively independent of, or it may interact with, the clean sand term. All the models reduce to the Archie water saturation equation when the fraction of shale is zero; for relatively small amounts of shaliness, most models and methods yield quite similar results.

Only a very few of these models will be reviewed here in order to provide some flavor and understanding for the evolution of shaly sand interpretation logic.

Laminated Sand-Shale Simplified Model

In this laminar shale model, R_t, the resistivity in the direction of the bedding planes, is related to R_{sh} (the resistivity of the shale laminae) and to R_{sd} (the resistivity of the clean sand laminae) by a parallel resistivity relationship,

$$\frac{1}{R_t} = \frac{1 - V_{lam}}{R_{sd}} + \frac{V_{lam}}{R_{sh}}, \quad \text{(Eq. 8-28)}$$

where V_{lam} is the bulk-volume fraction of the shale, distributed in laminae, each of more-or-less uniform thickness.

For clean-sand laminae, $R_{sd} = F_{sd} R_w / S_w^2$, where F_{sd} is the formation resistivity factor of the clean sand. Since $F_{sd} \cong a/\phi_{sd}^2$, (where ϕ_{sd} is the sand-streak porosity) and $\phi = (1 - V_{lam})\,\phi_{sd}$ (where ϕ is the bulk-formation porosity), then

$$\frac{1}{R_t} = \frac{\phi^2 S_w^2}{(1 - V_{lam})\, aR_w} + \frac{V_{lam}}{R_{sh}} \cdot \quad \text{(Eq. 8-29)}$$

To evaluate S_w by the laminated model, R_t, R_w, ϕ, V_{lam}, and R_{sh} must be determined.

For the determination of R_t, the problem is the same as for clean formations. If R_w is not known, its determination usually involves looking at a nearby clean sand and solving for R_w using the SP measurement or, if the formation is water bearing, using the resistivity and porosity measurements.

For the determination of ϕ and V_{lam}, a combination of porosity logs can be used. For example, as illustrated in Fig. 8-15, a crossplot of ϕ_N and ϱ_b from a density log is effective. The triangle of the figure is defined by the matrix point, water point, and shale point. In this example, the matrix point is at $\phi_N = 0$ (the neutron log was scaled in apparent sandstone porosity) and $\varrho_{ma} = 2.65$ g/cm^3 (quartz matrix). The shale point is at $\phi_N = 50$ pu and $\varrho_{sh} = 2.45$ g/cm^3. These values were taken in a nearby thick shale bed; it is assumed that shale laminae in the shaly sand under investigation are similar to the nearby massive shale beds. The water point is, of course, located at $\phi_N = 100$ pu and $\varrho_b = 1$ g/cm^3. The matrix-water line and shale-water line are linearly divided into porosity; the matrix-shale line and water-shale line are linearly divided into shale percentages.

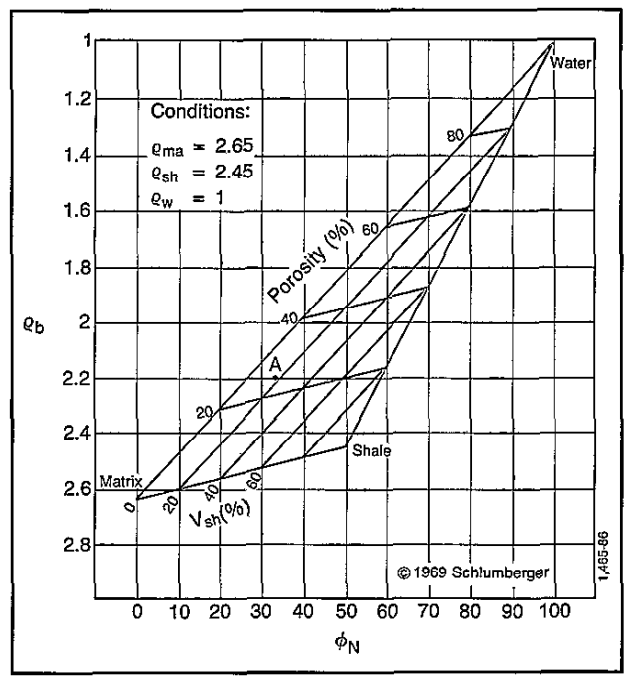

Fig. 8-15—Neutron-density crossplot showing matrix, water, and shale points, scaled for determination of V_{sh} and porosity.

Point A, plotted as an example, corresponds to log readings of $\varrho_b = 2.2$ g/cm^3 and $\phi_N = 33$ pu. Interpretation by the lines on the plot yields $\phi = 23\%$ and V_{sh} (or V_{lam}) = 16%.

Direct use of this crossplot assumes 100% water saturation in the zone investigated by the tools. Since oil has a density and hydrogen content normally not greatly different from water, this crossplot technique can be used with acceptable accuracy in oil-bearing formations. The presence of gas or light hydrocarbon, however, decreases ϕ_N and decreases ϱ_b. This would cause the point to shift in a northwesterly direction. When gas or light hydrocarbon are present, an additional shaliness indicator, such as GR or SP data, is needed in order to evaluate the amount of the shift.

Using the laminated model, an equation for R_{xo} analogous to Eq. 8-29 could be written. S_{xo} would replace S_w and R_{mf} would replace R_w. The other terms (ϕ, V_{lam}, R_{sh}) remain the same in the two equations. Assuming $S_{xo} = S_w^{1/5}$ (as in the flushed-zone ratio method) and the ratio of the PSP (SP deflection in the shaly sand) to the SSP (SP deflection in a nearby clean sand of similar formation water) is a measure of shaliness, V_{lam}, water saturation could be calculated from R_{xo}/R_t and PSP in the shaly sand and SSP (or R_{mf}/R_w) in a nearby clean sand. Chart Sw-2 performs the calculation.

Dispersed Shale Simplified Model

In this model, the formation conducts electrical current through a network composed of the pore water and dispersed clay. As suggested by L. de Witte, it seems acceptable to consider that the water and the dispersed shale conduct an electrical current like a mixture of electrolytes. Development of this assumption yields

$$\frac{1}{R_t} = \frac{\phi_{im}^2 \, S_{im}}{a}\left(\frac{q}{R_{shd}} + \frac{S_{im} - q}{R_w}\right), \quad \text{(Eq. 8-30)}$$

where

ϕ_{im} is intermatrix porosity, which includes all the space occupied by fluids and dispersed shale,

S_{im} is the fraction of the intermatrix porosity occupied by the formation-water, dispersed-shale mixture,

q is the fraction of the intermatrix porosity occupied by the dispersed shale,

and

R_{shd} is the resistivity of the dispersed shale.

Also, it can be shown that $S_w = (S_{im} - q)/(1 - q)$ where S_w is the water saturation in the fraction of true effective formation porosity.

Combining these relations and solving for S_w yields

$$S_w = \frac{\sqrt{\dfrac{aR_w}{\phi_{im}^2 \, R_t} + \left[\dfrac{q\,(R_{shd} - R_w)}{2\,R_{shd}}\right]^2} - \dfrac{q\,(R_{shd} + R_w)}{2\,R_{shd}}}{1 - q}. \quad \text{(Eq. 8-31)}$$

Usually, ϕ_{im} can be obtained directly from a sonic log since dispersed clay in the rock pores is seen as water by the sonic measurement. The value of q can be obtained from a comparison of a sonic and density log. Indeed, if $\rho_{shd} \cong \rho_{ma}$, then $q_{SV} \cong (\phi_{SV} - \phi_D)/\phi_{SV}$, where ϕ_{SV} and ϕ_D are the sonic and density derived porosities, respectively. In this case, ϕ_D approximates ϕ, the effective porosity available for fluid saturation.

The value of R_{shd} is more difficult to evaluate. It is usually taken as equal to R_{sh} in nearby shale beds. Fortunately, its value is not too critical if it is at least several times greater than R_w. In fact, when R_w is small compared to R_{shd} and the sand is not too shaly, Eq. 8-31 can be simplified to a form independent of R_{shd}:

$$S_w = \frac{\sqrt{\dfrac{a\,R_w}{\phi_{im}^2 R_t} + \dfrac{q^2}{4}} - \dfrac{q}{2}}{1 - q}. \quad \text{(Eq. 8-32)}$$

Total Shale Relationship

Based upon the above ideas, laboratory investigations and field experience, it has been found that a simple relationship of the following form works well for many shaly formations independent of the distribution of the shale and over the range of S_w values encountered in practice:

$$\frac{1}{R_t} = \frac{\phi^2 \, S_w^2}{a\,R_w\,(1 - V_{sh})} + \frac{V_{sh}\,S_w}{R_{sh}}. \quad \text{(Eq. 8-33)}$$

In using this equation, R_{sh} is taken equal to the resistivity of the adjacent shale beds and V_{sh} is the shale fraction as determined from a total shale indicator.

In recent years, it is equations of the form of Eq. 8-31 and -33 that have gained the widest acceptance in the evaluation of shaly sands. These equations have a general form

$$\frac{1}{R_t} = \alpha \, S_w^2 + \gamma \, S_w,$$

where α denotes a predominant sand term that is dependent on the amount of sand, its porosity, and the resistivity of the saturating water. The sand term always reduces to Archie's water saturation equation when the shale fraction is zero. γ denotes a predominant shale term that depends on the amount and resistivity of the shale.

Although the general form of shaly sand interpretation models may be quite similar, the methods of determining the amount of shale and its resistivity may differ greatly.

SARABAND* AND CORIBAND* MODELS

The response of the density log in a potential hydrocarbon-bearing shaly sand sequence is

$$\varrho_b = \phi\,[S_{xo}\,\varrho_{mf} + (1 - S_{xo})\,\varrho_h] \qquad \text{(Eq. 8-34)}$$
$$+ (1 - \phi)\,[V_{sh}\,\varrho_{sh} + (1 - V_{sh})\,\varrho_{ma}],$$

where ϱ_h is the density of the hydrocarbons and ϱ_{sh} is the shale/clay density. Assuming ϱ_{mf}, the density of the mud filtrate, is known and ϱ_{sh}, the density of the shale/clay, can be obtained from an adjacent shale bed, there are five unknowns in Eq. 8-34; they are ϕ, S_{xo}, ϱ_h, V_{sh}, and ϱ_{ma}.

Similar equations, with the same or relatable unknowns, can be written for the neutron log (similar to Eq. 8-34) and a microresistivity device (similar to Eq. 8-33) since these devices measure, more or less, the same volume of reservoir rock. The addition of a GR or SP curve, or some other measurement that is sensitive to clay volume would provide four measurements (equations) in five unknowns.

If the reservoir lithology is constant over a long interval and known, the number of unknowns is reduced to four. That is the case in sand-shale sequences; the reservoir lithology is sandstone (quartz). Thus, the combination of density, neutron, microresistivity, and, say, GR logs can be used to solve for formation porosity, flushed zone water and hydrocarbon saturations, hydrocarbon type, and volume of shale or clay. Furthermore, the addition of a deep resistivity measurement and R_w information (from the SP, for example) permits the determination of water and hydrocarbon saturation in the noninvaded, virgin formation. The Saraband program was designed to perform these computations.

Suppose, however, that lithology is not a sand-shale sequence but is more complex, as encountered in carbonate and/or evaporite sequences. To reduce the problem (Eq. 8-34) from the original five unknowns to four requires that one of the unknowns be estimated. Of the unknowns, hydrocarbon type is the obvious choice. It is often known; it is not critical to the various tool responses except when in gas or very light oil; it is generally the same over long intervals of the reservoir. Now, the combination of density, neutron, microresistivity, and GR logs can be used to solve for formation porosity, flushed zone water and hydrocarbon saturation, volume of shale, and matrix lithology. Addition of a deep resistivity measurement and R_w information gives water and hydrocarbon saturations in the noninvaded, virgin formation. The Coriband program was designed to perform these computations.

Because Saraband and Coriband are computer programs, advantage can be taken of the many features and capabilities of the computer to improve and expand the basic computations.

1. Extensive use is made of statistical methods. Frequency crossplots (both two- and three-dimensional) are used to evaluate various input parameters and data. Many parameters are automatically evaluated statistically by the programs.
2. In the case of a caved or rugose borehole, which affects the reliability of some logs, acceptable results can be achieved by checking against logs less affected by the borehole conditions and correcting for the rugosity.
3. The quality of the interpretation is checked by reconstructing certain log values from the interpretation results, by comparing these to the recorded log values, and by computing a figure of merit.
4. Additional log measurements, not part of the basic interpretation program, can be incorporated into the interpretation either to improve or expand the results. For example, sonic measurements are used in Saraband processing to correct other data for borehole rugosity; in Coriband, to provide a secondary porosity index.
5. All possible clay indicators (GR, SP, R_t, neutron, etc.) are evaluated to obtain clay volume and the most probable clay volume is selected.
6. The interpretations can be expanded, using statistical techniques, beyond a solution of the basic four unknowns to provide insight into other petrophysical parameters. These expansions do not detract from the validity of the basic interpretation.

The Saraband and Coriband techniques make extensive use of the neutron-density crossplot.

Saraband Model

The Saraband program uses a silt-shale-sand model in which the shales can be laminated, dispersed, or structural. The basic model is suggested by the groupings of the plotted points on the neutron-density crossplot of Fig. 8-16. This figure represents a typical crossplot through a sequence of sands, shales, and shaly sands. Most of the data belong to two groups: Group A, identified as sands and shaly sands, and Group B, identified as shales.

To explain the spread of points in Group B along the line from Point Q through Point Sh_0 to Point Cl, the shales are considered mixtures of clay minerals, water, and silt in varying proportions. Silt is fine grained and is assumed to consist predominantly of quartz, but it may

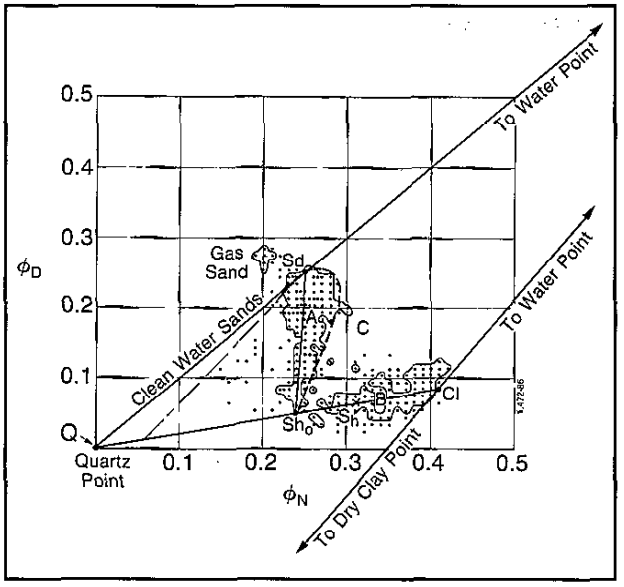

Fig. 8-16—Neutron-density frequency crossplot illustrating the shaly sand model used in Saraband processing.

also contain feldspars, calcite, and other minerals. Silt has, on the average, nearly the same neutron and density log properties as the matrix quartz; pure quartz silt would plot at the quartz point, Q. Silt, like quartz, is electrically nonconductive. Points near the "wet clay" point, Point Cl, correspond to shales that are relatively silt free. Point Sh_0 corresponds to shale containing a maximum amount of silt.

The shaly sands in Group A grade from shales, on Line Sh_0-Cl, to sands at Point Sd, on Line Q-Sd. The shale in these shaly sands may be distributed in various ways. When all the shale is laminar shale, the point will fall on the Sd-Sh_0 line. Dispersed shale causes the point to plot to the left of the line. Structural shale causes the point to plot to the right of the line.

Typically, few points plot in Area C. When they do, they usually represent levels where log readings have been affected by borehole rugosity, or where shale properties have been affected by hydration of the clay in contact with the mud, or where matrix lithology no longer corresponds to a shale-sand sequence (e.g., porous carbonates, lignite, etc.).

Once Points Sd, Sh_0, and Cl have been determined from inspection of the crossplot, the plot can be scaled for water-bearing sands and shales in terms of ϕ and V_{cl}, as shown in Fig. 8-17. The lines of constant ϕ are parallel to the shale line, Q-Sh_0-Cl. They range from $\phi = 0$ on the shale line to $\phi = \phi_{max}$ on the line through Point Sd. The lines of constant V_{cl} are parallel to the clean sand line, Q-Sd-Water Point; they range from $V_{cl} = 0$ on the clean sand line to $V_{cl} = 100\%$ at Point Cl. A similar scaling of V_{sh} is possible if the location of the laminar shale point, Point Sh_0, is fixed; the scaling ranges from $V_{sh} = 0$ on the clean-sand line to $V_{sh} = 100\%$ at Point Sh_0.

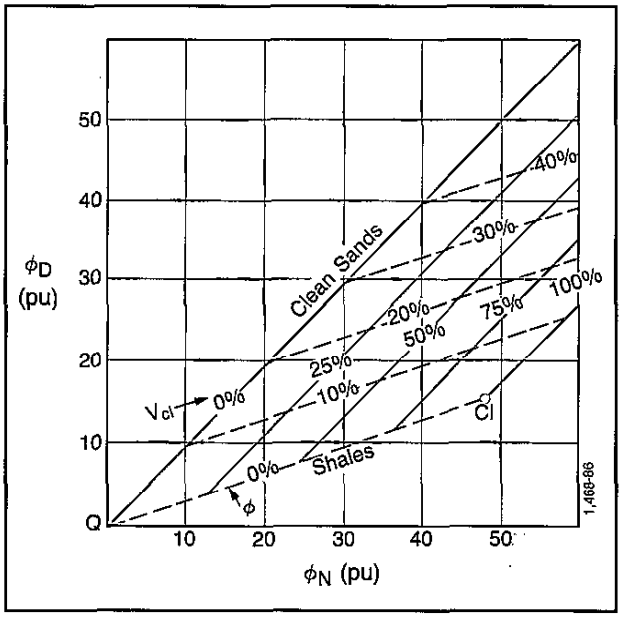

Fig. 8-17—Neutron-density crossplot scalings in terms of porosity and V_{cl}.

With a grid so established, the location of a point on the neutron-density crossplot defines its shale volume, V_{sh}; breaks down the total shale volume into clay volume, V_{cl}, and silt volume or silt index, I_{sl} (where $I_{sl} = (V_{sh} - V_{cl})/V_{sh}$); and defines effective porosity, ϕ, for water bearing-formations.

Because hydrocarbons, particularly gas and light hydrocarbons, can significantly affect the neutron and density log responses, hydrocarbon-bearing zones must be handled differently. Zone shaliness is first evaluated using a shale indicator (SP, GR, R_t, R_{xo}, etc.). The neutron and density logs are corrected for shaliness and then used to determine porosity and hydrocarbon density.

With ϕ, ϱ_h, V_{sh}, V_{cl}, I_{sl}, and S_{xo} now defined, water saturation in the noninvaded, virgin formation can be determined using the true resistivity from a deep resistivity log. Water saturation is calculated using Eq. 8-33.

Fig. 8-18 is an example of a Saraband log. Computed outputs include:

1. In Track 1, shale fraction (V_{sh}).
2. In Track 2, a hydrocarbon analysis consisting of water saturation (S_w), residual hydrocarbon volume (ϕS_{hr}), and residual hydrocarbon weight ($\phi S_{hr} \varrho_h$). Hydrocar-

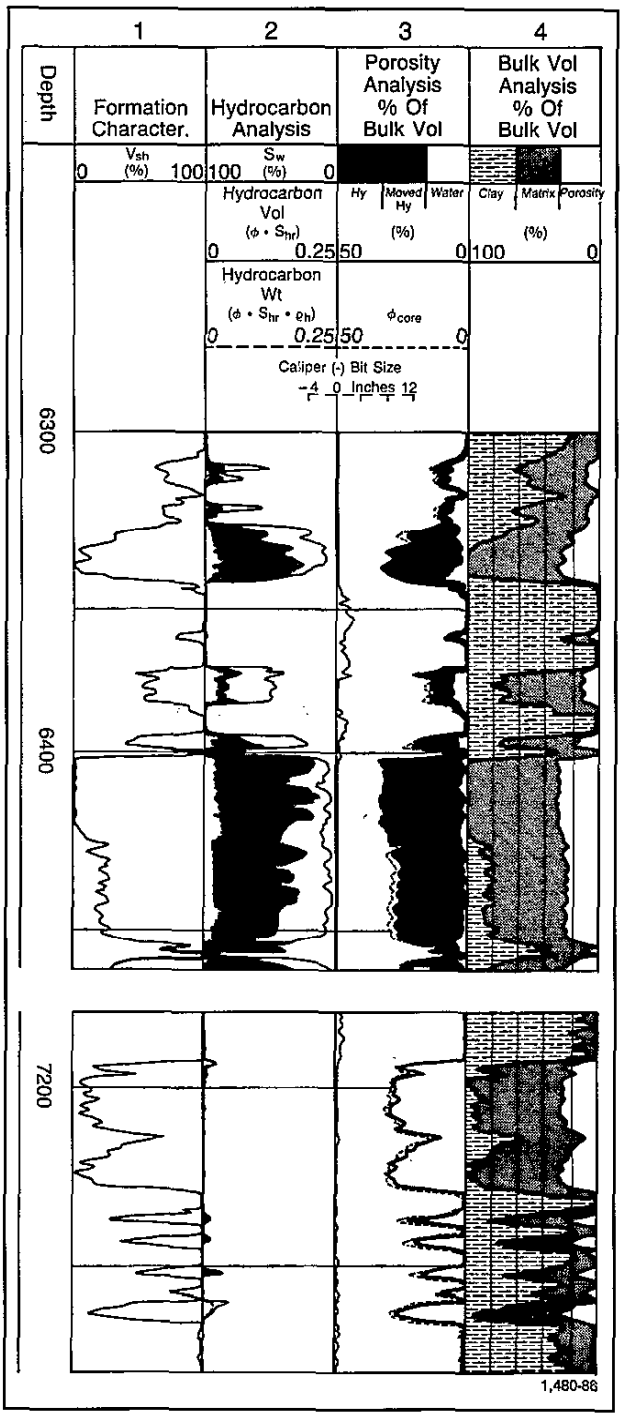

Fig. 8-18—Example of Saraband computation in hydrocarbon-bearing and water-bearing formations.

bon density can be determined by dividing the hydrocarbon weight by its volume.

3. In Tracks 2 and 3, a differential caliper (caliper minus bit size).
4. In Track 3, a porosity analysis showing effective porosity (ϕ), total "core" porosity (ϕ_{core}), bulk-volume water in the invaded zone ($\phi\ S_{xo}$) shown by the outline of the left edge of the dotted area, and bulk-volume water in the noninvaded zone ($\phi\ S_w$) shown by the outline of the left edge of the white area. The dotted area is, therefore, the bulk-volume of hydrocarbons moved by the invasion process, ($\phi\ S_{xo} - \phi\ S_w$). The shaded area represents the unmoved hydrocarbon in the invaded zone ($\phi - \phi\ S_{xo}$). Core porosity is a computed value that usually represents more closely the value of porosity from core analysis; it is found by adding to ϕ the water bound to the clays that are not laminated.
5. In Track 4 is a formation analysis showing the clay fraction (V_{cl}), a matrix-solids fraction, and the porosity. The matrix-solids fraction includes both the actual matrix and the nonclay materials (e.g., silt) in the shales.

Coriband Model

The Coriband program is a general interpretation method for mixed lithologies, including shaly formations. It provides hydrocarbon-corrected porosities in the standard lithologies (silica, limestone, dolomite, and anhydrite) and in cases where the lithology consists of a known mineral pair.

The Coriband program also uses a neutron-density crossplot, as shown in Fig. 8-19, to derive values of formation porosity and apparent matrix density. The crossplot is scaled into a series of ϱ_{ma} lines interpolated between the positions of the silica (quartz) line (ϱ_{ma} = 2.65), the limestone line (ϱ_{ma} = 2.71), and the dolomite line (ϱ_{ma} = 2.87). Neutron and density log values are plotted on Fig. 8-19 to obtain apparent values of porosity (ϕ_{ND}) and matrix density (ϱ_{ma}). These are applicable to clean, water-saturated formations.

A unique feature of this chart is that a point plotted on the chart and interpreted according to any binary mixture of the four most common minerals (silica, limestone, dolomite, and anhydrite) yields a reasonable value of porosity regardless of lithology. For example, the interpretation of Point A on Fig. 8-19, made with the assumption of different mineral pairs, would be the following:

1. If limestone and dolomite mixture (Line a-a): ϕ = 10.2%, ϱ_{ma} = 2.76 g/cm^3.
2. If dolomite and silica mixture (Line b-b): ϕ = 10.7, ϱ_{ma} = 2.77.
3. If silica and anhydrite mixture: ϕ = 11.0, ϱ_{ma} = 2.78.
4. If limestone and anhydrite mixture (Line c-c): ϕ = 10.5, ϱ_{ma} = 2.76.

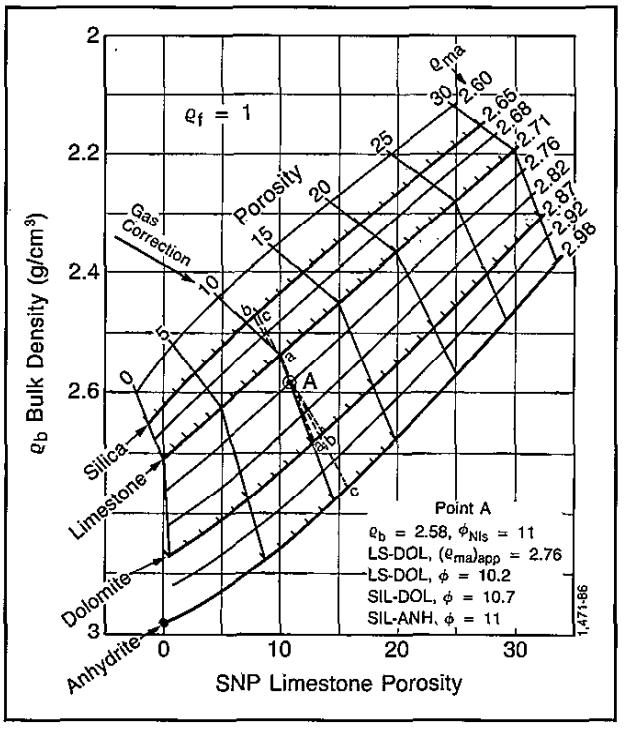

Fig. 8-19—Neutron-density crossplot scaled with interpolated ϱ_{ma} lines.

Thus, if it is known that only these four minerals are present but the composition is not further specified, the porosity of Point A will be 10.6 ± 0.4% and the matrix density will be 2.77 ± 0.01 g/cm³.

Before a set of neutron and density log data can be plotted on Fig. 8-19, the data must be corrected for clay content. The Coriband program looks at the clay fractions determined from many clay indicators (SP, GR, etc.). From these, the most probable value for the amount of clay (shale) is selected. Fig. 8-20 illustrates how the clay correction is made and values for ϕ and ϱ_{ma} are obtained.

Point L represents the log data (ϱ_b, ϕ_N) plotted for a given level. The location of the clay point (ϕ_{cl}, ϱ_{cl}) was determined from a study of the crossplot. Point X is the clay-corrected point location such that $\overline{XL}/\overline{XC} = V_{cl}$; V_{cl} was, of course, obtained from the clay indicator measurements (SP, GR, etc.). Point X corresponds to a formation having the same relative volume of matrix and pore space as the original formation, but with the clay removed.

Multiplying the porosity of Point X by $(1 - V_{cl})$ gives the approximate porosity of the original shaly formation. Using this porosity value, S_{xo} and S_{hr} can be computed. These values of ϕ and S_{hr} and the expected value of

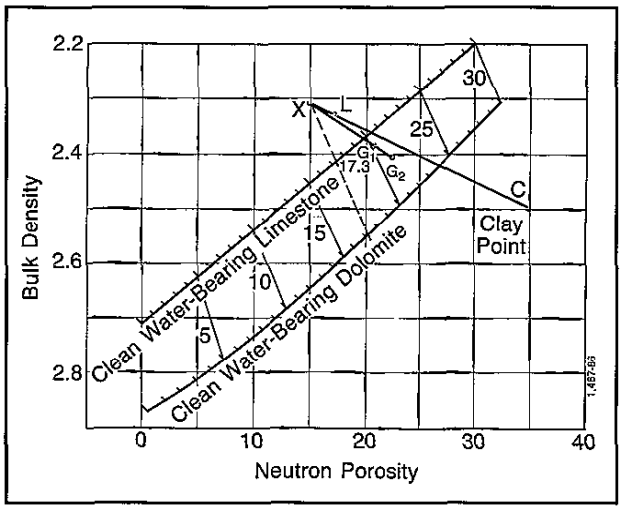

Fig. 8-20—Graphical illustration of clay and hydrocarbon corrections.

hydrocarbon density are used to compute the hydrocarbon effects on the clay-corrected, hydrocarbon-bearing formation of Point X.

The hydrocarbon effects are algebraically subtracted from the respective coordinates of Point X to locate Point G_1 (Point G_1 corresponds to the clay-corrected formation 100% water saturated). The crossplot porosity of Point G_1 is multipled by $(1 - V_{cl})$ to obtain the porosity of the original shaly formation corrected for the effect of shale and hydrocarbons. The value of ϱ_{ma} for Point G_1 is found from its position between the limestone and dolomite lines. If necessary, the result is refined by iterating the procedure, using the porosity last found, to locate a new Point G_2 with associated values of S_{xo}, S_{hr}, ϕ, and ϱ_{ma}. Several iterations might be needed to provide convergence.

With ϕ and V_{sh} defined and R_w and R_{sh} known or determined from resistivity log crossplots, the water saturation in the noninvaded formation is determined (Eq. 8-33) using the deep resistivity measurement.

Fig. 8-21 is an example of a Coriband log. Computed outputs include:

1. In Track 1, the average density of the formation solids, including the dry clay (ϱ_{ma}).
2. In Track 1, and if a sonic log is available, the secondary porosity index (SPI). The secondary porosity index is the difference between the neutron-density porosity and the sonic porosity.
3. In Track 2, the water saturation (S_w).
4. In Track 3, a porosity analysis showing: the porosity (ϕ), bulk-volume water in the invaded zone ($\phi\ S_{xo}$) shown by the outline of the left edge of the dotted area,

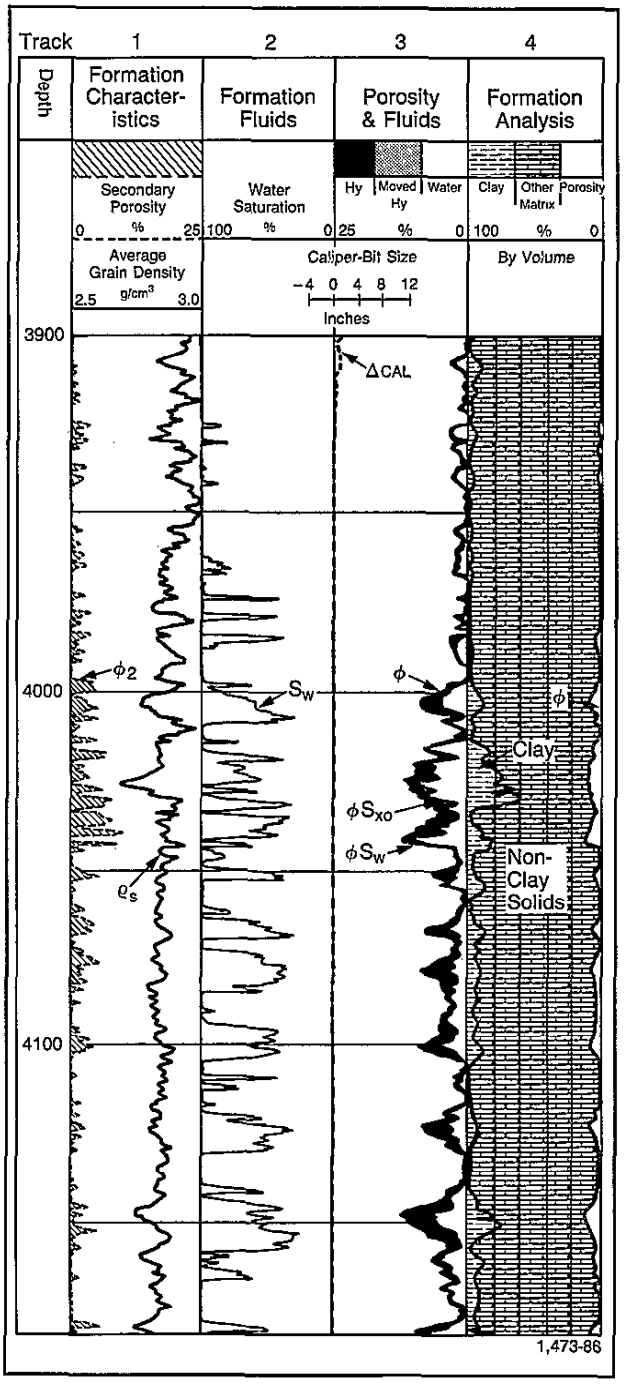

Fig. 8-21—Log presentation of computed Coriband results.

and bulk volume of water in the noninvaded zone (ϕS_w) shown by the outline of the left edge of the white area. The dotted area is, therefore, the bulk volume of hydrocarbons moved by the invasion process, and the solid area is the bulk volume of residual hydrocarbons.

5. In Track 4, a formation analysis showing the clay fraction, a matrix-solids fraction, and the porosity. The *matrix-solids fraction includes all the nonclay solid* materials (i.e., quartz, limestone, dolomite, anhydrite).

DUAL WATER MODELS

In 1968, Waxman and Smits proposed, based on extensive laboratory work and theoretical study, a saturation-resistivity relationship for shaly formations that related the resistivity contribution of the shale (to the overall resistivity of the formation) to the CEC of the shale. The Waxman-Smits relationship is

$$\frac{1}{R_t} = \frac{S_w^2}{F^* R_w} + \frac{BQ_v S_w}{F^*} \quad , \quad \text{(Eq. 8-35)}$$

where F^* is the formation factor of the interconnected porosity, S_w also relates to the interconnected pores, B is the equivalent conductance of the sodium clay-exchange cations as a function of the formation water conductivity, and Q_v is the CEC of the rock per unit pore volume.

Unfortunately, a continuous in-situ measurement of rock CEC was not available when this study was presented. As a result, the dual water model was developed as a practical solution. The dual water method is based on three premises:

1. The conductivity of clay is due to its CEC.
2. The CEC of pure clays is proportional to the specific surface area of the clay (Fig. 8-22).

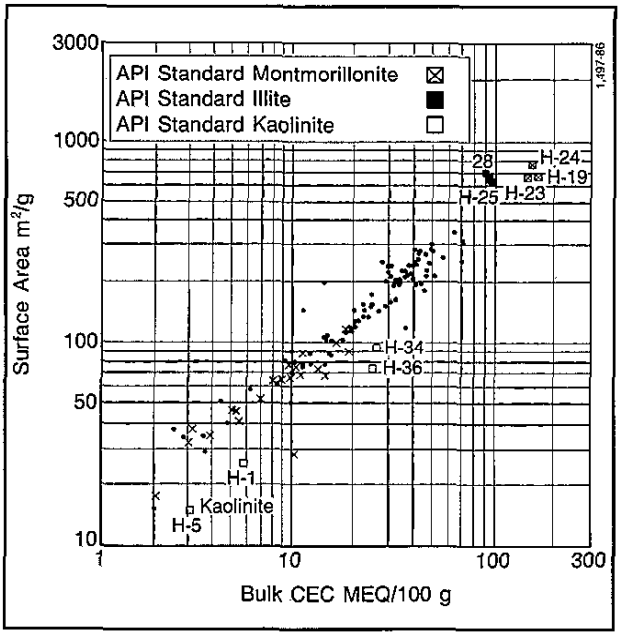

Fig. 8-22—Surface area of shale core samples versus CEC.

3. In saline solutions, the anions are excluded from a layer of water around the surface of the grain. The thickness of this layer expands as the salinity of the solution (below a certain limit) decreases (Fig. 8-23), and the thickness is a function of salinity and temperature.

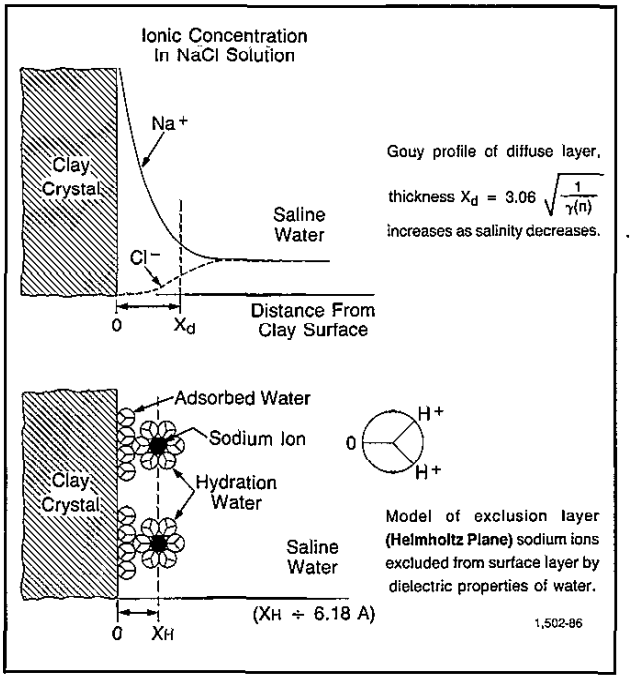

Fig. 8-23—Different models of the diffuse layer.

Therefore, since CEC is proportional to specific area (area per unit weight), it is proportional to the volume of water in the counter ion exclusion layer per unit weight of clay. Consequently, the conductivity of clay is proportional to the volume of the counterion exclusion layer; this layer being "bound" to the surface of the clay grains. For clays, this very thin sheet of bound water is important because of the large surface areas of clays relative to sand grains (several magnitudes greater).

Therefore, in the dual water model, a clay is modeled as consisting of two components, bound water and clay minerals.

The clay minerals are modeled as being electrically inert; the clay electrical conductivity is modeled as being derived from the conductivity of the bound water, C_{wb}. C_{wb} is assumed to be independent of clay type (from the second postulate above). The amount of bound water varies according to clay type, being higher for the finer clays (with higher surface areas), such as montmorillonite, and lower for coarser clays, such as kaolinite. Salinity also has an effect; in low-salinity waters (roughly <20,000 ppm NaCl) the diffuse layer expands.

The bound water is immovable under normal conditions; therefore, the volume it occupies cannot be displaced by hydrocarbons. Since the clay minerals (dry colloids) are considered electrically inert, they may be treated just as other minerals. Schematically, shaly formations are modeled with the dual water model as illustrated in Table 8-1.

Table 8-1
Dual Water Model

Solids			Fluids		
Matrix	Silt	Dry Clay	Bound Water	Free Water	Hydro-carbons
Matrix	Shale			Effective Porosity	
			Total Porosity		

1,509-86

For most rocks (except for conductive minerals such as pyrite, which cannot be treated in this way) only the porous part needs be considered when discussing electrical properties, and it is treated according to the Archie water saturation equation. The equation becomes

$$C_t = \frac{\phi_t^m \, S_{wt}^n}{a} \, C_{we} \, , \qquad \text{(Eq. 8-36)}$$

where

a, m, and n have the usual Archie connotations,

C_t is the conductivity of the noninvaded, virgin formation,

and

C_{we} is the equivalent conductivity of the waters in the pore space.

Note that ϕ_t and S_{wt} refer to total pore volume; this includes the pore volumes saturated with the bound water and the formation connate water (sometimes called the "free" water). The equivalent water conductivity, C_{we}, is

$$C_{we} = \frac{V_w \, C_w + V_{wb} \, C_{wb}}{V_w + V_{wb}} , \qquad \text{(Eq. 8-37a)}$$

where V_w and V_{wb} are the bulk volumes of formation water and bound water, respectively, and C_w and C_{wb} are their conductivities.

In terms of saturation, Eq. 8-37a becomes

$$C_{we} = \frac{\phi_t \, (S_{wt} - S_{wb}) \cdot C_w + \phi_t \, S_{wb} \cdot C_{wb}}{\phi_t \, (S_{wt} - S_{wb}) + \phi_t \, S_{wb}} \, ,$$

(Eq. 8-37b)

or

$$C_{we} = \left[\frac{(S_{wt} - S_{wb})}{S_{wt}}\right] C_w + \left[\frac{S_{wb}}{S_{wt}}\right] C_{wb} , \quad \text{(Eq. 8-37c)}$$

or

$$C_{we} = C_w + \left(\frac{S_{wb}}{S_{wt}}\right)(C_{wb} - C_w) , \quad \text{(Eq. 8-37d)}$$

where S_{wb} is the bound water saturation (i.e, the fraction of the total pore volume occupied by the bound water).

Eq. 8-37d describes the equivalent water conductivity as a function of the formation water conductivity plus the bound water conductivity. The saturation equation (Eq. 8-36) becomes

$$C_t = \frac{\phi_t^m S_{wt}^n}{a}\left[C_w + \frac{S_{wb}}{S_{wt}}(C_{wb} - C_w)\right]. \quad \text{(Eq. 8-38)}$$

The porosity and water saturation of the sand (clean formation) phase (that is the nonclay phase) of the formation is obtained by subtracting the bulk-volume fraction of bound water ($\phi_t S_{wb}$). Therefore, the effective porosity is

$$\phi = \phi_t (1 - S_{wb}) , \quad \text{(Eq. 8-39)}$$

and the water saturation is

$$S_w = \frac{S_{wt} - S_{wb}}{1 - S_{wb}} . \quad \text{(Eq. 8-40)}$$

In order to evaluate a shaly formation using the dual water model, four parameters must be determined. They are C_w (or R_w), C_{wb} (or R_{wb}), ϕ_t, and S_{wb}. A neutron-density crossplot provides a good value of ϕ_t. S_{wb} is obtainable from a variety of shale-sensitive measurements (SP, GR, ϕ_N, R_t, ϕ_N-ϱ_b, t-ϱ_b, etc.). R_{wb} and R_w are usually determined by the log analyst and entered as input parameters.

VOLAN* Model

The VOLAN program is a general computer interpretation program for clastic sequences and for carbonate lithologies; it uses the dual water model.

Resistivity, density, and neutron measurements are used to determine porosity, fluid saturations, hydrocarbon type and amount, permeability analysis, and a bulk-volume analysis of the matrix/fluid system — including clay, silt, and bound water. Other measurements can be used to improve and expand the interpretation results.

The program solves the model schematically depicted in Table 8-1 and the equations presented in the dual water model section. It is designed around the density-neutron crossplot. Fig. 8-24 shows how the crossplot is used to define, for each plotted level, values of ϕ_t, V_{sl}, and V_{cl} and to check S_{wb}. The four end points — quartz matrix (Q), water, dry clay (DC), and wet clay (CL), although reasonably fixed for most shaly sands, are located by a statistical crossplot of the density-neutron data (see Fig. 8-16). With these points located, the enclosed triangle can be divided into the various bulk volumes shown on Fig. 8-24.

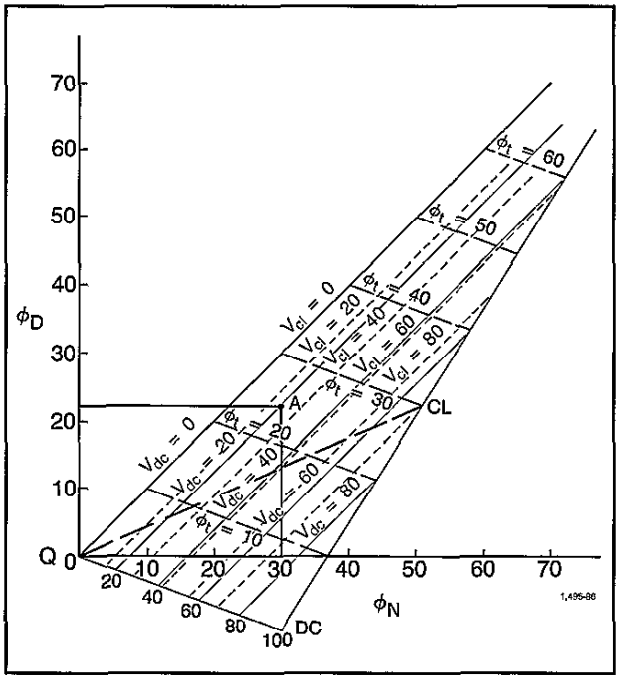

Fig. 8-24—Neutron-density crossplot.

1. Lines of constant ϕ_t are parallel to the Q-DC lines.
2. Lines of constant V_{cl} are parallel to the Q-Water Point line with the V_{cl} = 100% line passing through the Cl point.
3. Lines of constant V_{dc} are also parallel to the Q-Water Point line with the V_{dc} = 100% line passing through the DC point.
4. Lines of constant S_{wb} fan out from the Q point with S_{wb} = 0% lying on the Q-Water Point line and S_{wb} = 100% on the Q-Cl line.

As an example, consider Level A at ϕ_D = 0.22 and ϕ_N = 0.30. Fig. 8-24 indicates the following:

$$\phi_t = 24\%,$$

$$V_{dc} = 20\%,$$

$$V_{cl} = 28.6\%,$$

and

$$S_{wb} = 35.5\%.$$

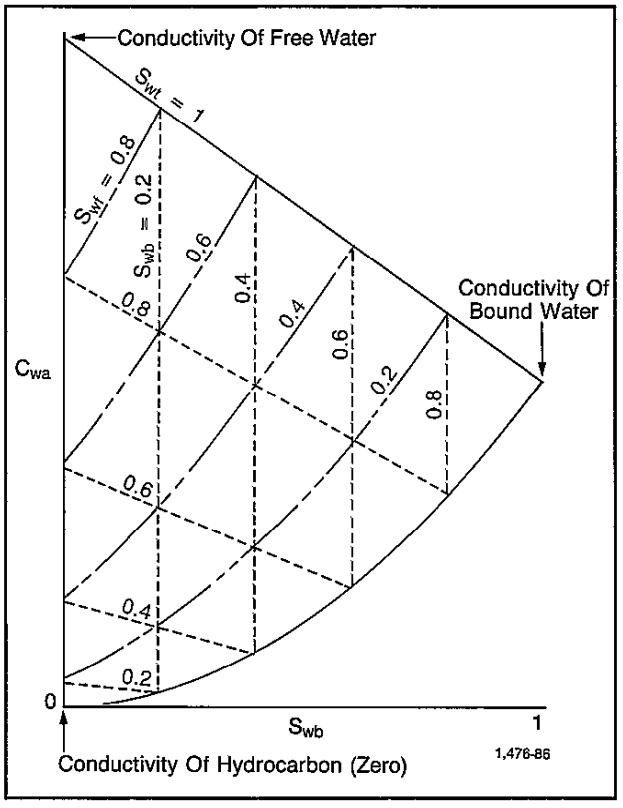

Fig. 8-25—C_{wa} S_{wb} crossplot as used in VOLAN processing.

Also, from the model of Table 8-1, it follows:

$$\phi_{wb} = V_{cl} - V_{dc} = 8.6\% ,$$

and

$$\phi = \phi_t - \phi_{wb} = 15.6\% .$$

These values assume that Level A represents a water-bearing horizon and that hole conditions are such that the density and neutron readings are valid. If there has been some displacement of Level A because of borehole rugosity or the presence of hydrocarbons, particularly light hydrocarbons, an external source of S_{wb} is required. S_{wb} is then used to assist in correcting the density and/or neutron data for hole rugosity or hydrocarbon effects.

There are several sources for S_{wb}. These include the density-neutron crossplot, SP, GR, resistivity, and sonic-density crossplot.

For the density-neutron crossplot, S_{wb} is given by

$$S_{wb} = \left(\frac{\phi_{tCl}}{\phi_t}\right)\left(\frac{V_{dc}}{V_{dcCl}}\right), \quad \text{(Eq. 8-41a)}$$

where the terms are as defined in Fig. 8-24 and ϕ_{tCl} and V_{dcCl} are the values of ϕ_t and V_{dc} of the Cl point, respectively.

For the GR,

$$S_{wb} = M\left(\frac{GR}{\phi_t}\right) + B , \quad \text{(Eq. 8-41b)}$$

where M and B are the slope and y-intercept of the regression analysis of an

$$S_{wb}\left(S_{wb} = \frac{GR - GR_w}{GR_{wb} - GR_w}\right) \text{ versus GR}/\phi \text{ crossplot.}$$

For the SP,

$$10^{SP/K} = \left[\frac{S_{wt}\,C_w + S_{wb}\,(C_{wb} - C_w)}{S_{xot}\,C_{mf} + S_{wb}\,(C_{wb} - S_{mf})}\right]\frac{S_{xot}}{S_{wt}} . \quad \text{(Eq. 8-41c)}$$

Good values of S_{wt}, S_{xot}, and C_{wb} are necessary; iteration is therefore needed to obtain a good S_{wb}.

For the resistivity,

$$S_{wb} = S_{wt}\left(\frac{C_{we} - C_w}{C_{wb} - C_w}\right), \quad \text{(Eq. 8-41d)}$$

where $C_{we} = FC_t/S_{wt}^n$ and S_{wt} is initially assumed to be 100%. Iteration is needed to obtain a good value of S_{wb}. Also, there must be a sufficient difference between C_{wb} and C_w to prevent S_{wb} from being overly sensitive to small anomalies in the data.

For the sonic-density crossplot,

$$S_{wb} = \frac{V_{cl}}{V_{dcCl}}, \quad \text{(Eq. 8-41e)}$$

where V_{cl} and V_{dcCl} are obtained in a manner analogous to the density-neutron crossplot.

From these various values of S_{wb}, a Hodges-Lehman technique is used to pick the most probable S_{wb}.

Other saturations can be determined from Eq. 8-38. If C_{wa} is defined as

$$C_{wa} = C_t\,F , \quad \text{(Eq. 8-42)}$$

where C_t is the conductivity of the noninvaded, virgin formation and F is the formation factor corresponding to ϕ_t, Eq. 8-38 becomes

$$C_{wa} = S_{wt}^2\left[C_w + \left(\frac{S_{wb}}{S_{wt}}\right)(C_{wb} - C_w)\right]. \quad \text{(Eq. 8-43)}$$

A plot of Eq. 8-43 is shown in Fig. 8-25. A comparison of C_{wa} and S_{wb} will yield S_{wt} and S_{wf} (the formation connate water saturation). Hydrocarbon saturation is, of course, $1 - S_{wt}$.

Fig. 8-25 is also used to screen data affected by bad hole (data falling outside the boundaries of the C_{wa} versus S_{wb} diagram) and to provide insight into the values of C_w and C_{wb}.

VOLAN results are presented as a continuous log (Fig. 8-26). Outputs include the following:

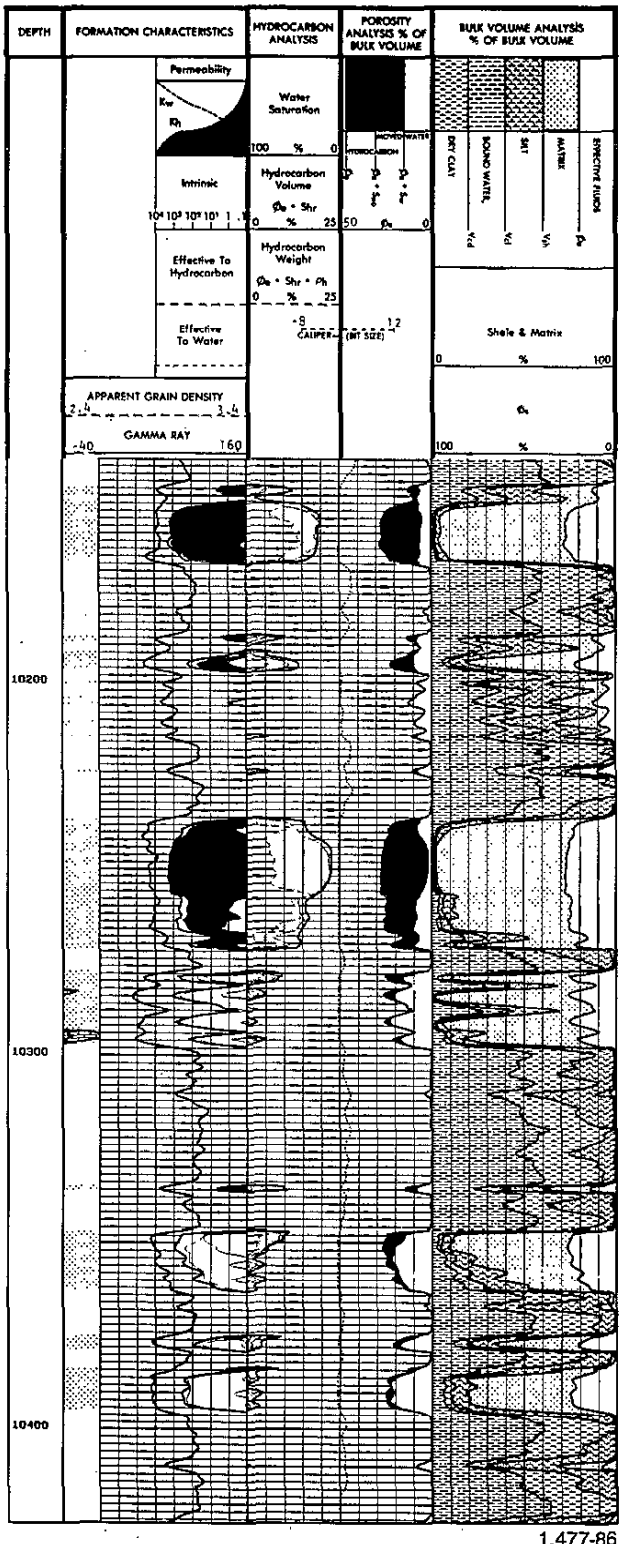

Fig. 8-26—VOLAN log.

1. In Track 1, the GR log for correlation, the apparent grain density (ϱ_{maa}), and a permeability analysis. The permeability analysis includes the intrinsic (absolute) permeability and the effective permeabilities to hydrocarbons and water.
2. In Track 1, if a Litho-Density log is available, the fractional volume of up to three constituent matrix minerals.
3. In Track 2, a hydrocarbon analysis consisting of water saturation (S_w), residual hydrocarbon volume ($\phi\ S_{hr}$), residual hydrocarbon weight ($\phi\ S_{hr}\ \varrho_h$). Hydrocarbon type (density) is identifiable by a comparison of hydrocarbon volume and hydrocarbon weight.
4. In Tracks 2 and 3, a differential caliper (hole caliper minus bit size).
5. In Track 3, a porosity analysis showing porosity (ϕ), bulk-volume water in the invaded zone ($\phi\ S_{xo}$), and bulk-volume water in the noninvaded zone ($\phi\ S_w$). The difference in the bulk volumes of water in the invaded and noninvaded zones is the bulk volume of moved hydrocarbons. The difference in the bulk-volume water in the invaded zone and the porosity is the bulk volume of residual hydrocarbons.
6. In Track 4, a formation analysis showing effective porosity (ϕ), matrix volume (V_{ma}), silt volume (V_{si}), bound water (ϕ_{wb}), and dry clay volume (V_{dc}). The bound water and dry clay add to the wet clay volume (V_{cl}); the wet clay and silt add to the shale volume (V_{sh}).

In addition to the "output result display," two diagnostic playbacks are generated. Reconstructed values of GR, SP, t, and ϱ_b are compared with the original logging curves (Fig. 8-27). The reconstructed t and ϱ_b have hydrocarbon effects removed (for subsequent use in the Geogram* program or for mechanical properties computation).

The second playback (Fig. 8-28) shows which measurements control the S_{wb} computation. In addition, ϕ_t (PHIT) is compared with density-neutron crossplot porosity and sonic sandstone porosity.

Cyberlook* Program

The Cyberlook program is a computer-assisted wellsite interpretation method. It uses the dual water model to account for the effects of clay fraction, lithology, and hydrocarbon in the derivation of reservoir parameters.

In the dual water model, the conductivity of a water-bearing shaly formation is given by (see also Eq. 8-38):

$$C_0 = \phi_t^2\ [S_{wb}\ C_{wb} + (1 - S_{wb})\ C_w]\ , \quad \text{(Eq. 8-44a)}$$

where a and m of the formation factor-porosity relationship are 1 and 2, respectively. Expressed in resistivity, Eq.

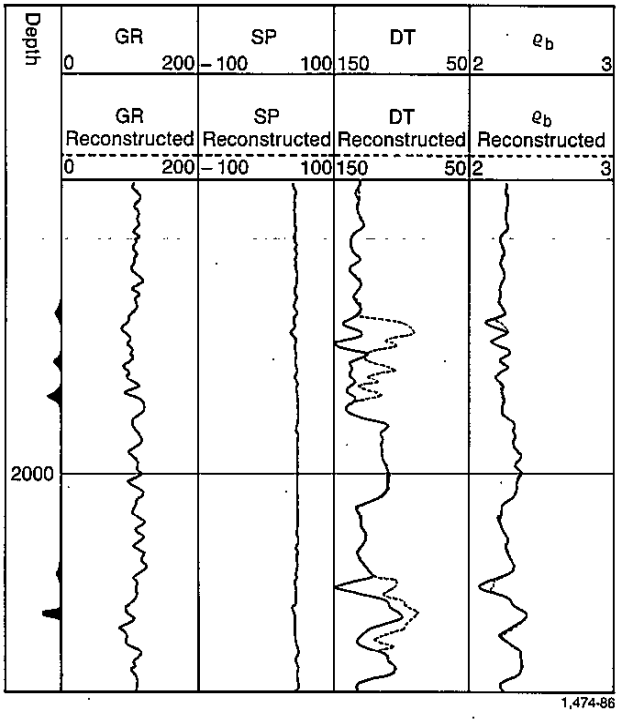

Fig. 8-27—VOLAN diagnostic playback: reconstructed openhole logs.

8-44a becomes

$$R_0 = \frac{R_w\, R_{wb}}{\phi_t^2\, [S_{wb}\, R_w + (1 - S_{wb})\, R_{wb}]} \cdot \quad \text{(Eq. 8-44b)}$$

In Cyberlook processing, the various parameters of this equation are evaluated and R_0 is calculated. A continuous plot, versus depth, of R_0 is made. R_0 can then be compared to the recorded deep resistivity (deep induction or deep laterolog). In water zones the calculated R_0 curve and deep resistivity R_t curve overlay (i.e., agree). This implies that the parameters required in Eq. 8-44b were properly evaluated. In hydrocarbon-bearing zones, the curves will separate with $R_t > R_0$. The Cyberlook water saturation is given by

$$S_w = \sqrt{R_0/R_t}\,. \quad \text{(Eq. 8-45)}$$

Porosity, ϕ_t, is derived from the neutron-density crossplot. S_{wb} is obtained from the traditional shale indicators. The Cyberlook program uses SP, GR, and neutron data. R_{wb} and R_w must be determined by the field engineer and entered as input parameters. The Cyberlook log, therefore, consists of two passes.

On Pass 1, a continuous computation of an apparent fluid resistivity, R_{fa}, is made, among many computations including ϕ_t. It is simply

$$R_{fa} = R_t\, \phi_t^2\,.$$

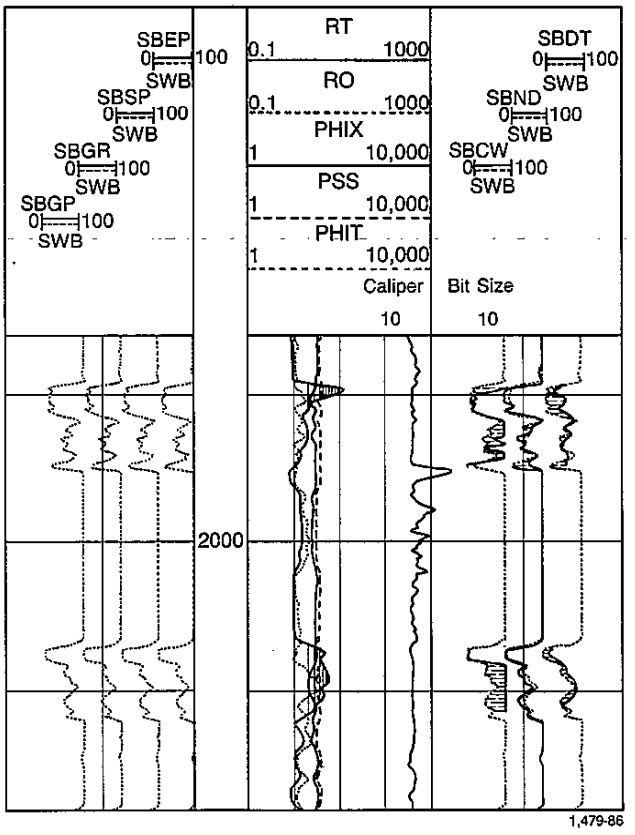

Fig. 8-28—Measurements controlling the S_{wb} computation in the VOLAN program.

From the R_{fa} curve, R_w and R_{wb} can be selected for use in Pass 2, the actual Cyberlook computation. R_w is read from the R_{fa} curve in clean and wet (water-bearing) zones. R_{wb} is read from the R_{fa} curve in shale intervals. If the R_{fa} curve indicates any changes in either R_w or R_{wb} from one interval to another, the Pass 2 computation can be "zoned" (separated into individual sections) and the desired R_w and/or R_{wb} values used in each interval. If there are no clean water-bearing zones, R_w may have to be estimated or taken from local experience.

Fig. 8-29 shows a Cyberlook log. Outputs are:

1. In Track 1, apparent grain density (ϱ_{maa}) and minimum shale index (MSI).
2. In Track 2, the computed R_0 curve from Eq. 8-45b (R_0) and the deep resistivity (R_t). These curves should overlay in water-bearing zones and separate ($R_t > R_0$) in hydrocarbon-bearing zones.
3. In Track 3, water saturation (S_w), a differential caliper (DCAL), and a porosity analysis consisting of effective porosity (ϕ_e), bulk-volume water in the invaded zone ($\phi\, S_{xo}$), and bulk volume water in the noninvaded zone ($\phi\, S_w$).

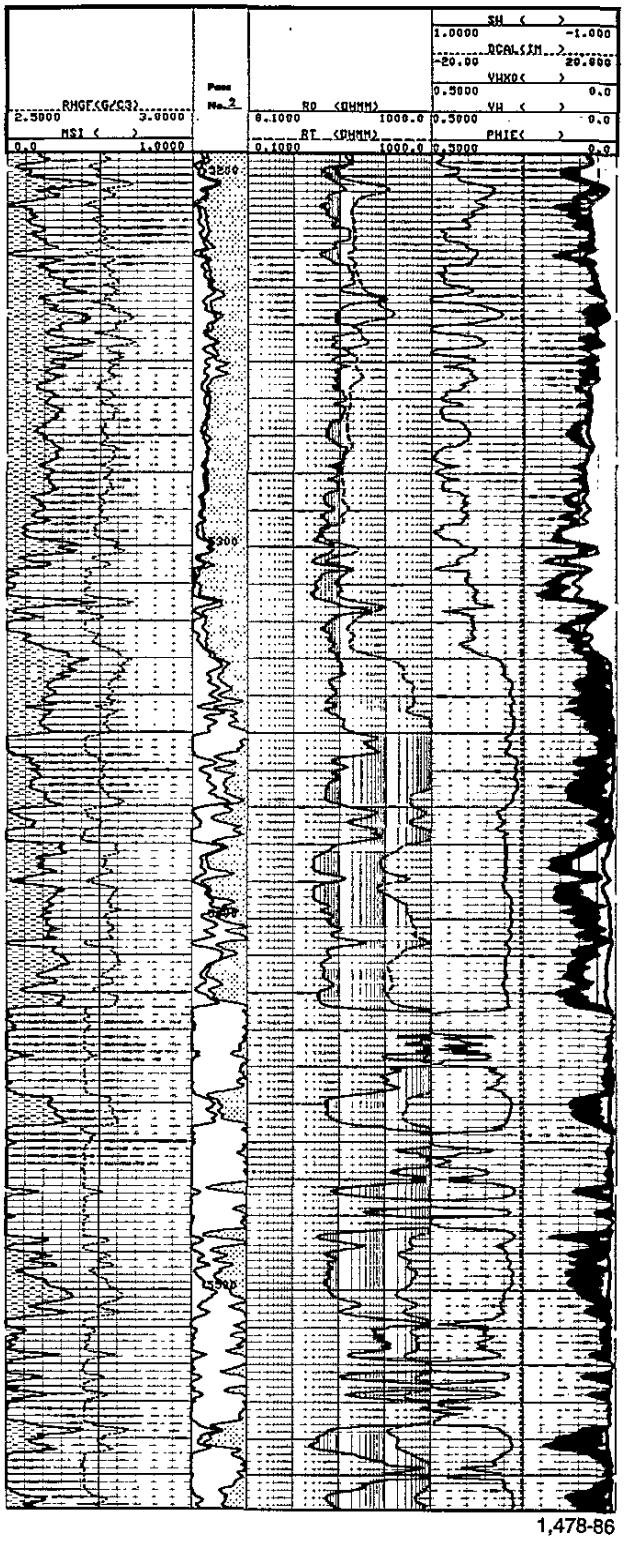

1,478-86

Fig. 8-29—Cyberlook/EPT log.

The term "effective" porosity is sometimes misleading. Effective porosity is that porosity associated with the nonshale phase of the shaly sand. It is the porosity that would exist if the shale and the water bound to the clays were removed, leaving only the clean sand phase. The effective pore space may contain fluids that are not movable. This means that formations with effective porosity are not necessarily permeable. It also means that not all the effective porosity is available for hydrocarbon saturation. Some portion of the effective porosity contains irreducible connate water bound to the sand grain surface by surface tension forces. Bound water, however, occupies a space that can only contain "clay" water; it cannot be displaced by hydrocarbons nor can it contribute to rock permeability.

GLOBAL* METHOD

Historically, log interpretation has been performed in a sequential process of logical operations. The log analyst determines one parameter, then another, and another, and so on, until the problem is solved. That approach has the advantage of being understandable, repeatable, and logically acceptable.

Most computer programs reproduce this step-by-step classical manual interpretation process. It was logical to do so. The process was well documented, and it was relatively easy to program the computer to duplicate that process.

Such techniques, however, have been outstripped by the evolution of log interpretation in its attempt to deal with the complexity of formations in which oil and gas are now being sought, and by the introduction of sophisticated new sensors to measure additional characteristics of reservoir rocks. As a result, it becomes increasingly difficult to define a sequential path through this maze of petrophysical measurements and interpretation models that makes the best use of all the available data and knowledge.

A more integrated approach to computer-processed interpretation is desirable and it should encompass the following objectives:

- Use all available information — log measurements, interpretation models, geological and physical constraints, local knowledge.
- Seek results that make optimum use of this complex body of knowledge.
- Have a potential for evolution, characterized by the easy introduction of new measurements and interpretation models.
- Provide a quality control of interpretation results.
- Use the *n*-dimensional capabilities of the computer rather than be limited to the 2-dimensional crossplot technique.

- Use probabilistic concepts to obtain the most probable solutions.

The GLOBAL program is a computer-processed log interpretation chain designed around these concepts. It uses a structure independent of model and logging suite. An error model relates tool measurements to petrophysical parameters such as porosity, lithology, and fluid saturation. Then, using a minimization routine, the GLOBAL program searches for the solution with the minimum error. This solution is considered the most probable answer.

The inputs of the GLOBAL program are, for each sample or level of the well, all the available environmentally corrected log measurements, which may be written in array notation:

$$a = (\varrho_b, \phi_N, t, R_{xo}, R_t, \text{GR, SP, etc.}) , \quad \text{(Eq. 8-46a)}$$

and a set of "zoned" parameters such as R_w, R_{mf}, clay parameters, etc. The outputs, or unknowns, in such a formation are all the desired petrophysical properties such as ϕ, S_{xo}, S_w, etc., which may also be written in array notation:

$$x = (\phi, S_{xo}, S_w, V_{cl}, \varrho_{ma}, \text{etc.}) . \quad \text{(Eq. 8-46b)}$$

The relationship between inputs and outputs can be expressed by a set of tool response equations, one equation for each tool. For example, the density relationship may be expressed as

$$\varrho_b = \phi\, S_{xo}\, \varrho_{mf} + \phi\,(1 - S_{xo})\, \varrho_h + V_{cl}\, \varrho_{cl} + \ldots$$

Using the array notation, the tool response equations may be written:

$$a_1 = f_1(x) ,$$
$$a_2 = f_2(x) , \quad \text{(Eq. 8-46c)}$$

where a, or $(a_1, a_2, \ldots)$, is a set of inputs at a particular level, and f_i is the tool response function. The function f_i may depend on variables other than x_1, x_2, etc. These variables, such as ϱ_{mf}, ϱ_{ma}, are called "zoned" parameters and are assumed to be constant within a given zone. They are determined prior to GLOBAL application.

The equations of Eq. 8-46c must be solved to find an interpretation solution. In addition, a solution must comply with certain constraints delineating the likely domain of the results:

- Purely physical (e.g., $0 \le \phi \le 1$, $0 \le S_w \le 1$, $0 \le V_{cl} \le 1$).
- Derived from geological knowledge (e.g., $2.70 < \varrho_{ma} < 2.88$ in carbonates $S_w \le S_{xo}$.
- Derived from a continuity hypothesis, which limits the vertical resolution of the results to the vertical resolution of the logs used.
- Imposed by the log analyst (e.g., a maximum porosity, a minimum water saturation, etc.).

Ideally, the program should be an overdetermined system; that is, there should be more equations than unknowns. Since there is no exact solution to an overdetermined system, the GLOBAL program searches for the most probable solution. This is consistent with the fact that the tool response equations are only approximations to the physical reality and that logs are subject to dispersion errors and statistics.

The incoherence function is a major component of the GLOBAL program. It expresses the lack of coherence between log measurements, computed results, response equations, and constraints. It takes into account the uncertainties on the log inputs, the uncertainties on the equation responses, geological impurities, and some penalty terms for the nonsatisfied constraints. The corresponding mathematical expression is given in Fig. 8-30.

For Each Level:

Inputs: $a = (a_1, a_2 \ldots, a_n)$
e.g., $(\varrho_b, \phi_N, \tau, P_e, R_t)$

Outputs: $x = (x_1, x_2 \ldots, x_n)$
(formation description)
e.g., $(\phi, S_{xo}, S_w, V_{cl}, V_{ma2}, \ldots)$

Tool Responses:

Functions: $a_i = f_i(\underline{x})$

Constraints: $g_j(\underline{x}) \ge 0$

Uncertainties: σ_i on logging measure a_i
τ_i on log response function f_i
τ_j on constraint g_j

Incoherence Function:

$$\Delta(a,x) = \sum_i \frac{[a_i - f_i(\underline{x})]^2}{\sigma_i^2 + \tau_i^2} + \sum_j \frac{g_j(\underline{x})^2}{\tau_j^2}$$

One Term Per Tool — One Term Per Constraint

1,481-86

Fig. 8-30—Construction of error-model (Incoherence Function) used in GLOBAL processing. A similar construction is used in the ELAN program; the major difference is that the equations are linearized.

The uncertainties on input logs come from sensor performance, dispersion in data acquisition during recor-

ding, or environmental corrections. For example, the uncertainty on the FDC log is calculated as a function of statistical variations, mudcake corrections, borehole diameter and rugosity, and depth-matching accuracy.

The uncertainties on the equation responses come from the simplifications adopted in writing the formula and from possible errors in the selection of the interpretative parameters.

The flow chart of the GLOBAL computation is shown in Fig. 8-31. The first step is to estimate a set of answers corresponding to the formation parameters to be determined. The definition of this set of answers depends on the interpretation model selected by the log analyst. In the second step, so-called "reconstructed" logs are derived from this set of answers using tool equation responses, one for each log. In the third step, the reconstructed logs are compared with the actual logs and an "incoherence" function measures the quality of the fit between the two sets of logs. The process is continued until minimal incoherence is obtained.

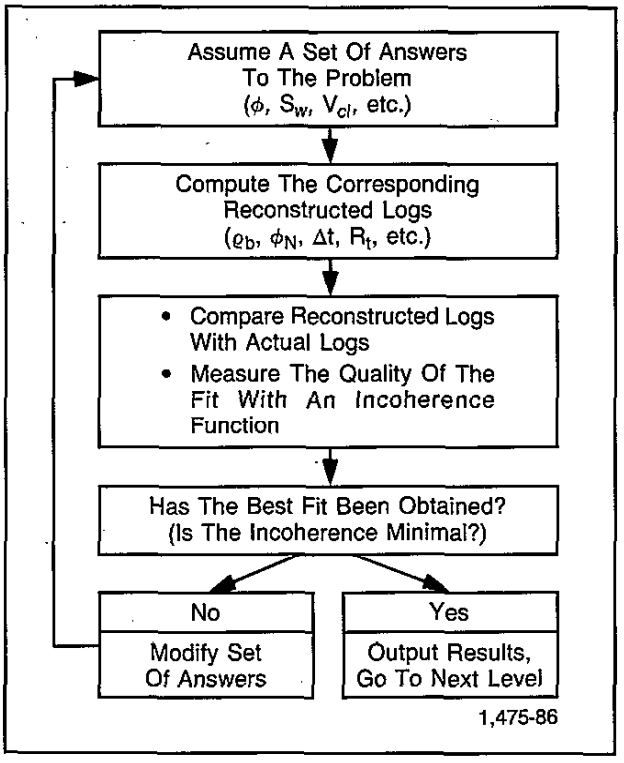

Fig. 8-31—Simplified flow chart of the GLOBAL method.

The GLOBAL results include a standard presentation of the computed formation parameters and a set of displays that are useful for quality control. An example is shown in Fig. 8-32.

The indicator shown as "reduced incoherence" is calculated at every level. It depends on the incoherence function, the number of logs considered, and the number of active constraints. Reliable results are indicated when the reduced incoherence is less than 1; the curve thus provides a quick and easy quality control.

The control display compares the actual logs with the reconstructed logs. The shaded area around the actual log represents the standard deviation of the log and equation responses. It can be considered as a confidence area; the reconstructed log should fall within this area if the response equation is within tolerance.

The example of Fig. 8-32 shows clearly the effects of rugosity on the density log; the uncertainty on ϱ_b is large over the Interval A. Although the reconstructed density log falls within the corresponding shaded area, very little weight is given to it over this interval because of the large uncertainty on ϱ_b.

Three GLOBAL programs have been developed so far. They are

- RTGLOB (R_t GLOBAL), which computes R_t, R_{xo}, and d_i from all available resistivity logs.
- RIG (Reservoir Interpretation by GLOBAL program), which is a full reservoir evaluation program and computes porosity, water saturation, etc.
- DWRIG (Dual Water Model Reservoir Interpretation by GLOBAL program), which is a reservoir evaluation program using the dual water model for saturation determination.

The interpretation model used in the GLOBAL program RTGLOB is a step profile of invasion. The corresponding set of unknowns is R_t, R_{xo}, and d_i; and all available resistivity logs (after environmental corrections) are used. The response equations contain the classical geometrical or pseudogeometrical factors. The problem of determining R_t, R_{xo}, and d_i becomes overdetermined if more than three resistivity logs are available; GLOBAL processing has the distinct advantage of using all the logs at every level.

In the example of Fig. 8-33, both ISF* and DLL*-MSFL logs were run in a reservoir composed of a series of permeable zones separated by tight sections. The figure displays the input logs (microresistivity, induction, shallow laterolog, deep laterolog), the computed results (R_t, d_i), and the reduced incoherence.

Interval C is a transition zone where R_t is smaller than R_{xo}. The pattern of resistivity profile is as expected:

$$R_t < R_I < R_{LLD} < R_{LLS} < R_{MSFL} .$$

Deep invasion (see the d_i curve) affects even the deep laterolog curve; the GLOBAL computation finds R_t smaller than R_{LLD} in the Intervals C1, C2, and C3.

All the resistivity logs read the same value at 5966 m,

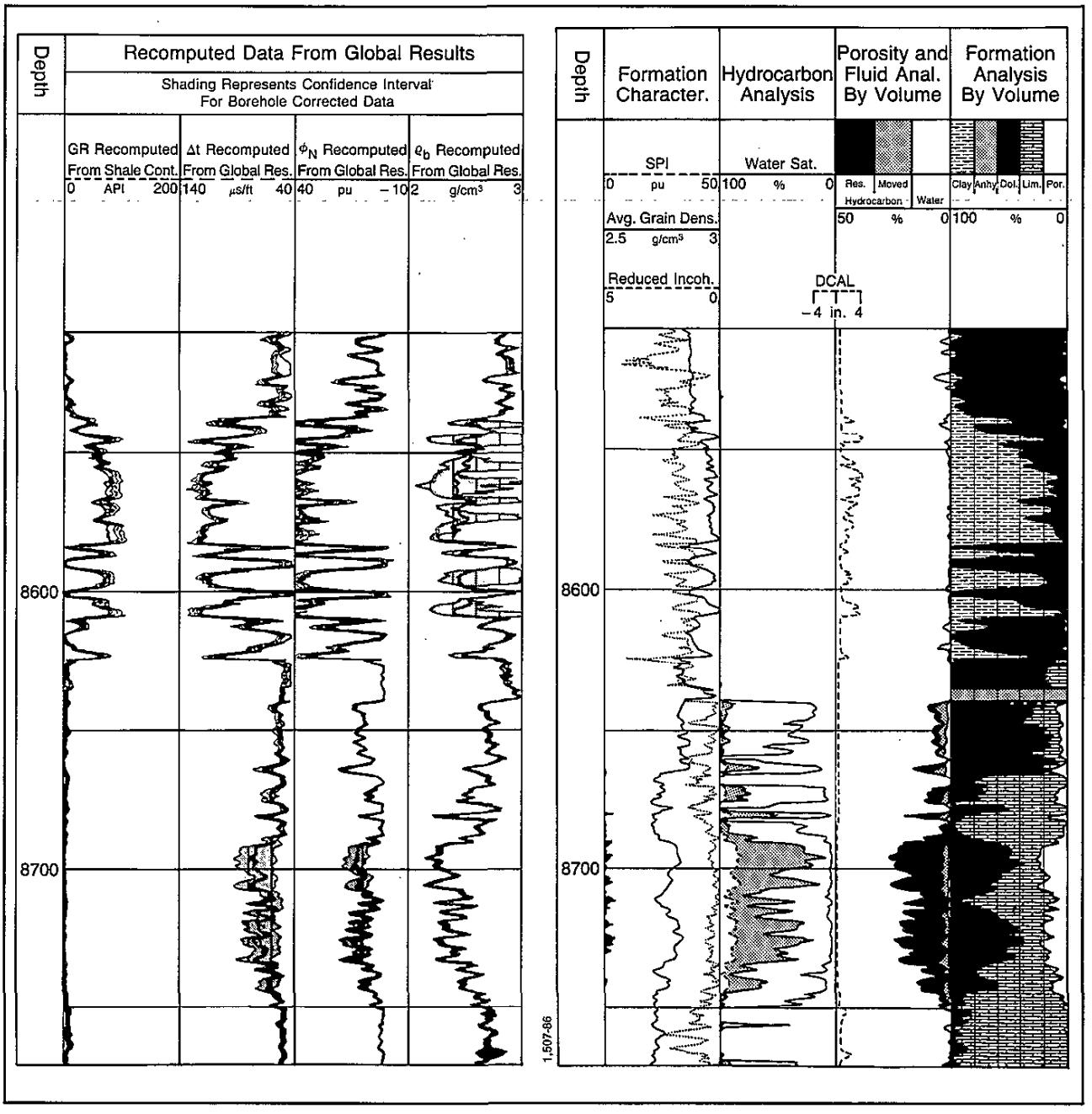

Fig. 8-32—Example of GLOBAL output with reconstructed logs.

indicating that R_t is equal to R_{xo} at this level. Above 5966 m in the permeable zones, R_t is higher than R_{xo} and the classical pattern of resistivity for a hydrocarbon zone is obtained:

$$R_t > R_I > R_{LLD} > R_{LLS} > R_{MSFL} .$$

The tight low-porosity zones show little invasion, as seen in Intervals D1 and D2. The three macroresistivity logs read approximately the same value, which is equal to R_t. The low value of the reduced incoherence over the entire interval indicates the consistency of the data and the validity of the invasion model assumed.

Many possibilities have been built into the GLOBAL evaluation program (RIG). At present, the interpretation models available include:

- A multimineral model handling up to six different

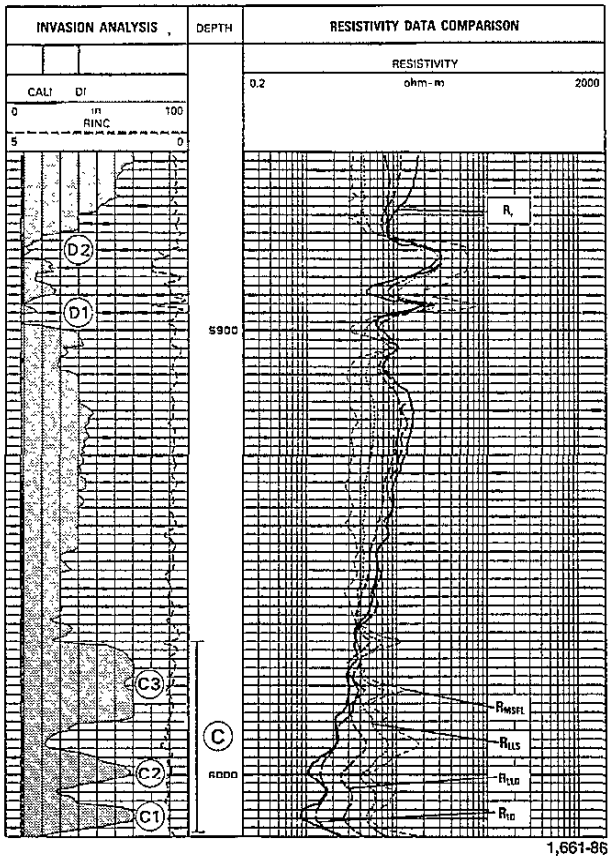

Fig. 8-33—Resistivity results from GLOBAL program.

minerals. The corresponding set of unknowns is:

$$(\phi_e, V_{cl}, S_w, S_{xo}, V_{m1}, V_{m2}, V_{m3}, V_{m4}, V_{m5}) .$$

- Dual mineral and shaly sand models are simple cases of the multimineral model.
- Dual water model, which may be preferred for determining water saturation in shaly formations. The set of unknowns is then:

$$(\phi_t, S_{wt}, S_{wb}, S_{xot}, V_{m1}, V_{m2}, V_{m3}, V_{m4}, V_{m5}) .$$

Most of available logs can be accommodated in the GLOBAL program. This includes:

- SP log.
- Porosity logs: neutron, density, and sonic.
- Photoelectric index from the Litho-Density tool.
- Natural radioactivity logs (GR or NGS* natural gamma ray spectrometry).
- GST* gamma spectrometry log (induced radioactivity).
- TDT* thermal decay time log.
- Propagation time and attenuation measurement from the EPT* electromagnetic propagation log.
- R_t and R_{xo} logs obtained from the RTGLOB program.

For each tool, a response equation has been established using classical formulae for the traditional logs or newly developed relationships for the recent logs. The structure of the program gives the possibility of adding other logs as necessary.

Naturally, the interpretation model selected by the log analyst depends a great deal on the logging program and the log responses. Ideally, the system should remain balanced or overdetermined; in other words, the number of log inputs should not be less than the number of unknowns.

REFERENCES

1. Archie, G.E.: "The Electrical Resistivity Log as an Aid in Determining Some Reservoir Characteristics," *J. Pet. Tech.* (1942) **5**.
2. Lindley, R.H.: "Use of Differential Sonic-Resistivity Plots to Find Movable Oil in Permian Formations," *J. Pet. Tech.* (Aug. 1961) **13**, No. 8.
3. Doll, H.G. and Martin, M.: "How to Use Electric Log Data to Determine Maximum Producible Oil Index in a Formation," *Oil and Gas J.* (July 5, 1954).
4. Rodermund, C.G., Alger, R.P., and Tittman, J.: "Logging Empty Holes," *Oil and Gas J.* (June 12, 1961).
5. Poupon, A., Clavier, C., Dumanoir, J., Gaymard, R., and Misk, A.: "Log Analysis of Sand-Shale Sequences — A Systematic Approach," *J. Pet. Tech.* (July 1970).
6. Poupon, A., Loy, M.E., and Tixier, M.P.: "A Contribution to Electrical Log Interpretations in Shaly Sands," *J. Pet. Tech.* (June 1954).
7. Poupon, A., Hoyle, W.R., and Schmidt, A.W.: "Log Analysis in Formations With Complex Lithologies," *J. Pet. Tech.* (Aug. 1971).
8. deWitte, L.: "Relations Between Resistivities and Fluid Contents of Porous Rocks," *Oil and Gas J.* (Aug. 24, 1950).
9. Waxman, W.H. and Smits, L.J.M.: "Electrical Conductivities in Oil-Bearing Sands," *Soc. Pet. Eng. J.* (June 1968).
10. Simandoux, P.: "Measures Dielectriques en Milieu Poreux, Application a Measure des Saturations en Eau, Etude du Comportement des Massifs Argileux," *Revue de l'institut Francais du Petrole,* Supplementary Issue (1963).
11. Smits, L.J.M.: "SP Log Interpretation in Shaly Sands," *Soc. Pet. Eng. J.* (June 1968).
12. Poupon, A. and Gaymard, R.: "The Evaluation of Clay Content from Logs," *Trans.*, 1970 SPWLA Annual Logging Symposium.
13. Patchett, J.G.: "An Investigation of Shale Conductivity," *Trans.*, 1975 SPWLA Annual Logging Symposium, paper V.
14. Clavier, C., Coates, G., and Dumanoir, J.: "Theoretical and Experimental Bases for the Dual-Water Model for Interpretation of Shaly Sands," *J. Pet. Tech.* (April 1984).
15. Best, D.L., Gardner, J.S., and Dumanoir, J.L.: "A Computer Processed Wellsite Log Computation," *Trans.*, 1978

SPWLA Annual Logging Symposium, paper Z.

16. Coates, G.R., Schultz, R.P., and Throop, W.H.: "VOLAN: An Advanced Computational Log Analysis," *Trans.*, 1982 SPWLA Annual Logging Symposium.
17. Mayer, C. and Sibbit, A.: "GLOBAL, A New Approach to Computer Processed Log Interpretation," paper SPE 9341 presented at the 1980 SPE Annual Technical Conference and Exhibition.
18. Waxman, W.H. and Thomas, E.C.: "Electrical Conductivities in Oil-Bearing Shaly Sands: I. The Relation Between Hydrocarbon Saturation and Resistivity Index; II. The Temperature Coefficient of Electrical Conductivity," *Soc. Pet. Eng. J.* (1974) **14**.
19. Worthington, P.F.: "The Evolution of Shaly-Sand Concepts in Reservoir Evaluation," *The Log Analyst* (Jan.-Feb. 1985).
20. *Log Interpretation Charts*, Schlumberger Well Services, Houston (1989).

9 Electromagnetic Propagation Logs

INTRODUCTION

Water saturation in reservoir rocks has historically been determined from a measurement of true formation resistivity. Since most formation waters are quite saline, resistivity measurements are most effective in distinguishing between hydrocarbon- and water-bearing formations. In addition, the resistivity measurement is somewhat unique in that, through proper tool design, it reflects the resistivity of the formation at some distance from the borehole with reasonable accuracy.

Unfortunately, not all formation waters are saline nor are all formations always saturated with waters of a constant salinity. As a water becomes less saline, its resistivity increases. Indeed, a water containing no dissolved salts exhibits a very high resistivity, similar to that of oil or gas. It is obvious that as formation waters become fresher, resistivity measurements lose their ability to distinguish between hydrocarbons and water.

Quantitative interpretation of the resistivity measurement into water and oil saturations requires knowledge of the formation water salinity. In some geological sequences the salinity varies greatly over a relatively short interval. Similarly, in fields that have been under waterflood for some time, the injection water salinity may have varied greatly over the life of the waterflood and from well to well. As a result, the formation water has become a mixture of waters of many chemical compositions.

A method that is less dependent upon water salinity, and knowledge of water salinity, has long been needed to determine water saturation. The measurement of dielectric permittivity offers one alternative. Table 9-1 gives laboratory-measured values of dielectric permittivity, ϵ, (relative to air) of some typical reservoir materials. With the exception of water, most materials in sedimentary rocks have low values (less than 8); therefore, the measured dielectric permittivity is primarily a function of the water-filled porosity. Although the dielectric permittivity of water is influenced by its salinity and its temperature, the range is relatively modest and much, much smaller than its range of resistivity.

Table 9-1
Relative dielectric constants and propagation times for common minerals and fluids.

Mineral	Relative Dielectric Constant	Propagation Time t_{pl}(ns/m)
Sandstone	4.65	7.2
Dolomite	6.8	8.7
Limestone	7.5-9.2	9.1-10.2
Anhydrite	6.35	8.4
Halite	5.6-6.35	7.9-8.4
Gypsum	4.16	6.8
Dry colloids	5.76	8
Shale	5-25	7.45-16.6
Oil	2-2.4	4.7-5.2
Gas	1	3.3
Water	56-80	25-30
Fresh water	78.3	29.5

1,568-86

Electromagnetic propagation can be described by Maxwell's equations:

$$\gamma = \alpha + j\,\beta\,, \qquad \text{(Eq. 9-1a)}$$

$$\omega^2\,\mu\,\epsilon = \beta^2 - \alpha^2\,, \qquad \text{(Eq. 9-1b)}$$

$$\omega\,\mu\,C = 2\,\alpha\,\beta\,, \qquad \text{(Eq. 9-1c)}$$

where

γ is the electromagnetic wave propagation,
α is the attenuation of the wave,
β is its phase shift,
ω is its angular velocity,
μ is the magnetic permeability,
ϵ is the dielectric constant,

and

C is the conductivity.

A measurement of α and β can, therefore, yield the dielectric constant (Eq. 9-1b) and the conductivity (Eq. 9-1c) of the formation in which the wave propagates (Fig. 9-2).

Schlumberger has two types of electromagnetic propagation tools: the EPT* and the DPT*. The EPT tool is a shallow investigating device that operates at a frequency of 1.1 GHz. The DPT tool is a much deeper investigating device that operates at a frequency of about 25 MHz.

EPT LOG

The EPT sonde is a pad-type tool, with an antenna pad attached rigidly to the body of the tool. A backup arm has the dual purpose of forcing the pad against the borehole wall and providing a caliper measurement. A standard microlog pad attached to the main arm allows a resistivity measurement to be made with a vertical resolution similar to that of the electromagnetic measurement. A smaller arm, which exerts less force, is mounted on the same side of the tool as the pad and is used to detect rugosity of the borehole. The borehole diameter is the sum of the measurements from these two independent arms.

Two microwave transmitters and two receivers are mounted in the antenna pad assembly in a borehole-compensated array that minimizes the effects of borehole rugosity and tool tilt.

Two tools are currently in use, the EPT-D tool and the ADEPT tool (Fig. 9-1). The ADEPT tool (also known as EPT-G) can utilize either of two configurations of new antenna arrays for deeper investigation or extended salinity range. Standard log outputs as labelled on the log heading are:

	EPT-D	ADEPT
Measured Propagation Time	TPL	TPL
Measured Attenuation	EATT	EATT
Corrected Propagation Time	—	TPPW
Corrected Attenuation	—	EAPW

A 1.1-GHz electromagnetic wave is sent sequentially from each of the two transmitters; at each of the receivers, the amplitude and the phase shift of the wavetrain are measured (Fig. 9-2). The propagation time of the wave, t_{pl}, (where $t_{pl} = \beta/\omega$) and the attenuation, A, over the receiver-spacing are determined from the individual measurements. In each case an average is taken of the measurements derived from the two transmitters. A complete borehole-compensated measurement is made 60 times per second; these individual measurements are accumulated and averaged over an interval of either 0.4, 1.2, 2, or 6 in. of formation prior to recording on film and magnetic tape.

*Mark of Schlumberger

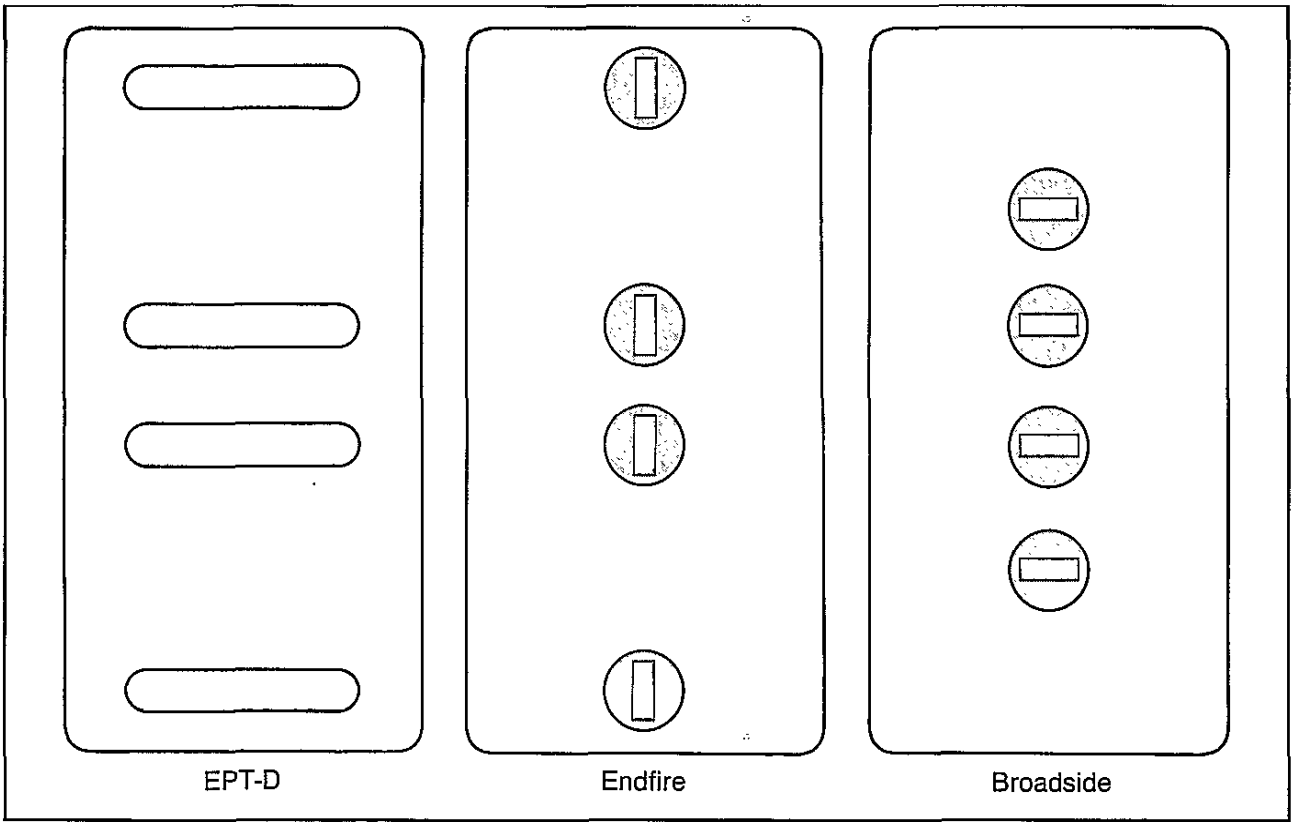

Fig. 9-1—Two microwave transmitters and two receivers are mounted in the antenna pad assemblies of the EPT-D, the ADEPT endfire array and the ADEPT broadside array.

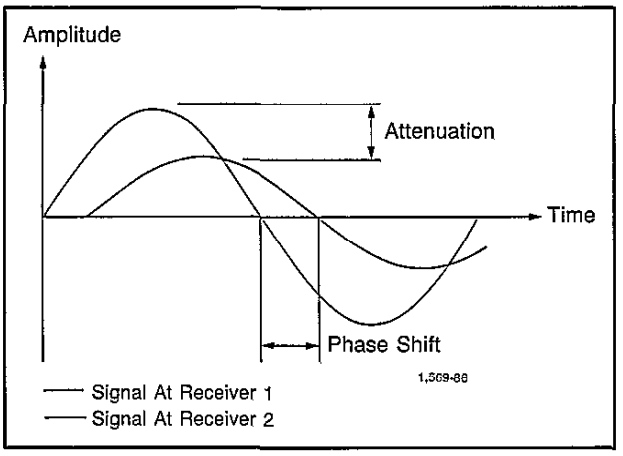

Fig. 9-2—Electromagnetic propagation signals.

Because of the close proximity of the receivers to the transmitters, spherical waves are being measured; therefore, a correction factor must be applied to the measured attenuation to compensate for the spherical spreading loss, *SL*. The corrected attenuation is given by the relationship

$$A_c = A - SL\,, \qquad \text{(Eq. 9-2)}$$

where

A_c is the corrected attenuation,

A is the measured attenuation,

and

SL is the spherical attenuation loss.

In air, *SL* has a value of about 50 dB, but laboratory measurements indicate it is somewhat porosity dependent. A more exact equation is

$$SL = 45 + 1.3\,t_{pl} + 0.18\,t_{pl}^2\,. \qquad \text{(Eq. 9-3)}$$

A graphical representation of this relationship is shown in Chart EPTcor-2.

An EPT log is shown in Fig. 9-3. Track 1 contains the borehole caliper and gamma ray curves. The electromagnetic wave attenuation in decibels per meter and propagation time in nanoseconds per meter are recorded in Tracks 2 and 3. The recorded attenuation, *A* (EATT on log heading), after correction for spreading loss, is directly proportional to the attenuation α of Eq. 9-1; the propagation time, t_{pl} (TPL on log heading), is proportional to the phase shift β ($t_{pl} = \beta/\omega$). The measurement of the smaller caliper arm is displayed in Track 2; it is used to monitor the borehole rugosity and, thereby, the quality of the EPT data.

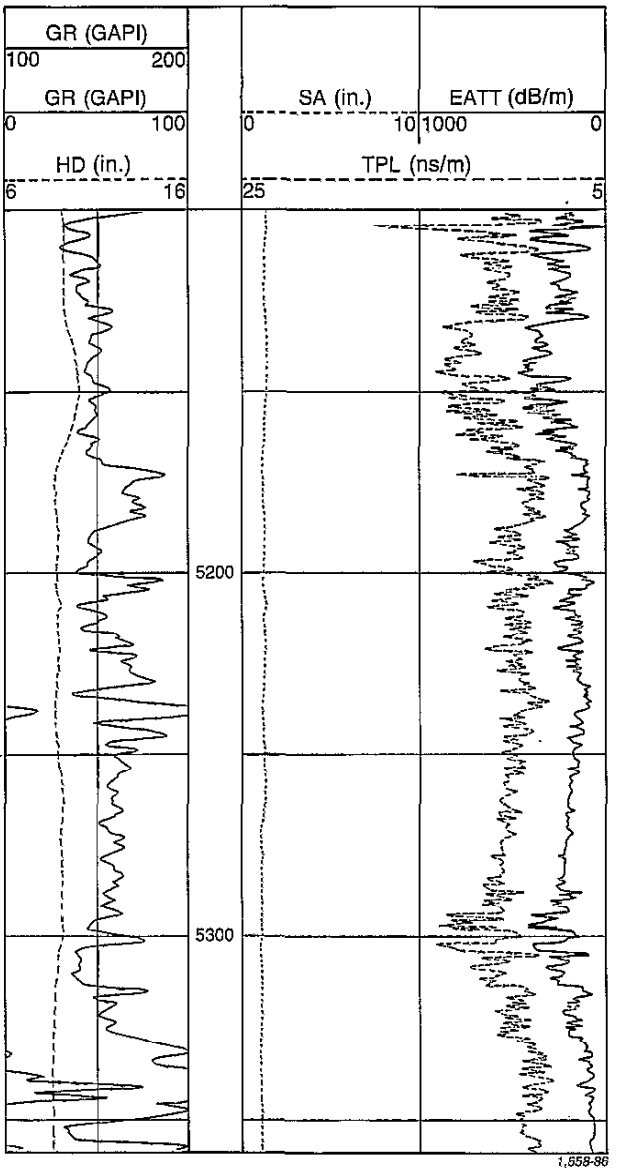

Fig. 9-3—Electromagnetic propagation log.

ADEPT: The ADaptable EPT Tool

The ADEPT tool was designed to provide a superior measurement in rugose boreholes and in the presence of mudcake. The tool uses new antennas which have simpler, more predictable properties. Measurement of attenuation and propagation time are very accurate since the tool response is well known and the "spreading loss" correction is predictable. Figure 9-4 shows a schematic comparison of the investigation patterns of the two optional antennas: *endfire* and *broadside* arrays.

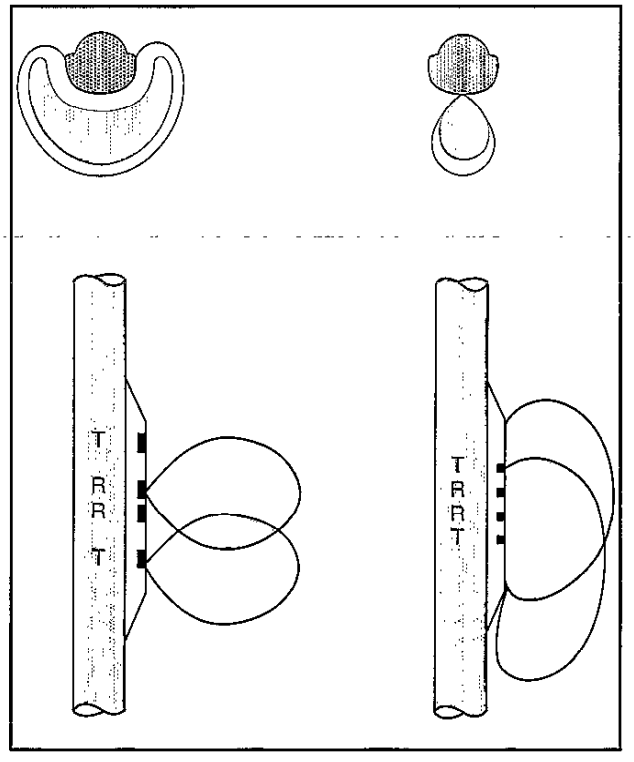

Fig. 9-4—Comparison of endfire and broadside arrays.

The optional *endfire* array is used to improve depth of investigation and significantly reduce mudcake and standoff effects without sacrificing vertical resolution. Depth of investigation is a function of formation resistivity; the endfire array has a depth of investigation greater than that of a conventional array. The endfire array would normally be used when invaded zone resistivity is greater than about 1 ohm-m.

If no other log information is available prior to EPT logging, invaded zone resistivity may be difficult to estimate. A simple, but less precise, guide for choosing the appropriate antenna option is: use the endfire array when mud resistivity exceeds 0.3 ohm-m.

The ADEPT tool allows use of an optional short-spacing *broadside* array which extends the effective operating range in high porosity and/or saline conditions. If log attenuations greater than 600 dB/m are seen in the zone of interest, a repeat pass with the broadside array should be considered.

Under normal fresh mud conditions, propagation time is essentially unaffected by water salinity (Fig. 9-5). However, for waters with resistivities less than 0.3 ohm-m, propagation time increases. Attenuation increases as porosity and water salinity increase. In porous formations containing very saline fluids, the electromagnetic waves are highly attenuated and detection can be difficult with the conventional array.

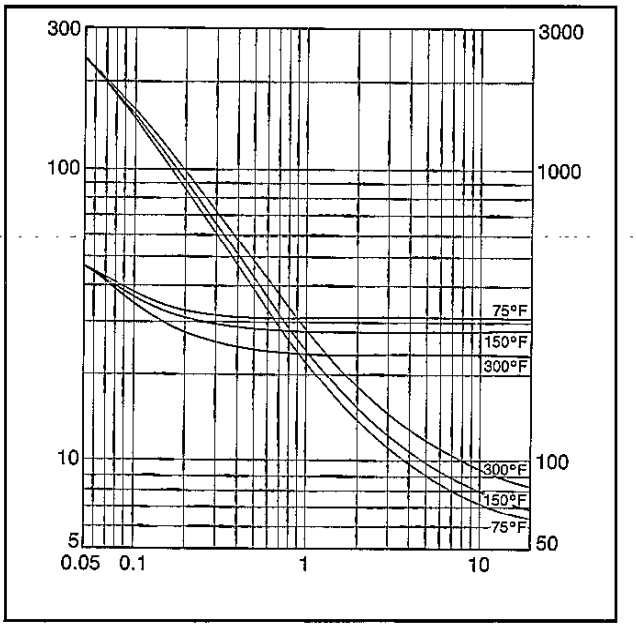

Fig. 9-5—Variation of t_{pf} and A_f vs. salinity and temperature.

Interpretation Methods

The EPT measurement responds mainly to the water content of a formation, rather than to the matrix or any other fluid. The water can be the original connate formation water, mud filtrate, or the bound water associated with shales. Because of the tool's shallow depth of investigation (1 to 6 in.), it can usually be assumed that only the flushed zone is influencing the measurement and that the water is primarily mud filtrate.

Electromagnetic wave propagation in mixtures of materials of differing electromagnetic wave propagation, dielectric constant, and conductivity has been explored theoretically and experimentally by several investigators. The most popular relationship to emerge from these studies is a simple weight-average equation (similar to that used in density evaluation of mixtures):

$$\gamma^* = \phi\gamma_f^* + (1 - \phi)\,\gamma_{ma}^* , \qquad \text{(Eq. 9-4)}$$

where

γ^* is the resultant electromagnetic wave propagation in the mixture,

γ_f^* is the electromagnetic wave propagation in the fluid saturating the pores,

γ_{ma}^* is the electromagnetic wave propagation in the rock matrix,

and

ϕ is the porosity.

The asterisk emphasizes that the electromagnetic wave propagation is a complex parameter containing both a real in-phase component and an imaginary out-of-phase component.

CRIM Method

Solution of Eq. 9-4 for water-filled porosity, ϕ_{EPT}, is called the CRIM (for complex refractive index) method of EPT interpretation. It is generally an iterative process in which the water-filled porosity and the saturating water electromagnetic wave propagation term, γ_w^*, are determined by iteration. To do so, Eq. 9-4 is translated into complex dielectric permittivity and then separated into real and imaginary parts:

$$\frac{\sqrt{\epsilon'}}{\sqrt{1-\tan^2\frac{\delta}{2}}} = \frac{\phi_{EPT}\sqrt{\epsilon'_w}}{\sqrt{1-\tan^2\frac{\delta_w}{2}}} + (1-\phi_{EPT})\sqrt{\epsilon'_m}, \quad \text{(Eq. 9-5a)}$$

and

$$\frac{\sqrt{\epsilon'}\tan\frac{\delta}{2}}{\sqrt{1-\tan^2\frac{\delta}{2}}} = \frac{\phi_{EPT}\sqrt{\epsilon'_w}\tan\frac{\delta_w}{2}}{\sqrt{1-\tan^2\frac{\delta_w}{2}}}, \quad \text{(Eq. 9-5b)}$$

where ϵ' and ϵ'_w are the real parts of the dielectric permittivity of the composite formation and waters and $\tan\delta$ and $\tan\delta_w$ are their respective loss tangents.

The dielectric constant of water as a function of temperature and salinity is given by

$$\epsilon'_w = 94.88 - 0.2317\ °F + 0.000217\ °F^2 - 0.1556 - 0.413\ (Kppm) + 0.00158\ (Kppm)^2 \quad \text{(Eq. 9-6a)}$$

and

$$\epsilon'_w \tan\delta_w = 5.66 + 2.65\ (Kppm) - 0.0045\ (Kppm)^2, \quad \text{(Eq. 9-6b)}$$

where °F is the temperature in degrees Fahrenheit and Kppm is the salinity in one thousand parts per million.

The EPT log provides t_{pl} and attenuation from which ϵ' and $\tan\delta/2$ can be computed:

$$\epsilon' = 0.09\,t_{pl}^2 - 2.4972 \times 10^{-5} A_c^2, \quad \text{(Eq. 9-7a)}$$

$$\epsilon'' = 1.832 \times 10^{-4} A_c\, t_{pl}, \quad \text{(Eq. 9-7b)}$$

and

$$\tan\delta = \epsilon''/\epsilon'. \quad \text{(Eq. 9-8)}$$

Eqs. 9-5a and -5b are solved for ϕ_{EPT} and water salinity iteratively using the following procedure. An initial value of salinity is assumed for the water in the invaded zone (usually the mud filtrate salinity is a good first approximation). Using the known temperature, the dielectric constant of this water, ϵ'_w, is computed from Eq. 9-6a. The loss tangent of water, $\tan\delta_w$, is computed from Eq. 9-6b. Substituting those values and using computed ϵ' and $\tan\delta/2$ from logs (Eq. 9-7 and Eq. 9-8), ϕ_{EPT} is determined from Eq. 9-5a. Using the computed ϕ_{EPT}, a corrected loss tangent of water is determined from Eq. 9-5b. This value of loss tangent is used to determine a new value for the water salinity, which is then used to find a new value of porosity, etc. The iteration is continued until the computed porosity and salinity converge to constant values. The technique determines not only water-filled porosity but also the salinity of the water in that region investigated by the EPT tool. The technique is most appropriate for computer solution.

CTA Model

The Complex Time Average (CTA) model is used in formation evaluation interpretation programs (Cyberlook*, GLOBAL* and ELAN*). The CTA method assumes that a petrophysical model can be constructed by using a weighted-average relationship similar to that used to interpret formation density logs. Two independent equations can be written, one for propagation time and one for attenuation:

$$t_{pl} = \phi S_{xo} t_{pw} + \phi(1-S_{xo}) t_{ph} + (1-\phi) t_{pma} \quad \text{(Eq. 9-9a)}$$

and

$$A = \phi S_{xo} A_w. \quad \text{(Eq. 9-9b)}$$

Before use in the above equations, measured values of propagation time (TPL) and attenuation (EATT) must be corrected for the propagation phenomena of *geometrical spreading and scattering*. For the EPT-D tool, the two effects have been determined empirically and lumped into a correction factor known as "spread loss correction", which must be applied to the EATT measurement. This has been published as Chart EPTcor-2.

The newer ADEPT tool uses antennas with a dipole propagation pattern, which allows more accurate characterization of the required corrections. ADEPT log outputs TPPW (propagation time, plane wave) and EAPW (attenuation, plane wave) have already been corrected for spreading. TPPW and EAPW may be used directly in Eqs. 9-9a and 9-9b, and are the preferred inputs for wellsite computations. Additional precision can be achieved if mudcake corrections are made using the Charts EPTcor-3 and -4.

The porosity determined in Eq. 9-9a and 9b is the water-filled porosity. The method assumes that the EPT tool responds to hydrocarbons in much the same manner as it responds to matrix. Eq. 9-9b also assumes that little signal attenuation occurs in the matrix.

Comparing ϕ_{EPT} with the actual porosity, ϕ, of the formation gives the water saturation of the zone investigated, most likely the flushed zone:

$$S_{xo} = \frac{\phi_{EPT}}{\phi}. \quad \text{(Eq. 9-10)}$$

Chart Sxo-1 graphically solves Eqs. 9-9a and -10 to yield S_{xo} from t_{pl}. Chart EPTcor-1 provides estimates of t_{pw} and t_{pma} for use in Eq. 9-9a and Chart Sxo-1. The t_{pw} estimate is based upon laboratory measurements. t_{pma} is estimated from knowledge of the apparent grain density, ρ_{maa}, from the density-neutron combination, and from the expected rock lithology.

Chart Sxo-2 graphically solves Eq. 9-9a and 10. The ADEPT tool's improved measurement of attenuation makes the use of this simple relationship practical. Porosity must be input, but in this case lithology is not required.

If water salinity is unknown, A_w can be redefined as a function of t_{pw} using Chart EPTcor-2, and the two equations may be used together to solve for both S_{xo} and t_{pw}.

t_{po} Method

In the t_{po} method of EPT interpretation all values are treated as if they were measured in a lossless formation. The measured propagation time, t_{pl}, must therefore be related to lossless conditions by applying a correction factor that is a function of the attenuation of the electromagnetic waves in the lossy medium. If the measured propagation time is t_{pl}, then the lossless formation propagation time, t_{po}, is (from Eq. 9-1b) given by

$$t_{po}^2 = t_{pl}^2 - \frac{A_c^2}{3604}, \qquad \text{(Eq. 9-11)}$$

where A_c is the attenuation corrected for spreading loss.

The EPT water-filled porosity is then given by

$$\phi_{EPT} = \frac{t_{po} - t_{pma}}{t_{pwo} - t_{pma}}. \qquad \text{(Eq. 9-12)}$$

The rock matrix is assumed to be a lossless medium, and the lossless propagation time of water (nonconductive) is obtained from the temperature-related equation

$$t_{pwo} = 20\ \frac{710 - T/3}{444 + T/3}, \qquad \text{(Eq. 9-13)}$$

where T is the temperature in degrees Fahrenheit.

If the presence of hydrocarbons is included in the response equation, the relationship takes the form

$$t_{po} = \phi_t S_{xo} t_{pwo} + \phi_t (1 - S_{xo}) t_{ph} + (1 - \phi_t) t_{pma} \qquad \text{(Eq. 9-14a)}$$

or

$$S_{xo} = \frac{(t_{po} - t_{pma}) + \phi_t (t_{pma} - t_{ph})}{\phi_t (t_{pwo} - t_{ph})}, \qquad \text{(Eq. 9-14b)}$$

where t_{ph} is the propagation time for hydrocarbons (also lossless) and ϕ_t is the total porosity. If the matrix and hydrocarbon propagation times are approximately the same, Eq. 9-14b reduces to Eq. 9-10.

A comparison of the EPT porosity measurement with the total porosity measured by the neutron, density, and/or sonic tools allows a quicklook determination of the water saturation in the flushed zone. Generally, the EPT porosity will be the same as the total porosity in water-bearing zones, but in hydrocarbon-bearing intervals the EPT porosity will be less than the total porosity. However, if total porosity is obtained from a neutron log, the separation between the neutron porosity and the EPT porosity will not be so apparent in gas zones because of the excavation effect on the neutron measurement. Fig. 9-6 illustrates these differences.

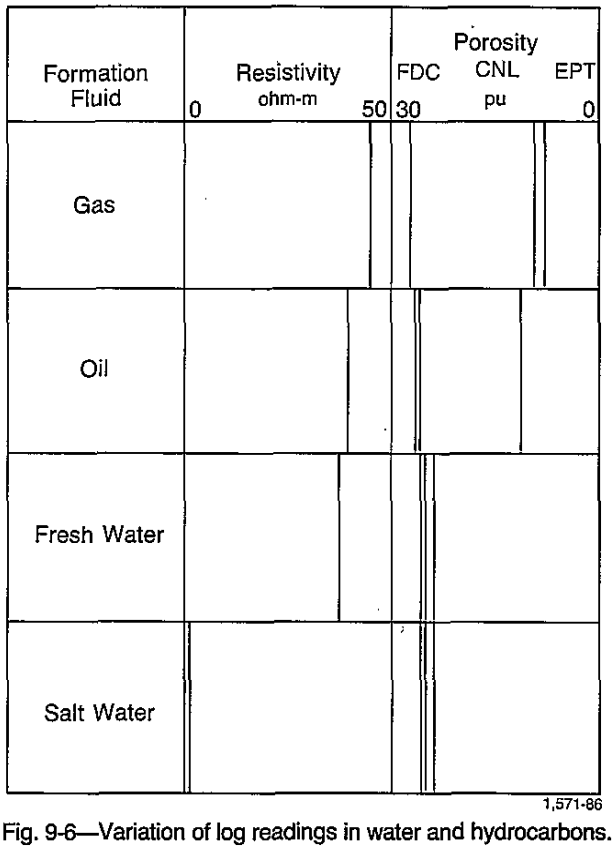

Fig. 9-6—Variation of log readings in water and hydrocarbons.

In Fig. 9-7, Zone A is obviously gas bearing, as evidenced by the neutron porosity reading less than the density porosity. The EPT porosity is near the neutron porosity and much less than the density porosity, which confirms the presence of hydrocarbons.

In Zone B, the wide separation between the density and EPT porosity values also indicates hydrocarbons. However, the neutron porosity is lower than in Zone A, which indicates Zone B contains more oil or condensate than Zone A. The three porosity logs read similar values in Zone C and indicate a water-bearing zone.

Fig. 9-8 shows an example of hydrocarbon detection in a freshwater zone in a South American well. The comparison of EPT porosity (EMCP on the heading) to neutron-density cross-

plot porosity (PHIA on the heading) clearly identifies the oil-water contact at 6850 ft; the resistivity curves show little difference.

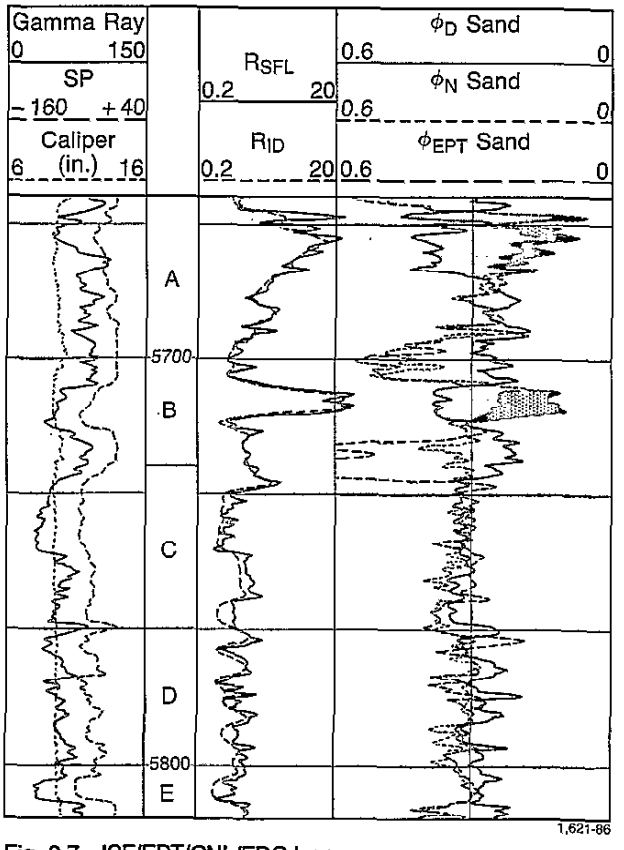

Fig. 9-7—ISF/EPT/CNL/FDC logs.

There are several methods for determining matrix propagation time, t_{pma}. If it is a simple, known lithology, the values of Table 9-1 can be used directly. In a dual-mineral formation containing two of the more common matrices, the chart of Fig. 9-9 can be used (Chart EPTcor-1). An apparent grain density, ρ_{maa}, is found from the neutron-density log combination. This apparent grain density is entered in Fig. 9-9 (or Chart EPTcor-1) to estimate t_{pma} for the appropriate two-mineral mixture. If another mineral is known to predominate in the formation, its matrix parameters can similarly be entered in the chart.

When the lithology is more complex, as it may be in many "hard-rock" areas, a three-mineral model may be necessary to properly evaluate t_{pma}. This can be done with a CNL*-Litho-Density* log combination. The ρ_b, ϕ_N, and P_e measurements can be combined to determine an apparent grain density and an apparent matrix volumetric cross section, U_{maa}, which are then used to find the proportions of the three minerals (V_1, V_2, V_3) in the matrix (Chart CP-21). A value of t_{pma} is assigned to each mineral in the model, and the t_{pma} of the composite matrix is given by

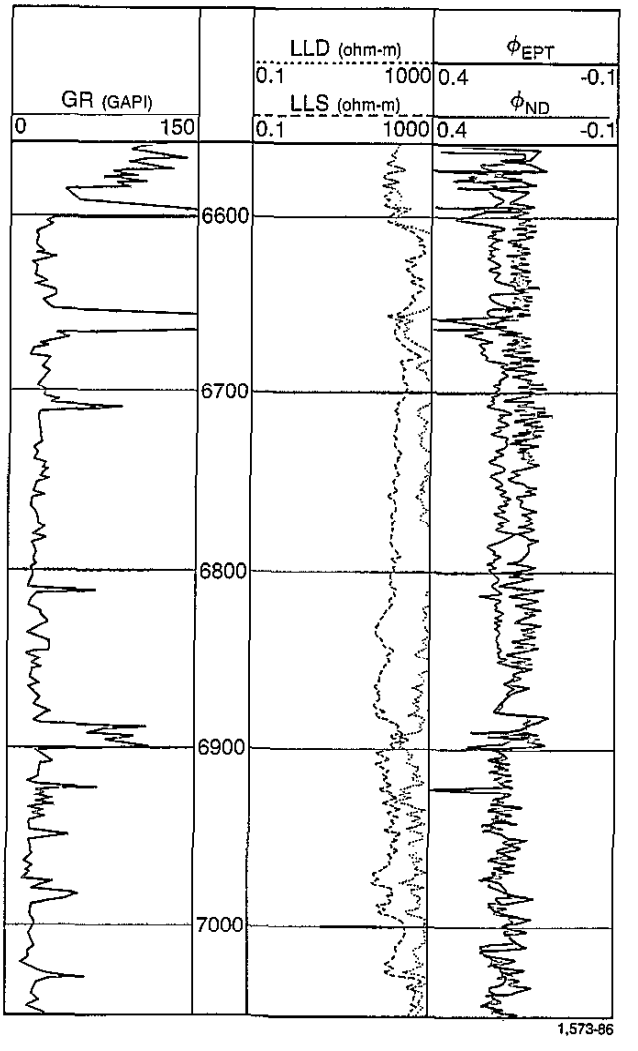

Fig. 9-8—Hydrocarbon detection in fresh water.

$$t_{pma} = t_{pma1} V_1 + t_{pma2} V_2 + t_{pma3} V_3, \qquad \text{(Eq. 9-15)}$$

where t_{pma1} and V_1 are the propagation time and the volumetric proportion of each mineral.

The Cyberlook* wellsite computation program computes the water volume from the EPT measurement using the t_{po} method and gives the amount of moved hydrocarbon (Fig. 9-10). The EPT measurements are used in advanced computer programs for determining accurate S_{xo} values, for improving clay and lithology determinations, and for analyzing laminated and thin beds.

ENDFIRE ARRAY

The ADEPT endfire array is less affected than a conventional antenna system by hole roughness and tool standoff from mudcake or other sources. This is clearly demonstrated by the example log through an interval of irregular borehole (Fig. 9-11).

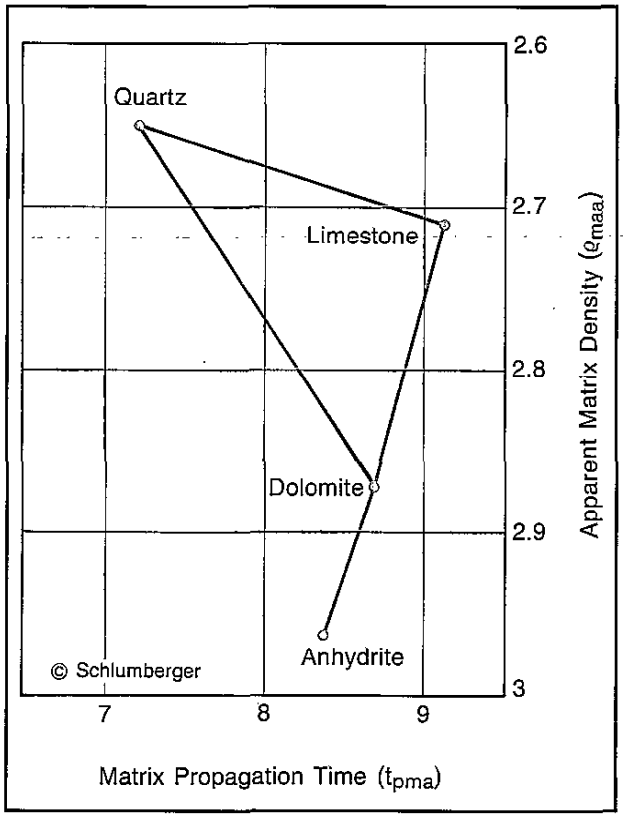

Fig. 9-9—Determination of EPT matrix propagation time.

The endfire propagation time, TPPW, gives a more nearly correct response than the conventional antenna's propagation time recording (TPL).

The logs of Fig. 9-12 illustrate the depth of investigation and standoff features of the ADEPT endfire array in a well in Kern County, California. The field is under steam injection, and formation water resistivity is high. Gas has broken out of solution in the top of zones A, B, and C. Zones D and E contain only liquid.

Agreement between the EPT-D and the ADEPT tool is good in shales and in zone E, which is water-bearing. However, in the other zones the EPT-D is adversely affected by invading mud filtrate. Saturations calculated from the EPT-D measurements averaged 65%, whereas those from the ADEPT tool ranged around 50%. The interpretations were confirmed by sidewall core analysis.

BROADSIDE ARRAY

The microwave signal is progressively attenuated as water salinity increases. When attenuation is too great, detection will be difficult. The ADEPT tool allows use of an optional short-spacing broadside array which extends the effective operating range.

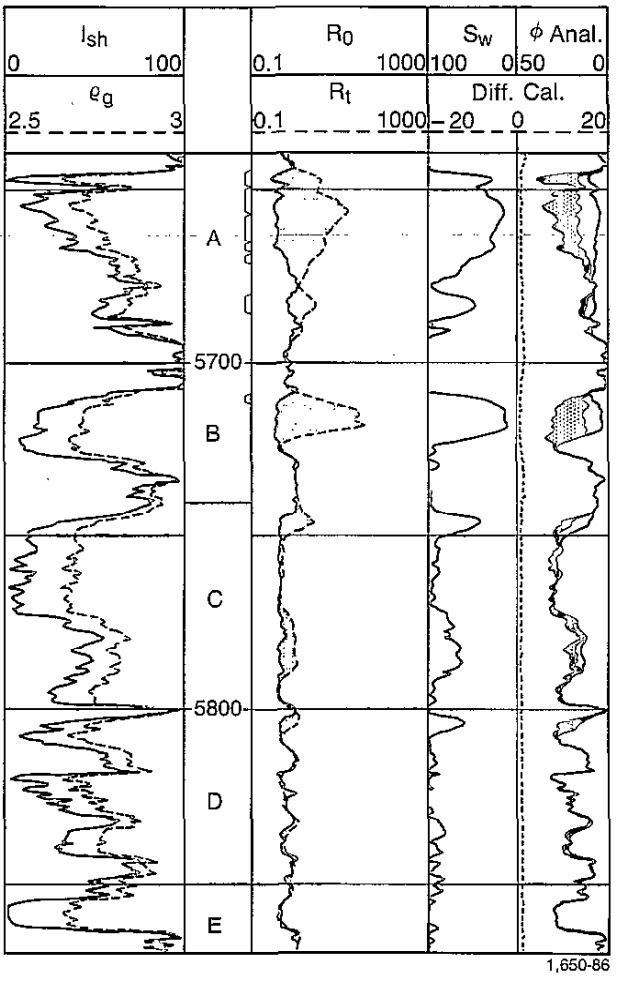

Fig. 9-10—Cyberlook computation using EPT data for movable-oil indication.

The well in Fig. 9-13 contained salt mud in the borehole, resulting in high attenuation levels averaging 700 dB/m. The zone above 114 m had low porosity. The lower section contained high porosity. Both the t_{pl} and the A readings from the EPT-D are not usable in this zone.

Use of the broadside array allowed an acceptable log, shown by the solid curve output TPPW (Time of Propagation, Plane Wave: the broadside array's propagation time).

DEEP PROPAGATION TOOL (DPT)

The DPT tool is a deep-investigating device which may be run in combination with the shallow-investigation Electromagnetic Propagation Tool. As with the EPT tool, an electromagnetic wave is launched from a transmitting antenna and its signal level and relative phase are measured at axially spaced receivers. These measurements are then transformed into attenuations and phase shifts. (For the EPT tool, the measured

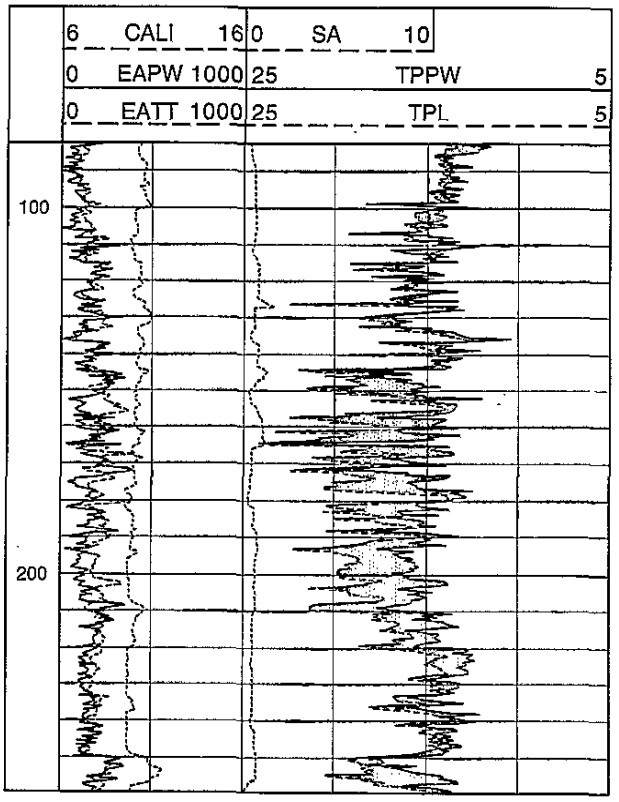

Fig. 9-11—Endfire and conventional array comparison in bad hole.

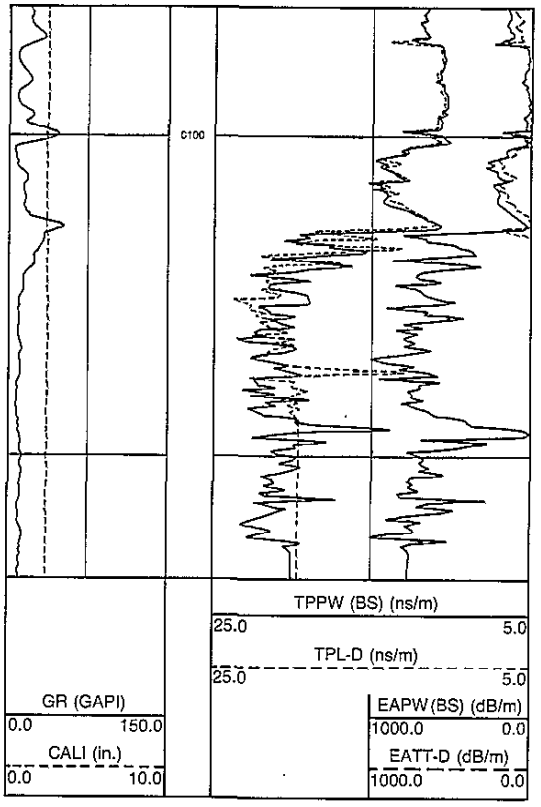

Fig. 9-13—High porosity and salt mud produces high attenuation, but the broadside array gives a useable log.

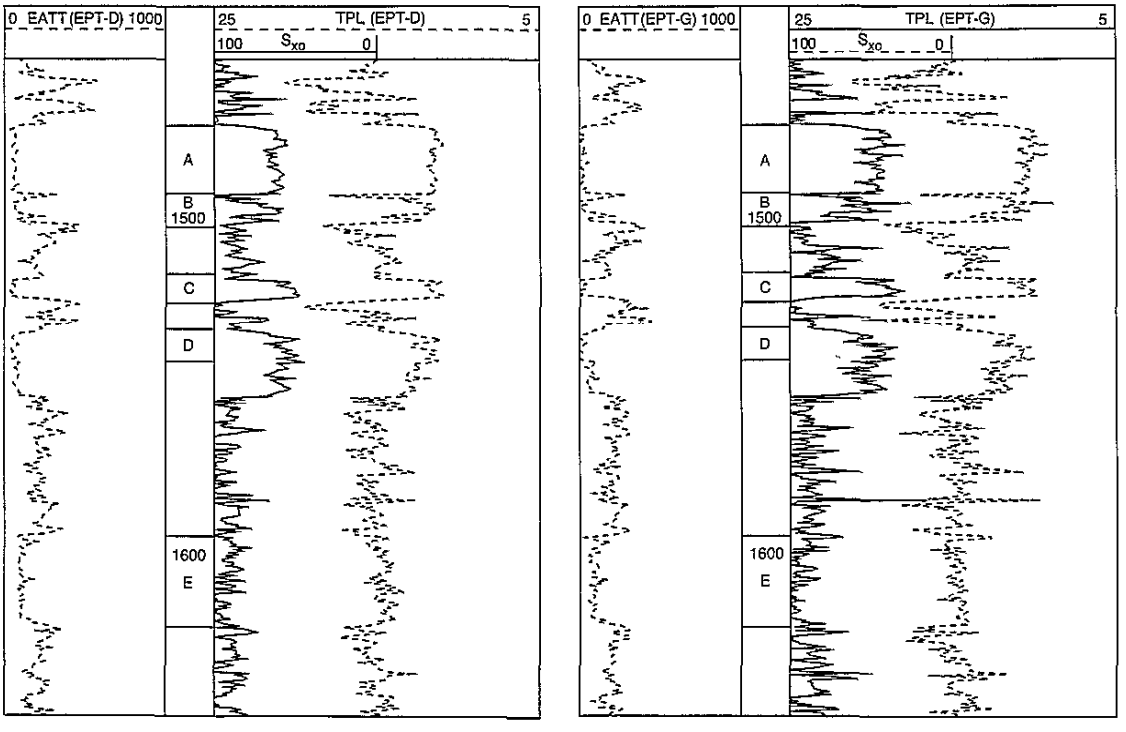

Fig. 9-12—Comparison of EPT-D and the ADEPT tool demonstrates the endfire array's improved depth of investigation.

propagation time is in reality also a phase shift measurement.) The computed attenuations and phase shifts can be used to determine the dielectric constant and resistivity of the formation. As measured by the DPT, these parameters will generally represent the undisturbed formation far away from the borehole.

The tool is a mandrel device. Its operating frequency of 25 MHz is about midway between that of the standard induction tools (20 kHz) and the EPT tool (1.1 GHz). It has one transmitting loop antenna, which radiates electromagnetic energy into the formation surrounding the borehole. Four receivers, also loop antennas, are located at staggered distances above the transmitting antenna (Fig. 9-14).

The receivers are grouped in two pairs (the "far" pair and the "near" pair); the signal attenuations and phase shifts between the two receivers of each pair are recorded. These attenuations and phase shifts are then used to compute, through Eq. 9-1, the apparent formation dielectric constant and apparent formation resistivity. Fig. 9-15 graphically illustrates the solution.

Depending on the signal origin, several computations of dielectric constant and resistivity are made. These are:

- The DPT "near" measurements, which use the near pair attenuation and phase shift.
- The DPT "far" measurements, which use the far pair attenuation and phase shift.
- The DPT "cross" measurements, which use the near pair attenuation and the far pair phase shift.
- The DPT "deep" measurements, which use a combination of attenuations and phase shifts from both receiver pairs.

The near measurement is the shallowest, followed by the far, and then the cross or the deep. These curves correctly indicate the invasion profile. Generally, the cross, far, and deep are rather similar. Since their accuracy starts to degrade when they separate, a comparison of the three provides a built-in quality control.

Environmental Effects

The receiver spacings and operating frequency for the DPT tool were chosen to be as sensitive as possible to the virgin, noninvaded formation parameters of dielectric constant and resistivity, over a large range of mud and formation resistivities. Unfortunately, the depth of investigation cannot be characterized in a simple fashion. It depends on the characteristics of both the virgin and invaded zones. Typical depths of investigations (diameters) are:

	$R_t > R_{xo}$	$R_t < R_{xo}$
Near	25 in.	20 in.
Far	45 in.	30 in.

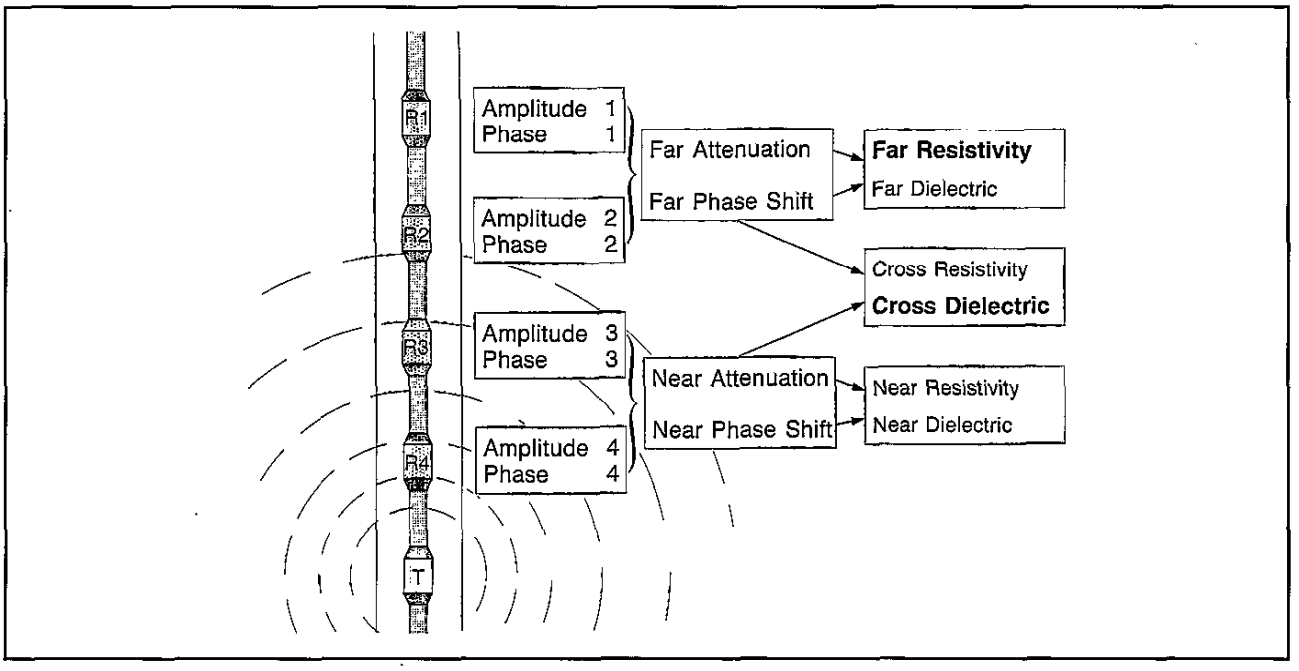

Fig. 9-14—Deep propagation tool.

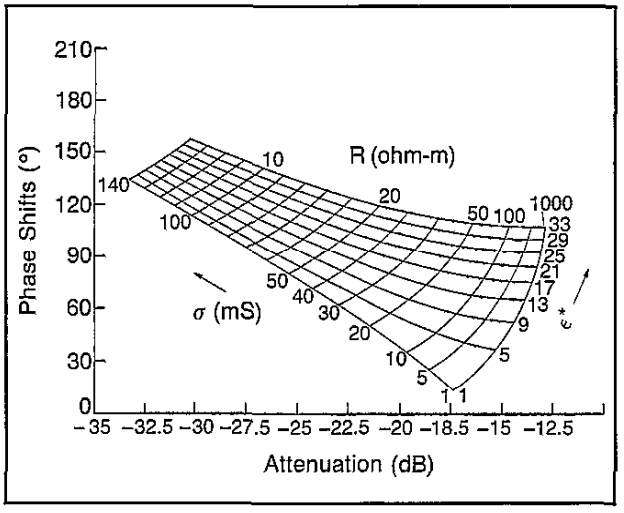

Fig. 9-15—DPT phase shift/attenuation to epsilon/sigma conversion chart.

Both mud and formation resistivities limit the tool's use. The lower the mud or formation resistivity, the lower are the received signal levels. In addition, the lower the formation resistivity, the less resolution there is in the measurement of dielectric constant. Acceptable accuracy is obtained in muds of 0.2-ohm-m resistivity or greater and in formations of 10-ohm-m resistivity or greater and in 8-in.-diameter boreholes. If there is little invasion, an acceptable dielectric constant measurement can be obtained in 0.1-ohm-m muds and 3-ohm-m formations using the near receivers. In this case, the resistivity measurement is accurate to 1 ohm-m.

Qualitative results can be obtained in beds 4 ft thick; for quantitative applications, bed thicknesses of 8 ft are required.

Interpretation Methods

The dielectric constant is, in fact, a quantity that is frequency dependent. The same also applies to conductivity. Dielectric constant increases when the frequency is decreased (Fig. 9-16). Conversely, conductivity decreases with decreasing frequency. "Dispersion" is the term used to describe these changes with frequency in the dielectric constant and conductivity. Dispersion also appears to be a function of salinity (e.g., in a water-saturated rock, dispersion increases as formation water resistivity, R_w, decreases).

Interpretation of the DPT dielectric constant measurement therefore requires that the technique accommodate dispersion and changes in dispersion. Two groups of DPT interpretation techniques have evolved. One assumes dispersion remains relatively constant; the other accommodates changes.

t_{po} Modified Method

The t_{po} modified method of DPT interpretation is applicable in constant-salinity or freshwater environments. It uses only the dielectric constant measurement of the DPT tool.

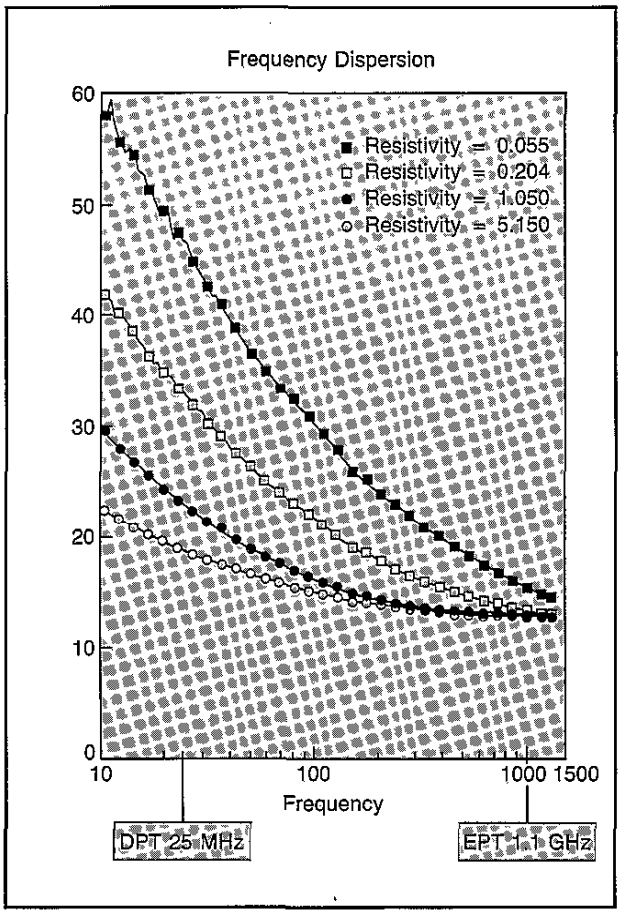

Fig. 9-16—Laboratory measurements of dielectric permittivity at different frequencies, on a single core sample saturated with water of four different salinities. This increase from the respective high and low frequency limits is termed "frequency dispersion".

$$\sqrt{\epsilon_{DPT}} = \phi S_w \sqrt{\epsilon_w^{\,p}} + \phi\,(1 - S_w)\sqrt{\epsilon_h} + (1 - \phi)\sqrt{\epsilon_{ma}}\,, \qquad \text{(Eq. 9-16)}$$

where

ϵ is the dielectric constant

and

p is a polarization exponent.

The subscripts, *DPT, w, h,* and *ma* refer to the DPT measurement, formation water, hydrocarbon, and matrix, respectively.

The physical significance of p is rather vague, but it characterizes in one term a number of possible dispersion causes, such as rock texture and fluid salinity. An unsatisfactory aspect of Eq. 9-16 is that, at 100% porosity, it does not predict the correct value for the dielectric constant of water. The equation is valid only over the range of most typical reservoir porosities, 0-40%.

The exponent p can be estimated from Fig. 9-15 as a function of water resistivity. A better method is to solve Eq. 9-16 for p in a clean, water-bearing formation where water salinity is constant. Fig. 9-18 shows a crossplot of ϵ_{EPT} versus ϕ for a series of clean, water-bearing sands. Lines of constant p (from Eq. 9-16 for $\epsilon_w = 68$ and $\epsilon_{ma} = 4.7$) are superimposed. The plot suggests a value of 1.09 for p in this well. (That is slightly greater than the value suggested by Fig. 9-17.)

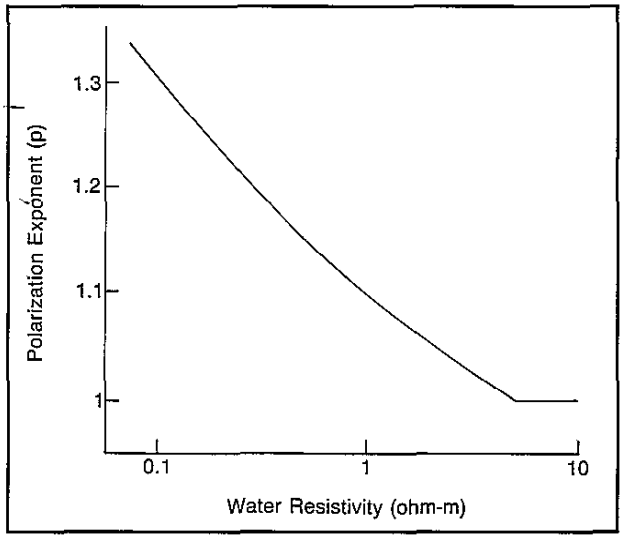

Fig. 9-17—Water resistivity vs. polarization exponent.

Dual Water t_{po} Modified Method

Dispersion is even greater in shales than in sands or carbonates. Laboratory core measurements show a relationship between dispersion and cation exchange capacity. From log data, dispersion appears to be a linear function of the volume of clay, V_{cl}. These observations led to the development of the dual water t_{po} modified method of DPT interpretation.

$$\sqrt{\epsilon_{DPT}} = \phi_t \left[(S_{wt} - S_{wb}) \sqrt{\epsilon_w^{\,p}} + (1 - S_{wt}) \sqrt{\epsilon_h} + S_{wb} \sqrt{\epsilon_{wb}^{\,p_b}} \right] + (1 - \phi_t) \left[(1 - S_{wb}) \sqrt{\epsilon_{ma}} + S_{wb} \sqrt{\epsilon_{dcl}} \right], \quad \text{(Eq. 9-17)}$$

where the terms are as defined in Eq. 9-16 and the additional subscripts *wt*, *wb*, and *dcl* refer to total water, bound water, and clay, respectively. p_b is the polarization exponent associated with the bound (to shale) water. The use of the bound water term is essentially a convenient manner with which to apply a shale correction. It would not be expected that bound water would have a particularly large susceptibility to polarization.

Both p and p_b can be determined by solving Eq. 9-17; in clean, water-bearing formations for p, and in shales for p_b. If a continuous computation of Eq. 9-17 is made, assuming all formations are water bearing (sands and shales), for an apparent polarization exponent, p_a, then the p_a found in water-bearing sands is p and the p_a found in shales is p_b. Fig. 9-19 is such an example (computed p_a shown in Track 1). p is indicated to be 1.07 and p_b is indicated to be 1.4.

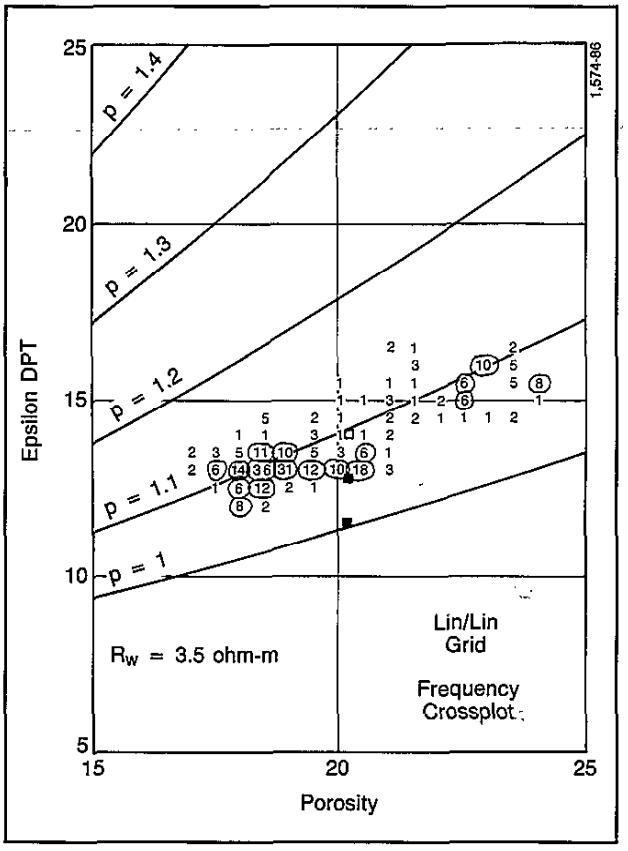

Fig. 9-18—Log data from a constant salinity water-wet sandstone section in Australia, showing p's independence to porosity changes.

Eq. 9-17 is also the basis of a wellsite interpretation. Fig. 9-19 is Pass 1 of that program. It is used to select p and p_b. Fig. 9-20 is the final Pass 2 of the interpretation. It is perfectly analogous with the wellsite Cyberlook program for conventional resistivity logs. An ϵ_0 curve (rock dielectric constant as if it were 100% water wet) is presented for comparison with the ϵ_{DPT} dielectric constant measurement. When ϵ_{DPT} is less than ϵ_0, hydrocarbon saturation is indicated.

The p_a Versus R_{fa} Plot

A plot of the apparent polarization exponent versus the apparent fluid resistivity, R_{fa}, (from Fig. 9-17, for example) gives a good approximation to a straight line graduated in bound water saturation, S_{wb}, when plotted on a log/log grid. The relationship for the apparent fluid resistivity is

$$R_{fa} = \frac{\phi_t^2 R_t}{0.81}, \quad \text{(Eq. 9-18)}$$

where R_t can be true resistivity from the deep laterolog, deep induction, or even the DPT tool.

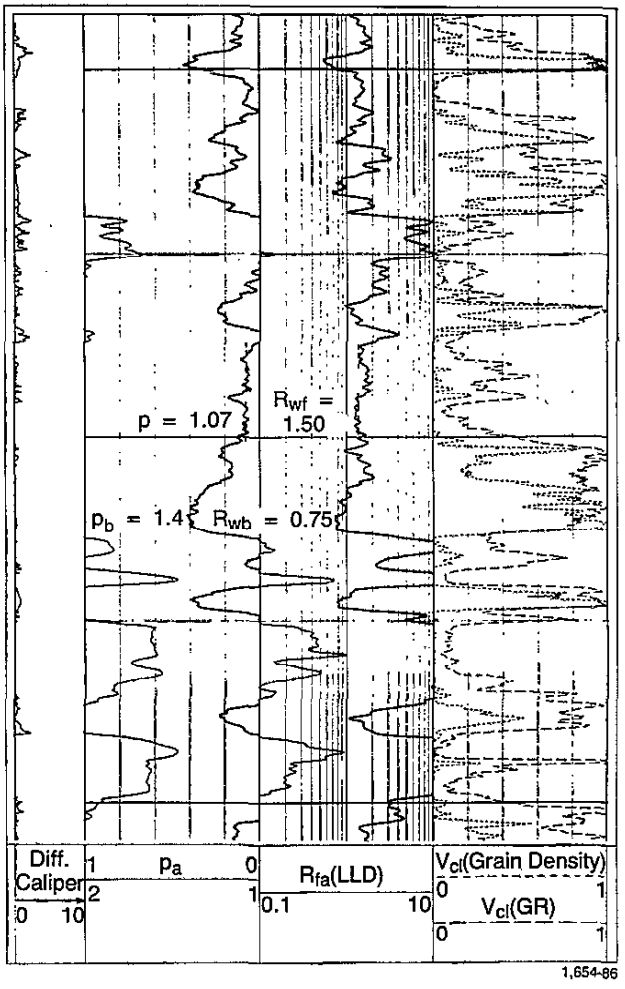

Fig. 9-19—CSU wellsite interpretation of a sand/shale series in Nigeria, first pass.

Fig. 9-21 shows an example plot. Shales, clean, water-bearing sands, and hydrocarbon-bearing sands are clearly delineated.

Other implications of this technique, which requires only the input of the DPT and porosity data (a conventional resistivity measurement can also be used), are that a water zone is not needed to normalize the interpretation (i.e., determined p) and that changes in zone-by-zone water salinity can be recognized. However, level-by-level salinity changes, such as those encountered in waterflood situations, cannot be handled.

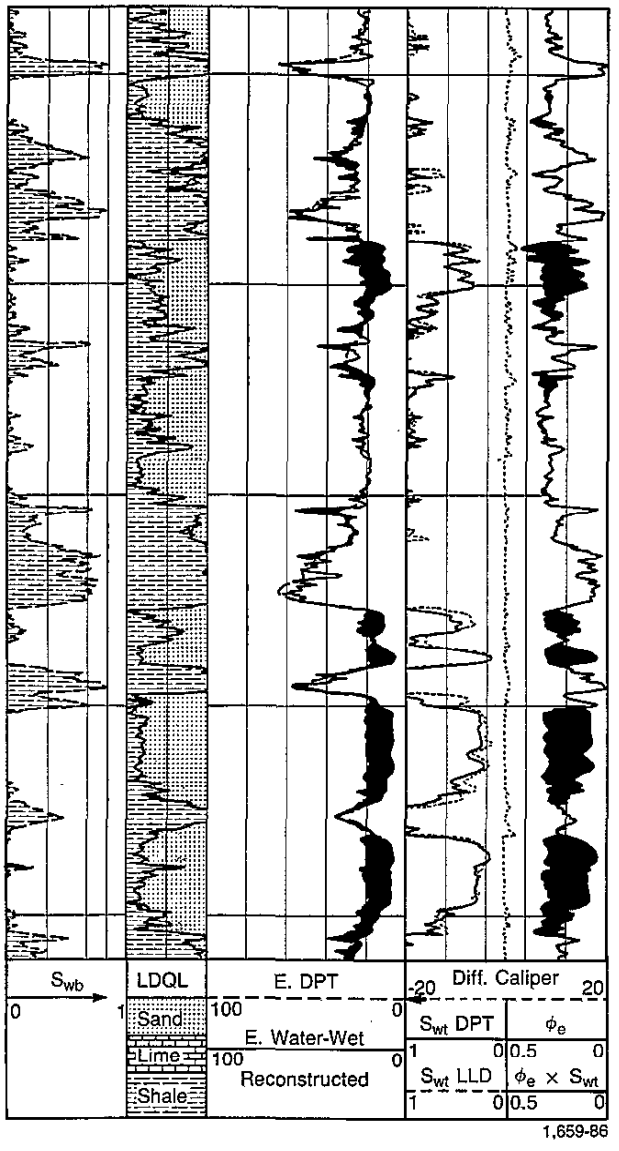

Fig. 9-20—CSU wellsite interpretation of a sand/shale series in Nigeria, second pass.

Dual Saturation Method

In constant-salinity or freshwater environments, the dual water t_{po} modified method gives valid water saturation information. However, the evaluation of the polarization exponent becomes quite difficult when variable-salinity, fresh-to-brackish water environments are encountered. To handle the situation of variable salinities, the dual saturation method of DPT interpretation can be used.

If a low-frequency resistivity measurement is available (usually the deep induction or deep laterolog) these three

simplified equations can be defined:

$$\sqrt{\epsilon_{DPT}} = \phi_t \left[S_{wt} \sqrt{\epsilon_w^{p_a}} + (1 - S_{wt}) \sqrt{\epsilon_h}\right] + (1 - \phi_t) \sqrt{\epsilon_{ma}}\,, \qquad \text{(Eq. 9-19a)}$$

$$S_{wt}^2 = \frac{0.81\, R_{fa}}{\phi_t^2\, R_t}\,, \qquad \text{(Eq. 9-19b)}$$

$$\log p_a = \text{"Gradient"}\ [\text{"Log Intercept"} - \log R_{fa}], \qquad \text{(Eq. 9-19c)}$$

where all terms are as defined in Eqs. 9-16, -17, and -18. In Eq. 9-19b, R_t and R_{fa} values are from the deep induction or deep laterolog. R_{fa} and p_a are as if the formation were water wet.

In Eq. 9-19c, the "Gradient" and "Log Intercept" values must be known from experience in the area or be derived from a continuous computation of Eq. 9-16 or -17.

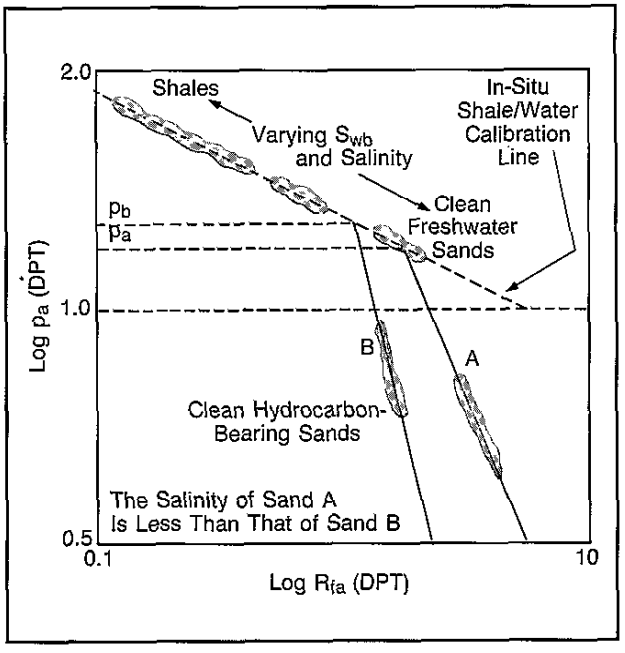

Fig. 9-21—Cartoon showing the model for the p_a/R_{fa} extrapolation technique.

Thus, there are three unknowns in the equations of Eq. 9-19 (S_{wt}, p_a, and R_{fa}). These can be solved simultaneously by varying the salinity in the p_a/R_{fa} relationship (Eq. 9-19c) until a balance in the two saturation equations is achieved.

Fig. 9-22 is a heavy oil example. In Track 2 the simultaneous solutions to p_a, R_{fa}, and S_{wtDual} have been plotted. In addition, S_{wtDPT} obtained by using the DPT t_{po} modified method and S_{wtLLD} obtained from a conventional dual laterolog are also shown. In the lower water zones, all three interpretations show 100% water. In the middle hydrocarbon sands with constant R_w, all three interpretations show the same S_{wt} of 40-60%. Their agreement implies that the salinity of the water associated with the hydrocarbon is the same as that in the lower water sands.

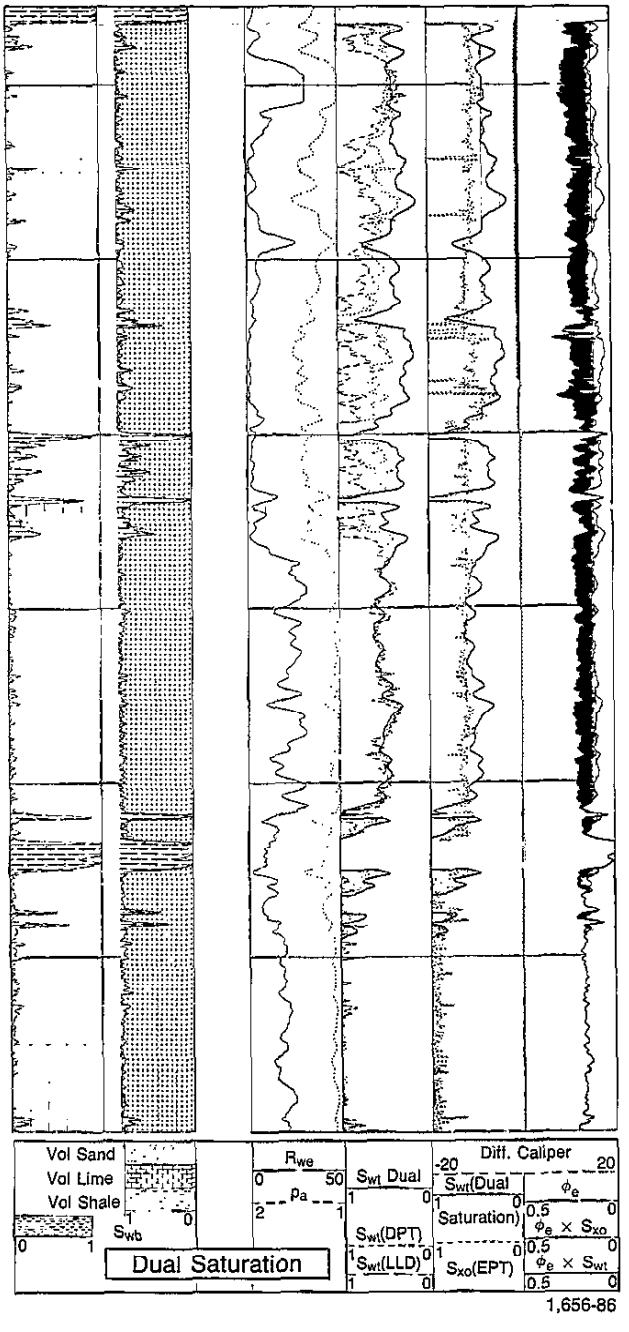

Fig. 9-22—Quantitative interpretation from Colombia, with the Dual Saturation approach, in varying salinity conditions.

The low R_{fa} and high p_a indicate the upper hydrocarbon sands to be of varying and higher fluid salnity. The S_{wt} obtained from the t_{po} modified method is superior to that obtained from the laterolog resistivity because it is less dependent on fluid salinity (i.e., dielectric constant is much less sensitive to salinity than is resistivity). The S_{wt} from the t_{po} modified method is always less than or equal to S_{xo} from the EPT interpretation. This is not always the case with the S_{wtLLD}. However, the S_{wtDPT} obtained with the dual saturation method is probably the closest to reality; the variations in fluid salinity were in accordance with other field data.

TOOL SPECIFICATIONS AND LIMITATIONS

The EPT tool provides simultaneous recording of propagation time and attenuation of a 1.1 GHz electromagnetic wave, hole diameter (long arm and short arm), and Microlog. The DPT tool is used to derive both resistivity and dielectric constant from the phase and attenuation measurements of a 25 MHz wave. Table 9-2 is a summary of tool specifications and limitations. Figure 9-23 provides a sketch of each downhole tool.

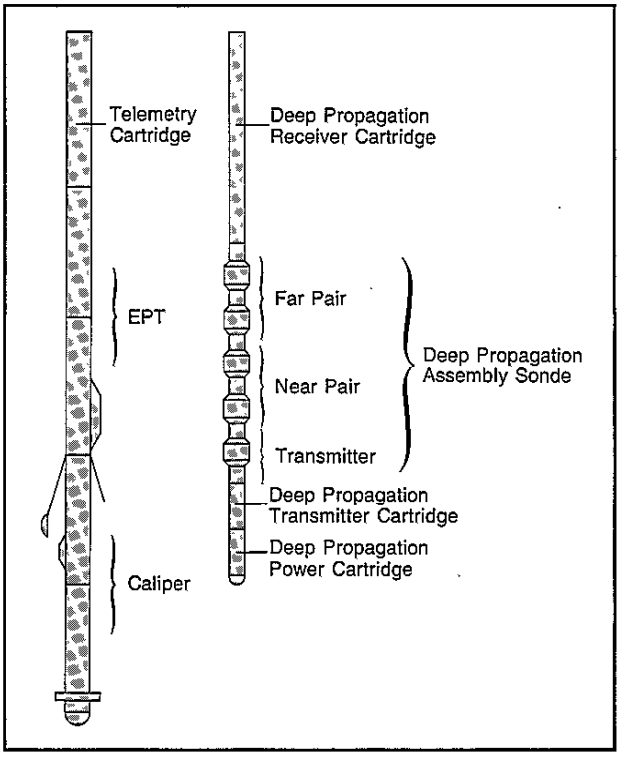

Fig. 9-23—Schematic of the EPT (left) and DPT (right).

Table 9-2

	EPT	DPT
Combinable with	DPT, AMS, CNT, LDT, NGT, SGT, DITE, SDT, PCD	EPT, CNT, LDT
Length	48 ft	28.5 ft
Outside diameter (max.)	4.5 in. (no Microlog) 5.875 in. with slim Microlog 6.875 in. with Microlog	4.5 in.
Logging speed	1800 ft/hr	3600 ft/hr
Sampling rate	6.0, 2.0, 1.2, 0.4 in.	6.0 in.
Vertical resolution	< 2 in.	8 ft
Approximate operating limit	EPTD - 1000 db/m Endfire - 680 db/m Broadside - 1250 db/m	R_m > 0.1 ohm-m (near) R_m> 0.2 ohm-m (far) R_t > 3 ohm-m (near) R_t>10 ohm-m (far)

REFERENCES

1. Calvert, T.J., Rau, R.N., Wells, L.E.: "Electromagnetic Propagation — A New Dimension in Logging," paper SPE 6542 presented at the 1977 SPE California Regional Meeting.
2. Wharton, R.P., Hazen, G.A., Rau, R.N., and Best, D.L.: "Electromagnetic Propagation Logging Advances in Technique and Interpretation," paper SPE 9267 presented at the 1980 SPE Annual Technical Conference and Exhibition.
3. Sen, P.N.: "The Dielectric and Conductivity Response of Sedimentary Rocks," paper SPE 9379 presented at the 1980 SPE Annual Technical Conference and Exhibition.
4. Rau, R.N. and Wharton, R.P.: "Measurement of Core Electrical Parameters at UHF and Microwave Frequencies," paper SPE 9380 presented at the 1980 SPE Annual Technical Conference and Exhibition.
5. Johnson, R. and Evans, C.J.: "Results of Recent Electromagnetic Propagation Time Logging in the North Sea," *Trans.*, 1983 SPWLA European Formation Evaluation Symposium.
6. Wharton, R.P. and Delano, J.M.: "An EPT Interpretation Procedure and Application in Fresh Water, Shaly, Oil Sands," *Trans.*, 1981 SPWLA Annual Logging Symposium.
7. Eck, M.E. and Powell, D.E.: "Application of Electromagnetic Propagation Logging in the Permian Basin of West Texas," paper SPE 12183 presented at the 1983 SPE Annual Technical Conference and Exhibition.
8. Huchital, G.S., Hutin, R; Thoraval, Y., and Clark, B.: "The Deep Propagation Tool (A New Electromagnetic Logging Tool)," paper SPE 10988 presented at the 1981 SPE Annual Technical Conference and Exhibition.
9. Kenyon, W.E. and Baker, P.L.: "EPT Interpretation in Carbonates Drilled With Salt Muds," paper SPE 13192 presented at the 1984 SPE Annual Technical Conference and Exhibition.
10. Cox, P.T. and Warren, W.F.: "Development and Testing of the Texaco Dielectric Log," *Trans.*, 1983 SPWLA Annual Logging Symposium.
11. Meador, R.A. and Cox, P.T.: "Dielectric Constant Logging: A Salinity Independent Estimation of Formation Water Volume," paper SPE 5504 presented at the 1975 SPE Annual Technical Conference and Exhibition.
12. Cheruvier, E. and Suau, J.: "Applications of Micro-Wave Dielectric Measurements in Various Logging Environments," *Trans.*, 1986 SPWLA Annual Logging Symposium.
13. Besson, C., Blenkinsop, M., and Trouiller, J.C.: "Environmental Effects on Deep Electromagnetic Logging Tools," *Trans.*, 1986 SPWLA Annual Logging Symposium.
14. Clavier, C., Blenkinsop, M., Baker. P., Kenyon, W., and des-Ligneris, S.: "Deep Electromagnetic Propagation Tool Interpretation," *Trans.*, 1986 SPWLA Annual Logging Symposium.
15. Allen, D.F.: "Laminated Sand Analysis," *Trans.*, 1984 SPWLA Annual Logging Symposium.
16. *Log Interpretation Charts*, Schlumberger Well Services, Houston (1989).
17. Blenkinsop, M., and Baker, P.: "Deep Electromagnetic Propagation Tool Interpretation," SPWLA Annual Symposium, 1986.
18. Cheruvier, E., and Suau, J.: "Applications of Microwave Dielectric Measurements in Various Logging Environments," SPWLA Annual Symposium, 1986.
19. Ellis, D.V.: *Well Logging for Earth Scientists*, Elsevier (1987).
20. Freedman, R., and Grove, G.: "Interpretation of EPT-G Logs in the Presence of Mudcakes," SPE Annual Meeting, 1988.
21. Buller, D., Kenyon, W., Rasmus, J., and Miller, S.: "Evaluating Porosity and Producibility in Oomoldic Carbonates," *The Technical Review* (July 1987) **35**, 3, 14-18.

10 Permeability and Productivity

PERMEABILITY

Permeability is a measure of the ease with which a formation permits a fluid to flow through it. To be permeable, a rock must have interconnected porosity (pores, vugs, capillaries, fissures, or fractures). Greater porosity usually corresponds to greater permeability, but this is not always the case. Pore size, shape, and continuity, as well as the amount of porosity, influence formation permeability.

Some fine-grained sands can have high interconnected porosity, although the individual pores and pore channels are quite small. As a result, the paths available through the narrow pores for the movement of fluid are quite restricted and tortuous; the permeabilities of very fine-grained formations may therefore be quite low.

Shales and clays, which are composed of exceedingly fine-grained particles, often exhibit very high porosity. However, because the pores and pore channels are equally small, most shales and clays exhibit, for all practical purposes, zero permeability.

Other formations, such as limestone, may be composed of a dense rock broken by a few small fissures of great extent. The porosity of the dense formation would surely be very low, but the permeability of a fissure can be enormous. Fissured limestones may thus have very low porosities, but high permeabilities.

The permeability of a given rock to the flow of a single homogeneous fluid is a constant, provided the fluid does not interact with the rock. Permeability determined for a single homogeneous liquid is called absolute, or intrinsic, permeability (k). Permeability measurements made using air or gas must be corrected for "slippage" effects, to equivalent liquid permeability, by using the Klinkenberg corrections.

The unit of permeability is the darcy. One darcy is that permeability which will allow the flow of one cubic centimeter per second of a fluid of one centipoise viscosity through a cross-sectional area of one square centimeter under a pressure gradient of one atmosphere per centimeter. A darcy is a very large unit so, in practice, the millidarcy (md) is the unit commonly used.

The range of permeabilities of producing formations is extremely wide — from less than 0.1 md to over 10,000 md. The lower limit of permeability for a commercial well depends on several factors: thickness of pay, whether production is oil or gas, hydrocarbon viscosity, formation pressure, water saturation, value (price) of the oil or gas, well depth, etc.

When two or more immiscible fluids (e.g., oil and water) are present in the formation their flows interfere. The effective permeability to oil flow (k_o) or water flow (k_w) is therefore reduced. Furthermore, the summation of effective permeabilities is always less than or equal to the absolute permeability (k). The effective permeabilities depend not only on the rock itself but also on the relative amounts and properties of the different fluids in the pores. In a given rock, k_o and k_w will vary as the oil and water saturations, S_o and S_w, vary.

Relative permeabilities are the ratios of the effective permeabilities to the absolute (single homogeneous fluid) permeability. Thus, for an oil-water system the relative permeability to water, k_{rw}, is equal to k_w/k; similarly, the relative permeability for oil, k_{ro}, is equal to k_o/k. It is apparent that relative permeabilities are usually expressed in percent or fractions and never exceed unity (1 or 100%).

Fig. 10-1 shows illustrative relative-permeability curves for a water-wet formation containing only oil and water. The values of k_{rw} and k_{ro} vary with the saturation. Complementary scales of S_w and S_o are shown at the bottom of the figure. The curves illustrate that at high oil saturation k_{ro} is large and k_{rw} is small; the oil flows easily and little water flows. At high water saturations k_{ro} is small and k_{rw} is large; now the water flows easily and little oil flows. The shapes of the relative permeability diagrams depend on the formation and pore characteristics and on the fluids present (water, oil, gas).

Most formations exhibit some directional permeability or permeability anisotropy. This is usually caused by layers of very fine-grained material, such as clay. The horizontal permeability (parallel to the bedding layers) is normally higher than the vertical permeability in non-fractured reservoirs.

Irreducible Saturations

When the k_{ro} value reaches zero, the oil remaining in the pore space is immovable; the corresponding value of oil saturation at which this occurs is the residual oil saturation (S_{or}).

The k_{rw} curve also becomes zero at an S_w value indicated on Fig. 10-1 as S_{wmin}. At this saturation only oil flows in the formation and the residual water is immobile. In a water-wet formation there is always a certain amount of water held in the pores by capillary forces. This water cannot be displaced by oil at pressures encountered in formations so the water saturation does not reach zero.

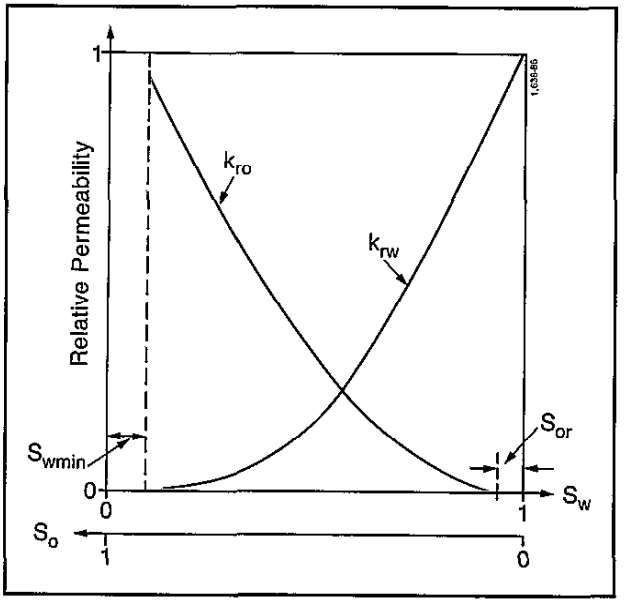

Fig. 10-1—Relative permeability vs. saturation (illustrative curves).

S_{wmin} is usually referred to as the irreducible water saturation, S_{wi}. S_{wi} is a function of both porosity and permeability. For most reservoir rocks, S_{wi} ranges from less than 10% to more than 50%.

When oil is produced from a formation, the relative amounts of oil and water produced at a given level will depend on the relative permeabilities at the given condition of saturation. As oil is produced and water saturation increases, a time will occur when some water will start being produced with the oil. As the level is further produced, more and more water will be produced.

The Transition Zone - Capillary Pressure Effects

In a thick reservoir that contains both water and hydrocarbon columns, the saturation may vary from 100% water at the bottom of the zone to a maximum oil saturation (and irreducible water saturation) at the top. There is a gradual transition between these two extremes in saturation. The transition interval may be very short for porous and permeable formations, or it may be quite long in formations of low permeability.

When both oil and water are present in the rock pores, the water, being the wetting phase, coats the pore walls and fills the smaller pore channels. The oil tends to accumulate in globules in the larger pores. The surface tension of the interface between water and oil causes the pressure within the oil globules to be greater than in the water. This difference in pressure is equal to the capillary pressure. Capillary pressure is a function of the elevation above the free water level and the difference in densities of the wetting (water) and nonwetting (oil) phases. The relationship is

$$P_c = \frac{h\,(\varrho_w - \varrho_o)}{2.3}, \qquad \text{(Eq. 10-1)}$$

where P_c is capillary pressure (psi), h is free water level (ft), and ϱ_w and ϱ_o are density of water and oil (g/cm^3), respectively.

The relation between the capillary pressure and the fraction of the pore space containing oil or gas depends on the pore size and the pore-size distribution within the rock and the nature of the fluids involved.

Fig. 10-2 shows typical capillary pressure curves for a series of rocks of different permeabilities. If the densities of the water and hydrocarbon are known, Eq. 10-1 can be used to transform the ordinate from capillary pressure to elevation above the free-water level, or vice versa.

The shape of the capillary pressure curve is related to porosity, ϕ, and permeability by the relationship

$$P_c = \sigma\,(\phi/k)^{1/2} J, \qquad \text{(Eq. 10-2)}$$

where J is a function of S_w that determines the basic shape of the $P_c - S_w$ plot, σ is the interfacial tension, and ϕ/k is the porosity-permeability ratio. The dependence of the capillary pressure curves on permeability is illustrated in Fig. 10-2.

Permeability From Resistivity Gradients

As a consequence of the decrease of S_w with height above the water table, there is an increase in formation resistivity. Assuming homogeneous porosity, formation resistivity increases from R_0 at the water table to a maximum R_t value in the zone of irreducible water saturation. It has been observed that this resistivity transition is linear with depth. The value of the resistivity gradient has been

used to estimate the order of magnitude of formation permeability. Chart K-1 relates resistivity gradient in ohm-m per foot of depth ($\Delta R/\Delta D$) to permeability as a function of oil gravity, water density, and R_0. The chart uses the equation:

$$K = C\left(a \times \frac{2.3}{\varrho_w - \varrho_h}\right)^2, \qquad \text{(Eq. 10-3a)}$$

$$a = \frac{\Delta R}{\Delta D} \times \frac{1}{R_0}, \qquad \text{(Eq. 10-3b)}$$

where

C is a constant, normally about 20,

ΔR is the change in resistivity (ohm-m),

ΔD is the change in depth corresponding to ΔR (ft),

R_0 is the 100% water-saturated formation resistivity (ohm-m),

ϱ_w is formation water density (g/cm^3),

and

ϱ_h is hydrocarbon density (g/cm^3).

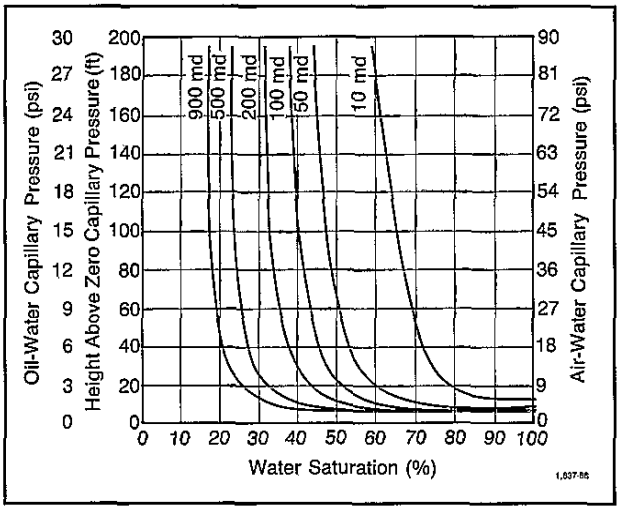

Fig. 10-2—Series of capillary pressure curves as a function of permeability.

Permeability Estimates From ϕ and S_{wi}

In many cases, there may exist relationships between the values of porosity and permeability, but such correlations usually are empirically derived for a given formation in a given area. They do not exhibit general application or validity. A more general empirical relationship, proposed by Wyllie and Rose, incorporates irreducible water saturation and has the form $k = C\phi^x/(S_{wi})^y$. The basis of the relationship is clearly illustrated on Fig. 10-2 by the correlation between permeability and irreducible water saturation. The dependency of permeability on porosity is not evident from this data, however.

Based on the general expression of Wyllie and Rose, several investigators have proposed various empirical relationships with which permeability can be estimated from porosity and irreducible water saturation derived from well logs:

Tixier

$$k^{1/2} = 250\,\frac{\phi^3}{S_{wi}}, \qquad \text{(Eq. 10-4a)}$$

Timur

$$k^{1/2} = 100\,\frac{\phi^{2.25}}{S_{wi}}, \qquad \text{(Eq. 10-4b)}$$

Coates-Dumanoir

$$k^{1/2} = \frac{300}{w^4}\,\frac{\phi^w}{S_{wi}^w}, \qquad \text{(Eq. 10-4c)}$$

Coates

$$k^{1/2} = 70\,\frac{\phi_e^2\,(1 - S_{wi})}{S_{wi}}, \qquad \text{(Eq. 10-4d)}$$

where

k is permeability (in md),

ϕ is porosity,

S_{wi} is irreducible water saturation,

and

w is a textural parameter related to the cementation and saturation exponents, $w \sim m \sim n$.

Fig. 10-3 plots these four relationships. Chart K-3 is the solution of Eq. 10-4b and Chart K-4 is the solution of Eq. 10-4d. All the relationships are based on intergranular porosity data. For this reason, their application is usually restricted to sandstones; it need not be.

To use these charts, ϕ and S_{wi} are entered. Their intersection defines the intrinsic (absolute) rock permeability.

A medium-gravity oil is also assumed. If the saturating hydrocarbon is other than a medium-gravity oil, a correction factor based on fluid densities, ϱ_w and ϱ_h, and elevation above the free water level, h, should be applied to S_{wi} before entering Chart K-3 or Chart K-4. The inset figure below Chart K-3 provides this correction factor. It can also be determined from the relationship

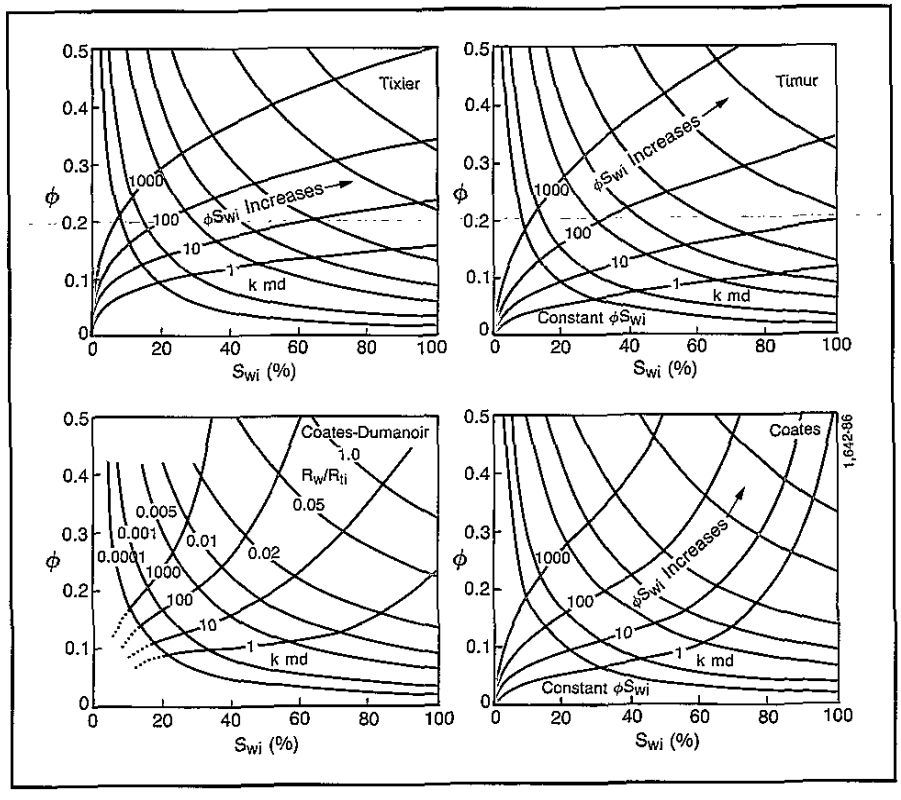

Fig. 10-3—Charts for estimating permeability from porosity and water saturation.

$$C' = 1 + (0.00083\ P_c^{1.3} + 0.02)$$
$$\sin\ (160\ \sqrt{S_{wi} - 0.04}), \qquad \text{(Eq. 10-5)}$$

where P_c is capillary pressure in psi and is equal to $h(\varrho_w - \varrho_h)/2.3$, S_{wi} is the irreducible water saturation at the P_c level (elevation), and the sin function is in degrees.

Modern logging programs provide good values of porosity and water saturation in most formations. However, these values alone do not define the expected fluid production. A zone at irreducible water saturation will produce no water. In the transition zone, however, some water will be produced, depending on the value of S_w.

For a given rock type, plots of ϕ versus S_{wi} fall in a fairly coherent pattern approximating a hyperbolic curve. This fact has been used to define zones at irreducible water saturation. Log-derived values of ϕ and S_w are plotted as shown in Fig 10-4. The points at irreducible water saturations fall lower left on the figure and conform roughly to a single hyperbolic curve, given by $S_{wi} = C/\phi$, where C is a constant for a given rock type and grain size. Points falling to the upper right of this line are from the transition zone and indicate water production, with or without oil.

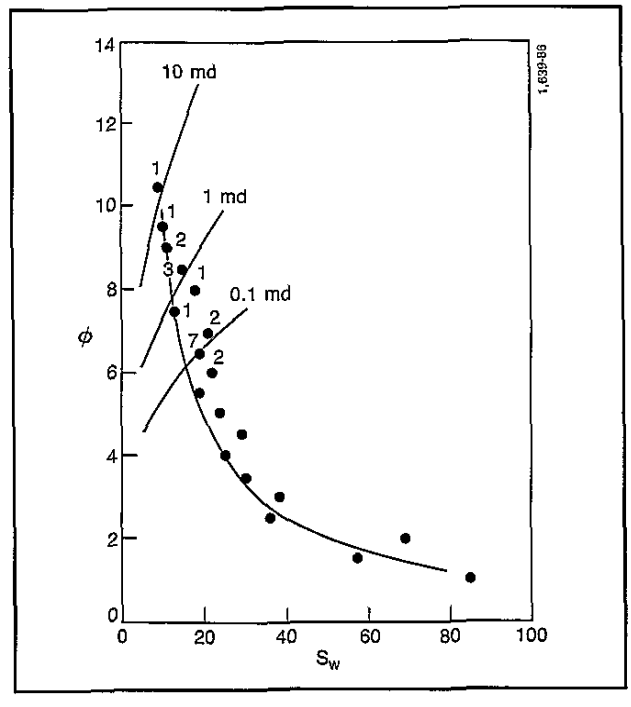

Fig. 10-4—Porosity vs. water saturation crossplot.

The permeability of the zone at each point on the irreducible saturation line can be determined from Chart K-3 or K-4. Permeability lines can be sketched on the crossplot, such as the dashed curves on Fig. 10-4 that use values transferred from the empirical charts.

It is possible, when the points are plotted from two different formation types, to find a different irreducible water saturation curve for each type. Fig. 10-5 illustrates such a case. The dolomite levels define one $\phi\ S_{wi}$ curve and the limestone levels define another. The implications of the two separate curves are that the dolomite exhibits less rock surface area per unit of porosity and higher permeability than does the limestone.

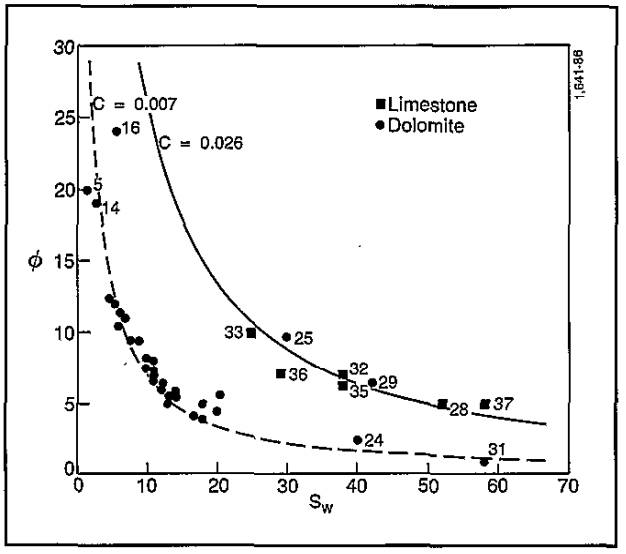

Fig. 10-5—Porosity vs. water saturation crossplot reflects change of lithology identified by lithology log.

Permeability and the Nuclear Magnetism Log

The two techniques discussed to derive permeability from log data require knowledge of either the irreducible water saturation (Eq. 10-4) or the resistivity gradient of the transition zone (Eq. 10-3). With these techniques, permeability can be predicted only in hydrocarbon-bearing formations. The NML* nuclear magnetism log provides a way to measure the irreducible water saturation of all formations, water bearing as well as hydrocarbon bearing, and another technique to estimate permeability.

Principle

The NML tool measures the free precession of proton nuclear magnetic moments in the earth's magnetic field. The principal of measurement is illustrated in Fig. 10-6. A strong DC polarizing magnetic field, H_p, is applied to the formation in order to align proton spins approximately perpendicular to the earth's field (H_E). The characteristic time constant for the exponential buildup of this spin polarization is called T_1 (spin-lattice relaxation time). The polarizing field must be applied for a period roughly five times T_1 for full polarization to occur. At the end of polarization, the field is turned off rapidly. Since the spins are unable to follow this sudden change, they are left aligned perpendicular to H_E and therefore process about the earth's field at the Larmor frequency, $f_L = \gamma H_E$, where γ is the gyromagnetic ratio of the proton ($\gamma = 4.2576 \times 10^3$ Hz/G). The Larmor frequency in the earth's field varies roughly from 1300 to 2600 Hz, depending on location. The spin procession induces in a pickup coil a sinusoidal signal of frequency f_L, whose amplitude is proportional to the number of protons in the formation. Inhomogeneities in H_E cause the spins to dephase as they process, resulting in an exponentially decaying sine wave with time constant T_2^* and frequency f_L as shown in Fig. 10-7.

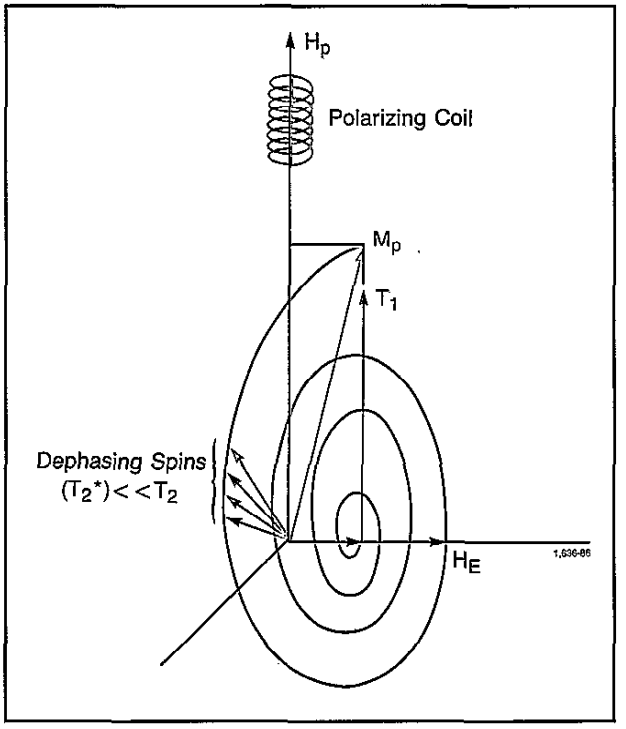

Fig. 10-6—Free induction decay in the earth's field following application of a DC polarizing field.

Because the large polarizing field cannot be turned off instantaneously, much of the signal amplitude could be lost. To compensate for this effect, the polarizing field is allowed to oscillate at the Larmor frequency for a few cycles; this "ringing" field keeps the proton spins aligned perpendicular to H_E.

*Mark of Schlumberger

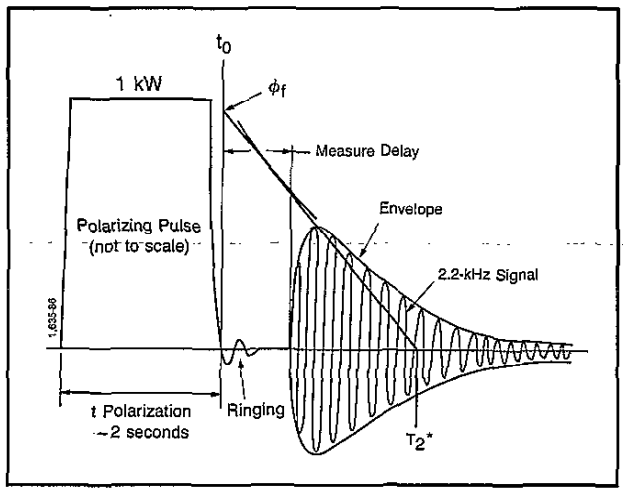

Fig. 10-7—NML signal and estimation of ϕ_f.

The NML tool measurement derives its unique quality from the dependence of the proton relaxation time T_1 on the environment. Hydrogen protons in solids or bound to surfaces have very short characteristic relaxation times, generally a few hundred microseconds at most. Bulk fluids in the pore space, however, have much longer relaxation times, usually hundreds of milliseconds. Since the observed free induction decay T_2^* must be less than or equal to T_1, one effectively discriminates against matrix and bound protons by delaying observation of the signal until 25-30 ms after the beginning of free precession. Hence, only bulk or "movable" fluid in the pore is measured by the NML tool. The measurement presented by the log is thus called free fluid index (FFI) or free fluid porosity (ϕ_f). This quantity is derived from the extrapolated signal amplitude at the beginning of free precession. In order to reduce the relaxation time of the borehole fluids, the drilling mud must be treated with a magnetite slurry before logging.

Because of the very small signals involved in nuclear magnetism logging, sophisticated processing is necessary to extract the desired information.

Applications/Interpretation

Applications for the NML survey include determination of irreducible water saturation, measurement of effective porosity, permeability estimation, heavy oil recognition, and determination of residual oil saturation.

A principal measurement of the NML tool is the free fluid index, FFI. It is the volume of fluid that is not bound electrically or chemically to the clay lattice, to the surface of the rock matrix, or to some other mineral lattice. It is the fluid that has some freedom of movement within the pore structure. This fluid volume includes oil and water but excludes irreducible water. Hence,

$$FFI = \phi\,(S_{xo} - S_{wi} + S_{or}), \quad \text{(Eq. 10-6a)}$$

or

$$FFI = \phi\,(1 - S_{wi}), \quad \text{(Eq. 10-6b)}$$

since $S_{xo} + S_{or} = 1$. The irreducible water saturation may therefore be determined in any formation by comparing the FFI measurement with a porosity measurement:

$$S_{wi} = 1 - \frac{FFI}{\phi}. \quad \text{(Eq. 10-6c)}$$

With S_{wi} available, any of the ϕ - S_{wi} permeability equations (Eq. 10-4) can be used. One such computation is a wellsite program called Cyberperm. Fig. 10-8 is the Cyberperm computation from a complex formation. Lithology is described as a shaly sand with calcareous cement. Over the interval shown, porosity varies from 7 to 18%; the FFI varies from near zero to about 8%. The resulting S_{wi} varies from about 40 to 100%. Permeability, presented in Track 2, varies from zero to about 3 md in those zones exhibiting some FFI. Those values agree with drawdown permeabilities obtained from the RFT* repeat formation tester.

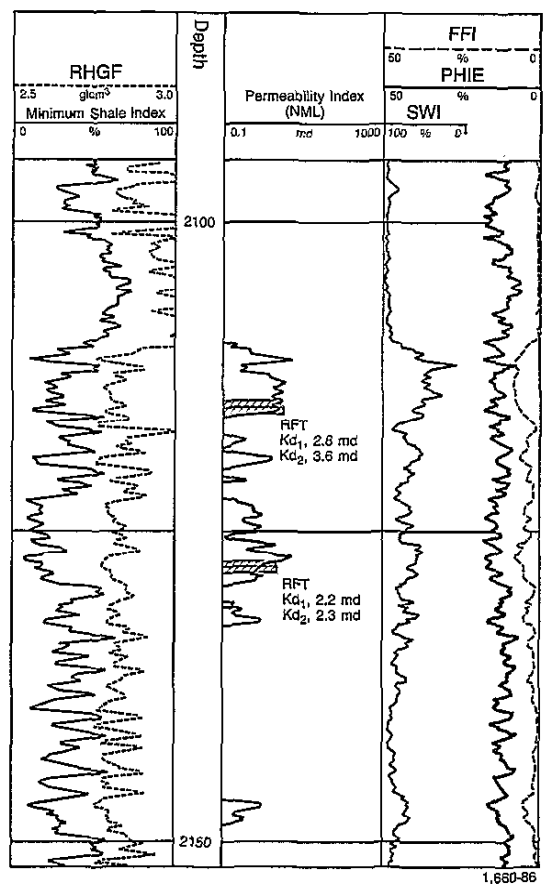

Fig. 10-8—Comparison; permeability index.

It is obvious that the FFI represents the "effective" porosity. Here, effective porosity is defined as that which contains free, movable fluid. The FFI measurement can also be a useful porosity log in hydrated minerals (such as gypsum, carnalite, polyhalite, etc.). The FFI is not affected by the water bound to the matrix lattice.

The NML measurement has been effectively used to identify water-productive intervals in heavy oil- or tar-bearing reservoirs. The NML log responds to these very heavy crudes as if they were solids; very little or no FFI is measured. Thus, any FFI signal indicates free water in the formation. Because of the large viscosity contrast between water (viscosity less than 1 cp) and these tar-like crudes (viscosity of several hundred centipoise), a formation with any free water will be predominately water productive.

The NML survey is the only logging technique that directly measures the S_{or} rather than infers it from other measurements. In addition, the technique does not depend on the choice or validity of the saturation equation. The procedure involves adding paramagnetic ions to the drilling fluid so that the mud filtrate which invades the formation is paramagnetic. This greatly reduces its relaxation time so that the FFI measurement responds only to the residual oil in the flushed zone, $\phi\, S_{or}$.

Effective and Relative Permeabilities

If the irreducible water saturation is determinable, the relative and effective permeabilities of the rock to the various saturating fluids can be predicted. Relationships proposed by Park Jones (and others) provide reasonable estimates in sands and shaly sands.

$$k_{rw} = \left(\frac{S_w - S_{wi}}{1 - S_{wi}}\right)^3, \qquad \text{(Eq. 10-7a)}$$

and

$$k_{ro} = \frac{(1 - S_w)^{2.1}}{(1 - S_{wi})^2}, \qquad \text{(Eq. 10-7b)}$$

where k_{rw} and k_{ro} are the relative permeabilities to water and oil, respectively; S_{wi} is the irreducible water saturation; and S_w is the actual water saturation. The water saturations refer to the porosity associated with the clean, nonshaly rock matrix.

Effective water and oil permeabilities are

$$k_w = k_{rw}\, k \qquad \text{(Eq. 10-8a)}$$

and

$$k_o = k_{ro}\, k, \qquad \text{(Eq. 10-8b)}$$

where k_w and k_o are the effective permeabilities (md) to water and oil, and k is the absolute or intrinsic rock permeability.

If a direct measurement of irreducible water saturation is not available, S_{wi} can sometimes be estimated. To do so requires that one or more hydrocarbon-bearing reservoirs at irreducible water saturation exist. If such a formation has a porosity, ϕ_1, and an irreducible water saturation S_{wi1}, then an approximate irreducible water saturation in another formation (not at irreducible water saturation) is given by the approximation

$$S_{wi2} = S_{wi1}\left(2 - \frac{\phi_2}{\phi_1}\right), \qquad \text{(Eq. 10-9)}$$

where ϕ_2 and S_{wi2} are the porosity and irreducible water saturation of the formation in question.

This relationship assumes that variations in porosity and S_{wi} are primarily due to grain size and grain sorting. The technique is not valid in conglomerates or secondary porosity systems.

Water-Cut Prediction

There is, of course, no initial water production from perforations above the transition zone where the actual water saturation equals the irreducible water saturation. However, intervals are often perforated in the transition zone, where the production will include water. The amount of water production depends upon the relative permeability ratio, k_{ro}/k_{rw}, and the fluid viscosity ratio, μ_w/μ_o.

$$\text{Water Cut} = \frac{1}{1 + \dfrac{k_{ro}}{k_{rw}} \cdot \dfrac{\mu_w}{\mu_o}}. \qquad \text{(Eq. 10-10)}$$

Log data may be used to estimate the water cut and thereby ascertain if it is within acceptable limits. The charts of Fig. 10-9 use log-derived values of S_w and S_{wi} to estimate water cut for a variety of oil gravities. The charts assume relative permeability responses similar to those given by Eq. 10-7.

Permeability From Geochemically Derived Mineral Abundances

A new experimental program that relates the geochemically derived mineral abundances to permeability shows good promise. Log data from gamma spectrometry, lithology-density, natural gamma ray spectrometry, and aluminum clay activation tools are used to determine the mineral abundances. These data are then used with a transform to estimate permeability in shaly sand environments.

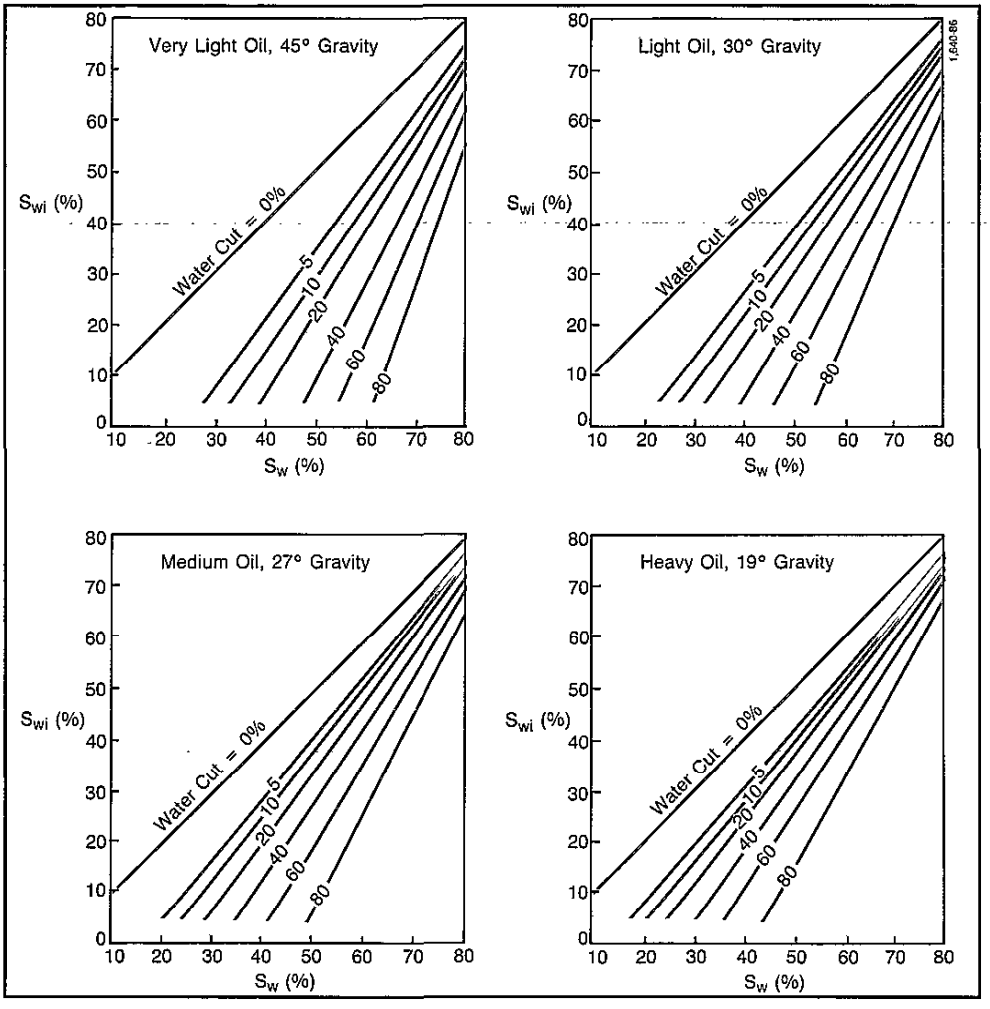

Fig. 10-9—Charts for prediction of water cut from transition-zone formations.

Fig. 10-10 shows measured porosity and permeability to air in core samples in a California well. In this example, samples of a given porosity value can vary in permeability by four orders of magnitude.

Permeability estimated from the geochemical mineralogy and porosity is compared to core permeability in Fig. 10-11. Most of the permeability variation in this well is caused by changes in clay content and in grain size — factors not reflected in the porosity variations.

Permeability From the Formation Tester Tools

Permeability can be estimated from the recovery data and pressure recording of the RFT tools. These include the original formation tester tools (FT and FIT) and the newer RFT tools. The tools provide a short production test. Once the tool is packed off against the borehole wall

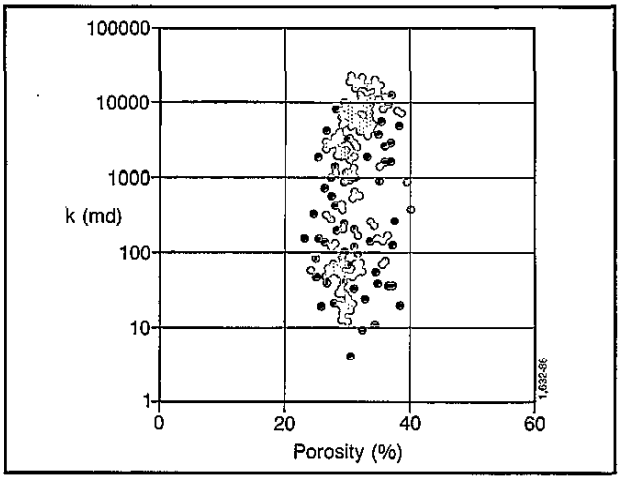

Fig. 10-10—Core porosity and permeability from California well.

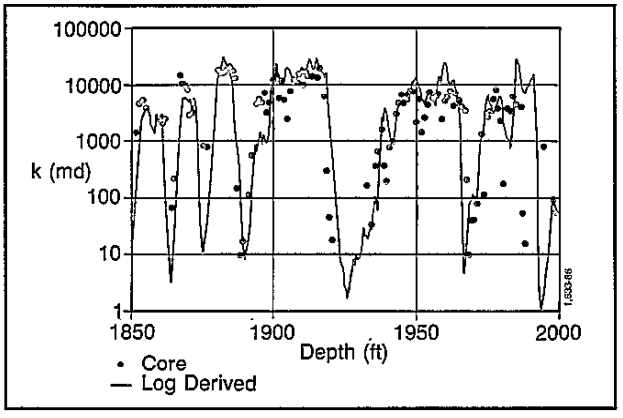

Fig. 10-11—Log permeability vs. core permeability.

(Fig. 10-12), a flow valve is opened and fluids from the formation flow into the tool's sample chamber. Sample chamber sizes vary, from the two small pretest chambers of 10 cm^3 each on the RFT tool to the regular 1-gal, 2¾-gal, or larger chambers available on all tools. Throughout the sampling (flow) period, a continuous recording of pressure is made. Pressure recording continues after the chamber is filled in order to obtain pressure buildup data.

With this technique, permeability can be estimated from the pressure drawdown data during fluid flow and from the pressure buildup data following the flow test.

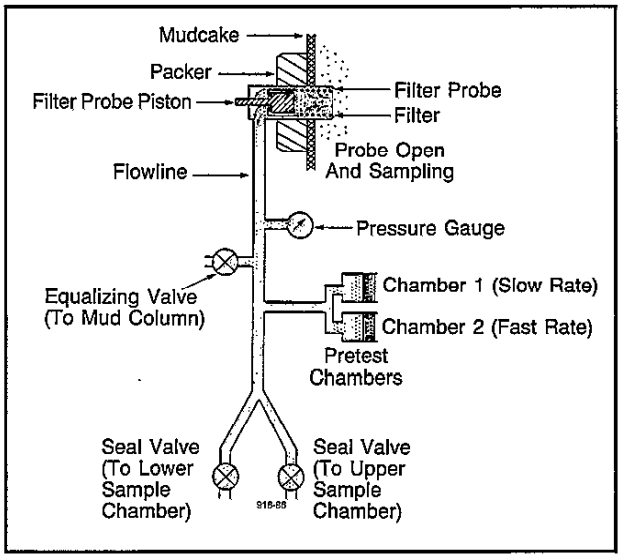

Fig. 10-12—RFT pretest and sampling system.

Drawdown Analysis

In the case of the very small 10-cm^3 pretest chambers of the RFT tool, fluid flow into the RFT probe is assumed to be spherical or hemispherical in nature. Because of the small amount of fluid actually moved during the pretests, steady-state quasihemispherical flow is rapidly established. The resulting pressure drawdown can be described as follows:

$$\Delta P = \frac{C\mu q}{2\pi r_p\, k_d}\left(1 - \frac{r_p}{r_e}\right), \quad \text{(Eq. 10-11a)}$$

where ΔP is the drawdown pressure, C is a flow shape factor, q is the flow rate, μ is the viscosity of the flowing fluid, r_p is the effective probe radius, r_e is the outer radius of the pressure disturbance, and k_d is the permeability that affects the flow regime.

Since r_p is very small relative to r_e, r_p/r_e is also small; the equation simplifies to

$$k_d = \frac{C\mu q}{2\pi r_p\, \Delta P}. \quad \text{(Eq. 10-11b)}$$

Evaluating the parameters in the term $C/2\pi r_p$ and converting to common oilfield units yields

$$k_d = 5660\,\frac{q\mu}{\Delta P}, \quad \text{(Eq. 10-11c)}$$

where

k_d is the drawdown permeability (md),

q is the pretest chamber flow rate (cm/sec),

μ is the viscosity of the flowing fluid, usually mud filtrate (cp),

and

ΔP is the drawdown pressure (psi).

The constant 5660 applies when the "standard" RFT probe is used. When the "large-diameter" or the "fast-acting" probe is used, the constant in Eq. 10-11c should be 2395. Similarly, when the "large-area packer" is used, the constant becomes 1107.

The two RFT pretest chambers are filled sequentially during a test, and drawdown permeability from each test can be compared. Fig. 10-13 shows a typical RFT pressure recording. A standard probe was used.

An example of drawdown analyses of the two pretests (10 cm^3 each) using data recorded on Fig. 10-13 gives:

$\Delta P_1 = 2050$ psi,

$T_1 = 15.4$ sec,

$q_1 = 10/15.4 = 0.65$ cm^3/sec,

$\Delta P_2 = 4470$ psi,

$T_2 = 6.1$ sec,

and

$q_2 = 10/6.1 = 1.64$ cm^3/sec.

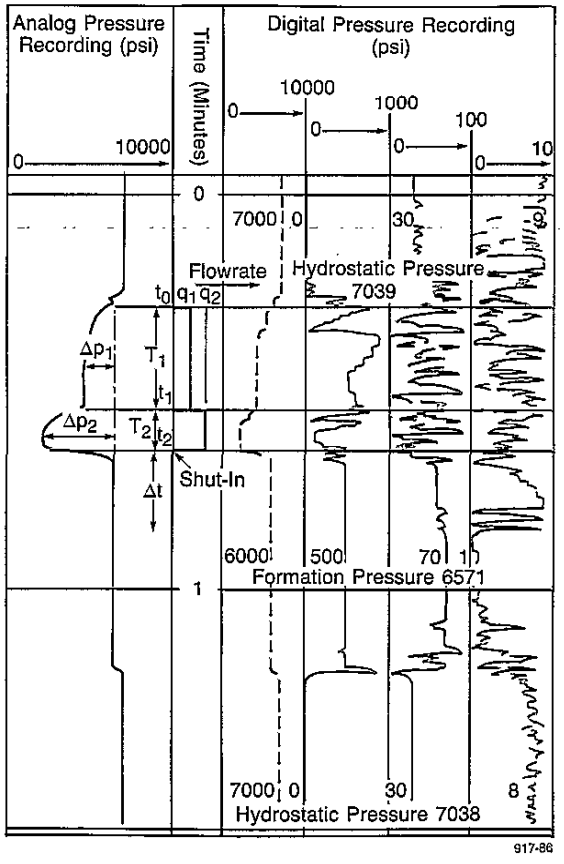

Fig. 10-13—Typical pressure recording during a pretest.

This well was drilled using an oil-base mud, and $\mu = 0.25$ cp was taken as the in-situ viscosity. The drawdown permeabilities can then be calculated as

$$k_{d1} = 5660 \times \frac{0.65 \times 0.25}{2050} = 0.45 \text{ md}$$

and

$$k_{d2} = 5660 \times \frac{1.64 \times 0.25}{4470} = 0.52 \text{ md.}$$

In this example, the two values of permeability agree quite well.

In the calculation of drawdown permeability from pressure and flow data recorded when recovering a 2¾-, 5½-, or 11-gal sample, a radial flow geometry is often more appropriate. This is because most formations usually contain thin laminae of impervious material (e.g., thin clay or shale laminae). Thus, even though the reservoir being tested might be quite thick, the thin clay laminae significantly reduce vertical permeability and cause the flow to be essentially radial.

Derivation of the equation for drawdown permeability in a radial flow geometry is similar to that for spherical flow geometry (Eq. 10-11). Related to the formation tester tools, the expression reduces to

$$k_d = \frac{600}{h} \frac{q\mu}{\Delta P}, \qquad \text{(Eq. 10-12)}$$

where the terms are as previously defined and h is the interval (thickness) tested. Ideally, one would carefully examine all the logs to locate the upper and lower permeability barriers or restrictions. That distance would be h in Eq. 10-12. In practice, h appears to be more a function of the tester probe than of the formation. For the formation tester tools that have shaped charge perforator probes, h is about 0.75 when one charge is employed, about 1.5 when two charges are used, and about 0.6 when only a probe (i.e., no shaped charge) is used.

Pressure Buildup Analysis

Permeability can also be estimated from an analysis of the pressure buildup recording following the flow test. When the two RFT pretest chambers are full, the pressure in the probe increases to the original static formation pressure, P_e, as the inward pressure propagation progresses.

The flow (and pressure propagation) geometry influences the calculation of permeability. The probe pressure response during buildup is obtained by the superposition of the two RFT pretest chambers drawdown responses. Calculations based on spherical flow in an infinite homogeneous medium lead to the expression

$$P_e - P_s = \frac{8 \times 10^4 \, q \cdot \mu \, (\phi \mu C_t)^{1/2}}{k_s} \times f_s(\Delta t), \qquad \text{(Eq. 10-13a)}$$

in which

$$f_s(\Delta t) = \frac{q_2/q_1}{\sqrt{\Delta t}} - \frac{(q_2/q_1 - 1)}{\sqrt{T_2 + \Delta t}} - \frac{1}{\sqrt{T_1 + T_2 + \Delta t}};$$

where

P_e is the initial static formation pressure (psi),

P_s is the probe pressure (spherical buildup) (psi),

ϕ is formation porosity,

C_t is the total compressibility of fluid in the formation (psi^{-1}),

k_s is the spherical buildup permeability (md),

Δt is the elapsed time after shut-in (seconds or minutes),

and

q_1, q_2, T_1, and T_2 are as previously defined.

A plot of P_s, the instantaneous observed pressures during buildup, versus $f_s\,(\Delta t)$, the spherical time function, on a linear-linear grid will ideally result in a straight line. Extrapolation of this straight line to $f_s\,(\Delta t) = 0$ yields the static formation pressure P_e. From the slope, m, of the spherical buildup plot, the spherical permeability can be calculated from Eq. 10-13. That equation, in terms of m, is

$$k_s = 1856\,\mu \left(\frac{q_1}{m}\right)^{2/3} (\phi C_t)^{1/3}. \quad \text{(Eq. 10-13b)}$$

Fig. 10-14 shows the buildup plot obtained using the data recorded on Fig. 10-13. Taking $q_1 = 0.65$ cm^3/sec and $q_2 = 1.64$ cm^3/sec as already computed, the points plot on a straight line and confirm the spherical flow hypothesis. Static formation pressure is indicated to be about 6573 psi. The slope of the straight line is 12.5 psi/sec$^{-1/2}$.

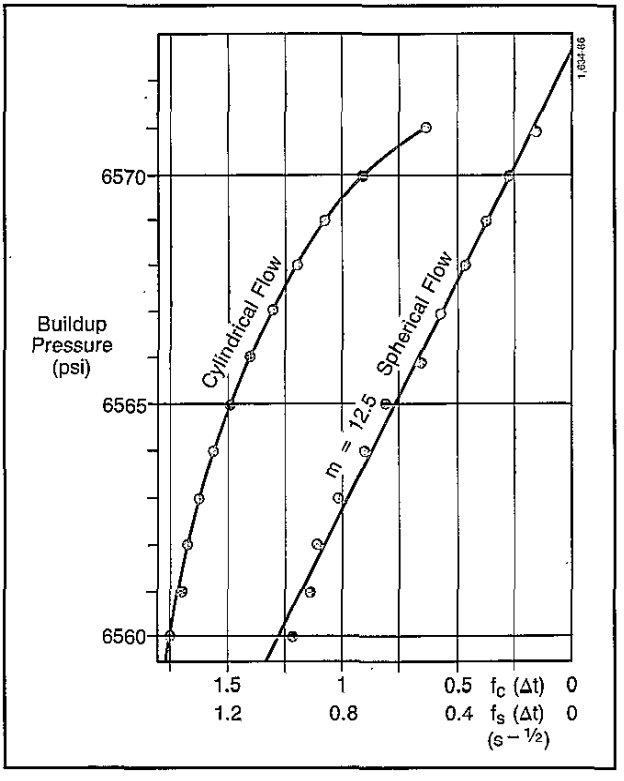

Fig. 10-14—Pressure plot in the case of a spherical flow.

If C_t is taken as 1.5 x 10^{-5} psi^{-1}, μ is 0.25 cp, and ϕ is 0.08 (porosity from well logs), $k_s = 0.69$ md (from Eq. 10-12b). This compares favorably to $k_d = 0.52$ md from the drawdown permeability.

Buildup and drawdown permeabilities need not agree. Drawdown permeability tends to reflect the lowest permeability in the fluid flow path. Buildup permeability tends to reflect the average permeability over the formation experiencing the pressure disturbance. Therefore, the "damaged" zone (damaged from mud invasion during drilling) of lower permeability surrounding the borehole influences the drawdown permeability calculation more than the buildup calculation.

For a radial-cylindrical flow pattern the buildup equation is given by

$$P_e - P_c = \frac{88.4\,q\mu}{k_r\,h} \times f_c\,(\Delta t), \quad \text{(Eq. 10-14a)}$$

in which

$$f_c\,(\Delta t) = \log \frac{T_1 + T_2 + \Delta t}{T_2 + \Delta t} + \frac{q_2}{q_1} \log \frac{T_2 + \Delta t}{\Delta t};$$

where

k_r is the cylindrical buildup permeability (md), h is the thickness of the producing bed, the distance between the upper and lower impermeable boundaries (ft), and the other terms are as previously defined.

Pressure readings from the formation tester pressure log are plotted versus the cylindrical time function $f_c\,(\Delta t)$ on a linear-linear grid. If the pressure propagation is cylindrical, the pressure versus cylindrical time function plot is then ideally a straight line that intersects the line $f_c\,(\Delta t) = 0$ at the static formation pressure, P_e. The slope of line, m, is used to determine permeability from the relationship (from Eq. 10-14a):

$$k_c = \frac{88.4\,q\,\mu}{mh}. \quad \text{(Eq. 10-14b)}$$

h can be estimated from openhole logs. However, as noted under the radial-cylindrical drawdown discussion, the effective bed thickness seems to be more a function of the number and type of probes used in the formation tester tool.

The pressure buildup data from the log of Fig. 10-13 were analyzed assuming a radial-cylindrical flow pattern. The plot of pressure versus time function $f_c\,(\Delta t)$ is shown on Fig. 10-14. It does not define a straight line, which indicates the flow pattern is not cylindrical. That comes as no surprise since analysis of the same data assuming spherical flow had confirmed the spherical flow assumption.

The radial-cylindrical flow pattern is, however, usually confirmed when dealing with the larger (1- to 11-gal) formation tester sample recoveries. Since only one chamber is involved (not the two small pretest chambers), the $f_c\,(\Delta t)$ term of Eq. 10-14a reduces to

$$f_c\,(\Delta t) = \log \frac{T + \Delta t}{\Delta t}. \quad \text{(Eq. 10-14c)}$$

Formation tester recoveries are flow tests. Therefore, the permeabilities calculated, whether derived from drawdown or buildup data, are essentially effective permeabilities.

Interpretation of RFT pretests or sample tests is available at either the wellsite with the RFTI program or at interpretation centers. Computations include Horner and spherical pressures, permeabilities, and mobility. Pressures are plotted versus depth for pressure profiles, fluid gradients, and pressure potential interpretations.

Fig. 10-15 is an example of a spherical and Horner plot computed automatically with the RFTI program. An example of the wellsite RFT interpretation results is shown in Fig. 10-16. Fig. 10-17 shows a spherical mobility-versus-depth plot.

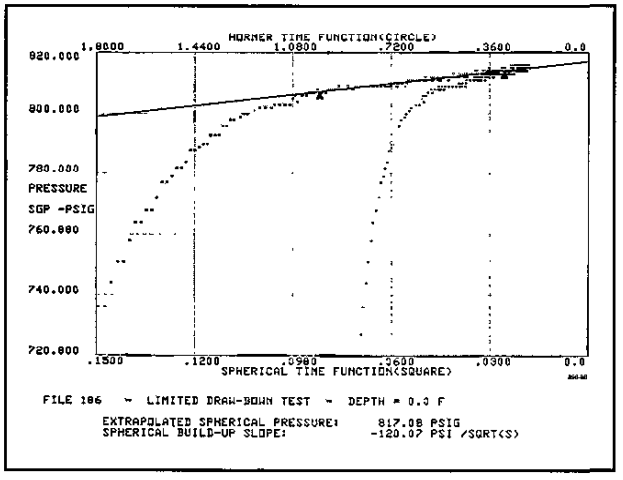

Fig. 10-15—RFTI Horner and spherical time function plot.

CTOT TOTAL FORMATION COMPRESSIBILITY
C1V PRETEST CHAMBER 1 VOLUME
C2V PRETEST CHAMBER 2 VOLUME
FP FORMATION PRESSURE
HMTP HORIZONTAL MOBILITY-THICKNESS PRODUCT
KD EFFECTIVE DRAW-DOWN PERMEABILITY
MHOR HORNER BUILD-UP SLOPE
MSPH SPHERICAL BUILD-UP SLOPE
PBU PRESSURE AT THE END OF THE BUILD-UP
PHI FORMATION POROSITY
PHOR EXTRAPOLATED HORNER PRESSURE
PHYA HYDROSTATIC PRESSURE AFTER PRETEST
PHYB HYDROSTATIC PRESSURE BEFORE PRETEST
PSPH EXTRAPOLATED SPHERICAL PRESSURE
RI DEPTH OF INVESTIGATION FOR SPHERICAL MOBILITY
SMOB MOBILITY FROM SPHERICAL BUILD-UP
TVD TRUE VERTICAL DEPTH
T1 DURATION OF PRETEST 1
T2 DURATION OF PRETEST 2
VISC VISCOSITY FOR DRAW-DOWN PERMEABILITY CALCULATION

FILE NUMBER	16	17	18	19	20
TEST NUMBER					
DEPTH (F)	4164.00	4134.00	4128.00	4115.00	4110.00
TVD (F)	4164.00	4134.00	4128.00	4115.00	4110.00
TEST TIME (HHMM)	04114	04122	04126	04130	04134
PHYB (PSIG)	2269.00	2252.59	2250.00	2242.65	2239.59
PHYA (PSIG)	2265.47	2249.71		2239.29	2237.47
PBU (PSIG)	815.33	841.50	839.83	879.00	881.67
PSPH (PSIG)	817.44	844.14	840.16	878.52	900.10
PHOR (PSIG)					
FP (PSIG)	817.44	844.14	840.16	878.52	900.10
T1 (S)	95.10	16.50	9.60	11.10	159.60
T2 (S)		3.00	3.60	2.40	
C1V (CB)	10.00	10.00	13.30	18.00	18.00
C2V (CB)	10.00	10.00	10.00	10.00	10.00
MSPH PSI /SQRT(S)	-126.94	-3.68	-43.49	-1.08	-519.05
MHOR PSI /CYCLE					
SMOB (MD/CP)	.251	5.982	1.434	15.070	.069
KD (MD)	1.582	69.829	19.416	192.676	.282
HMTP (MDFT/CP)					
PHI .15	.15	.05	.19	.15	.15
VISC (CP)	1.09	1.09	1.09	1.09	1.09
CTOT (1/PSI)	6.00000E-6	1.00000E-5	6.00000E-6	6.00000E-6	6.00000E-6
RI (F)	4.77	12.91	4.51	15.68	.58
SUPERCHARGING					YES

Fig. 10-16—RFT pressure interpretation results.

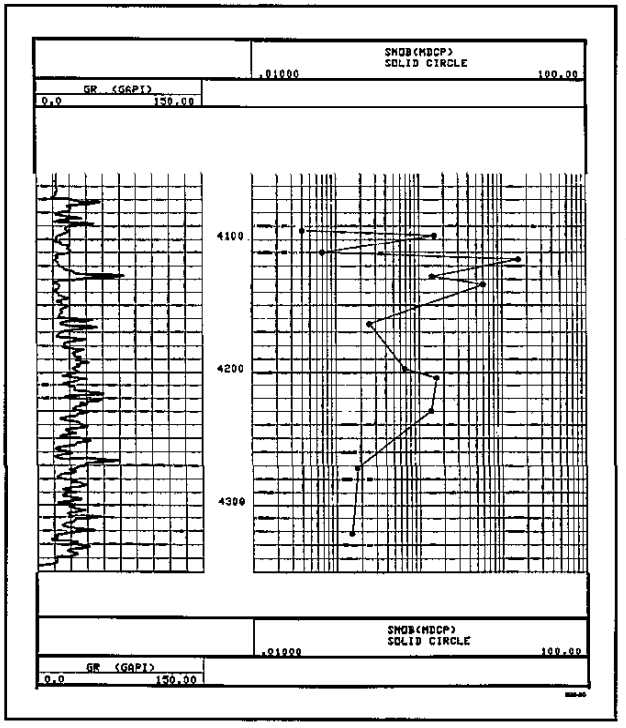

Fig. 10-17—Spherical mobility plot.

PRODUCTIVITY

With effective permeability, estimated by a formation tester or by log-derived methods, and formation pressure, available from formation tester measurements or elsewhere, the prediction of production rate as a function of the wellbore drawdown pressure is rather straightforward.

The Darcy relationship, in oilfield units, for liquid flow is

$$Q = \frac{7.07\ k\ h\ (P_e - P_w)}{\mu \ln (r_e/r_w)}, \quad \text{(Eq. 10-15a)}$$

where

Q is the flow rate (bbls/D),

k is the effective permeability (darcies),

h is the vertical extent of the productive interval (ft),

P_e is the static formation pressure (psi),

P_w is the pressure in the wellbore, such that $P_e - P_w$ is the drawdown pressure (psi),

μ is the viscosity of the produced fluid (cp),

r_e is the radius to the P_e pressure contour (ft),

and

r_w is the wellbore radius (ft).

The relationship for gaseous flow is

$$Q = \frac{39.76\ k\ h\ (P_e - P_w)}{B'g\ \mu\ \ln\ (r_e/r_w)}\ , \quad \text{(Eq. 10-15b)}$$

where

Q is the flow rate (cf/D).

$B'g$ is a volume factor that handles the gas expansion from reservoir to surface conditions,

$$B'g \sim \frac{2z\ P_s\ T_m}{T_s\ (P_e + P_w)}\ ,$$

and the other terms are as previously defined.

To calculate flow rate, the basic inputs needed include pressure, temperature, some fluid properties, approximate drainage radius, borehole size, reservoir thickness, and permeability.

Reservoir pressure, ideally, can be obtained from a formation tester log or a drillstem test; alternatively, it can be estimated from known pressure gradients, well logs, offset wells, or mud weight.

Fluid viscosity and other required parameters, such as fluid compressibility and formation volume factor, can either be measured or calculated using known correlations. These parameters can be computed if the specific gravity of the gas and the oil and the surface gas-oil ratio are given.

The approximate drainage radius can be estimated by dividing the well spacing in half, or it can be otherwise obtained. The number is relatively unimportant as long as it is of the correct order of magnitude. The reservoir thickness is obtained by considering only the zones of interest. Remember that the flow model assumes isotropic continuous reservoirs without permeability barriers and with radial drainage patterns. Vertical fluid movement within the reservoir is accounted for.

For an approximation of oil production rate, Eq. 10-15a can be simplified to

$$Q_o \sim \frac{k'h\ \Delta P}{1000\ \mu}\ , \quad \text{(Eq. 10-16a)}$$

where

ΔP is the pressure drawdown, i.e., $P_e - P_w$ (psi),

and

k' is the permeability (md).

A similar simplification for gas production rate is

$$Q_g \sim \frac{k'h\ (P_e^2 - P_w^2)}{100}\ . \quad \text{(Eq. 10-16b)}$$

The Producibility Log

The Producibility log is a computed log that uses the outputs from any formation evaluation computed log, such as a VOLAN* or GLOBAL* computation, and predicts the flow rates and reserves of the well. Three dependent segments of the well flow regime, any one of which can control the ultimate flow of the well, are considered: the formation, the perforation, and the tubing. In most cases, formation permeability is the primary controlling factor in well production — the key to producibility predictions is the calculation of permeability from well logs.

The permeability values are derived by the PERMS program, which provides four models for absolute permeability estimation. These include the Coates' free-fluid model, the total bulk volume irreducible water model (NML), the Timur model, and a logarithmic model to extend external permeability data (core). The relative permeabilities are based on the Naar-Henderson and Park-Jones correlations with modifications for residual oil saturation.

These permeability values and the physical properties of the fluid are used in the radial flow equation (Eq. 10-15) and continuously computed over the reservoir intervals. The results are then integrated over the total zone to give the total flow potential or rate. In much the same way, the flow restriction through a perforation or a gravel pack can be computed. The pressure drop in the tubing and its influence on uphole flow rates are also evaluated.

The program calculates flow rates from primary porosity represented by a natural completion or a gravel pack completion. It is not intended to handle skin damage, partial or damaged completions, or responses throughout the well's life cycle. The program can be used, however, to indicate many of these problems.

A Producibility log is shown in Fig. 10-18. Its output is presented in two parts:

1. A computed log consisting of a well sketch (borehole profile, casing string, tubing, packers, plugs, perforations, etc.), a permeability analysis (absolute and effective permeabilities to saturating fluids), a predicted flow profile (fraction of total production expected from each perforated, or potentially productive, interval), and a bulk volume analysis (fractions of porosity, rock matrix, and shale; fractions of water, movable hydrocarbons, and residual hydrocarbons).
2. A flow rate versus drawdown production performance analysis which, for a given zone, shows how the formation, the tubing, and the perforations interact to dictate the daily flow rate.

For example, in the production performance analysis shown in Fig. 10-18 of an extremely high volume gas well, the zone should flow about 30 MMcf/D through 3-in.

tubing at a wellhead pressure of 1500 psi if perforated with four shots per foot. A 2100-psi pressure drop occurs in the tubing, a 200-psi drop occurs in the formation, and an 1100-psi drop occurs across the gravel-packed perforations. Daily production could be increased to about 55 MMcfg/D if the zone were perforated with eight shots per foot.

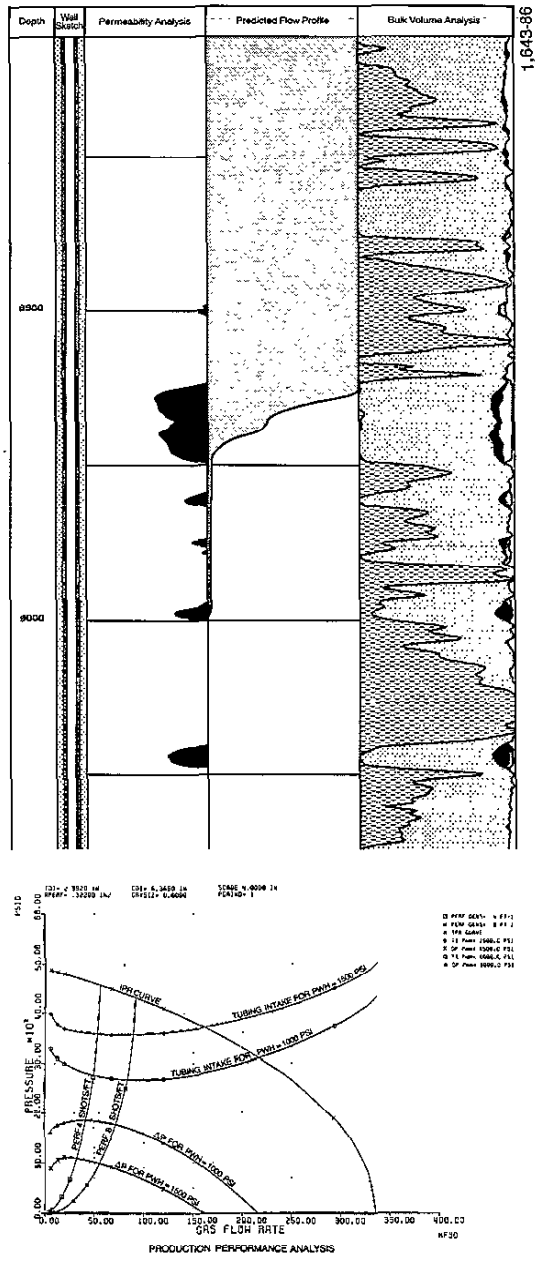

Fig. 10-18—Producibility log and production performance analysis plot.

Data listings give exact calculations, and tubing intake curves can be superimposed on the IPR curves.

Given the assumptions necessary, it should be clear that the well performance prediction from the Producibility log will be most successful in a relative sense. If predicted versus actual flow rates differ consistently, input parameters should be reviewed in an effort to improve the accuracy of the output. Once a log permeability transform has been determined to be accurate in a given reservoir, the program's power lies in application as a uniform model to a series of similar wells. An important application would be to indicate wells with performance less than predicted.

REFERENCES

1. Tixier, M.P.: "Evaluation of Permeability From Electric-Log Resistivity Gradients," *Oil and Gas J.* (June 16, 1949).
2. Wyllie, M.R.J. and Rose, W.D.: "Some Theoretical Considerations Related to the Quantitative Evaluation of the Physical Characteristics of Reservoir Rock from Electrical Log Data," *J. Pet. Tech.* (April 1950) 189.
3. Timur, A.: "An Investigation of Permeability, Porosity, and Residual Water Saturation Relationships for Sandstone Reservoirs," *The Log Analyst* (July-Aug. 1968) **9**, No. 4.
4. Morris, R.L. and Biggs, W.P.: "Using Log-Derived Values of Water Saturation and Porosity," *Trans.*, 1967 SPWLA Annual Logging Symposium.
5. Jones, Park J.: "Production Engineering and Reservoir Mechanics (Oil, Condensate, and Natural Gas)," *Oil and Gas J.* (1945).
6. Coates, G.R. and Dumanoir, J.L.: "A New Approach to Improved Log Derived Permeability," *The Log Analyst* (Jan.-Feb. 1974) **15**, No. 1.
7. Raymer, L.L.: "Elevation and Hydrocarbon Density Correction for Log-Derived Permeability Relationship," *The Log Analyst* (May-June 1981).
8. Stewart, G. and Wittman M.: "Interpretation of the Pressure Response of the Repeat Formation Tester," paper SPE 8362 presented at the 1979 SPE Annual Technical Conference and Exhibition.
9. Smolen, J.J. and Litsey, L.R.: "Formation Evaluation Using Wireline Formation Tester Pressure Data," paper SPE 6822 presented at the 1977 SPE Annual Technical Conference and Exhibition.
10. *RFT Essentials of Pressure Test Interpretation,* Schlumberger (1981).
11. Herrick, R.C., Couturie, S.H., and Best, D.L.: "An Improved Nuclear Logging System and Its Application to Formation Evaluation," paper SPE 8361 presented at the 1979 SPE Annual Technical Conference and Exhibition.
12. Brown, R.J.S. and Neuman, C.H.: "Processing and Display of Nuclear Magnetism Logging Systems: Application of Residual Oil Saturation," *Trans.,* 1980 SPWLA Annual Logging Symposium.
13. Herron, M.M.: "Subsurface Geochemistry: 1 Future Applications of Geochemical Data," Nuclear Data for Applied Nuclear Geophysics Meeting, Vienna, April 7-9, 1986.
14. Naar, J., Wygal, R.J., and Henderson, J.H.: "Imbibition Relative Permeability in Unconsolidated Porous Media," *Soc. Pet. Engr. J.* (1962).
15. *Log Interpretation Charts,* Schlumberger Well Services, Houston (1986).

11 Wellbore Seismic

In the early stages of planning exploration and development in a new area, surface seismic surveys are used extensively to delineate prospective structural or stratigraphic traps. Recent improvements in digital filtering and processing techniques have led to high-quality results under favorable conditions. The resolution of surface seismic surveys, however, is still fundamentally limited by low operating frequencies.

When wells are drilled, opportunities exist to improve this situation through the use of well logs. After editing and calibrating against check shots, openhole sonic and density logs can be used to generate synthetic seismograms. If openhole data are not available, in many instances a cased hole sonic log can be recorded for this purpose. These synthetics are extremely valuable in verifying reflection events in a seismic section and relating seismic features to geological structures. Velocity anomalies, which may cause exploration wells to be drilled off-structure, can be resolved.

A more recent geophysical application of wireline logging measurements involves the preparation of a vertical seismic profile (VSP). In this technique, an air gun vibroseis, or other seismic source on the surface generates the input signal that is detected by a downhole geophone. As the sound energy travels only once through the weathered surface layers, the resultant profile has much better resolution than the surface seismic around the borehole, and, in favorable cases, can identify reflectors far below the total depth of the well.

Unlike many wireline services, openhole and cased hole seismic results are similar since the casing typically does not affect the seismic signal. In fact, cased holes eliminate some of the openhole operational problems associated with poor hole conditions and highly deviated wells. Also, special multisensor array tools for VSP acquisition can be used in cased holes that are not practical for openhole operations.

WELL SEISMIC EQUIPMENT

The equipment shown in Fig. 11-1 consists of a downhole tool with geophones, the CSU surface recording system, offset shooting equipment, and an air gun system.

The most commonly used energy source offshore is the air gun. Its safety, reliability, cost, broad spectrum, simple signature, and transportability make the air gun a convenient seismic source. An array of synchronized air guns can be used if a large power output for deeper penetration is needed. The air gun firing chambers may incorporate a waveshaping kit that significantly reduces the bubble effect and provides a clean signal. The air compressor and air storage bottles provide an adequate air supply for fast, uninterrupted operations. Other sound sources, such as vibroseis units, are routinely used in the field depending on specific applications and local conditions.

When using an impulsive source such as an air gun, the source signal is recorded at the surface by a hydrophone. This allows a precise determination of the time break and permits continuous monitoring of the gun signature. The recorded source signature is used to enhance the signals recorded by the geophone in VSP processing.

The data are recorded digitally on magnetic tape with the CSU system. The seismic waveforms can also be stacked to improve the signal-to-noise ratio.

The downhole tools currently in use are the Well Seismic Tool (WST*), the Seismic Acquisition Tool (SAT*), and the Downhole Seismic Array tool (DSA*). The WST tool has four uniaxially stacked geophones that are primarily sensitive to movement in the vertical direction. The SAT tool has three mutually orthogonal geophones (which may also be gimbal-mounted for use in deviated wells) for 3-dimensional operation. This arrangement provides an x, y, z system of reference where each arriving ray can be represented by a vector. Among other applications, the ability to record and process signals in three axes allows the recording and interpretation of shear waves, salt proximity surveys, and long-offset VSP surveys. The DSA tool (Fig. 11-2) uses eight sensor packages (shuttles) which are positioned along an insulated multiconductor bridle cable at intervals of up to 50 ft. The sensor package contains a vertical geophone for signal acquisition, a magnetic clamping device to secure the package to the casing, a shaker element to generate mechanical vibrations for reference, and electronic circuitry to transmit

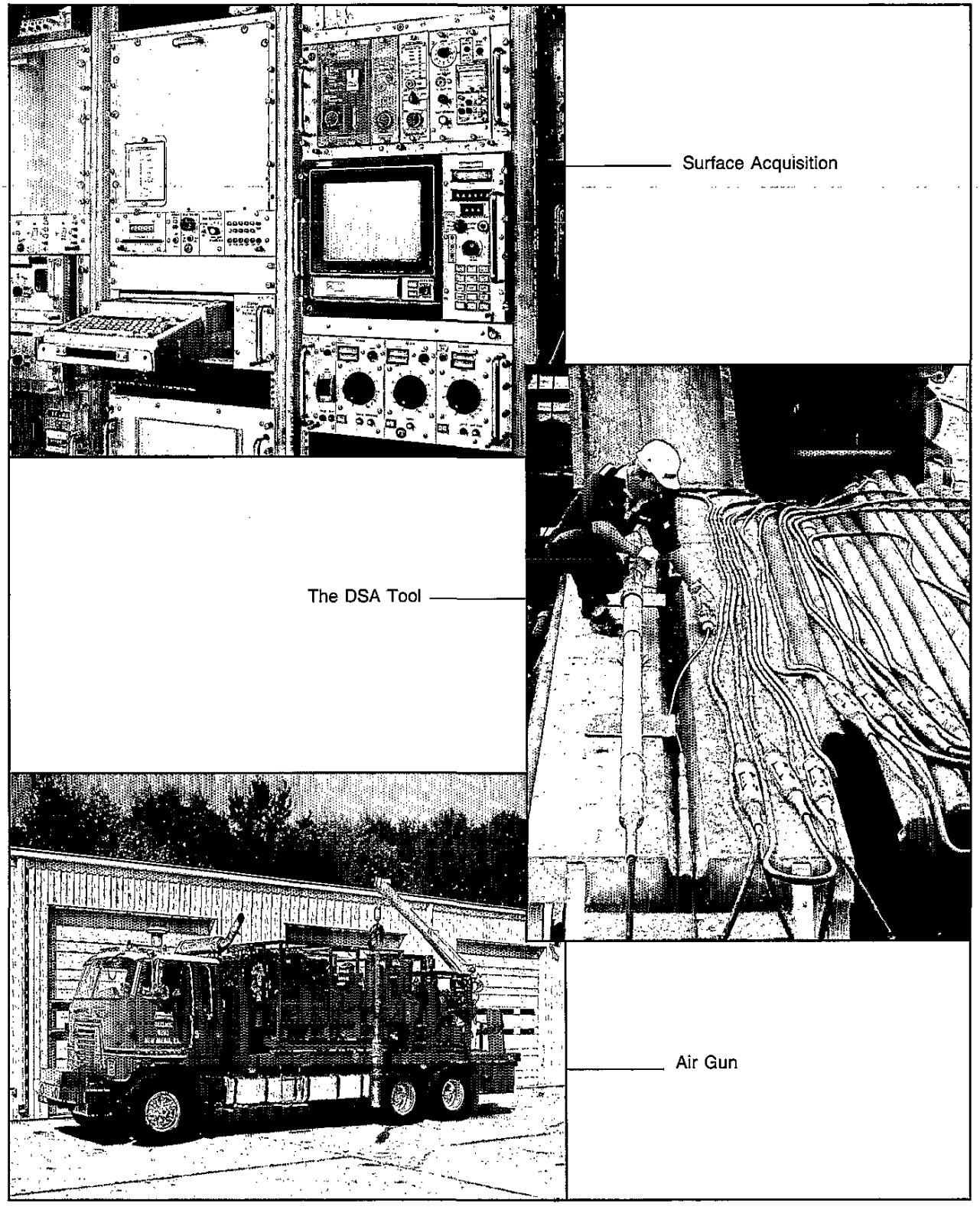

Fig. 11-1—Well seismic tool hardware.

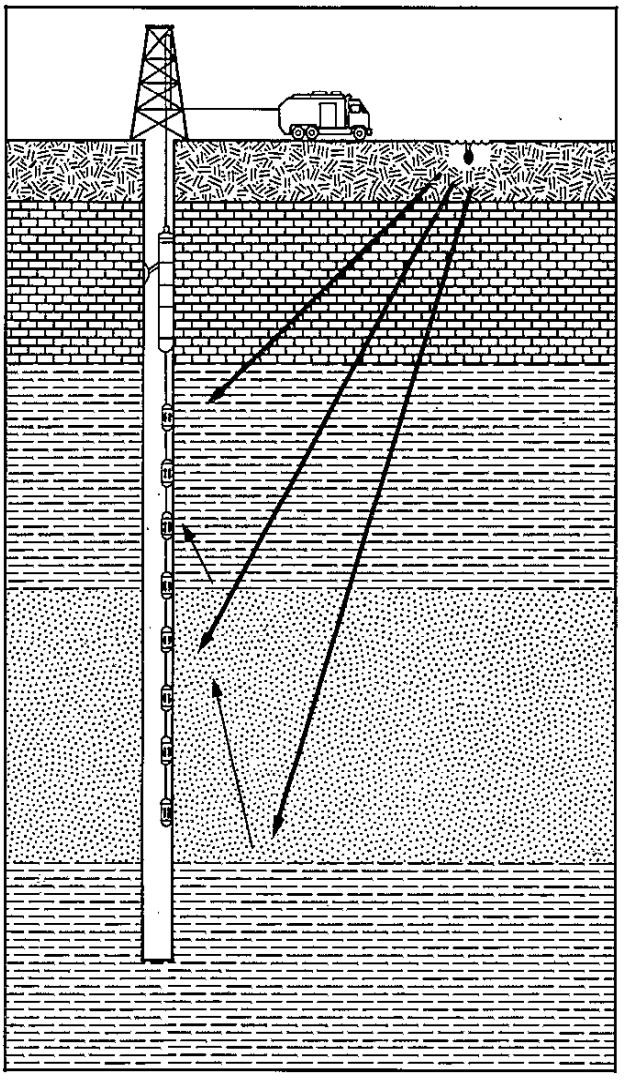

Fig. 11-2—Schematic of DSA tool in operation.

signals to the cartridge. In the cartridge, the signals pass through antialiasing filters, sample-hold circuits, and multiplexers, and are then digitized and telemetered to the surface. The tool can be combined with a casing collar locator for depth control.

DIGITAL CHECK-SHOT SURVEY

At each depth, the interval velocity of the formations between the source and the borehole geophone is measured. With an air gun source, the hydrophone monitors the signature and timing of the source signal, and the downhole geophone records the direct and reflected arrivals.

Transit time is measured from the first break of the hydrophone (surface) recording to the first break of the geophone (downhole) recording. Several shots are usually made at the same level and stacked in order to improve the signal-to-noise ratio.

If the hole is deviated or if there is a significant source offset, the transit times obtained must be converted to true vertical depth (TVD) transit times. Correction to the seismic reference datum (SRD) is also necessary if the source is above or below the seismic datum. The corrected, stacked magnetic tape data can then be converted to a standard SEG-Y tape format.

Time-To-Depth Conversion and Velocity Profile

Check-shot surveys are used to correct the velocities obtained by the integration of the sonic interval transit times. The adjusted sonic may then be used for the translation of surface seismic time into depth and in the calculation of formation acoustic impedance necessary for the generation of a Geogram* synthetic seismogram and for other applications.

Formation velocities obtained by the integration of sonic logs may differ from those obtained by surface and check-shot surveys for the following reasons:

- Because of velocity dispersion with frequency, seismic velocities (measured at roughly 50 Hz) may be as much as 6% lower than sonic velocities (measured at 20,000 Hz).
- Borehole effects, such as those caused by formation alteration, may decrease the apparent sonic log velocities.
- The sonic transit time measurement is fundamentally different from the surface seismic measurement. The sonic log velocity is measured in a continuous manner alongside the borehole, while the seismic waves reaching the geophone(s) take the most direct acoustic (shortest) path.

The long-spaced (LSS) or Array-Sonic tools are required for cased hole logs and provide better data than BHC sonics in open holes. However, all recorded sonic logs should be edited to correct for borehole effects. To adjust a sonic log correctly, check shots are required. Check shots should be made at the SRD, at the tops of significant formations, at the top of the sonic log, and spaced not greater than 500 ft apart.

Seismic time is normally referenced from the check shots, and sonic log measurements are adjusted accordingly. The adjustment consists of computing the raw drift, selecting the drift curve, adjusting the sonic log, and checking the validity of the result.

Raw drift is defined as the correct shot time minus the integrated sonic time. The selected drift curve is derived from the raw drift values. The knees of the selected drift curve are usually located at changes in lithology, borehole conditions, sonic log character, and the drift data. The correction determined by the selected drift curve is distributed to the sonic transit times over the interval defined by consecutive

knees. The check of the adjusted sonic is made by ensuring that the integrated sonic time and the corrected shot time agree at each shooting level within the accuracy of the shot time. Obviously, the more check shots, the more accurately this can be done.

A section of a sonic calibration log is shown in Fig. 11-3. The uncalibrated transit time, calibrated transit time, and gamma ray curve are displayed along with bulk density, spontaneous potential, and differential caliper data from open-hole logs. In the left track, vertical depth, shot numbers, corrected shot times, uncorrected 1-way integrated sonic times, and corrected 2-way integrated sonic times are displayed.

In addition to providing data for sonic calibration, check shots allow a time-to-depth conversion to be made when no sonic log has been recorded. A similar, related application is the determination of the weathering correction and the thickness of the weathered zone.

GEOGRAM PROCESSING

The seismic waveforms propagating through the earth are affected by each lithologic bed boundary. Specifically, at the interface of two formations of contrasting acoustic impedances, part of the energy will be transmitted across the interface and some will be reflected. The amount of seismic energy transmitted and reflected depends on the acoustic impedance contrast between the two formation beds. The acoustic impedance of a formation, Z_a, is given as:

$$Z_a = \rho v \,, \qquad \text{(Eq. 11-1)}$$

where ρ is the formation density and v is its interval velocity.

The amount of reflected energy between two adjacent beds depends on the relative impedances of the two beds. The reflection coefficient, R, is defined as:

$$R_{1,2} = \frac{Z_{a_2} - Z_{a_1}}{Z_{a_2} + Z_{a_1}} \,, \qquad \text{(Eq. 11-2)}$$

where Z_{a_2} and Z_{a_1} are the acoustic impedances of layers 2 and 1.

The subsurface can be approximated for seismic purposes by a series of layers having specific acoustic impedances, which can be used to produce a series of reflection coefficients at the boundaries (Fig. 11-4). Since a sonic log measures acoustic velocity and a density log measures bulk density, the sonic and density logs can be used to compute the reflectivity series, which can then be convolved with a suitable wavelet. The result is a Geogram display (synthetic seismogram).

Geogram processing produces an ideal seismic trace only if the sonic and density logs have been properly recorded, edited, and adjusted to represent the subsurface undisturbed by drilling. Special programs allow the recomputation of sonic velocities and bulk densities, taking into account the

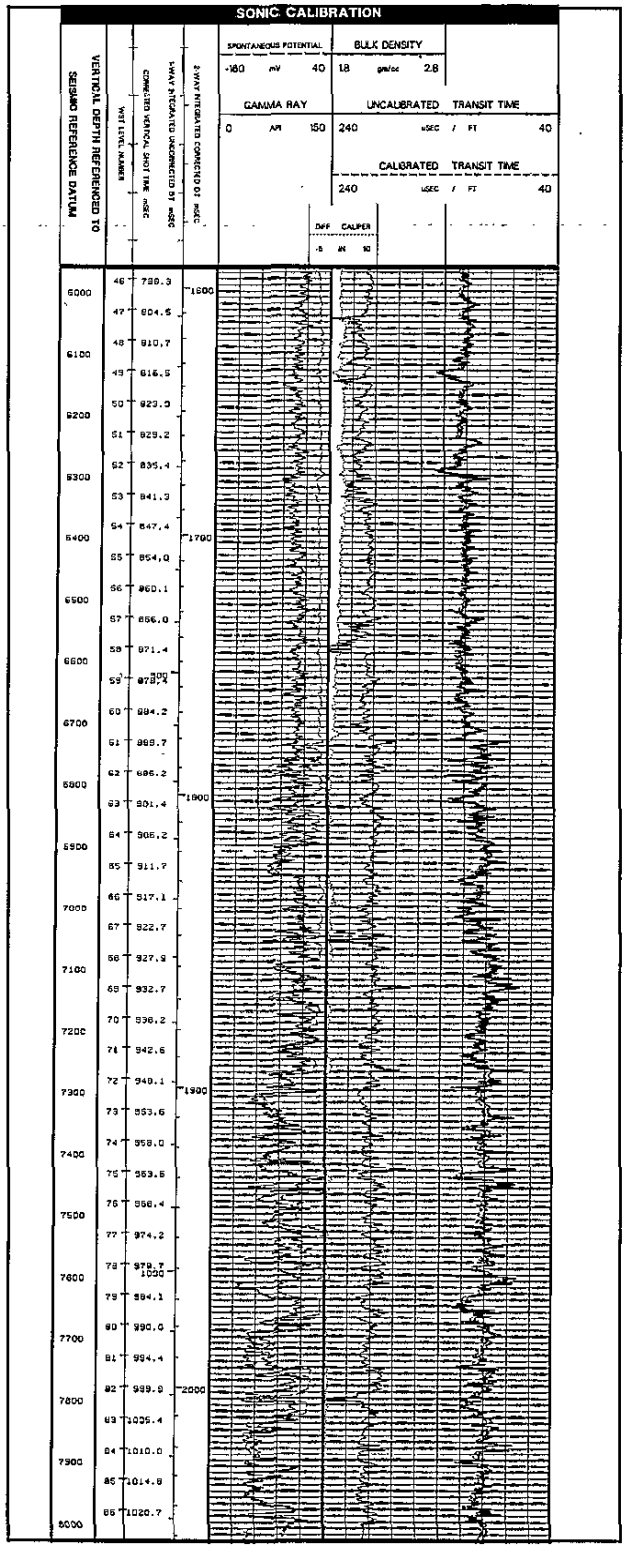

Fig. 11-3—Sonic calibration log.

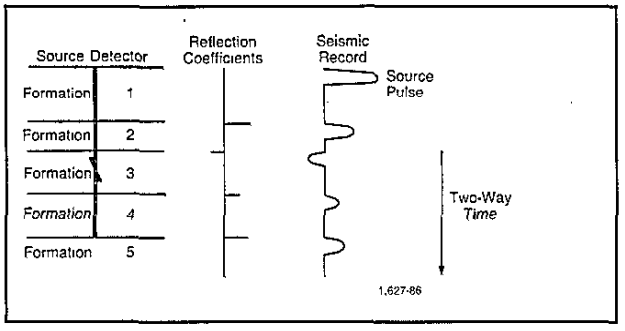

Fig. 11-4—Ideal seismic record giving position (in time) of reflector and value (amplitude) of reflection coefficient.

effect of the invaded zone; this is particularly important in gas-bearing formations. Geogram processing enables qualitative correlations as well as quantitative evaluations of seismic data to be made.

The Geogram processing sequence is shown in Fig. 11-5. The first two steps, which involve editing and sonic adjustments, are normally made during the time-to-depth conversion. Once the reflectivity series and transmission losses have been computed, the decision must be made on what type of wavelet to use for convolution. In order to give the best approximation of the actual source signature, several wavelets are available. These include Ricker minimum- or zero-phase, Klauder, spike with Butterworth filter, or other user-defined operators.

The Geogram display can be made with or without multiples and/or transmission losses, and with any desired frequency or band of frequencies. A typical Geogram display is shown in Fig. 11-6.

The structural dip, as interpreted from a dipmeter survey, can be incorporated into the presentation to permit the Geogram results to be projected away from the well (Fig. 11-7).

A Geogram display can help in the qualitative evaluation of the seismic sections by providing the following:

- an ideal seismic trace as a reference for the surface seismic data
- time-to-depth conversions
- detection of multiples
- seismic character correlation
- direct correlation with log intervals.

Seismic modeling can also be enhanced and processing time decreased by assuming a realistic model based on the Geogram computation. The original log data can be modified and used to generate new synthetic seismic traces. Other applications are inverse modeling and the design of the deconvolution operator. Furthermore, any log data, raw data, or

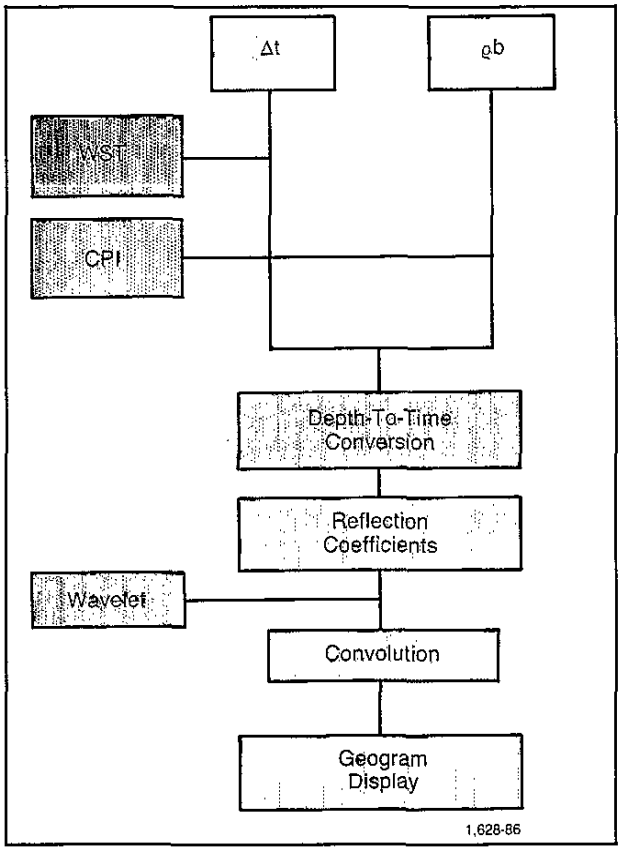

Fig. 11-5—Geogram processing chain.

processed data can be presented on a time scale for correlation with the seismic data.

VERTICAL SEISMIC PROFILE

Vertical seismic profiling is a technique of simultaneously recording the upgoing and downgoing wavetrains (Fig. 11-8). This represents a major advantage over the conventional surface reflection seismic technique, which records only the upgoing waves. By recording a sufficient number (50 or more) of fairly regularly spaced levels in the well, the upgoing and downgoing wavefields can be separated by computer processing. An analysis of the upgoing and downgoing components permits the detailed study of the change of the seismic wavetrain with depth. The acoustic properties of the earth can then be directly linked to and interpreted in terms of the subsurface lithology. The use of downhole sensors reduces the signal distortion caused by the low-velocity shallow layers since the signal passes only once through the surface layers.

The total wavefield recorded at the detector in the borehole consists of signals arriving from above the tool

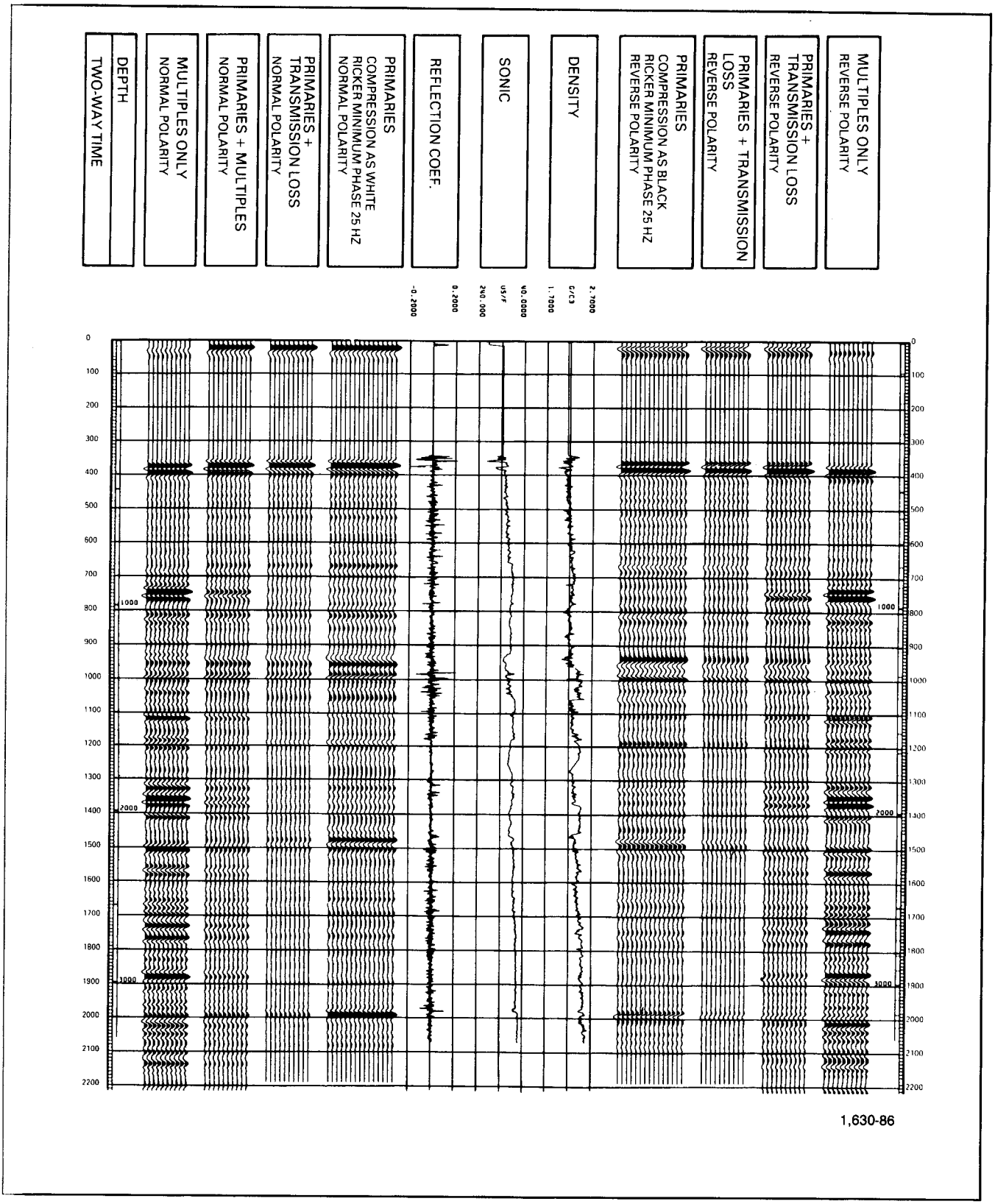

Fig. 11-6—Typical Geogram presentation.

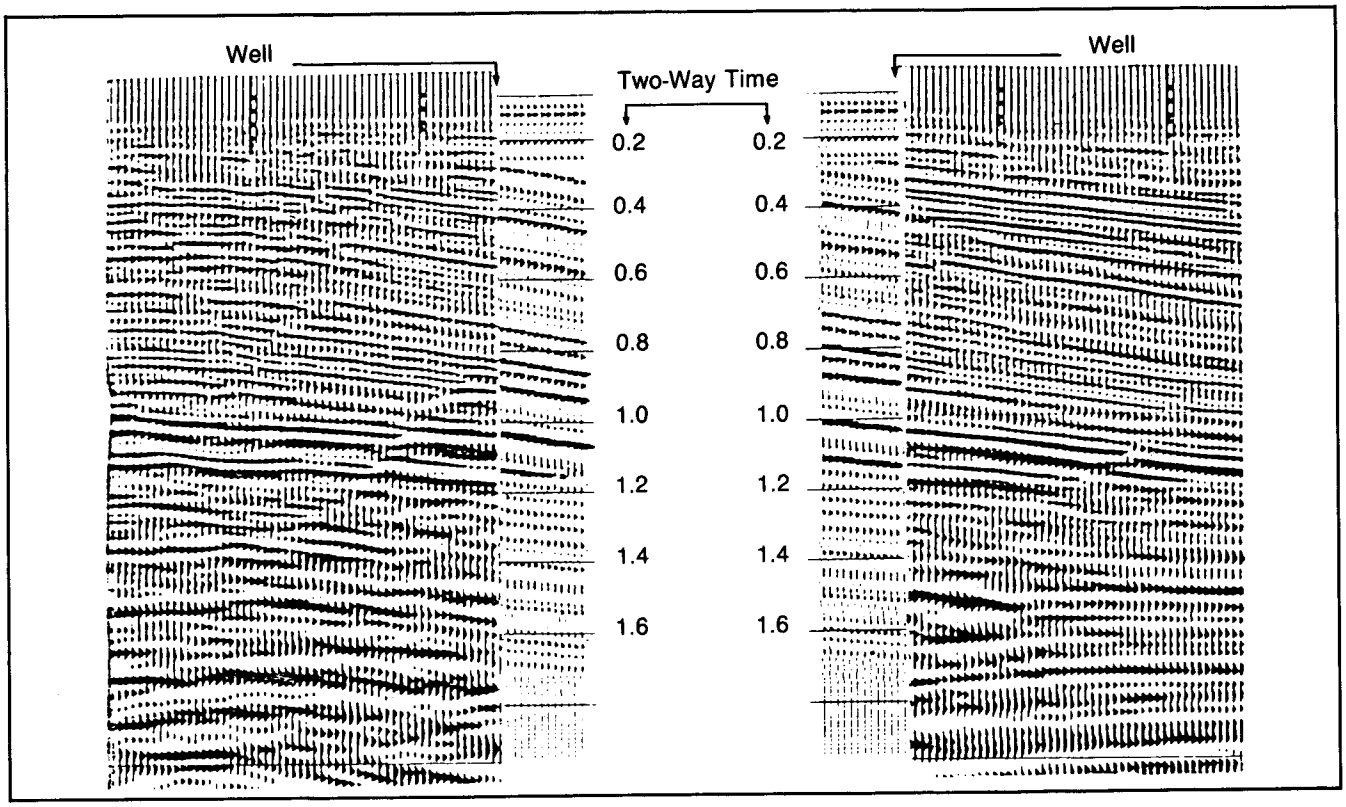

Fig. 11-7—Dip extrapolation: left part of section and right part of Geogram survey were put together and vice versa.

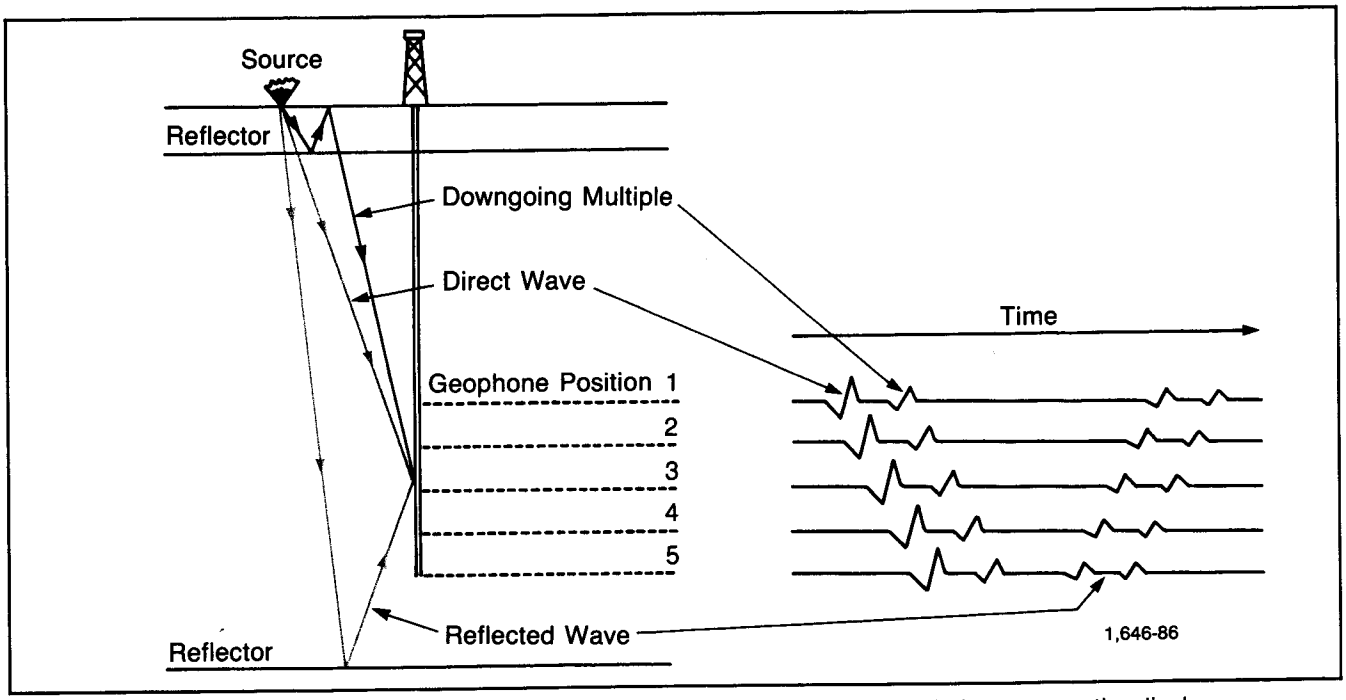

Fig. 11-8—A VSP trace contains upgoing and downgoing waves. Multiples can clearly be seen on the display.

(downgoing) and the signals arriving from below the tool (upgoing). The downgoing signals are the direct (first) arrivals and the downgoing multiples. The upgoing signals consist of the direct reflections and the upgoing multiples.

Advantages of the vertical seismic profile technique include:

- recording a real seismic trace in the borehole rather than relying on a synthetically generated seismogram
- measuring the spectral content of the downgoing seismic signal as a function of depth
- establishment of a precise link between the surface seismic results and well logs, since the VSP is a high-resolution measurement
- the recording of signals with an improved high-frequency content, since they cross the highly absorptive low-velocity layers near the surface only once
- improved seismic resolution of subtle stratigraphic features around the well, such as faults or pinchouts
- the recording of deep reflector signals that are not received at surface; this is particularly useful in structurally complex areas
- an excellent record of the band-limited reflection coefficient series through deconvolution of the VSP.

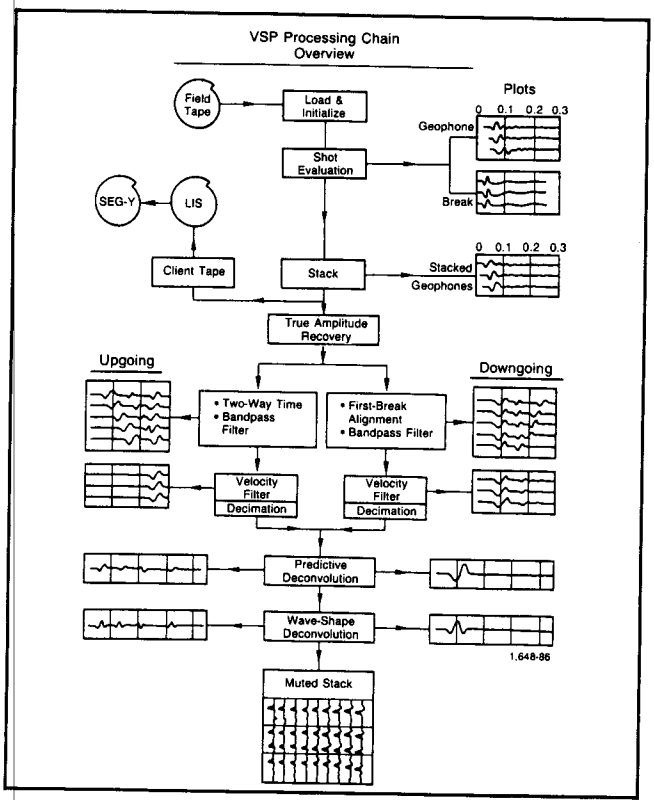

Fig. 11-9—Processing of VSP's involves three major steps: data editing for optimized shot quality, upgoing and downgoing wavetrain separation, and deconvolution.

VSP PROCESSING

The VSP processing sequence (Fig. 11-9) usually includes most of the following steps:

- shot selection by an analyst to reject the noisy, poor-quality shots
- consistency check of the surface hydrophone signal
- median stacking of shots
- check of coherence between a reference level and all others
- monitoring of phase shifts and acoustic impedance at all levels
- bandpass filtering to eliminate noise and remove aliased frequencies
- filtering to help eliminate tube waves
- true amplitude recovery by a time-variant function to compensate for spherical spreading
- velocity filtering to separate the upgoing and downgoing components of the total wavefield
- autocorrelation of the downgoing wave after filtering for selection of the proper deconvolution parameters using the downgoing wave field as a deterministic model
- predictive deconvolution to remove source signature effects and to improve resolution
- time-variant filtering to match the surface seismic data
- corridor stacking: summing all the upgoing waves recorded in a window following the first break.

A vertical seismic profile display using data from the Downhole Seismic Array tool is shown in Fig. 11-10. The corridor stack from this presentation is shown superimposed on the surface seismic section in Fig. 11-11.

OFFSET VERTICAL SEISMIC PROFILE

A normal VSP survey in a vertical borehole with horizontal bedding gives very limited lateral information. However, with dipping reflectors, a normal VSP survey can provide some information on the updip features (Fig. 11-12).

An offset VSP (Fig. 11-13), however, offers the possibility of large lateral coverage. Lateral coverage of up to one-half of the source offset distance can be achieved in the direction of the source. Profiling of a feature can be done by using a fixed offset source position some distance from the well and moving the geophone(s) in the well, or by having the geophone(s) fixed and moving the source.

WALKAWAY SURVEYS

A walkaway survey provides a 2-dimensional seismic picture of the formations on either side and below a well. This

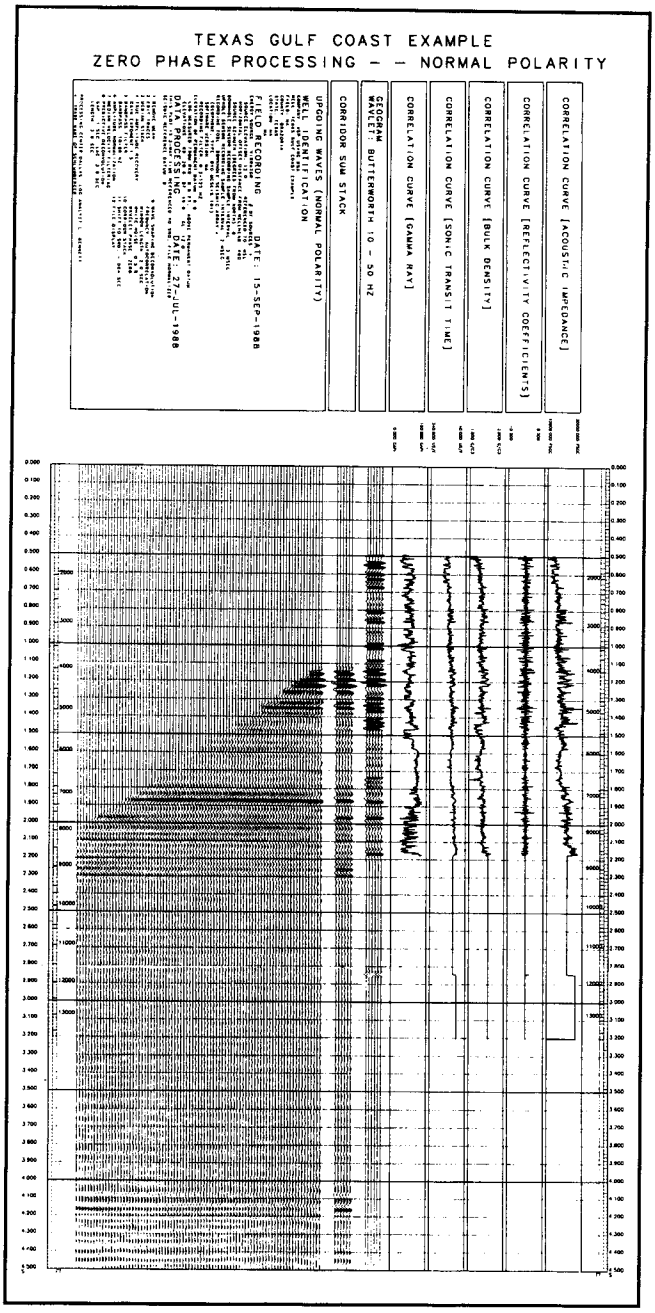

Fig. 11-10—VSP using DSA tool.

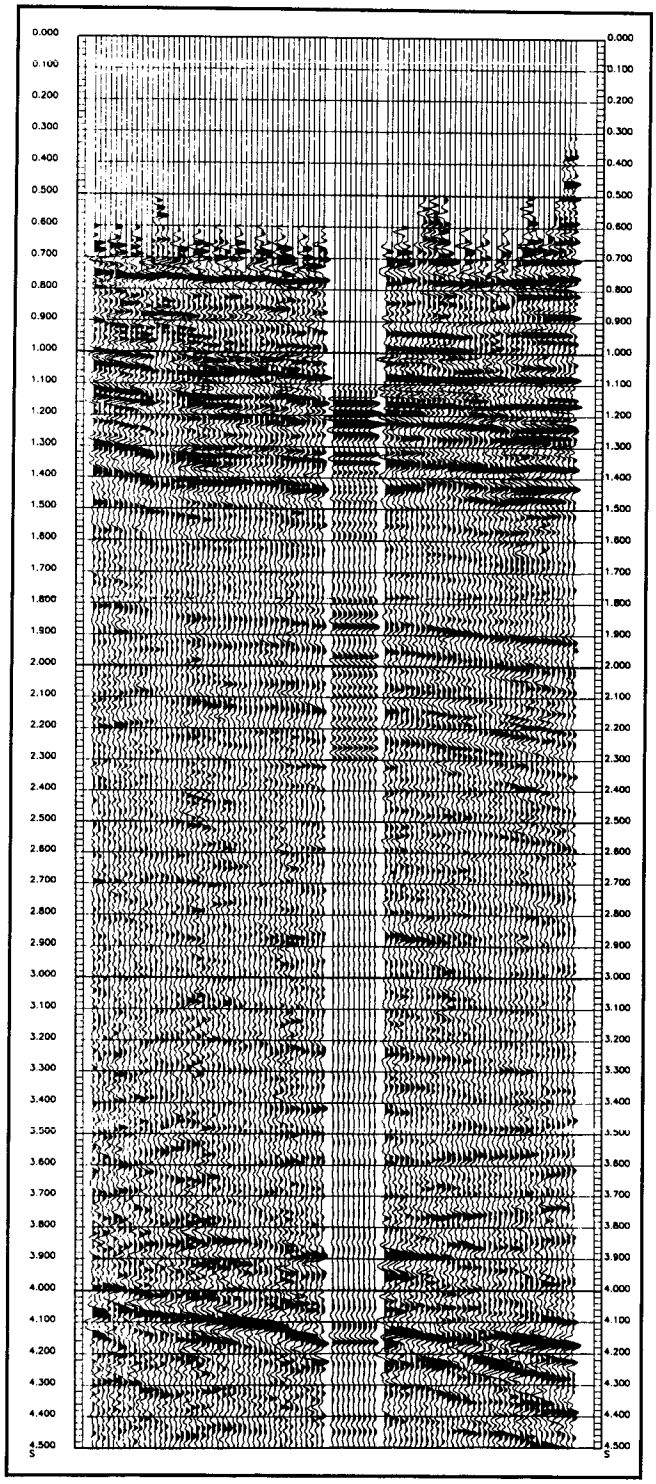

Fig. 11-11—VSP corridor stack from Fig. 11-10 superimposed on surface seismic section.

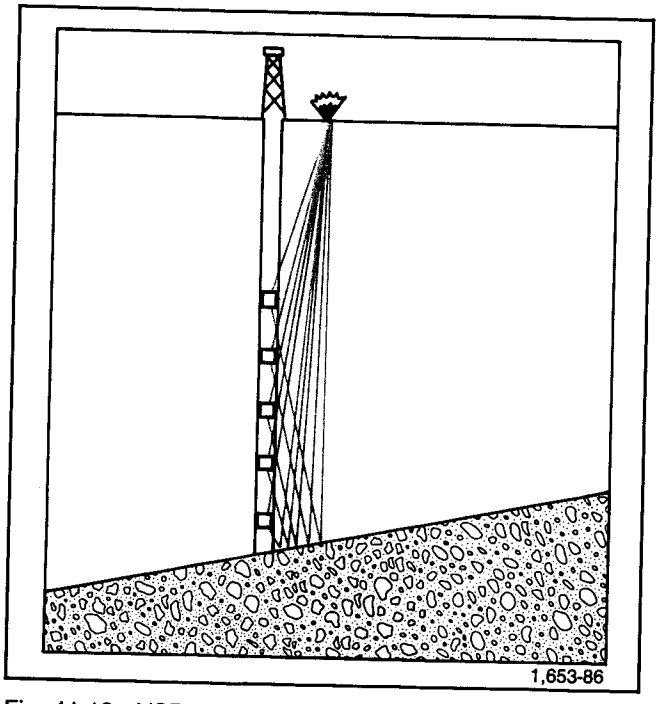

Fig. 11-12—VSP: stationary source, moving receiver.

is achieved by using survey techniques developed from Zero Offset VSP (ZVSP) and Offset VSPs (OVSP). Walkaway surveys are unique, however, in that they always employ a multiple source and single receiver arrangement.

A typical offshore walkaway survey would be carried out by a boat with the energy source, moving at a constant speed and direction along a 3 km line that passes close to the well. Seismic shots would be generated with an air gun at 30 m intervals along this line and a downhole geophone would monitor the arrivals. Each pass of the boat would generate 100 seismic wave traces at each geophone position. Accurate navigation fixes are obtained for each shot position along the survey line by placing navigation equipment on both the rig and boat. The seismic wave pattern created by this multi-source/single receiver arrangement is particularly useful in investigating complex formations.

The following illustrations show the family of borehole seismic surveys and the development of a walkaway survey. The first illustration (Fig. 11-14) shows the results of a check-shot survey. The impedance log (sonic × density) has been corrected with the check shot times to match the seismic times and a Geogram display computed from the data. Both logs are superimposed on the surface seismic section to allow correlation of the log data with the surface seismic events.

Figure 11-15 illustrates a ZVSP. In the ZVSP survey, the events beyond the check shot's first arrivals are recorded and interpreted, providing a time and depth record of upgoing reflected events. To obtain quality reflected data, a higher density of receiver positions is used than in the check-shot survey. A corridor stack of the VSP data is shown superimposed on the surface seismic section to allow correlation of depth and time.

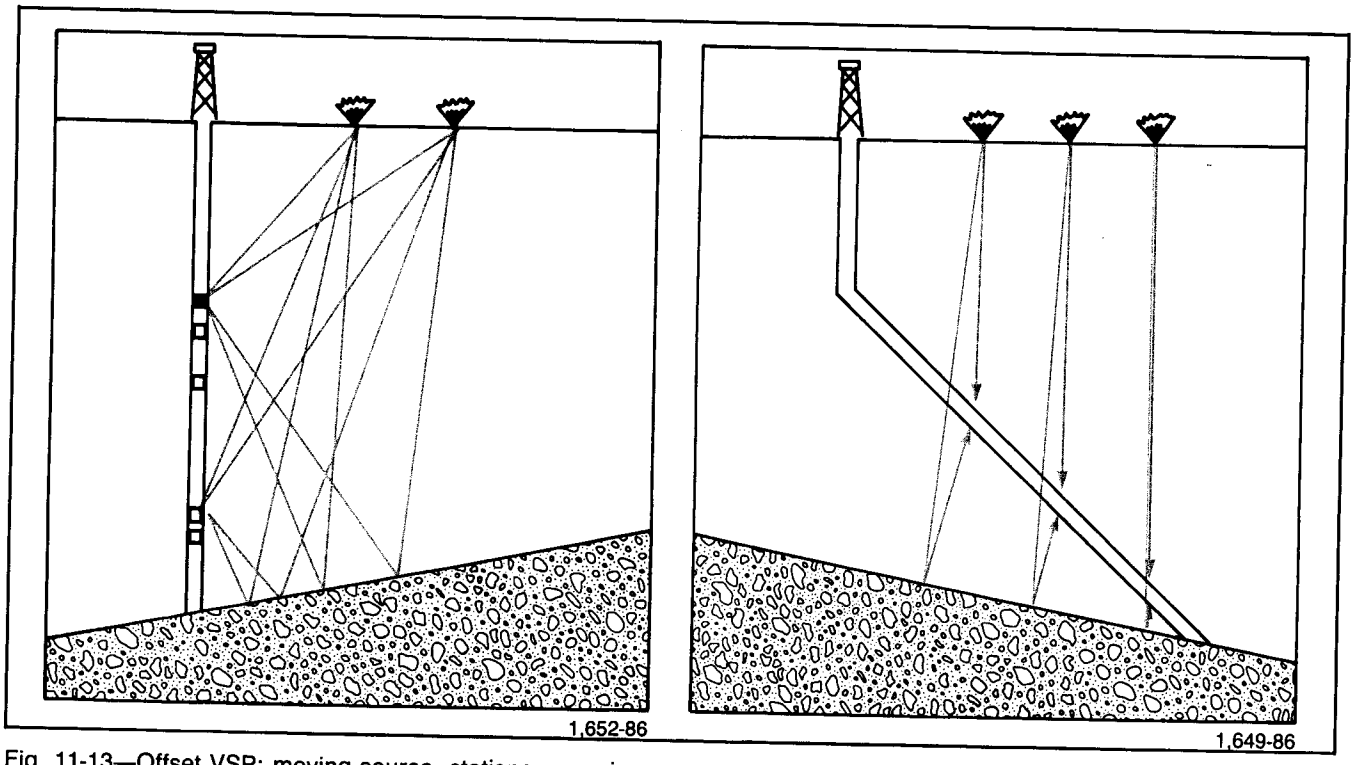

Fig. 11-13—Offset VSP: moving source, stationary receiver.

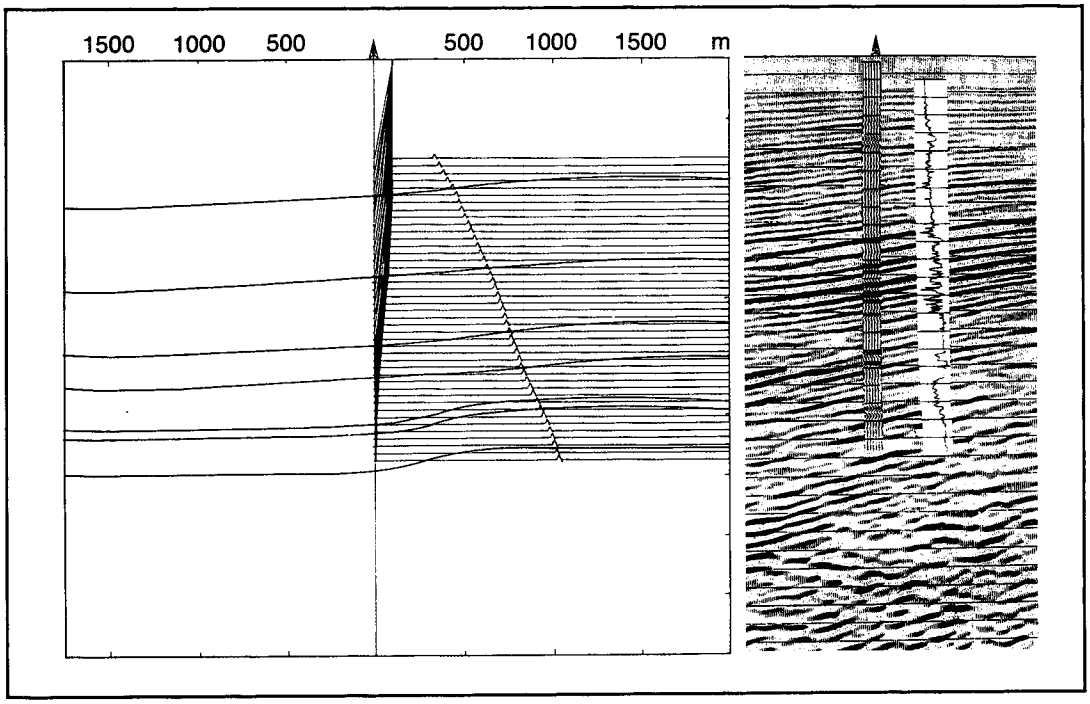

Fig. 11-14—An impedance log and Geogram log are shown superimposed on the surface seismic section.

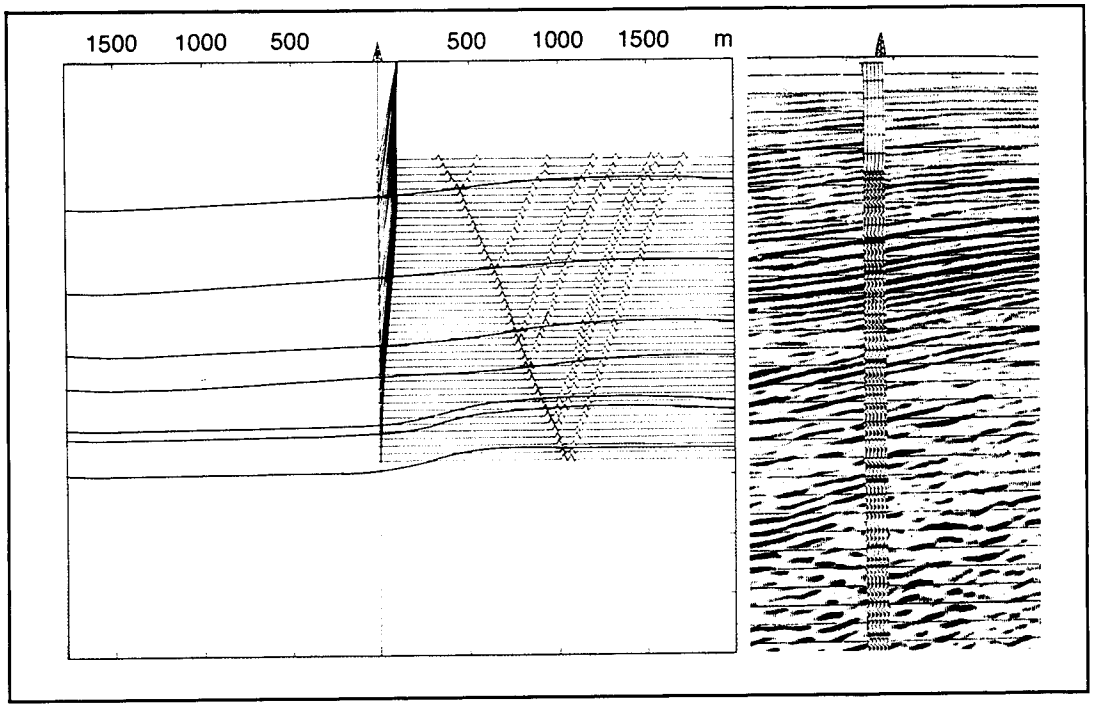

Fig. 11-15—Corridor stack of the VSP is superimposed on the surface seismic section to allow correlation of depth and time.

The same data from the previous acquisition has been processed with 2-dimensional model data to extend the offset position of reflection points on the dipping horizons (Fig. 11-16).

The OVSP is illustrated in display (a) of Fig. 11-17. In this case, the source is substantially offset from the well. This shifts the reflection points away from the well and produces coverage of an extended area around the well. This is

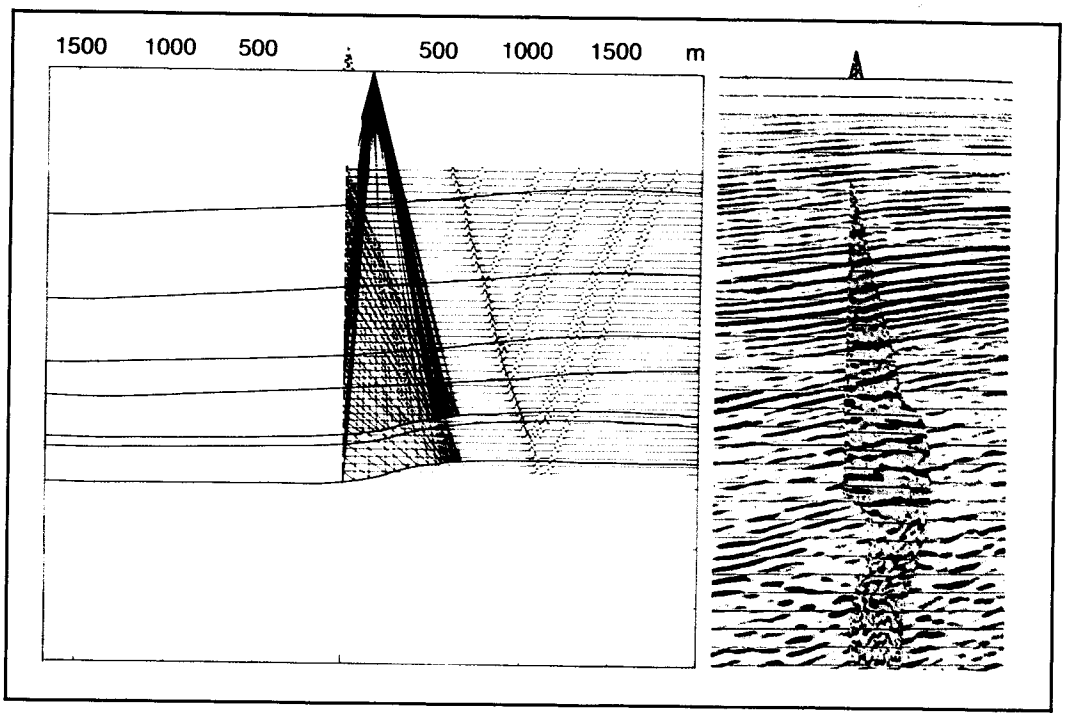

Fig. 11-16—Same data as Fig. 11-15, processed with 2-dimensional model data to extend the offset position of reflection points on the dipping horizons.

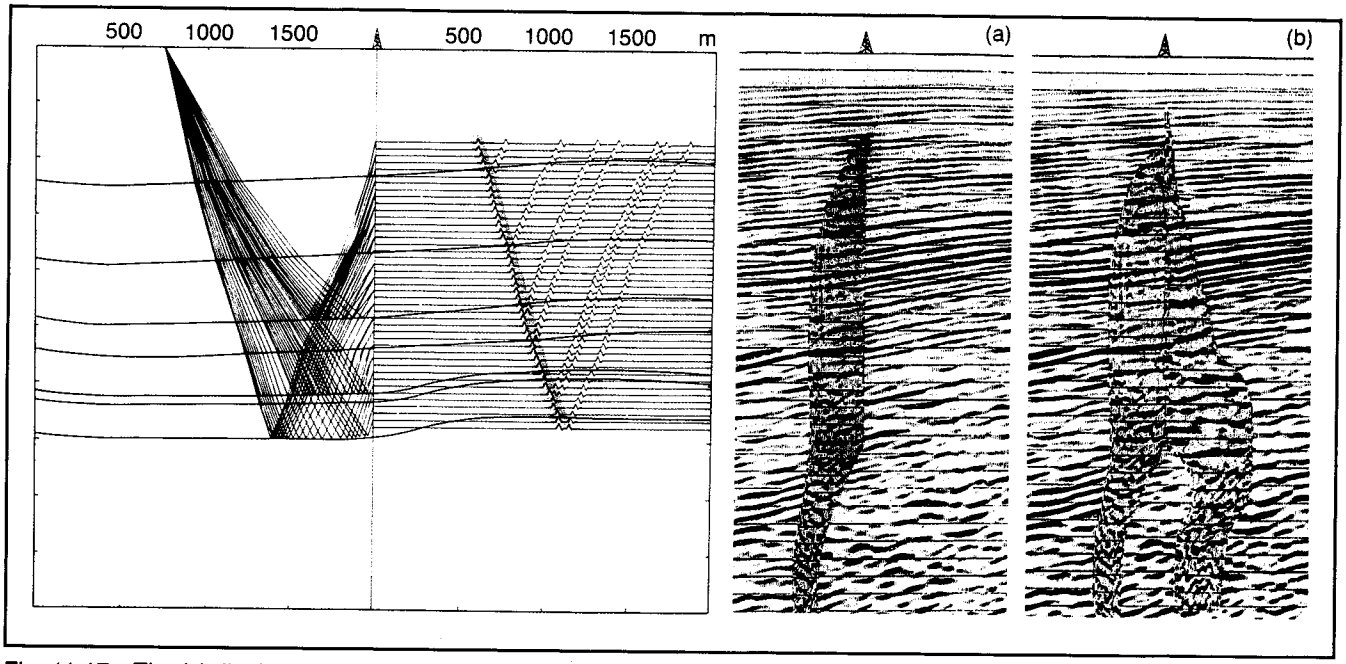

Fig. 11-17—The (a) display shows the Offset VSP events superimposed on the surface seismic section. The (b) display shows the combined results of the OVSP and modeled VSP data.

particularly useful for detection of faults and formation pinchouts. The OVSP events are shown superimposed on the appropriate part of the surface seismic data. The display (b) shows the combined results of the OVSP and modeled VSP data.

Note that there is no reflector coverage below total depth of the well. A particular attraction of walkaway surveys is that they provide better continuity and more complete coverage, especially below the bottom of the well.

The use of the Downhole Seismic Array tool to acquire the data can significantly reduce the acquisition time and improve the consistency of the seismic signal from level to level in the well. Figure 11-18 shows a schematic of the operational setup for a walkaway VSP job on land. Two vibrators, in radio contact with the logging unit, were used as the energy source. The shot points were located at 75 m intervals and were moved out 3 km from the well in each of the four orthogonal directions. At each shot position, eight levels were recorded with the DSA tool.

The east-west walkaway VSP results are shown on the left in Fig. 11-19. Faults, nearby and intersecting the well, were determined from this seismic section. The north-south walkaway section is shown on the right.

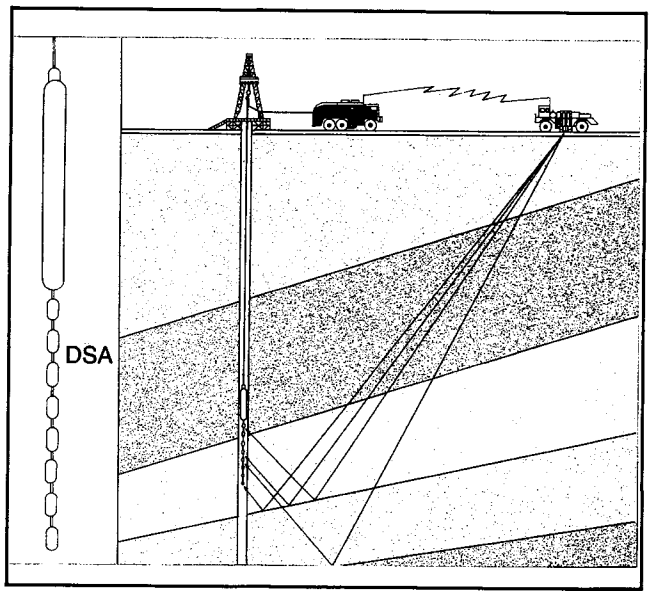

Fig. 11-18—Schematic of operational setup for a walkaway VSP job on land.

DSA TOOL FOR VSP ACQUISITION

The Downhole Seismic Array tool, with its eight single-axis geophone array configuration, provides several advantages over single level tools for VSP acquisition in cased holes:

- time savings. One obvious advantage is the savings in time since eight levels are recorded at each firing of the energy source.

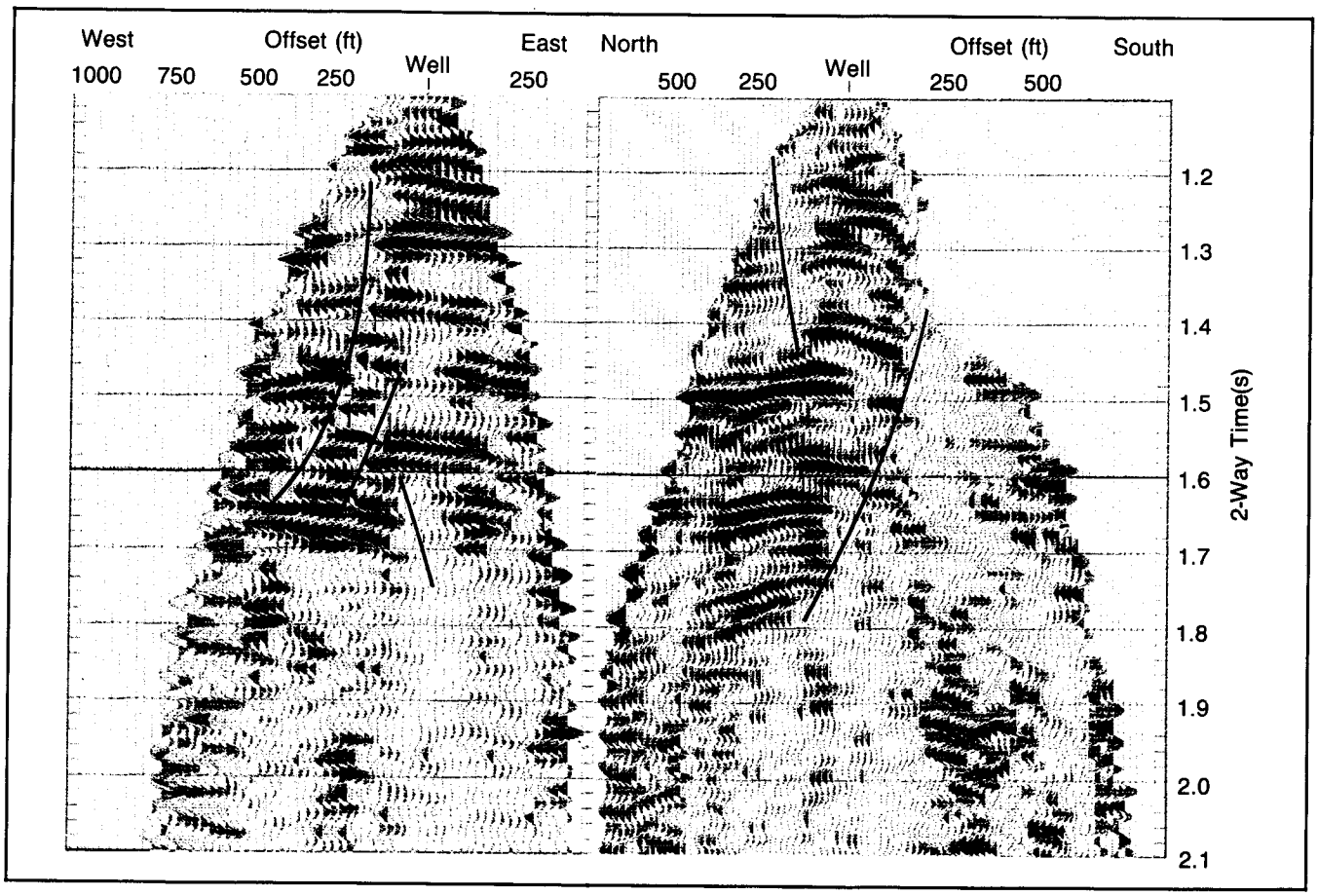

Fig. 11-19—The east-west walkaway VSP results are shown on the left, and the north-south results on the right.

- reduction in tube-wave effects. The DSA tool provides some advantages in areas where strong tube-waves may contaminate the waveform data. The strong clamping force, the small cross-sectional area, and the streamlined shape of the shuttle help to reduce the effect of tube-waves on the seismic data.
- reduction of navigation errors in walkaway VSP operations. In offshore multioffset operations, the seismic source is moved by a boat at a constant speed. The DSA tool acquires signals from eight levels while the boat is making a single path, reducing navigational errors over single level tools.
- reduction of effects of source signature changes. The effects of source signature changes due to such things as changes in gun pressure, gun pit alteration, or tide levels, are reduced because the eight shuttles receive signals which originate from the same shot.
- accurate transit times between levels. Since the DSA geophones are equally spaced on a cable, potential distance errors are eliminated.

PRIMARY USES OF THE VSP SURVEY

The enhanced resolution of the VSP makes it possible to verify or deny the presence of reflections that are indistinct or doubtful on seismic sections near the well. The VSP is particularly well suited to determine the conditions existing below the well's total depth. Overpressured zones, gas sands, and deep reflectors can be verified or recognized.

Since the downgoing wavefield is recorded, multiple reflections can be identified and removed. The same downgoing wave information can be used to reprocess surface seismic profiles traversing the vicinity of the well.

Perhaps the most common use for the VSP is a link between reflections observed on a surface seismic profile and specific petrophysical properties measured in the borehole. The correlation role of the VSP is important for reservoir development applications.

Finally, by positioning the seismic source a significant distance from the well, structural and stratigraphic features from hundreds to thousands of feet from the well can be delineated and verified against the surface seismic.

PROXIMITY SURVEY INTERPRETATION

Proximity surveys have been used for many years to define the shape of salt domes. Now a program is available to entirely mechanize the interpretation process. After a well has been drilled on the flank of a salt dome, a downhole sensor is lowered into the hole and anchored at numerous depths. An energy source is positioned directly over the top of the structure. A travel time is measured from the source to each of the downhole sensor locations. From prior knowledge of salt velocities, velocities of formations encountered in the well, and at least one salt tie point, distances from salt to sensor positions can be calculated, and the shape of the salt flank determined.

Given the layer velocities and the source and receiver locations, the transit times to each receiver are measured by ray tracing. Next, an initial model is generated on the computer containing the known source and receiver locations and the layer velocities. The program then calculates, for each source-receiver pair, all the possible travel paths the acoustic energy could have taken with the total time equal to the measured time. A line through all the refraction points contains all the possible locations for the salt interface calculated from one receiver. The resulting oval is called an aplanatic surface (Gardner, 1949). The computation can be performed for combinations of source and receiver, and will result in a series of aplanatic surfaces. The best fitting line, tangent to all the ovals, is the final solution for the location of the interface.

The technique is illustrated in a well in the Gulf of Mexico. Using accurate source-receiver travel times and the source-receiver positions, the initial model was generated. The salt was a known distance from one receiver, which enabled the use of the refraction oval technique for the determination of the salt top. The formation velocities adjacent to the salt were determined from a vertical check shot and the aplanatic surfaces were generated, as shown in Fig. 11-20. The salt flank was interpreted as the common tangent line illustrated in Fig. 11-21.

The mechanized proximity interpretation gives results consistent with the interpretation made with wavefront charts, but is much less time consuming.

REFERENCES

Anstey, N.A.: *Seismic Interpretation: The Physical Aspects*, IHRDC, Boston (1977).

Ausburn, B.E.: "Well Log Editing in Support of Detailed Seismic Studies," *Trans.*, 1977 SPWLA Annual Logging Symposium.

Gardner, L.W.: "Seismograph Determination of Salt Dome Boundary Deep on the Dome Flank," *Geophysics* (1949) **46**, 268-287.

Goetz, J.F., Dupal, L., and Bowler, J.: *An Investigation Into Discrepancies Between Sonic Log and Seismic Check-Shot Velocities*, Schlumberger Technical Services (1977).

Landgren, K.M. and Deri, C.P.: *A Mechanized Process for Proximity Survey Interpretation*, Schlumberger Offshore Services (1986).

McCollum, B. and LaRue, W.W.: "Utilization of Existing Wells in Seismograph Work," *Bull.*, AAPG (1931) **15**, 1409-1417.

Miller, D.E.: "Arrival Times and Envelopes - Inverse Modeling for Subsurface Seismics," 53rd Annual International SEG Meeting, Sept., 1983, Las Vegas, Expanded Abstracts, 449-467.

Mons, F. and Babour, K.: Vertical Seismic Profiling, SAID Quatrieme Colloque Annuel de Diagraphies (Oct., 1981).

Musgrave, A.W., Wooley, W.C., and Gray, H.: "Outlining of Salt Masses by Refraction Methods," *Geophysics* (1960) **25**, 141-167.

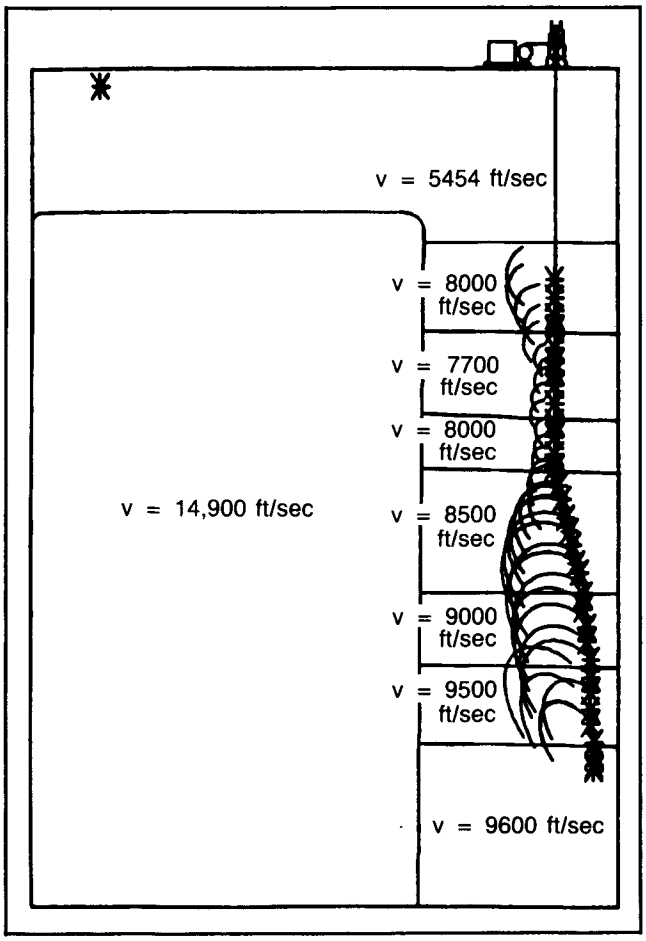

Fig. 11-20—Proximity Survey interpretation: refraction ovals.

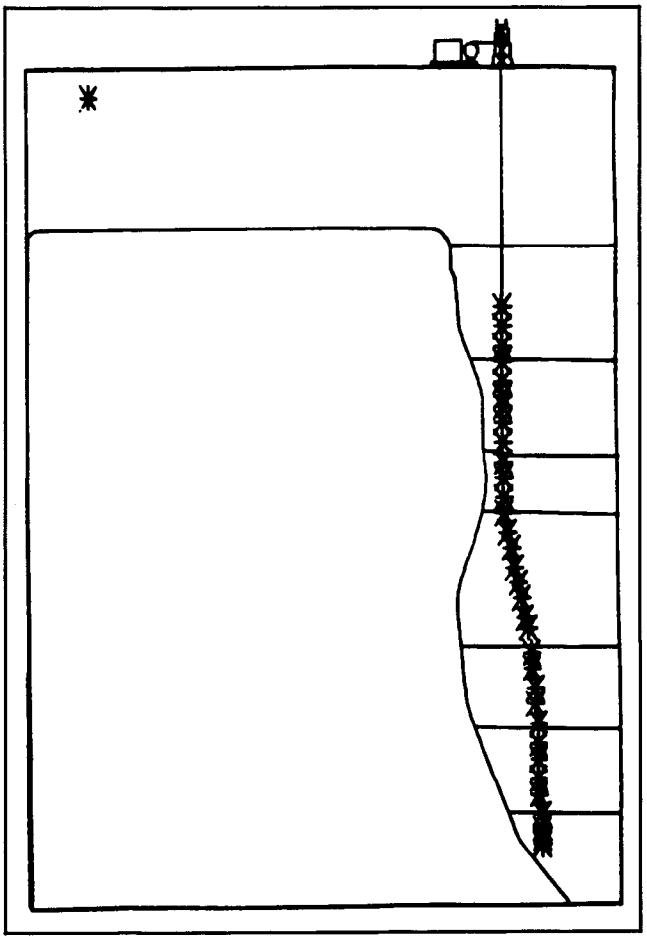

Fig. 11-21—Proximity Survey interpretation: final solution.

Robinson, E.A. and Treitel, S.: *Geophysical Signal Analysis*, Prentice-Hall Inc., New Jersey (1980).

Schlumberger Middle East Well Evaluation Review "Borehole Seismics", Schlumberger Technical Services, Paris (Autumn 1988).

Schlumberger West Africa Well Evaluation Conference, Schlumberger Technical Services, Paris (1983).

12 Geologic Services

INTRODUCTION

Wireline logs provide a continuous recording of formation parameters versus depth that can be very useful for geologic applications. These range from simple well-to-well correlations through stratigraphic information to the study of entire reservoirs.

Lithology determination from wireline logs was covered in Chapter 6. This chapter gives a brief overview of the applications of wireline logs for other geological information. The three fundamental geological parameters — composition, texture, and structure — can be related in some manner to the response of well-logging sensors.

The composition of a rock can be expressed as minerals or as chemical elements. The mineral composition provides the petrophysical properties, such as hardness, density, resistivity, and travel time. Some tools measure the concentration in elements, while others have a response that depends on the percentage and distribution of the minerals in the rock. Table 12-1 summarizes the relationship between rock composition and logging parameters.

Table 12-1
Relationship between composition of a rock and well logging parameters.

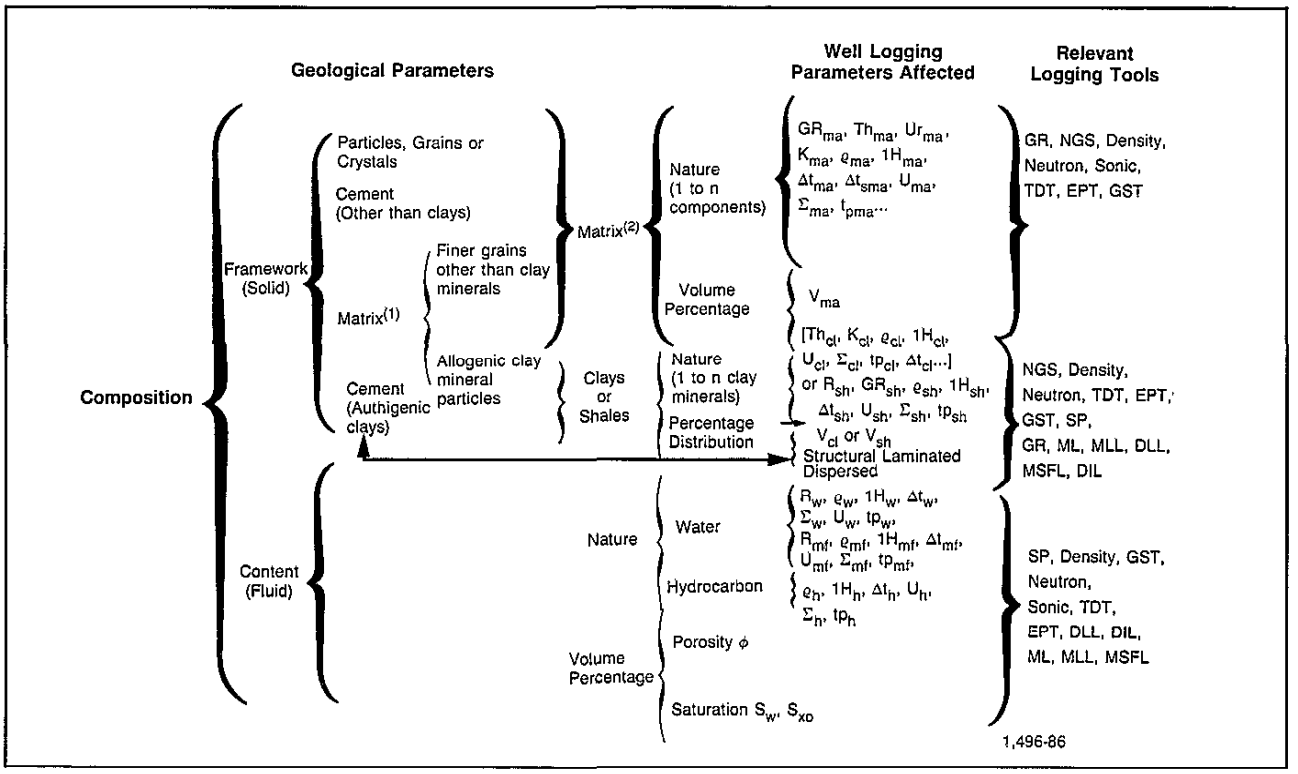

Texture relates to the geometrical aspects of the rock constituents, such as grain size sorting, packing, shape, and arrangement (fabric); matrix and cement arrangement; and the grain-grain, grain-matrix, or grain-cement contacts. The petrophysical properties of the rock, such as porosity and permeability, depend primarily on texture. Table 12-2 shows the relationship between rock texture and log parameters.

While texture deals with the grain-to-grain relations in a rock, sedimentary structures are related to the larger features that reflect the conditions at the time of deposition, such as energy and type of current. Structures constitute an important element of the facies of a sedimentary unit and aid in defining the depositional environment. The relationship between sedimentary features and log parameters is summarized in Table 12-3.

CORRELATION

One of the first uses of well logs was correlation of equivalent strata from one well to the next. This is still one of their most important uses. Intervals of logs from different wells are matched for similarity or for characteristic log responses to lithological markers.

Well logs have the advantage (for correlation) of providing a continuous record over the entire well. There are no missing sections as can be the case with core samples. Most important, because sonde depth is recorded, there is no ambiguity as to the depth of the various markers.

Well-to-well correlation studies thus permit accurate subsurface mapping and the determination of:

- The elevations of formations present in the well relative to other wells, outcrops, or geophysical projections.
- Whether or not the well is within a given major geological structure.
- Whether well depth has reached a known productive horizon, and, if not, approximately how much remains to be drilled.
- The presence or absence of faults.
- The existence of dips, folds, unconformities; the thickening and thinning of lithologic sections; or lateral changes of sedimentation or lithology.

Any continuously recorded log has some correlation potential, and every known openhole log has no doubt been used. For the best correlation, however, the log should respond to some property of the stratum that does not vary too much from well to well.

Table 12-2
Relationship between rock texture and well logging parameters.

Textural Parameters			Reservoir Characteristics Depending On Textural Parameters		Well Logging Parameters Affected	Relevant Logging Tools
Texture	Particles or Grains	Size	• Porosity	ϕ	R, ϱb, I_H, Δt, Σ, tpl, P_e	DLL, DIL, ML, MLL, MSFL
		Shape: Roundness, Sphericity	Total Porosity	ϕ_t		Density, Neutron Sonic, TDT, EPT, GST
		Sorting Packing Orientation	Primary Porosity	ϕ_1		
			Effective Porosity	ϕ_e		
			• Tortuosity or Cementation Factor	m	R, F, Δt, tpl	DIL, DLL, ML, MLL, MSFL, Sonic, EPT
	Matrix	Percentage	• Size Of Pores And Throats Which Control			
		Nature	Permeability	k	• S_{wi} • di • K, k_{rw}, k_{ro}	DLL, DIL, ML, MLL, MSFL SP
			Horizontal	k_H		
			Vertical	k_V	• SP curve shape	SP
			• Wettability			
	Cement	Percentage	• Anisotropy		• λ	DIL, DLL, MLL, MSFL
		Nature				

1,498-86

Table 12-3
Relationship between sedimentary features and well logging parameters.

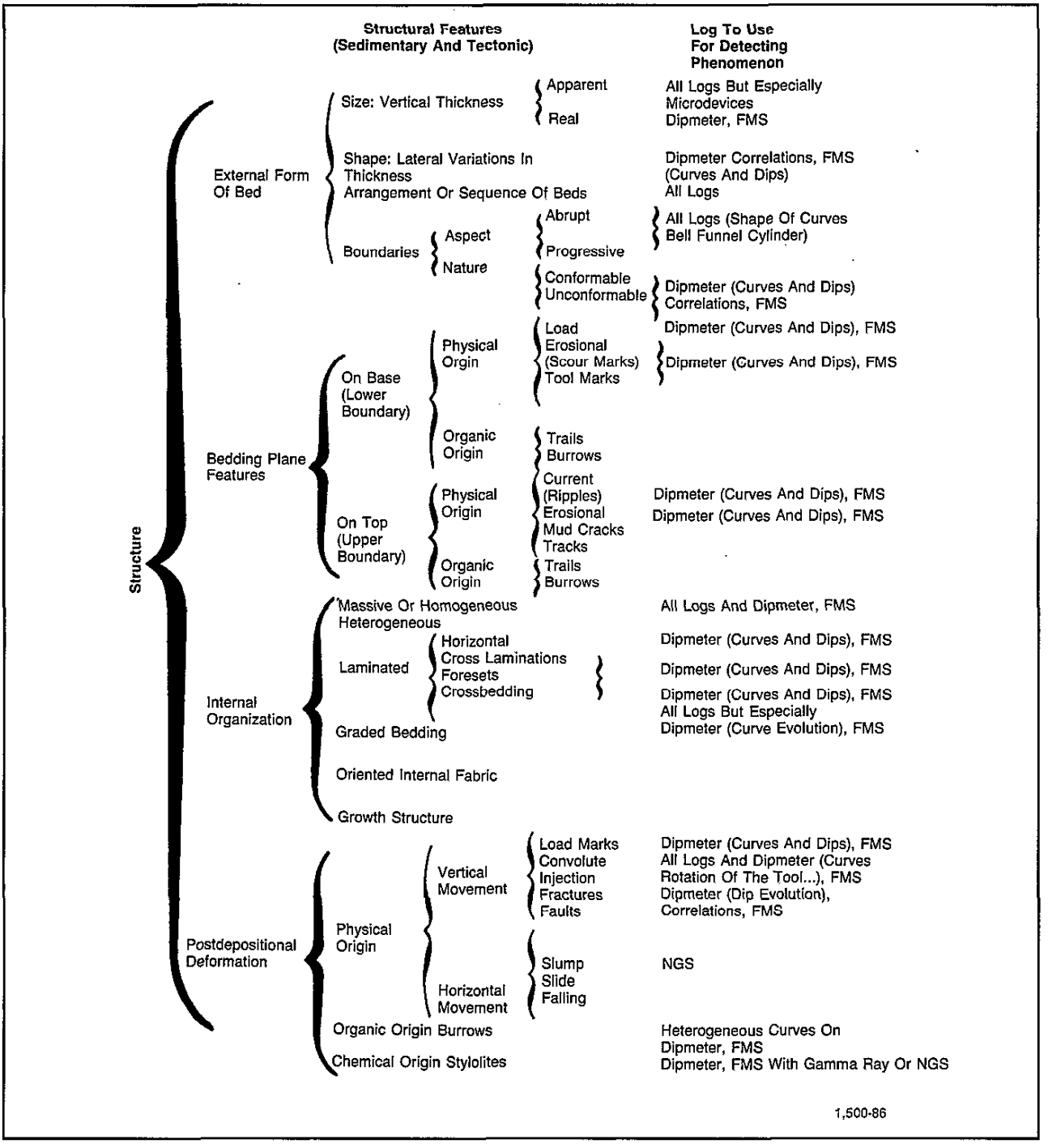

The logs most frequently used for correlation are the resistivity, SP, and gamma ray. The basic logs used in the majority of log-correlation studies are listed in Table 12-4 with their various uses and advantages. The dipmeter is a valuable supplement.

Some computed logs have good correlation features. Examples are the apparent-matrix-density (ϱ_{maa}) curve, the shale-fraction (V_{sh}) curve, the silt-fraction (V_{sl}) curve, lithology analysis, and Geocolumn* display (Fig. 12-1).

Table 12-4
Basic well logs used for correlation.

Log	Correlates On	Conditions For Best Use	Uses Or Advantages
SP	Permeable beds vs. shale beds.	Uncased hole. Good contrast between R_{mf} and R_w. Low-to-moderate formation resistivity. Fresh mud (but still useful in saline mud).	Displays easily read shale-sand profiles. Much used (usually with resistivity for correlation. Not affected by washed-out holes or deep or variable invasion.
Gamma Ray	Radioactivity associated with shaliness. Radioactive beds.	Moderate hole size with no large washed-out zones.	Insensitive to drilling fluid; thus can be used in oil- or salt-based muds and in air- or gas-filled holes. Can be used in cased hole.
Short-Spacing Resistivity (SN, LL8, SFL)	Invaded, porous beds. Deflection depends on formation factor, water resistivity, and shaliness. Dense strata (low water content and nonconductive matrix).	Uncased hole. Fresh mud. Invaded formations, not too resistive.	Much used (usually with SP or gamma ray) for correlation.
Amplified Short-Spacing Resistivity	Same as above.	Same as above.	Useful for correlation in shales or other low-resistivity sections.
Deep Laterolog	Same as above.	Uncased hole. Fresh to salt mud. High R_t/R_w ratio.	Useful for salt muds, resistive formations.
Induction Log	Variations of water content (and salinity) in beds with nonconductive matrix. (Porous-zone response varies with formation porosity and pore-fluid conductivity.)	Uncased hole. Fresh mud. Formation resistivity below 100 ohm-m.	The induction conductivity curve is useful for correlation in shales or other low-resistivity sections.
Sonic	Δt (dependent on lithology and porosity).	Liquid-filled gas-free holes.	Good porosity correlation, useful in low resistivities. Provides Δt parameter measurement for identification of lithological markers.
Neutron	Hydrogen content of formation. Large shale response.	Depends on tool type.	Good porosity correlation. Good in combination with other logs for gas detection. Provides ϕ_N parameter measurement for identification of lithological markers. Useful in cased holes. (Often run with gamma ray.)
Density	Formation density (dependent on lithology and porosity).	Uncased hole, with little mudcake and no hole-wall rugosity.	Chiefly useful for identification of lithological markers.
Caliper	Hole-size variations (washouts, noncircular boreholes, fracturing).	Uncased hole.	Seldom correlatable by itself, but often helps resolve ambiguities on other logs.

1503-86

*Mark of Schlumberger

The structural-dip angle from dipmeter logs is a valuable additional piece of information for well-to-well correlation, since it can be used to predict expected changes in elevations of strata from one well to the next (Figs. 12-2 and 12-3). This facilitates identification of corresponding beds and helps in the analysis of structural and stratigraphic anomalies such as faults and unconformities. Dip patterns associated with various geological structures and stratigraphic features are discussed in detail in Ref. 2.

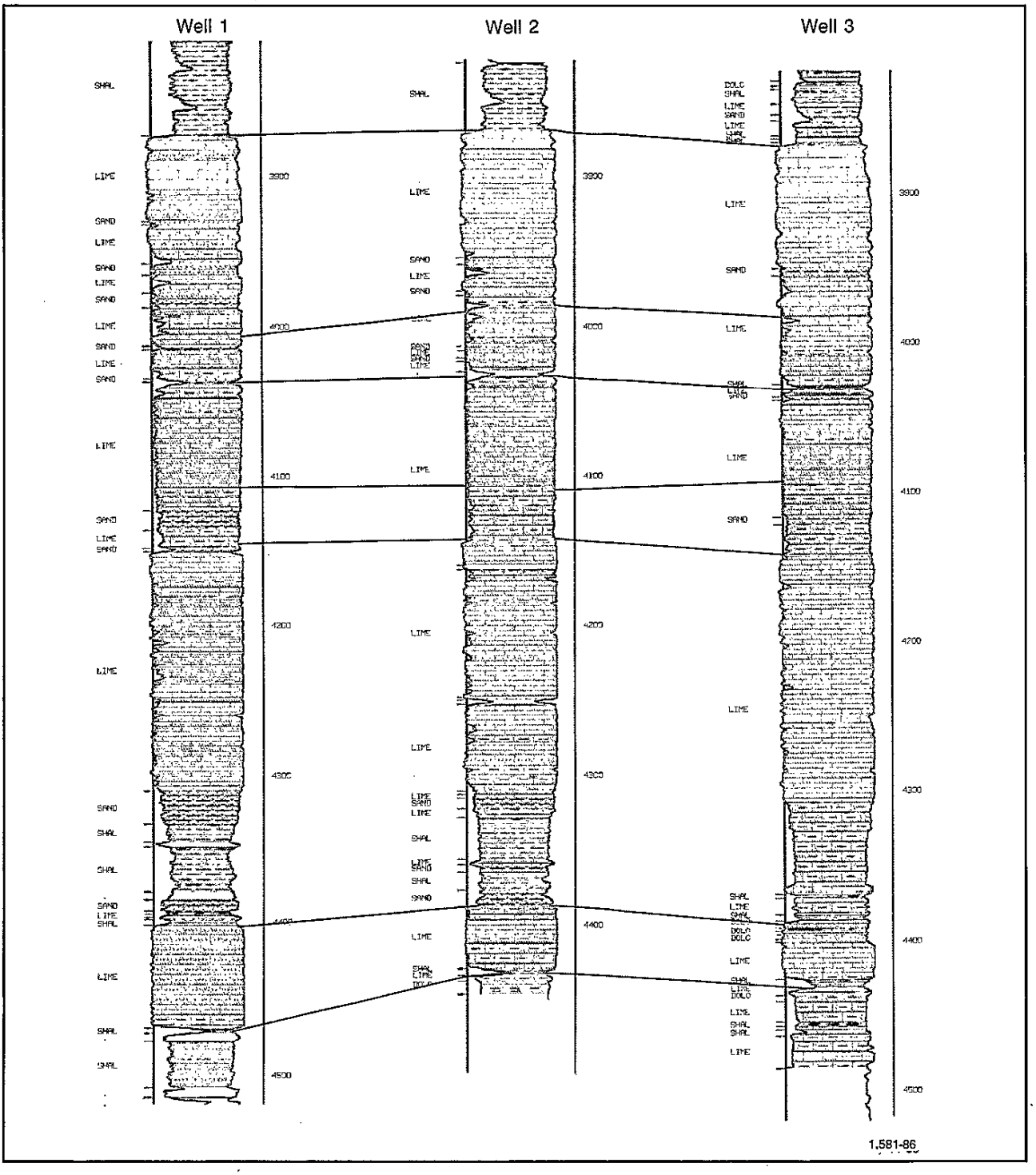

Fig. 12-1—Cross section showing detailed correlation with computed Geocolumn display.

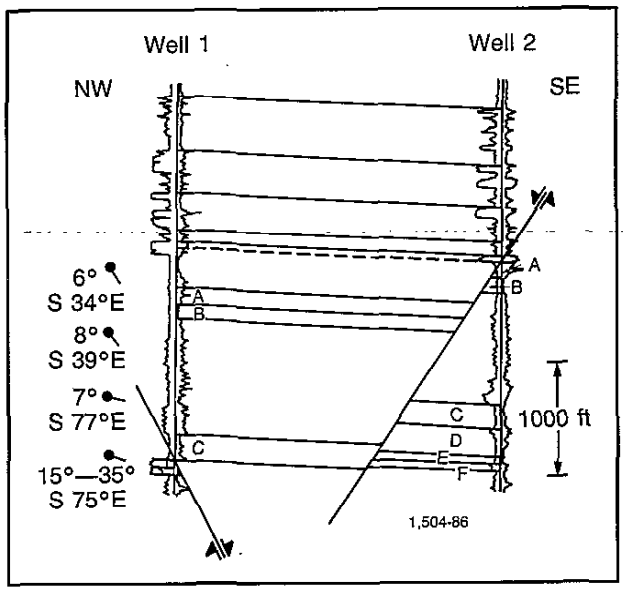

Fig. 12-2—Cross section showing faulting. The dipmeter in Well 1 confirmed the correlations in the upper parts of the two wells.

A useful presentation of dipmeter data for correlation use is the "stick plot." In a stick plot, the wellbore is represented by a (usually) vertical line; apparent dips in the plane of a given vertical cross section are shown by short line segments intersecting the wellbore line at the appropriate angles. Fig. 12-4 shows stick plots of three wells, with correlation lines drawn in. (These three wells are not in a line; the direction of the cross section from Well 1 to Well 2 is 360°-180°, whereas from Well 2 to Well 3 the direction is 317°-137°.) The particular stick plots of Fig. 12-4, along with stick plots of other nearby wells, were used to study geological structure in beds adjacent to a diapiric shale dome.

STRATIGRAPHIC INFORMATION FROM THE DIPMETER

All openhole logs can reflect sedimentary features, but, for most tools, the vertical resolution is not sufficient to detect thin events or sequences and give a detailed description of the rock. The dipmeter tools, however, can detect the very thin events that are related to sedimentary features. Here, the usefulness of the dipmeter for

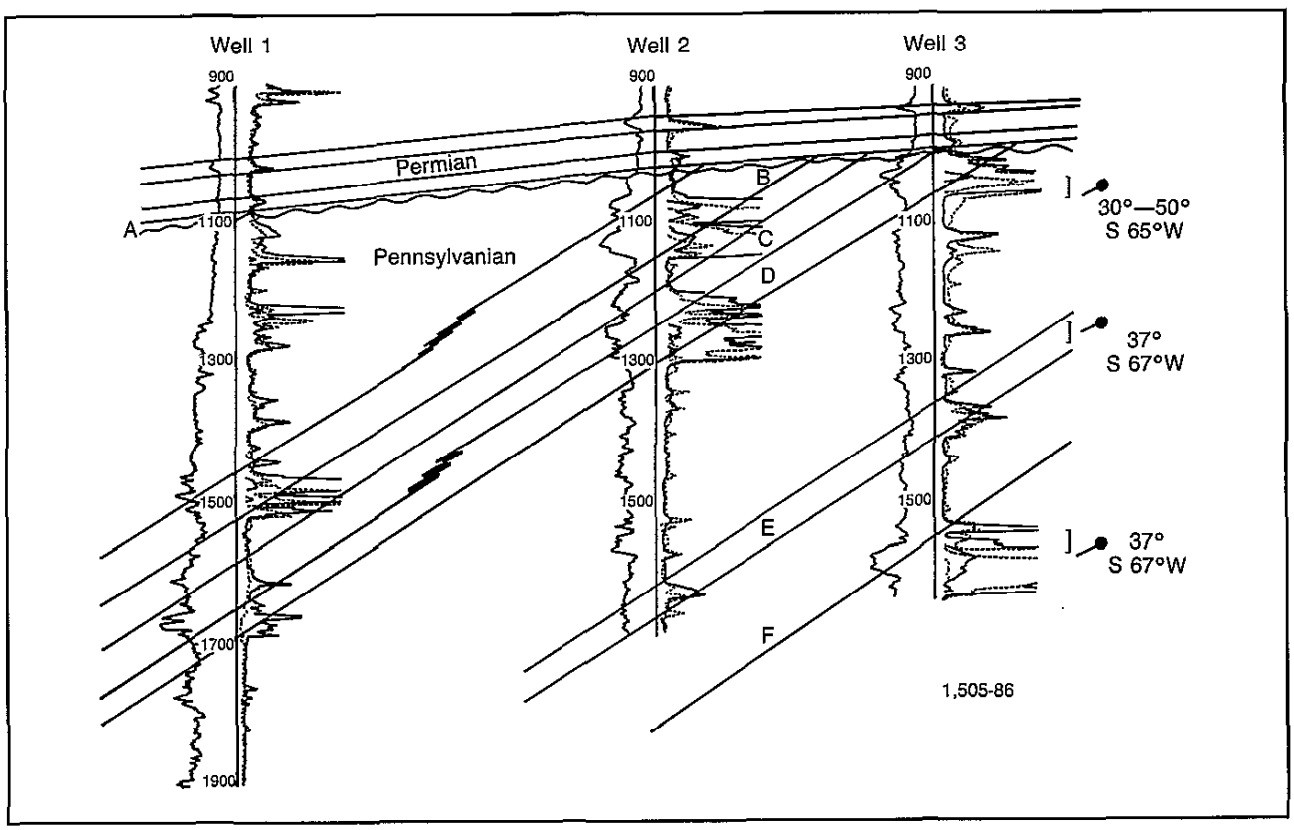

Fig. 12-3—Cross section in which correlation was not readily apparent from electric logs alone. Correlation was resolved by the dipmeter run in Well 3.

stratigraphic investigations is covered only briefly. More detailed information is available in Refs. 2-6 and 15.

With the introduction of electronic computers, dipmeter data can be interpreted in much more detail. Dips are computed at many more levels, and computations are made by correlating the dipmeter curves over shorter intervals. These short-interval correlations reveal the fine structure of current bedding and other sedimentation-related dips. In addition, the computer makes possible the use of statistical mathematics to pick the most probable solution. When long-interval correlations are made, this detailed information is averaged out, and essentially what remains is the structural dip. Even interpretation of dipmeter results can now be done by computer (see Dipmeter Advisor later in this chapter).

The geologic definition provided by short-interval correlations has been further enhanced by the use of the HDT* high-resolution dipmeter and the newer Dual Dipmeter* (SHDT) tools; these tools are designed to yield correlation curves of great detail. Data are also recorded for an automatic correction of variations in sonde velocity.

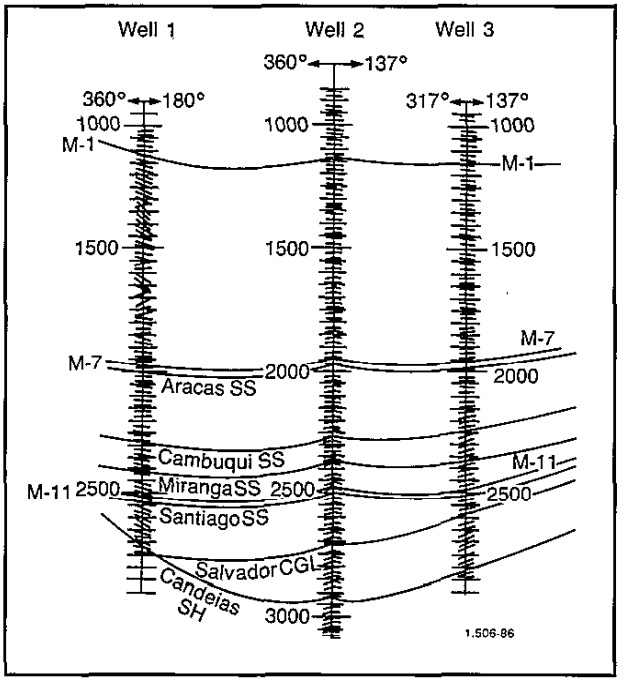

Fig. 12-4—Cross sections derived from dipmeter stick plots. The vertical lines represent the wellbores. The short line segments intersecting the wellbore indicate apparent dip in the indicated cross sections.

Dipmeter results are usually presented in "arrow" plots (or "tadpole" plots, as they are sometimes called) as illustrated in Figs. 12-5, -6, and -7. The stem on each plotting symbol indicates the direction of the dip. The displacement of the symbol from the left edge of the plot represents magnitude of dip angle. Vertically, the symbols are plotted versus depth.

It is common practice to identify various characteristic patterns on the plots by coloring them. In the jargon of the dipmeter interpreter the various patterns are called by the color names. Fig. 12-5 illustrates the red, blue, and green patterns.

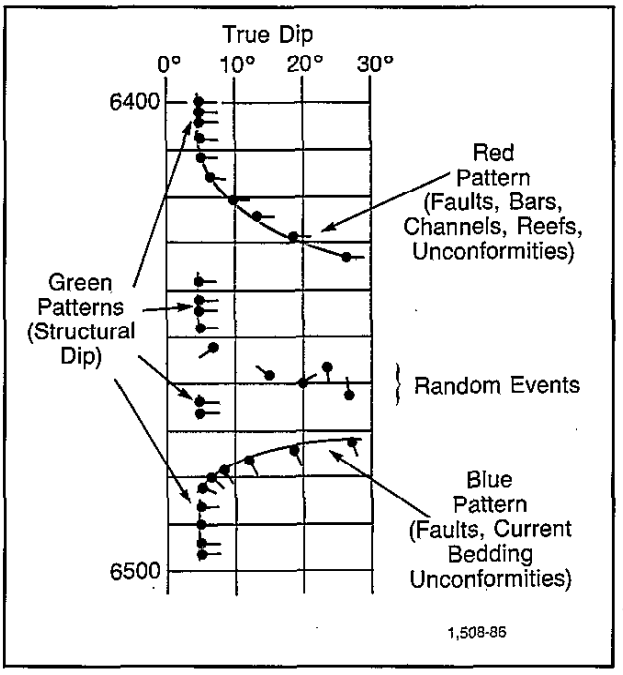

Fig. 12-5—Dip patterns and the geologic anomalies commonly associated with them.

In a red pattern, successive dips increase progressively with depth and keep about the same azimuth. As indicated in the figure, red patterns may be associated with faults, channels, bars, reefs, or unconformities. Fig. 12-6 illustrates red patterns seen over a bar or reef, or in a channel or trough.

In a blue pattern, successive dips with about the same azimuth decrease progressively with depth. Blue patterns may be associated with faults, current bedding, or unconformities. Fig. 12-7 illustrates schematically how crossbedding might show up as a blue pattern on a short-interval dipmeter arrow plot. The foreset current bedding shows larger dips at the top of each bed decreasing in a rather regular pattern toward the bottom of the bed.

A green pattern, shown on Fig. 12-5, corresponds to structural dip. It is consistent in azimuth and dip magnitude and is more prominent if structural dip is large.

To explore for a stratigraphic trap, it is necessary to know its type, internal crossbedding, direction of sand transport, and probable shape. The dipmeter provides data on the pattern of internal structures, direction of transport, and, in some instances, the direction of thickening of the depositional body.

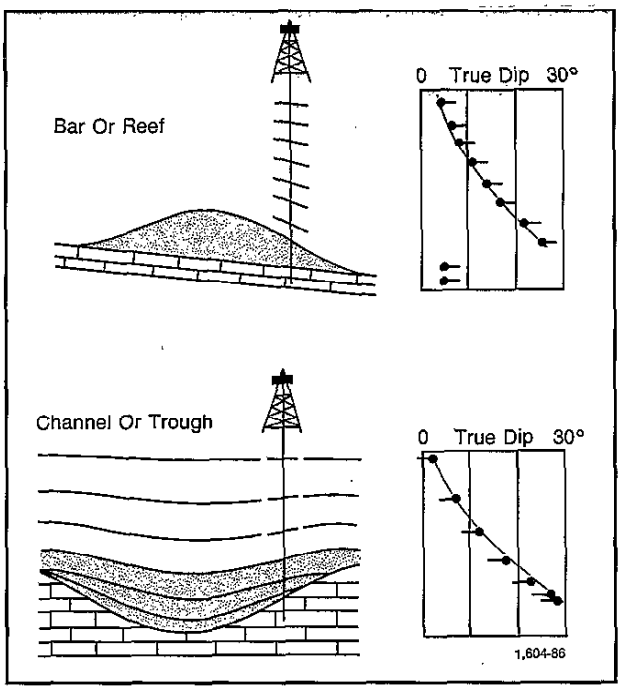

Fig. 12-6—Red patterns above a bar or reef or in a channel or trough. (After Ref. 5)

HDT Dipmeter Tool

The HDT dipmeter tool has four pad-type arms. Four microresistivity (or microconductivity) curves, spaced at 90° intervals around the borehole, are recorded. Although three curves are enough to define a dipping plane, the fourth curve provides valuable redundancy in the dip computation, particularly in rugose, irregular, or deviated boreholes in which one pad may not make good contact with the formation.

Opposite pairs of pads are independently linked to provide a dual caliper measurement of borehole diameter. One pad contains an additional electrode, vertically displaced from the dipmeter microresistivity measurement electrode. Data from this electrode permit dipmeter data to be automatically corrected for variations in sonde velocity.

A flux-gate compass and pair of pendulums permit the subsurface orientation of the dipmeter tool to be known. Thus, not only is the dip of subsurface beds calculated, but the direction of dip is also determined. Borehole deviation and direction are also determined.

CLUSTER* and GEODIP* processing are the two different types of processing commonly used for HDT data. In CLUSTER processing, various combinations of three of the four microresistivity dipmeters curves are used to calculate a group of possible dip planes at a given depth. Eight such solutions result. Ideally, all eight would define the same dip plane. In practice, they do not, but there is usually a tendency for many of them to "cluster" together. That clustered value is selected as the more pro-

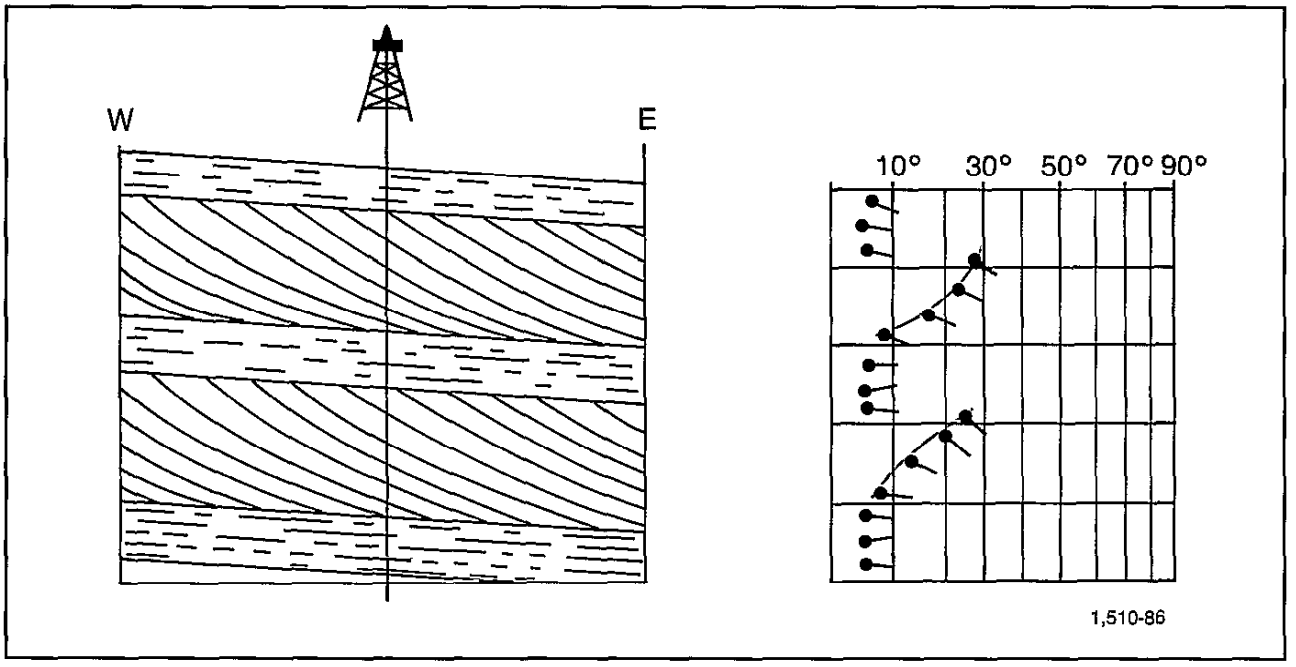

Fig. 12-7—Blue patterns resulting from foreset current bedding.

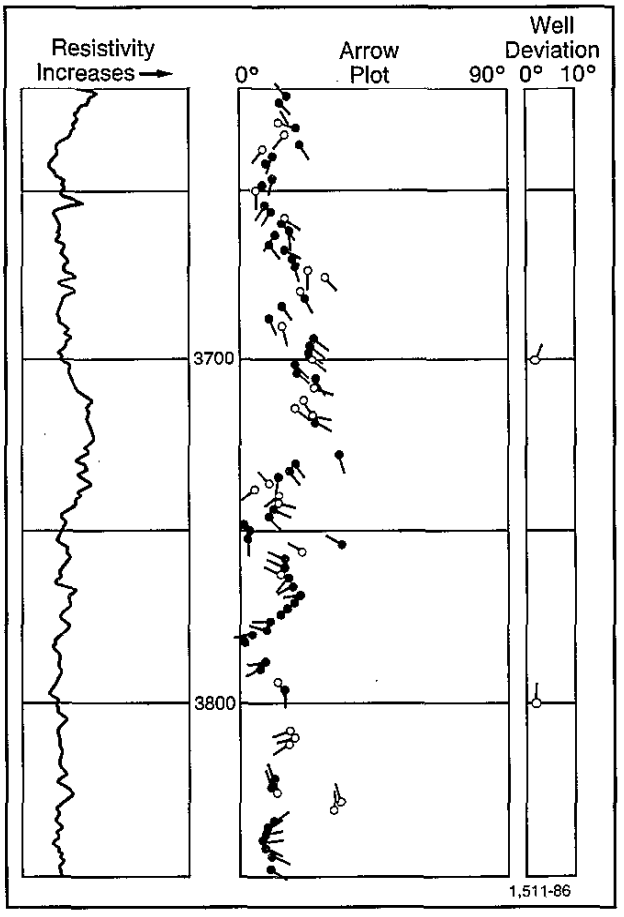

Fig. 12-8—Dipmeter results using the CLUSTER program.

bable. Fig. 12-8 shows the CLUSTER computation for the HDT data.

GEODIP processing is a pattern-recognition technique. It identifies and matches features from all four curves — much as the human eye would do. Because the program works from identifiable features on the curves, each one corresponds to a geological event. The density of the output data depends on the density of geological information at that level. This makes GEODIP processing particularly successful in fine-structured sedimentary sections. It may yield a large number of results over a short section of formation or relatively few results over a long interval. The GEODIP presentation is shown in Fig. 12-9.

Dual Dipmeter Tool

The Dual Dipmeter (SHDT) tool was designed to overcome some of the limitations of the previous generation of dipmeter tools:

- The sonde has been designed to maintain pad contact even in a deviated elliptical hole, thereby avoiding a "floating" pad and less reliable (three-pad) dip computations.
- The inclinometry system has been built with no moving parts to eliminate all frictional and inertial effects that can cause inaccurate measurements and slow response times. The system has an accuracy of ±0.2° for tool deviation and ±2° for azimuth.
- The (EMEX) survey current is automatically controlled at the optimum magnitude, thereby enabling quality dip resistivity curves to be obtained over intervals with both high- and low-resistivity formations.
- Each of the four pads has two "side-by-side" electrodes spaced 3 cm apart. This feature, together with a high data-sampling rate (0.1 in.), leads to the acquisition of more dip information (eight microresistivity dip curves).
- Tool-speed variation corrections can be made to the dip curves using data from two additional electrodes and a solid-state accelerometer.

Three different types of dip processing are available for Dual Dipmeter data. Two types search for pad-to-pad correlations in order to compute the dip of features crossing the entire borehole. The other computes displacements from side-by-side correlations on the same

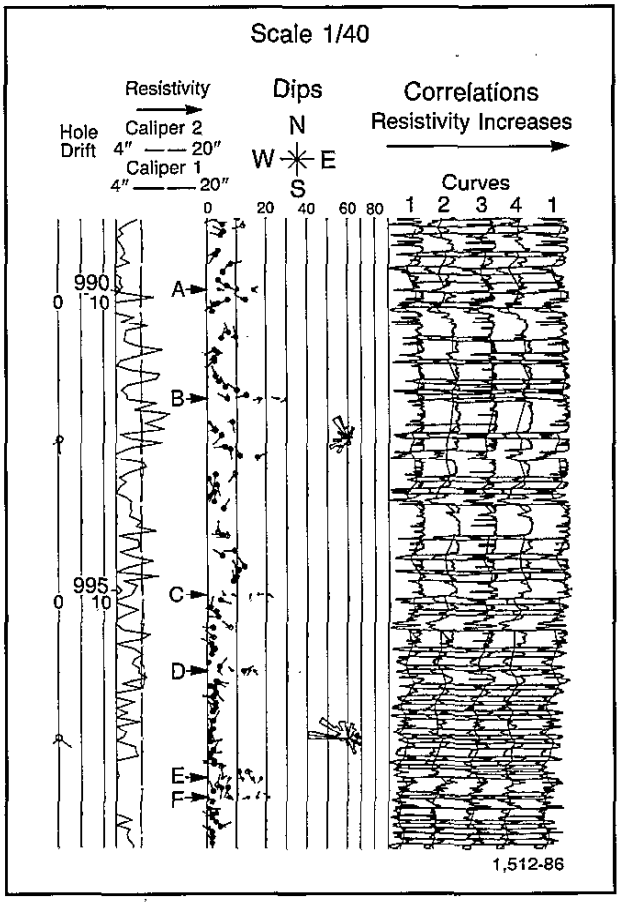

Fig. 12-9—Graphic presentation of GEODIP results. Note expanded depth scale.

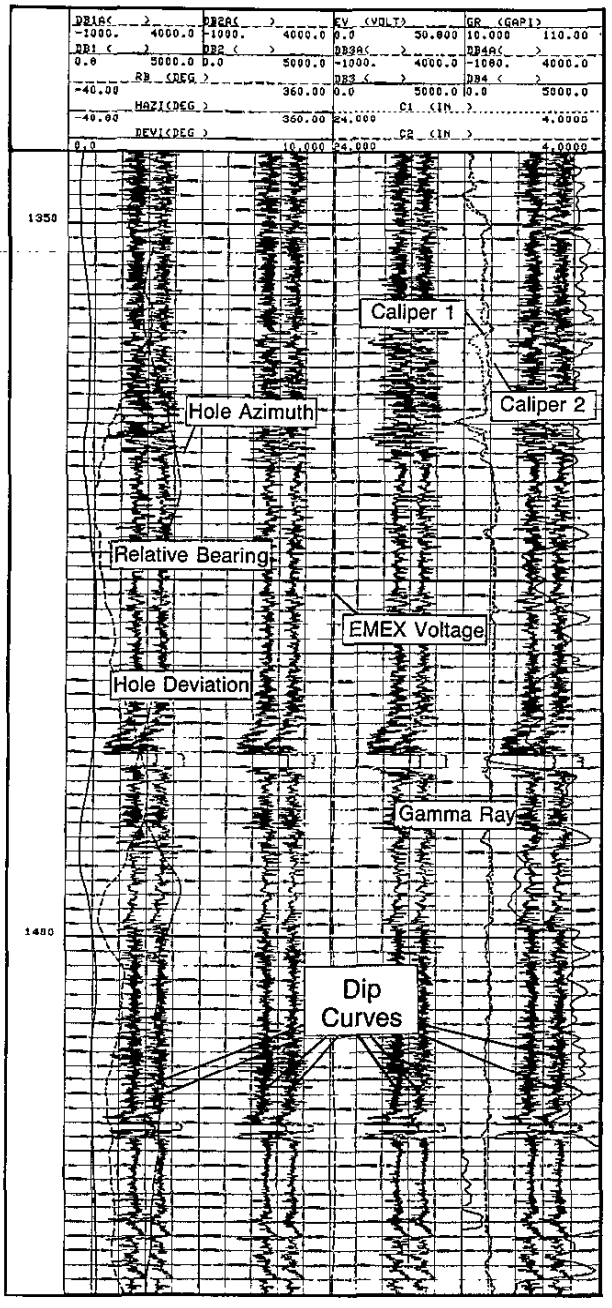

1,514-86

Fig. 12-10—Field presentation of Dual Dipmeter (SHDT) log.

pad in order to detect small events that do not necessarily have a wide extension.

Mean Square Dip (MSD) is a pad-to-pad processing of dip curve data that produces results similar to the CLUSTER processing of HDT dip curve data. It uses a specified correlation interval, step length, and search angle to determine displacements between curves. With eight microconductivity dip curves available from the Dual Dipmeter tool, a total of 28 crosscorrelations can be made, leading to 28 displacement values (if all are successful). Since only two adjacent displacements are needed to define a plane, there is tremendous redundancy in defining formation dip. The program searches for the best-fit plane that satisfies the majority of the 28 displacements. A quality rating is derived from the number of displacements contributing to each dip plane definition and their closeness to the resultant dip plane.

Local Dip (LOCDIP) is another pad-to-pad processing technique for Dual Dipmeter dip curve data. It detects features and correlates them in a way similar to that used by the GEODIP program on HDT dip curve data. Derivatives of all eight curves are produced, maxima are selected, and matching is performed between the maxima of different curves to compute the displacements between curves. Correlation lines are drawn across the dip resistivity curves. The dip and azimuth are computed if at least seven of the eight curves show the same feature. This derivative method recognizes the major borehole-crossing large-amplitude features that usually represent significant bed boundaries. The Local Dip program tends to recognize the major (primary) bed boundaries; the Mean Square Dip program tends to focus on the intrabed (secondary) features such as crossbedding.

Continuous Side-by-Side Dip (CSB) processing of the Dual Dipmeter data takes advantage of the very short distance (3 cm) between the two buttons on the same pad. The similarity between these two curves (see Fig. 12-10 and -11) usually permits a good correlation over a very short interval. If a good correlation cannot be made, the heterogeneous nature of the formation is clearly confirmed. Under certain conditions (deviated holes, for instance), the character of the dip curves may differ significantly from pad to pad, yet exhibit similarity from button to button (Fig. 12-11). In such cases, formation dip can be determined from side-by-side correlations (Fig. 12-12) if they are available from two adjacent pads (Fig. 12-13).

Fig. 12-14 further illustrates the large number of small details that can be correlated between the two buttons of the same pad. This leads to a better understanding of the sedimentary features and of the environment of deposition and, consequently, to a better definition of the facies. A short correlation interval (1 ft or less) is normally used in the side-by-side correlation in order to recognize this fine stratigraphic detail. The step distance is normally 3 or 4 in. Side-by-side correlation is also most efficient in the detection of high dip.

Before computing displacements between curves for dip determination, the data are processed for speed correction. The speed correction is achieved in two stages. First, the eight microresistivity dip curves and the two

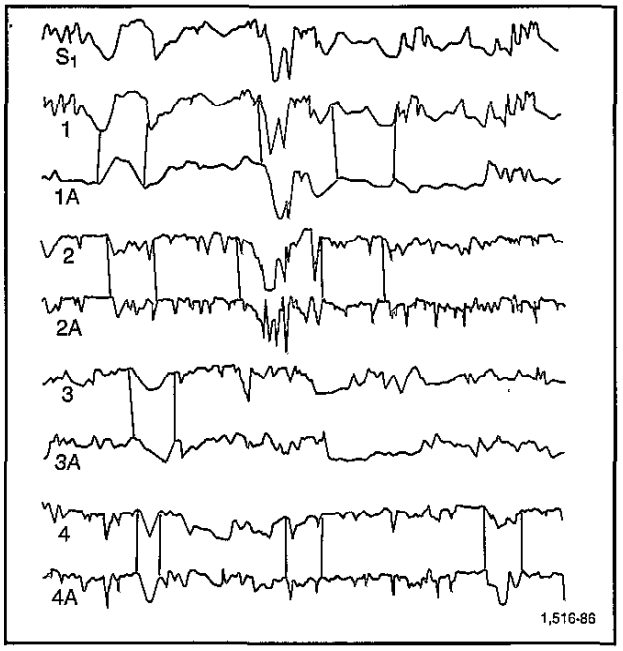

Fig. 12-11—Curve shape differs from pad to pad but not from button to button.

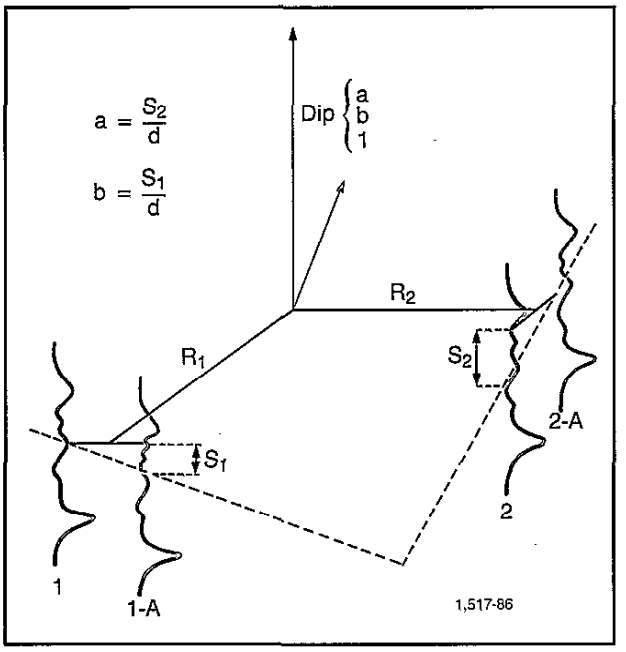

Fig. 12-13—Dip computation method from side-by-side data only.

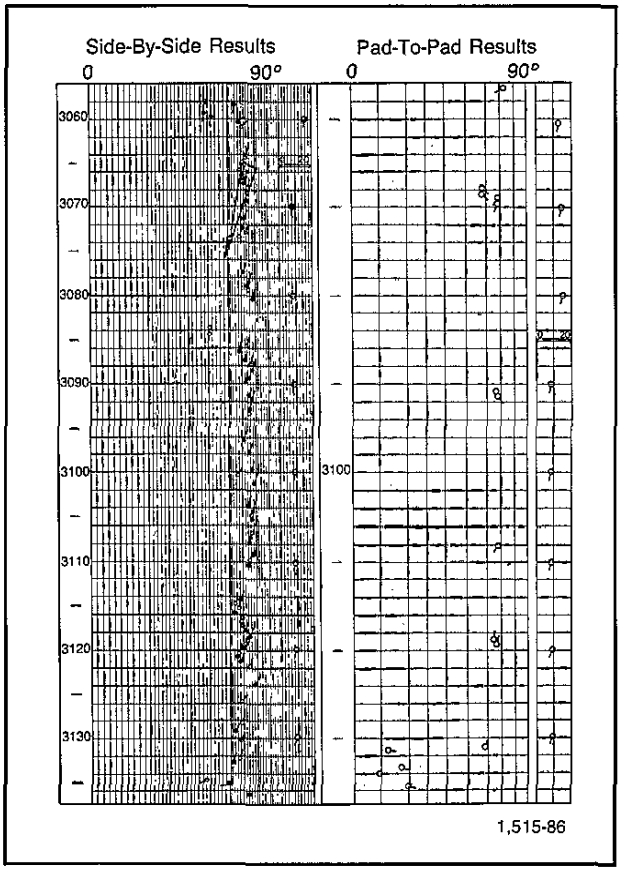

Fig. 12-12—High apparent dips on pad-to-pad results are confirmed by side-by-side results.

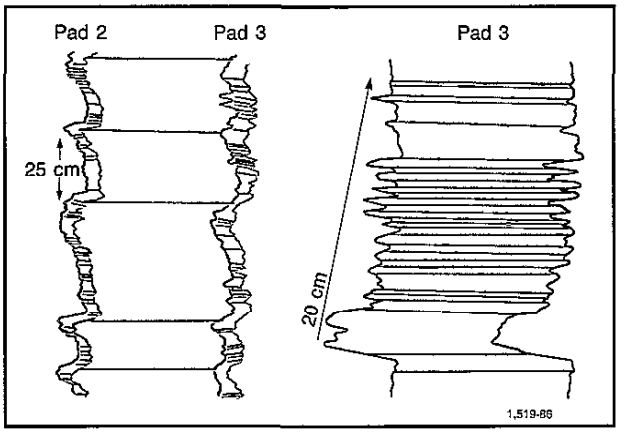

Fig. 12-14—Side-by-side and pad-to-pad correlations (left); detail of side-by-side correlations (right).

microresistivity speed curves are depth-shifted and reinterpolated using the accelerometer data. Second, the two speed curves are used during the dip computation stage to remove any remaining speed fluctuation.

For the different dip results, there are numerous combinations of presentations. The presentation used depends on the purpose of the dipmeter results and on personal preference. One presentation, using a 22-in. wide display, is shown in Fig. 12-15. From the left to the right are:

- Borehole depth, drift, and azimuth.
- Two calipers and a GR curve.
- Arrow plots corresponding to the two interval-correlation methods of dip computation: a triangular

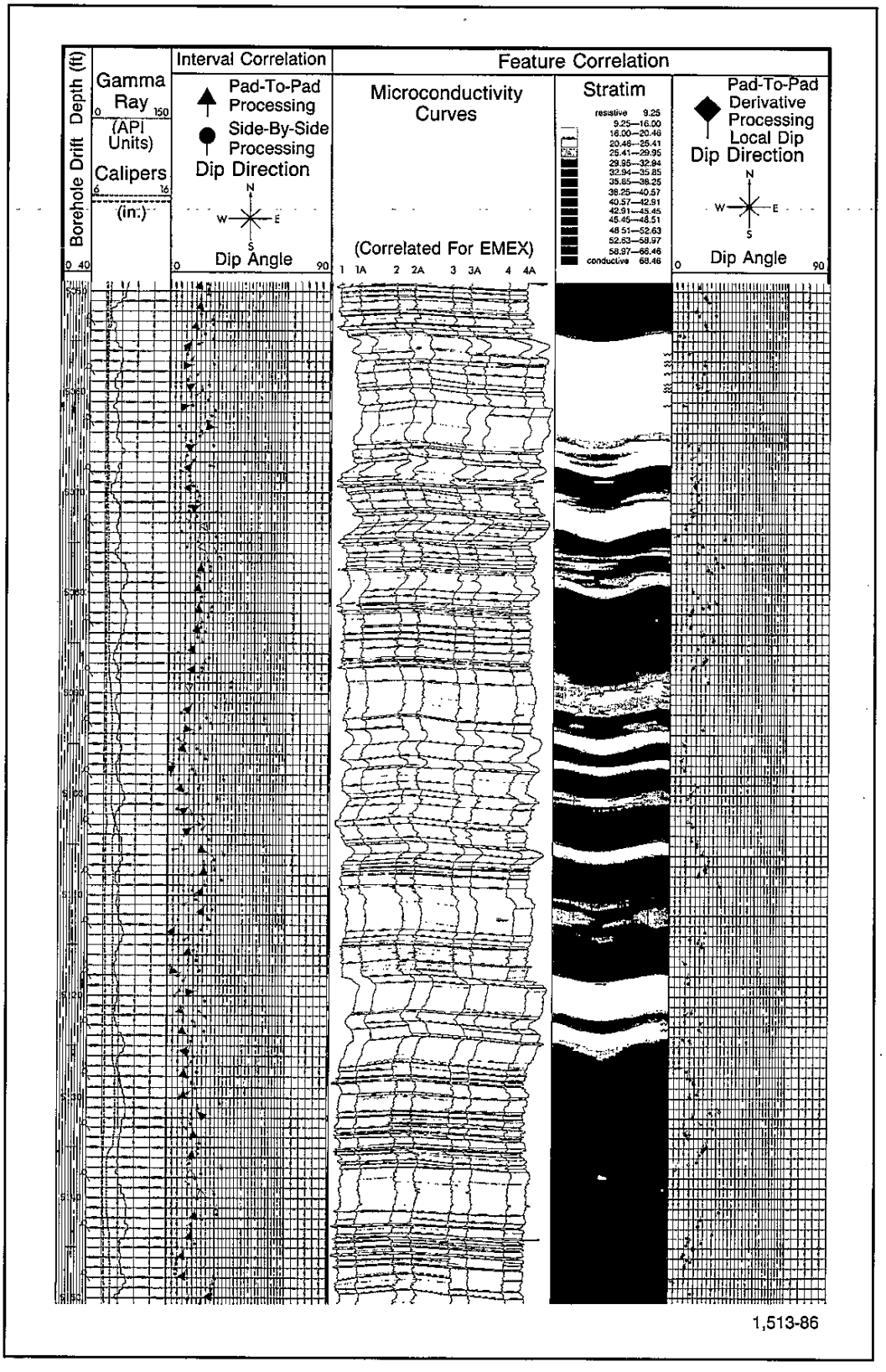

Fig. 12-15—Presentation of Dual Dipmeter (SHDT) data processing results.

tadpole for the MSD pad-to-pad correlations and a circular tadpole for the CSB side-by-side results.

- The eight microresistivity curves with dip Curve 1 repeated and the correlations found by the feature-correlation (LOCDIP) technique.
- STRATIM — a wrap-around image of the borehole based on interpolation between the eight microresistivity curves and the correlation links provided by the LOCDIP program.
- Arrow plot corresponding to the feature-correlation method; a square tadpole is used.

Wellsite Processing

A Cyberdip* arrow plot is available at the wellsite from HDT or Dual Dipmeter data. This processing is done after logging is completed and can save rig time by providing structural dip essential for drilling decisions.

Dipmeter Advisor* Program

The transformation of dipmeter dip computations into structural and stratigraphic information is a complex logic process. A great deal of experience is required. To capture the expertise of expert dipmeter interpreters, computer "artificial intelligence" is being employed. Dipmeter Advisor is a computer artificial intelligence program that can guide a less-proficient dipmeter interpreter through a dipmeter interpretation.

The Dipmeter Advisor program can be considered an "interpretation rule bank." Codified in the bank, in the language of a dipmeter interpreter, are the rules by which a geological feature can be identified using a continuous sequence of dip calculations. The rules are generated for a given sedimentological environment by correlating the observed dipmeter feature with cores, seismic data, and geological knowledge. Where it is recognized that a certain consistency and repetition exists, a rule can be written. This rule is then made a part of the computer knowledge base.

Associated with the knowledge base is the data base constituting the logging information available from a particular well. A program known as the "inference engine" correlates data with rules. This program performs such functions as scanning data, identifying doubtful data, and conducting searches for dip sequences of constant azimuth and magnitude and of increasing or decreasing dip with depth. During these operations, the program stores results, requests additional information, and finally presents displays of the operation and interpretation.

Fig. 12-16a is a typical display showing the potential of the system for stratigraphic analysis. Lithological information from the Geocolumn and SYNDIP* programs is presented in the left tracks. The user has selected scales that emphasize the trend of gradually increasing dip. Correlation links on the dip curves provide additional information on bedding characteristics. The SYNDIP computation derives synthetic curves from GEODIP or LOCDIP programs. The Geocolumn display is discussed later in this chapter.

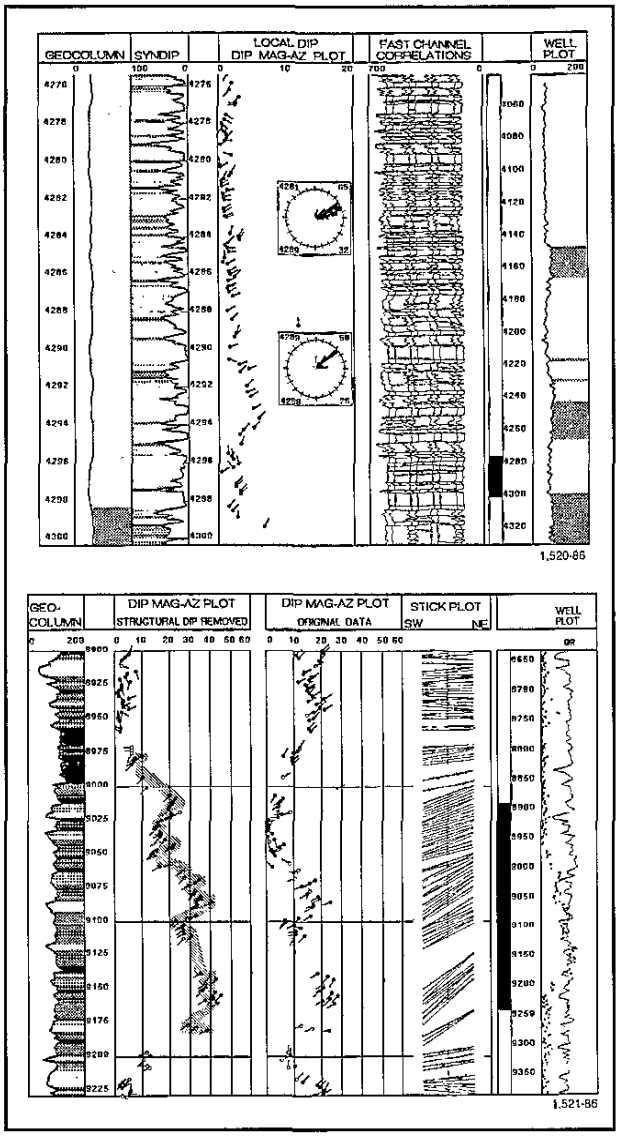

Fig. 12-16a,-16b—Examples of presentations by the Dipmeter Advisor program.

Fig. 12-16b is a display of the process. At the request of the interpreter, structural dip has been subtracted and the resulting display is presented adjacent to the original data. At this stage the Dipmeter Advisor program will display from its knowledge base, or bank, potential geological, sedimentary, and depositional environment interpretations of the various identified patterns.

The Dipmeter Advisor program allows the geologist to interact with the log data on a high-resolution screen

for displays of Wulff plots, Schmidt plots, stick plots, etc. (Fig. 12-17). Also, the geologist can select features from the raw data display and the program will make correlations and compute dip angles for those features.

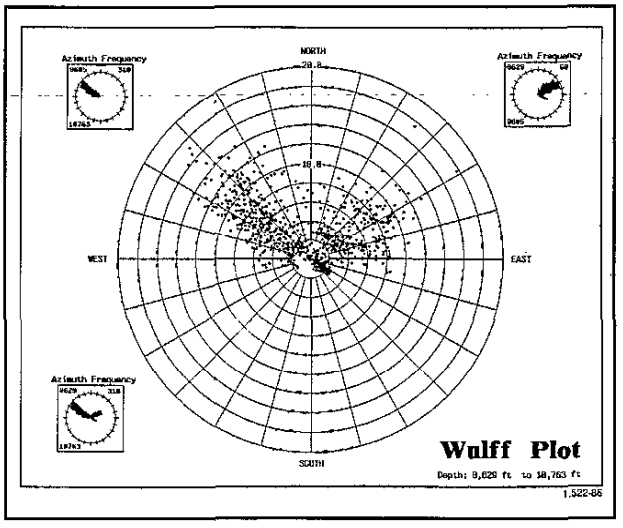

Fig. 12-17—The system will produce various plots over intervals selected from the screen image.

Formation MicroScanner* Service

The Formation MicroScanner (FMS) tool obtains oriented, two-dimensional, high-resolution imagery of microresistivity variations around the borehole wall. The measurement concept is an extension of Schlumberger dipmeter technology.

The tool has four articulated pads that contain two sets of electrodes. One set provides the standard Dual Dipmeter (SHDT) measurement and the other set provides the borehole imaging.

Fig. 12-18 shows the pad configuration for one of the imaging arrays, which are located on adjacent pads 90° apart. Each array has 27 electrodes with a lateral span of 2.8 in. The two arrays cover approximately 20% of an 8½-in. borehole.

The FMS service provides the geologist with formation details that were previously available only from full-hole cores. These features or heterogeneities may identify:

- Bedding deposited under a variety of flow regimes, such as trough and tabular crossbeds, ripples, very thin beds, and graded beds.
- Bedding subject to postdepositional distortions such as faulting, folding, or slumping.
- Nonbedding features such as fractures, burrowing, vugs, pebbles, concretions, fissures, stylolites, etc.

The log presentation includes the two-dimensional resistivity data and the gray-scale "core-like" borehole wall image mapped from the microresistivity data. The

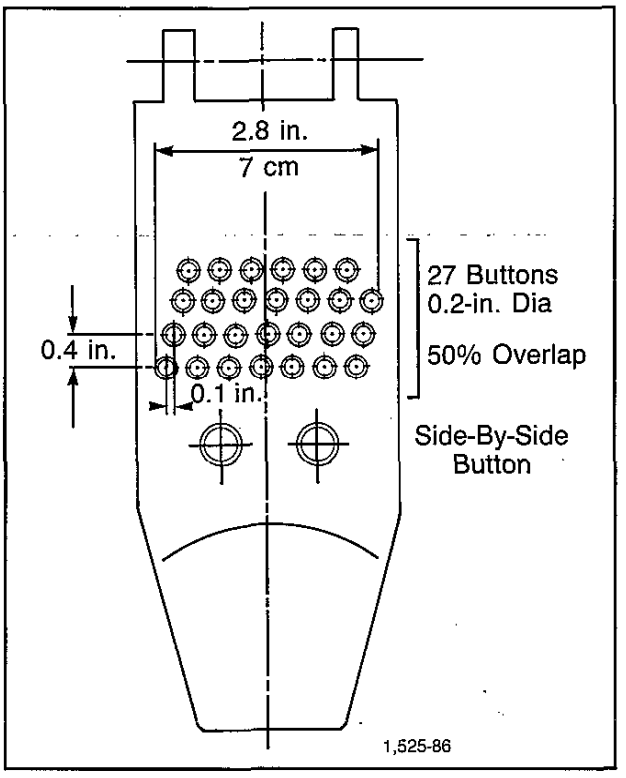

Fig. 12-18—Formation MicroScanner pad configuration.

gray-scale mapping is on a relative resistivity scale where black and white correspond to low and high values of resistivity, respectively. Color images are also available. Fig. 12-19 shows the FMS display with a core photograph through a calcilutite sequence that has been subjected to slumping. The individual laminae are broken up and present a brecciated appearance. A comparison of the FMS image and core photograph shows that the tool is capable of defining individual clasts on a centimeter scale.

A foreset bedded carbonate grainstone sequence, with open fractures, is shown on the FMS display in Fig. 12-20.

ELECTROFACIES IDENTIFICATION

For advanced reservoir studies, it is essential that reservoir parameters be well defined and zoned. It is equally important that identical parameters be associated with identical layers wherever they exist in the cross section of a particular field. Facies identification is therefore of utmost importance in modern reservoir evaluation.

A geological facies can be defined in terms of its geometry, lithology, paleontology, sedimentary structure, and paleocurrent patterns. These properties allow a particular geological facies to be identified and differentiated from any other. Thus, any technique that permits the recognition of these properties can form a basis for facies identification.

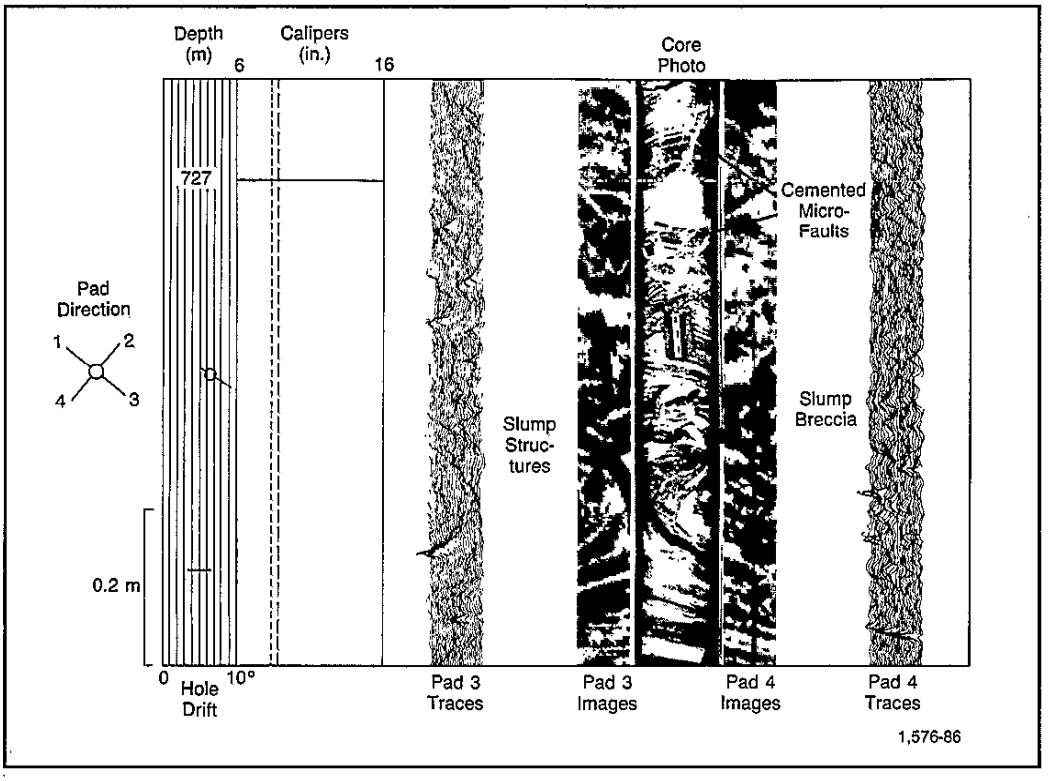

Fig. 12-19—Slump breccia developed in a calcilutite sequence.

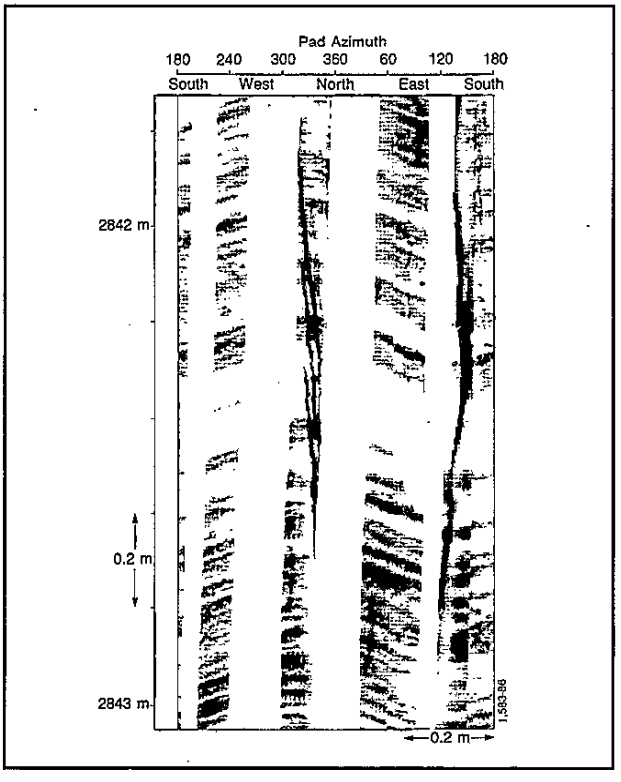

Fig. 12-20—FMS display showing open fractures.

A set of log measurements taken at a particular level in a well represents evaluation of some of these properties in terms of values of resistivity, density, acoustic transit time, hydrogen index, photoelectric cross section, electromagnetic wave propagation, etc.

Thus, a set of log signatures represents an electrofacies that can later be correlated with a geological facies. The Faciolog* program separates a sequence of formation beds into different electrofacies later linked to the geological facies.

Faciolog Computation

The objective of the Faciolog program is to segment a well, or part of a well, into log-consistent layers; i.e., layers where all levels of the layer have similar log responses. The number of levels, or clusters, is then reduced until each cluster can be related to a significant geological facies.

The environmentally corrected logs are transferred into principal component logs by the following procedures:

- In the multidimensional space of the normalized logs (i.e., a crossplot in n dimensions), new orthogonal axes are defined passing through the center of gravity, such that the first axis is in the direction of maximum variance and thus carries the greatest inertia. The second axis is orthogonal to the first and is in the direction of second greatest variance and so on.

- The normalized logs are then projected onto these principal component axes to derive the principal component logs.

The first principal component axis thus can be said to contain the most information, the second axis the next greatest amount, and so on. Further, as the axes are orthogonal, they are by definition uncorrelated. Fig. 12-21 shows principal component analysis in two dimensions using the neutron-density logs.

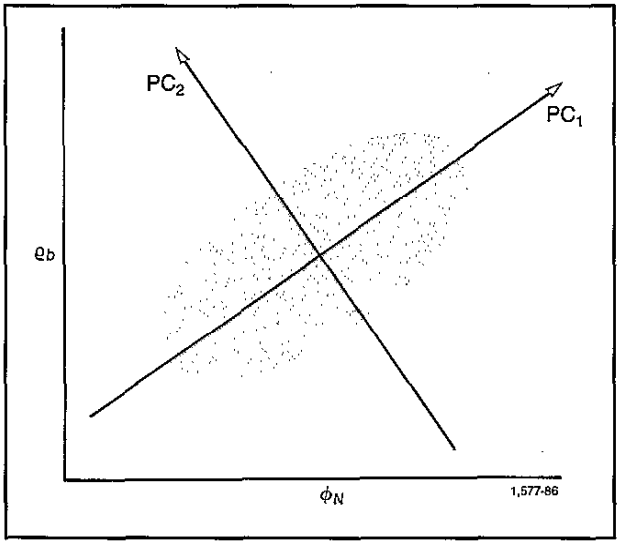

Fig. 12-21—Principal component logs are obtained by projection of data on the principal component axes.

Both principal component logs contain porosity and lithology information. The PC_1 log carries the most information in common with both logs; PC_2, the remaining information. In the neutron-density crossplot, PC_1 and PC_2 lie in the direction of porosity and lithology, respectively.

Data reduction is achieved through clustering of the PC log values into representative local modes. These local modes are then grouped together into larger clusters called terminal modes (Fig. 12-22). Terminal modes are representative of the final electrofacies. This is a critical step and recommendations from the local geologist are particularly valuable in the choice of the final facies and their geological meaning. Whenever possible, a comparison with core data should be used to control this clustering and naming process.

A composite presentation can be made to display Faciolog processing results and other computed log results. One such presentation is shown in Fig. 12-23.

Once a Faciolog data base has been established in an area, identical facies in other wells can be easily and automatically identified. Similarity in facies sequences can improve well-to-well correlations. The Faciolog processing can also be used to zone the logs prior to execution of other computer interpretation programs.

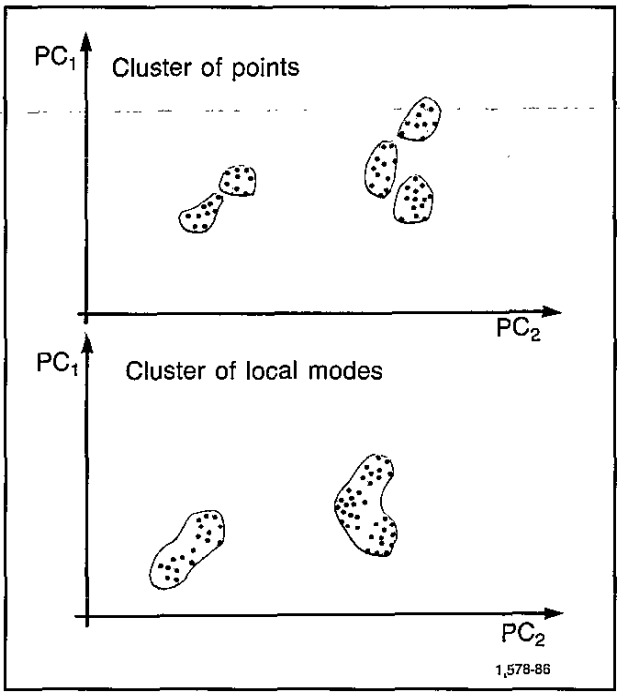

Fig. 12-22—Clustering of local modes.

Geocolumn Display

An electrofacies is an abstract mathematical concept that must be converted to geological terms to be understood and used by geologists. This conversion can be made by the Geocolumn display.

The Geocolumn display (Litho program) uses 192 electrofacies and 7 logging sensors to convert openhole log responses to lithology. Log measurements currently in the data base include density; neutron; photoelectric cross section (P_e); sonic transit time; natural gamma ray; and thorium, uranium, and potassium concentrations.

Each petrographic rock type is represented as a volume in the *n*-dimensional space of log response and not as a point. This allows for variations in both geology and data acquisition. The size of each volume reflects the amplitude of these variations.

Each electrofacies volume is represented as an ellipsoid in *n*-dimensional space by reference to the multivariant gaussian distribution. The model is simple but flexible enough to capture the main features of an electrofacies. The ellipsoids are constructed from their projections in two dimensions (crossplots), which are ellipses. The various ellipses must be consistent if they are to define a possible ellipsoid.

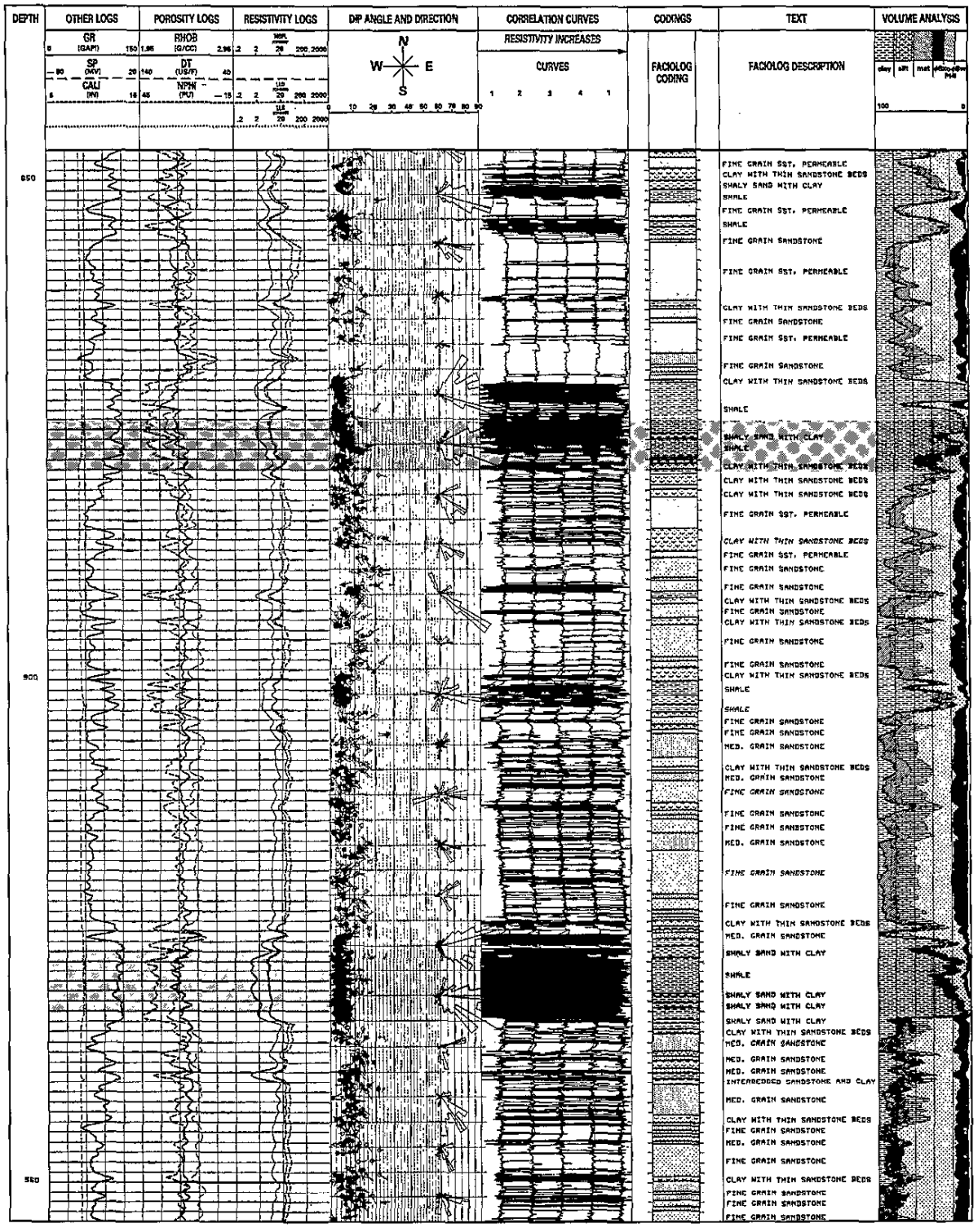

Fig. 12-23—Faciolog computation.

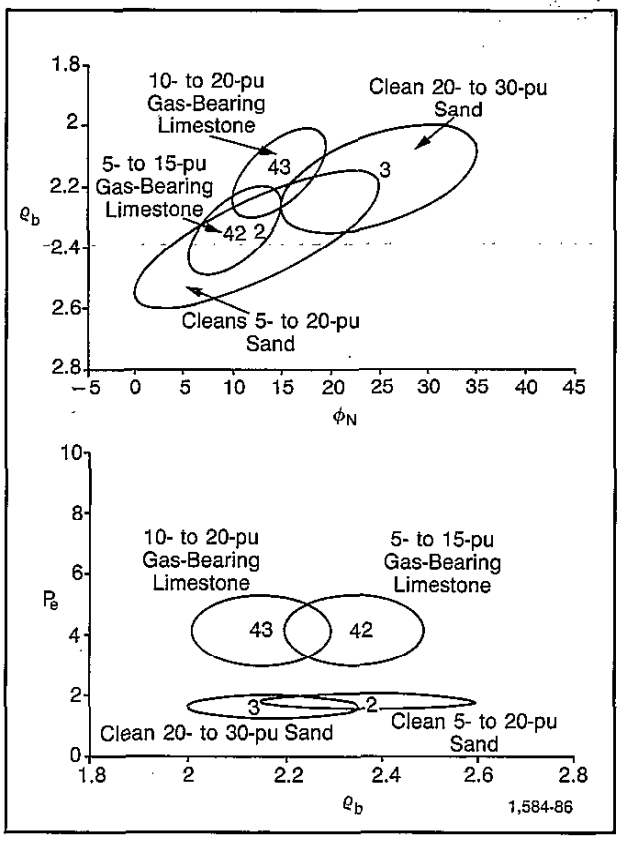

Fig. 12-24—Projection of two clean sands and two gas-bearing limestones on a density-neutron crossplot and a P_e-density crossplot.

Fig. 12-24 shows an example of electrofacies projections for two clean sands and two gas-bearing limestones on the density-neutron and P_e-density crossplots. The sandstones and limestones overlap in the density-neutron crossplot but are well separated on the P_e-density crossplot.

The 192 electrofacies included in the data base cover the most abundant sedimentary rocks and some igneous rocks. The major definitions include sandstones, limestones, dolomites, shales, coal, evaporites, and igneous rocks. These major definitions are further divided into subdefinitions by other factors, including porosity ranges, cementation, and special minerals. For example, the sandstone group is subdivided into over 30 categories. The data base is calibrated from cores and known lithology and can be fine-tuned to local conditions.

A statistical procedure, known as Bayes decision rule, helps to classify each depth level by reference to the data base. A probability distribution of log values is assigned to each lithofacies. The lithofacies with the highest probability is selected as the answer at each depth level. A point falling outside the ellipsoids is classified as "unidentified."

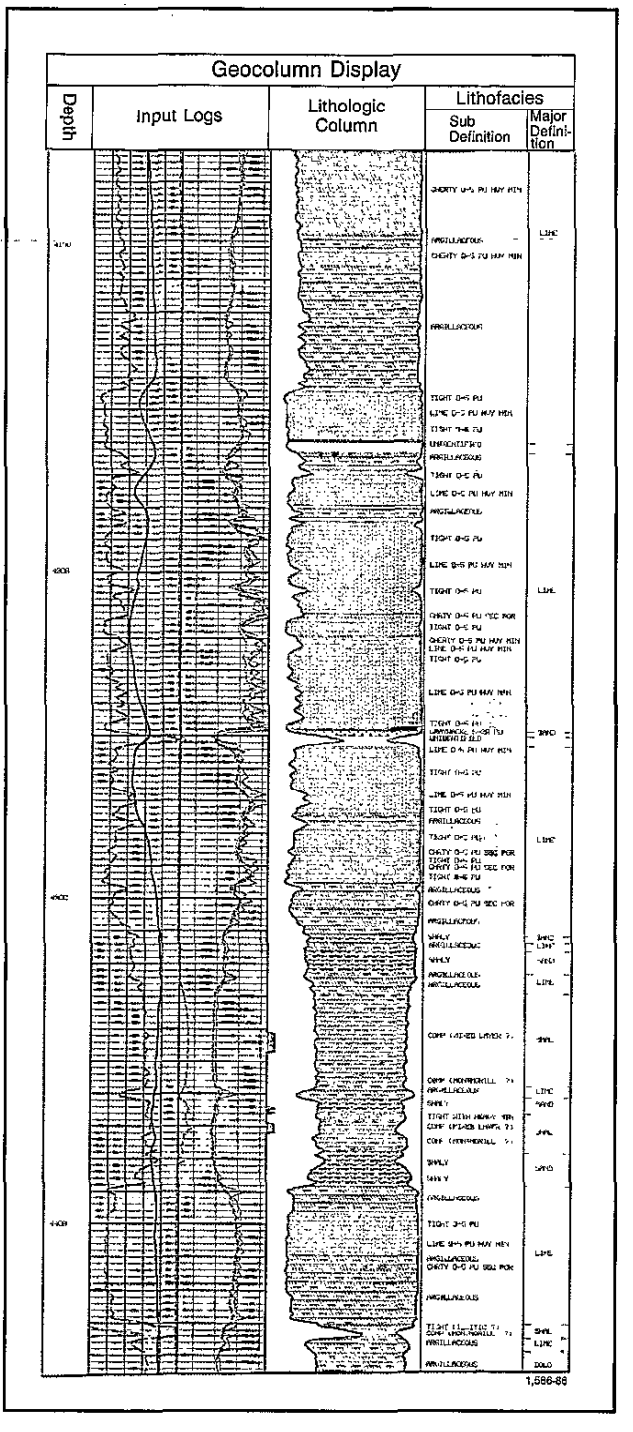

Fig. 12-25—Geocolumn display.

Fig. 12-25 shows a Geocolumn display through a carbonate zone. The lithologic column is bounded by the gamma ray curve on the left edge and the neutron-density crossplot porosity on the right edge. The lithofacies column is divided into major definitions and subdefinitions. The flags in the lithologic column indicate that one or

more of the sensors was affected by borehole conditions and that the answers in those intervals are not as reliable as those in other zones. The Geocolumn display can be computed at the wellsite with the CSU* unit or at field log computing centers. A color presentation is available from the computing centers.

In summary, both Faciolog and Geocolumn displays provide facies identification using different mathematical techniques. The Geocolumn display is a fast, automatic program while Faciolog processing is suitable for studies in great detail.

RESERVOIR DESCRIPTION SERVICES

The oil industry has become more and more aware that reservoirs exhibit complex variations of reservoir continuity, in particular of pore space-related properties (porosity, permeability, and capillary pressure). These variations reflect the original depositional process and subsequent diagenetic and tectonic changes. Simple models are often inadequate for predicting reservoir performance and for designing a field production management scheme that will optimize recovery. It is becoming increasingly apparent to reservoir engineers that the optimization of recovery is crucially dependent on the quality of the reservoir description. This is particularly true for heterogeneous reservoirs under water injection where the recovery factor is very sensitive to reservoir heterogeneity, and accurate knowledge of the vertical and lateral permeability distribution is essential. A more accurate initial reservoir description is definitely needed.

One key to a coherent reservoir description is the maximum utilization and integration of all reservoir data from all possible sources, since no one data source (on its own) can provide a complete reservoir description. Each data source is subject to some limitations and errors. Synergy can, however, arise from the intelligent amalgamation of all available reservoir data.

Static input data to the reservoir description come from:

- Openhole wireline logs.
- Core and cutting data.
- Seismic data.
- Reservoir fluid data.

Core and log data describe a very shallow region around the wellbore. The size of the typical core plug is small relative to the size of the reservoir layer. Core-determined reservoir properties therefore manifest more variation than data that are averaged over larger rock volumes. Other difficulties caused by the point nature of the core measurement are encountered when relating core permeability to large-scale layer flow properties and in defining vertical permeability, which is often controlled by very thin striations of tighter rock.

The modern trend, given the difficulty and cost of coring (particularly deviated wells offshore), is to core only a few key wells. These cores are then subjected to the detailed analysis necessary to develop the reservoir geologic model and to determine a relationship between the various formation petrophysical parameters (porosity, saturations, permeability, etc.) and the various formation parameters that can be determined from logs. With such a relationship established, the formation petrophysical parameters (including permeability distribution) can often be deduced from log data alone in wells or zones without core data. New techniques using multidimensional log data banks have been developed for this purpose. They provide continuous formation petrophysical parameter distributions coherent with core, geological, pressure, and other data for each well in the field and are thus an important addition to the techniques for improving reservoir description.

Log data have also been used successfully to define and correlate rock types — another often critical input to reservoir description.

Recent improvements in seismic recording techniques, sources, and processing have considerably enhanced the role of seismic information in reservoir description, particularly through stratigraphic modeling and interpretation. The dipmeter can also aid in the identification of structural and stratigraphic features and in the definition of the bedding dip and direction.

In most cases, the vast amount of log data and other rock data available, as well as all the computer processing interpretations, is not fully used in reservoir description. Although the objective of Reservoir Description Services (RDS) is to maximize the contribution of well logs to reservoir description, it is not a log-biased approach. It attempts a detailed reservoir description through the coherent use of all available data.

Missing Data

There are often gaps in logging data as a result of borehole conditions and inadequate logging programs. A key-well study and ensuing reservoir calibration evaluations allow a data bank of log responses and formation variables to be established for wells with favorable logging conditions and adequate logging programs. From this data bank, the required input parameters (e.g., R_w) and the desired formation petrophysical parameter (e.g., porosity, saturations, etc.) can be determined with confidence.

In those wells with less favorable logging programs or conditions, the desired petrophysical parameter must be estimated from the less than ideal data available. The method of estimation employs established transforms. Two basic assumptions are made:

- Geological continuity exists between wells in the data bank.
- Identical sets of responses yield identical sets of answers.

Therefore, it is implied that data banks be constructed for individual depositional units or environments.

As an example of the development of a porosity transform, gamma ray, sonic, and deep resistivity data for the reservoir calibrated wells were used to form a matrix cell (Fig. 12-26). This cell is subdivided into smaller cell elements, each of which might, among other things, represent a value of porosity. The size of the element cells can be changed, but, obviously, the smaller the element size, the more precise the estimation if sufficient porosity data are available to fill the elements.

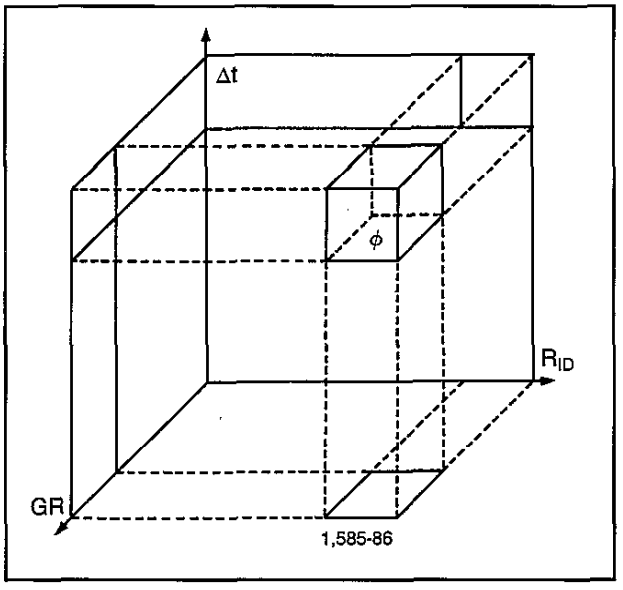

Fig. 12-26—Schematic representation of matrix and element cells.

If more than one value of porosity falls within the element cell, the data bank assumes a mean value of porosity. For each estimation, a standard deviation is computed for quality control. Smaller standard deviations imply closer porosity values within the element cells and hence better estimation of porosity.

Experience has shown that good estimations require three or four independent measurements. In this example, we have been restricted to three, where the contribution of resistivity in the porosity transform is probably small. Generally, at least five or six wells are needed to form the data base.

Fig. 12-27a compares the known porosity of one well with a four-well data bank estimation of the porosity of this well. All five wells are of the same group. The correlation is very good. Fig. 12-27b compares known porosity of a well from a second group of wells with the four-well porosity estimated from the first group. The correlation, although not quite as good, is still acceptable. Such displays are useful, both as a quality control of estimations and as indicators of geological continuity and lithologic model choice.

Similar statistical methods may be used to establish a data bank for estimation of a missing log over small intervals or permeability in uncored wells.

Estimation of Permeability

Many attempts have been made in the past to relate the permeability of a formation to other parameters measurable by wireline tools. Numerous formulas have been developed linking permeability to such parameters as porosity, irreducible water saturation, and clay content (see Chapter 10). Usually valid for the formation for which they were developed, no one formula has been universally applicable.

A computer program has been developed that relates permeability to a group of either log responses or computer results. The permeabilities used in this program are those obtained from laboratory measurements on cores. Therefore, the output is an estimated core permeability and requires dynamic matching to account for skin effects and relative permeabilities.

The theory of the method is identical to that for the estimation of missing logs and statistical transforms for wells with incomplete logging suites. The cells of the data bank are filled with core permeability values such that each cell can be described by the average of the values of the points in the cell and by their standard deviation. Inherent in the method are some of the reconciliations associated with the use of core data:

- The value of permeability measured on a core sample is limited not only by the precision of the measuring technique but also by the sampling of the core. The measurements are usually made on a very small sample of the reservoir; a large statistical error in representing the rock by such a small sample can therefore be expected.
- Depth matching of cores and logs is often difficult because of missing sections, physical deterioration of the core, etc. Depth matching is generally achieved by comparing the porosity values from cores and from logs.

Two considerations are paramount in choosing a permeability estimator from various well log measurements or from a combination of measurements.

- An evident correlation with permeability must, of course, exist.
- The permeability estimator must be able to discriminate between different classes of permeability.

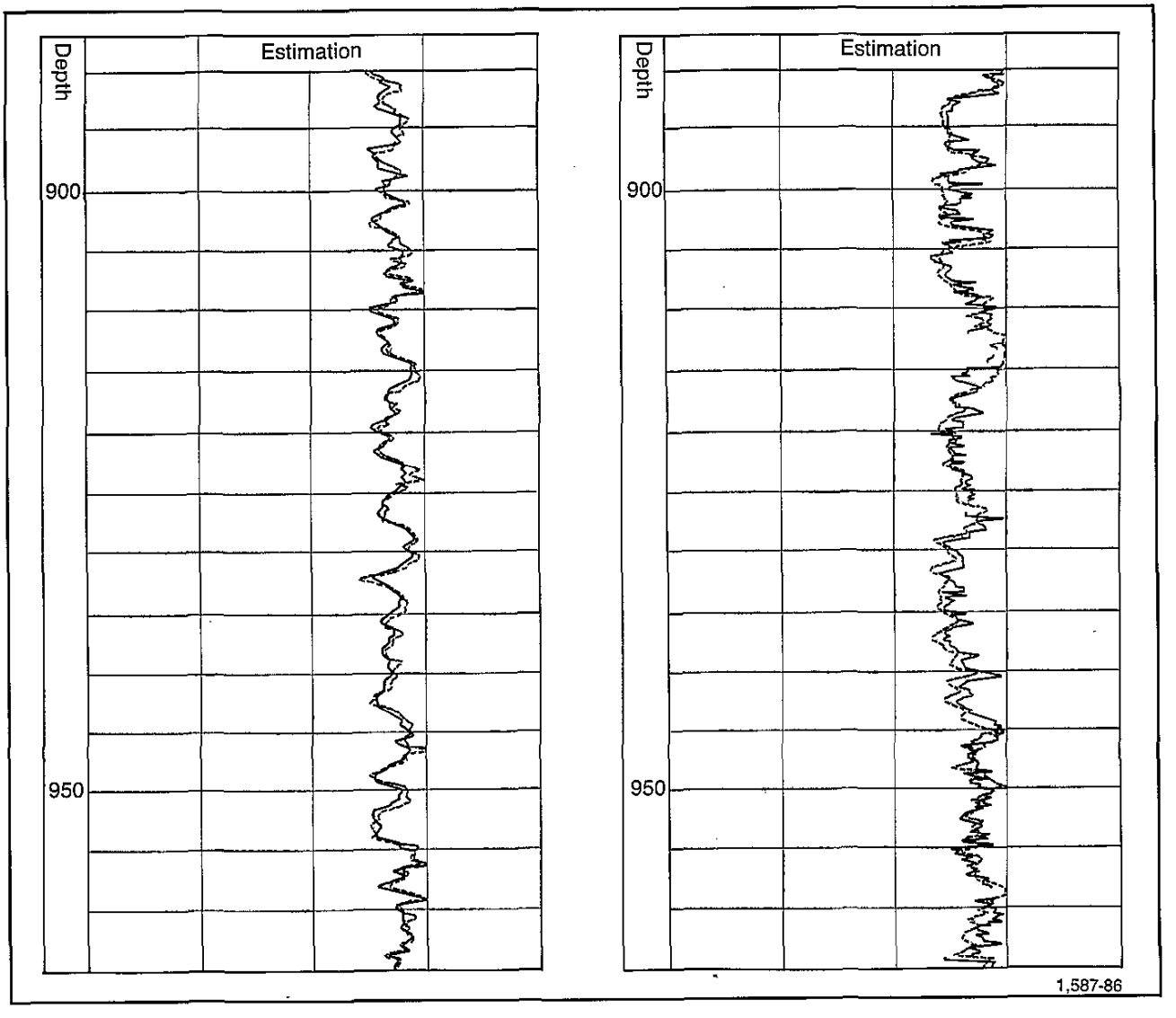

Fig. 12-27a—Group 1 well from Group 1 data bank.

Fig. 12-27b—Group 2 well from Group 1 data bank.

In the general case, porosity, water saturation, and clay content are used as estimators. To avoid ambiguities where different facies may have the same group of estimator values but different permeabilities, the results from a Faciolog computation may be helpful. For example, a number can be assigned to each facies and used as an estimator in the role of permeability discriminator.

Fig. 12-28 shows a comparison of estimated permeability and measured core permeability. Because of the small amount of core data initially available in this case, the match is not perfect. However, general trends are followed and a reasonably valid permeability estimator is available for use in nearby wells in which little or no direct permeability data may exist.

Lumping

The processing techniques described until now have all involved continuous log-type outputs with discrete calculations at half-foot intervals. For parameter gridding and mapping, a simplified description of the parameters in each reservoir subzone of each well is required.

This process is called lumping. The lumped value of a parameter in a zone is the cumulative value of that parameter in the zone. The cumulation is made over the whole zone (total thickness) or over selected intervals within the zone defined by such cutoffs as S_w, V_{cl}, ϕ_e (net and net-pay thickness).

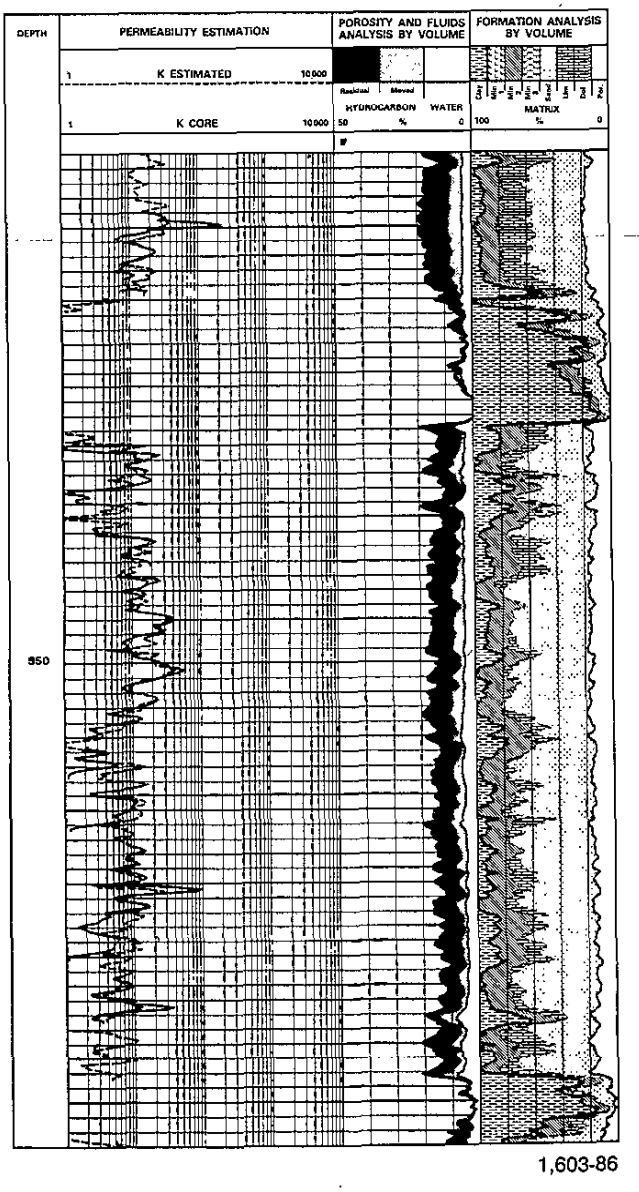

Fig. 12-28—Estimated permeability compared to core permeability.

The cumulative value is the sum of that parameter at each sampling depth multiplied by the sampling interval. Cumulation may be arithmetic, logarithmic, or harmonic.

An averaged value is the lumped value divided by the zone thickness as defined by total, net, or net-pay cutoffs.

Cutoffs, to eliminate nonproductive reservoir sections, must be determined from production, log, or core data, or from experience in the area.

Typically, average (porosity, water saturation, permeability) and cumulative (thickness, porosity/hydrocarbon feet) data are presented in tabular form with three reserve estimations (Fig. 12-29):

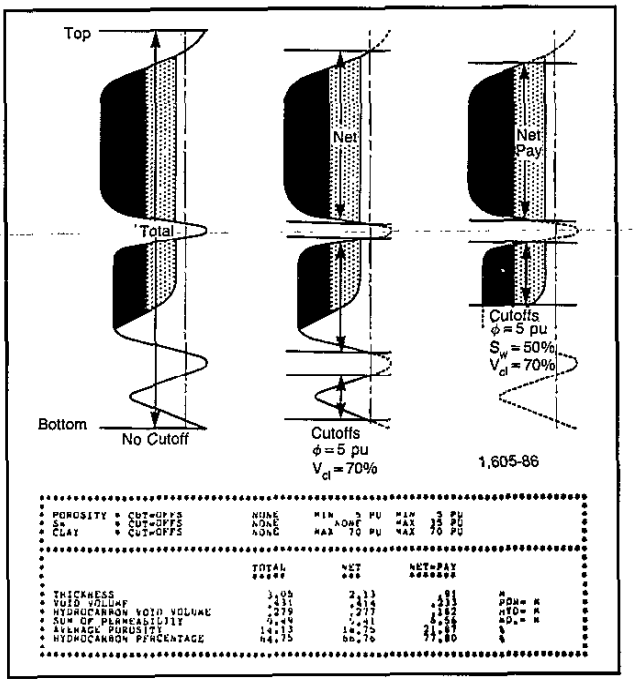

Fig. 12-29—Reservoir summary parameters (lumping and listing).

- Total pay — no cutoffs applied.
- Net — low-porosity and high-clay levels rejected.
- Net pay — rejection of low-porosity, high-clay, and high water-saturation zones.

For deviated wells, lumped parameters are calculated after correction for vertical thickness. Digital files suitable for reservoir mapping and gridding are also constructed.

Gridding and Mapping

The final modules in the reservoir description chain are designed to produce the maps and grids required for visual presentation, for input to a fieldwide simulator, and for estimations of reserves. There are three distinct phases to this process; gridding, contouring, and integrating. Fig. 12-30 shows a flow chart of the process.

The output of the lumping program consists of discrete data values for each well processed. The gridding program constructs a grid from these data points. The geostatistical technique employed is known as Kriging (after the mining engineer D. G. Krige). Kriging is an interpolation technique that considers the following points:

- The number of wells and the quality of the data for each well.
- The locations of the wells within the field.
- The distances between the wells and the area of interest.
- The spatial continuity of the interpolated variable.
- All other relevant information.

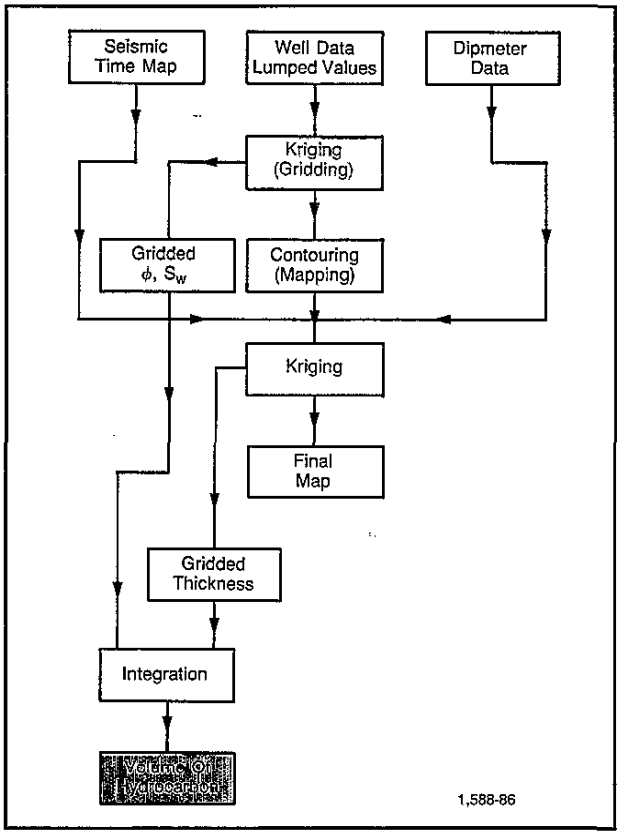

Fig. 12-30—Flow chart, gridding, and mapping.

For improved accuracy, particularly if only a few data points exist, it may be advantageous to introduce the results of surface seismic. The input may be either from seismic sections or from a digitized map of the structure top. Further options exist in the program to include the input of dipmeter data and to allow for discontinuities, such as faults.

Fig. 12-31 shows the development of a grid from eight discrete data points. This grid has then been contoured.

Fig. 12-32 shows the differences obtained when surface seismic has been combined with well data points from, in this case, 56 wells. The map with seismic is a substantial improvement over the map produced with only the well data points. For greater visual impact, color plots are available.

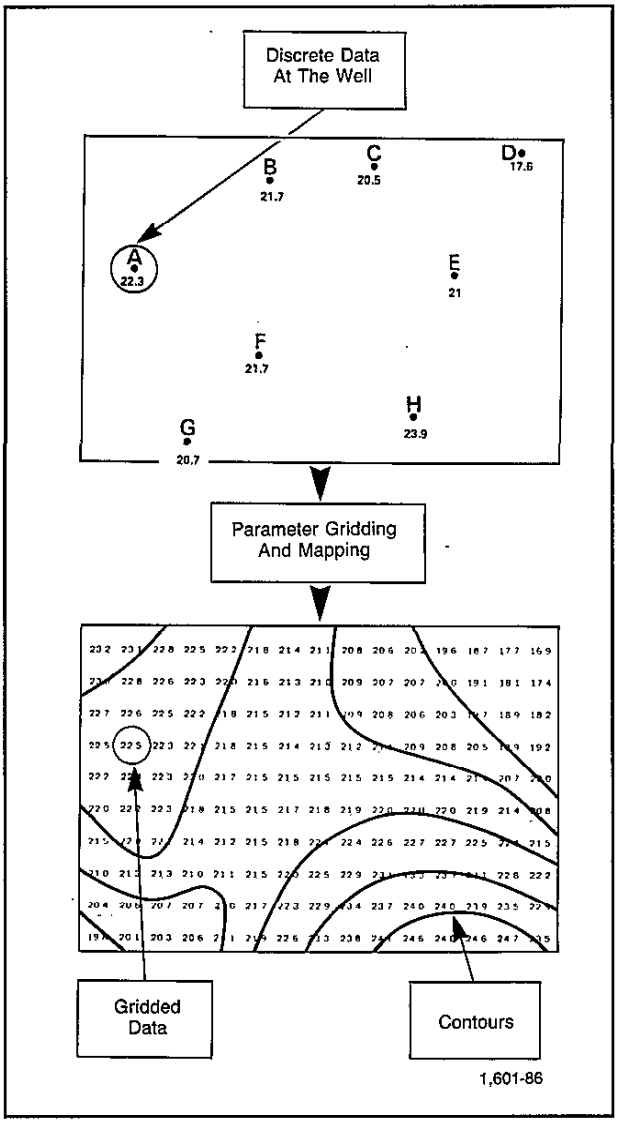

Fig. 12-31—Principle of reservoir gridding and mapping.

REFERENCES

1. Stratton, E.F. and Hamilton, R.G.: "Application of Dipmeter Surveys," *Trans.*, Petroleum Division of AIME Meeting, Tulsa (Oct. 1947).
2. *Fundamentals of Dipmeter Interpretation*, Schlumberger (1986).
3. Franke, M. and Hepp, V.: "Dipmeter Outlines Petroleum Entrapment on Flanks of Diapiric Shale Dome," *Trans.*, 1973 SPWLA Annual Logging Symposium.
4. Gilreath, J.A. and Maricelli, J.J.: "Detailed Stratigraphic Control Through Dip Computations," *Bull.*, AAPG (Dec. 1964) **48**, No. 12.
5. Campbell, R.L., Jr.: "Stratigraphic Applications of Dipmeter Data in Mid-Continent," *Bull.*, AAPG (Sept. 1968) **52**, No. 9.
6. Cox, J.W.: "The High-Resolution Dipmeter Reveals Dip-Related Borehole and Formation Characteristics," *Trans.*, 1970 SPWLA Annual Logging Symposium.
7. Allaud, L.A. and Ringot, J.: "The High Resolution Dipmeter Tool," *The Log Analyst* (May-June 1969) **10**, No. 3.
8. Vincent, Ph., Gardner, J-E., and Attali, G.: "GEODIP — An Approach to Detailed Dip Determination Using Correlation by Pattern Recognition," paper SPE 6823 presented at the 1977 SPE Annual Technical Conference and Exhibition.

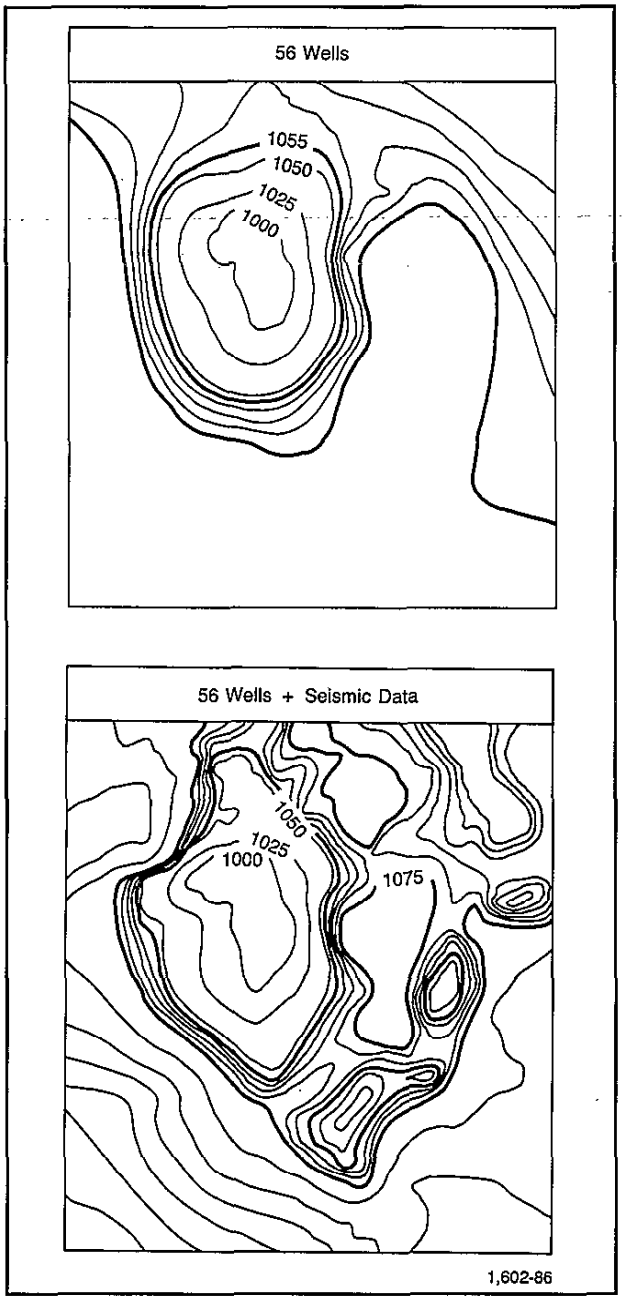

Fig. 12-32—Use of seismic data.

9. Serra, O. and Abbot, H.T.: "The Contribution of Logging Data to Sedimentology and Stratigraphy," paper SPE 9270 presented at the 1982 SPE Annual Technical Conference and Exhibition.
10. Wolff, M. and Pelissier-Combescure, J.: "FACIOLOG—Automatic Electrofacies Determination," *Trans.*, 1982 SPWLA Annual Logging Symposium.
11. Matheron, G.: *LeKrigeage Universel*, Les Cahiers du Centre de Morphologic Mathematic de Fountainebleau, Fascicule 1 (1969).
12. Boutemy, Y., Clavier, C., and Simond, R.F.: "Field Studies: A Progress Report on the Contribution of Logging," paper SPE 8178 presented at the 1979 SPE Annual Technical Conference and Exhibition.
13. Raymer, L.L. and Burgess, K.A.: "The Role of Well Logs in Reservoir Modelling," paper SPE 9342 presented at the 1980 SPE Annual Technical Conference and Exhibition.
14. Definer, P., Peyret, O., and Serra, O.: "Automatic Determination of Lithology from Well Logs," paper SPE 13290 presented at the 1984 SPE Annual Technical Conference and Exhibition.
15. Serra, O.: *Sedimentary Environments from Wireline Logs*, Schlumberger (1985).
16. Ekstrom, M.P., Dahan, C.A., Chen, M., Lloyd, P.M., and Rossi, D.J.: "Formation Imaging with Microelectrical Scanning Arrays," *Trans.*, 1986 SPWLA Annual Logging Symposium.
17. *Facies Models*, second edition, R.G. Walker (ed.), Geoscience Canada, Reprint Series 1, Geological Association of Canada (1984).
18. *Sedimentary Environments and Facies*, H.G. Reading (ed.), Elsevier, New York (1978).

13 Mechanical Properties Of Rocks

NATURAL FRACTURES

Naturally fractured zones are important, and sought after, in reservoir rocks because of the extra drainage and considerable increase in permeability they promise. Although fractures can have a very significant effect on the total permeability of a rock, they usually have very little effect on the porosity, saturations, or other petrophysical characteristics of the rock.

Natural fractures generally exhibit certain constant characteristics:

- They are usually approximately perpendicular to the dip; this does not, however, exclude the possibility of horizontal fractures, although horizontal fractures are much less frequent and less extensive than subvertical fractures.
- They are usually oriented according to one (or more) prevailing strikes. Since fractures are often the result of tectonic stresses, the prevailing strike of the fractures generally coincides with the orientation of the faults in the region.
- They frequently cause small amounts of rock to be broken off from the borehole wall by the drill bit or drillstring during drilling.
- They usually occur in compact, competent rocks where the hole would normally be cylindrical and in gauge in the absence of fractures.

Only fractures that are at least partially open are useful from the point of view of production.

Fracture Detection

Logging tools are designed to respond to different characteristics of the wellbore environment. Some tools respond primarily to lithology, some primarily to porosity, and others to fluid saturations. None, unfortunately, responds primarily to fractures although fractures, particularly open ones, may affect the response of some logging tools. The effect, however, is usually rather subtle. Thus, in the search for fractures using log measurements, it is necessary to understand both the basic tool physics and the geometry of all the measurements involved. Generally, only experience permits us to define the methods which, in a given location, will give the best results.

When looking for fractured zones on logs, the search is usually focused on areas where they are suspected for the following reasons:

- Local history of naturally occurring fractures.
- Lack of precision in seismic recordings.
- Extrapolation of observations on outcrops.
- Increase in the rate of penetration of the bit.
- Presence of crystals in the drill cuttings.
- Circulation losses during drilling.
- Poor core recovery.
- Fractured cores.
- Test results that are incompatible with the known or estimated porosities and permeabilities.
- Pressure interference between wells (production or injection).

Sonic Measurements

One of the oldest fracture indicators is the reverberation of sound waves in and around the borehole. Measurements based on sonic wave propagation respond to the mechanical properties of the rock and are little affected by the borehole environment.

In fractured zones, the appearance of the wavetrain, as recorded on the Variable Density* log (VDL), shows sudden changes — vague or blurred zones, chevron patterns, etc. (see Fig. 13-1). These features suggest interfaces of differing acoustic impedance between the transmitter and receiver of the sonic tool. Such propagation anomalies can be caused by open fractures. Unfortunately, similar anomalies can also occur with changes in the diameter of the borehole or because of thin beds of differing lithology or even a "healed" (closed) fracture system.

*Mark of Schlumberger

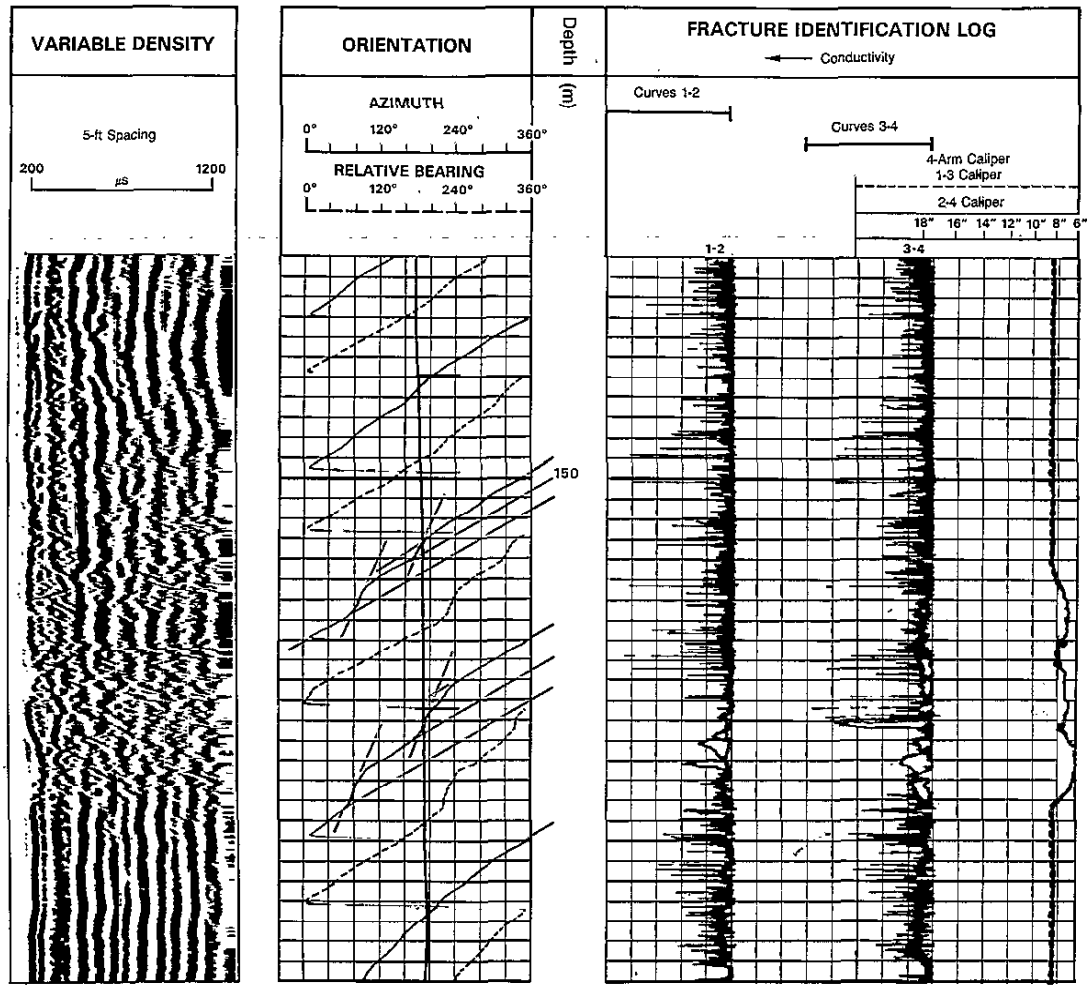

Fig. 13-1—Fracture identification with VDL display and fracture identification log.

Recently, the LSS* long-spaced sonic and Array-Sonic* tools have become popular for the recording of the sonic wavetrain. In addition to the two travel times (shear and compressional), the energy of the compressional and shear wave packets and their respective frequency contents can also be recorded. The Array-Sonic tool emits a given amount of energy. By measuring the amount of energy that arrives at the receiver, an indication of the competence and uniformity of the formation can be obtained. High signal strength at the receiver suggests a competent rock with a low probability of fractures; very low signal strength suggests a high probability of fractures, other things being equal. Fig. 13-2 is an example of a decrease in shear energy opposite a zone where fractures are suspected. At the fracture interface, some of the shear energy is reflected, some is converted to other modes of wave propagation, and some is refracted; as a result, the amount of shear energy reaching the receiver is significantly reduced.

Another promising technique is a study of the mode conversion effects that take place when acoustic energy encounters fluid-filled fractures. At the intersection of the borehole and the fracture, the coupling between borehole and formation is enhanced because of the large surface area of contact. This greatly facilitates the conversion of acoustic energy from one of the formation modes to one of the borehole modes [Stoneley (tube) waves and the various normal (pseudo-Rayleigh) modes] or vice versa. When the transmitter or receiver is opposite the fracture, this mode conversion causes a characteristic spike in formation mode amplitude. Two such spikes separated by the transmitter-receiver spacing provide a reliable means of detecting fractures.

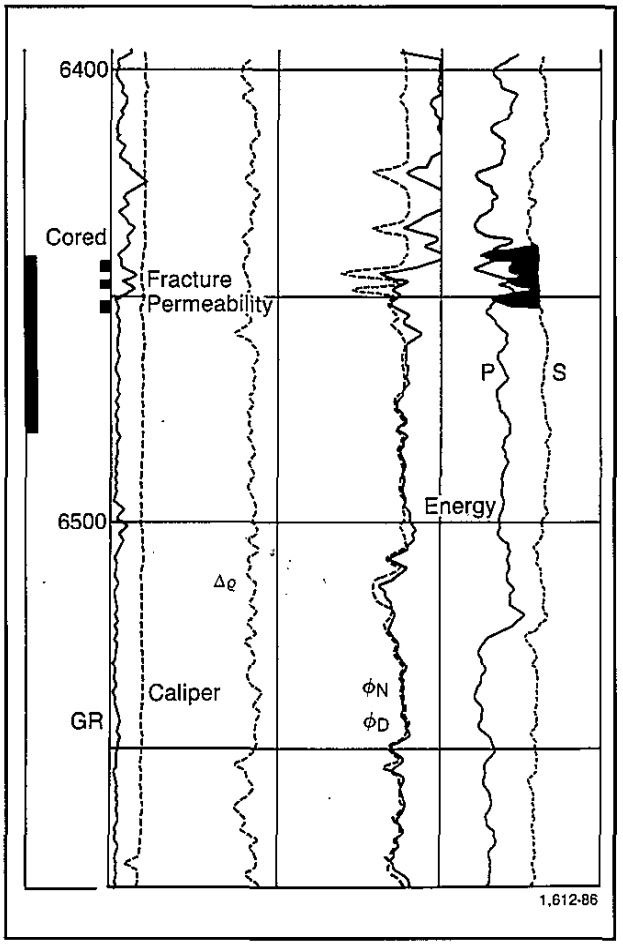

Fig. 13-2—Drop in shear energy indicates fractures.

Fig. 13-3 shows a 12-ft spacing sonic waveform in the vicinity of a large horizontal fracture. Points A and B are, respectively, the positions where transmitter and receiver are directly opposite the fracture. A sharp increase in the amplitude of the compressional and shear first arrivals can be easily seen.

Another feature, clearly discernible, is the criss-cross patterns originating in the compressional and shear waves. However, anomalies caused by vertical fractures are more subtle.

Poisson's ratio can be computed from the compressional and shear wave velocities (or transit times) (see Eq. 13-1). Rocks with a high Poisson's ratio are more likely to have fractured zones than those with a low Poisson's ratio. Thus, some insight into the likelihood of fracturing can be obtained from Poisson's ratio.

With the advent of the Array-Sonic and more sophisticated processing techniques, these sonic techniques for fracture recognition may be used in both open hole and cased hole.

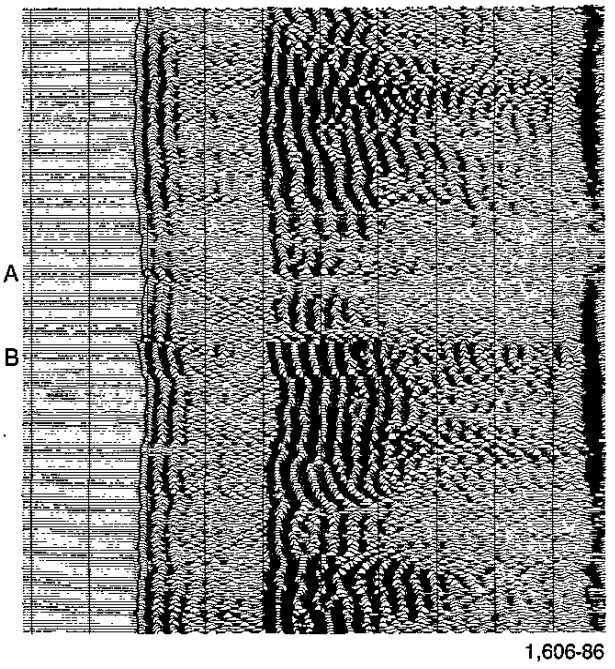

Fig. 13-3—Sonic waveform response over a large horizontal fracture.

Caliper Measurements

In drilling through a fractured zone, the rock edges of the fractures are often chipped away, thereby enlarging the borehole in the plane of the fracture system. Borehole enlargement and, particularly, borehole elongation in a formation expected to have an in-gauge and circular borehole can indicate fractures. To detect fractures with a caliper log, a multiarm, multidirectional caliper is preferred. The calipers recorded with the HDT* high-resolution dipmeter or Dual Dipmeter* (SHDT) tools are examples. These four-arm calipers record two borehole diameters 90° apart. One pair of arms is almost always aligned with the major axis of an elliptical borehole, the other pair with the minor axis. An elliptical or elongated borehole is thereby readily recognized.

In the absence of a four-arm caliper, borehole elongation can often be recognized from the comparison of a two-arm caliper (such as available on a density or microresistivity tool) with a three-arm caliper (from a sonic tool). Again, the two-arm caliper almost always follows the major axis of the borehole, whereas the three-arm caliper is heavily influenced by the minor axis diameter (see Fig. 13-4).

Extreme caution must be exercised in using the caliper for fracture detection. Borehole ellipticity can be caused by factors other than fractures. Directional drilling, deviated borehole, drilling through steeply dipping beds, an oriented pore structure, and other events can cause

an elongated borehole cross section. If lost-circulation material is used during drilling, fractures can sometimes have the opposite effect on the calipers; the caliper can read less than bit size in fractured zones because of the buildup of lost-circulation material in the fracture (see Fig. 13-1).

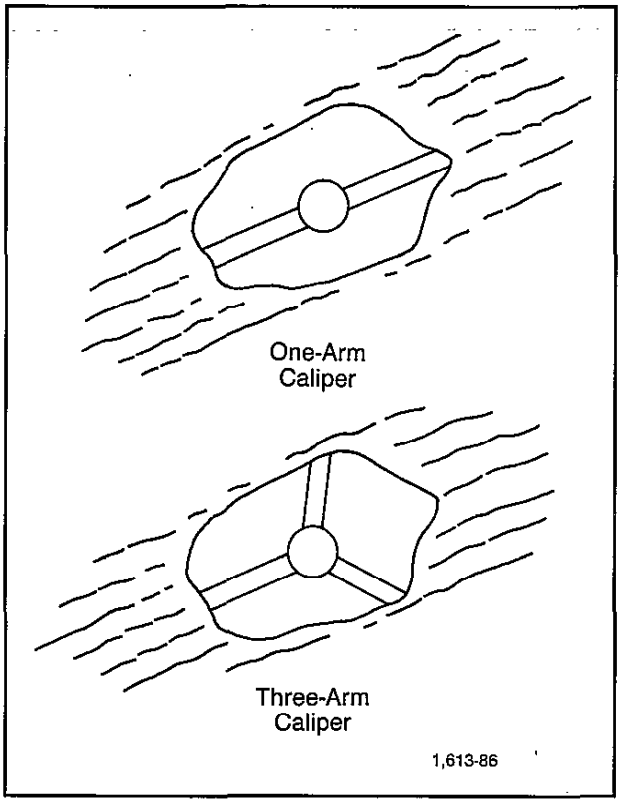

Fig. 13-4—Borehole ellipticity shown with two- and three-arm calipers.

Density Measurements

The correction curve on a density log, $\Delta\varrho$, is another potential fracture indicator. $\Delta\varrho$ is a measure of the correction made to the bulk density to compensate for mudcake and for the density tool not seating perfectly against the borehole wall. It normally responds to borehole rugosity and mudcake thickness, but it will respond to a fluid-filled fracture (particularly when the edges of the fracture have been chipped away by the drilling process). An active, erratic $\Delta\varrho$ curve may therefore indicate fractures when the hole is in gauge. Fig. 13-5 is an example. A disadvantage of the $\Delta\varrho$ curve for fracture detection is that it sees only a small portion of the borehole and may therefore miss the fracture. However, since the density tool will usually seek the long axis of the hole, the $\Delta\varrho$ correction curve normally follows the fracture plane. $\Delta\varrho$ also responds to washouts not associated with fractures; therefore, extreme care should be taken when using $\Delta\varrho$ as a fracture indicator.

Generally, fractures do not contribute significantly to the porosity of the rock; however, in some instances they may. Also, the "chipping-out" of the fracture by the drill bit during drilling may slightly increase the apparent porosity recorded by a shallow-investigating porosity device, such as the density tool. Thus, porosity anomalies between adjacent sides of the borehole may indicate fractures as well as provide a value for fracture porosity. This requires, of course, two passes with the density tool, one with the standard long-axis orientation and another with short-axis orientation.

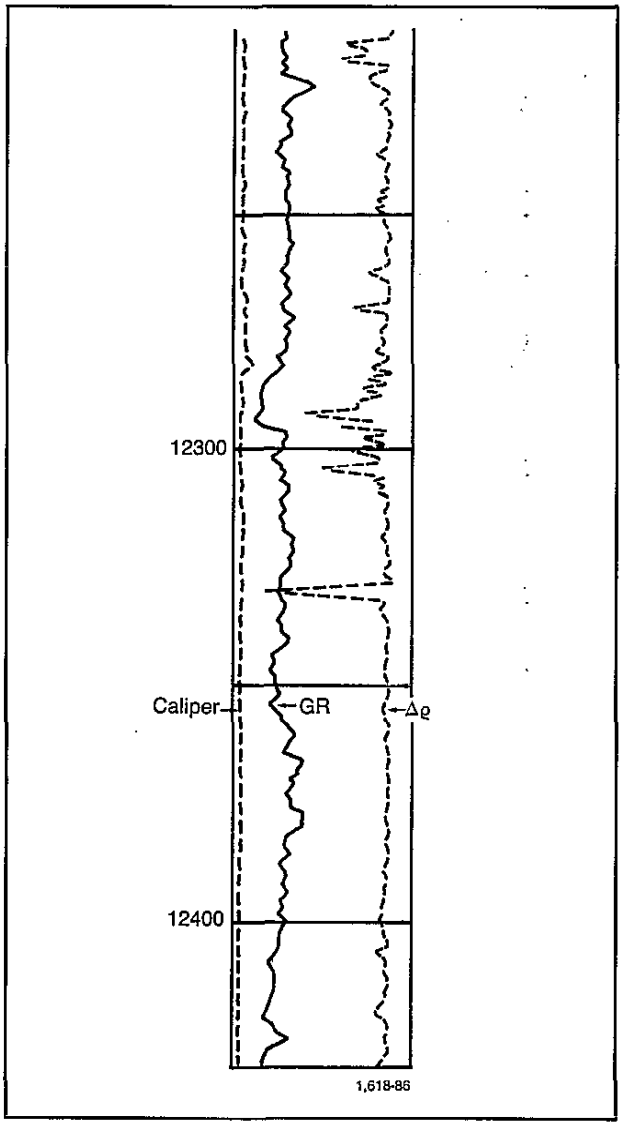

Fig. 13-5—High $\Delta\varrho$ activity opposite possible fractures.

Resistivity Measurements

Under the proper conditions, resistivity tools can be quite effective in locating fractured zones. Fracture detection is based on the principle that a device which looks deeper into the formation is less influenced by a fracture than is a shallow-reading device. For example, on a dual induction log, fractures may be indicated when the SFL* or LL8 curves exhibit spurious low-resistivity readings not evident on the deep or medium induction readings. The larger the separation, the stronger the fracture intensity, other things being equal. Fig. 13-6 is an example of fracture detection with the DLL*-MSFL log.

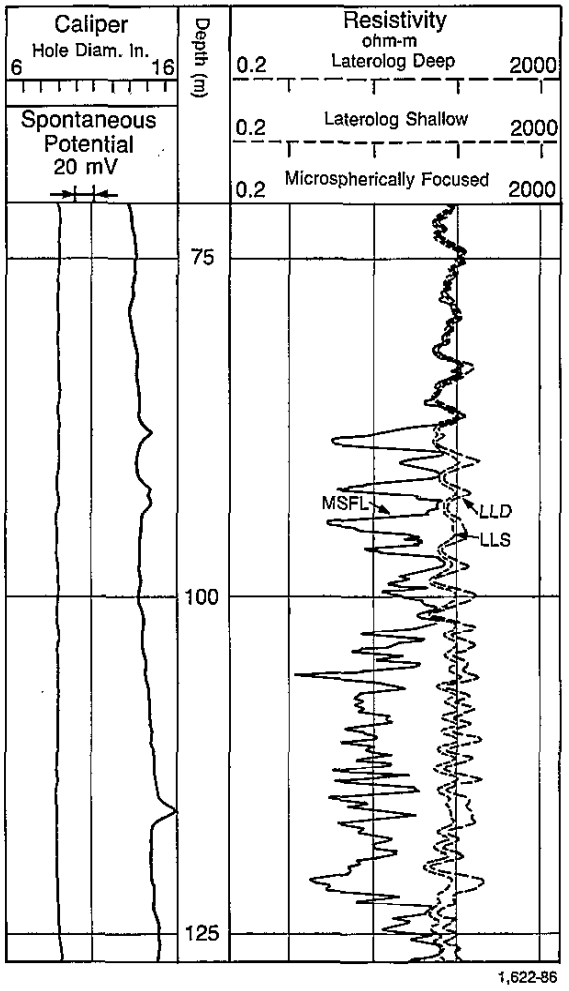

Fig. 13-6—Fracture identification with a DLL-MSFL log.

Photoelectric Absorption Measurements

The photoelectric absorption cross section, P_e, measurement from the Litho-Density* tool (LDT) can be used in heavy barite muds to detect mudcake and fluid loss in zones of low porosity. The photoelectric cross section of barite is 267, as opposed to 4.9 for limestone and 1.85 for sandstone. A mud-filled fracture should, therefore, be readily detectable with a P_e measurement. A high reading of P_e, with good tool-borehole contact established by the $\Delta\rho$ or caliper curve, can be a good indication of fractures.

Dipmeter Measurements

A special presentation of dipmeter microresistivity measurements, called the FIL* fracture identification log, is perhaps one of the simplest and most effective methods for fracture detection. When mud filtrate invades a fracture system, it usually causes a lower dipmeter microresistivity reading from the pad positioned opposite the fracture. A comparison of measurements from adjacent pads (i.e., 90° apart) indicates fractures. If no differences exist, the probability of fractures is low; if large differences exist, the probability is high. Such a difference is evident in Fig. 13-7. Dipmeter Curves 1 and 3 are

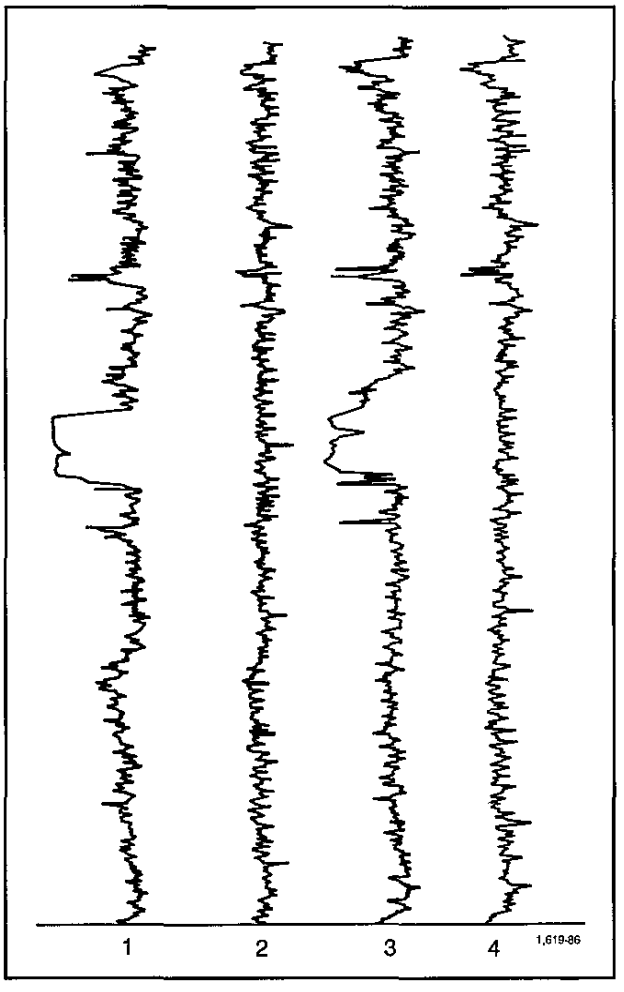

Fig. 13-7—Dipmeter data indicate anisotropy and, perhaps, fractures.

measuring much lower resistivities than are Curves 2 and 4 over a short interval of the example. Overlaying the adjacent pad microresistivity curves, as shown in the FIL log of Fig. 13-8, clearly highlights the probable fractured zone. Another FIL presentation is shown in Fig. 13-1.

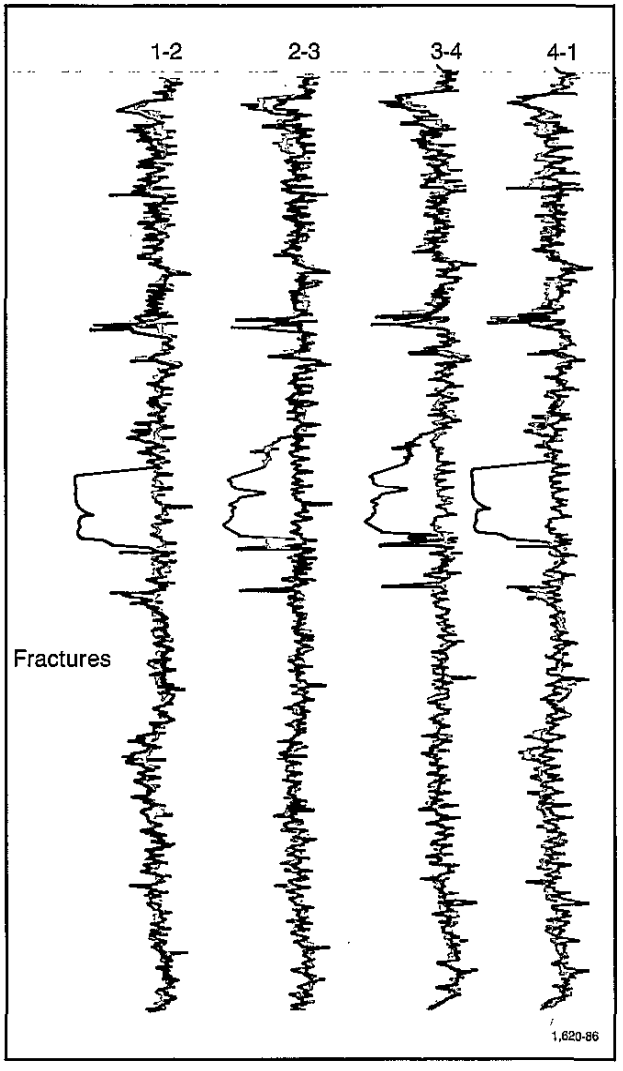

Fig. 13-8—Fracture indications on FIL presentation of dipmeter data in Fig. 13-7.

This method is not perfect since the pads cover only about 40% of the borehole wall surface in an 8-in. borehole. Severely shattered intervals, where all pads may read the same, and thin fractures in steeply dipping formations may not be easily detected by this method.

Fracture detection with the dipmeter and FIL log offers the added advantage of being able to orient the fracture system. By knowing which pads are against the fractures and the orientation of the dipmeter pads with respect to north, fractures can easily be oriented in the subsurface.

The grooves sometimes created in the borehole wall by the action of the bit and drillstring in fractured intervals are sometimes severe enough to restrict, for several feet, the customary rotation of a pad-tool ascent. The inclinometer curves of the dipmeter and Borehole Geometry tools (BGT) are good detectors of this phenomenon. When a dipmeter pad or caliper arm enters one of these grooves the normal tool rotation is modified until the pad leaves the groove; once through the fractured zone the normal tool rotation is reestablished. Note this phenomenon over the fractured intervals of Fig. 13-1.

Borehole Televiewer Tool

The borehole televiewer is an acoustic scanner. As it is pulled up the hole, it scans the borehole wall with a rotating transducer that emits a pulsed ultrasonic beam. A visual representation of the pattern of acoustic reflectivity off the borehole wall is displayed on a cathode-ray tube. The image shows the borehole wall as if it were split vertically and laid flat. Vertical fractures appear as straight lines, while fractures dipping between vertical and horizontal appear as sinusoidal traces.

Initial popularity of the tool waned because of the operational difficulty and environmental limitations. The results are poor in elongated, rugose, or collapsing boreholes; and these conditions are common in fractured intervals. The tool and signal processing have been improved to the point that the service is now regaining some of the lost popularity.

Formation MicroScanner* Tool

One of the most important applications of the Formation MicroScanner (FMS) tool, described in Chapter 12, is the detection of natural fractures. The FMS tool measures electrical conductivity from arrays of button electrodes on two pads 90° apart. It can detect fractures that range from a fraction of a millimeter to several centimeters across. The tool has excellent vertical resolution and can distinguish two fractures as close as 0.4 in. (1 cm). The FMS tool can also distinguish between open and closed fractures. Fig. 13-9 shows the dipping foreset beds in a carbonate grainstone. A steeply dipping series of linear conductive features are also evident. These are open fractures filled by the conductive drilling fluid. The lack of displacement of the bedding surfaces across these fractures indicates they were induced by tensional stress and not by shear stress.

Other Measurements

There are several other methods that sometimes provide insight into possible fractured intervals in specific locales. These include locating radioactive streaks with the gam-

ma ray or NGS* natural gamma ray spectrometry tools, special pulsed-neutron techniques, EPT* log response, temperature, and noise anomalies.

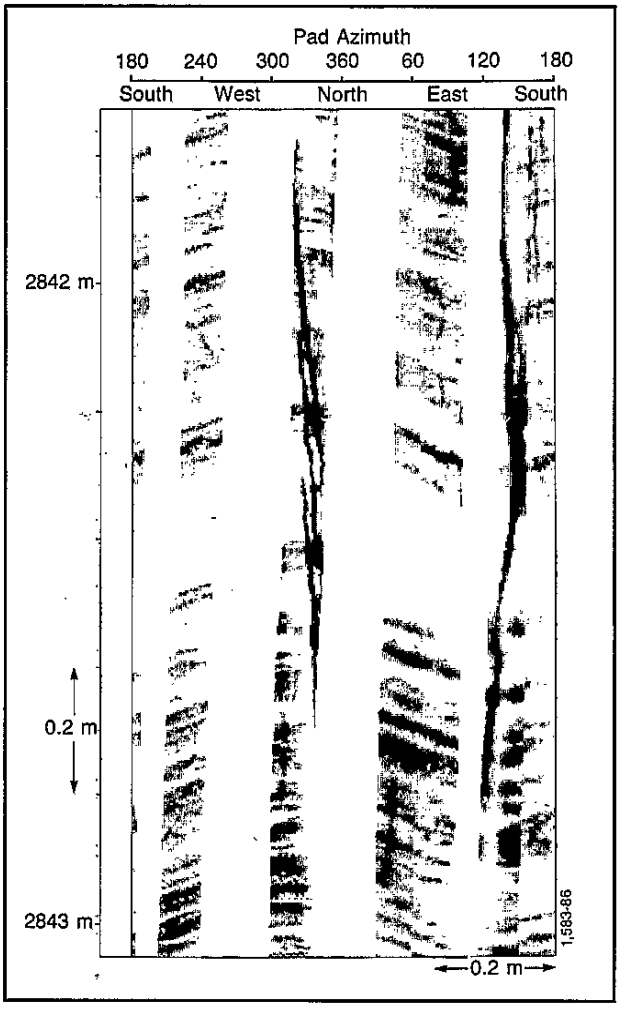

Fig. 13-9—FMS display showing open fractures.

Since fluid-filled fractures can cause anomalous readings on many openhole logs, a fracture probability program[13] was developed to use as many as 16 fracture indicators simultaneously to compute the likelihood of a zone being naturally fractured.

Conclusion

As can be deduced from the preceding explanations, no log, used alone, furnishes unequivocal proof of the presence of fractures. Fracture detection is most certain when several logs or techniques confirm their presence. The combination best adapted to the solution of local fracture identification problems must be defined after some experimentation and study, during which most of the logs offering fracture detection promise should be recorded and carefully analyzed.

ELASTIC CONSTANTS

The mechanical properties derived from testing rock samples in the laboratory, such as the measurement of the strain for a given applied stress, are static elastic constants. Dynamic elastic constants are derived from the measurement of elastic wave velocities in the material. Sonic logging and waveform analysis provide the means for obtaining continuous measurements of compressional and shear velocities. These data, in conjunction with a bulk density measurement, permit the in-situ measurement and calculation of the mechanical properties of the rock. The elastic moduli relationships, in terms of elastic wave velocities (or transit times) and bulk density, are shown in Table 13-1.

The standard practice is to use measured values of compressional travel time (t_c) and shear travel time (t_s). When shear travel time cannot be measured (i.e., in soft formations or poor cement jobs), predictions based on Poisson's Ratio and elastic moduli are not recommended. However, t_s data may be replaced with synthetic shear travel times computed from lithological models, using compressional travel times and bulk density that have been corrected for hydrocarbon effect. It should be noted that even though the hydrocarbon corrections are applied for the lithological model inputs for synthetic t_s computations, hydrocarbon corrections are not made when the raw data are used for the elastic properties computation.

The classic relationships in Table 13-1 do not account for the influence of fluid type on the sonic log responses. Generally this makes little difference in the case of carbonates, which have a large surface area of contact through solution welding or mineralization. Although minimal in low porosity sandstones, the effect should not be ignored, particularly

DYNAMIC ELASTIC PROPERTIES			
ν	Poisson's Ratio	$\frac{\text{Lateral strain}}{\text{Longitudinal strain}}$	$\frac{\frac{1}{2}(t_s/t_c)^2 - 1}{(t_s/t_c)^2 - 1}$
G	Shear Modulus	$\frac{\text{Applied stress}}{\text{Shear strain}}$	$\frac{\varrho_b}{t_s^{\nu}} \times a$
E	Young's Modulus	$\frac{\text{Applied uniaxial stress}}{\text{Normal strain}}$	$2G(1+\nu)$
K_b	Bulk Modulus	$\frac{\text{Hydrostatic pressure}}{\text{Volumetric strain}}$	$\varrho_b\left(\frac{1}{t_c^2} - \frac{4}{3t_s^2}\right) \times a$
C_b	Bulk Compressibility (with porosity)	$\frac{\text{Volumetric deformation}}{\text{Hydrostatic pressure}}$	$\frac{1}{K_b}$
C_r	Rock Compressibility (zero porosity)	$\frac{\text{Change in matrix volume}}{\text{Hydrostatic pressure}}$	$\frac{1}{\varrho_g\left(\frac{1}{t_{ma}^2} - \frac{4}{3t_{sma}^2}\right) \times a}$
α	Biot Elastic Constant	Pore pressure proportionality	$1 - \frac{C_r}{C_b}$

Table 13-1—Dynamic elastic properties.

when the reservoir fluids are highly compressible. An example would be when free gas is present at reservoir conditions.

The effect of fluid can be mathematically modeled. The ratio t_s/t_c, derived from the expressions for bulk modulus and shear modulus, is as follows:

$$t_s/t_c = (4/3 + K/G)^{1/2} . \qquad \text{(Eq. 13-1)}$$

If the rock were fluid-free, i. e., the pores contained a vacuum, K and G would be equal to the dry frame moduli, K_{dry} and G_{dry}. Since in-situ pores do contain a fluid, a stiffening term K_p should be included, so that $K = K_{dry} + K_p$. At low sonic frequencies, G and G_{dry} can be assumed equal. The shear/compressional ratio can then be expressed as:

$$t_s/t_c = \left(4/3 + \frac{K_{dry} + K_p}{G_{dry}}\right)^{1/2}, \qquad \text{(Eq. 13-2)}$$

where K_p (according to both Biot and Gassman theory) is a function of porosity, bulk modulus of both the dry frame and the grains, and the fluid compressibility. Assuming that $G_{dry} = G = \rho_b/t_s^2$, and knowing the parameters required for K_p, the derivation of the dry frame bulk modulus and Poisson's Ratio is straightforward.

INHERENT STRENGTH COMPUTATIONS AND THEIR RELATIONSHIP TO FORMATION COLLAPSE

To determine whether a formation will collapse under normal drawdown conditions it is first necessary to predict the critical wellbore pressure at which a cavity cannot maintain a stable shape. When the wellbore flowing pressure falls below the critical pressure, the failure of the cavity becomes "catastrophic" and results in formation collapse. Several criteria have been introduced that control the collapse phenomenon. The Mohr-Coulomb and extended Griffith failure criterions are by far the most widely applied and are used in the Sand Strength Analysis Program. Recent works by Morita et al have combined tensile failure with shear slippage in formation collapse modeling.

Stresses around a Producing Cavity

The effective principal stresses acting on an element at the surface of a cavity around a producing perforation are σ_r', σ_θ', and σ_ϕ' (Fig. 13-10). Radial stress due to the wellbore pressure is σ_r', while σ_θ' and σ_ϕ' are tangential to the cavity surface. The three principal stresses are orthogonal. The pore pressure at the surface of the cavity is equal to the well pressure, p_w. The total stresses at the cavity surface are:

$$\sigma_r = \sigma_r' + \alpha p_w = p_w \qquad \text{(Eq. 13-3a)}$$

$$\sigma_\theta = \sigma_\theta' + \alpha p_w \qquad \text{(Eq. 13-3b)}$$

$$\sigma_\phi = \sigma_\phi' + \alpha p_w , \qquad \text{(Eq. 13-3c)}$$

where:

$\alpha = 1 - (C_r/C_b)$

C_r = compressibility of rock matrix

C_b = bulk compressibility in psi^{-1}.

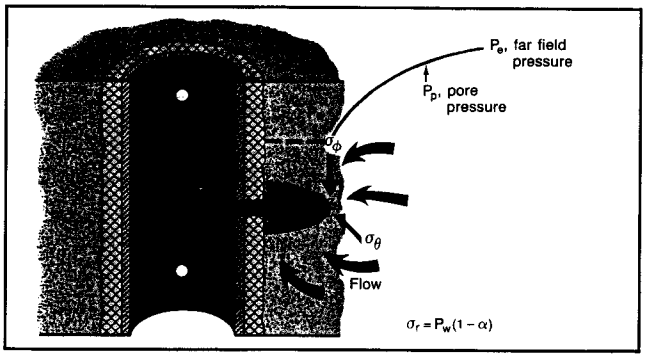

Fig. 13-10—Sanding model diagram.

A radial pore pressure differential ($p_p - p_w$) extends from the surface of the cavity to the far field where the reservoir pressure is p_e.

Far field vertical stress can be assumed to be equal to the overburden:

$$\sigma_z = p_{ob} . \qquad \text{(Eq. 13-4)}$$

The effective vertical stress is, therefore, the overburden minus the effect of pore pressure:

$$\sigma_z' = p_{ob} - \alpha p_p . \qquad \text{(Eq. 13-5)}$$

In the absence of a tectonic component, the minimum horizontal stress can be defined as:

$$\sigma_x = \left(\frac{\nu}{1-\nu}\right)(p_{ob} - \alpha p_p) + \alpha p_p \ , \quad \text{(Eq. 13-6)}$$

or, rearranging,

$$\sigma_x = p_{ob}\left(\frac{\nu}{1-\nu}\right) + \alpha p_p \left(1 - \frac{\nu}{1-\nu}\right) . \quad \text{(Eq. 13-7)}$$

Solution to the "Collapse" Problem

The total hydrostatic stress, $\overline{S}$, is defined as:

$$\overline{S} = \frac{1}{3}[\sigma_z + \sigma_x + \sigma_y] \quad \text{(Eq. 13-8)}$$

assuming horizontal stresses are equal (isotropic), $\sigma_x = \sigma_y$.

Therefore, from Eqs. 13-7 and 13-8:

$$\overline{S} = \frac{1}{3}\left[p_{ob} + 2p_{ob}\left(\frac{\nu}{1-\nu}\right) + 2\alpha p_p \left(\frac{1-2\nu}{1-\nu}\right)\right] \quad \text{(Eq. 13-9)}$$

The conceptual basis for determining formation collapse is founded on the stability of a cavity surrounding a producing perforation. The shape of a producing cavity is at its most stable form when the tangential stresses at the surface of the cavity are equal, i.e., when $\sigma_\theta = \sigma_\phi$. Therefore, the total hydrostatic stress at the cavity surface is:

$$\overline{S} = \frac{1}{3}[\sigma_r + \sigma_\theta + \sigma_\phi] . \quad \text{(Eq. 13-10)}$$

The stresses at the surface of a cavity with $\overline{S}$ applied and p_w in the wellbore are:

$$\sigma_r = p_w ,$$

and from Eq. 13-10,

$$\sigma_\theta = \sigma_\phi = \frac{3}{2}\overline{S} - \frac{1}{2}p_w . \quad \text{(Eq. 13-11)}$$

Tangential stress is reduced by $\Delta\sigma_\theta$ due to the radial pore pressure differential:

$$\sigma_\theta' = \sigma_\theta - \Delta\sigma_\theta - \alpha p_w ,$$

where the superposed tensile stress is:

$$\Delta\sigma_\theta = \alpha(p_p - p_w)\left(1 - \frac{\nu}{1-\nu}\right)$$

$$\sigma_\theta' = \frac{3}{2}\overline{S} - \frac{p_w}{2} - \alpha(p_p - p_w)\left(1 - \frac{\nu}{1-\nu}\right) - \alpha p_w . \quad \text{(Eq. 13-12)}$$

Effective principal stresses on element at surface of stable cavity are:

$$\sigma_\theta' = \frac{3}{2}\overline{S} - p_w\left(\frac{1}{2} + \alpha\right) - \alpha(p_p - p_w)\left(1 - \frac{\nu}{1-\nu}\right) \quad \text{(Eq. 13-13)}$$

when

$$\sigma_\phi' = \sigma_\theta'$$

$$\sigma_r' = p_w(1 - \alpha) . \quad \text{(Eq. 13-14)}$$

Griffith Failure Criterion

The Griffith failure envelope for the element at the surface of the cavity, extended to three dimensions by Murrell (Fig. 13-11) is:

$$(\sigma_\phi' - \sigma_\theta')^2 + (\sigma_\phi' - \sigma_r')^2 + (\sigma_\theta' - \sigma_r')^2 = 24T_o(\sigma_\theta' + \sigma_\theta' + \sigma_r'), \quad \text{(Eq. 13-15)}$$

where T_o = tensile strength.

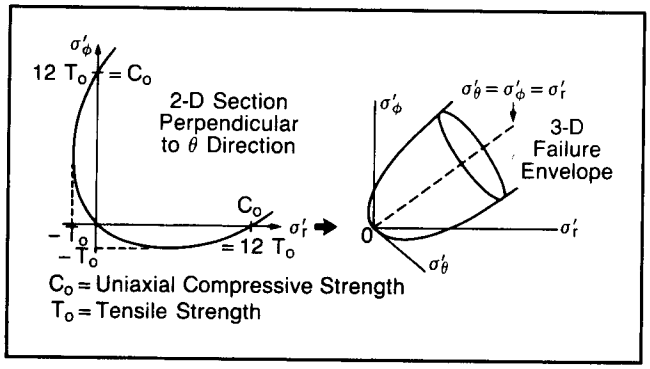

Fig. 13-11—The Griffith Failure Envelope extended to three dimensions by Murrell.

σ_ϕ', σ_θ', and σ_r' are substituted in the Griffith equation to solve for p_w. The value of p_w predicted to produce unstable conditions is designated p_c, the critical wellbore pressure for shear failure.

In Fig. 13-12, the pore pressure is shown on the left of track 1 scaled in psi/ft representing p_p/TVD. Anticipated drawdown is depicted by a band between p_p and the flowing well pressure p_w. Whenever p_w is less than p_c, the area between the curves is shaded to represent zones of potential failure. The interval 2873 to 2977 m is perforated over one of the zones predicted to fail. Sand production from this interval is confirmed by the cavity log recorded with a 2¾-in. density tool. The perforated interval 2887 to 2889 m has also caved. The other weak zones were avoided in the perforation program.

The mathematical properties of the Griffith Failure Criterion in Eq. 13-15 are such that if two out of the three stresses are set to zero, the third stress, being at the critical condition,

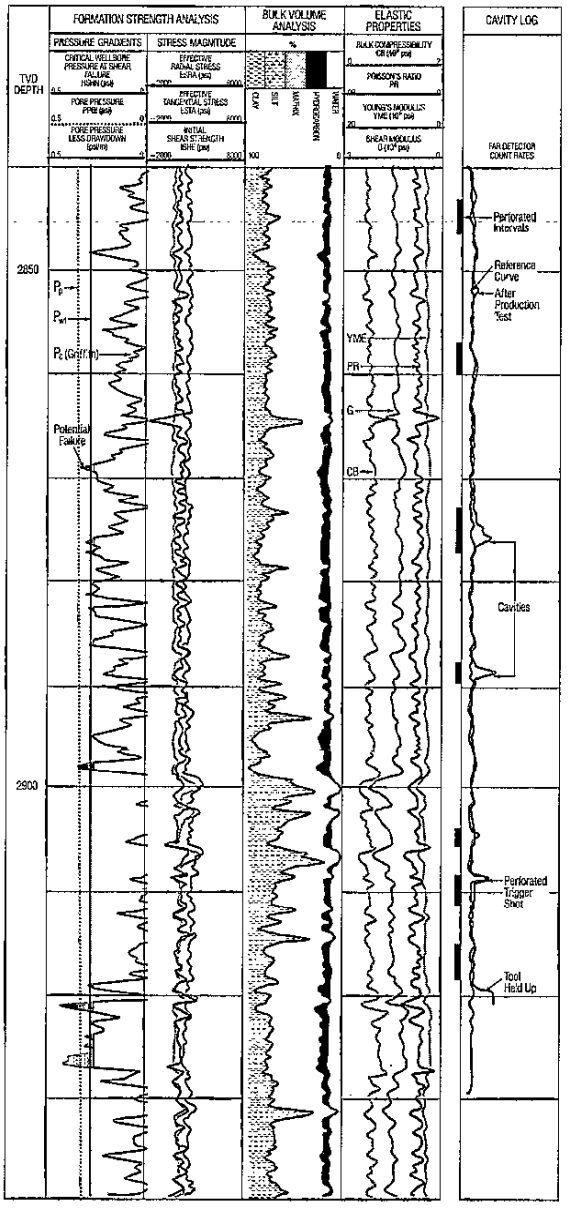

Fig. 13-12—Formation Strength Analysis log.

must be equal to the uniaxial compressive strength, C_o. Thus, $C_o = 12\ T_o$. By knowing C_o, the failure envelope is fully defined.

Mohr-Coulomb Failure Criterion

The Mohr-Coulomb Failure Criterion was used in the Sand Strength Analysis program prior to the introduction of the Griffith Model (Coates and Denoo, 1980 and 1981). Its application to sanding problems has been described in detail by Edwards et al (1983). In general, it differs from the 3-D Griffith Model in that an element on the borehole wall is examined rather than the cavity shape.

σ_x and σ_y are far field total stresses. σ_x is derived as shown in the next section. σ_y is the maximum horizontal stress and is equal to σ_z multiplied by the tectonic unbalance factor, σ_y/σ_x, which will be described later. Only two principal stresses on the element in the borehole wall are noted; effective radial stress, σ_r', and effective tangential stress, σ_θ'.

In the case of a "step" pore pressure profile, effective stresses on the element of borehole wall are:

$$\sigma_r' = p_w - \alpha p_p \qquad \text{(Eq. 13-16)}$$

and

$$\sigma'_\theta = 3\sigma_x - \sigma_y - p_w - \alpha p_p\ . \qquad \text{(Eq. 13-17)}$$

Mohr's Circle is a graphic representation of the variation in shear stress along a plane and the normal stress across the plane, as γ (the angle that the direction of the normal stress makes with the greater principal stress) changes from 0° to 90° (Fig. 13-13). The shear stress is:

$$\tau = \frac{1}{2}(\sigma_\theta' - \sigma_r')sin\ 2\gamma\ . \qquad \text{(Eq. 13-18)}$$

The normal stress is:

$$\sigma_n' = \frac{1}{2}(\sigma_\theta' + \sigma_r') + \frac{1}{2}(\sigma_\theta' - \sigma_r')cos\ 2\gamma \qquad \text{(Eq. 13-19)}$$

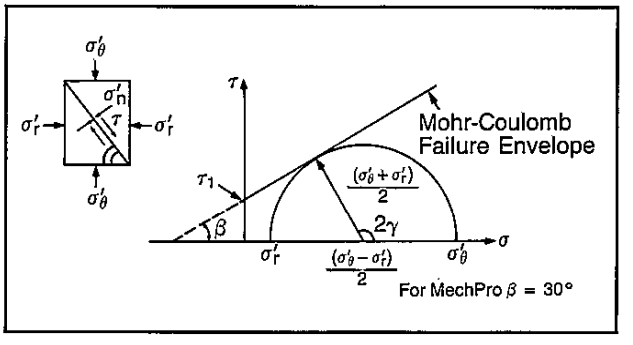

Fig. 13-13—Mohr's circle showing 30-degree failure-envelope line.

The initial shear strength, τ_i, is derived from an empirical model based on Deere and Miller's work (1969) and elaborated by Coates and Denoo (1981):

$$\tau_i = \frac{0.026E}{C_b \times 10^6}\left[0.008V_{clay} + 0.0045(1 - V_{clay})\right]\ , \qquad \text{(Eq. 13-20)}$$

where:

E = Young's Modulus in psi

C_b = bulk compressibility in psi^{-1} and
V_{clay} = the volume of clay.

A formation collapses due to shear failure when the induced shear stress exceeds an amount depicted by the failure envelope. If the Mohr's Circle just intercepts the failure line, the point of contact identifies both the critical shear stress and the angle γ between the normal to the shear plane and the direction of the maximum stress.

The Coulomb failure line is a linear approximation of the Mohr failure envelope. It is depicted as follows:

$$\tau = \tau_i = \sigma \cos \beta \,, \qquad \text{(Eq. 13-21)}$$

where β = angle of friction.

The condition of instability occurs when:

$$\frac{\sigma'_\theta - \sigma'_r}{2} = \left[\tau, \cos \beta - \frac{\sigma'_r - \sigma'_\theta}{2}\right] \sin \beta \quad \text{(Eq. 13-22)}$$

By substituting σ'_θ and σ'_r from Eq. 13-16 and Eq. 13-17 in Eq. 13-22, a solution for p_w is provided.

The model is more representative of producing conditions by allowing for a radial pore pressure gradient from the wellbore to the far field. Critical wellbore pressure, p_c, using the Mohr-Coulomb Criterion becomes:

$$p_c = \frac{1.5\sigma_x - 0.5\sigma_y - 0.5\alpha p_p\left(\frac{1-2\nu}{1-\nu}\right) - 1.732\tau_i}{1 - 0.5\alpha\left(\frac{1-2\nu}{1-\nu}\right)}$$

(Eq. 13-23)

Experience has shown that the results are pessimistic in competent sands, but closely match the Griffith results in unconsolidated formations.

In an example from a chalk reservoir in the North Sea (Fig. 13-14), the well pressure desired by the operator is compared with the critical well pressure estimated to cause failure. Intervals where well pressure is lower than the critical pressure (blue) were considered susceptible to failure.

Producing the well at the desired production rate would cause most of the upper oil-bearing zone to collapse, a catastrophe that had previously occurred in other wells. In this case the weak zones were sealed, zones below them were perforated, and communication was re-established to the producing horizons through hydraulically-induced fractures.

STRESS ANALYSIS IN RELATION TO HYDRAULIC FRACTURING

A known regional overburden gradient can be used in the computation. However, the MechPro program has the capability for integrating openhole density log and pseudodensity data to the surface to obtain the cumulative weight or to extrapolate from density log data along predefined trends (Fig. 13-15).

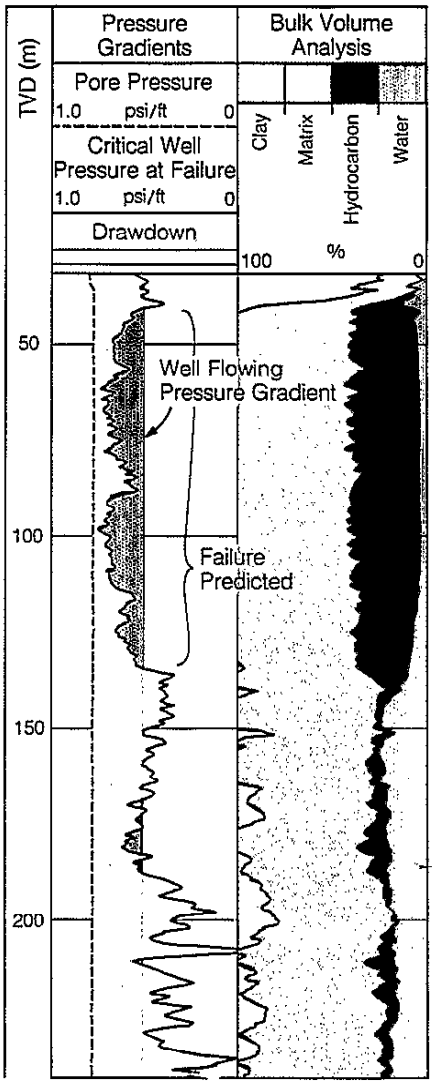

Fig. 13-14—MechPro failure prediction example from a well drilled into a North Sea chalk formation.

The vertical stress, σ_z, is assumed to be equal to the overburden pressure:

$$\sigma_z = p_{ob} \,. \qquad \text{(Eq. 13-24)}$$

The minimum horizontal stress, σ_x, is obtained assuming a horizontally constrained elastic model. Three options are available:

- the classical or Terzaghi equation:

$$\sigma_x = \frac{\nu}{1-\nu}(p_{ob} - p_p) + p_p \,. \quad \text{(Eq. 13-25)}$$

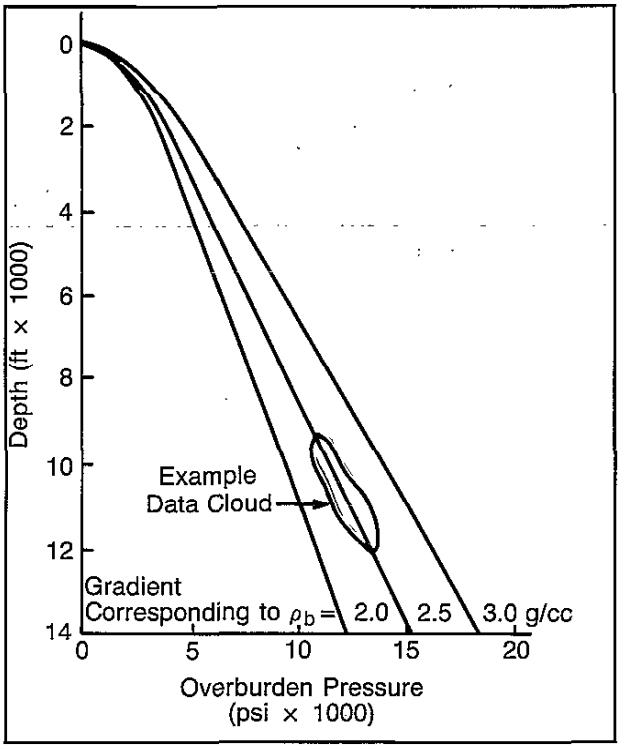

Fig. 13-15—Overburden pressure extrapolation.

- A modified version for anisotropically stressed formations with unidirectional microcracks is currently under investigation. Termed "hard rock", the experimental equation simplifies to:

$$\sigma_x = \frac{\nu}{1-\nu}(p_{ob} - \alpha p_p) + p_p \quad \text{(Eq. 13-26)}$$

- The equation to derive the radial and tangential stress inputs to the Griffith and Mohr-Coulomb Failure Criteria is:

$$\sigma_x = \frac{\nu}{1-\nu}(p_{ob} - \alpha p_p) + \alpha p_p \quad \text{(Eq. 13-27)}$$

All three equations ignore the magnitude of the tectonic stress. For simplicity, the term "tectonic component" is used to represent that part of the horizontal stress which is not due to overburden. In the minimum horizontal stress direction the magnitude is T_x.

The tectonic component can still be present in seismically inactive areas. It is assumed that for a given structure, T_x is constant. The three equations are examined on a plot of the Poisson's Ratio term $\frac{\nu}{1-\nu}$ against minimum horizontal stress (Fig. 13-16). Equations 13-25 and 13-26 intercept the stress axis at the pore pressure, p_p. Equation 13-27 intercepts the stress axis at αp_p, and is, therefore, highly influenced by the ratio of rock grain compressibility to framework compressibility. As C_r/C_b approaches one, α approaches zero.

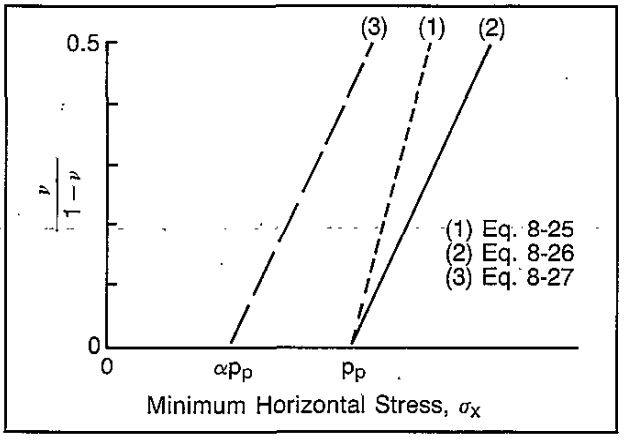

Fig. 13-16—Determination of "tectonic component".

If a tectonic component T_x exists, all three relationships should move an amount equivalent to T_x along the stress axis. The slope is equal to the effective overburden stress, $p_{ob} - \alpha p_p$. In the Terzaghi case α is one.

Calibration with Mini-Frac Data

Analysis of downhole pressure and spinner flow rate during a mini-frac operation can help to determine the minimum horizontal stress. A mini-frac is a series of pumping tests carried out to determine parameters required to plan a hydraulic fracture operation. It is preferably conducted with the same fluid specifications that will be used in the full hydraulic fracture treatment, but without the proppant. The operation consists of:

- pumping at stepped rates and measuring the downhole pressure for fracture initiation, extension, and reopening.
- shut-in by instantaneously switching off the pumps and measuring the falloff in downhole pressure and spinner response.

Several plotting techniques are available to help identify the wellbore pressure which exactly balances the minimum horizontal stress at the point when the fracture closes. This is called the closure pressure (or stress) and is deemed to be equal to the minimum horizontal stress at the fracture interval (Nolte, 1979). A recent innovation by A. Amin (1984) accounts for wellbore storage effects by examining the downhole spinner response following shut-in. This technique is derived from the investigations into "after-flow analysis" by Meunier et al (1983).

The procedure for calibrating the log-derived results is to plot the computed effective minimum horizontal stress against $\frac{\nu}{1-\nu}$. Points representing the effective closure stress obtained from the mini-frac pressure analysis, plotted against the computed $\frac{\nu}{1-\nu}$, should be marked on the same plot.

The calibration technique can be improved by conducting the mini-frac in several intervals with straddle packers. Ideally, the mini-frac tests should be in zones of different Poisson's Ratio to give sufficient range on the crossplot to derive a scaling factor.

The calibration method is illustrated in Fig. 13-17. The most appropriate equation is selected, considering the tectonic nature of the region. The effective closure stress is obtained by subtracting the pore pressure component. For Eq. 13-25 or Eq. 13-26:

$$\sigma_x' = \sigma_x - p_p \,, \qquad \text{(Eq. 13-28)}$$

or for Eq. 13-27:

$$\sigma_x' - \sigma_x - \alpha p_p \,, \qquad \text{(Eq. 13-29)}$$

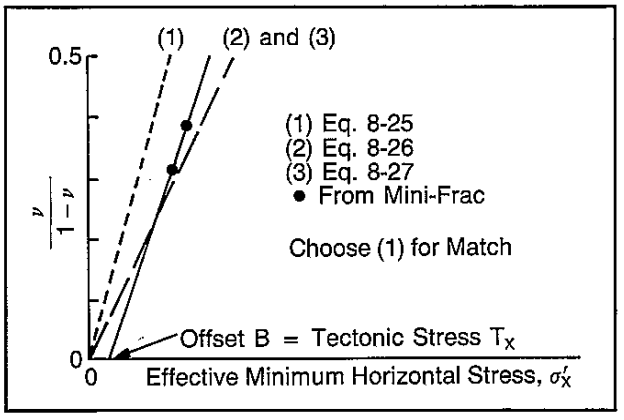

Fig. 13-17—Calibration of closure stress.

a scaling factor A and offset B are selected to obtain the best match with the test data. Calibrated closure stress, σ_x, can now be defined:

$$\sigma_x' \text{ (calibrated)} = A\ \sigma_x' + B \,. \qquad \text{(Eq. 13-30)}$$

For the Terzaghi case:

$$\sigma_x \text{ (calibrated)} = A\ (\sigma_x - p_p) + B + p_p \,. \text{(Eq. 13-31)}$$

The offset B is considered to represent the tectonic component, T_x.

Figure 13-18, from a study by Draxler and Edwards (1984), shows that the minimum computed σ_x value, within the frac test interval, was about equal to the test value, indicating a negligible T_x component.

Fracture Pressure Computations

Fracture initiation pressure, or formation breakdown pressure, p_b, is a function of:

$$p_b = 3\sigma_x - \sigma_y - \alpha p_p + T_o \,, \qquad \text{(Eq. 13-32)}$$

where:

σ_x = minimum horizontal stress
σ_y = maximum horizontal stress
p_p = pore pressure
α = Biot poroelastic constant
T_o = tensile strength.

Models for σ_x computations were shown in the previous section. σ_y is usually defined in terms of the tectonic unbalance factor σ_y/σ_x. This factor is elusive in current oil industry practice, though frequently measured in mining engineering and indirectly obtained in geological and geophysical survey holes. The existence of tectonic unbalance can be inferred from borehole deformation tests or from breakout identification from multiple-diameter caliper logs. Pore pressure is obtained from wireline formation tests or from pressure buildup tests.

Alpha is made unity whenever the Terzaghi or "hard rock" relationship for σ_x is used, simplifying the calculation of fracture initiation to:

$$p_b = 3\sigma_x - \sigma_y - p_p + T_o \,. \qquad \text{(Eq. 13-33)}$$

To compute the fracture reopening pressure, p_{fr}, the tensile strength, T_o, is made zero:

$$p_{fr} = 3\sigma_x - \sigma_y - p_p \,. \qquad \text{(Eq. 13- 34)}$$

In a naturally-fractured zone, an interval selected for hydraulic fracturing would be intersected by many joints. Although individual pieces of rock could possess a high tensile strength, the interval as a whole would have negligible tensile strength. In such a case, the reopening pressure would be the same as the initiation pressure.

After fracture initiation, continual pumping would result in the fracture propagating in a plane parallel to the maximum stress and perpendicular to the minimum stress. Fracture extension pressure is lower than the reopening pressure, but must exceed the minimum horizontal stress. It is a function of the minimum horizontal stress, pump rate, hydraulic fluid characteristics, leakoff due to microfissures, and matrix permeability.

HYDRAULIC FRACTURE GEOMETRY ANALYSIS

Hydraulic stimulation has proven to be a dominant factor in the success of marginal wells in low-permeability, low-porosity, dense rocks. Twenty percent or more of the total well cost can be involved in fracturing; proper treatment design is a must if low-production wells are ever to reach payout. The treatment design is critical. Too small a fracture treatment may result in such inadequate drainage of the reservoir that the well remains unprofitable. Conversely, too large a treatment can be an unnecessary waste of completion funds

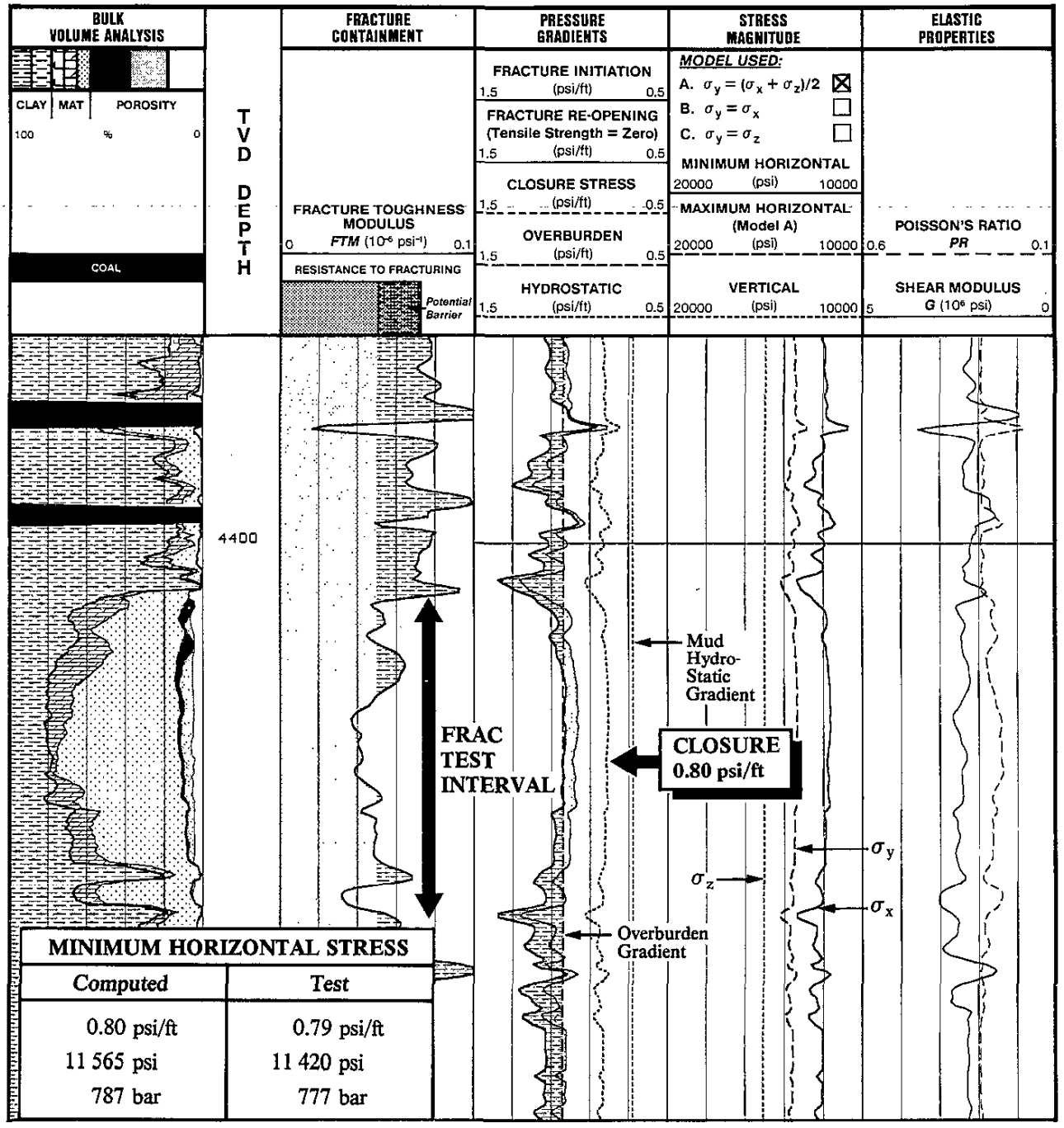

Fig. 13-18—Example showing a negligible T_x component within the frac test interval.

and render the well unprofitable; worse, the fracture may migrate into a nearby aquifer.

Fracture Height

When pressure is increased in the borehole, rupture occurs in the plane that is perpendicular to the direction of least compressive stress (σ_x or σ_y). The pressure required to induce this fracture is called the initial or breakdown pressure. Once a fracture has been initiated, the pressure necessary to hold the fracture open (in the case of a vertical fracture) will be

equal to the minimum total horizontal stress, Ahmed (1988). This stress is often referred to as closure stress. In tectonically relaxed areas, the least principal stress is generally horizontal. Fracturing should therefore occur along vertical planes.

Hydraulic fracture design depends on two sets of variables: the distribution and magnitude of in-situ minimum horizontal stress in the producing and surrounding formations, and the flow behavior of the fracturing fluid. These variables determine:

- the direction and geometry (height, length, and width) of the created fracture,
- whether multiple zones should be fractured one at a time, in groups, or simultaneously,
- design parameters of hydraulic fracturing, such as horsepower, pumping pressure, and proppant transport, and
- the fracturing fluid flow behavior and efficiency.

During a fracturing job, the fracture fluid creates tension. In a vertical fracture, its pressure counteracts the earth's compressive horizontal stress. The fracture grows vertically if the stress-intensity factor, K, top or bottom, exceeds the formation's fracture toughness, K_{Ic}. Predicting vertical propagation therefore depends on calculating the stress-intensity factor at the fracture's vertical extremities.

The crucial variables in this calculation are fracture height, fluid pressure in the fracture, and the magnitude of minimum horizontal stress, which varies with depth, z. Several theorists have proven the fundamental result as follows:

$$K_{top} = \frac{1}{\pi\sqrt{2h}} \int_{-h}^{h} (S_H(z) - p_{wf}) \frac{\sqrt{h - z}}{h + z} dz , \qquad \text{(Eq. 13-35)}$$

and

$$K_{bot} = \frac{1}{\pi\sqrt{2h}} \int_{-h}^{h} (S_H(z) - p_{wf}) \frac{\sqrt{h + z}}{h - z} dz .$$

K_{top} and K_{bot} are the stress-intensity factors at the top and bottom of the fracture. The fracture height, $2h$, is normal to the minimum horizontal stress.

Disregarding friction losses in the fracture, fluid pressure is assumed equal to borehole fluid pressure, p_{wf}. Determining whether a vertical fracture extends is a matter of calculating K_{top} and K_{bot}, and determining where fracture toughness is exceeded, if at all. Each time the fracture extends, stress-intensity factors must be recalculated.

The FracHite* Program

The FracHite program calculates the fracture's vertical extension using the continuous horizontal-stress values from the MechPro program and an approximation to the integrals, which includes the fluid-gravity effects within the created fracture. It does this for a sequence of increasing pumping pressures. The FracHite log also provides a picture of the fracture geometry, assuming a 2-dimensional, wedge-shaped fracture. If more than one zone is being fractured simultaneously, the program calculates the percentage of fracturing fluid that enters each fracture, based on zone thickness and material balance, and provides a picture of each fracture's geometry.

Figure 13-19 shows FracHite log results for an East Texas well with two producing zones. Both zones were fractured simultaneously. The left track shows the expected vertical propagation as fracture pressure increases in 300-psi steps. The middle track depicts the vertical and horizontal extent of each fracture. The right track is a lithologic analysis from openhole logs. According to the program, fracture-initiation pressure in the top zone is 600 psi lower than in the bottom zone. FracHite results predict the consequence of this difference. The top zone opens first and takes most of the fracturing fluid. This is exactly what happened during the fracture job with the fracturing fluid pumped at 900 psi.

To monitor the vertical extent of the fracture, the proppant was tagged with a radioactive marker and gamma ray logs were run before and after the fracture operation. Increased radioactivity, indicating successful fracture initiation, was noted in the vertical intervals predicted by the FracHite log for borehole fluid at 900 psi. Production logs show that only the top zone contributed to production as predicted by the FracHite log. A second FracHite result (Fig. 13-20) shows what would have happened had the zones been fractured independently.

Fracture Propagation Azimuth

In areas where the overburden exceeds the minimum horizontal stress, the hydraulic fracture plane would tend to be vertical and to propagate normal to the minimum stress direction.

The minimum stress direction can be inferred from the breakout orientation (Fig. 13-21). Programs now exist to help in the task of identifying breakouts and their azimuth from multiple-diameter, oriented caliper logs. Fig. 13-22 shows an example of a breakout orientation log computed from a 4-arm dipmeter tool.

In very shallow holes, the least principal stress would likely be the vertical stress. Therefore, fracturing would tend to be horizontal and the fracture pressure would be sufficient to lift the overburden.

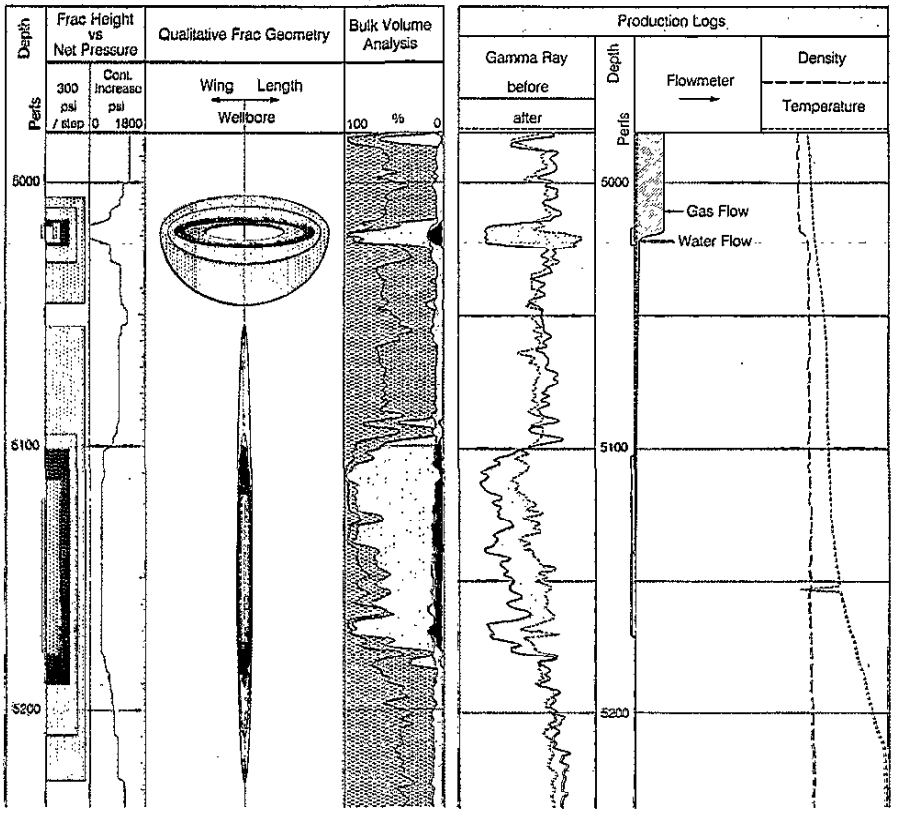

Fig. 13-19—FracHite log and production logs showing the results from fracturing both zones simultaneously.

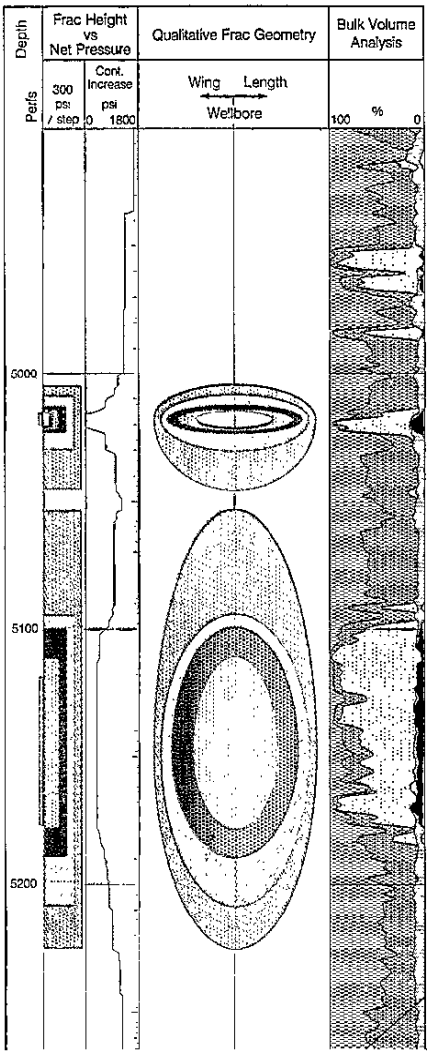

Fig. 13-20—FracHite log predicting results of fracturing each zone separately.

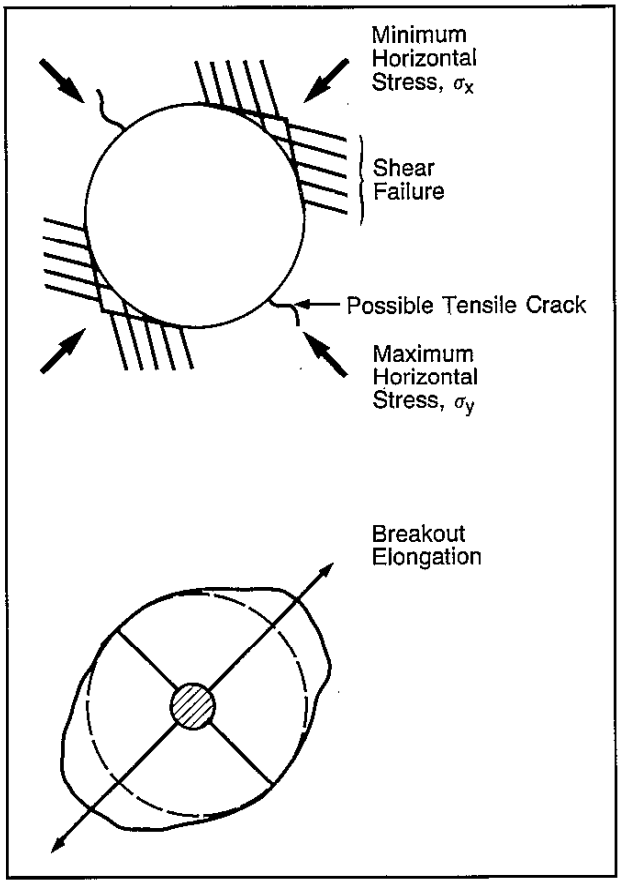

Fig. 13-21—The breakout mechanism in borehole elongation.

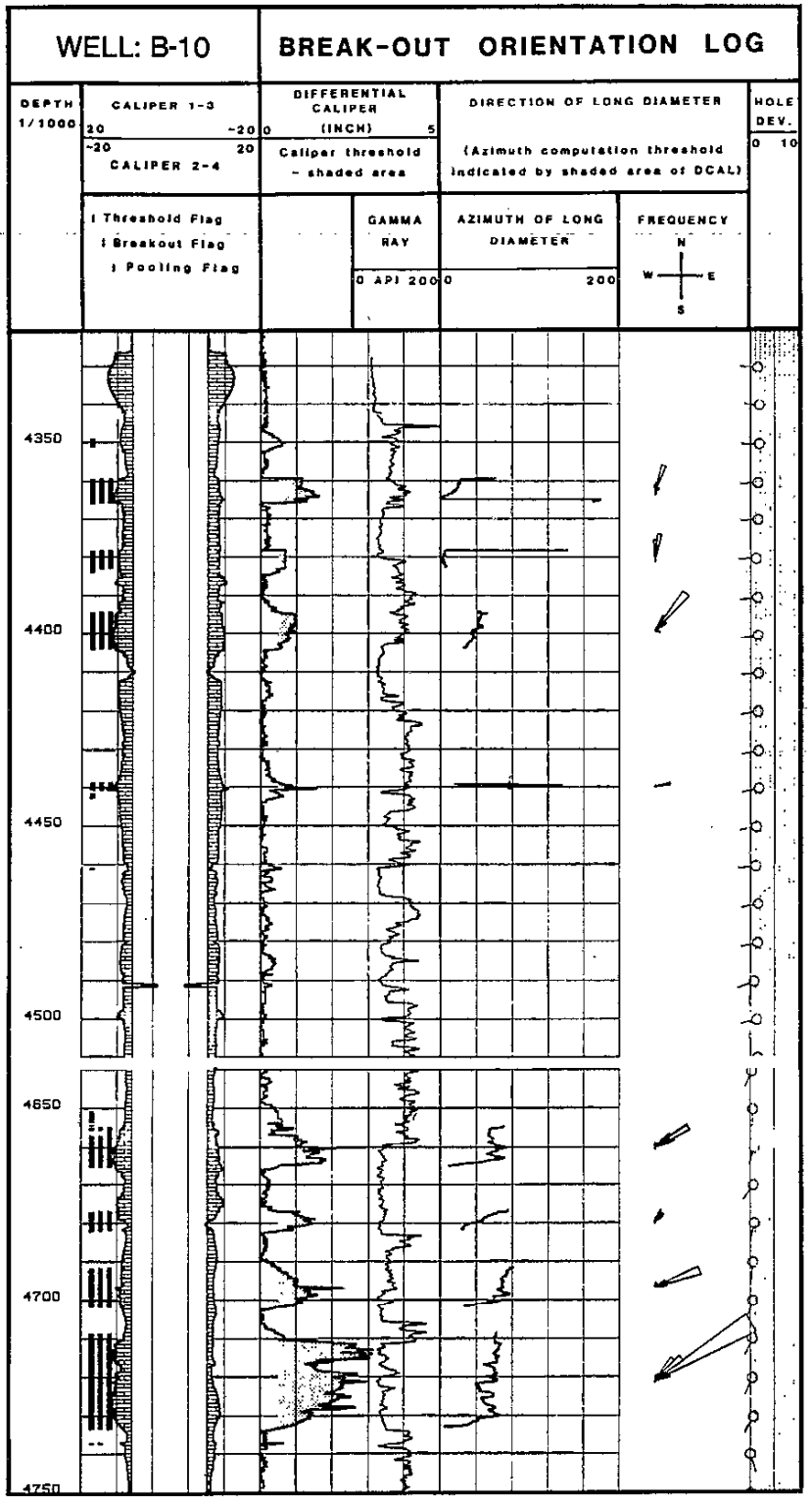

Fig. 13-22—Breakout orientation log computed from a 4-arm dipmeter tool.

REFERENCES

1. Tixier, M.P., Loveless, G.W., Anderson, R.A.: "Estimation of Formation Strength From the Mechanical Properties Log," paper SPE 4532 presented at the 1973 SPE Annual Meeting.
2. Coates, G.R. and Denoo, S.A.: "Mechanical Properties Program Using Borehole Stress Analysis and Mohr's Circle," *Trans.*, 1981 SPWLA Annual Logging Symposium.
3. Hottman, C.E. and Johnson, R.K.: "Estimation of Formation Pressures From Log-Derived Shale Properties," *J. Pet. Tech.* (June 1965).
4. Anderson, R.A.: *A Review of the Elastic Solution for Fracture Pressure*, Amer. Soc. of Mech. Engineers (1976).
5. Anderson, R.A., Ingram, J.S., and Zanier, A.M.: "Fracture Pressure Gradient Determination from Well Logs," paper SPE 4135 presented at the 1972 SPE Annual Meeting.
6. Newberry, B.M., Nelson, R.F., and Ahmed, U.: "Prediction of Vertical Hydraulic Fracture Migration Using Compressional and Shear Wave Slowness," paper SPE/DOE 13895 presented at the 1985 SPE/DOE Low Permeability Gas Reservoirs Symposium.
7. Ahmed, U., Newberry, B.M., and Cannon, D.E.: "Hydraulic Fracture Treatment Design of Wells with Multiple Zones," paper SPE/DOE 13857 presented at the 1985 SPE/DOE 1985 Low Permeability Gas Reservoirs Symposium.
8. Massa, P., Ruhland, M., and Thowvenin, J.: *Structure et fracturation du champ d'Hass: Nessaiyd (Algeria)*, Revuede 1 I.F.P., **XXII** (1972).
9. Beck, J., Schultz, A., and Fitzgerald, D.: "Reservoir Evaluation of Fractured Cretaceous Carbonates in South Texas," *Trans.*, 1977 SPWLA Annual Logging Symposium.
10. Brown, R.O.: "Application of Fracture Identification Logs in the Cretaceous of North Louisiana and Mississippi," *Trans.*, 1978 GCAGS Meeting, **XXIII**.
11. R.A. Anderson, D.P. Edwards, and L. Ormerod: "Log Interpretation Techniques to Evaluate Formation Collapse in the North Sea Chalk," paper presented at the Symposium on North Sea Chalk, May 21-22, 1985, Stavanger, Norway.
12. "Rock Mechanics," *The Technical Review* (October 1986) **34**, No. 3.
13. "Fracture Detection," *The Technical Review* (January 1987) **35**, No. 1.
14. Ahmed, U.: "Fracture Height Prediction," *JPT* (July 1988) 813-815.
15. Anderson, R.A., Edwards, D.P., and Ormerod, L.: "Log Interpretation Techniques to Evaluate Formation Collapse in the North Sea Chalk, paper presented at the Symposium on North Sea Chalk, Stavanger (1985).
16. Morita, N., Whitfill, D.L., Fedde, O.P., and Lovik, T.H.: "Parametric Study of Sand Production Prediction," paper 16990 presented at the 62nd Annual SPE Fall Technical Conference, 1987.